Supramolecular self-assemblies of triarylamines : fundamental studies and applications

Artem Osypenko

UNIVERSITÉ DE STRASBOURG

ÉCOLE DOCTORALE 222

UPR 22

THÈSE

présentée par :

Artem OSYPENKO

soutenue le : **26 septembre 2016**

pour obtenir le grade de : **Docteur de l'université de Strasbourg**
Discipline/ Spécialité : CHIMIE

SUPRAMOLECULAR SELF-ASSEMBLIES OF TRIARYLAMINES: FUNDAMENTAL STUDIES AND APPLICATIONS

THÈSE dirigée par :
M. GIUSEPPONE Nicolas Professeur, Université de Strasbourg, Strasbourg, France

RAPPORTEURS :
M. PRINS Leonard Professeur, Université de Padoue, Padoue, Italie
Mme. ESCUDER Beatriu Professeur, Universitat Jaume I, Castelló, Espagne

---

AUTRES MEMBRES DU JURY :
M. KLYMCHENKO Andrey Docteur, Université de Strasbourg, Strasbourg, France

Artem OSYPENKO

SUPRAMOLECULAR SELF-ASSEMBLIES OF TRIARYLAMINES: FUNDAMENTAL STUDIES AND APPLICATIONS

Résumé

Dans cette thèse, nous avons étudié le mécanisme fondamental du processus d'auto-assemblage thermoréversible des trisamides triarylamines chiraux. Nous avons ensuite étudié les utilisations possibles de dérivés de triarylamine dans différents domaines de recherche liés à la science des matériaux. Premièrement, en utilisant une approche biocatalytique, nous avons réussi à contrôler l'auto-assemblage d'amphiphiles à base de TAA-peptide conjugués dans l'eau. Deuxièmement, de nouveaux dérivés de triarylamine ont été incorporés avec succès en tant que couches conductrices de trous dans des cellules solaires de type pérovskite. Troisièmement, nous avons démontré la possibilité de déclencher électrochimiquement l'auto-assemblage de triarylamines pour la construction anisotrope contrôlée de nanofils conducteurs. Enfin, nous avons développé une technique qui permet l'alignement hautement ordonné de nanoparticules d'or sur une couche de nanofils de triarylamines à l'interface liquide-liquide.

MOTS-CLES : chimie supramoléculaire, auto-assemblage, triarylamine, pérovskite, polymérisation supramoléculaire, auto-assemblages biocatalytiques, alignement anisotrope, chiralité supramoléculaire

Résumé en anglais

In this thesis, we have explored the fundamental mechanism of the thermally initiated self-assembly process of chiral triarylamine trisamides. The results demonstrate a cooperative nucleation and growth mechanism with well-defined thermal hysteresis and memory effect. We have then studied the possible implementation of triarylamine derivatives in various fields of materials science. First, by taking advantage of a biocatalytic approach, we managed to control the self-assembly of TAA-peptide amphiphiles in water. Second, new triarylamine derivatives were successfully inserted as hole transporting layers in perovskite solar cells. Third, the self-assembly of triarylamines was triggered electrochemically, leading to an anisotropic construction of conducting nanowires. Finally, we developed a technique that allows for the highly ordered alignment of gold nanoparticles over a layer of triarylamine nanowires at the liquid-liquid interface by simple centrifugation of a biphasic mixture.

KEYWORDS: supramolecular chemistry, self-assembly, triarylamine, perovskite, supramolecular polymerization, biocatalytic self-assembly, anisotropic alignment, supramolecular chirality

This work has been carried out in the SAMS research group in the Institute Charles Sadron CNRS, the University of Strasbourg under the supervision of Prof. N. Giuseppone and has received funding from the European Commission's Seventh Framework Program (FP7-PEOPLE-2011-ITN) under the grant agreement n^{o} 289723.

I would firstly like to give my sincerest thanks to my PhD supervisor Professor Nicolas Giuseppone, for giving me this fantastic opportunity to be a part of his diligent and hard-working research group during last four years. I am grateful for the interesting projects that I have been involved in and for the freedom granted to me to develop them in my artistic and disorganised manner. I have deeply appreciated his enduring patience and kind support, particularly during the past months,.

I express my gratitude to Prof. Beatriu Escuder from the Jaume I University, Prof. Leonard Prins from the University of Padova and Dr. Andrey Klymchenko from the University of Strasbourg for examinating my work and I appreciate them consecrating time.

I owe thanks to Dr. Emilie Moulin for her enormous effort to decrease the level of my entropy in general. Her help and advice during the writing of this manuscript in particular were at all times constructive and suitable for the progress. In many aspects, her perseverance and thoroughness should be taken as an example to follow.

I thank Dr. Cristina Misuraca, my dear "microchief", with whom I started the work in the group and whose Zen, warmth and wisdom have always fascinated me.

I thank Dr. Gad Fuks for the extravagant discussions on various topics and for his advice and help concerning the teaching of chemistry and, of course, for his help in elucidating the structure of my assemblies. I wish to thank Prof. Maaloum for the real AFM "magic" that he does and to Dr. Eric Busseron and Dr. Yves Ruff for their experience and advice which they shared with me in chemistry and also on general matters. I would like to acknowledge our dear Odile, Julie and Mélodie for their constant friendliness and care towards us.

It was an honour for me to work on common projects with such amazing scientists as Tom Ellis and Joe Armao. A big thanks, guys for your great ideas and scientific atmosphere.

I thank all my labmates: Eric, Valentina, Adrian, Quan, Yunjie, Justin, Qing, Ting, Jean-Rémy, Junjun, Manick, Thomas, Yuya, Damien, Joachim and even Stefano for the fun time which we have spent together while doing all kinds of things: singing, traveling, climbing, partying, playing Mahjong, learning Chinese, discussing Japanese shows or watching strange YouTube videos and doing chemistry of course. I would like to express my gratitude for Susanne and Antoine's vivid nature, curiosity and support, especially during the time of writing. « Un pour tous, tous pour un! »

I greatly thank Cris Rețe, Simon McKie and Dr. Daniel Funeriu for being on the same wave with me and for the pleasure they gave me to talk to them about anything. You are the best!

The stay here would not have been so marvelous without Artem K., Iuliia "Kurochka" K., Anna "Kurochka" D., Olga S., Natallia Sh., Marek T. and Anna M. and, of course,

amazing Dr. Michel Rawiso. I would also like to thank Laure Biniek and Morgane Diebold for their friendliness and helpfulness.

I also thank the former and current director of the ICS, Prof. Jean-Michel Guenet and Prof. Christian Gauthier respectively, for accepting me and my project. I also want to thank the administrative staff: Virginie Oberlé, Lea Koch, Magali Meyer, Paule Vannson and Odile Lemblé together with Jean-Marc Chauvelot for their administrative support.

As a part of Marie Curie network, I had the opportunity to meet and collaborate with great people from all over the world. I would like to thank my friends from ReAd: Elena, Giulia, Ivica, Yousef, Julia, Rakesh, Sergio, Leonardo, Ziya and Elnaz for the amazing time we have spent together during our meetings. I hope our paths will cross again! I show my appreciation to Prof. R.V. Ulijn and Prof. K. Severin for the opportunity to work for some time as a part of their research teams during my internships. I would also like to thank all the members of Ulijn and Severin groups for their hospitality, hearty welcome and openness which made my stay extremely joyful and comfortable. Especially I would like to acknowledge Dr. S.K.M. Nalluri, Dr. Y. Abul-Haija and Léonard Eymann for introducing their projects to me and for the interesting discussions which broadened my knowledge in these fields. I express my gratitude to Prof. Grätzel from École polytechnique fédérale de Lausanne for his willingness to collaborate and especially to Dr. Paul Gratia who performed the experiments.

Different people helped me to make this manuscript look nice and I would like to acknowledge them again: first of all Emilie, but also Simon, Susanne and Cris. I thank Junjun for “saving” me technically in the last days of the intense work.

I would like to thank all my friends outside of the institute for all the moments we had together: Sergii, Ihor & Alina, Yura, Nico, Jerome & Valia, Nina, Olia, Vika P., Nastia, Ania Z., Myshka, Vika M., Oleksii D., Bohdan, Sasha G., Mariana & Sergei, Iuliia, Marian, Nataliia G., Lesia, Ira, Katia, Vasyl, Eugen Sh., Olezhko & Juliia, Anna Zh., Anais, Meghna, Raimonda, Thomas, Mathias, Marion, Sylvain and Eric. Especially to ID&AS, SK, OD, AD for feeding me. And again ID for having the courage to listen to my crazy ideas.

I would like to acknowledge a few people who are far from Strasbourg, but who have always been around: S. Shevchuk, A. “Pigallizza”, Zhekach, 4zhen, Aliosha P., Clema, Vova & Vika, S. Denysenko., Nastya & Nataliia Makhotkina, Vika D., 4uk, Andrii B., Zoya Voitenko, Olga Berezan and Svitlana Litkovets.

With all my gratitude to OK and DT for being with me and being the part of me.

And finally (but I will tell them to read from the end) I thank my family, my parents and my bro Stas, for their support over all these years. Ваша підтримка і ваша віра в мене завжди були дуже важливими, адже легко іти вперед відкривати нові горизонти коли знаєш, що є місце, де на тебе завжди чекають, незалежно від того, ким ти став і чи є в тебе титули.

TABLE OF CONTENT

ABSTRACT

Triarylamine molecules are among the best hole transporting materials used in organic electronics. For two decades, they have demonstrated impressive physical properties in a variety of devices such as organic light-emitting diodes, field effect transistors, in xerography (Xerox® process), and for nonlinear optic materials. Recently, our group discovered that triarylamine molecules, when substituted with amide groups, can self-assemble to produce a variety of supramolecular polymers. Further studies of this new type of supramolecular building block revealed its outstanding performance as soft conducting and plasmonic organic materials.

In this thesis, we have first explored the fundamental mechanism of the thermally initiated self-assembly process of chiral triarylamine trisamides. The results obtained demonstrate a cooperative nucleation and growth mechanism with well-defined thermal hysteresis and memory effect. We have then studied the possible implementation of triarylamine derivatives in various fields of research related to materials science. First, by taking advantage of a biocatalytic approach, we managed to control the self-assembly of TAA-peptide amphiphiles in water. This method led to the formation of supramolecular hydrogels, which were proved to be inaccessible using conventional synthetic techniques. Second, new photoactive triarylamine derivatives were successfully inserted as hole transporting layers in perovskite solar cells, reaching solar cell performances as high as 7.5%. Third, we demonstrated the possibility to electrochemically trigger the self-assembly of triarylamines for the controlled anisotropic construction of conducting nanowires between electrodes at the micrometric scale. Finally, we developed a technique that allows for the highly ordered alignment of gold nanoparticles over a layer of triarylamine nanowires at the liquid-liquid interface by simple centrifugation of a biphasic mixture.

Overall, this work produces knowledge for a better understanding of structure-properties relationship in triarylamine-based supramolecular polymers, and it further highlights their interest for applications in various fields of materials science.

RÉSUMÉ EN FRANÇAIS

Le premier objectif de ce travail était d'étudier le mécanisme de polymérisation supramoléculaire des triarylamines (TAAs) chirales et d'étudier l'influence du biais chiral sur la chiralité supramoléculaire de ses auto-assemblées. Lorsque les triarylamines étaient décorées avec les groupements contenants des centres stéréogènes, notre hypothèse était qu'elles s'auto-assemblent en hélices avec une chiralité préférentielle. En outre, à cause de la chiralité hélicoïdale présente dans les molécules de triarylamine, la combinaison de ces deux niveaux d'asymétrie pourrait aboutir à un phénomène d'amplification de chiralité intéressant et à un niveau de complexité plus élevé pour contrôler le processus d'assemblage.

Notre second objectif était d'explorer une nouvelle méthode pour la construction de systèmes originaux hautement organisés à base de TAAs. Pour cela, nous avons planifié en collaboration avec le groupe de Prof. R.V. Ulijn de développer un processus d'auto-assemblage initié par une action enzymatique sur un précurseur non-assemblé. Dans ce cas, une enzyme appropriée pourrait catalyser la transformation chimique d'un conjugué TAA-peptide menant à la formation d'auto-assemblages *in situ* qui ne pourraient pas être obtenus par la voie purement chimique.

Notre troisième objectif était de tester le potentiel des polymères supramoléculaires de TAAs comme matériaux de transport des trous dans les cellules solaires de type pérovskite. Les structures moléculaires des TAAs ont été conçues pour qu'elles correspondent au niveau énergétique de la pérovskite tout en conservant leurs habilités à s'auto-assembler.

Notre quatrième objectif visait à l'auto-assemblage contrôlé de TAAs entre des microélectrodes commerciales, qui possèdent des géométries différentes. Pour cela, une étude profonde des propriétés électrochimiques des TAAs et de leurs auto-assemblages a été envisagée, dans le but ultime de déclencher la polymérisation supramoléculaire initiée uniquement par le potentiel électrique.

Enfin, une dernière étude a été orientée vers la possibilité d'utiliser cette famille de polymères supramoléculaires en tant que matrices nématiques. En particulier, nous avons étudié la formation de films interfaciaux formés à une interface liquide-liquide dans laquelle un auto-assemblage hautement anisotrope de fibres de TAAs et de nanoparticules d'or peut être obtenu, conduisant à la formation de guides d'ondes plasmoniques.

Ce travail touche donc de nombreux domaines, allant de la chimie supramoléculaire et des polymères en général à l'électronique organique et plasmonique. Le manuscrit est donc

organisé en commençant par une introduction générale sur les polymères supramoléculaires et la chimie de triarylamines (*Chapitre I*), tandis que chaque chapitre décrivant les résultats sera précédé par une introduction plus spécifique sur le sujet particulier décrit.

De manière générale, la chimie supramoléculaire étudie des processus parfois très complexes, dont les attributs caractéristiques sont influencés par les interactions non-covalentes. En outre, elle est utilisée pour tenter de répondre à des questions fondamentales, telles que l'apparition de l'ordre à partir du désordre, comment la vie a-t-elle émergé et évolué... Au cours des dernières décennies, la chimie supramoléculaire a aussi été utilisée comme un outil dans les domaines de la science des matériaux, des nanosciences et nanotechnologies tels que l'électronique, les machines moléculaires, l'énergie verte ou la catalyse. L'approche « bottom-up » supramoléculaire est très utile pour la conception de nouveaux objets et systèmes possédant des propriétés nouvelles dues à la nature non-covalente des auto-assemblages (réponse à un stimulus, propriétés d'autoréparation...).

En 2010, notre équipe a mis en évidence un phénomène très intéressant d'auto-assemblage des dérivés triarylamines, modifiées avec des groupements amides. Le mécanisme de ce processus, initié par un stimulus lumineux dans les solvants chlorés, est très complexe, mais l'étape clé est la formation d'une quantité catalytique de radicaux-cations qui initie la formation de structures supramoléculaires présentant des propriétés électroniques particulières. En effet, des études sur des dispositifs d'électrodes séparées de 80 nm ont mis en évidence le caractère métallique des fils supramoléculaires et la conductivité supérieur à 5×10^3 S m^{-1}.

À partir de ces résultats, une $2^{ème}$ génération de TAAs possédant trois groupements amides décorés avec différentes chaines alkyles : les triarylamines tris-amide (TATAs) a été développée. Notre équipe a montré que grâce aux liaisons hydrogènes et aux interactions-π, les TATAs s'auto-assemblent dans le chloroforme en longues fibres hélicoïdales, même sans irradiation lumineuse. Quand les fibres préassemblées sont exposées à la lumière, l'apparition d'une bande de transfert de charge dans la région proche infra-rouge est observée ainsi que la diminution du nombre de défauts structurels dans les structures assemblées. D'autres études sur ce nouveau type de « building blocks » supramoléculaires ont révélé des propriétés remarquables, notamment en termes de la conductivité électronique et plasmonique.

Depuis notre première publication dans le domaine de chimie de TAA auto-assemblées en 2010, plusieurs travaux fondamentaux liés à leur mécanisme de polymérisation supramoléculaire, ainsi que leurs propriétés fonctionnelles uniques et leurs applications sont apparus dans la littérature.

En particulier, l'objectif de cette thèse était d'explorer et de mieux comprendre les relations entre la structure moléculaire, la structure supramoléculaire des assemblées à base de triarylamine et leurs propriétés physiques, menant enfin vers leur implémentation en tant que matériaux fonctionnels.

La plupart des études sur les auto-assemblés de TAA/TATA ont été effectuées dans des solvants chlorés. Cependant, grâce à ces études nous savons que les molécules TATA peuvent produire de longues fibres hélicoïdales sans irradiation lumineuse. Nous nous sommes ensuite intéressés à l'étude du mécanisme d'auto-assemblage de TATAs dans des solvants non halogénés. Ici, notre intérêt portait sur deux aspects: (***a***) la thermodynamique et la cinétique du processus d'auto-assemblage et (***b***) les propriétés chirales de ce processus. Dans cette direction, un ensemble de molécules TATA chirales et achirales a été synthétisé en quelques étapes avec des rendements élevés et leur auto-assemblage a été étudié (**Figure A**). La présence de substituants alkyles chiraux près du noyau de TAA a été utilisée pour étudier le mécanisme d'auto-assemblage de ces dérivés dans divers solvants, en utilisant le modèle de nucléation-croissance coopérative, initialement développé par Oosava et Kasai (1962), et ensuite adapté pour le processus de polymérisation supramoléculaire par Van der Schoot (2005).

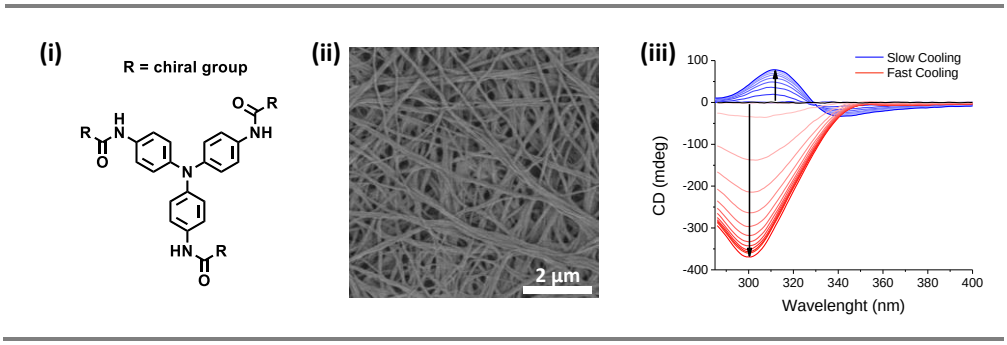

Figure A | (i) Structure de TATAs décorées avec des substituants alkyles ; **(ii)** Image de microscopie électronique à balayage de l'auto-assemblage de TATA dans le toluène; **(iii)** Spectres de dichroïsme circulaire obtenus pour une solution de TATA à 0,5 mM dans le toluène pour différents régimes de refroidissement: refroidissement lent (1 K/min, lignes bleues); refroidissement rapide (10 K/min, lignes rouges).

Nous avons mis en évidence que ces molécules s'auto-assemblent dans des solvants non chlorés, tels que le toluène, en longues structures fibrillaires (**Figure A(ii)**). Les TATAs forment des organogels thermoréversibles à de très faibles concentrations dans différents solvants organiques (OGC (*Onset Gelation Concentration*) : 0,1% en masse ou 0,75 mM dans le toluène). La structure de ces auto-assemblages a été étudiée par microscopie optique et

électronique à transmission et à balayage (MET et MEB). La formation de très longues fibres (plusieurs centaines de micromètres) a été observée dans les deux régimes de concentration – en-dessous et au-dessus de la OGC.

Nous avons ensuite étudié l'auto-assemblage des TATAs dans le toluène à différentes concentrations par spectroscopie UV-Vis à température variable. Les courbes non-sigmoïdales observées ont été modélisées avec deux modèles – isodesmique et coopératif. Les données obtenues suggèrent que la polymérisation supramoléculaire de TATAs se produit par un mécanisme coopératif de nucléation-croissance. De plus, la présence d'une hystérèse thermique entre le processus d'assemblage et de désassemblage a été observée, indiquant l'existence d'une barrière cinétique pendant le processus d'agrégation, qui est liée à une forme particulière hélicoïdale (« propeller-like structure ») des molécules TATA, avec deux composantes possibles: (***a***) entropique (pourrait être majeure), liée à la rotation intramoléculaire et (***b***) conformationnelle, liée à l'incompatibilité hétérochirale des conformères Δ et Λ, qui ne peuvent pas former un dimère. Les paramètres thermodynamiques, extraits lors de l'ajustement des données expérimentales, sont en accord avec des valeurs reportées pour des systèmes à trois liaisons hydrogènes similaires.

Différentes voies d'auto-assemblage ont été observées en utilisant la spectroscopie de dichroïsme circulaire (CD) en fonction de la vitesse de refroidissement (**Figure A(iii)**). L'analyse cinétique des courbes de fusion ainsi que l'imagerie AFM suggèrent que la différence de chiralité est liée à la formation de structures d'ordres supérieurs, qui se forment facilement lors d'un refroidissement lent. Durant le processus de refroidissement rapide, à des concentrations plus élevées, les fibres ont tendance à s'agréger également, mais en raison des déviations rapides en température, le degré d'enchevêtrement est beaucoup plus faible. Ce type de réglage fin de l'auto-assemblage peut être important pour changer les propriétés de ces matériaux, tant d'un point de vue application que d'un point de vue recherche fondamentale.

Le contrôle de la structure des auto-assemblages est un point très important pour maitriser le transfert de charges intermoléculaire. Ce genre de structure est extrêmement utile dans la nature, par exemple au sein de systèmes photosynthétiques, où les antennes et les capteurs de photons sont situées parallèlement l'une par rapport à l'autre, afin d'assurer le transfert d'énergie sans perte vers le centre réactionnel. L'histoire de la science comporte de nombreux exemples de chimistes qui, inspirés par la nature, ont essayé de développer des structures bien organisées à l'aide de molécules biologiques : protéines, ADN/ARN, peptides,

acides-aminés, etc. Précédemment nous avons vu que l'arrangement colonnaire des unités de triarylamine dans les nanofibres, obtenues par l'introduction des groupements amides autour du noyau de TAA, est crucial à leurs propriétés conductrices exceptionnelles. Il a été démontré que de telles fibres supramoléculaires peuvent être utilisées pour différentes applications telles que des cristaux liquides, des guides d'ondes organiques, des interconnexions plasmiques ou des technologies de spintronique. Dans notre groupe, nous sommes également intéressés à explorer d'autres approches supramoléculaires afin de contrôler l'arrangement des fonctions de triarylamines à l'intérieur des auto-assemblages.

Lors de la recherche de motifs structurants, la nature est une source d'inspiration abondante, car elle utilise des éléments de construction simples, tels que les acides aminés, les glucides, les lipides et les nucléotides pour construire des objets de haute complexité. Au cours des dernières décennies, une approche « bottom-up » a été appliquée avec succès par les chimistes supramoléculaires pour obtenir de nouveaux matériaux fonctionnels dans tous les domaines de la nanoscience, des applications biomédicales jusqu'à l'électrochimie de matière molle. L'une de ces stratégies hiérarchiques est axée sur l'utilisation de différentes molécules bioconjuguées constituées de parties fonctionnelles et de peptides auto-assemblés, qui sont responsables de la structuration contrôlée de la partie fonctionnelle. Ces dernières années, cette approche a abouti à la construction de différents systèmes supramoléculaires à base de conjugués peptidiques comprenant les motifs du ferrocène, des azobenzènes, du tetrathiafulvalene, du naphtalène ou du pyrène et présentant des propriétés électroniques intéressantes. De plus, l'utilisation de biomolécules ayant des fonctions spécifiques, telles que les enzymes, elles peuvent être utilisées pour produire des nanostructures, qui ne sont pas accessibles par des techniques conventionnelles. Récemment, une telle approche biocatalytique a été utilisée par le groupe d'Ulijn qui a obtenu un hydrogel à base de conjugué naphtalène diimide-peptide avec des propriétés optoélectroniques intéressantes.

Inspirés par ces résultats, nous étions curieux de savoir si cette approche pourrait être utilisée pour organiser les TAAs conducteurs. Dans le *chapitre III*, nous avons rapporté la synthèse et l'étude des propriétés supramoléculaires des triarylamines décorées avec des résidus d'acides aminés et de peptides à l'état natif et en présence d'enzymes différentes.

L'étude sur l'auto-assemblage biocatalytique a été réalisée en collaboration avec le groupe du Prof. R.V. Ulijn. Les expériences ont été en partie conduites à l'Université de Strathclyde au Royaume-Uni, conjointement avec le Dr S.K.M. Nalluri dans le cadre du programme de mobilité de l'action Marie Curie ITN ReAd.

Un ensemble de précurseurs « building blocks » à base de triarylamine (les conjugués TAA avec acides aminés et peptides) a été synthétisé pour produire des assemblages à l'aide de différentes enzymes. Deux types de molécules ont été conçus avec le noyau TAA comme unité aromatique d'APA: le premier type, avec une branche peptidique et deux groupes methoxy autour du noyau TAA. Le second type est décoré de deux branches peptidiques et possède un groupe amide. Bien que le premier type de peptides amphiphiles aromatiques (avec d'autres fragments aromatiques) a été décrit plusieurs fois, le deuxième type, avec deux branches d'acide aminés/peptides reliées à un noyau hydrophobe, n'a jamais été reporté à notre connaissance.

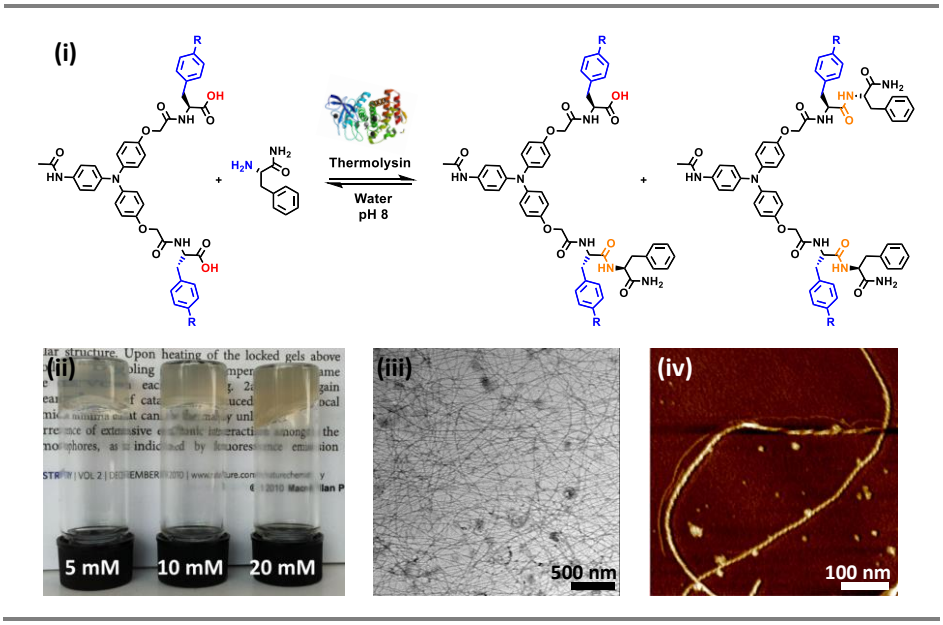

Figure B | (i) Structure des TAAs bio-conjuguées synthétisées : R – Phe ou Tyr, X – –OH ou –NH_2 et schéma de réaction enzymatique; **(ii)** Hydrogels obtenus *via* l'auto-assemblage biocatalytique ; **(iii)** Image MET de fils supramoléculaires obtenus à partir de la TAA modifiée avec la phénylalanine.

Nous avons ensuite étudié le processus de formation des structures supramoléculaires biocatalysées à l'aide de thermolysine – une protéase contenant du Zn(II). En milieu biologique, cette enzyme catalyse l'hydrolyse de la liaison peptidique, mais si la structure de l'agrégat est énergétiquement plus favorable, elle peut aussi catalyser la formation de liaison peptidique entre des acides aminés correspondants.

Après 24h de réaction enzymatique, des hydrogels ont été obtenus pour toutes les molécules (**Figure B(ii)**). La structure microscopique de ces gels a été étudiée par la microscopie électronique à transmission (**Figure B(iii)**) ainsi que par la microscopie à force atomique (**Figure B(iv)**). Il a été démontré que ces gels sont constitués des fibres supramoléculaires, dont le composant majoritaire est le dipeptide, synthétisé

enzymatiquement *in situ* par la bio-conjugaison de la TAA et de l'acide aminé présent dans le milieu.

Il est intéressant de noter qu'il est impossible de former des structures supramoléculaires issues des dipeptides obtenus directement par voie classique de synthèse car ces composés ne sont pas solubles dans le milieu aqueux.

Pour conclure, dans ce chapitre nous avons montré que les approches biocatalytiques s'avèrent très utiles pour produire des auto-assemblages hiérarchiques sous forme d'hydrogels, lorsque ces matériaux ne sont pas accessibles directement à partir des précurseurs synthétiques. De plus, l'inversion de la chiralité thermique a été observée pour les auto-assemblages Y-TAA-bioconjugués, ce qui suggère une transition possible du produit cinétique à la thermodynamique.

D'autres analyses seront faites pour déterminer la conductivité de ces nanofibres à l'aide d'AFM, mais aussi pour élucider par FTIR et SAXS l'agencement moléculaire de fibres hélicoïdales, telles que déterminées par des expériences CD et de microscopies.

Une étude permettant une meilleure compréhension des effets dépendant de la température sera également menée dans la continuation de ce projet.

Ensuite, nous avons concentré nos études sur les applications de systèmes à base de TAAs auto-assemblés dans des domaines différents tels que le photovoltaïque, l'électronique supramoléculaire et les nanotechnologies plasmoniques.

Depuis plusieurs décennies, le développement des cellules solaires organiques a conduit à la découverte de nombreux composés photo-actifs, notamment des dérivés triarylamines, dont les efficacités peuvent atteindre plus de 10%. Ces systèmes offrent divers avantages par rapport aux cellules solaires à base de silicium: plasticité, faible poids, fabrication plus facile, etc. Cependant, les faibles rendements de conversion observés pour ces composés purement organiques par rapport au silicium ont, pour l'instant, limité leurs applications. Récemment, des cellules solaires à base de pérovskite ont été mises au point. Dans ce type de cellules solaires, la pérovskite joue le rôle de matériau photo-actif transportant les électrons, et présentant des efficacités prometteuses de plus de 20% de rendement. Notamment, le groupe de Grätzel a mis en évidence l'efficacité d'un dispositif incorporant des triarylamines comme transporteurs de trous (24 % de conversion).

Inspirés par ces succès, nous avons développé et synthétisé une série de dérivés TAAs auto-assemblées (**Figure C(i)**), incorporant deux ou trois centres redox avec différents substituants de chaînes latérales (**2 redox-TAAs** et **3 redox-TAAs**) et présentant théoriquement les meilleures propriétés de bande interdite pour les cellules à base de pérovskite. L'incorporation du groupe amide est conçue pour faciliter l'auto-assemblage en induisant une interaction de type liaison hydrogène entre les molécules. Les chaînes latérales liées au noyau ont été modifiées afin d'évaluer leur influence sur l'assemblage, la solubilité et la conduction.

Tous les composés synthétisés ont été caractérisés par des méthodes physico-chimiques de caractérisation : RMN, UV-Vis, électrochimie (**Figure C**). Le comportement RMN classique pour ce type de molécules a été observé dans le chloroforme – la disparition des signaux correspondant au cœur aromatique des TAAs après l'irradiation, indiquant la formation de radicaux délocalisés au sein de l'auto-assemblage. Au cours de l'irradiation des solutions de TAAs étudiées, une large bande d'absorption dans la région proche infra-rouge est apparue, correspondante à une bande caractéristique d'un transfert de charge intramoléculaire. Une étude plus détaillée de l'auto-assemblage réalisée avec de la MET a révélé des structures de fibres pour différentes TAAs.

Bien que ces molécules conservent leurs propriétés d'auto-assemblage lors de l'irradiation par la lumière (**Figure C(ii)**), des expériences de voltampérométrie cyclique (VC) ont montré que ces TAA pourraient convenir en termes de niveaux d'énergie pour une utilisation comme HTM dans des cellules solaires de type pérovskite, ce qui était en accord avec les calculs théoriques réalisés pour les valeurs d'énergies d'ionisations (**Figure C(iii)**).

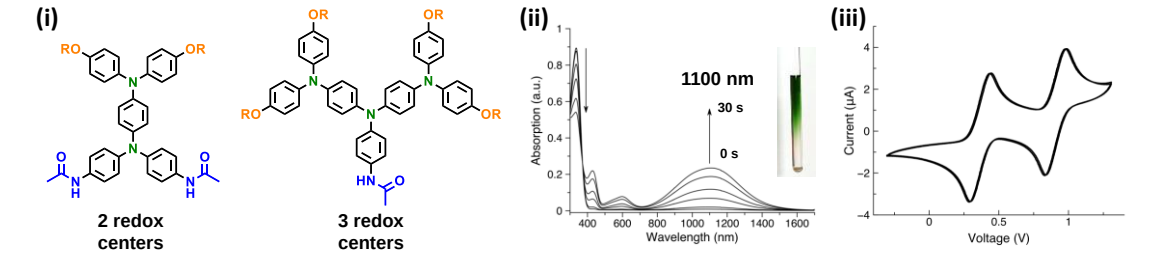

Figure C | (i) Structures des TAAs synthétisées : 2 redox et 3 redox TAAs; **(ii)** Spectres d'absorption obtenus au cours de l'irradiation d'une solution de 2 redox-TAA dans du chloroforme. Dans la fenêtre, l'image d'une solution de 2 redox-TAA dans une tube RMN dans le chloroforme est presentée. La partie haute de la solution a été irradiée avec la lumière et la partie basse de la solution a été protégée de l'irradiation lumineuse. **(iii)** Le voltampèrogramme cyclique de 2 redox-TAA.

La performance de toutes les molécules a été testée à Lausanne au sein de laboratoire de Nazeeruddin et Grätzel. Jusqu'à présent, nous avons démontré que les TAA, ayant un

niveau d'énergie approprié, peuvent être utilisés comme HTM dans les cellules solaires de pérovskite sans aucun additif. Nous avons également constaté que le photo-dopage améliorait les performances des appareils. Bien que le PCE aussi élevé que 7,5% puisse être enregistré pour les mêmes dérivés, toutes les molécules synthétisées n'ont pas surpassé la performance de la référence-or dans ces cellules.

En outre, l'une de nos principales questions demeure sans réponse, à savoir est-ce que le processus d'auto-assemblage a une quelconque influence sur les PCE des appareils. Nous envisageons maintenant de construire des cellules photovoltaïques en utilisant le dépôt de nos HTM à partir de solvants où les TAA ne s'assemblent pas, tels que le THF par exemple, et de comparer les performances de ces dispositifs avec ceux construits en utilisant des procédures standards.

Des études mécanistiques détaillées sur le processus d'auto-assemblage de la première génération de TAA ont démontré que la quantité critique de radicaux (supérieure à une concentration critique de 10 nM), générée par photo- ou chimio-oxydation (par exemple tetrabromobenzoquinone) déclenche la polymérisation supramoléculaire des TAA dans des nanofibres conductrices. De plus, nous avons prouvé que les quantités de cation radicalaire peuvent être dosées en utilisant différentes sources lumineuses conduisant au contrôle de la morphologie des nanostructures à base de TAA.

D'autre part, nous étions curieux de savoir s'il serait possible d'induire et de contrôler l'auto-assemblage des TAA en utilisant un courant électrique comme oxydant. En effet, les méthodes électrochimiques trouvent un grand nombre d'applications dans différents domaines de la science et de la technologie tels que la galvanoplastie, l'électrolyse (production de différents matériaux et composés tels que l'aluminium, etc.) ou la synthèse électrochimique de composés à états d'oxydation exotique) car l'électricité est un oxydant très puissant, mais en même temps, est aussi un agent réducteur très puissant. De plus, une méthode électrochimique permettrait la manipulation de substances très délicates, dû à la possibilité technique de contrôler facilement divers paramètres du courant électrique tels que le type, l'intensité du champ, la densité du courant, etc. Dans le domaine de l'électronique organique, l'électrochimie a été utilisée avec succès pour construire divers polymères conducteurs covalents tels que les polyanilines, les polithiophènes, les polypyrènes, les polypyrroles. Pourtant, il n'y a que quelques exemples de polymérisation supramoléculaire électro-initiée dans la littérature. Dans ces exemples, le polymère supramoléculaire se forme en raison des

interactions « host-guest », qui peuvent être influencées par des stimuli électrochimiques, en changeant la constante d'association entre le « host » et le « guest » dû à leurs états d'oxydation et de réduction.

Dans le *chapitre IV*, nous reportons les résultats d'un travail collaboratif réalisé avec le Dr T. Ellis (ancien chercheur postdoctoral au SAMS Group), le Dr J.J. Armao IV (ancien doctorant au SAMS Group) et le Dr D. Martel (chercheur permanent à l'Institut Charles Sadron) sur la polymérisation supramoléculaire du mono-amide de TAA initiée électrochimiquement. De plus, nous démontrons la possibilité d'utiliser le champ électrique continu pour l'alignement macroscopique *in situ* des nanofibres de TAA entre des microélectrodes d'or de différentes morphologies.

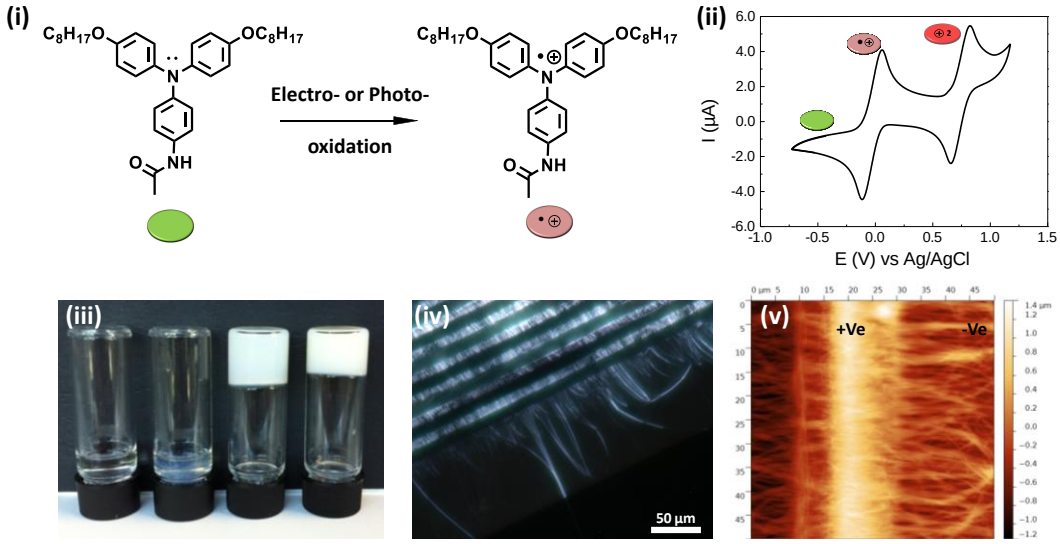

Figure D | (i) Schéma réactionnel d'oxydation d'une TAA de la première génération ; **(ii)** Le voltampèrogramme cyclique de la TAA qui indique deux vagues d'oxydation, correspondantes à la formation du cation radicalaire et à du dication correspondant ; **(iii)** L'image électronique démontrant la formation des gels thermoréversibles ; **(iv)** Image de microscopie optique polarisé effectué sur le dispositif des électrodes interdigitales avec les fibres auto-assemblées alignées ; **(iv)** Image de microscopie électronique à balayage du même dispositif.

Tout d'abord nous avons étudié quelques aspects très importants dans ce projet : (***a***) la possibilité d'utiliser le courant électrique pour initier l'auto-assemblage et (***b***) l'influence de l'électrolyte présent dans un milieu à haute concentration sur ce processus. En effet, par la (VC) il a été montré que la TAA s'oxyde réversiblement par le courant, premièrement en cation radicalaire et ensuit en dication correspondant (**Figure D(i-ii)**). La comparaison des systèmes obtenus par les voies photo- et électrochimique par la spectroscopie UV-Vis a indiqué la présence des mêmes espèces moléculaires obtenues dans le chloroforme pur ainsi qu'avec du tetrabutylammonium chlorure (TBACl) en tant

qu'électrolyte. Par contre, quand le $TBAPF_6$ ou le $TBAClO_4$ ont été utilisés, le maximum d'absorption de la bande radicalaire a subit un shift hypsochromique de 785 vers 760 nm, indiquant une certaine différence de l'interaction entre la TAA cation-radicalaire et l'ion chlorure par rapport à l'ion hexafluorophosphate ou perchlorate.

Connaissant la possibilité de déclencher électrochimiquement la nucléation de molécules supramoléculaires de triarylamines, et de les faire croître sur une surface par reconnaissance supramoléculaire, nous avons étudié la possibilité de polymériser et d'aligner ces fibres directement entre des électrodes commerciales en présence d'un champ électrique. Un tel alignement a déjà été observé pendant une photo-irradiation sur une distance très courte (de 100 nm). Pourtant, nous n'avons pas réussi à atteindre une telle organisation sur de longues distances avec des procédures expérimentales identiques. Nous avons postulé que la raison de cet échec provenait en partie de l'utilisation de chloroforme ou de tetrachloroethane comme solvant pour les molécules de TAA. En prenant en compte les valeurs de leurs potentiels redox et de leurs constantes diélectriques, le grand champ électrique nécessaire pour aligner les fibres sur de longues distances était masqué par les cations-radicaux de triarylammonium électrogénérés (ou photo-générés) et leurs contre-ions respectifs. Si cet effet peut en effet être surmonté en utilisant des nanoélectrodes dans lesquelles la longueur de Debye est supérieure à la distance entre les électrodes, un choix de solvant approprié (avec une constante diélectrique inférieure) doit être considéré pour des échelles plus grande. Cependant, les solvants avec des constantes diélectriques inférieures sont moins appropriés pour solubiliser des molécules de TAA, ce qui fait perdre l'avantage de déclencher un processus de nucléation/croissance orienté à la surface de l'électrode.

Il est intéressant de constater que la TAA se dissout à des températures élevées dans des alcanes tels que l'heptane qui est au centre de cette étude et qu'elle forme un organogel thermoréversible après refroidissement (avec une concentration initiale de gélification de 2,5 mg/ml à T ≈ 10 °C, **Figure D(iii)**). Une propriété intéressante de ce système est sa grande hystérèse thermique qui montre que, après la gélification, le gel est assez stable jusqu'à T = 30 °C. Nous nous sommes donc tournés vers des dispositifs potentiellement plus informatifs en utilisant la géométrie latérale des électrodes interdigitées d'or et de platine (IDE) séparées par des gaps parallèles avec une distance entre 10 et 50 μm et utilisant une force de champ de 5×10^7 $V \cdot m^{-1}$. La procédure de dépôt impliquait: (***a***) le chauffage de la matière (5 mg/mL) jusqu'à la dissolution complète du système; (***b***) un refroidissement de la solution à température ambiante (5 °C au-dessus de la température de gélification); et (***c***) le dépôt de la solution (typiquement 5 μL sur le substrat interdigité en présence du champ

électrique en courant continu et jusqu'à l'évaporation du solvant). Les substrats ont ensuite été analysés par POM et AFM montrant un très fort degré d'alignement homogène des fibres supramoléculaires entres les électrodes (**Figure D(iv-v)**). Une expérience de contrôle utilisant la même procédure mais sans champ électrique n'a révélé que la présence de matériau amorphe et non localisé.

Ainsi, nous avons démontré la possibilité d'obtenir le positionnement et l'orientation de polymères supramoléculaires en combinant un mécanisme de nucléation/croissance avec un champ électrique appliqué entre des électrodes sur des dizaines de micromètres. Pour cela, nous avons utilisé des molécules de TAA qui présentent des caractéristiques clés pour atteindre un tel procédé entièrement contrôlé et, en particulier: (***a***) la capacité de former un nucléus électrochimiquement, (***b***) une stabilité élevée sur la surface de l'électrode, (***c***) la capacité à initier la croissance de la fibre à l'électrode sans processus redox permanent, (***d***) la capacité à s'aligner dans des champs électriques sur de grandes distances. Les champs relativement élevés requis pour cet alignement limitent le type de solvants qui peuvent être utilisés – en général, excluant les solvants à constantes diélectriques élevées, qui peuvent être réduites ou oxydées électrochimiquement à l'interface. Néanmoins, des solutions expérimentales peuvent être trouvées comme cette étude le montre. Un tel contrôle élevé dans tous les aspects des processus de polymérisation supramoléculaire, y compris la localisation et l'orientation sur de telles distances, est à l'heure actuelle tout à fait unique dans la littérature. Les implémentations possibles résultant de ce travail incluent: (***a***) le contrôle spatial du processus d'auto-assemblage dans divers dispositifs optoélectroniques nécessitant un transport de charge efficace et allant des capteurs aux cellules solaires, (***ii***) l'utilisation de couples redox pour créer des systèmes redox hors d'équilibre pour l'auto-assemblage dynamique, (***iii***) une croissance des fibres conductrices en 3D dans les organogels.

La possibilité de manipuler la lumière par le couplage de plasmon entre les nanoparticules plasmoniques (surtout les métaux nobles) excite l'intérêt des scientifiques de différents domaines de la nanoscience. Cette technologie a été exploitée pour des différentes applications telles que la diffusion en surface de Raman (SERS), la biodétection, les nanorègles plasmoniques, pour la construction de puces photoniques et de sources lumineuses et même pour le développement des cellules photovoltaïques. La nanotechnologie plasmonique devrait amener l'informatique à un niveau qualitativement nouveau et surmonter ses limites actuelles.

Cependant, le problème majeur est de parvenir à contrôler l'alignement de telles structures plasmoniques ; ce qui a jusqu'à présent abouti au développement de techniques avancées d'ingénierie et de bioingénierie.

Dans le *chapitre VI*, après une brève introduction bibliographique sur les bases des phénomènes plasmoniques en nanoscience, nous avons présenté une nouvelle méthode rapide et simple d'alignement des nanoparticules d'or (AuNPs) à l'interface liquide-liquide (LLI) en utilisant des assemblées de TAA. Cette méthode a été découverte dans notre groupe par le Dr J.J. Armao IV et le développement de cette approche a abouti à ce travail collaboratif entre les chercheurs de notre groupe ainsi que le Dr R. Arenal de l'Institut de Nanoscience d'Aragon à Zaragosa et le groupe théorique de notre institut (Dr I. Nyrkova et Dr A. Semenov).

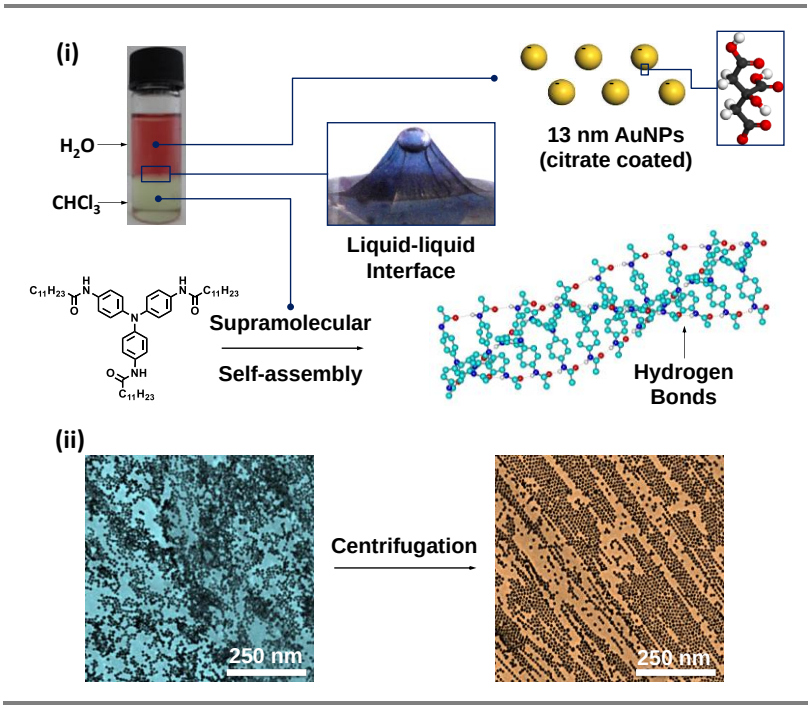

Figure E | (i) Différents composants impliqués dans la formation du film hybride TATA/Au à l'interface liquide/liquide. l'image du système biphasique avec les phases chloroforme (couche basse) et eau (couche haute). La couche de chloroforme contient des nanofibres supramoleculaires de TATA, dopés par irradiation lumineuse avec des cations-radicaux. La couche aqueuse contient une suspension de nanoparticules d'or de taille de 13 nm stabilisées au citrate (Au NPs). Une bulle d'air, piégée sous le film hybride, formée à l'interface ; **(ii)** Images MET démontantes les films hybrides obtenues sans (gauche) et avec la centrifugation (droite).

Sachant que les TATAs s'auto-assemblent en longues nanofibres chargées après irradiation lumineuse, nous avons été curieux de voir s'il est possible d'obtenir des matériaux conjugués AuNPs/TAA, dans lesquels les NPs seraient organisés le long de ces fibres. Nos hypothèses étaient les suivantes: (***a***) les nanofibres de TATA, lorsqu'elles sont dopées avec des cations radicaux sont chargées positivement, avec des contre-ions chlorure, (***b***) d'autre part, les AuNPs lorsqu'elles sont stabilisées en solution avec des molécules de citrate, sont

chargés négativement, (***c***) à cause des interactions électrostatiques entre la double couche chargée négativement des NPs et les TATA-nanofibres chargés positivement, il pourrait être possible d'obtenir un matériau hybride AuNPs/TATA.

Pour prouver notre hypothèse, un système biphasique, contenant des TATA-nanofibres et des Au NPs a été préparé (**Figure E(i)**). La couche basse contenait une solution de TATA-nanofibres dans le chloroforme, dopée avec environ 50% de cations-radicaux par oxydation photo-induite. La couche haute aqueuse contenait la solution colloïdale de NPs à 13 nm stabilisées au citrate. Après avoir secoué cette système pour seulement 10 – 15 s, une observation intéressante a été faite : un film coloré bleu foncé intense a été formé à l'interface. De même, le film a été formé lorsque le système biphasique n'a pas été perturbé pendant la nuit.

L'imagerie par la MET a montré que le film était composé de nanofibres et de AuNPs sans ordre particulier, ni pour les nanofibres ni pour les NPs. Il est intéressant de noter que lorsqu'une centrifugation a été utilisée pour accélérer la formation du film hybride, une amélioration remarquable du degré d'ordre a été observée par la MET (**Figure F(ii)**).

Une nouvelle méthode simple et rapide pour la formation des films hybrides plasmoniques TATA/Au a été développée. Les étapes clés de ce processus ont impliqué: (***a***) le dopage des TATA-nanofibres avec des cations-radicaux positivement chargés; (***b***) la migration et l'alignement de ces fibres sur la LLI, provoqués par le transfert d'anions chlorure dans la phase aqueuse; (***c***) la diffusion accélérée par centrifugation des AuNPs vers la LLI et l'adsorption sur la couche de TATA-nanofibres. Dû à l'alignement des fibres et de l'attraction latérale entre les AuNPs, causée par la polarisation supplémentaire par les TATAs, des structures avec un ordre élevé d'anisotropie ont été obtenues. Nous supposons que cette méthode pourrait être universelle pour toutes structures supramoléculaires capables de former un assemblage chargé et organisé en 1D, ce qui peut être en fait un outil utile pour la préparation de nanostructures plasmoniques anisotropes.

Pour conclure, dans ce manuscrit, j'ai décrit les résultats de mon travail de doctorat orienté vers la compréhension des différents aspects fondamentaux de la chimie supramoléculaire des triarylamines et leurs applications potentielles.

Dans le *chapitre II*, j'ai élucidé le mécanisme des polymérisations supramoléculaires activées thermiquement de tris-amides de triarylamine. Il a été montré que le processus d'assemblage se fait par l'intermédiaire d'un mécanisme de nucléation et de croissance coopératif. La présence d'hystérèse thermique entre les processus d'assemblage et de dissociation indique l'existence d'une barrière cinétique, qui peut être liée à la « chiralité hélicoïdale » inhérente pour les triarylamines. La chiralité supramoléculaire des assemblages hiérarchiques dépend du taux de changement de température, comme le montrent les spectroscopies CD et l'imagerie AFM. Ces résultats peuvent contribuer à un meilleur contrôle des propriétés fonctionnelles des polymères supramoléculaires et aux matériaux qui en sont issus. D'autres études devraient être réalisées à l'avenir pour corréler les propriétés optiques, électroniques, magnétiques et plasmoniques en fonction de la voie utilisée pour l'auto-assemblage.

Dans le *chapitre III*, en collaboration avec le groupe du Prof. R. Ulijn, nous avons démontré la possibilité d'utiliser une approche enzymatique pour la construction de structures basées sur TAAs qui ne sont pas accessibles par d'autres moyens. L'incubation de l'auto-assemblage déclenché enzymatiquement à différentes températures a permis de contrôler la morphologie et la chiralité des assemblages. Il a été démontré que de petits changements dans la structure du conjugué TAA-peptide, tels que l'échange de Tyr par Phe, conduisent à de grands changements au niveau macroscopique. Là encore, des mesures optiques et de conductivité devront être effectuées à l'avenir pour extraire une relation structure/fonction de ces systèmes.

Le *chapitre IV* décrit l'application de dérivés de TAAs à deux et trois centres redox auto-assemblés en tant que matériaux de transport de trous « dopant-free » dans des cellules solaires de type pérovskite. La photo-conversion des dispositifs incorporant nos molécules a démontré une efficacité assez élevée. Toutefois, elle n’est pas en concurrence avec les meilleurs dispositifs de référence en raison des problèmes d'extraction de charges et de résistance en série. Cependant, nous avons clairement souligné l'aspect bénéfique de l'auto-assemblage supramoléculaire sur la photo-conversion.

Dans le *chapitre V,* nous avons démontré la possibilité de déclencher électrochimiquement la polymérisation supramoléculaire. La croissance unidirectionnelle des fibres a été réalisée sous un champ électrique *in situ* à l'échelle micrométrique entre les

électrodes. Ce type de processus d'auto-construction ouvre de nombreuses possibilités pour la conception de systèmes complexes, tels que le nanofilage 3D par exemple.

Le *chapitre VI* explore des caractéristiques structurelles des triarylamines. Notamment, nous avons décrit le processus de formation de films hybrides organiques-inorganiques à l'interface liquide-liquide entre les nano-fibres TAA et les nanoparticules d'or causée par une attraction électrostatique. Il a été observé un haut degré d'ordre des nanoparticules d'or lorsqu'une force gravitationnelle supplémentaire a été introduite pour faciliter la formation du film, en utilisant une simple centrifugation d'un système biphasique. À notre opinion cette méthode simple et rapide peut être utilisée comme un outil général pour la préparation des matériaux ordonnés de manière anisotrope.

Dans l'ensemble, à mon avis, ces résultats poussent un peu plus loin notre connaissance et la compréhension de la chimie supramoléculaire des triarylamines, ce qui aidera pour le développement de nouveaux systèmes avec des propriétés améliorées. De manière plus générale, nous avons tenté de contribuer à la compréhension des relations complexes entre la structure de petites molécules et la manière dont elle est exprimée au niveau supramoléculaire sous l'influence de changements environnementaux. J'espère que ce travail de recherche contribuera au développement futur de la chimie supramoléculaire comme «*quelque part, quelque chose d'incroyable attend d'être découvert*».

ABBREVIATIONS AND SYMBOLS

α	mole fraction
Å	angstrom
A-D	acceptor-donor
Ac	acetyl
AC	alternate current
ACQ	aggregation caused quenching
AFM	atomic force microscopy
AIE	aggregation induced emission
APA	aromatic peptide amphiphile
BINAP	2,2'-bis(diphenylphosphino)-1,1'-binaphthyl
Bn	benzyl
BTA	benzene-1,3,5-tricarboxamide
Bu	butyl
°C	Celsius degree
CBT	carbonyl-bridged triarylamine
CD	circular dichroism
CMC	critical micelle concentration
CPL	circularly polarized light
C_T	total concentration
CT	charge-transfer
CV	cyclic voltammetry
CW	clockwise
CCW	counterclockwise
D	diffusion coefficient
δ	chemical shift
DAC	1,2-diaminocyclohexane
DC	direct current
DCM	dichloromethane
DDA	discrete dipole approximation
DFT	density functional theory
DLS	dynamic light scattering
DMF	dimethylformamide
$_{Dm}Fc/_{Dm}Fc^+$	decamethylferrocene/decamethylferrocenium
DMSO	dimethylsulfoxide
DNA	deoxyribonucleic acid
DOSY	diffusion-ordered spectroscopy
DPPF	1,1'-bis(diphenylphosphino)ferrocene
DSC	differential scanning calorimetry

ε	dielectric constant
$E_{1/2}$	redox potential
EELS	electron energy loss spectroscopy
EDTA	ethylenediaminetetraacetic acid
EPR	electron paramagnetic resonance
eq	equivalent
ESI-MS	mass spectrometry with electrospray ionization
eV	electron-volt
EWG	electron withdrawing group
F	Faraday constant
Φ	quantum yield
Fc/Fc^+	ferrocene/ferrocenium
FDTD	finite difference time domain
FF	fill-factor
FTIR	fourier transform infrared spectroscopy
G	Gibbs Free Energy
H	enthalpy
h	hour
HEEDTA	hydroxy-2-ethylenediaminetriacetic acid
HOMO	highest occupied molecular orbital
HPLC	high performance liquid chromatography
HTM	hole transporting material
ILCT	intra-ligand charge transfer
IVCT	intervalence charge transfer
IPA	isopropyl alcohol
IR	infrared
ITO	indium tin oxide
J	coupling constant
J	joule
K	kelvin
K_a	activation constant
K_e	elongation constant
K_d	dissociation constant
L	liter
λ	wavelength
LC/MS	liquid chromatography coupled to mass spectrometry
LED	light-emitting diode
LLI	liquid-liquid interface
LUMO	lowest unoccupied molecular orbital
m	meter

MCH	methylcyclohexane
MeCN	acetonitrile
µL	microliter
mL	milliliter
MLCT	metal to ligand charge transfer
µmol	micromole
mmol	millimole
MS	mass spectrometry
mV	millivolt
NIR	near infrared
nm	nanometer
nA	nanoampere
NMR	nuclear magnetic resonance
NP	nanoparticle
OFET	organic field-effect transistor
OGS	onset gelation concentration
OLED	organic light-emitting diode
OPM	optical polarized microscopy
OPV	organic photovoltaic
OPV	oligo(p-phenylenevinylene)
ORD	optical rotatory dispersion
PCE	photoconversion efficiency
PEG	poly(ethylene glycol)
pH	pondus hydrogenii
ppm	parts per million
PSC	perovskite solar cell
PyBOP	benzotriazol-1-yl-oxytripyrrolidinophosphonium
R	ideal gas constant
R_f	retardation factor
RIR	restriction of intramolecular rotations
RPM	revolutions per minute
r.t.	room temperature
S	siemens
S	entropy
S	orientation parameter
s	second
SAXS	small angle X-ray scattering
SEM	scanning electron microscopy
SERS	surface-enhanced raman scttering

SOMO	singly occupied molecular orbital
spiro-OMeTAD	N2,N2,N2′,N2′,N7,N7,N7′,N7′-octakis(4-methoxyphenyl)-9,9′-spirobi[9H-fluorene]-2,2′,7,7′-tetramine
STANW	self-assembled triarylamine nanowires
T	temperature
T_e	elongation temperature
T_m	melting temperature
TAA	triarylamine
TATA	tris-amide triarylamine
TBQ	tetrabromoquinone
TBA	tetrabutylamine
TBACl	tetrabutylammonium chloride
$TBAClO_4$	tetrabutylammonium perchlorate
TBAHFP	tetrabutylammonium hexafluorophosphate
TCE	tetrachloroethane
TCNQ	tetracyanoqoinodimethane
TEA	triethylamine
TEM	transmission electronic microscopy
THF	tetrahydrofuran
TLC	thin layer chromatography
TPA	triphenylamine
TPB	N,N,N',N'-tetraphenylbenzidine
TTF	tetrathiafulvalene
UPLC	ultra-performance liquid chromatography
UV	ultra-violet
Vis	visible
Ω	ohm
WAXS	wide-angle X-ray scattering

GENERAL INTRODUCTION AND OBJECTIVES

The possibility to access ordered supramolecular polymers by the stacking of triarylamine molecules, in particular when substituted by amide moieties, was first published in 2010 by our research group. Since then, several interesting fundamental works related to their supramolecular polymerization mechanism, as well as to their unique functional properties and related applications appeared in the literature.

The objective of this thesis was to explore further and thus gain a better understanding of the relationship between chemical structure and the physical properties of triarylamine-based supramolecular polymers with a view toward their implementation as functional materials.

In particular, the first goal of my work was to investigate the mechanism of supramolecular polymerization of chiral TAA molecules and to study the influence of chiral bias on their supramolecular chirality. It was expected that, when decorated with stereogenic substitutes, triarylamines would assemble into helices with preferential handedness. Moreover, due to the "propeller chirality" in triarylamine molecules, the combination of these two levels of asymmetry could result in interesting chirality amplification phenomenon and higher level of complexity for controlling the assembly process.

Our second objective was to explore a new method for the construction of ordered triarylamine systems with original structures. For that, in collaboration with the group of R. Ulijn, we wanted to develop an enzymatically triggered self-assembly process where an appropriate enzyme could catalyse the chemical transformation of a triarylamine-peptide conjugate to yield the *in situ* formation of self-assemblies that could not be reached by self-assembly of the preformed building blocks.

Our third objective was to probe the potential of triarylamine-based supramolecular polymers as a hole-transporting material in perovskite solar cells. In this direction, we carefully designed the molecular structure of triarylamines to match with the HOMO level of perovskite, while keeping their self-assembling characteristic.

Our fourth objective targeted the directed self-assembly of triarylamine-based supramolecular polymers precisely between a series of commercially available microelectrodes of different geometries. For this, a careful study of the electrochemical properties of the triarylamine molecules and of their self-assemblies was envisioned, with the ultimate goal to trigger said supramolecular polymerization solely using electrical potential.

Finally, a last study was oriented towards the possibility to use this family of supramolecular polymers as nematic templates. In particular, we studied the formation of interfacial films formed at a liquid-liquid interface in which a highly anisotropic self-assembly of triarylamine fibres and gold nanoparticles can be co-self-assembled, leading to the formation of plasmonic waveguides.

This work touches many domains, going from supramolecular chemistry and polymers at large to organic electronics and plasmonics. The thesis will thus be organized with a general introduction on supramolecular polymers and triarylamine chemistry (*Chapter I*), and each chapter, describing the results, will be started with a more specific introduction on each particular topic.

CHAPTER I.
GENERAL BIBLIOGRAPY

1. SUPRAMOLECULAR CHEMISTRY AND SUPRAMOLECULAR POLYMERS

A. Supramolecular Chemistry

Supramolecular chemistry is a very broad field of chemical science studying processes governed by non-covalent interactions. Supramolecular chemistry has been defined in 1978 by J.-M. Lehn as "a chemistry beyond the molecule"[1] and, in 1987, D. Cram, J.-M. Lehn and C. Pedersen received the Nobel Prize for "their development and use of molecules with structure-specific interactions of high selectivity". The key concepts and applications of supramolecular chemistry are defined by the distinct nature of non-covalent interactions, as opposed to covalent bonds, involving: (*a*) bond energy (noncovalent interaction usually are weaker than covalent ones); (*b*) dynamics (*i.e.* kinetic lability at ambient conditions), (*c*) directionality (which partly governs selectivity aspects). The main types of non-covalent forces that define supramolecular interactions are represented in **Table 1** in order by descending strength of the interaction.

Table 1 | Comparison of different noncovalent interactions

Interaction	Strength, kJ/mol	Example
Ion-ion	200 – 300	$(n\text{-Bu})_4N^+Cl^-$
Ion-dipole	50 – 200	Sodium and [15]crown-5
Dipole-dipole	5 – 50	Acetone
Hydrogen bonding	4 – 120	Nucleotides within DNA
Cation-π	5 – 80	K^+ in benzene
π-π	0 – 50	Benzene and graphite
Van der Waals	<5 (but variable depending on surface area)	Liquid gases, packing in molecular crystals
Hydrophobic	Related to solvent-solvent interaction energy	Cyclodextrin inclusion compounds

1. Lehn, J.-M. Supramolecular Chemistry—Scope and Perspectives Molecules, Supermolecules, and Molecular Devices (Nobel Lecture). *Angew. Chem. Int. Ed.* **27,** 89–112 (1988).

Domains of particular interest based on supramolecular chemistry are: (***i***) *molecular recognition*; (***ii***) *molecular self-assembly*; (***iii***) *molecular topology*; (***iv***) *dynamic covalent chemistry*.

Molecular recognition is one of the most fundamental aspects of supramolecular chemistry, which refers to a *specific* noncovalent interaction between two or more molecules. A classical, naturally occurring example of molecular recognition is the enzyme-substrate interaction (popularized by the lock and key principle of E. Fischer in 1894).[2] Another classical example is the binding of alkali metal cations to crown-ethers.

Molecular self-assembly is a process of structural organisation of molecular building blocks into supramolecular structures by means of noncovalent interactions, which can lead to the formation of discrete objects (such as molecular capsules, cages, micelles, *etc.*) or infinite self-assemblies (fibers, membranes, networks). In a *hierarchical* self-assembly, molecular organisation occurs at multiple scales.[3]

Molecular topology is involves particular molecular structures, which are linked together only due to mechanical constraints (mechanically interlocked molecules) such as catenanes, rotaxanes, molecular knots *etc.*[4] When the parts of these molecules are set in controlled motion this gives rise to a new object such as *molecular machines* and *molecular motors*.[5]

Dynamic covalent chemistry deals with reversibly connected molecules, which can make use of supramolecular bonds but also of reversible covalent bonds such as imine bond, disulphide bond, *etc.* Dynamic covalent chemistry is at the origin of a dynamic combinatorial chemistry, which is a powerful synthetic tool allowing the screening of a large number of compounds in order to design new drugs or for the discovery of new functional materials.

Related topics important for biology have been nurtured by these basic concepts, such as *systems chemistry* and *chemical evolution.* In *material science*, supramolecular chemistry plays also an important role, being responsible for novel properties of materials such as self-healing, stimuli responsiveness, tunability *etc.* It is used as a bottom-up approach to design new materials with properties that occur because of specific intermolecular recognition between structural elements, such as enhanced conductivity, improved mechanical properties

2. Fischer, E. Einfluss der Configuration auf die Wirkung der Enzyme. *Berichte der Dtsch. Chem. Gesellschaft* **27,** 2985–2993 (1894).
3. Whitesides, G. M. & Grzybowski, B. Self-Assembly at All Scales. *Science* **295,** 2418–2421 (2002).
4. *Molecular Catenanes, Rotaxanes and Knots: A Journey Through the World of Molecular Topology*. (Wiley-VCH Verlag GmbH, 1999). doi:10.1002/9783527613724
5. Erbas-Cakmak, S., Leigh, D. A., McTernan, C. T. & Nussbaumer, A. L. Artificial Molecular Machines. *Chem. Rev.* **115,** 10081–10206 (2015).

etc. In particular, a large class of molecular self-assemblies for (bio)material science comprise the so-called supramolecular polymers.

B. Supramolecular Polymers

Supramolecular polymers are reversible unidirectional assemblies of molecules held together by means of noncovalent interactions. This branch of supramolecular chemistry has developed enormously since the first publication by Lehn and co-workers[6,7] and is constantly growing. Due to the reversible nature of non-covalent bonds, supramolecular polymers have several distinct features compared to covalent polymers: (***i***) a degree of polymerisation that depends on the concentration of monomer; (***ii***) self-healing properties; (***iii***) responsive properties. These interesting features of supramolecular polymers have attracted much attention to this topic in recent decades, and resulted in a high number of fundamental studies and in various applications in material science.

In this section, we will give a brief introduction of the field of supramolecular polymers using a classification based the supramolecular interactions involved.

i. Hydrogen Bonding Polymers

Hydrogen bonds play a crucial role in bio-macromolecules that represent a source of inspiration for the design of artificial supramolecular polymers. They ensure functions such as protein folding (L. Pauling and R. Corey (1951)[8]), polycarbohydrate assembly (cellulose and chitin structure), functioning of enzymes (specific catalysis), storage and translation of the genetic information supported by the desoxyribonucleic acic DNA (J. Watson together with F. Crick (1953)[9]). The structure of a canonical double strand of B-DNA is represented in **Figure 1A**. Its backbone is constructed from alternating carbohydrate molecules (desoxyribose) connected by phosphodiester bonds in positions 5' and 3'. The purine (adenine, A and guanine, G) and pyrimidine bases (cytosine, C, thymine, T and uracil, U) form complementary pairs: A-T, C-G *via* double or triple hydrogen bonds (**Figure 1B**).

6. Gulik-Krzywicki, T., Fouquey, C. & Lehn, J. Electron microscopic study of supramolecular liquid crystalline polymers formed by molecular-recognition-directed self-assembly from complementary chiral components. *Proc. Natl. Acad. Sci.* **90,** 163–167 (1993).
7. Fouquey, C., Lehn, J.-M. & Levelut, A.-M. Molecular recognition directed self-assembly of supramolecular liquid crystalline polymers from complementary chiral components. *Adv. Mater.* **2,** 254–257 (1990).
8. Pauling, L. & Corey, R. B. Configurations of Polypeptide Chains With Favored Orientations Around Single Bonds: Two New Pleated Sheets. *Proc. Natl. Acad. Sci. U. S. A.* **37,** 729–40 (1951).
9. Watson, J. D. & Crick, F. H. C. Molecular Structure of Nucleic Acids: A Structure for Deoxyribose Nucleic Acid. *Nature* **171,** 737–738 (1953).

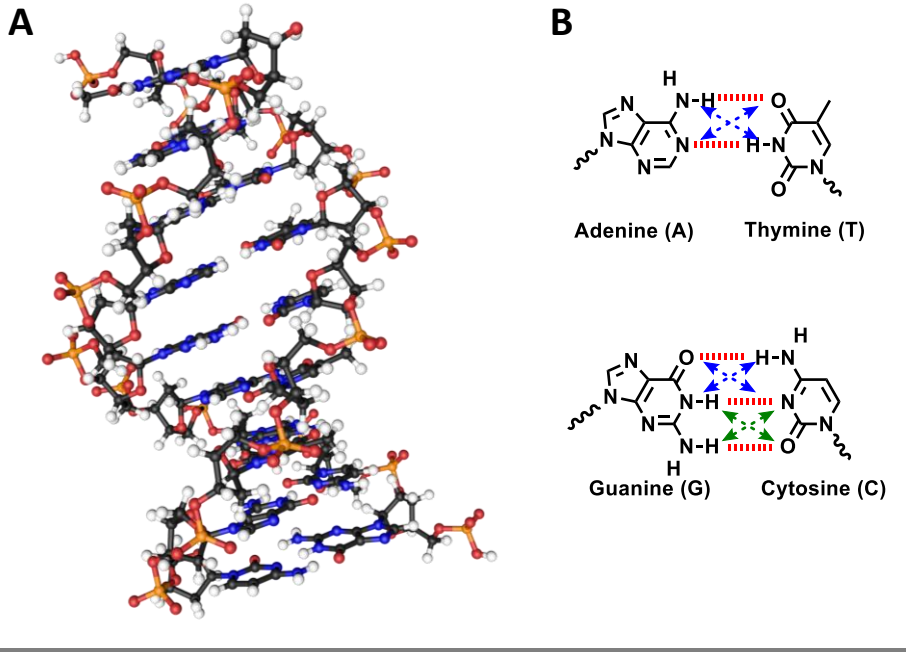

Figure 1 | (A) Fragment of self-complementary double DNA strand. **(B)** Hydrogen bonding between nucleotides. Red dashed lines represent hydrogen bonds, blue arrows represent secondary repulsive interactions and green arrows represent secondary attractive interactions. DNA strand was modeled with Avogadro software and visualised with Cinema 4D using ePMV plug-in.[10]

The energy of hydrogen bonding, and consequently the association constant in these types of structures, is strongly influenced by the secondary attractive (depicted as green arrows) and repulsive (blue arrows) electrostatic interactions. Therefore, the association constant involving an array of 3 hydrogen bonds can change dramatically from 90 M^{-1} to 10^{10} M^{-1}. [11,12]

The first synthetic example of a supramolecular polymer based on multiple hydrogen interactions was reported in 1990s by Lehn and collaborators (**Figure 2**).[6,7] Triple hydrogen-bonding self-complementary precursors with DAD-linker-DAD (***a***) and ADA-linker-ADA (***b***) structures have been synthesized (**Figure 2A**). Here, the DAD (donor-acceptor-donor) motif is 2,6-diacetylamidopyridine (P) and the ADA (acceptor-donor-acceptor) motif is uracil (U). Mixing the precursors in a chloroform solution lead to the formation of a supramolecular polymer (***[a-b]$_n$***), which further formed liquid crystalline hexagonal phase made of helical superstructures as seen by SEM microscopy (**Figure 2B,C**).

10. Johnson, G. T., Autin, L., Goodsell, D. S., Sanner, M. F. & Olson, A. J. ePMV embeds molecular modeling into professional animation software environments. *Structure* **19,** 293–303 (2011).
11. Jorgensen, W. L. & Pranata, J. Importance of secondary interactions in triply hydrogen bonded complexes: guanine-cytosine vs uracil-2,6-diaminopyridine. *J. Am. Chem. Soc.* **112,** 2008–2010 (1990).
12. Blight, B. A. *et al.* AAA−DDD Triple Hydrogen Bond Complexes. *J. Am. Chem. Soc.* **131,** 14116–14122 (2009).

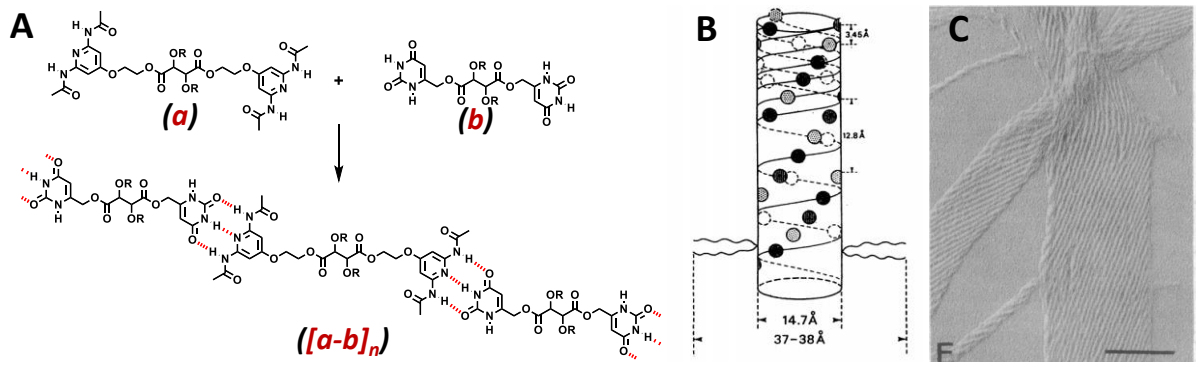

Figure 2 | First example of an artificial hydrogen bonded supramolecular polymer. (**A**) Reactional scheme of supramolecular polymer formation from complementary precursors ***a*** and ***b*** *via* triple hydrogen bonding. (**B**) Schematic representation of the columnar superstructure, each spot represents a P-U or U-P base pair; spots of the same type belong to the same strand of a triple helix. (**C**) SEM image of the air dried thin layers deposited on TEM grids. Figure is adapted from refs. 6,7

ii. Ionic and Coordination (Metal-Ligand) Polymers

The implementation of ionic and metal-ligand interactions have been nicely combined, as demonstrated in the work of the Schmuck group (**Figure 3**).[13] Here, ditopic motif (***c***) displays terpyridine function at one side, which can coordinate metal ions, and an orthogonal self-complementary hydrogen bonding/ionic function at the other side (**Figure 3A**). The reaction scheme on **Figure 3B** describes the possible pathways of supramolecular polymerization. *State A*: no metal ions are present, the pH is low, the molecule is protonated, and exists uniquely in monomeric state. The situation changes either when a metal ion, such as iron(II) is added, shifting the system to a coordination dimer formation (*state B*); or by basifying the solution, which causes the ionization of the protonated part, zwitterion formation and consequently dimerization by means of self-complementary ionic interactions between the carboxyl of one molecule and the guanidinium function of another one (*state C*). The supramolecular polymer formation can be induced from both *B* and *C* states either by adding the base (*state B* to *D*) or iron(II) (*state C* to *D*). All these interstate transitions are reversible, and the polymer can be easily transformed to the initial monomer by addition of EDTA or/and acid.

13. Gröger, G. *et al.* Switchable Supramolecular Polymers from the Self-Assembly of a Small Monomer with Two Orthogonal Binding Interactions. *J. Am. Chem. Soc.* **133,** 8961–8971 (2011).

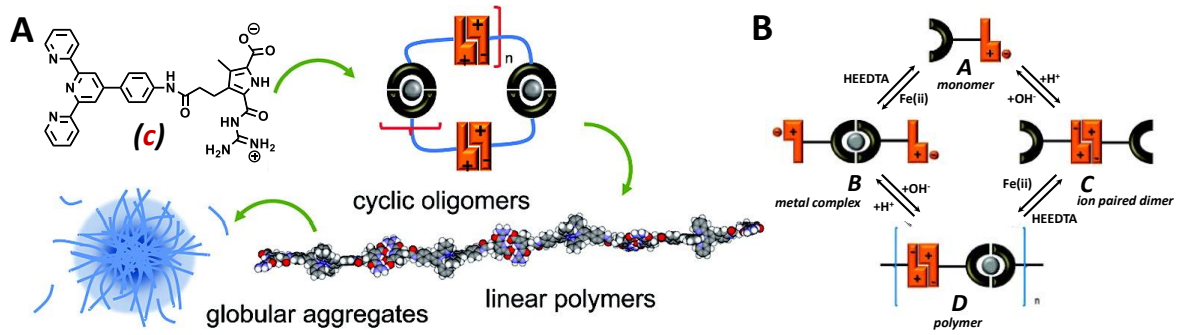

Figure 3 | Self-Assembly of a heteroditopic monomer ***c*** based on two orthogonal binding interactions, metal–ligand binding and ion pair formation. (**A**) General scheme of the self-assembly. (**B**) Pathways of supramolecular polymerization using pH and metal ions. Figure is adapted form ref. 13

iii. π-π Interactions

π-π interactions[14] are also fundamental in the stabilization of DNA along the helix axis and they can be a cause of severe dysfunctions when competing planar aromatic molecules, such as thalidomide, intercalate between the nucleotide pairs, thus preventing efficient transcription.[15] This interaction can also be targeted positively in chemotherapy of intensively growing tumours, with for instance doxorubicin intercalating into DNA of abnormal cells.[16]

π-π interactions play an important role for the optical and electronic properties of materials, and additionally for the structure determination of supramolecular aggregates, especially in aqueous media. For instance, the group of Häner has worked on DNA mimicking synthetic systems, intensively exploiting π-π interactions between the polyaromatic analogues of nucleobases, such as pyrene.[17–19] They recently communicated the cooperative π-π-interaction driven self-assembly of pyrene-DNA bioconjugates in water (**Figure 4**).[19] Oligopyrene units, which consist of seven dialkylpyrene monomers, connected one to another in a linear heptamer by phosphodiester bonds (similarly as nucleotides are connected within DNA strand), were decorated with single-strand DNA containing 9 bases (***d***). In an aqueous medium the heptamer adopts a compact stair-like conformation due to the π-π-interactions, while the ionisable phosphate groups ensure solubility.

14. Hunter, C. A. & Sanders, J. K. M. The Nature of pi-pi Interactions. *J. Am. Chem. Soc.* **112,** 5525–5534 (1990).
15. Koch, H. P. & Czejka, M. J. Evidence for the intercalation of thalidomide into DNA: clue to the molecular mechanism of thalidomide teratogenicity? *Zeitschrift für Naturforschung. C, J. Biosci.* **41,** 1057–61
16. Yang, F., Teves, S. S., Kemp, C. J. & Henikoff, S. Doxorubicin, DNA torsion, and chromatin dynamics. *Biochim. Biophys. Acta - Rev. Cancer* **1845,** 84–89 (2014).
17. Vyborna, Y., Vybornyi, M. & Häner, R. From Ribbons to Networks: Hierarchical Organization of DNA-Grafted Supramolecular Polymers. *J. Am. Chem. Soc.* **137,** 14051–14054 (2015).
18. Rudnev, A. V. *et al.* Cooperative and Noncooperative Assembly of Oligopyrenotides Resolved by Atomic Force Microscopy. *Macromolecules* **45,** 5986–5992 (2012).
19. Vyborna, Y., Vybornyi, M., Rudnev, A. V. & Häner, R. DNA-Grafted Supramolecular Polymers: Helical Ribbon Structures Formed by Self-Assembly of Pyrene-DNA Chimeric Oligomers. *Angew. Chem. Int. Ed.* **54,** 7934–7938 (2015).

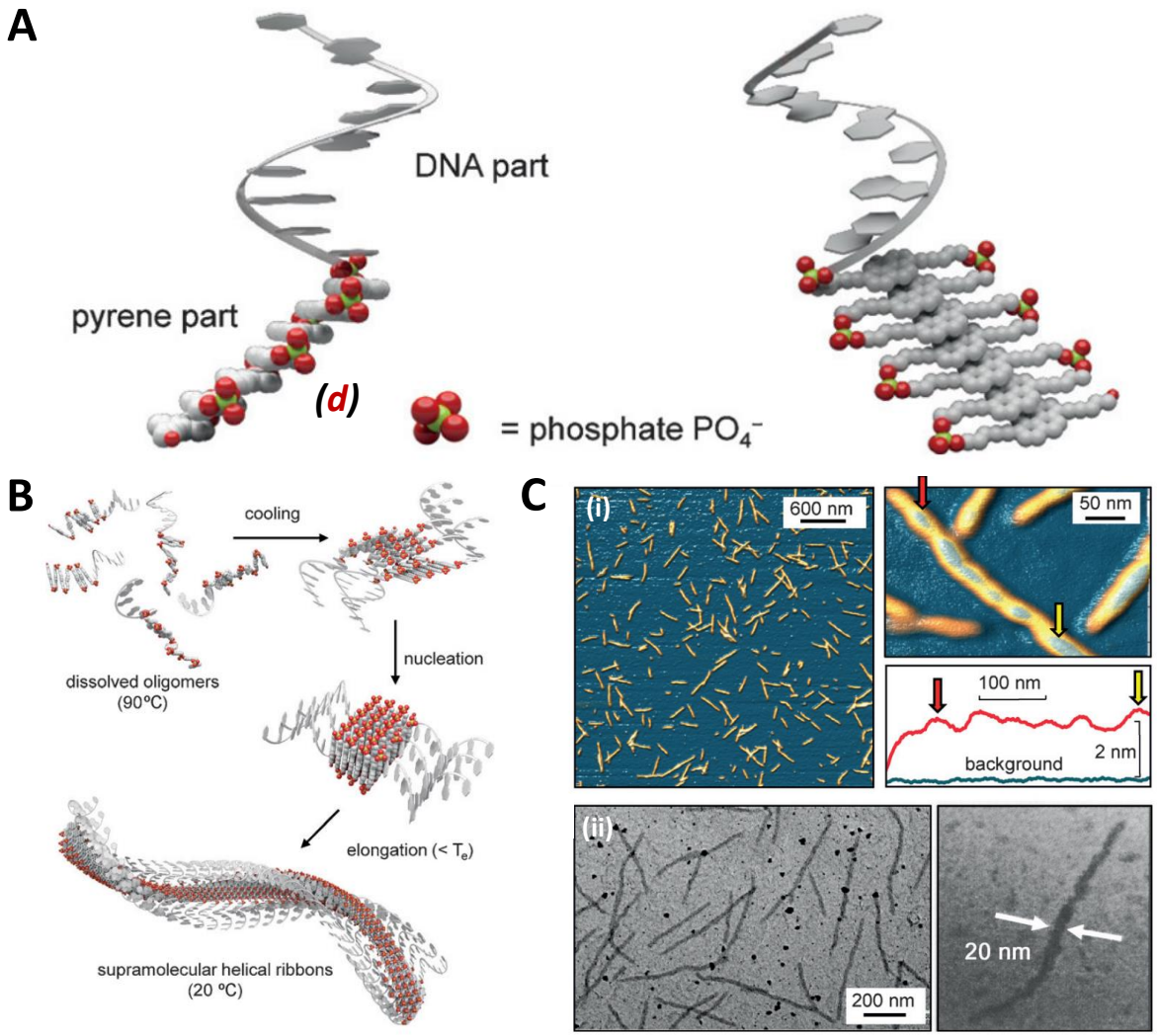

Figure 4 | Pyrene-DNA bioconjugate self-assembly. (**A**) Model of the pyrene–DNA chimeric oligomer ***d***. (**B**) Formation of DNA-grafted supramolecular polymers from chimeric DNA-pyrene oligomers through a nucleation–elongation process. (**C**) Microscopy studies of the pyrene-based supramolecular polymers (**i**) AFM images; (**ii**) TEM images. Conditions for the polymer formation: 10 mm phosphate buffer, pH 7, 250 mM sodium chloride; total strand concentration 10 μM. Figure is adapted from ref. 19

iv. Charge Transfer Interactions

The Group of Zhang demonstrated the possibility to exploit charge transfer interactions in hierarchical self-assembly of aromatic super-amphiphiles (**Figure 5**).[20] The designed system contains an electron deficient cationic viologen surfactant (***e***) and an electron rich anionic 6,8-dihydroxypyrene-1,3-disulfate (***f***). The association of these molecules, driven by electrostatic attraction and charge transfer complex formation between electron-donor and electron-acceptor molecules, leads to the formation of so-called superamphiphiles (**Figure**

20. Wang, C., Guo, Y., Wang, Z. & Zhang, X. Superamphiphiles Based on Charge Transfer Complex: Controllable Hierarchical Self-Assembly of Nanoribbons. *Langmuir* **26,** 14509–14511 (2010).

5**A**). At pH 9 and higher, long and flexible single layer nanoribbons are formed, while at pH 8 rod-like multilayer assemblies are observed (**Figure 5B**).

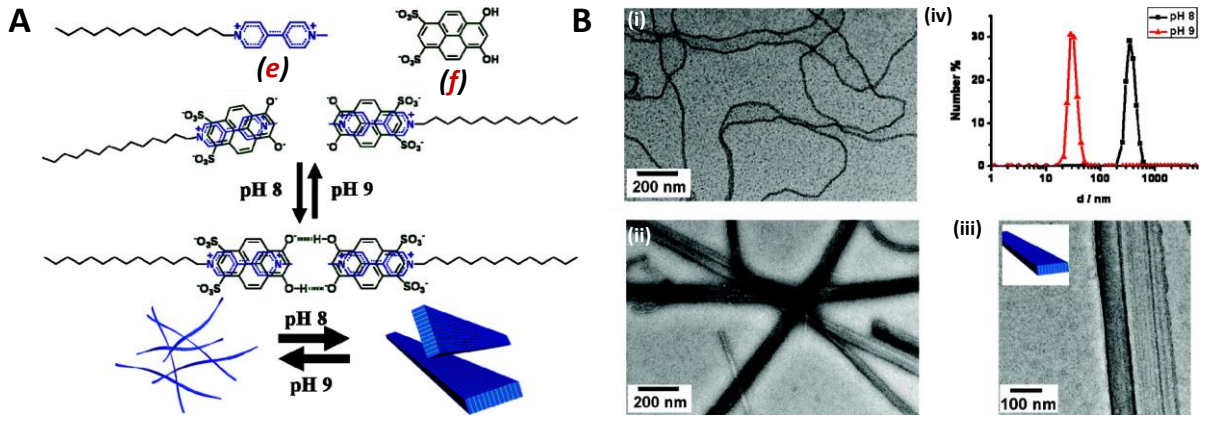

Figure 5 | (**A**) Schematic illustration of the hierarchical nanoribbons self-assembly of aromatic amphiphiles. (**B**) TEM images of the aggregates of (***e-f***) at pH 9 (**i**). (**ii** and **iii**) Magnified TEM images of the aggregates at pH 8. (**iv**) Distribution of the hydrodynamic diameter of (***e-f***) at pH 9 and pH 8. Figure is adapted from ref. 20

v. Hydrophobic Interactions

Hydrophobic interactions are also crucial in biological systems, they are a strong driving force in the folding of proteins or the self-sustaining of cellular membranes. Artificial systems involving hydrophobic forces were designed for instance by the group of van Esch who studied self-assemblies of multisegment amphiphiles based on 1,3,5-cyclohexyltrisamide scaffold (***g***).[21] Schematic structure of this class of supramolecular amphiphilic building blocks is represented in **Figure 6A(i)**: the dark-blue segments correspond to the hydrophobic part while the light-blue ones to the polar, hydrophilic part. To study the influence of hydrophobic interactions on the self-assembly pathway, the symmetrical amphiphile was decorated with C_8 alkyl chains. The hierarchical self-assembly occurred when a hot solution was cooled to room temperature and depending on the concentration resulted in the increase of the solution viscosity or in hydrogelation. At first, individual fibrils formed *via* multiple noncovalent interactions including threefold hydrogen bonding between amide groups, π-interactions between phenyl moieties of phenyl alanines and lateral hydrophobic interactions between alkyl chains **Figure 6B(i)**. Cryo-TEM investigations clearly demonstrated the formation of single fibrils at low gelator concentration. With gradual increase of concentration, the bundle of fibrils and tapes were formed. Fluorescent spectroscopy with Nile Red dye showed strong blue shift of the emission

21. Boekhoven, J., van Rijn, P., Brizard, A. M., Stuart, M. C. A. & van Esch, J. H. Size control and compartmentalization in self-assembled nano-structures of a multisegment amphiphile. *Chem. Commun.* **46,** 3490 (2010).

maximum from 660 nm in pure water to 622 nm in water solution of amphiphile, indicating the existence of hydrophobic domains.

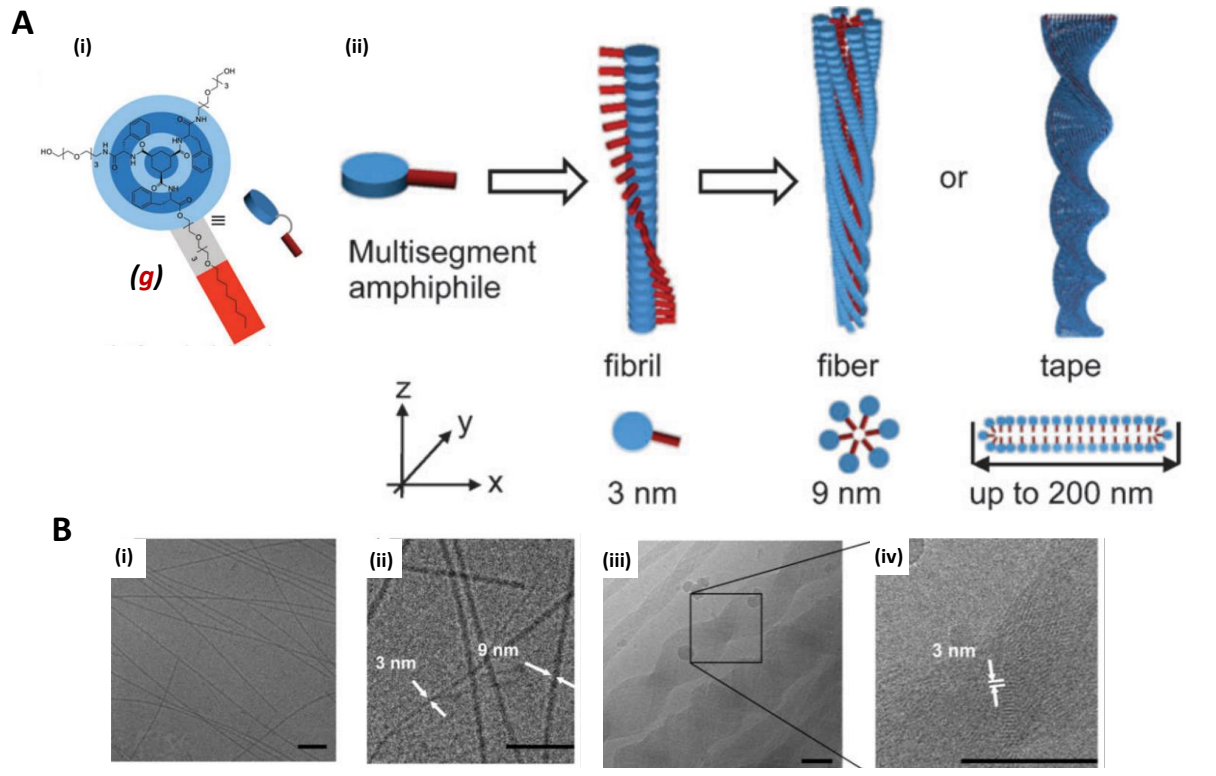

Figure 6 | (**A**) (**i**) Multisegment amphiphile ***g***, where light areas represent hydrophilic domains whereas dark areas represent hydrophobic domains. (**ii**) Schematic representation of the self-assembly of ***g*** into fibril, hydrogen bonded in the z-direction. Additionally, due to hydrophobic interactions between the surfactant segments, 5 to 7 fibrils assemble into 9 nm fibers or up to 200 nm tapes depending on the concentration. (**B**) Cryo-TEM images of (**i**) fibrous network of ***g*** at 0.25 mM displaying fibers with a diameter of 9 nm; (**ii**) magnification of **Fig. B(i);** (**iii**) fibrous network of ***g*** at a concentration above 0.25 mM. Polydisperse twisted tapes of 50 to 200 nm in diameter are formed; (**iv**) magnification of **Fig. B(iii)** showing substructures consisting of fibrils of 3 nm in diameter. Scale bar: 100 nm. Figure is adapted from ref. 21

These examples presented in this section highlight the role and importance of noncovalent interactions in the formation of supramolecular polymers. As one might have noticed, several types of weak interactions are often combined in such self-assembly processes – being sometimes cooperative and sometimes anti-cooperative.

In the next section, we will discuss the chemistry and supramolecular chemistry of one particular building block – the triphenylamine derivatives, which will serve as the basis this PhD work.

2. Chemistry and Supramolecular Chemistry of Triarylamines

It would not be an exaggeration to say that the derivatives of triarylamines are one of the most widely used compounds in various fields of organic electronics due to their remarkable conducting properties and relatively high stability. They have been used for decades in xerography (Xerox® process)[22,23] in laser printers, in organic light emitting diodes (OLEDs),[24,25] organic field effect transistors (OFETs),[26] organic photovoltaic cells (OPCs),[27] perovskite solar cells,[28–30] two photon absorption and emission[31], etc.

However, until recently, supramolecular self-assemblies based on triarylamine cores were totally unknown in the literature. In this section, we will discuss molecular and supramolecular chemistry of triarylamines, as well as their use in organic electronics.

A. Methods of Preparation of Triarylamines

i. Historical Overview

Triphenylamine (TPA) was obtained for the first time, and in a poor yield, by Merz and Weith in 1873 when reacting aniline or diphenylamine with potassium in the melt, followed by addition of bromobenzene to the reaction mass (**Scheme 1 A**).[32]

22. Karam, R. E. Method for the preparation of an electrostatographic photoreceptor. (1975).
23. Turner, S. R.; Yanus, J. F.; Renfer, D. S. Process for preparing arylamines. (1988). at <https://worldwide.espacenet.com/publicationDetails/biblio?CC=US&NR=4764625A&KC=A&FT=D&ND=&date=19880816&DB=&locale=>
24. Tao, Y., Yang, C. & Qin, J. Organic host materials for phosphorescent organic light-emitting diodes. *Chem. Soc. Rev.* **40,** 2943 (2011).
25. Jou, J.-H., Kumar, S., Agrawal, A., Li, T.-H. & Sahoo, S. Approaches for fabricating high efficiency organic light emitting diodes. *J. Mater. Chem. C* **3,** 2974–3002 (2015).
26. Chou, Y.-H. *et al.* Nonvolatile transistor memory devices using high dielectric constant polyimide electrets. *J. Mater. Chem. C* **1,** 3235 (2013).
27. Lin, Y., Li, Y. & Zhan, X. Small molecule semiconductors for high-efficiency organic photovoltaics. *Chem. Soc. Rev.* **41,** 4245 (2012).
28. Yu, Z. & Sun, L. Recent Progress on Hole-Transporting Materials for Emerging Organometal Halide Perovskite Solar Cells. *Adv. Energy Mater.* **5,** 1500213 (2015).
29. Völker, S. F., Collavini, S. & Delgado, J. L. Organic Charge Carriers for Perovskite Solar Cells. *ChemSusChem* **8,** 3012–3028 (2015).
30. Ameen, S. *et al.* Perovskite Solar Cells: Influence of Hole Transporting Materials on Power Conversion Efficiency. *ChemSusChem* **9,** 10–27 (2016).
31. Lartia, R. *et al.* Synthetic Strategies to Derivatizable Triphenylamines Displaying High Two-Photon Absorption. *J. Org. Chem.* **73,** 1732–1744 (2008).
32. Merz, V. & Weith, W. Vermischte Mittheilungen. *Berichte der Dtsch. Chem. Gesellschaft* **6,** 1511–1520 (1873).

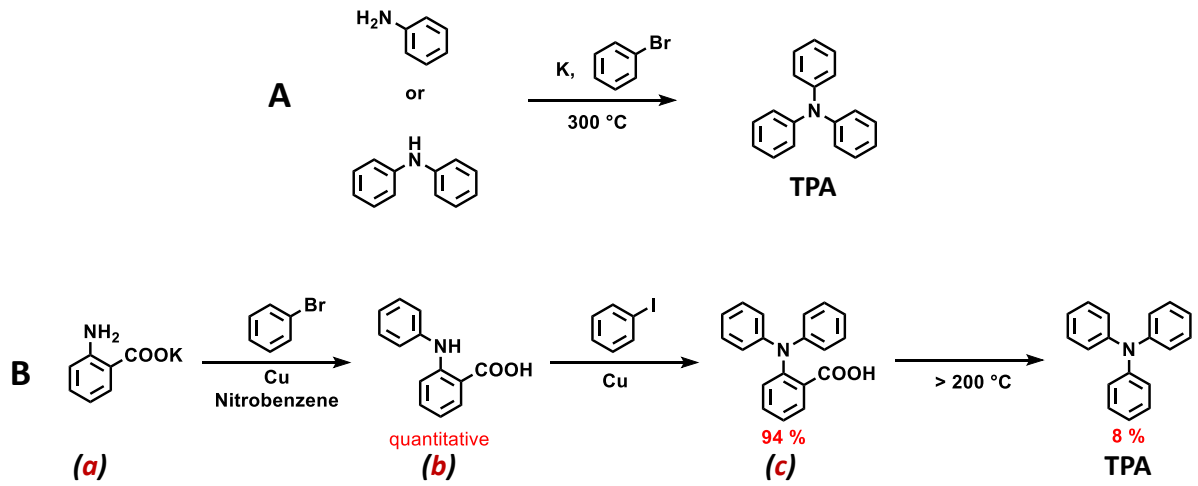

Scheme 1 | Syntheses of the pristine triphenylamine (TPA) starting (**A**) from aniline or diphenylamine and bromobenzene using potassium as a base according to Merz and Weith procedure [32] and (**B**) according to Goldberg and Nimerovsky method starting from anthranilic acid (***a***) (in a form of potassium salt) using copper.[33,34]

Goldberg and Nimerovsky in 1907 developed a three-step synthesis of TPA starting from anthranilic acid (**Scheme 1 B**).[33,34] The authors took advantage of a stoichiometric Ullmann-coupling reaction[35] to obtain diphenyl amine precursor (***b***) in quantitative yield by reacting the anthranilic acid potassium salt (***a***) with bromobenzene. The triphenylamine precursor (***c***) was subsequently synthetized by the reaction of diphenylamine with four-fold excess of iodobenzene also in high yield. Finally, the decarboxylation of TPA carboxylic acid resulted in pristine TPA in 8% yield.

ii. Modern Methodologies

The classic Ullmann reaction required the use of stoichiometric amount of copper and quite harsh reaction conditions. Further developments of this methodology resulted in number of different varieties of this method, where the catalytic amount of copper(I) salts such as bromide or iodide and an appropriate ligand such as proline or phenantrhroline, were used to promote the coupling reaction.[36–38] This new copper-catalyzed Ullmann method allows one to

33. Goldberg, I. & Nimerovsky, M. Über Triphenylamin und Triphenylamin-carbonsäure. *Berichte der Dtsch. Chem. Gesellschaft* **40,** 2448–2452 (1907).
34. Goldberg, I. Ueber Phenylirungen bei Gegenwart von Kupfer als Katalysator. *Berichte der Dtsch. Chem. Gesellschaft* **39,** 1691–1692 (1906).
35. Ullmann, F. Ueber eine neue Bildungsweise von Diphenylaminderivaten. *Berichte der Dtsch. Chem. Gesellschaft* **36,** 2382–2384 (1903).
36. Gorvin, J. H. The synthesis of di- and tri-arylamines through halogen displacement by base-activated arylamines: comparison with the Ullmann condensation. *J. Chem. Soc. Perkin Trans. 1* 1331 (1988). doi:10.1039/p19880001331
37. Ma, D., Cai, Q. & Zhang, H. Mild Method for Ullmann Coupling Reaction of Amines and Aryl Halides. *Org. Lett.* **5,** 2453–2455 (2003).
38. Cho, S. H., Kim, J. Y., Kwak, J. & Chang, S. Recent advances in the transition metal-catalyzed twofold oxidative C–H bond activation strategy for C–C and C–N bond formation. *Chem. Soc. Rev.* **40,** 5068 (2011).

obtain substituted di- and triphenylamines in high yields under mild reaction conditions (**Figure 7**).

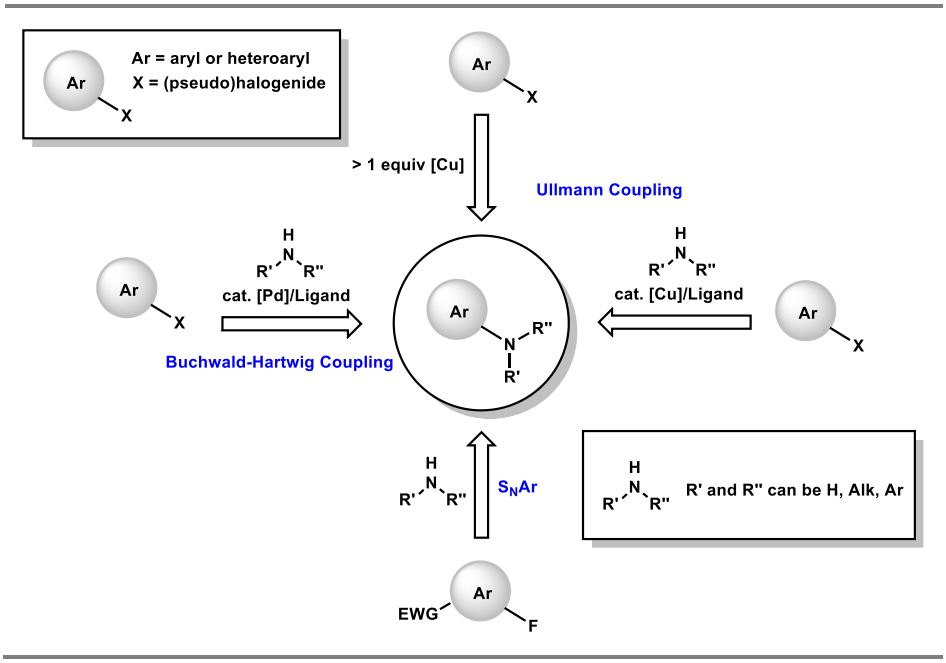

Figure 7 | Summary of modern triarylamine synthesis methods.

Simultaneous development of a palladium catalysed coupling by Buchwald[39] and Hartwig[40] in the 1990s extended the scope of the synthetic methodologies for the aromatic amine synthesis. Various di- and triarylamine derivatives can be synthetized starting from anilines and diphenylamines and aryl halogenides using Buchwald-Hartwig procedure. The use of sterically hindered ligands such as BINAP or DPPF favours the formation of diarylamines in comparison with relatively small ligands such as *tert*-butyl phosphine for example. Some recent reports propose to use cheaper nickel[41] or iron[42] catalyst instead of expensive palladium.

Another very useful method for the synthesis of triarylamines is the aromatic nucleophilic substitution (S_NAr) of a fluorine atom in fluorobenzenes substituted in *p*-position with EWGs such as nitro or cyano-. Starting from *p*-phenylenediamine and *p*-fluoronitrobenzene the triarylamine core is obtained in high yield.[43]

39. Guram, A. S. & Buchwald, S. L. Palladium-Catalyzed Aromatic Aminations with in situ Generated Aminostannanes. *J. Am. Chem. Soc.* **116,** 7901–7902 (1994).
40. Paul, F., Patt, J. & Hartwig, J. F. Palladium-catalyzed formation of carbon-nitrogen bonds. Reaction intermediates and catalyst improvements in the hetero cross-coupling of aryl halides and tin amides. *J. Am. Chem. Soc.* **116,** 5969–5970 (1994).
41. Ackermann, L., Sandmann, R. & Song, W. Palladium- and Nickel-Catalyzed Aminations of Aryl Imidazolylsulfonates and Sulfamates. *Org. Lett.* **13,** 1784–1786 (2011).
42. Hatakeyama, T. *et al.* Iron-Catalyzed Aromatic Amination for Nonsymmetrical Triarylamine Synthesis. *J. Am. Chem. Soc.* **134,** 20262–20265 (2012).
43. Różalska, I., Kułyk, P. & Kulszewicz-Bajer, I. Linear 1,4-coupled oligoanilines of defined length: preparation and spectroscopic properties. *New J. Chem.* **28,** 1235 (2004).

iii. Reaction Mechanism

The proposed catalytic cycles for both Ullmann and Buchwald-Hartwig metal-catalysed reactions are represented in **Figure 8**. Despite the Ullmann amination reaction being developed more than a century ago, there is still ongoing debate concerning its mechanism.[44,45] Generally, however, it is agreed that the modified Ullmann reaction mechanism implies: (***i***) coordination of the nucleophile to the copper, promoted by the deprotonation of former, followed by (***ii***) the oxidative addition of the aryl halogenide, with a subsequent (***iii***) reductive elimination resulting in the desired arylamine and recovered copper halide. Usually, this reaction requires the use of appropriate ligands, so that the active catalyst exists in a coordinated state. Some authors believe that the oxidation state of copper after the addition of aryl-halide is III,[44] while others argue that it is II.[45]

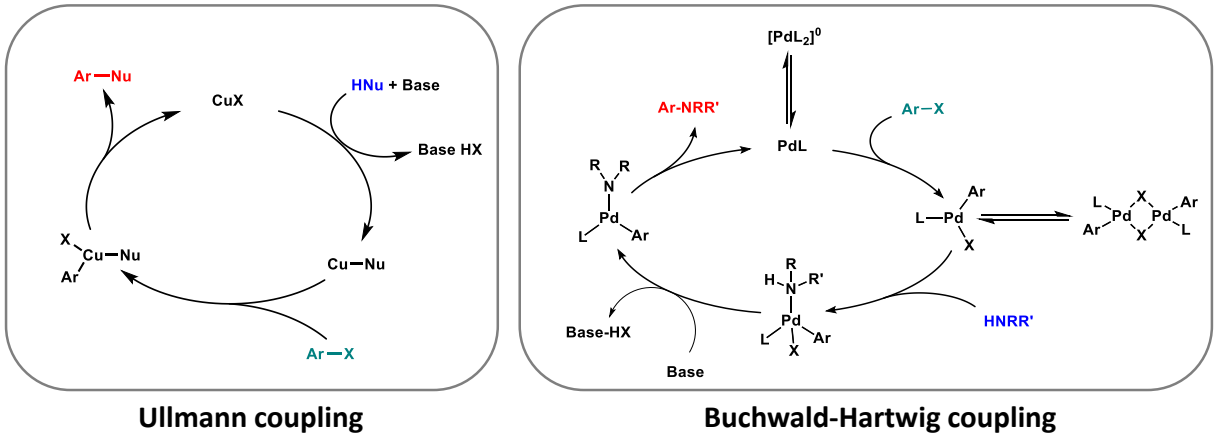

Figure 8 | Proposed mechanisms for the modern Ullmann coupling and palladium catalised Buchwald-Hartwig coupling reactions of aromatic amine formation.

The mechanism of palladium catalysed Buchwald-Hartwig reaction is similar to some extent to the modern Ullmann reaction. It consists of the following steps: (***i***) oxidative addition of the arylhalide to the active catalytic Pd^0L species, (***ii***) amine coordination followed by the deprotonation of the amine, and subsequent (***iii***) reductive elimination producing an active catalyst and the desired arylamine. The oxidation state of palladium after the oxidative addition is believed to be II.

44. Sperotto, E., van Klink, G. P. M., van Koten, G. & de Vries, J. G. The mechanism of the modified Ullmann reaction. *Dalt. Trans.* **39,** 10338 (2010).
45. Sambiagio, C., Marsden, S. P., Blacker, A. J. & McGowan, P. C. Copper catalysed Ullmann type chemistry: from mechanistic aspects to modern development. *Chem. Soc. Rev.* **43,** 3525 (2014).

B. Structure and Properties of Triarylamines

i. Structure of Triarylamines

The structure of triarylamines, in general, and pristine triphenylamine, in particular, is a very interesting subject from a fundamental point of view (see **Figure 9**).[46] According to the general assumption, TPA molecules should have a C_3-cymmetry, similarly to the analogous triphenylarsine for example[47] or trimethylamine (**Figure 9C**).

However, unlike its analogues,[48] the geometry around the nitrogen atom in the triphenylamine in the solid state was found to be almost planar (**Figure 9B**). Single crystal X-ray diffraction revealed a CNC valence angle of 119.6° and 119.9° for triphenyl- and tri-*p*-tolyl- amines respectively, which are very close to the value for the valence angle of 120° corresponding for the sp^2-hybridization of the central atom.[47,49] Although Sasaki *et al.* in 1959 reported the value of the valence angle of 116±2°,[46,50] recent studies of the TPA structure by electron diffraction in the gas phase[51] and the vibrational spectroscopy in the argon matrix[52] together with a number of computational studies confirmed the almost planar structure of TPA giving a CNC angle of 119.9°.

The dihedral angles in the TPA molecule $\tau(l_pNC^3C^4)$ (see **Figure 9B**) describing the conformation of the phenyl rings relative to the C_3-axis of the molecule were found to be 47.8°, suggesting a propeller-like structure of the TPA. Volden and co-workers performed the DFT calculations of the conformer energy change depending on the dihedral angle of the phenyl rings, when transforming from *Δ*-propeller to *Λ*-propeller configurations *via* different pathways (**Figure 9E,F**).[51] Diagram (**i**) on **Figure 9F** represents the conformer energy change (white circles) and the l_pNC^3 angle change depending on the dihedral angle $\tau(l_pNC^3C^4)$ for the transition **I-II-I'**, showing the two energy minima, corresponding to the propeller like conformations **I** and **I'** and a local maximum corresponding to a conformation **II**. Diagram **ii** of the same figure represents the energy change for the second transition **I-III-I'**, imposing a C_2-symmetry on the TPA molecule with a C_2-axis passing through one of the phenyl rings and

46. Sasaki, Y., Kimura, K. & Kubo, M. Electron Diffraction Investigation of Triphenylamine. *J. Chem. Phys.* **31,** 477 (1959).
47. Sobolev, A. N., Belsky, V. K., Romm, I. P., Chernikova, N. Y. & Guryanova, E. N. Structural investigation of the triaryl derivatives of the Group V elements. IX. Structure of triphenylamine, C18H15N. *Acta Crystallogr. Sect. C Cryst. Struct. Commun.* **41,** 967–971 (1985).
48. The trigonal pyramid geometry of a trimethylamine is a result of sp^3-hybridisation of electron orbitals of a nitrogen atom giving the C-N-C angle of approximately 111°. The pyramidal structure of a C_3-symmetry analogues of the 15th group of elements (PX_3, AsX_3, *etc.*) is a result of so called p^3-hybridisation, which means that only *p*-orbitals take part in the formation of a chemical bonds, hence the valence bond is closer to 90°.(**Figure 9D**)
49. Wang, B.-C., Liao, H.-R., Chang, J.-C., Chen, L. & Yeh, J.-T. Electronic structure and molecular orbital study of hole-transport material triphenylamine derivatives. *J. Lumin.* **124,** 333–342 (2007).
50. Kemmitt, R. D. W., Nuttall, R. H. & Sharp, D. W. A. 10. The basic properties, infrared spectra, and structures of triphenylamine and tri-p-tolylamine. *J. Chem. Soc.* 46 (1960). doi:10.1039/jr9600000046
51. Naumov, V. A., Samdal, S., Naumov, A. V., Gundersen, S. & Volden, H. V. Molecular Structure of Triphenylamine in the Gas Phase. *Russ. J. Gen. Chem.* **75,** 1956–1961 (2005).

one CN bond. These peculiar structural features of TPA are largely extended to the whole family of triarylamines, which might be a cause of their remarkable electronic properties such as conductivity, charge and energy transfer.

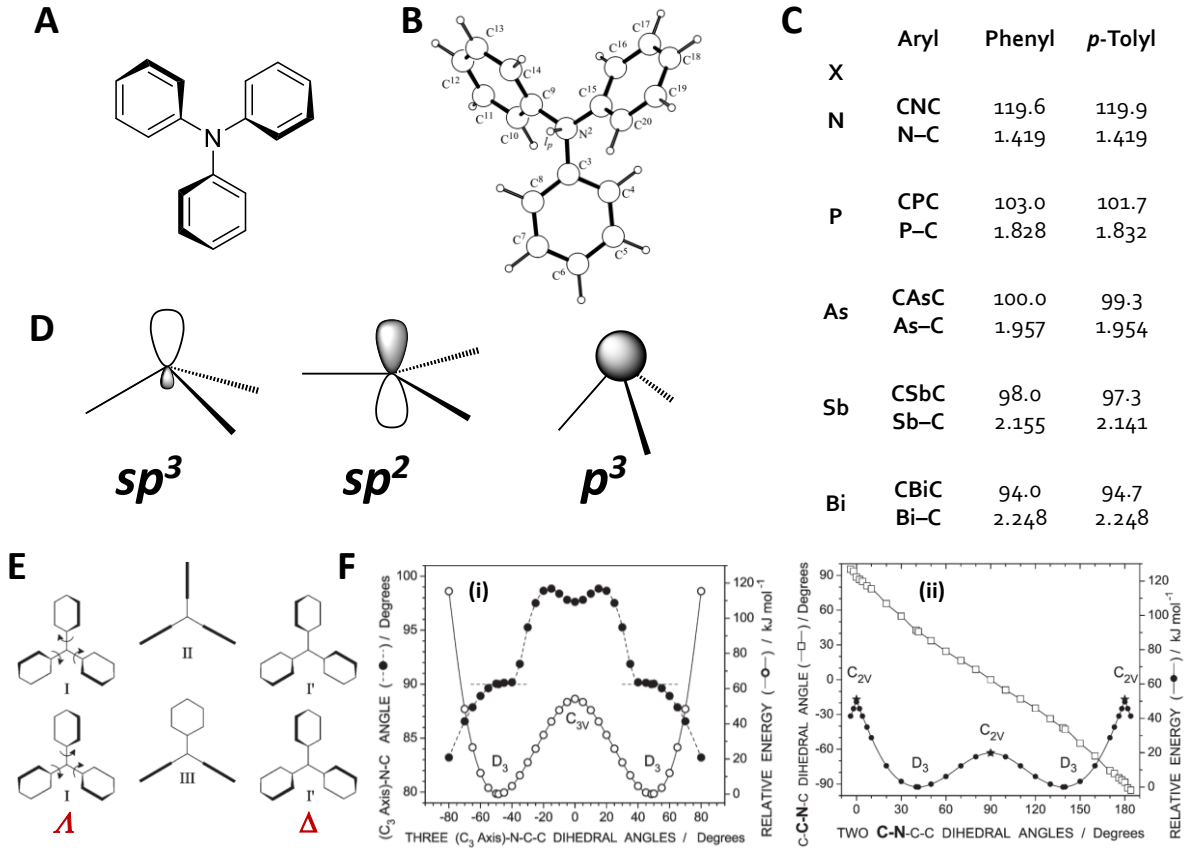

X	Aryl	Phenyl	*p*-Tolyl
N	CNC	119.6	119.9
	N–C	1.419	1.419
P	CPC	103.0	101.7
	P–C	1.828	1.832
As	CAsC	100.0	99.3
	As–C	1.957	1.954
Sb	CSbC	98.0	97.3
	Sb–C	2.155	2.141
Bi	CBiC	94.0	94.7
	Bi–C	2.248	2.248

Figure 9 | Structural parameters of triphenylamine. (**A**) Chemical structure of TPA. (**B**) Conformation of TPA determined using DFT calculations in the gase phase.[51] (**C**) Experimental data for Ar_3X TPA analogs (where *X* is a 15 group element) representing *CXC* angle and *X–C* distance.[47,53] (**D**) Molecular geometries of EXA_3-type of molecules resulted from the orbital hybridizetion: sp^3, sp^2 and p^3 hybridizations (*X–A* bonds are represented as solid lines, electron pair *E*, is represented as an orbital). (**E**) Possible pathways for transformation of TPA from the minimum energy structure **I** to its mirror-like counter-part **I'**. (**F**) Calculated relative energies of the TPA conformers depending on the dihedral CNCC angles for (**i**) **I-II-I'** transition and (**ii**) for **I-III-I'** transition.[52] Figure is adapted form refs.51, 52

52. Reva, I., Lapinski, L., Chattopadhyay, N. & Fausto, R. Vibrational spectrum and molecular structure of triphenylamine monomer: A combined matrix-isolation FTIR and theoretical study. *Phys. Chem. Chem. Phys.* **5,** 3844–3850 (2003).
53. Adams, E. A., Kolis, J. W. & Pennington, W. T. Structure of triphenylstibine. *Acta Crystallogr. Sect. C Cryst. Struct. Commun.* **46,** 917–919 (1990).
54. Cauquis, G. & Serve, D. Anodic voltammetry of some aromatic amines in chloroform. Absorption spectra and association phenomena of the corresponding cation radicals. *Anal. Chem.* **44,** 2222–2224 (1972).
55. Cauquis, G., Delhomme, H. & Serve, D. Les proprietes electrochimiques des diphenylamines et de leurs produits d'oxydation en milieu organique—III. Les diphenylamines p.p′-disubstituees et l'evolution de leur radical cation primaire. *Electrochim. Acta* **21,** 557–565 (1976).
56. Schmidt, W. & Steckhan, E. Über organische Elektronenüberträgersysteme, I. Elektrochemische und spektroskopische Untersuchung bromsubstituierter Triarylamin-Redoxsysteme. *Chem. Ber.* **113,** 577–585 (1980).
57. Dapperheld, S., Steckhan, E., Brinkhaus, K.-H. G. & Esch, T. Organic Electron Transfer Systems, II Substituted Triarylamine Cation-Radical Redox Systems – Synthesis, Electrochemical and Spectroscopic Properties, Hammet Behavior, and Suitability as Redox Catalysts. *Chem. Ber.* **124,** 2557–2567 (1991).
58. Seo, E. T. *et al.* Anodic Oxidation Pathways of Aromatic Amines. Electrochemical and Electron Paramagnetic Resonance Studies. *J. Am. Chem. Soc.* **88,** 3498–3503 (1966).

ii. Redox and Optical Properties of Triarylamines

Numerous experimental and theoretical investigations of the electrochemical properties of triarylamines have been reported since the1960s.[54–64] For instance, Lambert and colleagues carried out a systematic study of the oxidation potentials and optical properties of different symmetrically and asymmetrically *p*-substituted triarylamines (**Table** 2**, Figure** 10).[59]

Table 2 | Structure of TAAs with different substituents at the *p*-position and their corresponding half-wave oxidation potentials and absorption maxima for neutral and radical cation molecules. Data reproduced from ref. 59

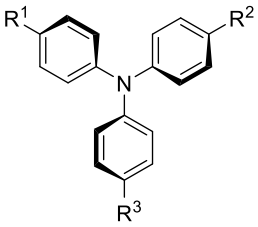

Compound	R_1	R_2	R_3	$E_{1/2}^{ox}$, mV in DCM	UV-vis data in MeCN (DCM), λ_{max}, nm (neutral TAA)	UV-vis data in MeCN, λ_{max}, nm ($TAA^{\bullet+}$)
(*a*)	*OMe*	*OMe*	*OMe*	109	296 (300)	718; 633
(*b*)	*Me*	*Me*	*Me*	332	299 (303)	667; 576
(*c*)	*Me*	*OMe*	*OMe*	180	296 (300)	725; 590
(*d*)	*Me*	*Cl*	*Cl*	576	301 (304)	681; 573
(*e*)	*OMe*	*Me*	*Me*	250	297 (301)	706; 575
(*f*)	*OMe*	*Cl*	*Cl*	463	300 (302)	717; 578
(*g*)	*Cl*	*Me*	*Me*	460	299 (302)	677; 569
(*h*)	*Cl*	*OMe*	*OMe*	290	294 (300)	748; 590
(*i*)	*Cl*	*Cl*	*Cl*	691	304 (307)	684; 590
(*j*)	*Cl*	*OMe*	*Me*	359	296 (300)	715; 578

59. Amthor, S., Noller, B. & Lambert, C. UV/Vis/NIR spectral properties of triarylamines and their corresponding radical cations. *Chem. Phys.* **316,** 141–152 (2005).
60. Yurchenko, O. *et al.* Electrochemically Induced Reversible and Irreversible Coupling of Triarylamines. *J. Phys. Chem. B* **116,** 30–39 (2012).
61. Cias, P., Slugovc, C. & Gescheidt, G. Hole Transport in Triphenylamine Based OLED Devices: From Theoretical Modeling to Properties Prediction. *J. Phys. Chem. A* **115,** 14519–14525 (2011).
62. Murata, H. & Lahti, P. M. Synthesis and oxidation of triarylamine derivatives bearing hydrogen-bonding groups. *J. Org. Chem.* **72,** 4974–7 (2007).
63. Pan, J.-H., Chiu, H.-L., Chen, L. & Wang, B.-C. Theoretical investigations of triphenylamine derivatives as hole transporting materials in OLEDs: Correlation of the Hammett parameter of the substituent to ionization potential, and reorganization energy level. *Comput. Mater. Sci.* **38,** 105–112 (2006).
64. Yuan Chiu, K. *et al.* Novel trends of electrochemical oxidation of amino-substituted triphenylamine derivatives. *J. Electroanal. Chem.* **575,** 95–101 (2005).

Cyclic voltammetry, performed on triarylamines in dichloromethane, revealed one reversible oxidation process corresponding to the one electron oxidation of the neutral TAA to its radical cation. The second oxidation peak, corresponding to further oxidation of the radical cation into a dicationic form, was observed only for tri-*p*-anysilamine (***a***) (**Figure** 10**A**).[59] The redox potentials $E_{1/2}$ of the first oxidation wave are summarized in **Table** 2**.** As expected, electron withdrawing substituents such as chlorine atoms shift the redox potential to higher values (691 mV) while the electron donating methoxy substituents shift it to lower values (109 mV) compared to alkyl substituents (332 mV) for symmetrically substituted TAAs. Interestingly, the authors noticed that the relationship between the position of a first oxidation peak ($E_{1/2}$ (**I**)) and the number of chlorine and methoxy substituents in the TAA can be described by an empirical linear equation:

$$E_{\frac{1}{2}}(I) \approx 332 + 110 \times n(Cl) - 75 \times n(OMe) \qquad \textbf{(1)}$$

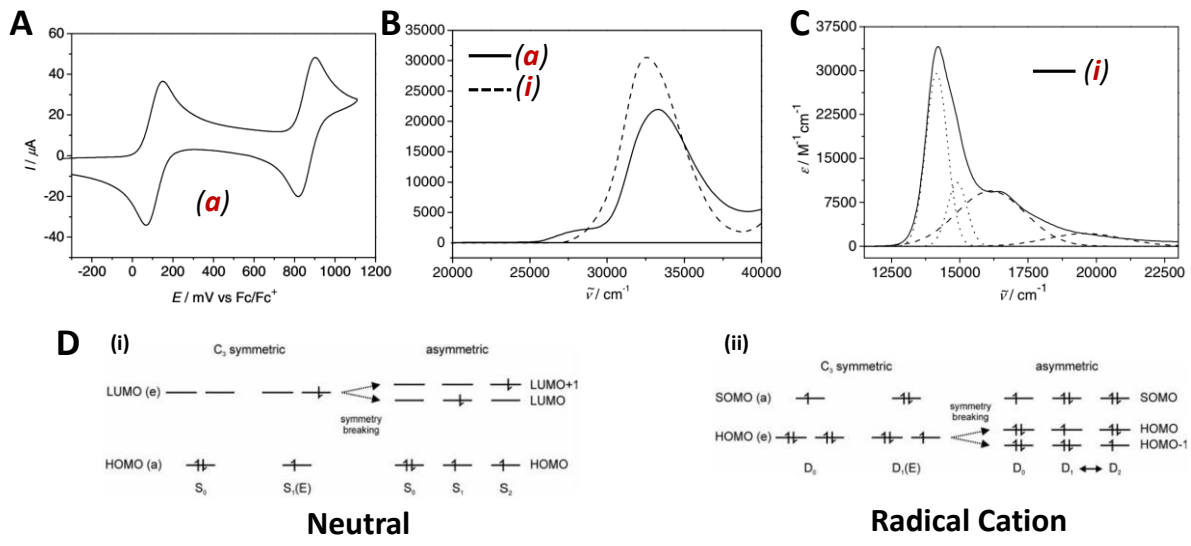

Figure 10 | (**A**) Cyclic voltammograms in dichloromethane (TBAH) at *v* = 250 mV·s^{-1} with redox potentials $E_{1/2}$ of 109 and 860 mV *vs* Fc/Fc^{+}. (**B**) UV/Vis absorption spectra of TAAs ***a*** and ***i*** in dichloromethane. (**C**) Experimental spectrum of ***a*** $^{\bullet+}$ and ***i*** $^{\bullet+}$ in dichloromethane, deconvolution by four Gaussian functions ($D_0 \rightarrow D_1$ dotted lines, $D_0 \rightarrow D_2$ dashed lines). (**D**) (**i**) Configuration diagram for the ground state and excited state of a neutral symmetric TAA and the ground state and excited states of an asymmetric TAA. (**ii**) Configuration diagram for the ground state and excited state of a symmetric TAA$^{\bullet+}$ radical cation and the ground state and excited states of an asymmetric TAA$^{\bullet+}$ radical cation. Figure is adapted from ref. 59

The absorption spectra of neutral TAAs (***a***) and (***i***), recorded in dichloromethane, are shown in **Figure 10B**. They are typical of the triarylamine family and have one intense absorption maximum near 300 nm (33 000 – 34 000 cm^{-1}). The substitution of the methyl

groups in tri-*p*-tolylamine by more electron acceptor chlorine groups causes a bathochromic shift of the absorption maximum, while the substitution with electron donating methoxy function leads to a hypsochromic shift.

The absorption spectra of neutral TAAs can be explained by a single π-π^* electron transition localised on the phenyl rings: HOMO → LUMO ($S_0 \rightarrow S_1$) into a degenerate (E) S_1 state **Figure 10D(i)**. However, for the dissymmetrical TAAs the degenerate state splits into two, resulting in the appearance of two transitions: HOMO → LUMO ($S_0 \rightarrow S_1$) and HOMO → LUMO+1 ($S_0 \rightarrow S_2$).

The typical absorption spectra of TAA radical cations are characterised by three absorptions: the first, very intense one is around 670 – 730 nm (13 000 – 14 990 cm^{-1}) and a second one, less intense near 570 – 630 nm (15 300 – 17 570 cm^{-1}). The third, high-energy absorption is situated in the blue region around 350 nm. The energy of the main electron transition for the radical cation is lower in comparison with the neutral molecule. The absorption spectrum of TAA (***a***) radical cation is represented in **Figure 10C** with the Gaussian fit of the corresponding bands. The absorption of the radical cation can be explained by the electron transition HOMO → SOMO ($D_0 \rightarrow D_1$), where the D_1 state is degenerated in the case of C_3-symmetrical molecules and splits into two states with the corresponding transitions: HOMO → SOMO ($D_0 \rightarrow D_1$) and HOMO-1 → SOMO ($D_0 \rightarrow D_2$) (**Figure 10D(ii)**). This can explain the presence of two absorption maxima in the spectra of dissymmetric TAAs. For symmetric molecules, which also exhibit similar optical properties, the authors suggest a possible C_3-symmetry breaking caused by to the interaction with solvent and/or planarization of the radical cation similar to the structure **III** in **Figure 9E**, which results in the appearance of two absorptions.

The fluorescent properties of various TAAs were studied by the group of Audebert.[65,66] The typical absorption and emission spectra of TAAs are represented in **Figure 11A** for TAA (***a***) in acetonitrile. The observed emission spectrum is a mirror image of the absorption one, with the emission maxima at 384 nm (Stokes shift 101 nm).[67] The quantum yield of fluorescence (Φ) measured compared to quinine sulphate was found to be 0.06 for (***a***) with a lifetime (τ) of 3.6 ns. The extension of the aromatic system by the insertion of the

65. Quinton, C. *et al.* Redox-controlled fluorescence modulation (electrofluorochromism) in triphenylamine derivatives. *RSC Adv.* **4,** 34332 (2014).
66. Quinton, C. *et al.* Design of New Tetrazine-Triphenylamine Bichromophores - Fluorescent Switching by Chemical Oxidation. *European J. Org. Chem.* **2012,** 1394–1403 (2012).
67. We should mention that the position of the absorption maximum for the tri-*p*-methoxyphenylamine reported by Audebert[65] (283 nm) is somehow lower values reported by group of Lambert[59]and group of Gopidas[69] (both reported 296 nm for the absorption maximum of the neutral TAA).

phenyl group between the methoxy substituent and the triarylamine core leads to a dramatic increase of quantum yield up to 0.37.

The influence of oxidation of the TAA on the fluorescence was also studied. The oxidation was carried out in acetonitrile solutions using copper(II) perchlorate as a mild electron oxidant.[68] The titration UV-Vis and fluorescent spectra are reported on **Figure 11B,C**. Upon addition of Cu^{2+} the intense bands, corresponding to the radical cation appeared in the UV-Vis spectra (360 nm and 706 nm). The maximum intensity was reached when 1.5 equivalents of added Cu^{2+}. The fluorescence intensity gradually decreased upon oxidation, however there was no influence on the quantum yield nor the lifetime. The authors suggest that these redox controlled absorption and fluorescent properties of triarylamines can be used in electrochromic devices.

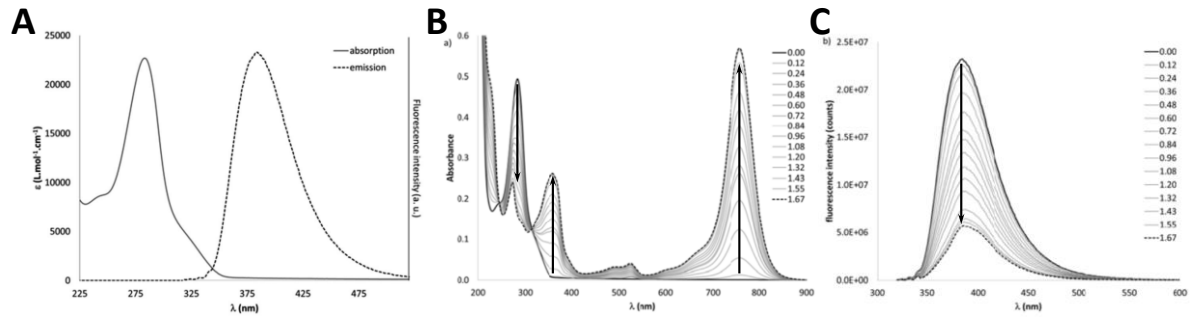

Figure 11 | (**A**) Absorption (solid line) and emmission (dash line) spectra of *p*-methoxy-substituted TAA in acetonitrile (λ_{ex} = 309 nm). (**B** and **C**) Absorption and fluorescence spectra of ***a*** respectively, recorded in acetonitrile, upon addition of Cu^{2+} salt as an oxidant. Arrows represent the intensity change. Figure is adapted from ref. 65

Interestingly, although the redox potential of the Cu^{2+}/Cu^{+} system is lower than the second redox potential of the tri(*p*-anisyl)amine (***a***), meaning that the oxidation process in energetically unfavoured, Gopidas and co-workers reported on oxidation of the triarylammonium radical cation into its dication by using copper(II) perchlorate in acetonitrile solutions (**Figure 12A**).[69,70] Starting the titration of the neutral colourless solution of TAA in acetonitrile, the authors observed the expected behaviour: the decrease of the absorption band corresponding to the neutral triarylamine at 296 nm and the increase of the bands corresponding to the radical cation at 717 nm, maximum intensity was reached when the amount of added copper(II) was near one equivalent (**Figure 12B(i)**). Further addition of the

68. The redox potential of Cu^{2+}/Cu^{+} couple in acetonitrile is 600 mV *vs* Fc/Fc^{+}.
69. Sreenath, K., Thomas, T. G. & Gopidas, K. R. Cu(II) mediated generation and spectroscopic study of the tris(4-anisyl)amine radical cation and dication. Unusually shielded chemical shifts in the dication. *Org. Lett.* **13,** 1134–7 (2011).
70. Sreenath, K., Suneesh, C. V., Gopidas, K. R. & Flowers, R. a. Generation of triarylamine radical cations through reaction of triarylamines with Cu(II) in acetonitrile. A kinetic investigation of the electron-transfer reaction. *J. Phys. Chem. A* **113,** 6477–83 (2009).

Cu^{2+} results in the decrease of the band at 717 nm and the appearance of a broad absorption band at 520 nm, leading to its maximal intensity when two equivalents of copper(II) was added together with the full disappearance of the 717 nm band. The newly appeared band at 520 nm corresponds to a dication triarylamine form. Remarkably, while the TAA → $TAA^{\bullet+}$ oxidation was almost immediate, the further oxidation $TAA^{\bullet+}$ → TAA^{2+} was relatively slow, so that each spectrum in plot (**ii**) in **Figure 12B** was recorded 30 min after Cu^{2+} addition. The change in colour of the TAA solution upon oxidation is depicted on **Figure 12C** passing from colourless (neutral TAA) to intense blue (radical cation TAA) to pink-red (dication TAA).

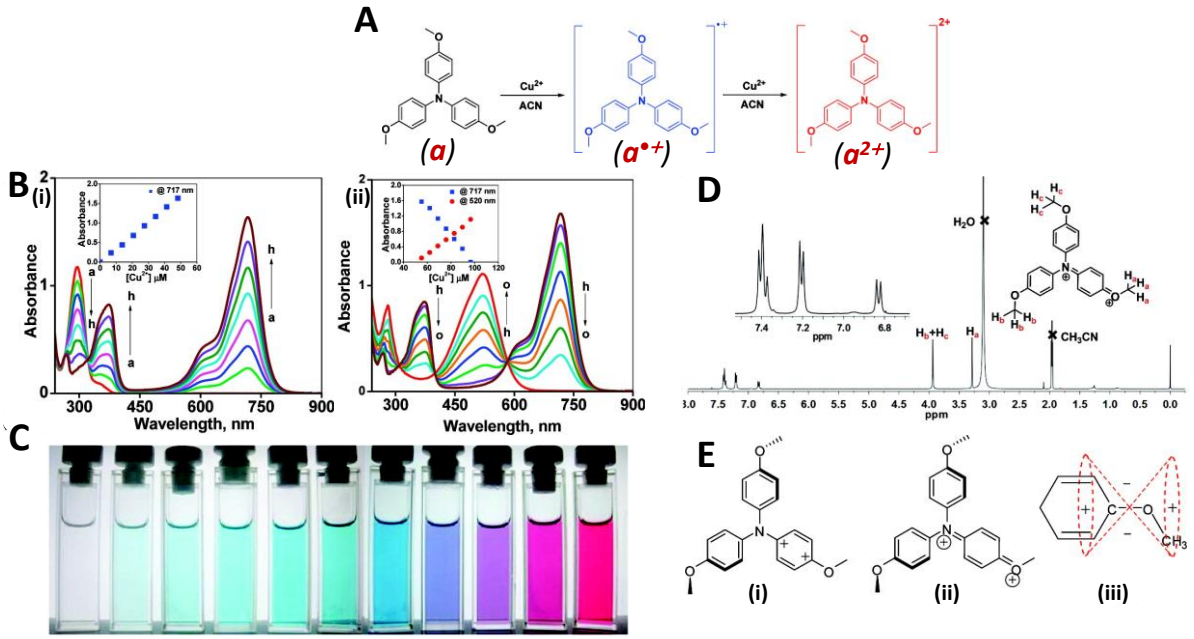

Figure 12 | (**A**) The reaction of TAA (***a***) with Cu^{2+} ion leading to the formation of the TAA radical cation and dication. (**B**) UV-Vis spectroscopy studies of the effect of adding $Cu(ClO_4)_2$ to TAA (5×10^{-5} M) in acetonitrile; (**i**) a-h, [Cu^{2+}] varied from 0 to 1 equiv. (**ii**) h-o, [Cu^{2+}] varied from 1 to 2 equiv. Insets show variations of absorbances as a function of [Cu^{2+}]. (**C**) Change of colors in the reaction of TAA-***a*** (5×10^{-5} M) with Cu^{2+}. Cu^{2+} concentrations were 0, 0.2, 0.4, 0.6, 0.8, 1.0, 1.2, 1.4, 1.6, 1.8, and 2.0 equiv. (**D**) ^{1}H-NMR spectra of TAA^{2+} (recorded at 263 K) in acetonitrile. (**E**) Possible structures of TAA^{2+}. Figure is adapted from ref. 69

Interestingly, when neutral TAA was added to a solution of the dication the band at 520 nm disappeared with a simultaneous appearance of a band at 717 nm following the reaction:

$$TAA^{2+} + TAA \rightarrow 2TAA^{\bullet+} \qquad \textbf{(2)}$$

Another interesting observation was done by using ^{1}H NMR spectroscopy (**Figure 12D**). The resonance signals of dicationic TAA were well defined, unlike in the case of

radical cation which, due to the spin-spin relaxation, has extremely broad signals. In comparison with a symmetrical neutral molecule, which has three signals in ^{1}H-NMR, the symmetry of dicationic TAA is broken, as can be deduced from the splitting of the NMR signals in two groups. This effect can be possibly explained by the formation of resonant structures **i** and **ii** represented on **Figure 12E.** Furthermore, unexpectedly, one of the signals corresponding to the methoxy group, as well to one of the phenyl rings were shifted up-field. The authors suggest that this peculiarity can be explained by the inversion of magnetic susceptibility, causing the shielding effect on the groups situated in the positive region of the magnetic anisotropy conus (**Figure 12E(iii)**).

The understanding of the structure-properties relationship is crucial for the design of TAAs with expected electronic behaviour and thus their use in various devices such as solar cells or OLEDs. Cias *et al*. reported on the theoretical studies of various parameters, such as geometry, energies of HOMO and LUMO, redox potentials and hole transporting properties for TAAs with different electron donor and electron acceptor substituents, covering a broad range of Hammett parameters from –NH_2 to –NO_2 groups (**Figure 13**).[61]

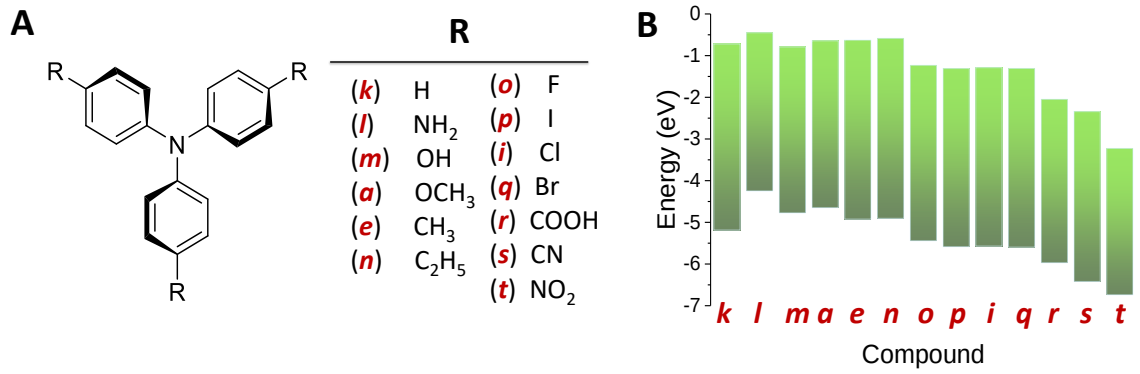

Figure 13 | (**A**) Structure of TAAs with different *p*-substituents R. (**B**) Corresponding calculated HOMO-LUMO energy levels reported by Cias *et al.*[61]

From the diagram **Figure 13B** it is clear that the HOMO energy level increases with the increase of electron donating properties of the substituents from -6.74 eV to -4.25 eV for the nitro and amino substituted TAAs respectively (causing the decrease of the ionisation potential).[71] This effect can be explained by the increase of the electron density in the aromatic system with donor substituents and a decrease with acceptor substituents. The same trend is observed for the LUMO energy levels. Interestingly, the HOMO-LUMO gap changes

71. Almost linear relationship between the Hammett parameters of the substituents and the HOMO level (ionization potential) is observed.

with the substituent change, however the dependence in this case is more related to the absolute value of the Hammett parameter of the substituents: the biggest change in the HOMO-LUMO gaps, in comparison with non-substituted TPA, is observed for the substituents with both the strongest electron donor and acceptor properties, such as nitro (***t***), cyano (***s***), amino (***l***), methoxy (***a***) and hydroxyl (***m***).

iii. Oxidation of Aromatic Amines in Chlorinated Solvents

Previous examples demonstrate the possibility to generate oxidized states of TAAs by electrochemical methods as well as by using appropriate chemical oxidants, such as copper(II). However, other non-invasive methods of radical cation synthesis exist in the literature, such as radiation induced oxidation[72–74] or photo-oxidation.[75–80] Recently, our group took advantage of the light-induced oxidation of triarylamines to trigger the self-assembly process in chloroform leading to the formation of highly conducting nanowires.[81–83] This light-triggered self-assembly process is governed by two distinct processes: (***i***) photo-oxidation of triarylamine and (***ii***) cooperative self-assembly. We will describe the first step (photo-oxidation) in this section, leaving the explanation of the second step (self-assembly) to the following section.

The photosensitisation of aromatic amines was intensively studied in the 1960s. For instance, Meyer reported on the study of the photo-oxidation of the N,N,N',N'-tetramethyl-*p*-phenylenediamine in various solvents, covering a broad range of dielectric constants from acetonitrile (ε = 37.5) to dichloromethane (ε = 9.1) and toluene (ε = 2.4) (see **Table S1** in

72. Maroz, A., Hermann, R., Naumov, S. & Brede, O. Ionization of Aniline and Its N -methyl and N -phenyl Substituted Derivatives by (Free) Electron Transfer to n -butyl Chloride Parent Radical Cations. *J. Phys. Chem. A* **109,** 4690–4696 (2005).
73. Brede, O., Maroz, A., Hermann, R. & Naumov, S. Ionization of cyclic aromatic amines by free electron transfer: Products are governed by molecule flexibility. *J. Phys. Chem. A* **109,** 8081–8087 (2005).
74. Han, J.-M. M. *et al.* γ radiation induced self-assembly of fluorescent molecules into nanofibers: a stimuli-responsive sensing. *J. Mater. Chem. C* **3,** 4345–4351 (2015).
75. Richtol, H. H., Fitzgerald, E. A. & Wuelfing, P. Photochemical oxidation of some substituted aromatic amines in chloroform. *J. Phys. Chem.* **75,** 2737–2741 (1971).
76. Meyer, W. C. Halogen-sensitized photoionization of N,N,N',N'-tetramethyl-p-phenylenediamine in liquid halomethanes. *J. Phys. Chem.* **74,** 2118–2121 (1970).
77. Wyrzykowska, K., Grodowski, M. & Wen, K. MECHANISM OF THE PHOTOCHEMICAL REACTION OF DIPHENYLAMINES WITH CARBON. 192–193 (1978).
78. Meyer, W. C. Halogen-sensitized photoionization of aromatic amines in molded polymer films. *J. Phys. Chem.* **74,** 2122–2126 (1970).
79. Meyer, W. C. Correlation of the luminescence perturbation of N,N,N',N'-tetramethyl-p-phenylenediamine with the path of halogen-sensitized photoionization. *J. Phys. Chem.* **74,** 2127–2132 (1970).
80. Budyka, M. F. & Alfimov, A. V. Photochemical Reactions of Complexes of Aromatic Amines with Polygalomethanes. *Russ. Chem. Rev.* **64,** (1995).
81. Moulin, E. *et al.* The Hierarchical Self-Assembly of Charge Nanocarriers: A Highly Cooperative Process Promoted by Visible Light. *Angew. Chem. Int. Ed.* **49,** 6974–6978 (2010).
82. Faramarzi, V. *et al.* Light-triggered self-construction of supramolecular organic nanowires as metallic interconnects. *Nat. Chem.* **4,** 485–490 (2012).
83. Nyrkova, I. *et al.* Supramolecular self-assembly and radical kinetics in conducting self-replicating nanowires. *ACS Nano* **8,** 10111–10124 (2014).
84. The polarity of solvents generally plays an important role in the intermolecular electron transfer process.

annexes). The increased photoionization was observed for halogenated solvents such as chloroform, bromoform, *etc.* independently of their dielectric constant.[84]

One year later, the mechanism of the photo-oxidation of various primary, secondary and tertiary aromatic amines in chloroform was proposed by Richtol and collaborators (see **Figure S1** in annexes for structures of studied compounds).[75] It was found that, in chloroform, aromatic amines undergo a photo-oxidation using light with energies much lower than their ionization potentials 3.5 eV *vs* 6 – 7 eV respectively. The authors hypothesise that the key process of the photoinduced oxidation is the electron attachment reaction, the transfer of the electron onto the chloroform molecule, generating a chlorine anion and a dichloromethyl radical:

$$CHCl_3 + e^- \rightarrow CHCl_2^{\bullet} + Cl^- \qquad \textbf{(3)}$$

Importantly, it was found that the oxidation quantum yields depended on the oxygen concentration, showing a more than twofold increase in oxidation efficiency for air-saturated solutions in comparison with degassed ones, suggesting that it may play a role in the radical cascade process. The photo-oxidation performed in ethanol solutions with the addition of chloroform was also observed, with the rate depending on the amount of added chloroform. The main by-products of oxidation were found to be: H^+ ions (1 mole of H^+ per 1 mole of oxidized amine), phosgene, chloride anions (Cl^-) and ethyl formate (when ethanol was added to chloroform solution, suggesting the presence of formyl chloride). Based on these results the following oxidation mechanism was proposed:

$$\begin{gathered} A \xrightarrow{h\nu} {}^1A^* \\ {}^1A^* \rightarrow A + h\nu \\ {}^1A^* \rightarrow {}^3A^* \rightarrow A \\ {}^1A^* + CHCl_3 \rightarrow A^{\bullet+} + Cl^- + CHCl_2^{\bullet} \\ CHCl_2^{\bullet} + O_2 \rightarrow CHCl_2OO^{\bullet} \\ CHCl_2OO^{\bullet} \rightarrow CHClO + ClO^{\bullet} \\ CHClO \rightarrow HCl + CO \\ ClO^{\bullet} + CHCl_3 \rightarrow COCl_2 + HCl + Cl^{\bullet} \\ Cl^{\bullet} + A \rightarrow A^{\bullet+} + Cl^- \end{gathered} \qquad \textbf{(4)}$$

Where, after the photoexcitation, amine molecules transfer one electron to the chloroform molecule, thereby starting a radical cascade reaction.

iv. Triarylammonium Radical Cation Reactions

Another interesting aspect of the behaviour of triarylamine radical cations was discovered upon its electrochemical formation: the formation of dimers. Adams and colleagues reported that, upon CV studies of the redox process of pristine TPA in acetonitrile after several redox cycles, new redox peaks appeared, which corresponded to a different compound.[58] It was found that the TPA radical cation undergoes a fast dimerization forming a dicationic σ-dimer, which transforms into a tetraphenylbenzidine (TPB) after a loss of two protons (**Scheme 2**). The TBP in turn has a lower redox potential compared to TPA and easily undergoes two oxidations.

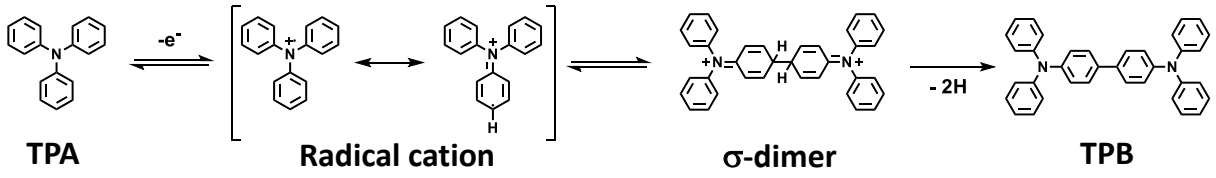

Scheme 2 | Scheme of pristine TPA oxidation into its radical cation, which can reversibly form a σ-dimer. The deprotonation of a later produces the tetraphenylbenzydin (TPB).[58]

TAAs with substituents in *p*-positions do not form stable dimers, however Ludwigs and co-workers demonstrated that they can readily form corresponding carbazoles *via* intramolecular radical recombination after the second oxidation step (**Scheme 3**).[60]

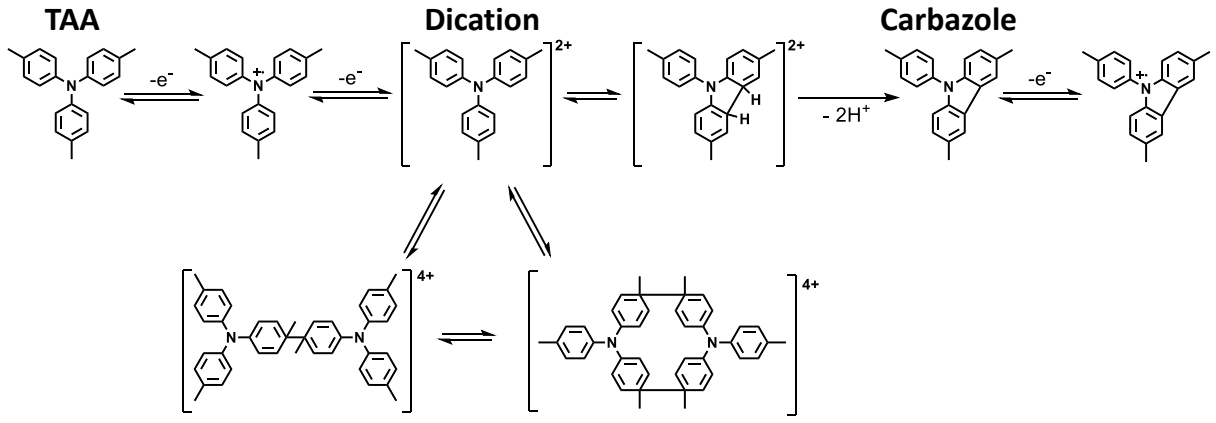

Scheme 3 | Reactional pathways occuring during the oxidation process of a TAA with *p*-substituents.[60]

This property of triarylamine radical cations to dimerise was exploited numerous times as a mild method to synthesize different benzidines and *p*-substituted (pseudo) halogenides of TAAs.[85]

85. Kirchgessner, M., Sreenath, K. & Gopidas, K. R. Understanding reactivity patterns of the dialkylaniline radical cation. *J. Org. Chem.* **71,** 9849–52 (2006).

v. Charge Transfer in Triarylamine Systems

In the previous section, we discussed the possible dimerization of the radical cation upon the oxidation of TAA. Interestingly, when corresponding TPB (**Scheme 1**) is oxidised to its radical cation, no characteristic absorption band around 720 nm is observed, but the instead an intense and broad band in near infra-red (NIR) region. This band corresponds to an intramolecular photoinduced inter-valance charge transfer (IVCT), which occurs in systems having chemically equivalent centres with different oxidation states. The photo-induced CT is a very fundamental natural process, which occurs in various living systems (photosynthetic systems for example)[86] and plays an important role in the electronic devices such as OLEDs, solar cells, OFETS *etc.* For his contribution to the study of electron transfer reactions in chemistry, Rudolph A. Marcus received the Nobel Prize in 1992.[87] Marcus' works were mainly focused on the intramolecular charge transfer in inorganic systems. The studies of CT in organic molecules began in recent decades, where the triarylamines, due to the high stability of their radical cations, play an important role in understanding of the IVCT.[88–93]

The group of Lambert extensively studies the intramolecular charge transfer in organic systems based on various molecules including triarylamines. **Figure 14** describes the CT phenomenon on the example of *p*-methoxytriarylamines (***a*** – ***c***) connected with linkers of different length.[91] After the single oxidation of the studied compounds to their corresponding radical cations, molecules with mixed-valence states were obtained (**Figure 14A**), in which two nitrogen centres are chemically identical, but have a different oxidation state. The UV-Vis-NIR spectroscopy in different solvents such as nitrobenzene, acetonitrile or dichloromethane revealed the appearance of broad bands in the NIR region for all of the compounds, indicating the existence of photoinduced intramolecular IVCT (**Figure 14B**).

Interestingly, molecules ***b*** and ***c*** showed the presence of the radical absorption band and a very broad IVCT band, with the position of the maxima depending strongly on the solvent polarity, which suggests a class II of the charge transfer systems, meaning that interaction between redox centres exists, however their position is rather localised. On the

86. Brettel, K. & Leibl, W. Electron transfer in photosystem I. *Biochim. Biophys. Acta - Bioenerg.* **1507,** 100–114 (2001).
87. The Nobel Prize in Chemistry 1992. at <http://www.nobelprize.org/nobel_prizes/chemistry/laureates/1992/index.html>
88. Lambert, C. & Nöll, G. The Class II/III Transition in Triarylamine Redox Systems. *J. Am. Chem. Soc.* **121,** 8434–8442 (1999).
89. Lambert, C. & Nöll, G. One- and Two-Dimensional Electron Transfer Processes in Triarylamines with Multiple Redox Centers. *Angew. Chem. Int. Ed.* **37,** 2107–2110 (1998).
90. Lambert, C., Nöll, G. & Schelter, J. Bridge-mediated hopping or superexchange electron-transfer processes in bis(triarylamine) systems. *Nat. Mater.* **1,** 69–73 (2002).
91. Lambert, C. *et al.* How fast is optically induced electron transfer in organic mixed valence systems? *Phys. Chem. Chem. Phys.* **18,** 19405–19411 (2016).
92. Heckmann, A. & Lambert, C. Organic Mixed-Valence Compounds: A Playground for Electrons and Holes. *Angew. Chem. Int. Ed.* **51,** 326–392 (2012).
93. Lambert, C. in *Organic Redox Systems* 245–268 (John Wiley & Sons, Inc, 2015). doi:10.1002/9781118858981.ch7

contrary, molecule ***a*** exhibits a relatively narrow intense charge transfer band with almost no solvent influence on its position, indicating fully delocalised nature of the radical. This is the class III of charge transfer systems.[94]

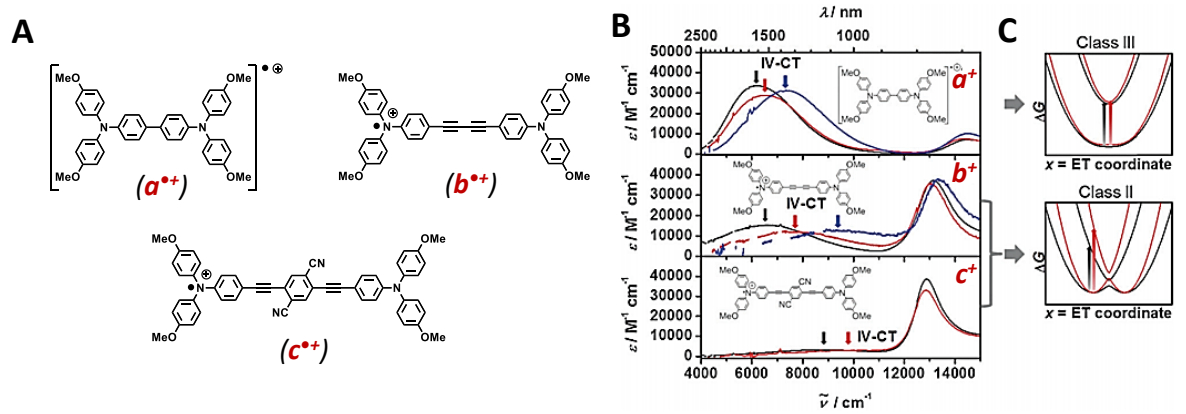

Figure 14 | (**A**) Chemical structures of mixed-valence molecules containing two triarylamine redox centers connected *via* different linkers. (**B**) Vis-NIR absorption spectra of mixed valence monoradical cation compounds ***a***$^{•+}$ - ***c***$^{•+}$. The arrows indicate the maximum of the IVCT band in different solvents: black (dichloromethane), red (nitrobenzene), and blue (acetonitrile). The band at ca. 13000 cm^{-1} for ***b***$^{•+}$ and ***c***$^{•+}$ is caused by localized π–π* excitations of the triphenylamine radical cation. Missing data points refer to spectral areas where the solvent dominates the spectra. (**C**) The diagrams at the right hand side sketch the Gibbs potential energy surface for low (black) and high (red) reorganization energy for a Class III situation (top) and a Class II situation (bottom). IVCT absorptions are indicated by black and red arrows. Figure is adapted from ref. 91

In order for the charge transfer to occur, it is not necessary for the system to have the same type of redox centres, rather any redox system with appropriate energy levels, for instance triarylamines coupled with triphenylmethane radical or tricoordinated organoboron compounds (**Figure 15A**). Triphenylboranes (TPBs), similarly to triarylamines, have recently found various applications in the field of organic electronics.[95] While TAAs are excellent electron donors and hole transporting materials, due to the presence of easily ionisable electrons, TPBs, because of the existence of an unoccupied *p*-orbital of a central boron atom (**Figure 15B**), act as efficient electron accepting and transporting materials, for example in OLEDs.[95] When conjugated with an appropriate electron donor, namely TAAs, new optical properties can emerge, such as nitrogen-boron charge transfer. Wang and co-workers has developed a class of nitrogen-boron conjugated molecules (**Figure 15A**), which exhibit highly intense emission, strongly influenced by the solvent polarity (shifting from around 400 nm in hexane to 490 nm in acetonitrile for ***d***, which is characteristic of a donor-acceptor charge transfer.

94. Mixed-valence systems with no interaction between redox centers comprise Class I of charge transfer systems.
95. Hudson, Z. M. & Wang, S. Impact of Donor−Acceptor Geometry and Metal Chelation on Photophysical Properties and Applications of Triarylboranes. *Acc. Chem. Res.* **42,** 1584–1596 (2009).

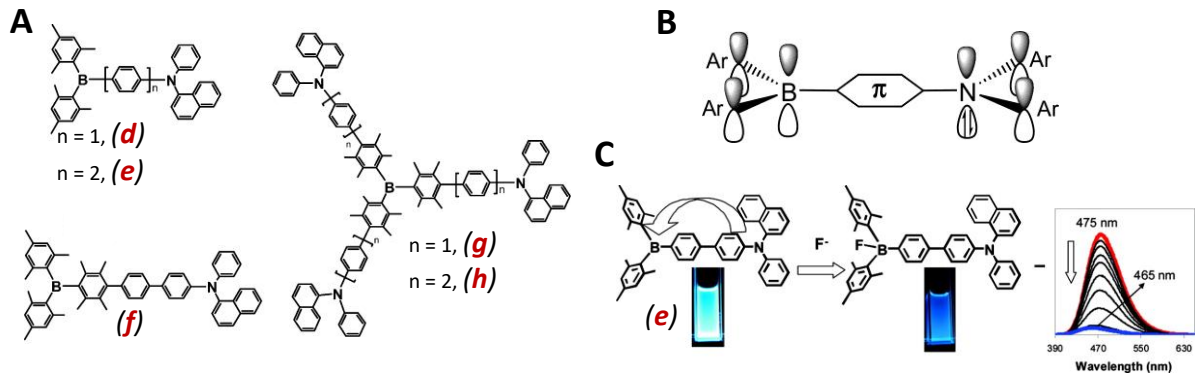

Figure 15 | (**A**) Chemical structure of conjugated triarylamine and triarylborane containing molecules (B-N molecules). (**B**) Schematic representation of the generic B-N conjugate, indicating the free *p*-orbital of a boron atom and occupied *p*-orbital of a nitrogen atom. (**C**) Photographs and the emission spectral change of ***e*** before and after the addition of TBAF in dichloromethane (all titration spectra were recorded at ~1.0 × 10^{-5} M). Figure is adapted from ref. 95

Remarkably, when boron coordinates some ligands (such as fluoride or cyanide anions) the N→B charge transfer is disrupted, resulting in the disappearance of the CT band in the absorption spectra and fluorescence quenching (**Figure 15C**). The authors suggest the possible applications of these effects for the highly selective fluorine sensing.

Moreover, the charge transfer can take place between TAA moieties and metals, as depicted in **Figure 16**, representing so-called organic-inorganic mixed-valence systems.[96] Recently Nie *et al.* reported on the synthesis of the mixed-valence state organic-inorganic compounds with a donor triarylamine part and an acceptor organometallic part with Ru (***i***) and Os (***j***) in initial oxidation states (+2) (**Figure 16A**).[96] Both compounds are characterised by two redox peaks at 0.27 eV/0.68 eV and 0.18 eV/0.59 eV for Ru and Os compounds respectively. All three oxidation states ($[N^0\text{-}M^{II}]^+$; $[N\text{-}M]^{2+}$ and $[N^{\bullet+}\text{-}M^{III}]^{3+}$) have distinctly different colours, which makes them interesting candidates as electrochromic materials (**Figure 16C**). The UV-Vis-NIR absorption spectroscopy reveals the absorption in a broad range from the visible to the NIR region. In the initial localised state $[N^0\text{-}M^{II}]^+$ the absorption in the visible region is related to metal to ligand charge transfer (MLCT) and intra-ligand charge transfer (ILCT) transitions. In the NIR region, Os complexes (***j***) display triplet ILCT transition extended to 1100 nm, which is not present for the Ru compound (***i***). Upon oxidation into MV state $[N\text{-}M]^{2+}$, the intense IVCT band appears in the NIR region at 1050 nm and 972 nm for Ru and Os respectively, additionally the Os containing system exhibits a broad CT band around 1960 nm which is assigned to Os^{III} *d-d* transitions. The authors assign the studied

96. Nie, H.-J., Shao, J.-Y., Yao, C.-J. & Zhong, Y.-W. Organic–inorganic mixed-valence systems with strongly-coupled triarylamine and cyclometalated osmium. *Chem. Commun.* **50,** 10082 (2014).

molecules to a class III charge transfer systems with delocalised mixed-valence states. Finally, the second oxidation leads to the formation of localized systems $[N^{\bullet+}\text{-}M^{III}]^{3+}$ with the intense absorption at around 720 nm characteristic to a radical cation (with a characteristic colour of the solutions). The Os compound also shows Os^{III} *d-d* transitions in the NIR region.

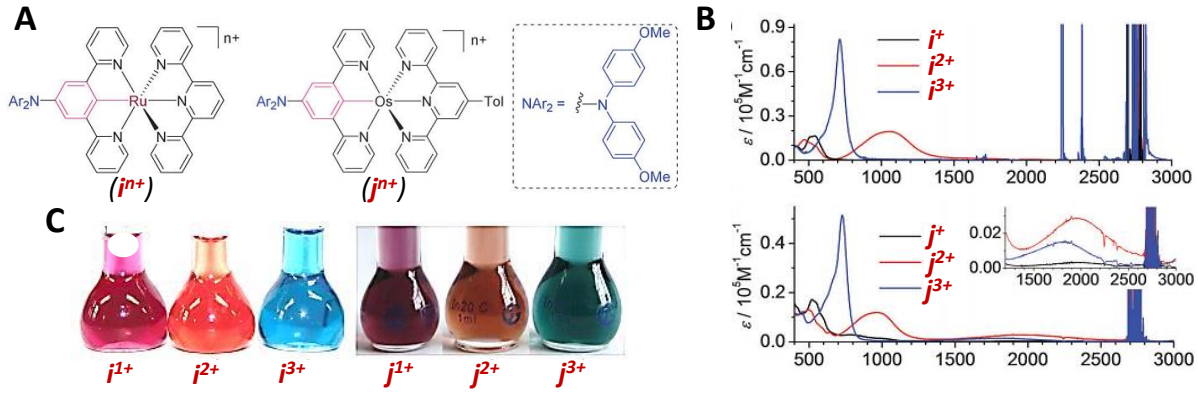

Figure 16 | (**A**) Chemical structures of TAA-Ru and TAA-Os mixed-valence compounds. Tol is the *p*-tolyl group. (**B**) Absorption spectra of (***i*** and ***j***) at different oxidation states in dichloromethane. Insets show the enlarged plots in the NIR region. (**C**) Solutions of ***i*** and ***j*** at different oxidation states in dichloromethane at 1×10^{-4} M. Figure is adapted from ref. 96

These examples highlight the great importance of various TAA based systems in understanding, not only, very fundamental concepts, such as electron/charge transfer, but also the possibility of their application in different fields of materials and analytical science.

vi. Application of Triarylamines

The major domain of the application of small molecule and polymer TAAs are, without doubt – organic electronics, where these materials are used as hole transporting materials. Here we briefly highlight a few examples of the use of small molecule TAAs in OLEDs, organic photovoltaic devices, and perovskite solar cells.

Triarylamine-based molecules in **Figure 17A** represent a general class of hole transporting materials (HTM) used in OLEDs. Their main role is to deliver electron holes from the anode to the light emissive layer where they can recombine with electrons resulting in energy emission in the form of light. Thus the key parameters of the HTM are ***i***) the efficiency of hole injection from anode to the HTM, ***ii***) the efficiency of hole injection from HTM to the emissive layer, and ***iii***) the efficiency of electron blocking properties of HTM. These properties are defined by an appropriate position of the HOMO level relative to the anode and light-emitter. Other important parameters are the level of crystallinity (the more

amorphous the better) and, obviously, the cost of production, which is related to the method of synthesis.

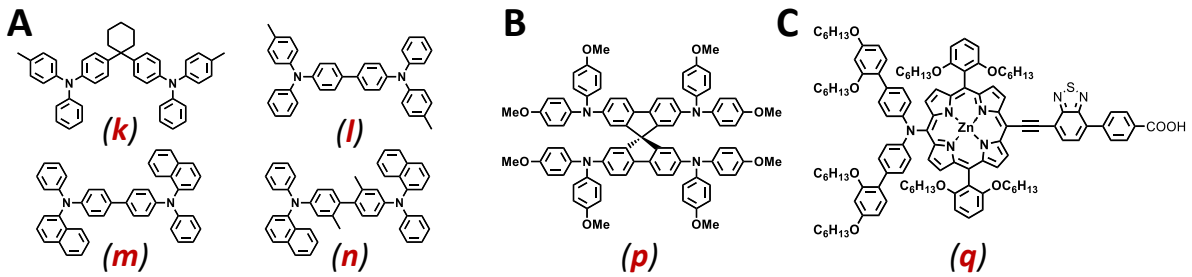

Figure 17 | Some examples of different triarylamine-based molecules which found various applications in (**A**) OLED devices, (**B**) organic solar cells, (**C**) perovskite solar cells.[25,29,30,97]

Triarylamine-based molecules have recently been used and extensively studied in perovskite solar cells, a topic that will be discussed further in *Chapter IV* of this thesis. Here we will briefly acknowledge one example of the large family of these molecules, *spiro*-OMeTAD (***p***) which is represented in **Figure 17B**. This molecule was initially used as a HTM in OLEDs. The general criteria for the HTM in perovskite solar cells are similar to the ones for OLEDs. This molecule satisfies these criteria having the corresponding HOMO-LUMO levels. It has good physical properties such as high glass transition temperature. The only disadvantage is its relatively high price, which demands the search of efficient cheap alternatives.

Triarylamine compounds are also used in organic solar cells. For instance, Grätzel and co-workers recently reported on the unprecedented efficiency for the dye synthesised solar cells of 13%.[97] The photoactive compound such as molecule (***q***) (**Figure 17C**) was designed as a D-A type molecule, containing diarylamine moiety, which played the electron donor role, connected to a Zn^{2+} coordinated porphyrin, acting as electron acceptor.

Among other applications in the field of materials sciences, TAA derivatives proved to be promising in biomedical applications as fluorescent probes. Due to their rich chemistry, the varying substituents may lead to the emergence of nonlinear optical properties, such as two-photon absorption.

97. Mathew, S. *et al.* Dye-sensitized solar cells with 13% efficiency achieved through the molecular engineering of porphyrin sensitizers. *Nat. Chem.* **6,** 242–247 (2014).

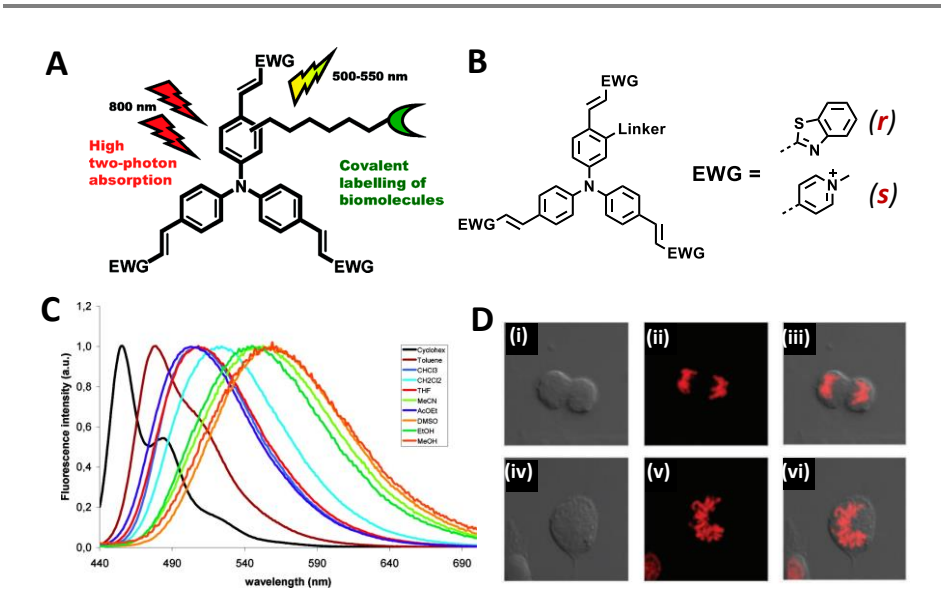

Figure 18 | (**A**) Generic structure of a triarylamine-based two-photon absorption molecules and representation of two-photon absorption. (**B**) Chemical structure of studied molecules. (**C**) Normalized emission spectra of compound benzothiazole (***r***) recorded in various solvents. (**D**) Laser scanning confocal microscopy pictures of CHO-K1 cells in different states of mitosis; cells treated with (***s***) (2 μM). Phase-contrast picture of the cells (**i** and **iv**), fluorescence of (***s***) in the chromosomes of the cells (**ii** and **v**), and overlay of phase-contrast and fluorescence image (**iii** and **vi**). Figure is adapted from refs. 31,98

Figure 18 shows the application of TAAs conjugated with various electron withdrawing groups (EWG) in fluorescent bioimaging. In this work, the authors demonstrated that the positively charged TAAs, having good solubility in biological medium, exhibited high affinity to DNA, which can be seen from the fluorescent photograph in **Figure** 18**D.**[31,98–100]

98. Bordeau, G. *et al.* New triarylamine-based far-red DNA stainers with high two-photon absorption properties. *Nucleic Acids Symp. Ser. (Oxf).* 155–156 (2008). doi:10.1093/nass/nrn079
99. Allain, C. *et al.* Vinyl-pyridinium triphenylamines: Novel far-red emitters with high photostability and two-photon absorption properties for staining DNA. *ChemBioChem* **8,** 424–433 (2007).
100. Bordeau, G. *et al.* Trinaphthylamines as Robust Organic Materials for Two-Photon-Induced Fluorescence. *J. Am. Chem. Soc.* **130,** 16836–16837 (2008).

C. Self-Assembling Triarylamines

In this section, we will discuss the recent advances in the supramolecular chemistry of triarylamines. As will be stated below, the first supramolecular polymers based on triarylamine stacks were published only six years ago by our group. However, we will start by mentioning other self-assembled systems, using other supramolecular recognition motifs than triarylamines stacks but including triarylamines in their structures, as well as undefined aggregates of triarylamines.

i. Coordination Compounds and Cages Including Triarylamines

The first reported supramolecular assemblies including triarylamines in their structures were organic and organometallic polyhedrons[101–103] and frameworks.[104–108] For instance, in 2002, Field *et al.* reported on the spontaneous self-assembly of triarylamine carboxylic acid (***a***) into tetrahedron cages through intramolecular hydrogen bonding (**Figure 19A**).[101] Since then, other groups have reported on the metal-driven formation of polyhedral cages and their application *in vivo*, for example as spin-traps for NO detection.[103]

Triarylamine derivatives have also been utilised as trigonal building blocks for the construction of various metal-organic frameworks with interesting structural and redox properties, *etc.* In 2005 Sun *et al.* have used a tetraphenylenediamine carboxylate (***b***) to construct a MOF by coordination with copper(II) (**Figure 19B**).[105] Interestingly, due to the dynamic structure of the tetraphenylenediamine molecule, it can adopt two conformations: C_{2h} or D_2-symmetry (**Figure 19B(i-ii)**). Two crystal topologies could be obtained, corresponding to either the first or the second conformation depending on conditions.

101. Field, J. E., Combariza, M. Y., Vachet, R. W. & Venkataraman, D. Spontaneous assembly of a hydrogen-bonded tetrahedron. *Chem. Commun.* **0,** 2260–2261 (2002).
102. Roberts, D. A., Castilla, A. M., Ronson, T. K. & Nitschke, J. R. Post-assembly Modification of Kinetically Metastable $Fe^{II}_2L_3$ Triple Helicates. *J. Am. Chem. Soc.* **136,** 8201–8204 (2014).
103. Wang, J., He, C., Wu, P., Wang, J. & Duan, C. An Amide-Containing Metal–Organic Tetrahedron Responding to a Spin-Trapping Reaction in a Fluorescent Enhancement Manner for Biological Imaging of NO in Living Cells. *J. Am. Chem. Soc.* **133,** 12402–12405 (2011).
104. Hua, C., Baldansuren, A., Tuna, F., Collison, D. & D'Alessandro, D. M. In Situ Spectroelectrochemical Investigations of the Redox-Active Tris[4-(pyridin-4-yl)phenyl]amine Ligand and a Zn^{2+} Coordination Framework. *Inorg. Chem.* **55,** 7270–7280 (2016).
105. Sun, D., Ke, Y., Mattox, T. M., Ooro, B. A. & Zhou, H.-C. Temperature-dependent supramolecular stereoisomerism in porous copper coordination networks based on a designed carboxylate ligand. *Chem. Commun.* **0,** 5447 (2005).
106. Venkateswarulu, M., Pramanik, A. & Koner, R. R. Novel metal–organic framework with tunable fluorescence property: supramolecular signaling platform for polynitrophenolics. *Dalt. Trans.* **44,** 6348–6352 (2015).
107. Qiao, C. *et al.* Instant high-selectivity Cd-MOF chemosensor for naked-eye detection of Cu(II) confirmed using in situ microcalorimetry. *Green Chem.* **18,** 951–956 (2016).
108. Yao, Q. *et al.* Series of Highly Stable Isoreticular Lanthanide Metal–Organic Frameworks with Expanding Pore Size and Tunable Luminescent Properties. *Chem. Mater.* **27,** 5332–5339 (2015).

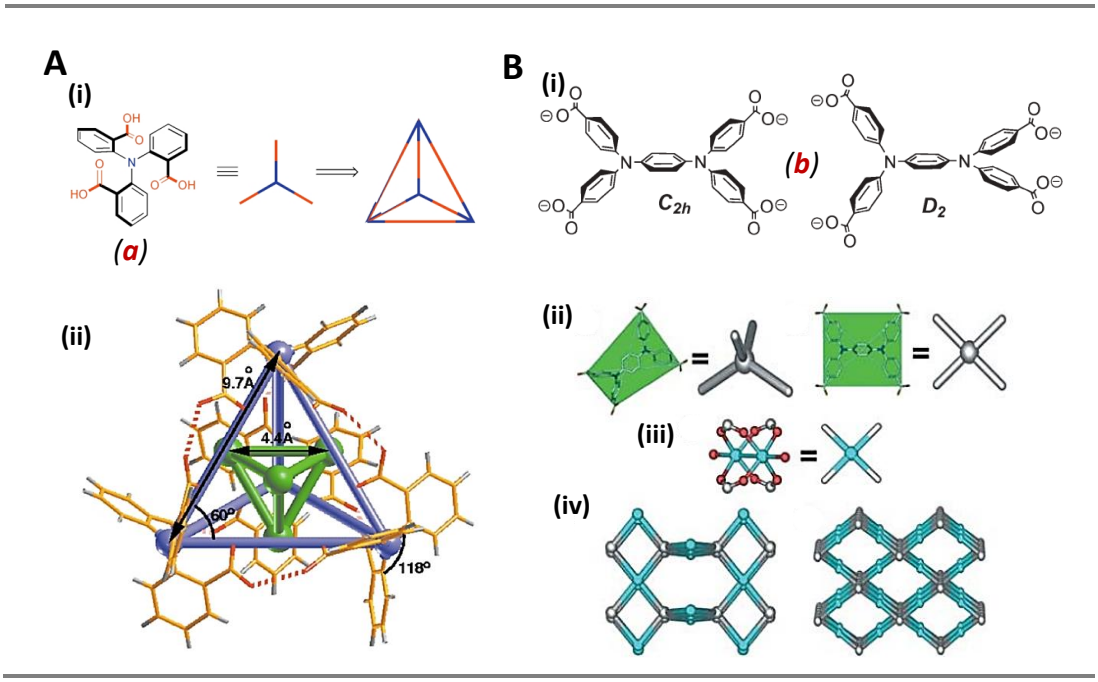

Figure 19 | (**A**) Spontaneous assembly of a hydrogen-bonded tetrahedron. (**i**) Schematic representation of (***a***) as a tetrahedral synthon. (**ii**) Illustration of the supramolecular structure of (***a***) from single crystal X-ray diffraction.[101] (**B**) (**i**) The designed carboxylate ligand: the tetra-anions of N,N,N',N'-tetrakis(4-carboxyphenyl)-1,4-phenylenediamine (***b***). (**ii**) View of (left) the approximate tetrahedral conformation of D_2-***b***, (right) the near square-planar conformation of C_{2h}-***b***. (**iii**) The paddlewheel SBU as a square-planar node, and the resulting (**iv**) PtS net (left) and NbO net (right). (Colour scheme: aqua, Cu; red, O; and grey, C.).[105] Figure is adapted from refs**.** 101,105

ii. Aggregation Induced Emission in Triarylamine Systems

Aggregation induced emission (AIE) is a relatively novel concept,[109,110] which is characterised by the increase of fluorescence of a compound caused by the aggregation process. Most organic fluorophores, such as perylene derivatives, while highly emissive in diluted solutions when aggregate, do not exhibit fluorescent properties due to π-π interactions. The quenching of emission upon aggregation of such molecules is called *aggregation caused quenching* (ACQ) (**Figure 20A**). Unlike classical fluorophores, compounds exhibiting AIE properties, such as hexaphenylsilole (HPS) usually have non-planar propeller-like structures, with a high degree of intramolecular motion. Such compounds do not fluoresce in solutions, however, upon aggregation, due to the restriction of intramolecular rotations (RIR) of phenyl rings, which blocks non-irradiative pathways, the aggregation induced emission takes place (**Figure 20B**).

Pristine triphenylamine, although being a propeller-like molecule, does not possess AIE properties, however its various derivatives, especially decorated with electron accepting groups, were shown to exhibit enhanced fluorescence upon aggregation.[109–111]

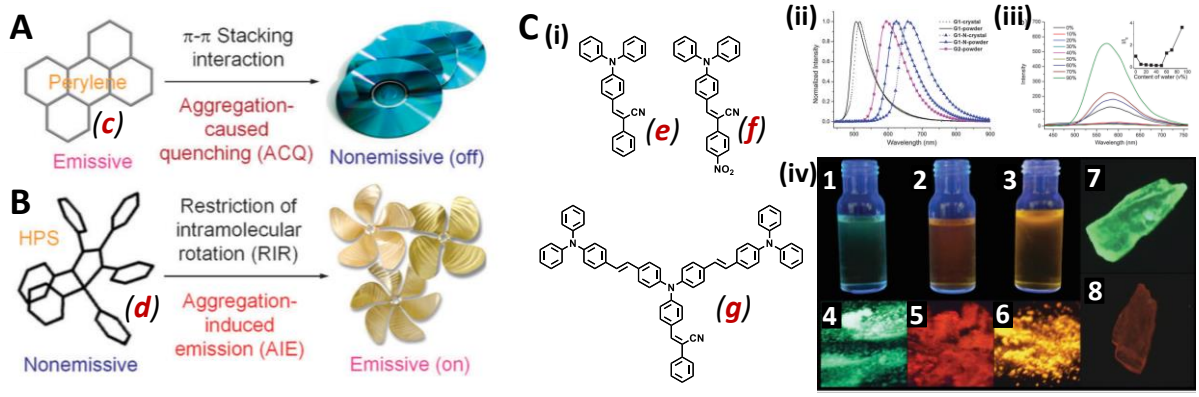

Figure 20 | (**A**) Planar luminophoric molecules such as perylene tend to aggregate as and discs pile up, due to strong π- π stacking interactions between the aromatic rings, which commonly turns ‘‘off’’ light emission. (**B**) Non-planar luminogenic molecules such as hexaphenylsilole (HPS) behave oppositely, with their light emissions turned ‘‘on’’ by aggregate formation, due to the restriction of the intramolecular rotation (RIR) of the multiple phenyl rotors against the silole stator in the aggregate state. (**C**) Aggregation-induced emission of triphenylamine substituted cyanostyrene derivatives. (**i**) Chemical structure of studied molecules. (**ii**) Fluorescence emission spectra of ***e***, ***f*** and ***g*** in solid states (λ_{ex} = 365 nm). (**iii**) Fluorescence emission spectra (λ_{ex} = 365 nm) of ***g*** (10^{-5} M) in THF–water with different amounts of water (% volume). The inset shows a plot of PL integral versus water content of the solvent mixture for ***g***. (**iv**) Photos of ***e***, ***f*** and ***g*** in THF (1, 2 and 3, respectively) and in powders (4, 5 and 6, respectively) under UV illumination (365 nm), and fluorescent microscope (λ_{ex} = 330–385 nm) images of ***e*** (7) and ***f*** (8) in crystals.[111] Figure is adapted from refs. 109,111

For instance, in a recent report, Zhao *et al.* studied AIE of triphenylamines, decorated with cyano- and nitro- groups (**Figure 20C**), which were introduced to tune fluorescent properties (**Figure 20C(ii)**). The introduction of a nitro group into ***f***, shifts the emission maximum batochromically from 506 nm to 624 nm compared to ***e***. All studied compounds exhibited AIE properties, which were observed when diluting THF solutions of luminophores with water, causing their aggregation (**Figure 20C(iii)**). Fluorescence photographs of powders are represented in **Figure 20C(iv)** showing intensively emitting samples.

109. Hong, Y., Lam, J. W. Y. & Tang, B. Z. Aggregation-induced emission. *Chem. Soc. Rev.* **40,** 5361 (2011).
110. Mei, J. *et al.* Aggregation-Induced Emission: The Whole Is More Brilliant than the Parts. *Adv. Mater.* **26,** 5429–5479 (2014).
111. Zhao, X. *et al.* Aggregation-induced emission of triphenylamine substituted cyanostyrene derivatives. *New J. Chem.* **38,** 1045 (2014).

iii. Supramolecular Polymerization of Triarylamines

1) Light-Triggered Supramolecular Polymerization

Our group first reported that some triarylamines, such as the one depicted in **Figure 21,** can undergo supramolecular polymerization by stacking of triarylamine units.[81] In addition to the triarylamine core, the presence of an amide function was shown to be crucial for the self-assembly process to occur. It was also shown that the presence of long alkyl chains participates in supramolecular stabilization, and ensures a good solubility in organic solvents.

Interestingly, and in a quite unique manner, this type of self-assembly can be (although not necessarily) triggered by simple light irradiation from solution. Upon exposure to visible light for a few minutes, the colour of the solution turns green, and a set of ^{1}H NMR resonance signals disappear, corresponding to the TAA core, the acetamide moiety, and the methylene protons of the octyl chains neighbouring the aromatic core (**Figure 18B**). This disappearance was shown to be a combination of the presence of paramagnetic species – triarylammonium radical cation – together with the formation of dense supramolecular structures.

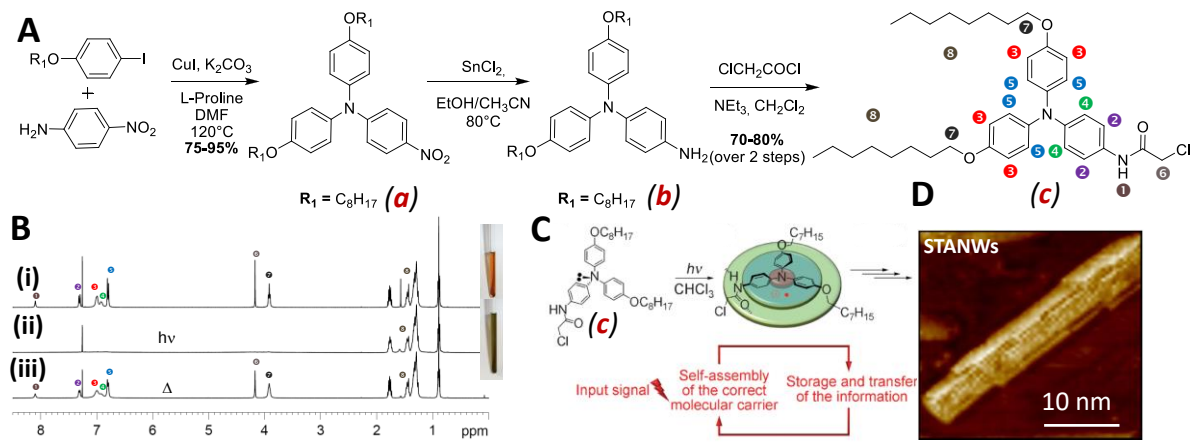

Figure 21 | Light-triggered self-assembly of triarylamine nanowires. (**A**) Synthetic scheme and chemical structure of a first generation self-assembling triarylamines (***c***). (**B**) ^{1}H-NMR spectra of ***c*** in chloroform (**i**) immediately after the purification, (**ii**) after irradiation with visible light and (**iii**) after heating for 60 °C overnight. The insets shows the solution of ***c*** in the NMR tube before and after irradiation. (**C**) Schematic representation of the light-induced self-assembly process. (**D**) AFM image of the supramolecular corn-like TAA fiber. Figure is adapted from ref. 81

Further investigation of this phenomenon revealed several peculiar facts: (***i***) the initial spectrum remained identical for the sample kept in dark for one week and (***ii***) no changes in the NMR behaviour were observed for the irradiated sample, which was also kept in the dark for one week. The NMR signals could be recovered after heating of the sample at 60 °C

overnight and this process could be repeated several times without detectable degradation of the TAA molecules. EPR studies revealed that after one hour of light-irradiation the concentration of radicals reaches ≈ 10% of the total amount of triarylamines. When left in dark, a smooth decay of 12 hours was observed until reaching a value of around 6 radicals per 1000 neutral TAAs.

Self-assembly was first confirmed by DLS experiments showing changes in the autocorrelation curve after the light irradiation, and then by high resolution AFM imaging, revealing the formation of supramolecular fibrillar structures with a well-defined internal ordering (**Figure 18D**).[81]

2) Mechanism of the Light-Triggered Polymerization

In order to understand the structure and the mechanism of formation of this light-induced self-assembly, experimental and theoretical investigations were combined.[83]

The structural organisation of TAA molecules within self-assemblies was determined by AFM, powder X-ray diffraction, and DFT (**Figure 22(I)**). The supramolecular stacking of TAAs within a snow-flake double columnar packing was demonstrated (**Figure 22(I)d,e**).

The mechanism of this photo-induced self-assembly was proposed based on kinetic EPR, NMR and UV-Vis-NIR measurements and on analytical theory. In breif, the proposed mechanism consists of three main steps: (***i***) photo-oxidation of TAA molecule; (***ii***) nucleation step; (***iii***) fibrillar growth. The first step, photo-oxidation, is identical to that already discussed in the previous section. However, the second, nucleation step, is of particular interest and should be detailed. Initially, after the photo-oxidation, due to relatively low dielectric constant of chloroform, the triarylammonium radical cation is bound with a chloride anion in the charge transfer complex (**Figure 22(II)b)**. Due to electrostatic attraction, these charge transfer of TAA-Cl start forming strings of dipoles, where the triarylammonium molecules alternate with chloride anions in a so-called loose state (**Figure 22(II)c-f).** Reaching a certain length,, and thus having a notable energetic gain by approaching the triarylamine at a close contact, chloride anions then migrate to the periphery of the stacked fibre in its tight state (**Figure 22(II)f-h**). Finally, the double columnar nucleus is formed *via* hydrogen bonds between two columns in a tight state **Figure** 22**(II)i**. This nucleus finally initiates further growth of TAA fibre by the addition of neutral molecules (**Figure 22(II)j**).

Importantly, during the elongation process, the fibres grow from both sides of the nucleus. Moreover, above a certain length, it was shown that brakeage of fibres occurs,

increasing the number of tips capable of piling new neutral triarylamines, and initiating a sigmoidal shape of the kinetic curves, as expected for an auto-catalytic process.[83]

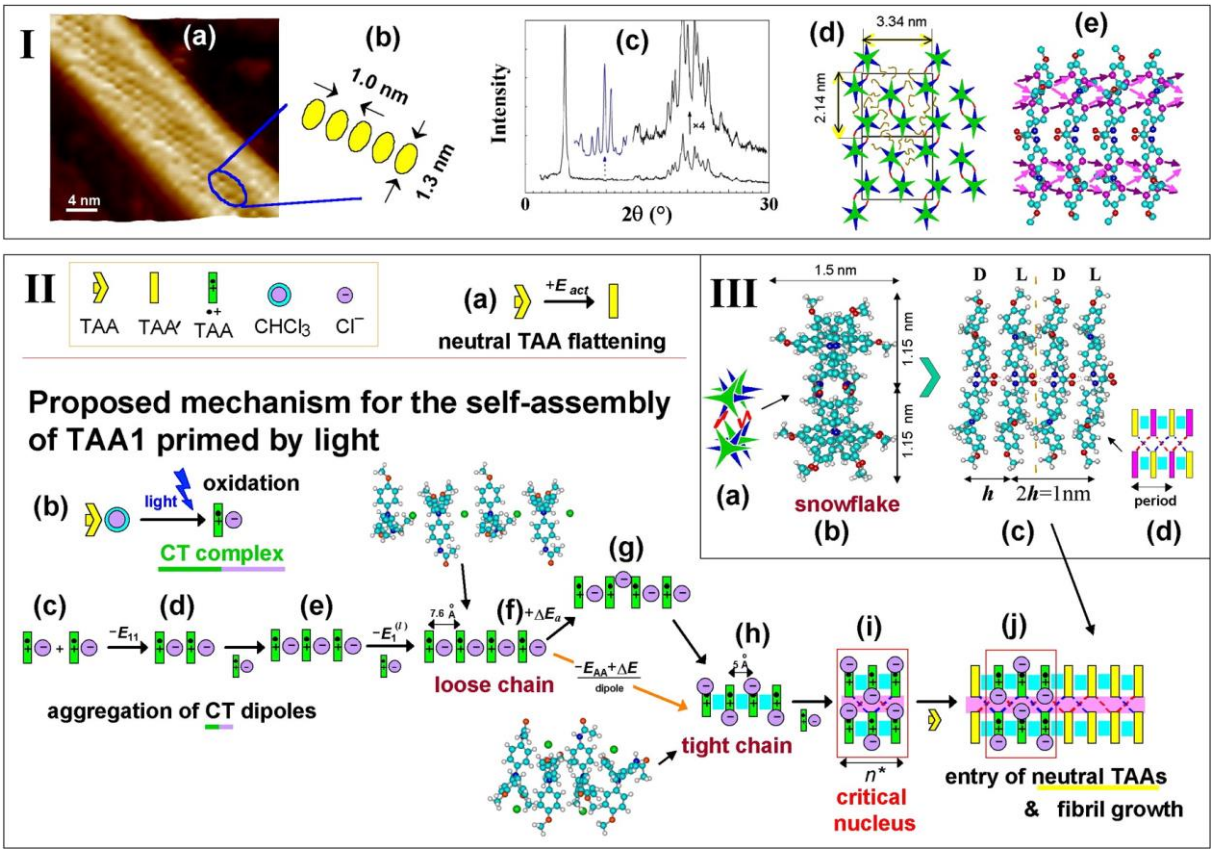

Figure 22 | TAA fibrils in chloroform after 1 h exposition to white light. (**I**) (**a,b**) AFM height image. (**c**) XRD pattern from 10 mM TAA-***c*** sample (bottom, black) its magnification in the WAXS range (top, black) and in the SAXS range (top, blue). (**d**) The proposed molecular organization of TAA-***c*** fibrils based on the XRD. (**e**) The simulated all-atomic structure of snowflake double column. (**II**) Light-induced aggregation kinetics in TAA solutions. (**a**) Spontaneous flattening of isolated neutral TAA molecule (transition TAA → TAA′). (**b**) Light induces oxidation of a neutral TAA producing TAA^{+} radical and Cl^{-} anion. (**c,d**) Two free radicals $TAA^{\bullet+}$ complexed with the Cl^{-} counterions attract each other head-to-tail. (**e,f**) A growing stack of radical dipoles. (**f,g,h**) Tightening of the stack: chloride ions move sideways (**g**); aromatic rings of TAA molecules benefit from closer contacts, while chloride anions are finally accommodated in the gaps between ether tails of TAA molecules (**h**). (**i**) Formation of double-columnar nuclei stabilized by H-bonds between the columns. (**j**) Growth of the structure by attachment of neutral TAA molecules. (**III**) Molecular arrangements in bicolumnar "snowflake" stacks of neutral TAA: (**a**) A cartoon showing alternating molecular orientation in the columns. (**b**) The top view (along the main axis), and (**c**) the side view of the structure. (**d**) A cartoon with zigzag chain of H-bonds connecting the columns. Figure is reproduced from ref. 83

3) Second Generation of Self-Assembling Triarylamines

As the presence of at least one amide function was proved crucial for the self-assembly process, we also explored a second generation of triarylamines having three amide

functions (trisamide-triarylamines (TATAs)) (**Figure 23A**). Remarkably, due to strong three-fold hydrogen bonding, these molecules self-assemble in many organic solvents, even without light irradiation, and often lead to organogelation above a certain concentration.[112] The fine structure of these aggregates was proposed based on X-ray diffraction and microscopy data suggesting helical columnar arrangement, *via* threefold hydrogen bonding, with N-N distances of 4.85 Å and a helical pitch of 18 molecules, and with all aromatic groups of the TATAs engaging π-π staking interactions with their neighbours. These experimental data were fully corroborated by DFT calculations (**Figure 23G**).

TATAs assemble into long fibrillar structures in chloroform even before light irradiation (**Figure 23F**), making the self-assembly difficult to study by NMR in this solvent. In order to disrupt supramolecular interactions, the studies were carried out in a mixture of methanol/toluene, resulting in good resolution NMR spectra (**Figure 23B**). The addition of 5% of chloroform to this solution with a consequent irradiation with visible light causes the disappearance of resonance signals corresponding to the aromatic core and neighbouring methylene protons of alkyl chains (**Figure 23B(ii)**) indicating the photo-induced oxidation of TATAs and subsequent self-assembly also in that mixture of solvents.

Interestingly, when preformed fibres were irradiated in chloroform, an intense IVCT band in the NIR region appeared with a maximum at 1150 nm (**Figure 23C**). The symmetry of the CT band, which dominates during the first 15 minutes of irradiation is characteristic of partially delocalised CT, corresponding to a class II CT systems. Upon further irradiation, when nearly 50% radical cations are formed, the symmetry of the CT band changes indicating the transition to class III with full delocalisation. When photo-oxidation is continued to 100% the system exhibits fully localised radical cation character, characteristic of class I (**Figure** 23**C(ii)**). These transitions were also confirmed by time dependent EPR spectroscopy.[113] Upon oxidation for only 5 min, the fluorescence of TATA was fully quenched due to radical formation and delocalization in the supramolecular polymer (**Figure** 23**D**). Remarkably, SAXS measurements, performed with samples before and after irradiation, revealed considerable narrowing of the coherence length for irradiated sample (**Figure 23E**), suggesting fewer structural defects and better organisation of the fibres. This improvement of the fibres' quality by light-irradiation was also demonstrated by AFM (**Figure 23F** transition from **i** to **ii**).

112. We should mention that the organogelation of a TATA molecule was already reported by Shirota and colleagues, although they never proposed any supramolecular structure/organization of the gel except that it should involve hydrogen bonds.[224].
113. Armao IV, J. J. *et al.* Healable Supramolecular Polymers as Organic Metals. *J. Am. Chem. Soc.* **136,** 11382–11388 (2014).

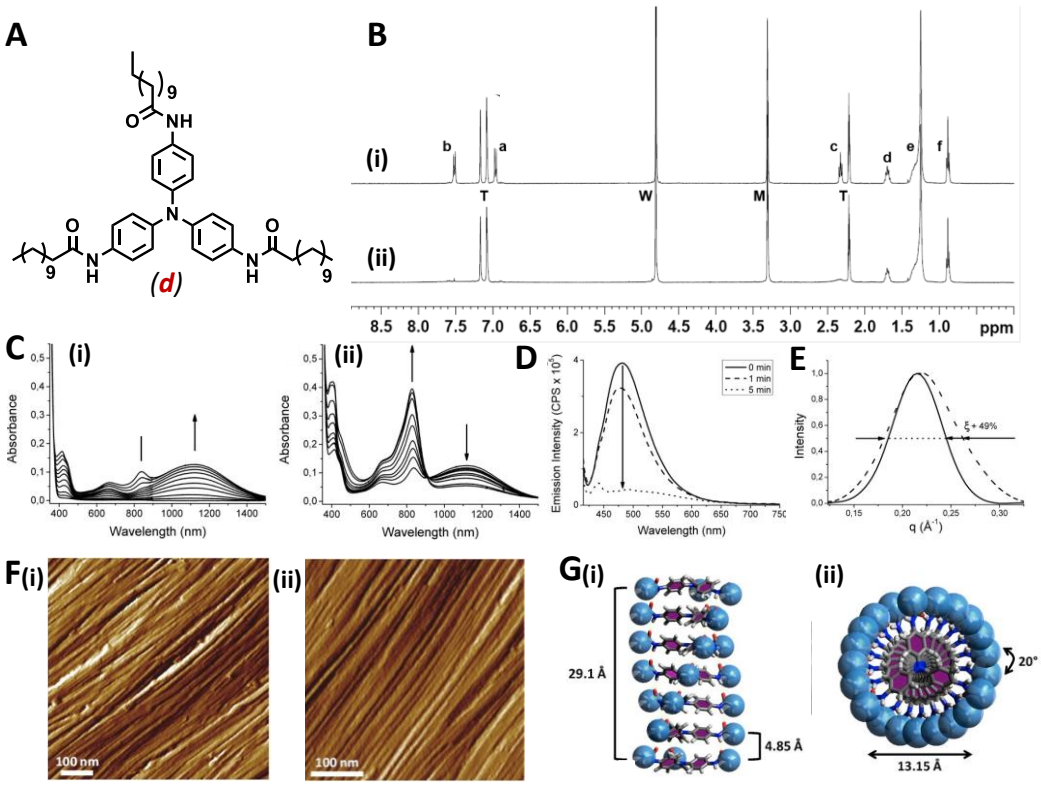

Figure 23 | Second generation of self-assembling triarylamines. (**A**) Chemical formula of TATA-***d*** and (**B**) associated ^{1}H NMR of TATA-***d*** in a 5:3 methanol:toluene mixture, in the presence of $CDCl_3$ (5 vol %) before (**i**) and after (**ii**) light irradiation. (**C**) Effect of light irradiation on TATA self-assemblies. (**i,ii**) Sequential absorbance spectra taken during light irradiation of a 0.1 mM solution of TATA-***d*** in $CHCl_3$; (**i**) first 6 min of light irradiation, (**ii**) from 7 to 73 min of light irradiation. (**D**) Fluorescence emission of TATA-***d*** upon light irradiation showing the quenching induced by the polaron formation. (**E**) SAXS of nonirradiated (dotted line) and irradiated (full line) thin films demonstrating a 49% increase in the correlation length (calculated as 4π/fwhm). (**F**) AFM image of TATA-***d*** obtained from the drop cast of a chloroform solution before light irradiation (**i**) and after 15 min of light irradiation (**ii**) showing the healing of structural defects. (**G**) Side view (**i**) and top view (**ii**) of the proposed stacking structure of TATA-***d***, as obtained from DFT calculations, and with a longitudinal periodicity of 29.1 Å, a nitrogen–nitrogen distance of 4.85 Å between adjacent molecules, and a dihedral angle of 20° between each plateau. Figure is adapted from ref. 113

4) Derivations of the Triarylamine Core

Our research group has been particularly interested in the functional properties of these supramolecular polymers, and the possibility to implement these new dynamic structures in materials science. Importantly, other scientific groups have also started to contribute to these developments and we will highlight them hereafter.

The first important aspect is that the triarylamine amide unit is its ability to organize even with substitutents baring numerous (and even bulky) fragments. For instance, we reported that triarylamine-fullerene conjugates (***e***), designed as donor-acceptor molecules, exhibit remarkable self-assembly behaviour depending on the light source used to induce their aggregation (**Figure 24**).[114] After irradiation with a halogen lamp fibres were formed, upon exposure to sunlight, nanospheres were obtained. This difference in morphology is caused by the difference in the light intensity in the UV range: *a*) low intensity halogen lamp produces small amount of nuclei and, as a consequence, long fibres; *b*) high intensity produces the formation of larger amount of nuclei and, as consequence, short rods that subsequently aggregate in nanospheres.

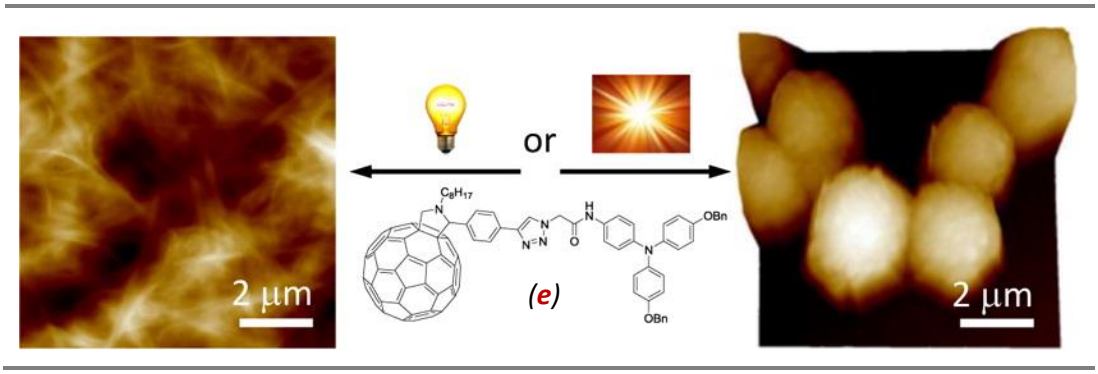

Figure 24 | TAA-fullerene conjugate self-assemblies. Chemical structure and AFM images of the self-assemblies, formed upon irradiation with different light sources. (Left image) nanofibres obtained after irradiation with visible light emited by halogen lamp; (right image) nanospheres formed upon irradiation with sun light. Figure is reproduced from ref. 114

Following similar lines, various scaffolds based on triaryalmine and including metal-ligand associations,[115] rotaxanes,[116–118] and benzene-1,3,5-tricarboxamide (BTA)[119] moiety were also shown to produce interesting responsive supramolecular self-assemblies.

Due to their special structural features (star shape, propeller-like structure), triarylamines are of a great fundamental interest as a model compound for the study of different pathways of supramolecular polymerisation and chirality amplification.[120] Recently, almost simultaneously, a few groups reported on the study of the mechanism of supramolecular polymerisation for gallate-decorated TAAs (Aida, Miyajima *et al.* 2016)[121]

and planar carbonyle-bridged TAA-derivatives (Meijer *et al.* 2016, see **Figure 25**).[122] The planar carbonyle-briged TAA (CBTs) core, which was also recently used by the group of Hildner and Schmidt as conductive core unit for long-range energy transfer in previously reported studies,[123,124] was decorated with trialkylgallate functions with chiral *R/S* citronellol-derivatives (*R/S*-***f***) (**Figure 25A)**. The self-assembly process of these molecules was studied in *o*-dichlorobenzene. Upon cooling a hot solution containing molecularly dissolved ***f***, the formation of nanofibers of approximately 4 nm was observed by AFM studies, corresponding to a diameter of a single fibre. Electron diffraction of the fibres gave the intermolecular distance of 3.3 Å (**Figure 25A,B)**. This value is significantly shorter than the N-N distance within TATA self-assemblies (4.85 Å)[113] which is related to two main factors: (***i***) the restricted planar structure of CBT compared to the propeller like structure of the TAA and (***ii***) the introduction of electron accepting carbonyl groups reduces the electron density on the nitrogen atom, therefore reducing the electrostatic repulsion between electronegative nitrogens.

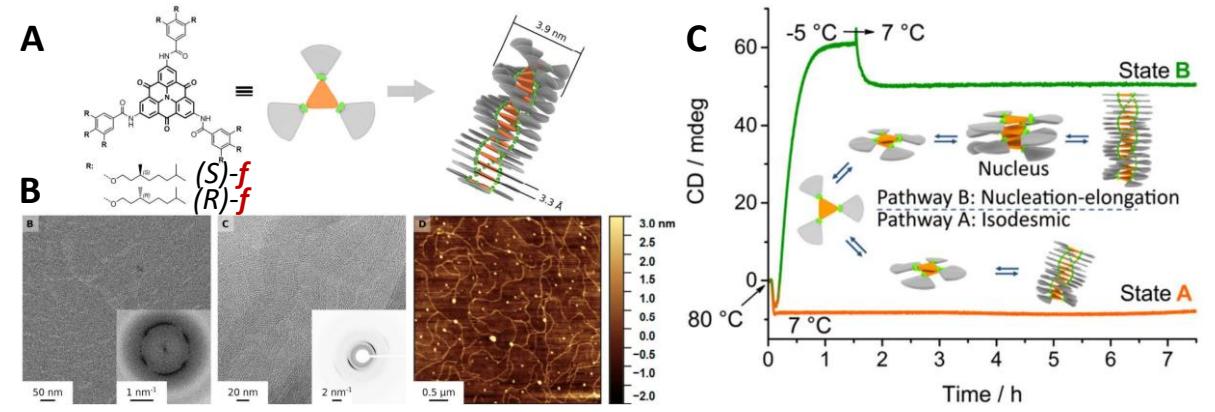

Figure 25 | Pathway complexity in self-assembly of chiral carbonyl-bridged TAAs. (**A**) Chemical structure amd schematic representation of structural TAA unit ***f***, assembling into helical aggregate. (**B**) TEM and AFM mstudies of self-assemblies. (**C**) Time dependent CD measurements, demonstrating different self-assembly pathways into state A and state B, which are schematically described by molecular model cartoon. Figure is adapted from ref. 122

Importantly, the authors noticed that, depending on the temperature regime, the CBT molecules assembled with different mechanisms. Namely, when a hot solution of CBT was

114. Busseron, E. *et al.* Light-Controlled Morphologies of Self-Assembled Triarylamine–Fullerene Conjugates. *ACS Nano* **9,** 2760–2772 (2015).
115. Moulin, E. *et al.* Light-triggered self-assembly of triarylamine-based nanospheres. *Nanoscale* **4,** 6748–51 (2012).
116. Wolf, A. *et al.* pH and light-controlled self-assembly of bistable [c2] daisy chain rotaxanes. *Chem. Commun.* **51,** 4212–4215 (2015).
117. Chang, J.-C., Lai, C.-C. & Chiu, S.-H. A Redox-Controllable Molecular Switch Based on Weak Recognition of BPX26C6 at a Diphenylurea Station. *Molecules* **20,** 1775–1787 (2015).
118. Mandal, A. K., Gangopadhyay, M. & Das, A. Photo-responsive pseudorotaxanes and assemblies. *Chem. Soc. Rev.* **44,** 663–676 (2015).
119. Moulin, É. *et al.* Self-assembly of benzene-tris(bis(p-benzyloxy)triphenylamine)carboxamide. *Comptes Rendus Chim.* **19,** 117–122 (2016).

cooled down from 80°C to 7°C, the system assembles *via* an isodesmic mechanism into a kinetically trapped *state A* (**Figure 25C,** orange curve) whereas when it is overcooled first to -5 °C before letting warm it up to 7 °C, it assembles *via* the cooperative mechanism into a thermodynamically stable *state B* (**Figure 25C,** green curve).

Trialkyl-gallate was also used by our group to decorate the first generation TAAs in different ways in order to investigate their properties in bulk and in solutions (**Figure 26**).[125]

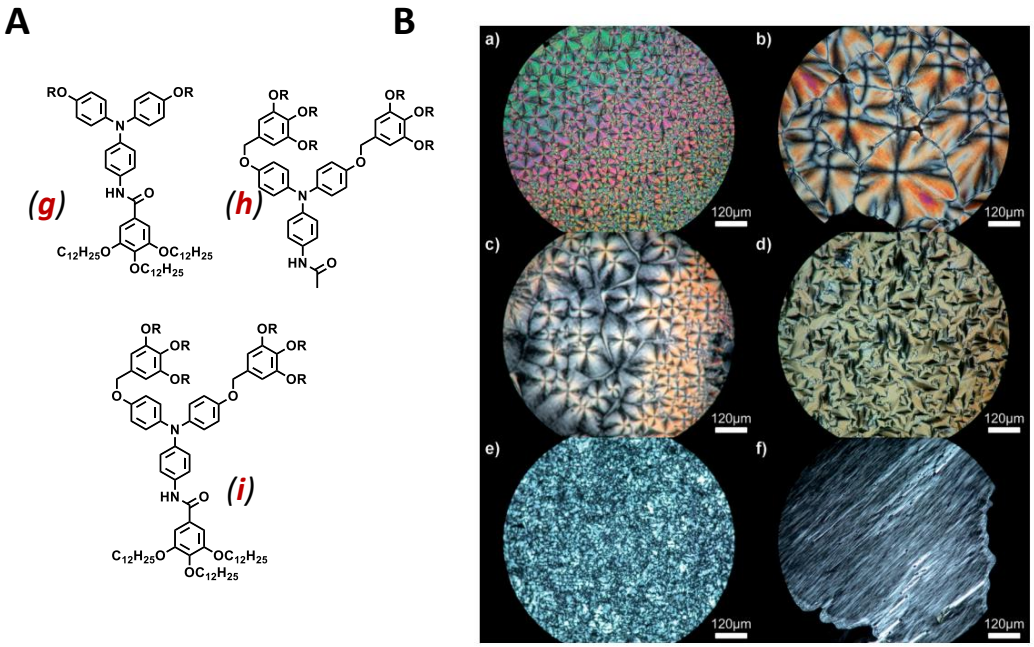

Figure 26 | Liquid crystal Triarylamines. (**A**) Chemical structures of triarylamines decorated with trialkyl gallate maieties (***g*** - ***i***). (**B**) Cross-polarised OPM images of TAA liquid crystals. Figure is adapted from ref. 125

Three types of TAA molecules were synthesised with one, two, and three gallate moieties as represented in **Figure 26A**. All molecules exhibited characteristic for self-assembling TAAs behaviour under light irradiation in chloroform, indicating their self-assembly, and all the TAA-gallates demonstrated formation of liquid crystal phases (**Figure** 26**B**).

120. Kim, J. *et al.* Induction and control of supramolecular chirality by light in self-assembled helical nanostructures. *Nat. Commun.* **6,** 6959 (2015).
121. Kim, T., Mori, T., Aida, T. & Miyajima, D. Dynamic Propeller Conformation for The Unprecedentedly High Degree of Chiral Amplification of Supramolecular Helices. *Chem. Sci.* **00,** 1–6 (2016).
122. Haedler, A. T. *et al.* Pathway Complexity in the Enantioselective Self-assembly of Functional Carbonyl-bridged Triarylamine Trisamides. *J. Am. Chem. Soc.* jacs.6b05184 (2016). doi:10.1021/jacs.6b05184
123. Haedler, A. T. *et al.* Synthesis and photophysical properties of multichromophoric carbonyl-bridged triarylamines. *Chem. Eur. J.* **20,** 11708–11718 (2014).
124. Haedler, A. T. *et al.* Long-range energy transport in single supramolecular nanofibres at room temperature. *Nature* **523,** 196–199 (2015).
125. Domoto, Y., Busseron, E., Maaloum, M., Moulin, E. & Giuseppone, N. Control over Nanostructures and Associated Mesomorphic Properties of Doped Self-Assembled Triarylamine Liquid Crystals. *Chem. Eur. J.* **21,** 1938–1948 (2015).

5) Physical Properties and Applications of Self-Assembling Triarylamines

Conduction Properties and Construction of Interconnects

The molecular packing of triarylamine molecules within self-assemblies suggests the possibility of an efficient electron transfer due to its delocalisation along the nanowire. This was first demonstrated by our group, reporting on the outstanding metal-like conductivity of the first generation TAA self-assemblies (**Figure 27**).[82] A solution of TAA was dropcasted on the surface of lithographically manufactured gold electrodes, with an 80 nm gap and under 0.3 – 0.8 V DC electric field. The conductivity between the electrodes was monitored during the deposition process, and practically no significant changes were detected in the dark, after the solution was deposited. However, after just a few seconds of light irradiation, conductivity increased dramatically by more than six orders of magnitude indicating the construction of low resistance interconnects between the electrodes. Further investigation of the electrodes by AFM confirmed the formation of uniformly aligned nanofibers in the nanotrench. Based on this work, the theoretical calculations, performed by the group of Sanvito[126], estimate the electron mobility values for pristine defect free self-assemblies at room temperature to be of the order of 10 $cm^2 \cdot V^{-1} \cdot s^{-1}$. The same authors also theorised on the use of STANWs in organic spintronic devices.[127]

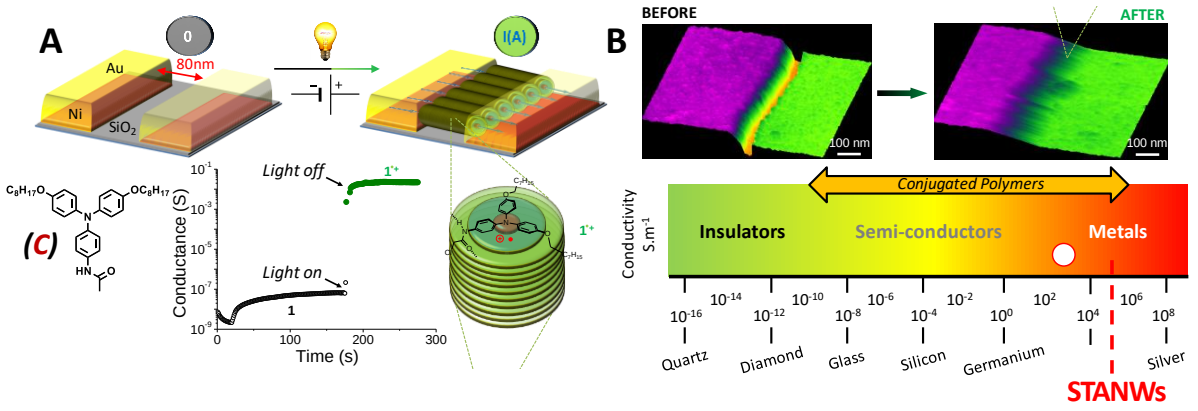

Figure 27 | Construction of nanocircuit with conducting supramolecular triarylamine nanowires. (**A**) Schematic representation of experimental set-up: TCE solution of TAA-***c*** was casted on litographically constructed gold electrodes with a 80 nm gap, after illumination with light, self-assembly occurred causing dramatic increase in conductivity. (**B**) AFM height image of the nanotrench before and after fibre self-assembly. Figure is adapted form ref. 82

126. Bhattacharya, S., Akande, A. & Sanvito, S. Spin transport properties of triarylamine-based nanowires. *Chem. Commun.* **50,** 6626 (2014).
127. Akande, A., Bhattacharya, S., Cathcart, T. & Sanvito, S. First principles study of the structural, electronic, and transport properties of triarylamine-based nanowires. *J. Chem. Phys.* **140,** 074301 (2014).

In a collaboration between our group and the group of Barboiu in Montpellier, these TAA nanowires were introduced in biocompatible hybrid electrodes.[128] The conducting fibres were self-assembled directly into oriented mesoporous silica, which by itself is an insulator, thus bringing electron conducting properties to the system. The biocompatible electrode was further used as an efficient laccase-based biocathode to reduce oxygen into water.

Plasmonic Properties and Energy Transfer

The presence of metallic electrons in the organic fibres was also exploited towards the design of plasmonic supramolecular polymers. Plasmonics will be discussed in details in *chapter VI*. For instance, our group designed a simple system connecting clusters of gold nanoparticles with triarylamine nanowires as shown in **Figure 28.** [129]

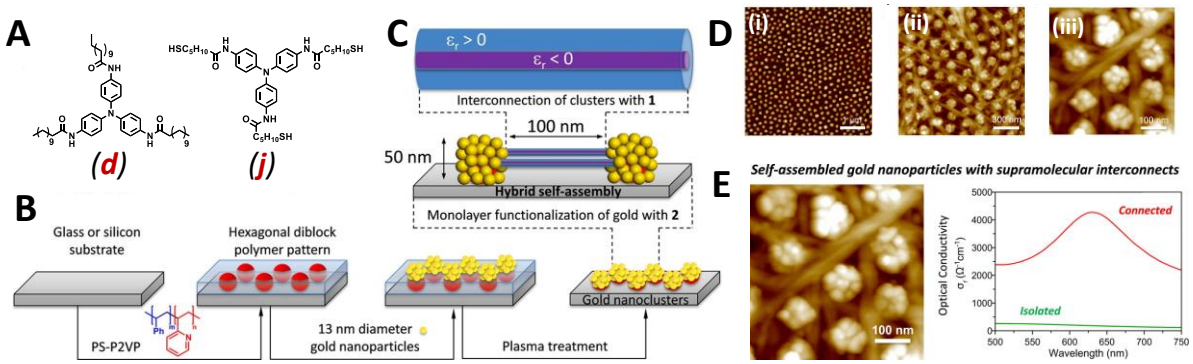

Figure 28 | (**A**) Chemical structure of the TATAs used in the study. TATA-***g*** to construct nanowires, and TATA-***j*** for the surface functionalization. (**B**) Schematic construction of the array of gold nanoclusters, using the patterning of the substrate by microphase separation of a block copolymer, selective deposition of nanoparticles, and plasma treatment. (**C**) Interconnection of clusters with supramolecular TATA nanowires. (**D**) (**i**) AFM height image of the patterned array of naked gold nanoclusters, as obtained after the construction process depicted in **Fig. B**. (**ii**) AFM height image of the hybrid array of organic fibers with gold nanoclusters, as obtained after the construction process depicted in **Fig.C**, that is including STANWs as interconnects. (**iii**) Magnification of the AFM height image obtained in (**ii**). Figure is adapted from ref. 129

The gold surface of the nanoparticles was first functionalised with a monolayer of TATA molecules decorated with thiols (***j***) to ensure strong contact between the nanowires and the gold surface through hydrogen bonding recognition. The interconnection of the clusters with the nanowires was done by the incubation of functionalised surfaces with a light irradiated chloroform solutions of nanowires, resulting in the formation of a hybrid surface **Figure 28C,D(ii, iii)**. The study of optical properties of these hybrid systems revealed significant changes for photo-doped nanowires, compared to undoped ones. For instance, the

128. Licsandru, E.-D. *et al.* Self-Assembly of Supramolecular Triarylamine Nanowires in Mesoporous Silica and Biocompatible Electrodes Thereof. *Nanoscale* **8,** 5605–5611 (2016).
129. Armao IV, J. J. *et al.* Supramolecular Organic Nanowires as Plasmonic Interconnects. *ACS Nano* **10,** 2082–2090 (2016).

optical conductivity of interconnected nanoparticle clusters increased from 260 to 4270 $\Omega^{-1}\cdot cm^{-1}$ suggesting the interaction between hot electron/hole couples of gold nanoparticles and the polaronic band of TATA nanowire. In another example organic crystals constructed with acetylated TATA were used as microscopic plasmonic waveguides.[130]

Organic Solar Cells

Triarylamines are widely used in the form of amorphous films in organic and hybrid photovoltaics. The first examples of self-assembling triarylamines in this field have been reported only very recently by the groups of Holmes (2013)[131,132] and Stupp (2016) (**Figure** 29).[133]

The group of Holmes took advantage of the light-induced self-assembly of triarylamines to investigate its influence on the organic solar cell performance. For this reason, two TAA-based donor-acceptor molecules (***k*** and ***l***) were synthesised (**Figure** 29**A**). The light-induced self-assembly was confirmed by NMR spectroscopy, with the disappearance of all the resonance signals, corresponding to a π-conjugate system for both molecules (**Figure 29B**). The authors report the increase in photo-conversion efficiency from 0.65% to 0.90% for molecule ***k*** before and after irradiation respectively.

Stupp and co-workers report on the use of donor-acceptor tripodal compound in organic heterojunction solar cells (**Figure 29B**). A set of molecules with different alkyl substituents: short linear (C_6, C_8) short brunched (ethylhexyl) and long linear (C_{12}) chains were synthetized. The C_6 and C_8 decorated molecules had low solubility and were not suitable for device fabrication. The performance of the devices prepared with ethylhexyl-TAA (***m***) and C_{12}-TAA (***n***) was 2.9% and 4.4% respectively. This difference is explained by the fact that the molecule ***n*** assembles in small supramolecular wires, while molecule ***m*** forms a uniform film.

130. Armao IV, J. J., Rabu, P., Moulin, E. & Giuseppone, N. Long-Range Energy Transport *via* Plasmonic Propagation in a Supramolecular Organic Waveguide. *Nano Lett.* **16,** 2800–2805 (2016).
131. Kumar, R. J. *et al.* Enhanced photovoltaic efficiency via light-triggered self-assembly. *Chem. Commun.* **49,** 6552 (2013).
132. Kumar, R. J., Subbiah, J. & Holmes, A. B. Enhancement of efficiency in organic photovoltaic devices containing self-complementary hydrogen-bonding domains. *Beilstein J. Org. Chem.* **9,** 1102–1110 (2013).
133. Aytun, T. *et al.* Self-Assembling Tripodal Small-Molecule Donors for Bulk Heterojunction Solar Cells. *J. Phys. Chem. C* **120,** 3602–3611 (2016).

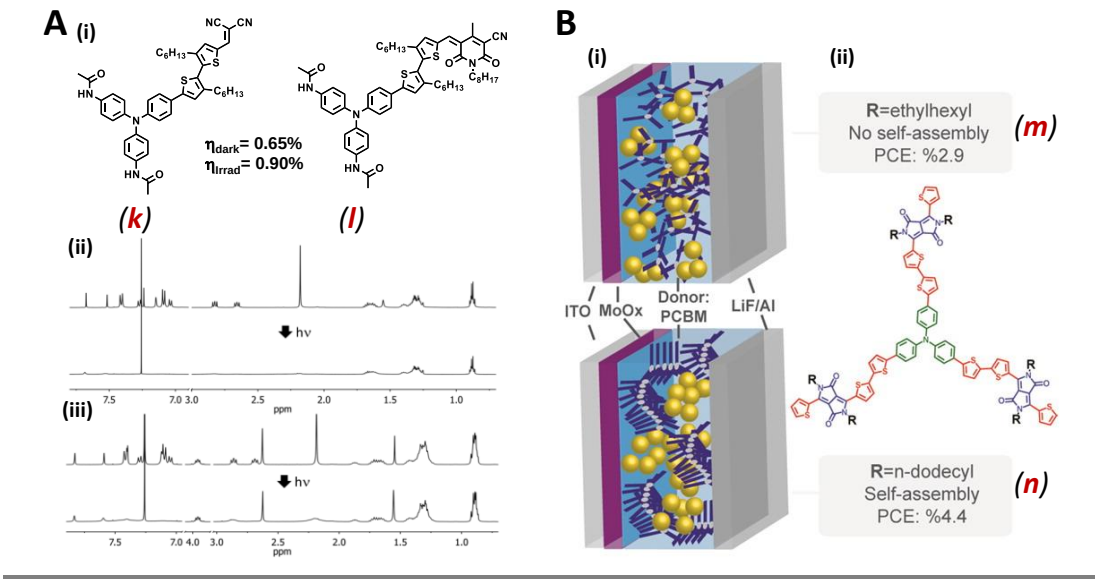

Figure 29 | Self-assembling triarylamine-based materials used in organic photovoltaic cells. (**A**) (**i**) Chemical structure of triarylamine bis-imides decorated with thioophene moieties. Change in the ^{1}H NMR spectrum of a 5 mM solution of ***k*** (**ii**) and ***l*** (**iii**) in chloroform following 2 hours of irradiation with white light.[131] (**B**) (**i**) Schematic representation of the solar cells with non-assembling (top) and assembling (bottom) triarylamine derivative (**ii**) Chemical structure of used triarylamine-based donor molecules ***m*** and ***n***. The photoconversion efficiencies are 2.9% and 4.4% for non-assembling (***m***) and assembling (***n***) molecule respectively.[133] Figure is adapted from refs. 131,133

Chemo and Biosensing

In the section dedicated to molecular triarylamines, we acknowledged their use to detect different analytes. Similarly, in recent years, the use of supramolecular triarylamines was reported to detect explosives,[134–136] organic vapours,[137] metal ions (mercury,[138] copper and iron[139]) or fluoride anion,[140] γ-radiation detection[74] and bioimaging[141] *etc.*

For instance, the group of Ziqiang reported on the use of triarylamine derivatives (***o*** and ***p***) depicted on **Figure 30** for the detection of picric acid (trinitrophenol).[135] The studied molecules formed rod-like assemblies in THF solutions (**Figure 30C (i, iii)**), which showed intense fluorescence both in solution and in solid state. However, upon the addition of picric acid, the florescence was gradually quenched, due to the donor-acceptor intermolecular

134. Ma, H. *et al.* Supramolecular self-assembly carbazolyl radicals nanospheres triggered by ultraviolet light for explosives sensing. *Talanta* **160,** 133–137 (2016).
135. Wenfeng, L., Hengchang, M. & Ziqiang, L. Self-assembled triphenylamine derivative for trace detection of picric acid. *RSC Adv.* **4,** 39351 (2014).
136. Shanmugaraju, S. & Mukherjee, P. S. π-Electron rich small molecule sensors for the recognition of nitroaromatics. *Chem. Commun.* **51,** 16014–16032 (2015).
137. Jiang, Y. *et al.* Multibranched triarylamine end-capped triazines with aggregation-induced emission and large two-photon absorption cross-sections. *Chem. Commun.* **46,** 4689 (2010).
138. Shi, W. *et al.* Barbituric acid-triphenylamine-adduct as AIEE-type molecule and optical probe for mercury(II). *New J. Chem.* **00,** 1–3 (2016).
139. Wenfeng, L. *et al.* A self-assembled triphenylamine-based fluorescent chemosensor for selective detection of Fe^{3+} and Cu^{2+} ions in aqueous solution. *RSC Adv.* **5,** 6869–6878 (2015).
140. Xu, D. *et al.* New dendritic gelator bearing carbazole in each branching unit: selected response to fluoride ion in gel phase. *Org. Biomol. Chem.* **9,** 1523 (2011).
141. Kong, L. *et al.* Self-assembly of metal ion induced highly emissive fluorophore-triphenylamine nanostructures: enhanced two-photon action cross-section for bioimaging applications. *J. Mater. Chem. C* **3,** 570–581 (2015).

charge transfer taking place between the electron donor TAA molecules and highly electron deficient picric acid. Remarkably, the addition of picric acid had a strong influence on the aggregate formation, which greatly decreased in size (**Figure 30C(ii-iv)).** Generally, the detection of common aromatic explosives is based on their D-A interaction with triarylamines.

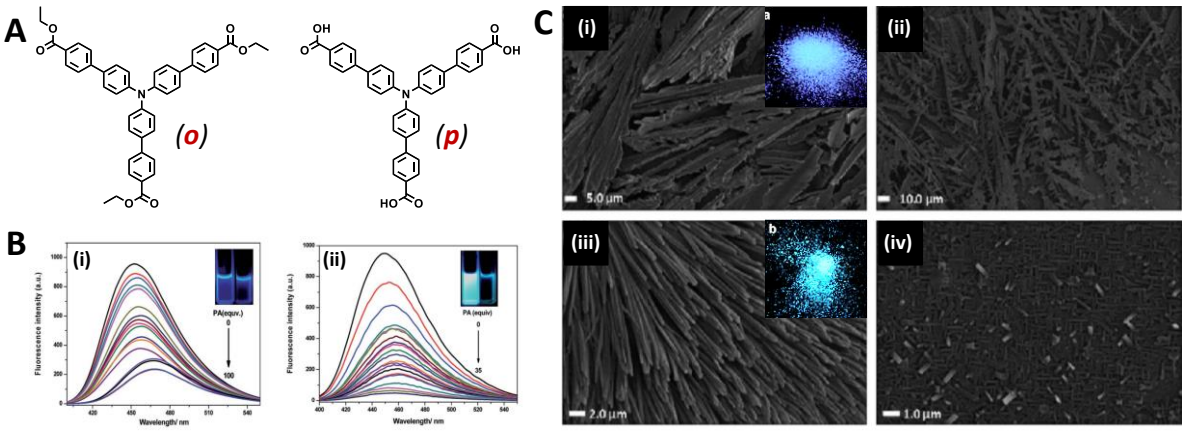

Figure 30 | Self-assembled triphenylamine derivative for trace detection of picric acid (PA). (**A**) Chemical structure of ester (***o***) and acid (***p***) triarylamine derivatives. (**B**) Fluorescence spectra of ***o*** and ***p*** (10 μM) on addition of PA in THF respectively. Insets show the quenching in fluorescence of ***o*** (**i**) and ***p*** (**ii**) after addition of PA. All images are taken under 368 nm UV lamp. (**C**) SEM images of aggregates of compounds ***o*** (**i**) and ***p*** (**iii**) in THF; SEM images of [***o*** + PA] (**ii**) and [***p*** + PA] (**iv**). Insets show the fluorescense of compounds in a powder state. Figure is adapted from ref. 135

The use of triarylamine systems for biomedical applications is also interesting, as was discussed in the previous section. Recently, Barboiu *et al.* reported on the use of self-assembling triarylamine derivative for DNA length determination.[142] The authors used a one-step straightforward approach for the synthesis of TAA derivatives, taking advantage of a hydrazone formation starting from tri-formyl-phenylamine (***q***) and corresponding hydrazide (**Figure 31A**). Using this method, various TAA derivatives can be easily synthetized. The introduction of hydrazone moieties ensures the efficient hydrogen bonding between molecules and the positively charged groups provide both good solubility in aqueous media and electrostatic binding to negatively charged DNA molecules. The titration of a 25 base single strand DNA by TAAs-***r*** controlled by CD spectroscopy (**Figure 31B)** revealed a very interesting observation. Firstly, pure TAA-***r*** did not exhibit a CD signal. After its addition to the solution of DNA, the distinct CD signal, corresponding to the absorption of triarylamine core gradually increased to the point at which the ratio DNA/TAA was 1 to 8.33 which exactly corresponds to the charge balance between DNA^{25-} and 8.33 $(TAA\text{-}r)^{3+}$, indicating the formation of stable hybrid DNA-TAA self-assemblies (**Figure 31C**).

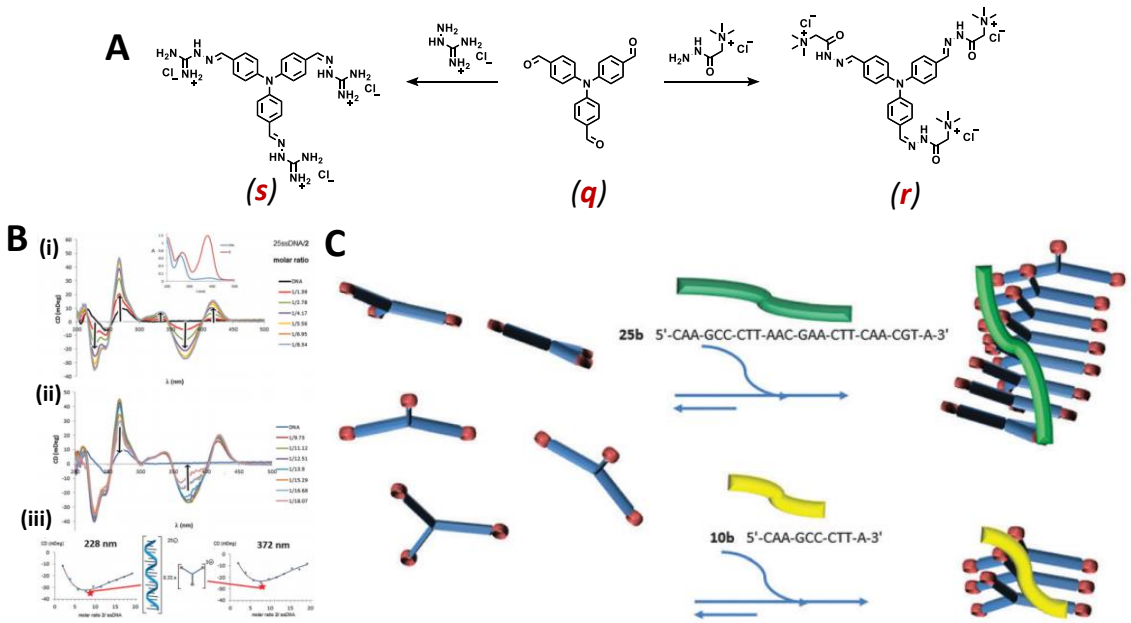

Figure 31 | (**A**) Chemical structure of positively charged ionic triarylamines obtained from corresponding hydrazides and triarylamine aldehyde. (**B**) Circular dichroism spectra obtained by titrating a solution of 25 base ssDNA with TAA-***r***: (**i**) before and (**ii**) after equivalence point corresponding charge balance equilibration of $ssDNA^{25-}$ with about 8.33 molecules of $(TAA\text{-}\boldsymbol{r})^{3+}$. Inset: UV-Vis spectra of 25 base ssDNA and of compound ***r***. (**iii**) Representation of CD signal intensity variation as a function of the ***r***/ssDNA molar ratio at 228 nm (left), respectively, at 372 nm (right); the charge balanced $ssDNA^{25-}/(\boldsymbol{r}^{3+})8.33$ composition at the charge balance equilibration point represented as a red star. (**C**) Proposed self-assembly mechanism of ssDNA-TPA complexes of different dimensional behaviour function of the length of ssDNA, obtained at the charge equivalence point where the charge ratio between negatively charged ssDNA and positively charged ***r*** or ***s*** is 1: 1. Figure is adapted from ref. 142

These examples underline the possibility to use self-assembling triarylamines not just in the field of material sciences but also for sensing of biological molecules in aqueous medium.

142. Kocsis, I., Rotaru, A., Legrand, Y.-M., Grosu, I. & Barboiu, M. Supramolecular rulers enabling selective detection of pure short ssDNA via chiral self-assembly. *Chem. Commun.* **52,** 386–389 (2016).

CHAPTER II. COOPERATIVE SELF-ASSEMBLY OF TRIARYLAMINE-BASED ORGANOGELATORS

1. INTRODUCTION

As we can see from the previous chapter, most studies of self-assembling TAAs/TATAs were in chlorinated solvents. However, we know from these studies that TATA molecules can produce long helical fibres without light irradiation.[113]

Here we will report on the synthesis of chiral TATAs and study their self-assembling properties in various organic solvents. The presence of chiral alkyl substituents near the TATA core (**Figure 32**) will be used to study the self-assembly mechanism of TATA derivatives in these solvents, according to the self-assembly model originally developed by Oosava and Kasai (1962)[143], and adapted to supramolecular polymerization processes by van der Schoot (2005)[144] and widely used by many groups [145–151].

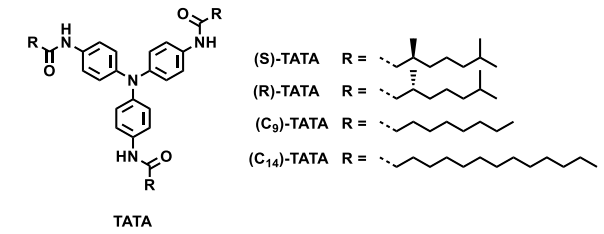

Figure 32 | Molecular structures of C_3-symmetrical TATAs, bearing different alkyl substituents.

143. Oosawa, F. & Kasai, M. A theory of linear and helical aggregations of macromolecules. *J. Mol. Biol.* **4,** 10–21 (1962).
144. *Supramolecular Polymers, Second Edition*. (CRC Press, 2005).
145. Jonkheijm, P., van der Schoot, P., Schenning, A. P. H. J. & Meijer, E. W. Probing the solvent-assisted nucleation pathway in chemical self-assembly. *Science* **313,** 80–3 (2006).
146. Smulders, M. M. J., Schenning, A. P. H. J. & Meijer, E. W. Insight into the mechanisms of cooperative self-assembly: The 'sergeants-and-soldiers' principle of chiral and achiral C 3-symmetrical discotic triamides. *J. Am. Chem. Soc.* **130,** 606–611 (2008).
147. Smulders, M. M. J. *et al.* How to Distinguish Isodesmic from Cooperative Supramolecular Polymerisation. *Chem. Eur. J.* **16,** 362–367 (2010).
148. Ogi, S., Sugiyasu, K., Manna, S., Samitsu, S. & Takeuchi, M. Living supramolecular polymerization realized through a biomimetic approach. *Nat. Chem.* **6,** 188–195 (2014).
149. Yamauchi, M., Ohba, T., Karatsu, T. & Yagai, S. Photoreactive helical nanoaggregates exhibiting morphology transition on thermal reconstruction. *Nat. Commun.* **6,** 8936 (2015).
150. García, F., Viruela, P. M., Matesanz, E., Ortí, E. & Sánchez, L. Cooperative Supramolecular Polymerization and Amplification of Chirality in C3-Symmetrical OPE-Based Trisamides. *Chem. Eur. J.* **17,** 7755–7759 (2011).
151. Ogi, S., Stepanenko, V., Sugiyasu, K., Takeuchi, M. & Würthner, F. Mechanism of Self-Assembly Process and Seeded Supramolecular Polymerization of Perylene Bisimide Organogelator. *J. Am. Chem. Soc.* **137,** 3300–3307 (2015).

2. BIBLIOGRAPHY

A. Supramolecular Chirality

i. Generalities

Chirality (handedness from Greek) is a property of symmetry and represents an extremely important fundamental phenomenon in nature. An object is said to be *chiral* if it cannot be superimposed on top of its mirror image. Conversely, if an object and its mirror image are superimposable, then it is said to be *achiral*. Chirality manifests itself through many different natural phenomena, from elementary particles to galaxies, but also in biological systems (**Figure 33**). The first chiral organic molecule was recently discovered in interstellar space.[152]

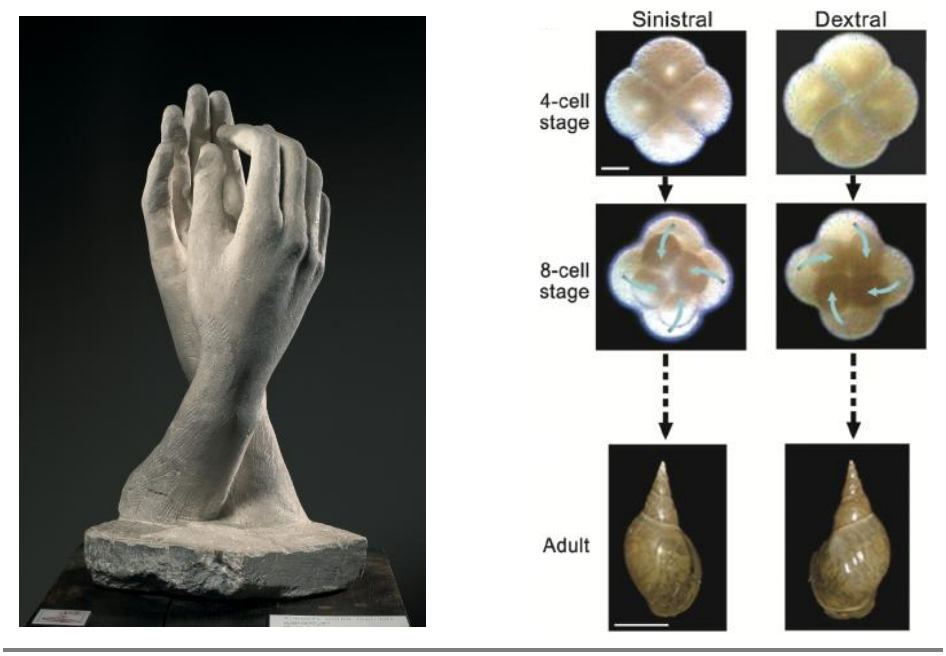

Figure 33 | Photograph of the sculpture "The Cathedral" by A. Rodin, taken from the web-page of the Musée Rodin[153] **(left);** Development of a sinistral and dextral snails, observed olready at 4 and 8-cell stages. And correspondent adult snails. (**right**). Image is reproduced from ref. 154

In chemistry, chirality is of great interest regarding both practical applications in industry, such as enantio-selective synthesis, catalysis and development of bioactive compounds; and fundamental aspects, such as chiral information, recognition and amplification or even the existence of homochirality in living organisms.[155]

152. McGuire, B. A. *et al.* Discovery of the interstellar chiral molecule propylene oxide (CH_3CHCH_2O). *Science* **352,** 1449–1452 (2016).
153. Museé Rodin. at <http://www.musee-rodin.fr/>
154. Shibazaki, Y., Shimizu, M. & Kuroda, R. Body Handedness Is Directed by Genetically Determined Cytoskeletal Dynamics in the Early Embryo. *Curr. Biol.* **14,** 1462–1467 (2004).

Molecules which relate to each other as mirror images are a special type of stereoisomers called *enantiomers.* When stereoisomers are not mirror images of one another, they are called *diastereomers*.

Enantiomers have the same energy potential and therefore the same chemical and physical properties and cannot be distinguished by conventional methods. Diastereomers on the other hand have different energies and consequently different physico-chemical properties.

A molecule is chiral when it contains *stereogenic* centre, usually an atom connected with four unique substituents.[156] Many chiral molecules do not possess a stereogenic centre. In these cases, it is said that they have *axial*, *planar* and *helical* chirality.

Chirality in supramolecular structures originates from the asymmetrical arrangement of molecules by means of non-covalent interactions. The molecules themselves can be chiral, achiral, or even a mixture of chiral and achiral molecules, which assemble in to chiral supramolecular structures. The comparison between molecular and supramolecular chirality is summarised in **Table 3**.

Table 3 | Comparison between molecular and supramolecular chirality.

	Molecular Chirality	**Supramolecular Chirality**
Composition	Atom	Molecule, binding block, tecton
Bond	Covalent bond	Non-covalent bond
Chiral Geometry	Tetrahedron*, axis, plane	Helical, spiral, chiral sheet, chiral domain
Manifestation of Chirality	Point, axis, plane	Conformation, secondary and tertiary structures, helicity, induced chirality *etc.*
Naming Convention	R/S, L/D, Δ/Λ M/P	M/P
Special Feature	Fixed chirality, recognition	Dynamic, sergeant-soldier rule, majority rule, chiral memory, recognition

* and higher symmetry

156. Stereogenic atom should not be necessarily a carbon atom. Theoretically, it may be almost any atom from the periodic table. Moreover, stereogenic centre could be positioned not at an atom at all, but somewhere in space between atoms like in chiral adamant.

In the following sections, after a short discussion on the techniques used to characterize supramolecular chirality, we will present selected examples of chiral supramolecular aggregates built from:

(***i***) purely chiral or a mixture of chiral and achiral molecules;

(***ii***) chiral and/or achiral molecular units under the influence of external physical or chemical stimuli;

(***iii***) exclusively achiral molecules *via* spontaneous symmetry breaking.

ii. Characterization of Supramolecular Chirality

Chirality can be observed directly at the molecular level by X-Ray diffraction, which gives the absolute configuration of a molecule. Unfortunately, most supramolecular structures do not produce monocrystals, suitable for the X-Ray diffraction. The main method, used to study chirality at both molecular and supramolecular levels is circular dichroism spectroscopy (CD). This non-invasive method measures the interaction of chiral electromagnetic irradiation (circularly polarised light) with matter.[157] CD in the UV-Vis region is most commonly used and is strongly related to absorption spectroscopy. If the compound of interest does not absorb in the UV-Vis region, it will be inactive in CD as well. Technically CD represent the difference in absorption of the sample between left circularly polarised light (*L-CPL*) and right circularly polarised light (*R-CPL*).[158]

$$CD = \Delta Abs(\lambda) = Abs(\lambda)_{L-CPL} - Abs(\lambda)_{R-CPL} \quad \textbf{(5)}$$

If the CD signal has a shape of a peak or a valley (**Figure 34**, red lines), it is said that Cotton effect is observed[159]. Cotton effect is called positive, if the CD intensity increases when moving to lower wavelengths (**Figure 34A**) and negative if it decreases (**Figure 34B**). Usually the Cotton effect corresponds to the maximum of the absorption spectra. Whereas UV-Vis spectra of enantiomers are identical, their CD and ORD (Optical Rotatory Dispersion)[160] spectra are the mirror images of one another.

For a mixture of compounds, the resulting CD spectrum is a superposition of the signals from each chiral chromophore present in the system: individual molecules, primary aggregates, aggregates of higher orders. This as well as the dynamic nature of supramolecular

157. Being a type of optical spectroscopy CD spectroscopy is categorised by the light energy regions: Electron Circular Dichroism spectroscopy (UV-Vis-NIR-region) and Vibrational Circular Dichroism spectroscopy (IR).
158. Rodger, A. in *Encyclopedia of Analytical Chemistry* 1–34 (John Wiley & Sons, Ltd, 2006). doi:10.1002/9780470027318.a5402
159. Named after the French physicist Aimé Cotton (1869–1951) who discovered this phenomenon in 1895.
160. ORD is defined as optical rotation of a compound measured as a function of the wavelength.

systems are the main reasons why the interpretation of the CD spectra of self-assemblies is sometimes not a trivial task. Nevertheless, CD spectroscopy in supramolecular systems is a very important tool to provide information on: (***i***) the dynamics of the chiral nano-objects and (***ii***) the intermolecular interactions involved in the formation of the chiral supramolecular aggregates.

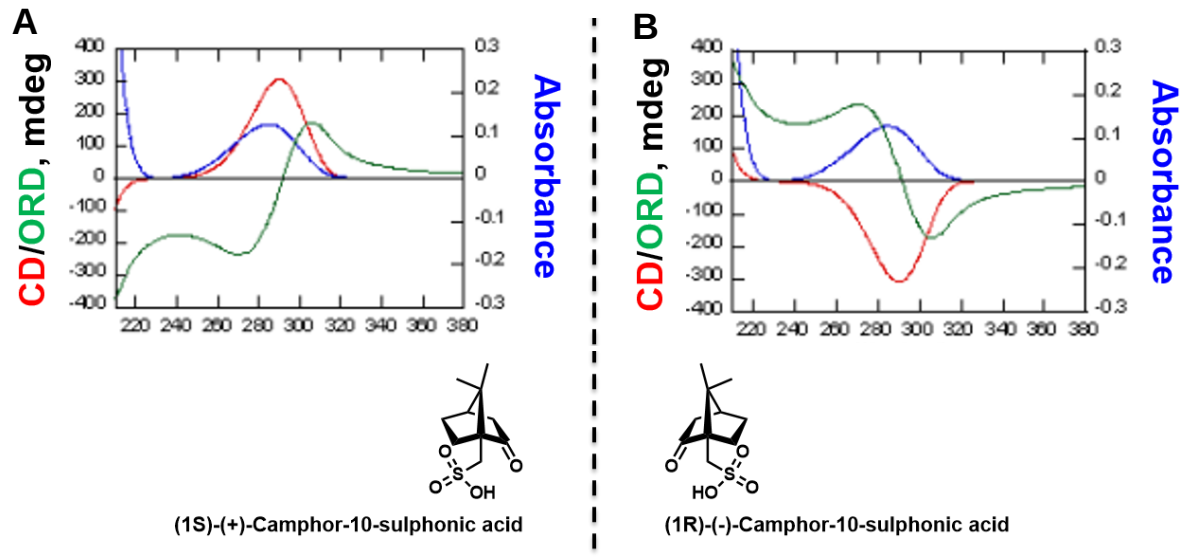

Figure 34 | Typical CD (red line), ORD (green line) and UV (blue line) spectra of (**A**) (1*S*)-(+)-camphor-10-sulphonic acid and (**B**) (1*R*)-(–)-camphor-10-sulphonic acid. Figure is adapted from the web-page of Applied Photophysics.[161]

Supramolecular chirality can also be studied by direct observation of the morphology using microscopy techniques such as TEM, SEM together with AFM and STM. These techniques enable the study of chirality at the nano/micro-level.

Overall, although observed objects will correspond to aggregates of higher orders *i.e.* superstructures, formed from primary aggregates during further assembling process, microscopy will complement CD analyses and provide global information on the morphology of the chiral supramolecular aggregates. Unfortunately, these objects are rarely primary aggregates; most frequently they represent aggregates of higher orders – superstructures, formed from primary aggregates during further assembling processes.

For instance, when chiral assemblies are built from achiral precursors, an equimolar mixture of chiral M and P twisted helixes, which are enantiomers, is expected to form. In this particular case, although the CD of such system will be silent, microscopy techniques should provide imaging of the aggregates of both types of "handedness".

161. AppliedPhotophysics. at <https://www.photophysics.com/resources/tutorials/circular-dichroism-cd-spectroscopy>

iii. Supramolecular Chirality via Chirality Transfer

Chirality transfer (or transfer of chiral information) is the first mechanism through which chiral self-assemblies are produced. There are two possibilities: ***a***) supramolecular structure is built uniquely from chiral monomers, and the chirality of a monomer dictates handedness of a whole assembly; ***b***) supramolecular chirality of the system is defined by the chirality transfer from a small fraction of chiral molecules in a mixture of chiral and achiral monomers. The efficiency of chirality transfer depends on a number of parameters such as the nature and the strength of the supramolecular bond, and the distance from the stereogenic centre to the assembly site.

There are many reported examples of chirality transfer in supramolecular systems, in which chiral assemblies were obtained from chiral precursors: artificial and natural amphiphiles such as amino acids, peptides[162,163] or nucleobase derivatives[17], discotic molecules such as derivatives of naphthalene, pyrene[17,164], perylene[165], hexabenzocoronenes, oligo-phenylenes,[145,166] porphyrins,[148,167] BTAs,[146,168–178] *etc.*

162. Ulijn, R. V. & Smith, A. M. Designing peptide based nanomaterials. *Chem. Soc. Rev.* **37,** 664–675 (2008).
163. Fleming, S. & Ulijn, R. V. Design of nanostructures based on aromatic peptide amphiphiles. *Chem. Soc. Rev.* **43,** 8150–8177 (2014).
164. Micali, N. *et al.* Hydrodynamic and Thermophoretic Effects on the Supramolecular Chirality of Pyrene-Derived Nanosheets. *Chem. Eur. J.* **21,** 9505–9513 (2015).
165. Würthner, F. *et al.* Perylene Bisimide Dye Assemblies as Archetype Functional Supramolecular Materials. *Chem. Rev.* **116,** 962–1052 (2016).
166. Korevaar, P. a. *et al.* Pathway complexity in supramolecular polymerization. *Nature* **481,** 492–496 (2012).
167. Helmich, F. *et al.* Dilution-Induced Self-Assembly of Porphyrin Aggregates: A Consequence of Coupled Equilibria. *Angew. Chem. Int. Ed.* **49,** 3939–3942 (2010).
168. Markvoort, A. J., ten Eikelder, H. M. M., Hilbers, P. A. J., de Greef, T. F. A. & Meijer, E. W. Theoretical models of nonlinear effects in two-component cooperative supramolecular copolymerizations. *Nat. Commun.* **2,** 509 (2011).
169. Gillissen, M. A. J. *et al.* Triple Helix Formation in Amphiphilic Discotics: Demystifying Solvent Effects in Supramolecular Self-Assembly. *J. Am. Chem. Soc.* **136,** 336–343 (2014).
170. Stals, P. J. M., Artar, M., Vendrig, P., Palmans, A. R. A. & Meijer, E. W. Consequences of Subtle Chiral Effects: From 'Majority-Rules' to 'Minority-Rules'. *Aust. J. Chem.* **68,** 622–626 (2015).
171. Nieto-Ortega, B. *et al.* On the handedness of helical aggregates of C $_3$ tricarboxamides: a multichiroptical characterization. *Chem. Commun.* **51,** 9781–9784 (2015).
172. Nakano, Y. *et al.* Conformational Analysis of Chiral Supramolecular Aggregates: Modeling the Subtle Difference between Hydrogen and Deuterium. *J. Am. Chem. Soc.* **135,** 16497–16506 (2013).
173. Desmarchelier, A., Raynal, M., Brocorens, P., Vanthuyne, N. & Bouteiller, L. Revisiting the assembly of amino ester-based benzene-1,3,5-tricarboxamides: chiral rods in solution. *Chem. Commun.* **51,** 7397–7400 (2015).
174. Smulders, M. M. J. *et al.* C 3 -symmetrical self-assembled structures investigated by vibrational circular dichroism. *Chirality* **20,** 1016–1022 (2008).
175. Stals, P. J. M., Smulders, M. M. J., Martín-Rapún, R., Palmans, A. R. A. & Meijer, E. W. Asymmetrically Substituted Benzene-1,3,5-tricarboxamides: Self-Assembly and Odd-Even Effects in the Solid State and in Dilute Solution. *Chem. Eur. J.* **15,** 2071–2080 (2009).
176. Smulders, M. M. J. *et al.* Tuning the Extent of Chiral Amplification by Temperature in a Dynamic Supramolecular Polymer. *J. Am. Chem. Soc.* **132,** 611–619 (2010).
177. Stals, P. J. M. *et al.* Dynamic Supramolecular Polymers Based on Benzene-1,3,5-tricarboxamides: The Influence of Amide Connectivity on Aggregate Stability and Amplification of Chirality. *Chem. Eur. J.* **16,** 810–821 (2010).
178. Stals, P. J. M. *et al.* Symmetry Breaking in the Self-Assembly of Partially Fluorinated Benzene-1,3,5-tricarboxamides. *Angew. Chem. Int. Ed.* **51,** 11297–11301 (2012).

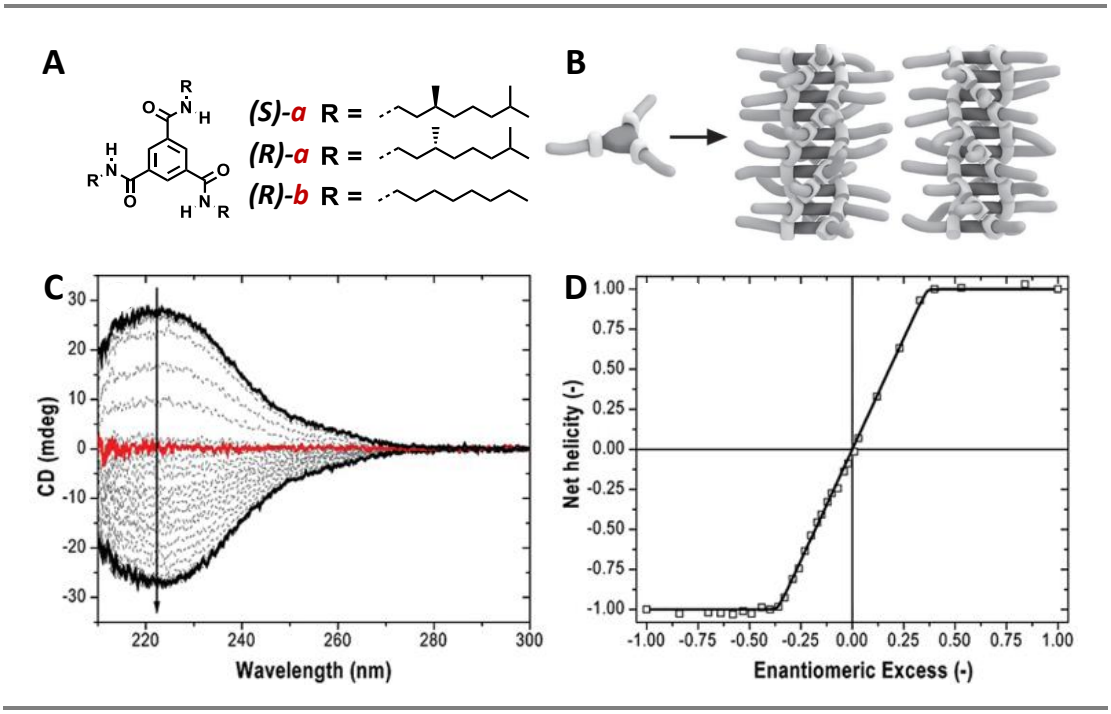

Figure 35 | (**A**) Chemical structure of BTA molecules decorated with chiral (*S*/*R*)-***a*** and achiral alkyl chains (***b***). (**B**) Schematic representation of right and left-handed helices formed during the self-assembling process. (**C**) CD spectra of pure (*R*)-BTA (top black), pure (*S*)-BTA (bottom black) and their equimolar mixture (red). (**D**) Dependence of the helicity of the system based on its composition. Figure is adapted from ref. 176

One family of molecules, which has been extensively studied to understand the various chirality transfer events leading to supramolecular chirality, is the benzene tricarboxamide (BTA) one, largely developed by Meijer and co-workers.[146,168–171,174–177] BTAs assemble in many organic solvents as well as in aqueous media (depending on the nature of side chain) into columnar aggregates. The driving force of this process is the formation of three-fold hydrogen bonds between neighbouring molecules within a stack. The assembly is additionally stabilised by the aromatic and van der Waals interactions. The combination of various experiments such as molecular modelling, IR, and crystal structure suggests the helical arrangement of the BTA molecules within the assembly.[179]

Importantly, when BTA is decorated with achiral alkyl chains, no CD signal of the assemblies is detected as an equimolar mixture of right and left-handed helices is produced (**Figure 35**). In contrast, if the alkyl chains are chiral, chirality transfer from the stereogenic carbon atom to the supramolecular assembly takes place, as indicated by the appearance of a CD signal.[180] A distinct Cotton effect is observed for the aromatic core chromophore: positive

179. Lightfoot, M. P., Mair, F. S., Pritchard, R. G. & Warren, J. E. New supramolecular packing motifs: π-stacked rods encased in triply-helical hydrogen bonded amide strands. *Chem. Commun.* 1945–1946 (1999). doi:10.1039/a905245c
180. Brunsveld, L. *et al.* Chiral Amplification in Columns of Self-Assembled N,N',N''-Tris((S)-3,7-dimethyloctyl)benzene-1,3,5-tricarboxamide in Dilute Solution. *Chem. Lett.* 292–293 (2000). doi:10.1246/cl.2000.292

in the case of (*R*)-BTA and negative for (*S*)-BTA.[176] In both cases, CD signals have the same shape, but are the mirror images of one another, indicating enantiomeric relationship between the BTA helices (**Figure 35**). This example highlights the chirality transfer event which takes place from the molecular building block to the whole supramolecular aggregate.

Some particular cases of chirality transfer are observed when enantiomers or achiral and chiral molecules are mixed. When (*R*)-BTA and (*S*)-BTA were mixed together in different proportions, a nonlinear relationship between the enantiomeric excess, *ee* and the net helicity of the system was observed (**Figure 35C** and **D**)[176]. When (R)- and (S)- enantiomers were mixed in equal proportions, the measured helicity of this mixture was equal to zero (**Figure 35C,** red line). Surprisingly, upon increasing the *ee* of one or another enantiomer, the increase of helicity happened much faster than *ee* increase, reaching a plateau when the *ee* is above 40%. Such observation indicates the existence of homochirality in the system. This effect is called the "*majority-rule*", *i.e.* the major chiral component in a two-component system dictates the chirality of the whole system.

Another particular case of chirality transfer or *chiral amplification* is the so-called *sergeant-and-soldier principle*, which happens when a chiral molecule (which is called *sergeant*) is added to achiral molecules (*soldier*). As already mentioned, due to the presence of both enantiomeric *M* and *P* helixes in a solution of achiral BTA the CD is silent.[180] However, upon addition of a small quantity of chiral molecules ((*S*)-BTA in this case), the CD signal showed a large increase reaching the CD value of pure (*S*)-BTA upon addition of around 15% of sergeant (**Figure 36**). This example highlights how a sergeant molecule can force the whole system to adopt its chirality.

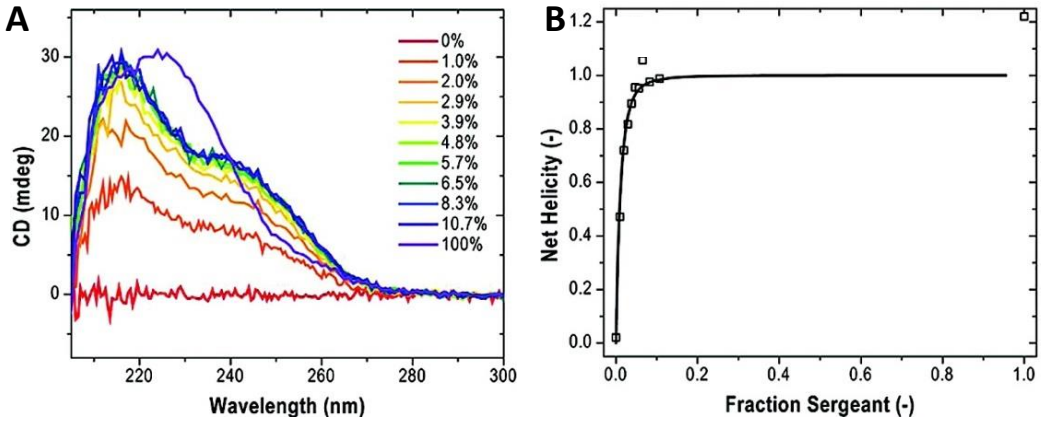

Figure 36 | Experimental demonstration of the "sergeant-soldier" principle. (**A**) CD spectra of mixtures of (*R*)-BTA (sergeants) and (*A*)-BTA (soldiers) with different fraction of "sergeant" (**B**) Dependence of the normalised net helicity on the fraction of "sergeant" in the system. Figure is adapted from ref. 176

iv. External Bias

1) Chemical additives

Chirality transfer can also occur upon addition of a chiral dopant to an achiral self-assembly as reported by Liu and co-workers.[181] The self-assembly process of a water soluble porphyrin TPSS (***c***) was studied in an organic solvent (mixture of chloroform and methanol) in which ***c*** has a bad solubility (**Figure 37A**). However, the formation of long nanofibers was observed. The CD spectra recorded for this suspension of self-assemblies showed a low intensity ambiguous signal, with a stochastic detection of Cotton effect, thus indicating the formation of chiral aggregates of both handednesses.

Interestingly, if a chiral amine (diaminocyclohexane, DAC) was added to the system in different proportions (DAC:***c*** 2:1, 1:1, 1:2) distinct Cotton effects were observed. Importantly, enantiomeric amines produced mirror CD signals showing the formation of aggregates with different handednesses. Moreover, SEM imaging proved to be very informative to demonstrate the chirality of these aggregates by SEM, clearly showing the formation of right and left twisted nanorods (**Figure 37**).

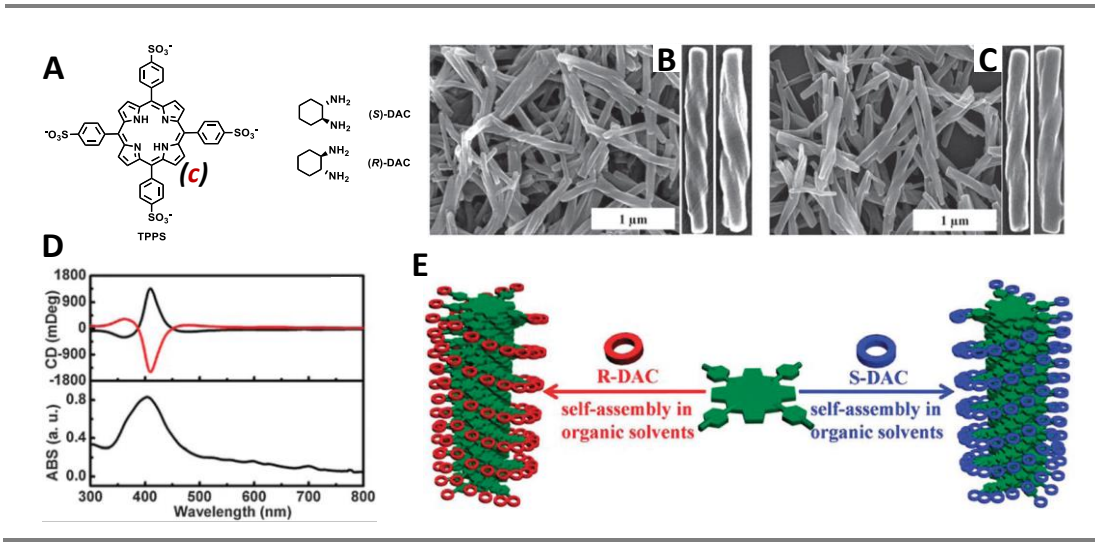

Figure 37 | (A) Chemical structure of water soluble porphyrin, TPPS (***c***) and chiral (*S)*-DAC and (*R*)-DAC diamines. (**B,C**) SEM image of *M* and *P* twisted nanorods, obtained after the coassembly of TPPS with chiral diamines. (**D**) CD (top, black and red line corresponds to *R*- and *S*-DAC respectively) and UV-Vis (bottom) spectra of coassemblies. (**E**) Schematic representation of the supramolecular chirality transfer occuring during the co-assembling process. Figure is adapted from ref. 181

181. Rong, Y., Chen, P. & Liu, M. Self-assembly of water-soluble TPPS in organic solvents: from nanofibers to mirror imaged chiral nanorods. *Chem. Commun.* **49,** 10498 (2013).
182. George, S. J., Tomović, Ž., Schenning, A. P. H. J. & Meijer, E. W. Insight into the chiral induction in supramolecular stacks through preferential chiral solvation. *Chem. Commun.* **47,** 3451 (2011).

2) Solvent

One should not forget that solvent plays a critical role in the stabilisation/destabilisation of supramolecular structures in solutions. The importance of such interactions can be demonstrated when a solvent is used as a chiral bias during the self-assembling process. Some years ago, the group of Meijer reported that achiral OPVs (***d***) in alkanes assemble into a racemic mixture of *P* and *M* helical aggregates. However, the introduction of a chiral side chain on the OPV backbone leads to the formation of helical supramolecular polymers of chiral OPVs (**Figure 38**).[145] When aggregation was carried out in the presence of a chiral co-solvent, however, such as *R*/*S* citronellol, a well-defined CD spectra were detected, with either positive or negative Cotton effect depending on the chirality of the co-solvent.[182] This example demonstrates that chirality transfer can occur from the solvent to the self-assembly.

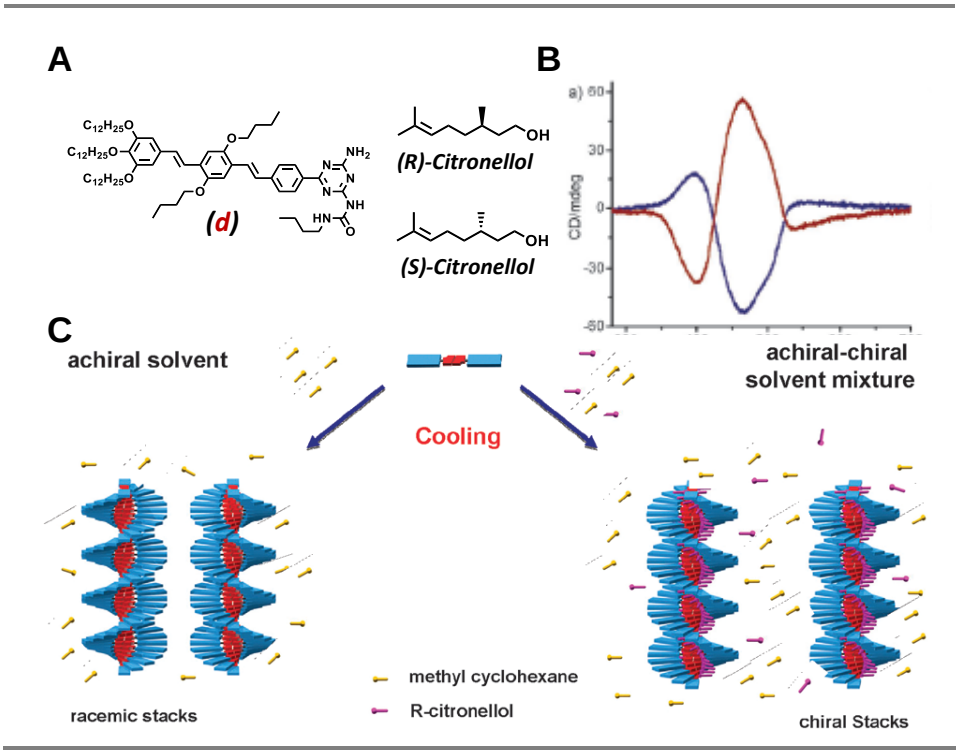

Figure 38 | (A) Chemical structure of OPV molecule (***d***), and chiral co-solvents (*R*/*S* citronellol). (**B**) CD spectra of chiral self-assemblies, thanks to the chirality transfer from the solvent molecules. (**C**) Schematic representation of studied process of chiral induction process. Figure is adapted from ref. 182

In another example, the same group also studied the influence of solvent composition on the self-assembling process of amphiphilic BTA derivative (***e***) (**Figure 39**).[169] The self-assembly process of these molecules was studied in water. For a high water content, using cryo-TEM and SAXS, the authors suggested the formation of a triple helical bundle of fibres due to hydrophobic interactions between alkyl chains. However, when isopropyl alcohol

(IPA) was added to the system, the formation of one-dimensional fibres was observed for high fraction of IPA. The CD signal in both regimes showed different CD, suggesting the different chirality.

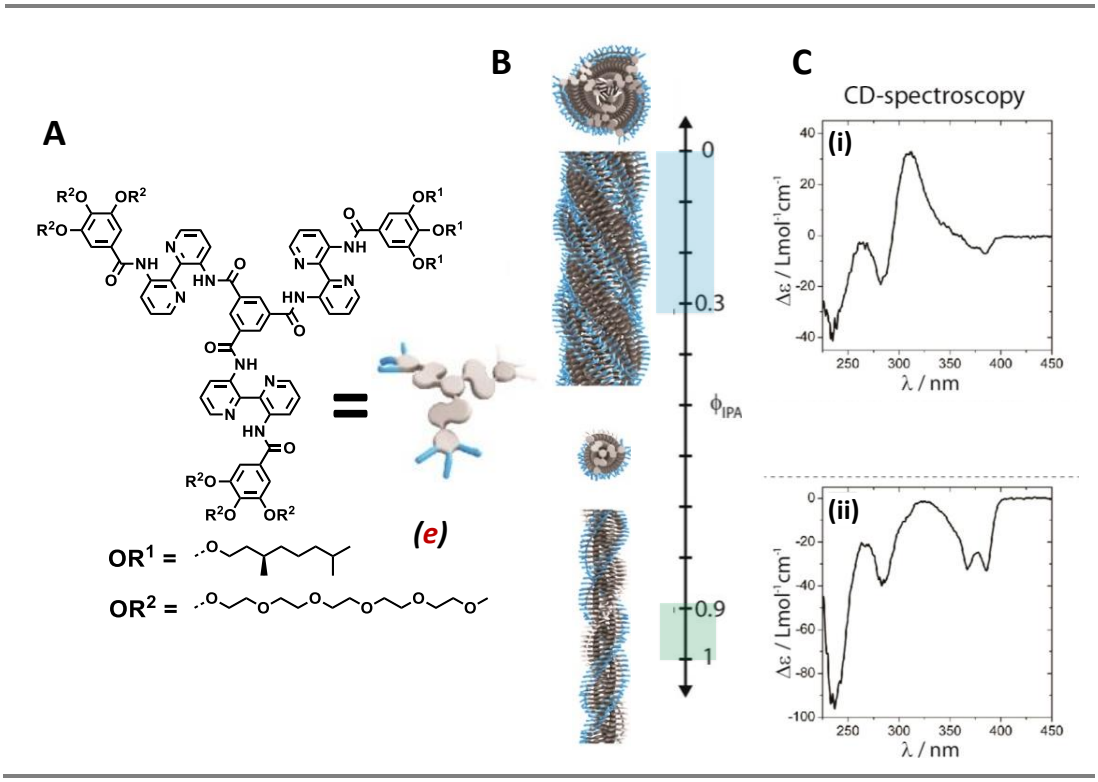

Figure 39 | (A) Chemical structure of BTA derivative (***e***) and **(B)** model of different assemblies (triple helix and single fibre). Scale represent the solvent composition, different colour indicates ranges of the existance of each type of aggregates. (**C**) Corresponding CD spectra in the (**i**) high fraction of IPA and (**ii**) low fraction of IPA. Figure is adapted from ref. 169

3) Temperature effects

Wan and collaborators reported on the formation of sugar-based thermoreversible gels of a sugar derivative **(*f*)** in mixtures of solvents (**Figure 40**).[183] Interestingly, different CD responses were detected, depending on the cooling rate. When a hot solution (where the compound is molecularly dissolved) was cooled slowly, a positive Cotton effect was observed, whereas when the solution was cooled fast, a negative Cotton effect was observed. The formation of the fibrillar structures with different helicities was confirmed by SEM for the slow and fast cooling regimes. This observation was in agreement with CD spectra. This example clearly indicates the importance of thermodynamic parameters on the control of supramolecular chirality.

183. Cui, J. *et al*. Tuning the Helicity of Self-Assembled Structure of a Sugar-Based Organogelator by the Proper Choice of Cooling Rate. *Langmuir* **26,** 3615–3622 (2010). 184. Yagai, S. *et al.* Control over Hierarchy Levels in the Self-Assembly of Stackable Nanotoroids. *J. Am. Chem. Soc.* **134,** 18205–18208 (2012).

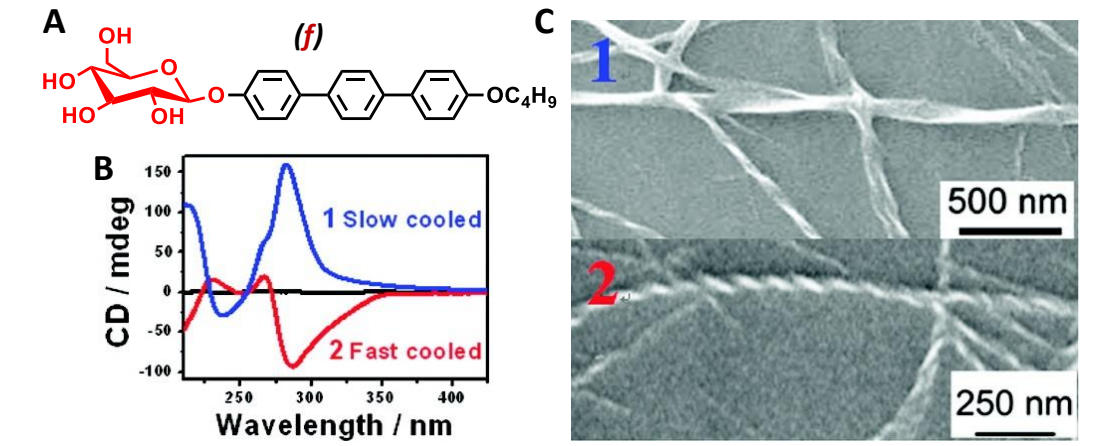

Figure 40 | (**A**) Chemical structure of sugar-based gelator (***f***). (**B**) CD spectra corresponding to the slow cooling and the fast cooling gels. (**C**) SEM images of aggregates, obtained during the slow cooling (**1**) and fast cooling (**2**) processes. Figure is adapted from ref. 183

4) Light

Nonpolarised light was used to tune chirality in supramolecular systems composed of molecules, with photoactive groups, such as azobenzene for instance.[184–186]

The group of Liu described the self-assembly of a chiral azobenzene organogelator (***g***) (**Figure 41**).[185] It aggregates into fibrillar structures in various organic solvents, and forms thermoresponsive gels at appropriate concentrations. Interestingly, the reversible sol-gel transition was observed upon subsequent irradiation of these gels with UV and visible light, due to the structural changes in assemblies, caused by cis-trans photoisomerisation of azobenzene moieties. Moreover, the CD intensity was found to change, depending on light irradiation, suggesting different supramolecular organisation for *E*- and *Z*- isomers. (**Figure** 41).

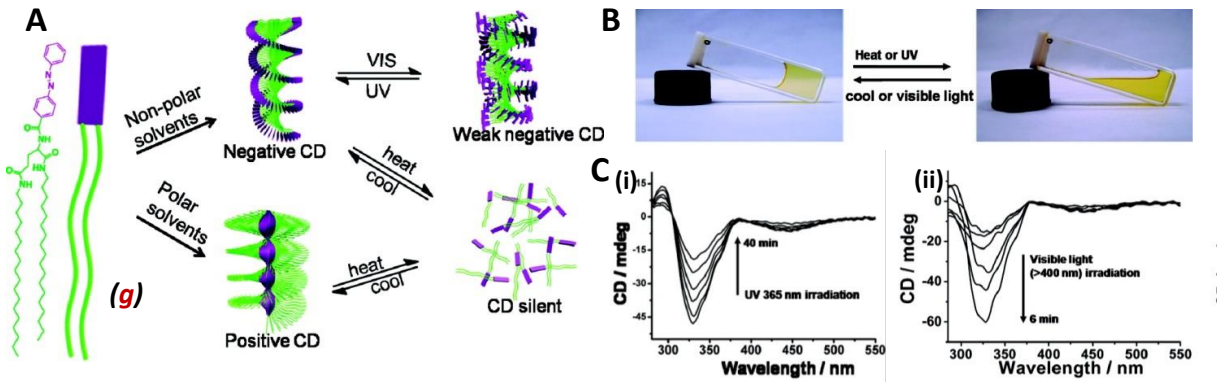

Figure 41 | (**A**) Schematic representation of the self-assembling process of chiral azobenzene molecue (***g***) in polar and apolar organic solvents. (**B**) Digigat photographs of the reversible photo/thermo sol-gel transition. (**C**) CD spectra of studied assemblies in toluene and DMSO. Figure is adapted from ref. 185

Moreover, circularly polarised light can be used to control the chirality of self-assemblies built from achiral molecules. In a recently published paper, left circularly polarised light (*L*-CPL) and right circularly polarised light (*R*-CPL) were claimed to control the helicity of TATA self-assemblies in dichloroethane (**Figure 42**).[120] TATA molecules (***h***) were decorated with the diyne moieties in order to potentially polymerize the self-assembled structures. Upon irradiation with "normal" light, no CD signal was observed, because of the formation of racemic mixture of supramolecular fibres. However, when CPL was used, the self-assembled fibres showed positive Cotton effect with *R*-CPL and *L*-CPL and negative one with *L*-CPL. The intensity of the CD signal increased when irradiation time, upon reaching a plateau after 10 min of irradiation. Moreover, when chiral aggregates, obtained upon irradiation with *L*-CPL, were irradiated with *R*-CPL, the chirality of the system could be reversed and vice-versa. Importantly, the inversion of chirality was not possible anymore after photopolymerization of the diyne side chains, which leads to a freezing of chirality. This example highlights the dynamic nature of supramolecular polymerization process and demonstrated how symmetry breaking can occur using external bias on purely achiral molecule.

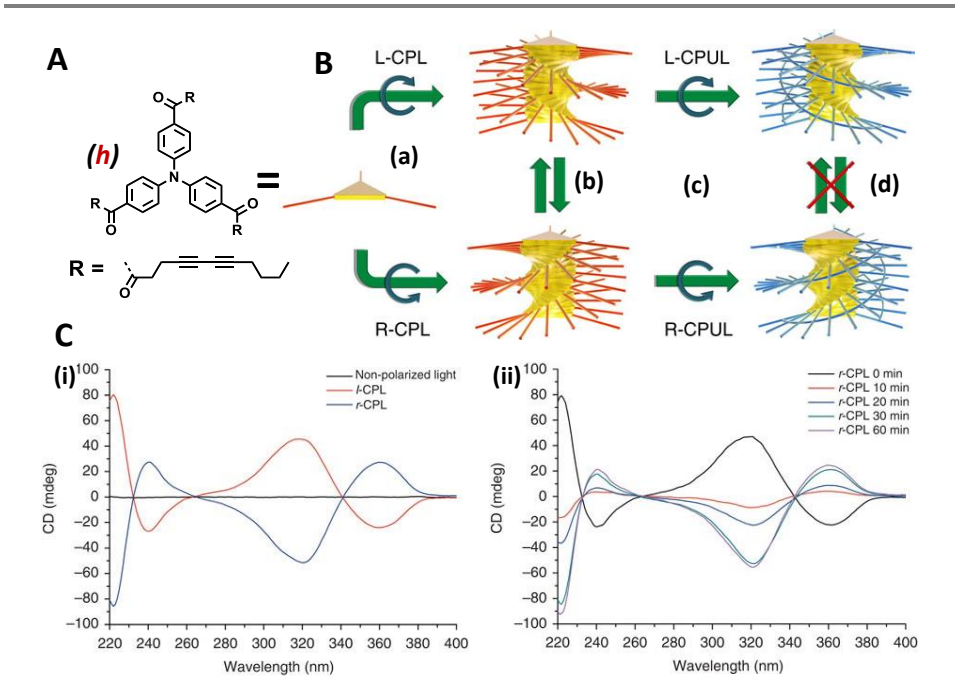

Figure 42 | (**A**) Chemical structure of achiral TATA molecule (***h***) decorated with diyne side-chaines. (**B**) Schematic representation of the self-assembling process. (**a**) *R*-CPL or *L*-CPL dictates the helicity of nanofibres of TATA, (**b**) *M/P* helix transformations upon irradiation with corresponding CPL. (**c**) Cross-photopolymarization of dyine-functions with corresponding CPUL. (**d**) After the polymerisation chirality of assemblies do not change upon irradiation with CPL. (**C**) CD spectra of self-assemblies. (**i**) CD spectra demonstrating process (**a**) of **Fig.B**. (**ii**) CD spectra, demonstrating chirality inversion, described as (**b**) on **Fig.B**. Figure is adapted from ref.120

v. Emergence of Supramolecular Chirality by Symmetry Breaking

The fundamental phenomenon of symmetry breaking *i.e.* induction of asymmetry in the system, starting from achiral compound or a racemic mixture of chiral compounds, is believed to be at the origin of homochirality in living organisms. It is supposed that a number of mechanisms could be responsible for the symmetry breaking:[155]

(***i***) chiral nature of some physical laws, such as electroweak interaction;

(***ii***) chiral environment (circularly polarized light, chiral quartz crystals or even earth rotation);

(***iii***) statistical fluctuations in distribution of chiral molecules.

In order to better understand the complex nature of this event chemists study and model the symmetry breaking in artificial chemical systems.

For the first time, the spontaneous symmetry breaking was observed in stilbene liquid crystals, published in the paper by Young and collegues.[187] Since then, this property was found in different types of liquid crystals, such as banana-shaped (bent-core) molecules.[188]

For instance, Hough, Clark and co-workers reported on the formation of chiral twisted filaments, produced from achiral bent-core molecules.[189] Due to the structural restrains in these compounds, the competition between layering and twisting during their packing, produces nanophase segregation with different degree of hierarchical order. This caused the appearance of both macroscopic chirality and layering in an exotic liquid crystal phase.

Another interesting example of chirality breaking in liquid crystalline phase was communicated by Cheng and colleagues.[190] The authors observed chiral propeller-patterned structures, self-assembled from achiral molecule, derivative of 4-biphenylecarboxylic acid (***i***), which readily formed head-to-head dimers (**Figure 43A**). Different twisting of the dimers leads to the formation of nematic chiral phases. Interestingly, when propeller-patterned droplets with same handedness merged, it resulted in the formation of a bigger droplets, having identical handedness (**Figure 43B(i)**); in contrast, when merging droplets were of the opposite handednesses, this resulted in the formation of large achiral droplet (**Figure 43B(ii)**).

185. Duan, P., Li, Y., Li, L., Deng, J. & Liu, M. Multiresponsive Chiroptical Switch of an Azobenzene-Containing Lipid: Solvent, Temperature, and Photoregulated Supramolecular Chirality. *J. Phys. Chem. B* **115,** 3322–3329 (2011).
186. Gopal, A., Hifsudheen, M., Furumi, S., Takeuchi, M. & Ajayaghosh, A. Thermally assisted photonic inversion of supramolecular handedness. *Angew. Chem. Int. Ed.* **51,** 10505–10509 (2012).
187. Young, W. R., Aviram, A. & Cox, R. J. Stilbene derivatives. New class of room temperature nematic liquids. *J. Am. Chem. Soc.* **94,** 3976–3981 (1972).
188. Lubensky, T. C. LIQUID CRYSTALS: New Banana Phases. *Science* **288,** 2146–2147 (2000).
189. Hough, L. E. *et al.* Helical Nanofilament Phases. *Science* **325,** 456–460 (2009).
190. Jeong, K. U. *et al.* Construction of chiral propeller architectures from achiral molecules. *Adv. Mater.* **18,** 3229–3232 (2006).

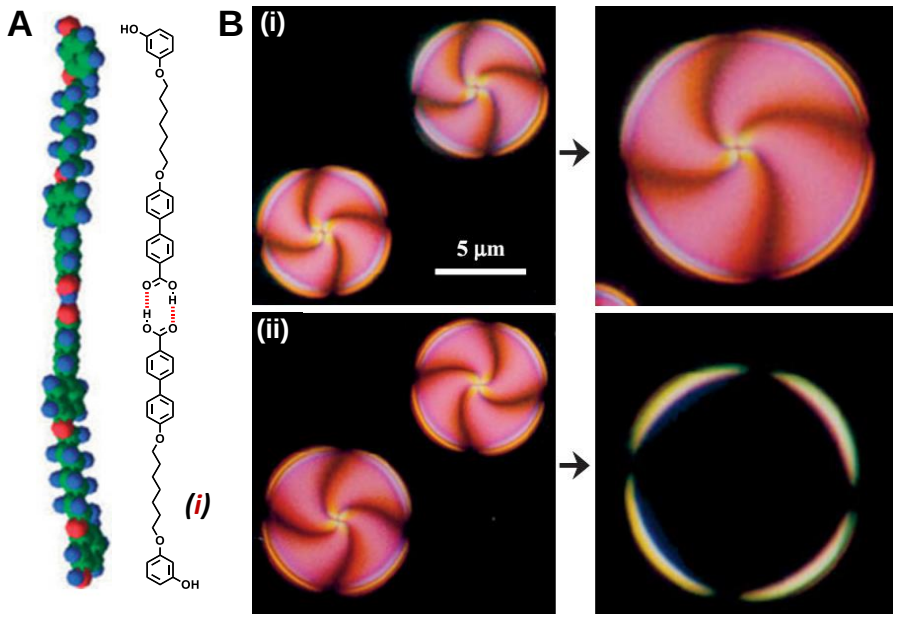

Figure 43 | (**A**) Chemical structure and molecular model of twisted head-to-head dimer (***i*$_2$**). (**B**) OPM images of chiral microdroplets, (**i**) merging droplets of the same chirality produce chiral droplets of a larger size, (**ii**) droplets with oposuit chiralities produce achiral droplets. Figure is adapted from ref. 190

Examples, discussed above, underline the possibility to observe the formation of chiral structures from achiral molecules through the spontaneous symmetry breaking phenomenon in liquid crystalline phases. However, similar chiral symmetry breaking phenomena were also observed in solutions.

In 2012 the group of Meijer demonstrated that partially fluorinated BTA derivatives undergo spontaneous symmetry breaking during the two-step self-assembling process.[178] Upon cooling a hot solution of achiral BTA molecules, during the first step, the racemic mixture of primary *M* and *P* helices is formed, demonstrating no optical activity at the thermodynamic equilibrium conditions. Strikingly, further aggregation of primarily formed fibres (second self-assembling step), resulted in the appearance of the CD signal, indicating formation of supramolecular aggregates of higher orders, with one preferential handedness. Authors suggest that the crucial factor in the observed symmetry breaking is the presence of week interactions between fluorine atoms and electron deficient hydrogens of terminal -**CF_2H** groups, causing the bundling of supramolecular fibres during the second step of aggregation, during which the statistically emerged chiral bias is dramatically amplified.

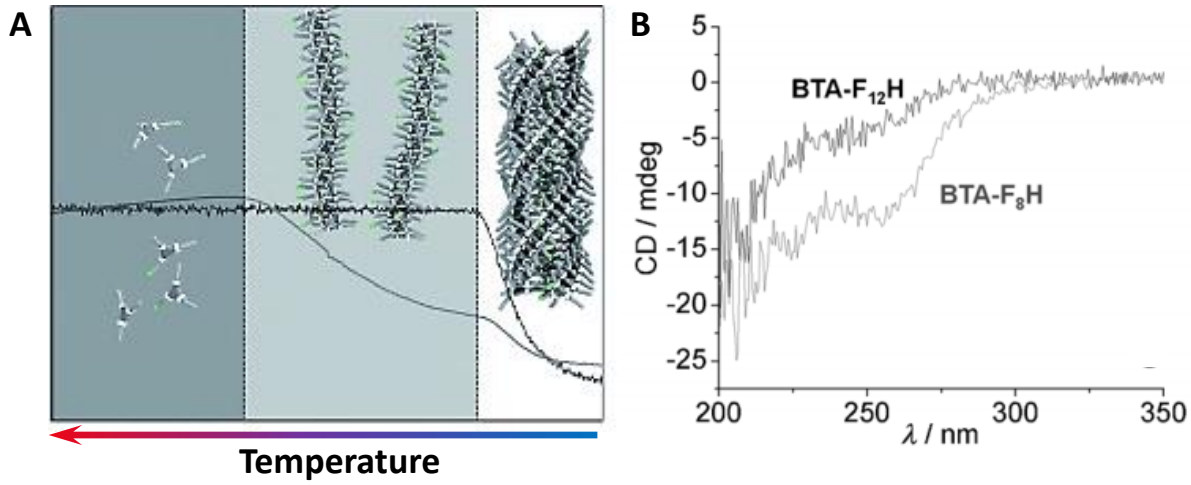

Figure 44 | (**A**) Temperature dependent CD (black) and UV (grey) traces recorded upon cooling of hot solutions of partially fluorinated BTAs. Dashed lines indicate the borders of three regimes: nucleation (dark grey region), 1D elongation (grey region), higher order elongation (white region). (**B**) CD spectra of self-assembled partially fluorinated BTAs with different amount of introduced fluorine atoms. Figure is adapted from ref. [178]

Moreover, it was shown that even mechanical bias such as vortex flow, can also induce the symmetry breaking in achiral systems.[164,191–198] Aida's group performed studies on the influence of stirring on the macroscopic chirality of systems, containing achiral dendric zinc porphyrins (***j***) which self-assemble in fibrous aggregates in benzene (**Figure** 45).[193] It was found that upon stirring in a particular CW or CCW directions, benzene solutions exhibited persistent CD effect. Importantly, mirror images CD signals were detected for different opposite direction of stirring. Moreover, non-stirred solution demonstrated silent CD. The authors conclude that their example shows an interesting possibility to align nanofibers in chiral helical way using rotary stirring. Unlike other examples, where aggregates with a particular handedness are formed, they cannot switch it to opposite, their system exhibit high chiral dynamics depending on the input (**Figure** 45**D**). The supramolecular chirality emerges not only in 1D structures. In the recent work published by Vilari, Häner and colleagues[164], the influence of the stirring on the aggregation of achiral pyrene derivatives in aqueous medium was studied. Upon cooling a hot solution, 2D

191. Tsuda, A. Hydrodynamic Helical Orientations of Nanofibers in a Vortex. *Symmetry (Basel).* **6,** 383–395 (2014).
192. Hotta, Y. *et al.* A physical operation of hydrodynamic orientation of an azobenzene supramolecular assembly with light and sound. *Chem. Commun.* **50,** 5615 (2014).
193. Tsuda, A. *et al.* Spectroscopic Visualization of Vortex Flows Using Dye-Containing Nanofibers. *Angew. Chem. Int. Ed.* **46,** 8198–8202 (2007).
194. D'Urso, A., Randazzo, R., Lo Faro, L. & Purrello, R. Vortexes and Nanoscale Chirality. *Angew. Chem. Int. Ed.* **49,** 108–112 (2010).
195. Okano, K. & Yamashita, T. Formation of chiral environments by a mechanical induced vortex flow. *ChemPhysChem* **13,** 2263–2271 (2012).
196. Sorrenti, A. *et al.* Kinetic Control of the Supramolecular Chirality of Porphyrin J-Aggregates. *Chem. Eur. J.* **18,** 8820–8826 (2012).
197. Micali, N. *et al.* Selection of supramolecular chirality by application of rotational and magnetic forces. *Nat. Chem.* **4,** 201–207 (2012).
198. Petit-Garrido, N., Claret, J., Ignés-Mullol, J. & Sagués, F. Stirring competes with chemical induction in chiral selection of soft matter aggregates. *Nat. Commun.* **3,** 1001 (2012).

supramolecular aggregates (nanosheets) were formed. Surprisingly, when the solution with molecularly dissolved precursor was stirred upon cooling, a well-defined CD signal was observed, which was explained by the presence of nanosheets with a preferential curvature. Importantly, the CD clearly indicated the formation of structures with opposite supramolecular chirality, depending on the direction of stirring.

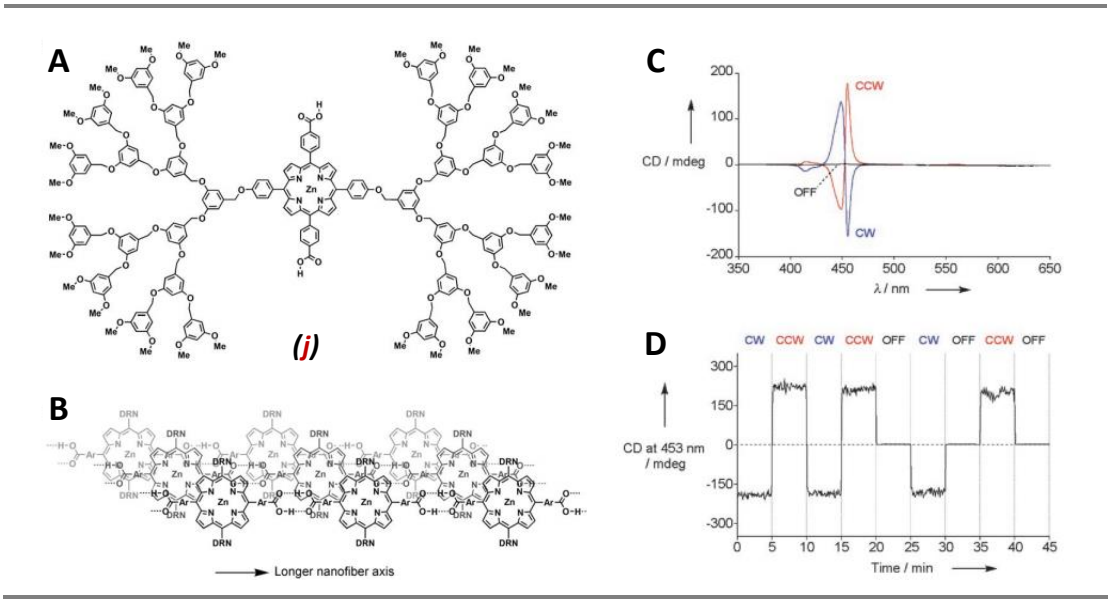

Figure 45 | (**A**) Dendrimeric porphirin derivative (*j*) (**B**) Schematic representation of porphirin arrangement in the supramolecular aggregate. (**C**) CD spectra recorded during CW, CCW and OFF stirring. (**D**) CD intensity measured at 453 nm. Figure is adapted from ref. 193

These examples of symmetry breaking using relatively week and poorly controlled physical forces, sparked considerable interest in the scientific community both for their possible role in the origin of homochirality and for their potential applications in chiral separation. For instance, recently Grzybowski and colleagues reported on the possibility to separate enantiomeric nanoobjects using chiral hydrodynamic flows.[199]

199. Hermans, T. M., Bishop, K. J. M., Stewart, P. S., Davis, S. H. & Grzybowski, B. A. Vortex flows impart chirality-specific lift forces. *Nat. Commun.* **6,** 5640–5648 (2015).
200. De Greef, T. F. A. *et al.* Supramolecular polymerization. *Chem. Rev.* **109,** 5687–5754 (2009).

vi. Conclusions

Studies of chiral phenomena in supramolecular systems may potentially elucidate the fundamental problem on the emergence of homochirality in living organisms. In addition, the potential use of supramolecular chirality in different domains of science make these studies important and interesting. Chiroptical responsiveness, chiral recognition and sensing, supramolecular chiral catalysis are just few examples of the most promising domains of science.

Moreover, in many examples, the use of chiral precursors as building blocks for supramolecular structures with preferential handedness makes it possible to use a very sensitive method, CD spectroscopy, to study the self-assembling process. This can also be instrumental in the determination of the pathways of the self-assembling process and its mechanism.[200]

B. Mechanisms of Supramolecular Polymerization

As already stated in the first chapter of this thesis, due to the dynamic nature of non-covalent forces, supramolecular polymerisation is a dynamic process, during which monomers, oligomers and polymeric molecules exist in equilibrium. The pathway leading to this supramolecular polymerization process on several variables such as: (***i***) the nature of monomer, (***ii***) the concentration of monomer units, which could, for instance, give considerable amount of aggregated species only when using high concentrations of monomers, and (***iii***) the temperature at which polymerisation event occurs (**Figure 46**). For this last parameter, in some cases, a critical concentration of monomers is necessary for the supramolecular polymerization to take place.

The need for supramolecular chemists to understand the thermodynamic parameters that govern supramolecular polymerization events and to explain some of their properties led to the development of theoretical models which are based on the way the Gibbs free energy of a supramolecular polymer evolves with the conversion.[200] These models are inspired by the first theoretical models described in the 1960s to elucidate protein aggregation, such as actin polymerization.[143,201,202] In the following sections, we will briefly classify the different supramolecular polymerization mechanisms based on the evolution of the Gibbs free energy and then explain how thermodynamic parameters can be extracted for each mechanism from experimental data.

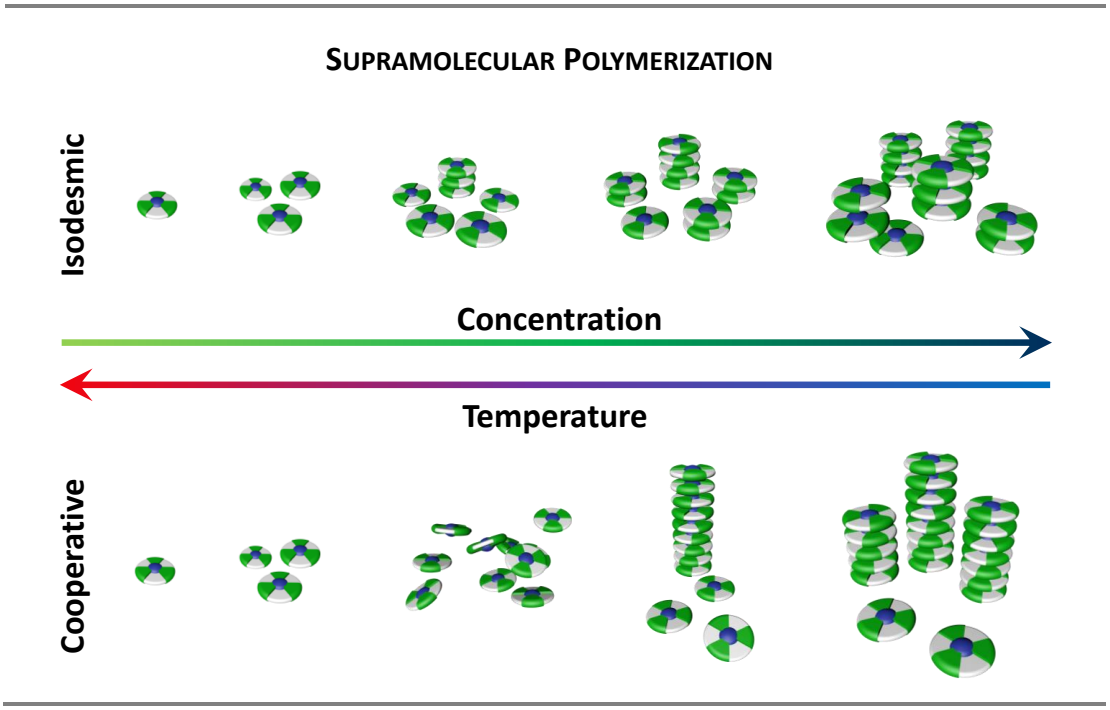

Figure 46 | Graphical representation of isodesmic and cooperative mechanisms of supramolecular polymerization.

i. Classification of Supramolecular Polymerization

Although supramolecular polymers could be classified based on the nature of the non-covalent interactions involved or the type and number of monomers used, the most used classification in the literature is based on the thermodynamics of the supramolecular polymerisation event, which takes into consideration the association constant – K of each monomer addition.[144,147,200,203–206]

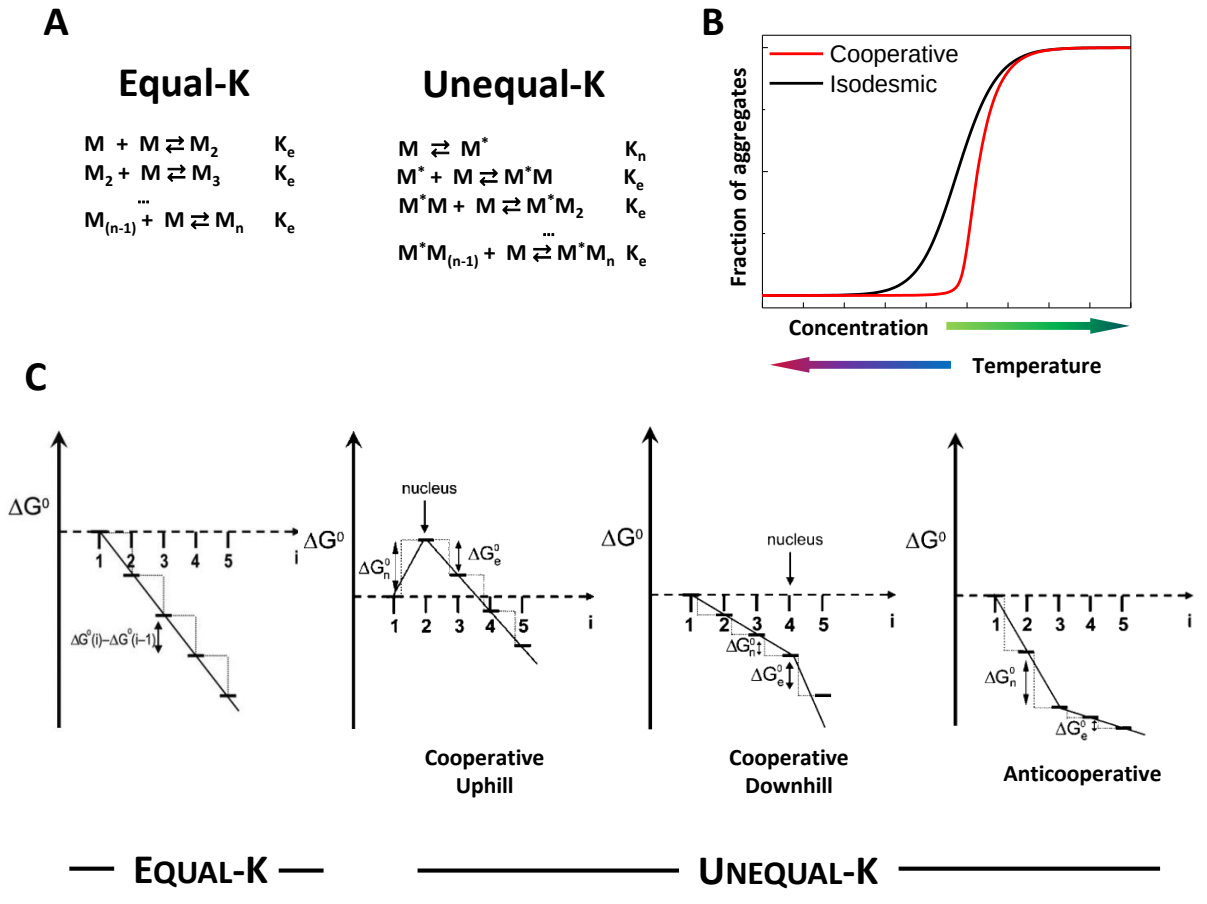

Figure 47 | (**A**) Chemical equilibria existing in the isodesmic (Equal-K) and cooperative (Unequal-K) supramolecular polymerization; (**B**) Graphical representation of the fraction of aggregated molecules as a function of concentration and temperature for the isodesmic and cooperative supramolecular polymerizations; (**C**) Schematic diagram of the free energy changes for the different types of supramolecular polymerization. X-axis represents the size of aggregate, and Y-axis represent free energy in arbitrary units.

Meijer and co-workers identify three mechanisms of supramolecular polymerization: *isodesmic*, *ring-chain* and *cooperative*.[200] The specificity of the ring-chain supramolecular polymerization mainly comes from the nature of the unimers to form inter- or intra-molecular cyclic products, which are in equilibrium with the open-chain species. The supramolecular bonds are formed mainly *via* an isodesmic mechanism. Nevertheless, it was shown that

secondary interactions lead to a certain degree of cooperativity in such systems.[207] Therefore, I will not discuss ring-chain mediated mechanism here, but instead, will focus on the isodesmic and cooperative ones (**Figure 47**).

When the association constant is equal for all steps of the polymerization, *i.e.* it does not depend on the degree of polymerisation, the process is described as an *isodesmic* supramolecular polymerisation. However, when the association constant depends on the degree of polymerization, the supramolecular polymer is produced by a *cooperative* mechanism, also named *Unequal-K* model. This model can be subdivided into three different categories: cooperative nucleated uphill, cooperative nucleated downhill and anticooperative, which will be discussed in details in section **iii** of this chapter.

Each of these models were developed based on two seminal papers: (***i***) a mathematical model reported by Oosawa and Kasai in 1962 to describe the protein assembly[143] and (***ii***) model developed by Goldstein and Stryer in 1986 which describes the cooperativity in polymerization reactions.[208]

ii. Equal-K Supramolecular Polymerization (Isodesmic Supramolecular Polymerization)

The isodesmic supramolecular polymerisation is similar to a step-growth polymerisation, such as polycondensation reactions. Such polymers are formed by the successive addition of a monomer to an oligomer or to another monomer. The nature of the reversible non-covalent bond, involved in the polymerization process is identical at all steps and does not depend on the size of aggregate. This implies that the reactivity of the end-groups in such supramolecular aggregate is equal to the reactivity of the monomer. Many different species with various degree of polymerisation coexists during an isodesmic process, but high degree of aggregation can only be achieved only for relatively high concentrations of monomers.

201. Pantaloni, D., Hill, T. L., Carlier, M. F. & Korn, E. D. A model for actin polymerization and the kinetic effects of ATP hydrolysis. *Proc. Natl. Acad. Sci.* **82,** 7207–7211 (1985).
202. Morris, A. M., Watzky, M. A. & Finke, R. G. Protein aggregation kinetics, mechanism, and curve-fitting: A review of the literature. *Biochim. Biophys. Acta* **1794,** 375–397 (2009).
203. Zhao, D. & Moore, J. S. Nucleation–elongation: a mechanism for cooperative supramolecular polymerization. *Org. Biomol. Chem.* **1,** 3471–3491 (2003).
204. Kulkarni, C., Balasubramanian, S. & George, S. J. What Molecular Features Govern the Mechanism of Supramolecular Polymerization? *ChemPhysChem* **14,** 661–673 (2013).
205. Gershberg, J., Fennel, F., Rehm, T. H., Lochbrunner, S. & Würthner, F. Anti-cooperative supramolecular polymerization: a new K 2 –K model applied to the self-assembly of perylene bisimide dye proceeding via well-defined hydrogen-bonded dimers. *Chem. Sci.* **7,** 1729–1737 (2016).
206. Chen, Z., Lohr, A., Saha-Möller, C. R. & Würthner, F. Self-assembled π-stacks of functional dyes in solution: structural and thermodynamic features. *Chem. Soc. Rev.* **38,** 564–584 (2009).
207. Goujon, A. *et al*. Hierarchical Self-Assembly of Supramolecular Muscle-Like Fibers. *Angew. Chem. Int. Ed.* **55,** 703–707 (2016).
208. Goldstein, R. F. & Stryer, L. Cooperative polymerization reactions. Analytical approximations, numerical examples, and experimental strategy. *Biophys. J.* **50,** 583–599 (1986).

1) Monomer-Dimer Equilibrium

Even though the dimerization of low molecular weight monomers does not lead to the formation of macromolecules, it could be considered as the simplest example of isodesmic supramolecular polymerization, where the degree of polymerization equals two. In this process two active monomers, M and its dimer, M_2, which does not polymerise further, are considered. The dimerization equilibrium is the following:

$$M + M \rightleftarrows M_2 \quad \textbf{(6)}$$

with the dimerization equilibrium constant K_2 which is equal to:

$$K_2 = \frac{[M_2]}{[M]^2} \quad \textbf{(7)}$$

The concentration of dimer M_2 could be expressed then as:

$$[M_2] = K_2\,[M]^2 \quad \textbf{(8)}$$

Consider the, total concentration of monomeric species in the system (usually considered as the initial monomer concentration) C_T:

$$C_T = 2[M_2] + [M] \quad \textbf{(9)}$$

The molar fraction of monomer molecules, α_{mono}[209] is given by:

$$\alpha_{mono} = \frac{[M]}{C_T} \quad \textbf{(10)}$$

and accordingly, the molar fraction of dimers α_{agg} then is expressed as:

$$\alpha_{agg} = 1 - \alpha_{mono} = \frac{2[M_2]}{C_T} \quad \textbf{(11)}$$

Taking into consideration equations **(8)** and **(9)** the concentration of monomer $[M]$ can be expressed as a function of K_2 and C_T by solving the corresponding quadratic equation for $[M]$:

209. In the literature also denoted as α, φ, η for instance.
210. Chen, Z., Fimmel, B. & Würthner, F. Solvent and substituent effects on aggregation constants of perylene bisimide π-stacks – a linear free energy relationship analysis. *Org. Biomol. Chem.* **10,** 5845 (2012).

$$[M] = \frac{\sqrt{8K_2C_T + 1} - 1}{4K_2} \quad \textbf{(12)}$$

Considering equations **(10), (11)** and **(12),** the fraction of monomeric and dimeric species can be expressed as follows:

$$\alpha_{mono} = \frac{\sqrt{8K_2C_T + 1} - 1}{4K_2C_T} \quad \textbf{(13)}$$

$$\alpha_{agg} = 1 - \frac{\sqrt{8K_2C_T + 1} - 1}{4K_2C_T} \quad \textbf{(14)}$$

2) Isodesmic Model

In the isodesmic model (also known as ***Equal-K (EK) Model*** or ***Multistep Open Association*** – **MSOA**), as the association constant does not depend on the size of the aggregate, the free energy change is equal for each elongation step. Thus, the isodesmic polymerisation equilibrium can be described as:

$$\begin{aligned}
M + M &\rightleftarrows M_2 && [M_2] = K_2[M]^2 \\
M_2 + M &\rightleftarrows M_3 && [M_3] = K_3[M_2][M] = K_2K_3[M]^3 \\
M_3 + M &\rightleftarrows M_4 && [M_4] = K_4[M_3][M] = K_2K_3K_4[M]^4 \\
&\bullet\bullet\bullet && \bullet\bullet\bullet \\
M_{n-1} + M &\rightleftarrows M_n && [M_n] = K_n[M_{n-1}][M] = K_2K_3 \dots K_n[M]^n
\end{aligned} \quad \textbf{(15)}$$

where $[M]$, $[M_2]$, $[M_3]$… $[M_n]$ are the molar concentrations of monomer, dimer, trimer and n-mer respectively, and K_2, K_3, K_4 and K_n are the equilibrium constants for the formation of the dimer, for the trimer from the dimer, for the tetramer from the trimer, and for a $n-1$-mer respectively. For an isodesmic polymerization mechanism we consider that:

$$K_2 = K_3 = K_4 = \cdots = K_n = K$$

The concentration of n-mer C_n can be given as:

$$C_n = K^{n-1}[M]^n \quad \textbf{(16)}$$

And the total concentration C_T of molecules M accordingly:

$$\begin{aligned} C_T &= ([M] + 2K[M]^2 + 3K^2[M]^3 + \cdots + nK^{n-1}[M]^n) \\ &= [M](1 + 2K[M] + 3K^2[M]^2 + \cdots + nK^{n-1}[M]^{n-1}) \end{aligned} \quad \textbf{(17)}$$

Considering that for $(0<x<1)$ the $1 + 2x + 3x^2 + \cdots + nx^n = 1/(1-x)^2$, equation **(17)** becomes:

$$C_T = \frac{[M]}{(1 - K[M])^2} \quad \textbf{(18)}$$

Solving the quadratic equation **(18)**, provides the concentration of monomer as a function of KC_T:

$$[M] = \frac{2KC_T + 1 - \sqrt{4KC_T + 1}}{2K^2C_T} \quad \textbf{(19)}$$

Using equations **(10)**, **(11)** and **(19)** we obtain α_{mono} and α_{agg} respectively:

$$\alpha_{mono} = \frac{2KC_T + 1 - \sqrt{4KC_T + 1}}{2K^2C_T^2} \quad \textbf{(20)}$$

$$\alpha_{agg} = 1 - \frac{2KC_T + 1 - \sqrt{4KC_T + 1}}{2K^2C_T^2} \quad \textbf{(21)}$$

Typically, the fraction of aggregated species for different total concentration of molecules is obtained from experimental UV-Vis or CD measurements. The value of *K* can then be extracted by using a least-square analysis of the experimental concentration dependent data. This operation can be performed using any data analysis software, such as Origin. This model was successfully applied by several groups, for instance, the group of Würthner extensively used it to study the aggregation process of various perylene bisimides dye molecules.[165] **Figure 48** demonstrates the fitting of the experimental UV-Vis data, using isodesmic model described above **(21)**.[210]

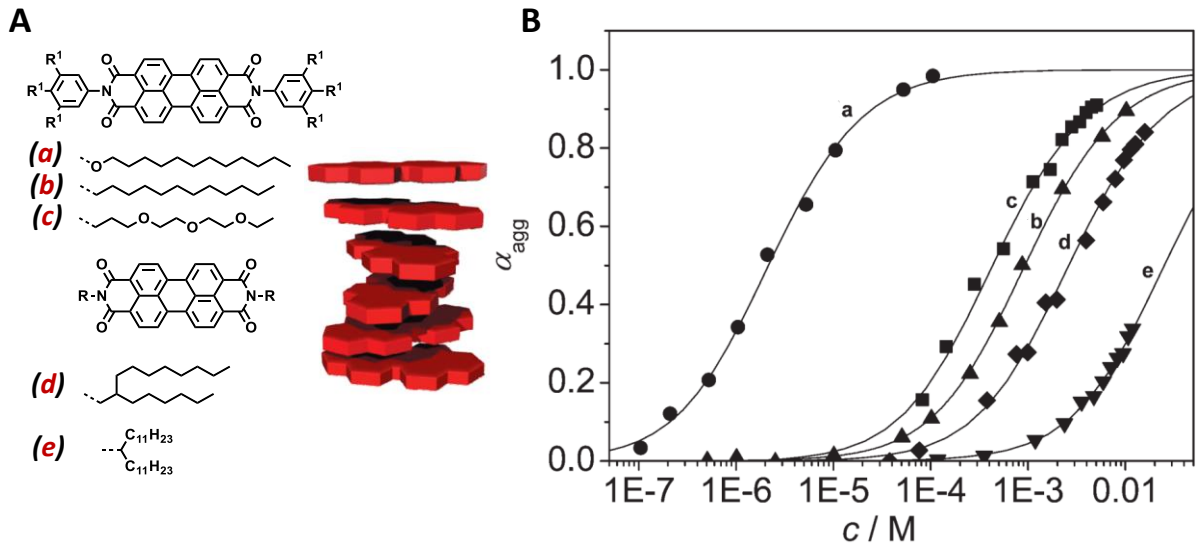

Figure 48 | Application of isodesmic model to concentration dependent spectroscopic data. (**A**) Chemical structure of various perylene bisimide (PBI) molecules studied by concentration dependent UV-Vis spectroscopy. (**B**) Molar fraction of aggregated molecules α_{agg} as a function of concentration of the PBI dyes *(**a** – **e**)* in tetrachloromethane. The lines were obtained by fitting the concentration-dependent UV-Vis data with the isodesmic model **(21)**. Figure is adapted from ref. 210

iii. Non-equal-K Supramolecular Polymerization

1) K_2-K Supramolecular Polymerization Model

The non-equal-K supramolecular polymerization, also commonly called as cooperative supramolecular polymerization, is characterised by the presence of two regimes of aggregation, having two different association constants. In the most general case, this kind of polymerization can be considered as a combination of two isodesmic supramolecular polymerizations: one of which occurs before the a degree of aggregation s is reached (with a nucleation equilibrium constant, K_n) and a second one after (with an elongation equilibrium constant, K_e). In the simplest case, when the nucleus is a dimer, the first association constant (dimerization) is not equal to the second and following ones:

$$K_2 \neq K_3 = K_4 = \cdots = K_n$$

The cooperative polymerisation event can be described as follows:

$M + M \rightleftarrows M_2$	$[M_2] = K_2[M]^2$
$M_2 + M \rightleftarrows M_3$	$[M_3] = K[M_2][M] = K_2K[M]^3$
$M_3 + M \rightleftarrows M_4$	$[M_4] = K[M_3][M] = K_2K^2[M]^4$
•••	•••
$M_{n-1} + M \rightleftarrows M_n$	$[M_n] = K[M_{n-1}][M] = K_2K^{n-2}[M]^n = \sigma K^{-1}(K[M])^n$ where $\sigma = \frac{K_2}{K}$

The total concentration C_T of molecules is given by: [o]

$$C_T = [M] + \sum_{n=2}^{\infty} n\sigma K^{-1}(K[M])^n = (1-\sigma)[M] + \sigma[M]/(1-K[M])^2 \qquad \textbf{(22)}$$

From expression **(22)** one can see that $[M]$ is necessarily smaller than $1/K$. Although the equation **(22)** could be solved analytically[211], it might require some time. However for a given σ, considering equation **(22),** KC_T could be expressed as a function of $K[M]$:

$$KC_T = (1-\sigma)K[M] + \sigma K[M]/(1-K[M])^2 \qquad \textbf{(23)}$$

211. Using Wolfram Alpha. *Wolfram Alpha LLC* at <https://www.wolframalpha.com/input/?i=((1-p)y%2Bpy%2F(1-y)%5E2)%3Dx> for example.

Taking into consideration that:

$$\alpha_{Agg} = 1 - \alpha_{mono} = 1 - \frac{[M]}{C_T} = 1 - \frac{K[M]}{KC_T} \quad \textbf{(24)}$$

α_{Agg} can be calculated as a function of KC_T. [212]

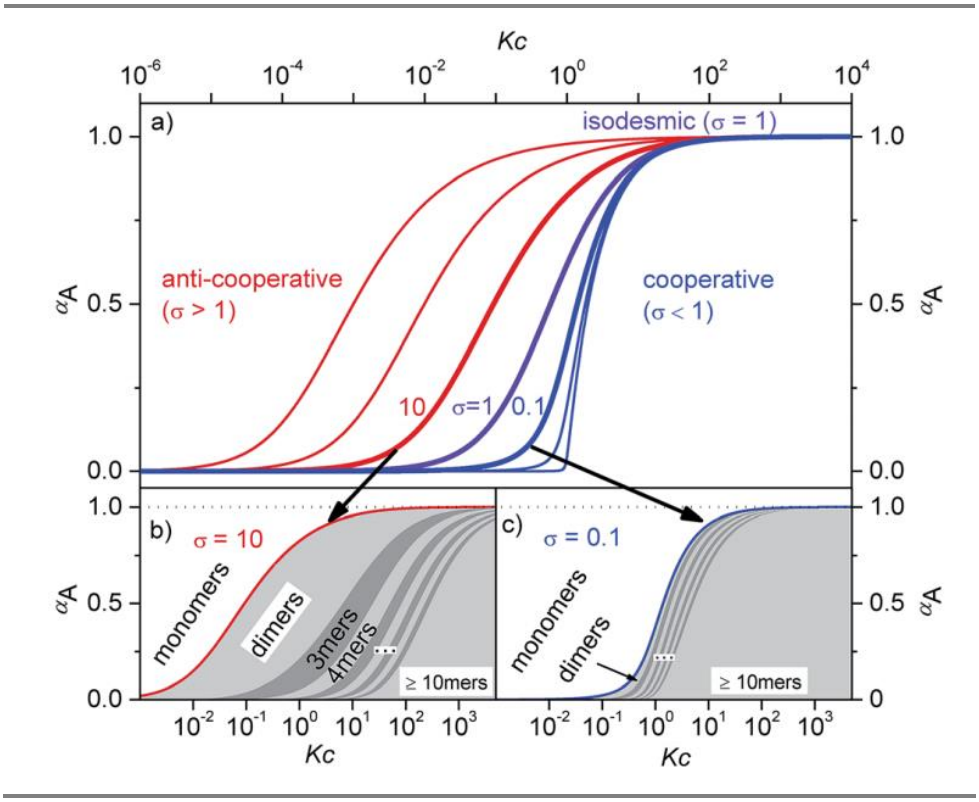

Figure 49 | Graphical representation of the degree of aggregation $\boldsymbol{\alpha_{Agg}}$ as a function of $\boldsymbol{KC_T}$ for the monomer-dimer equilibrium, and K_2-K model for different $\boldsymbol{\sigma}$ values. When $\boldsymbol{\sigma > 1}$, the process is called anticooperative when $\boldsymbol{\sigma < 1}$, the process is cooperative and when $\boldsymbol{\sigma}$ equals 1, it is said isodesmic. Figure is reproduced from ref. 205

σ is an important parameter which describes the degree of cooperativity. The smaller σ is, the higher the degree of cooperativity is. When σ equals one, the first association constant is equal to all following associations and thus, equation **(22)** corresponds to equation **(18)** which is characteristic of an isodesmic process. When $\sigma \ll 1$, the formation of dimer is less favoured than the elongation and thus the process is highly cooperative, whereas for $\sigma > 1$, the process becomes anticooperative, and the dimer corresponds to the major product.

212. First for each value of $K[M]$, taken from 10^{-6} to 0.9999 with as many points as needed, KC_T values are calculated using equation **(23)** for each given σ. After that, α_{Agg} is calculated for each point of KC_T using equation **(24)**. And finally α_{Agg} can be plotted as a function of KC_T for each value of σ.

2) Multiple Nucleation Supramolecular Polymerization

Obviously, the nucleus is generally not restricted to a dimer, but could be an s-mer. In this case, the nucleation process is governed by the nucleation constant K_N and the elongation one K_E, leading to equations for the expression of KC_T:

$$KC_T = \sum_{n=1}^{s} n\sigma^{n-1}(K[M])^n + \sum_{n=s+1}^{\infty} n\sigma^{s-1}(K[M])^n =$$
$$= \frac{s(K[M])^s\sigma^{s-1}}{1-K[M]} + \frac{(K[M])^{s+1}\sigma^{s-1}}{(1-K[M])^2} + \frac{K[M](s(\sigma K[M])^{s+1}-1)}{\sigma K[M]-1} - \frac{\sigma(K[M])^2((\sigma K[M])^{s-1}-1)}{(\sigma K[M]-1)^2} \quad \textbf{(25)}$$

where $\sigma = \frac{K_N}{K_E}$ and s corresponds to the is a nucleus size.

A full fitting procedure has been described by the group of Wurthner,[205,213] which involves that experimental data are fitted iteratively with randomly chosen initial parameters s, K. However, such procedure proved to be difficult and new procedures using temperature dependent experiments have been developed to model such mechanism (see section **iv** of this chapter).

3) Anticooperative Supramolecular Polymerization

When σ is larger than one, *i.e.* the nucleation step is more favoured than the subsequent elongation process, the supramolecular polymerization process is called *anticooperative*.[200,205] Despite the fact that many molecules readily form dimers, surprisingly there were no reports describing such a mechanism until recently. In this case, the formation of dimers is preferential, and subsequent polymer growth is less favoured.[205] The distribution of species in the anticooperative supramolecular polymerisation in comparison with isodesmic or cooperative, is shifted towards dimers. Importantly, the concentration of even-number aggregates (dimer, tetramer *etc.*) is higher that the concentration of odd-number aggregates. Recently, Würthner and co-workers communicated the use of the K_2-K model which was modified to be suitable for the characterisation of the anticooperative aggregation process (**Figure** 50).[205]

213. Fennel, F. *et al.* Biphasic Self-Assembly Pathways and Size-Dependent Photophysical Properties of Perylene Bisimide Dye Aggregates. *J. Am. Chem. Soc.* **135,** 18722–18725 (2013).
214. Martin, R. B. Comparisons of Indefinite Self-Association Models. *Chem. Rev.* **96,** 3043–3064 (1996).

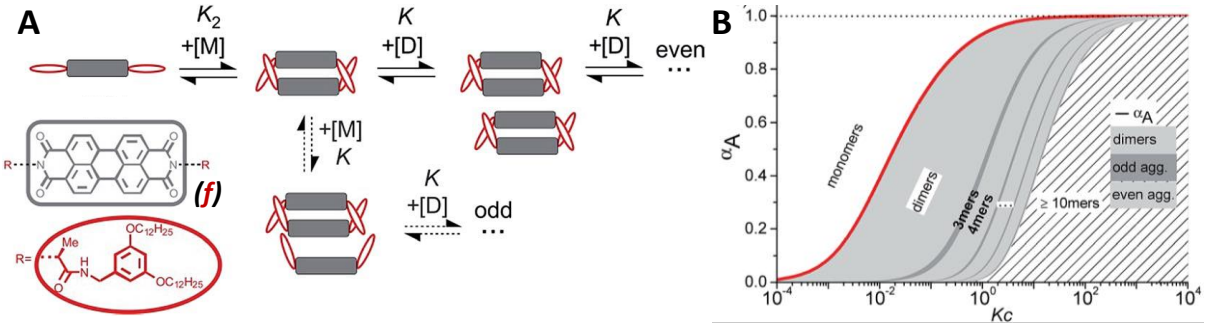

Figure 50 | (**A**) Molecular structure of perylene bisimide derivatives, which aggregate *via* anticooperative mechanism together with schematical explenation of the odd/even effect for the species distribition. (**B**) Theoretical dependence of the degree of aggregation from KC_T modeled using modified K_2-K model. Figure is adapted form ref. 205

The equations below describe the mass balance of the anticooperative process:

$$C_A^{odd} = K[M]\frac{[M_2](3-K[M_2])}{(1-K[M_2])^2}$$
$$C_A^{even} = \frac{2[M_2]}{(1-K[M_2])^2} \qquad \textbf{(26)}$$
$$C = C_M + C_A^{odd} + C_A^{even}$$

4) Other Models

Some other models have been proposed to describe the self-association process, and the general features of these models are reported hereafter. An exhaustive explanation of indefinite self-association models may also be found in the review by B. Martin[214].

The ***Attenuated K (AK) Model*** is described as an entropically unfavoured stepwise polymer growth so that the value of each next association constant should decrease according to the prescription:

$$K_n = K_A/n \quad \text{to give:} \quad K_A = 2K_2 = 3K_3 = \cdots = nK_n.$$

The ***Increasing K (IK) Model*** considers that successive constants increase according to:

$$K_n = \frac{K(n-1)}{n} \quad \text{so that} \quad K_2 = \frac{K_I}{2}, K_3 = \frac{2K_I}{3} \quad \text{or} \quad K_I = 2K_2 = \frac{3K_3}{2} = \cdots = \frac{nK_n}{n-1}.$$

The ***Middling K (MK) Model*** is established as the mild decrease of the subsequent constants according to:

$\mathrm{K_n} = \frac{K_M(n-1)}{n-2}$ for n ≥ 3, so that $K_3 = 2K_M,\ K_4 = \frac{3}{2}K_M,\ K_5 = \frac{4}{3}K_M$ or

$$K_M = \frac{K_3}{2} = \frac{2K_4}{3} = \frac{3K_5}{4} = \cdots = \frac{(n-2)K_n}{n-1}.$$

In the ***"Overall" Model*** the association process is simplified, so that all aggregated molecules are considered as one component:

$$nM \rightleftarrows M_n, \text{ where } K_O = \frac{[M_n]}{[M]^n}$$

This model is a two-stage process (such as a dimerization model) and all the intermediary stages are ignored.

These models can be used to roughly estimate the association constant; however with the development of specialised computer programs more precise K_2-K models have replaced them.

iv. Thermally Activated Supramolecular Polymerization

Modelling of concentration dependent data sometimes proves to be quite challenging. Indeed, the number of experimental data points should be high enough to avoid errors with the chosen model (if the amount of points is not high enough, two models can give a perfect fit).[147] On the other hand, for thermally activated supramolecular polymerization, the number of experimental points is limited by either the temperature control apparatus and/or boiling/melting points of the solvent. Furthermore, models, which have been developed for the thermally activated assembling process, can be easily implemented.

1) Isodesmic Model

The isodesmic model based on temperature dependent experimental data was developed by Meijer and colleagues, and the reader is referred to the original paper for complete derivation.[147]

The degree of aggregation is related to the "melting" temperature T_m (temperature at which half of molecules exist in aggregated state, α_{Agg}= 0.5) and to the enthalpy release ΔH during the aggregation process through the expression:

$$\alpha_{Agg} \cong \frac{1}{1 + \exp(-0.908\Delta H \frac{T - T_m}{RT_m^2})} \quad \textbf{(27)}$$

Where R is an ideal gas constant.

The number-averaged degree of polymerization DP_N can be calculated from the degree of aggregation:

$$DP_N(T) = \frac{1}{\sqrt{1-\alpha_{agg}(T)}} \quad \textbf{(28)}$$

Furthermore, the equilibrium constant K_e is related to the number-averaged degree of polymerization and to the total concentration of molecules C_T through:

$$DP_N(T) = \frac{1}{2} + \frac{1}{2}\sqrt{4K_e(T)C_T + 1} \quad \textbf{(29)}$$

From this equation, the entropy change ΔS can be extracted *via* the Van 't Hoff equation. Equations **(27) - (29)** clearly demonstrate that K_e is temperature dependent.

2) Cooperative Model

The cooperative model, proposed by Oosawa and Kasai,[143] was modified by van der Schoot[144] to be suitable for thermally activated supramolecular polymerization and successfully implemented by several groups.[145,146,148,149,151,215]

Experimental melting curves (temperature dependent degree of aggregation) for a cooperative supramolecular polymerization are characterised by two distinct regimes. The nucleation regime exists above the critical temperature, the so called elongation temperature, T_e. In the nucleation regime, molecules exist in monomeric state and no aggregates are observed. In the elongation regime, below the T_e, the supramolecular polymerisation occurs.

In the elongation regime, the self-assembly process is governed by the nucleation equilibrium constant K_a and the degree of aggregation is given by:

$$\alpha_{Agg} = \alpha_{Sat}\left(1 - \exp\left[\frac{-\Delta H_e(T - T_e)}{RT_e^2}\right]\right) \quad \textbf{(30)}$$

Where ΔH_e is the enthalpy release during the elongation process, T is the absolute temperature, R is the gas constant and parameter α_{Sat} is introduced so that $\alpha_{Agg}/\alpha_{Sat}$ does not exceed unity. The nonlinear least-squares analysis of the experimental data affords three parameters: ΔH_e, T_e and α_{Sat}.

In the nucleation regime ($T_e < T$) α_{Agg} is given by the following equation:

$$\alpha_{Agg} = \alpha_{Sat}\left\{\sqrt[3]{K_a}\, exp\left[\left(\frac{2}{3\sqrt[3]{K_a}} - 1\right)\Delta H_e\left(\frac{(T - T_e)}{RT_e^2}\right)\right]\right\} \quad \textbf{(31)}$$

where K_a is the dimensionless activation equilibrium constant at T_e and can be obtained by nonlinear least-squares analysis. Using equation **(31)** one can estimate the average length of nuclei, $\langle N_n(T_e)\rangle$, averaged over the nucleated species at T_e:

$$\langle N_n(T_e)\rangle = \frac{1}{\sqrt[3]{K_a}} \qquad \textbf{(32)}$$

From this equation, it is obvious that the smaller value of K_a, the larger nucleus should be formed before the elongation process occurs.

In the elongation regime, the number-averaged degree of polymerisation, averaged over all species present in the solution, $\langle N_n\rangle$ is given by the following equation:

$$\langle N_n\rangle = \frac{1}{\sqrt{K_a}}\sqrt{\frac{\alpha_{Agg}}{\alpha_{Sat} - \alpha_{Agg}}} \qquad \textbf{(33)}$$

If K_a << 1, the aggregation process is characterised by a high degree of cooperativity. The concentration of monomer in this case, above T_e, could be approximated as the total concentration C_T. Thus K_e is equal to the inverse of C_T. K_e is governed by the free energy change in the elongation process (ΔG_e), R and T, thus $K_e(T_e)$ is given by following equation:

$$K_e(T_e) = \frac{1}{C_T} = exp\left[-\frac{\Delta G_e}{RT_e}\right] = exp\left[-\frac{(\Delta H_e - T_e\Delta S_e)}{RT_e}\right] = exp\left[\frac{\Delta S_e}{R} - \frac{1}{T_e}\frac{\Delta H_e}{R}\right] \qquad \textbf{(34)}$$

Assuming that K_a is equal to K_n/K_e in the nucleation regime at T_e, the free energy changes of nucleation (ΔG_n) at temperatures above T_e is given by equation **(35)**.

$$\Delta G_n(T_e) = -RT_e\ln(K_n) = -RT_e\ln(K_aK_e) = -RT_e\ln\left(\frac{K_a}{C_T}\right) \qquad \textbf{(35)}$$

The temperature dependence of the degree of aggregation can be expressed as a function of absolute temperature by using the Van 't Hoff equation:

$$\ln\big(K_e(T_e)\big) = \ln\left(\frac{1}{C_T}\right) = -\frac{\Delta G_e}{RT_e} = -\frac{\Delta H_e}{R}\frac{1}{T_e} + \frac{\Delta S_e}{R} \qquad \textbf{(36)}$$

The thermodynamic parameters ΔH_e and ΔS_e can be obtained after least-square linear fitting of the plotted data: natural logarithm of the reciprocal C_T *vs* reciprocal T_e:

$$\ln\left(\frac{1}{C_T}\right) = f\left(\frac{1}{T_e}\right) \quad \textbf{(37)}$$

These parameters may be obtained as well from the nonlinear least square fit of the data plotted in the coordinates: $C_T\ vs\ T_e$.

$$C_T = \frac{1}{\exp\left[\frac{\Delta H_e}{RT_e} + \frac{\Delta S_e}{R}\right]} \quad \textbf{(38)}$$

Numerous reports exist in the literature, where thermally activated supramolecular polymerization is studied, due to its simpler and faster procedure. Both isodesmic and cooperative model generally give good fitting results. **Figure 51** demonstrates the application of isodesmic and cooperative models to fit the experimental absorption data for perylene bisimides derivatives, one without hydrogen bonding motifs (**Figure 51A**) which assembles *via* isodesmic mechanism[147] and one, containing amide groups, for hydrogen bonding between molecules (**Figure 51B**), which assembles *via* cooperative model.[151] In both cases the temperature dependent absorption data were recorded at appropriate wavelength. After the normalization procedure, the melting curves were plotted, describing degree of aggregation as a function of temperature (**Figure 51A(iii), B(ii)**). Each melting curve was fitted with corresponding model, to afford thermodynamic parameters as a result of least-square analysis.

For both processes the fitting of temperature dependent data afforded results in good agreement with parameters, obtained with concentration dependent studies respectively: 1.6×10^5 M^{-1} *vs* 2×10^5 M^{-1} for isodesmic polymerization,[147] and 4.6×10^5 *vs* 4.1×10^5 for cooperative polymerisation. This demonstrates high practical interest of thermally activated studies of supramolecular polymerisation mechanism.

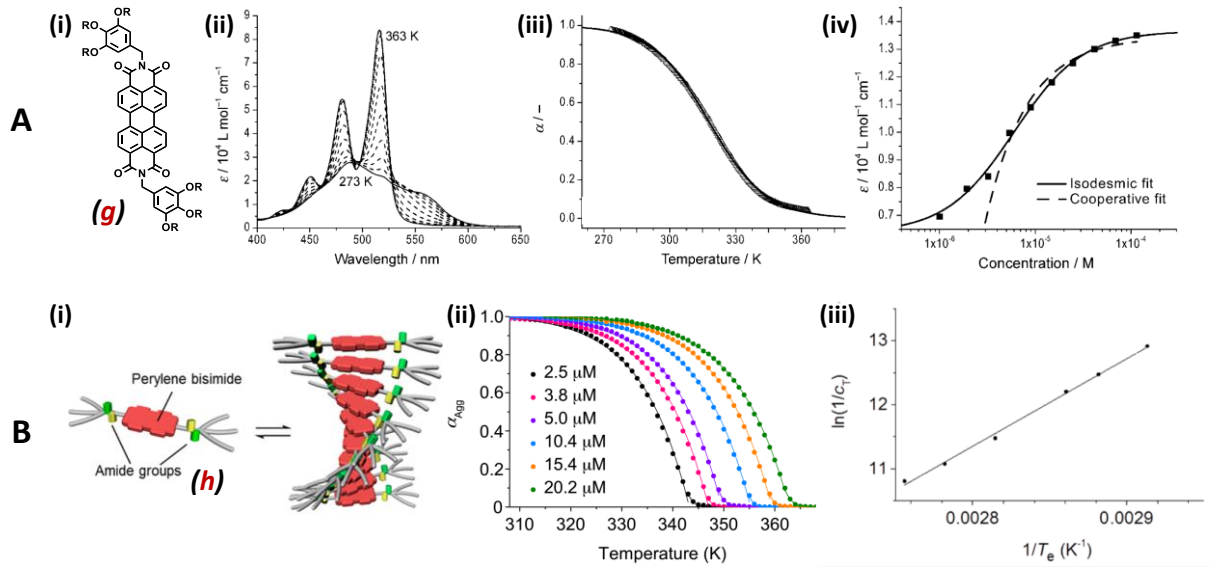

Figure 51 | Application of isodesmic (**A**)[147] and cooperative (**B**)[151] models to fit experimental spectroscopic data for thermaly activated supramolecular polymerisation. (**A**) Isodesmic supramolecular polymerization. (**i**) Chemical structure of perylene bisimide (***g***), which assembles according to equal-K model. (**ii**) Temperature dependent UV-Vis data recorded for ***g***. (**iii**) Melting curve recorded at 556 nm (black squares) and isodesmic fit described by Eq. **(24)**. (solid line). (**iv**) Absorption at 556 nm for different concentration of (***g***) (squares) fitted with equal-K and K_2-K model concentration dependent model. (**B**) Cooperative supramolecular polymerisation. (**i**) Schematic representation of perylene bisimide (***h***) self-assembly. (**ii**) Experimental melting curves recorded during the heating of toluene/cyclohexane solutions of ***h*** with different concentrations (circles) and cooperative fit (solid lines). (**iii**) van't Hoff plot built for determination of standart thermodinamic parameters. Figure is adapted form refs. 147,151

In this section, we described the most commonly used methods and models to study the mechanism of supramolecular polymerisation. In the next part of this chapter, the application of these method to the study triarylamine self-assembly process will be discussed.

3. RESULTS AND DISCUSSIONS

The self-assembly of triarylamine molecules in chloroform under light irradiation has been previously reported,[81,83,113] however no reported investigation of the self-assembly mechanism in non-halogenated solvents have been carried out until two recent examples, on which we discussed above.[121,122] Here our interest will be focused on two aspects: (***i***) thermodynamics and kinetics of the self-assembly process and (***ii***) chiral behaviour of this process. In this direction, a set of chiral and achiral TATAs have been synthesised and their self-assembly has been investigated.

A. Synthesis

Different TATAs with chiral (**(*S*)-TATA**), and achiral (**(C_9)-TATA** and **(C_{14})-TATA)** substituents were synthetized with high yields in few steps (**Scheme 4**).

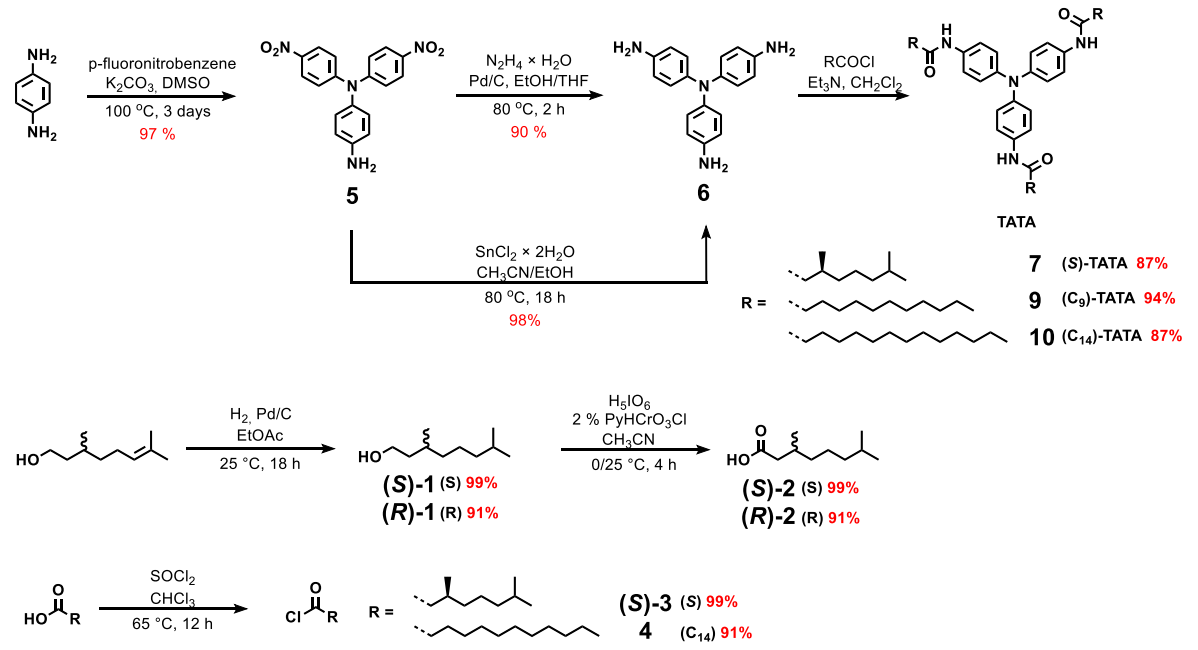

Scheme 4 | Synthetic scheme for TATAs.

(*R/S*) stereogenic acids were synthetized from optically pure commercially available (+) and (–) citronellol in few steps (**Scheme 4B**).[216] Citronellol was first hydrogenated under hydrogen atmosphere using palladium on activated carbon as a catalyst at atmospheric pressure in almost quantitative yield. Then fully saturated alcohol **(*R/S*)-1** was oxidised into the corresponding carboxylic acid **(*R/S*)-2** by periodic acid in acetonitrile. Only 2 % of pyridinium chlorochromate was used as a catalyst in this greener version[217] of a commonly

used procedure of Jones oxidation with Cr(VI) reagents.[218,219] Final treatment of the acids with thionyl chloride yielded the corresponding acyl chlorides with high yield.

The formation of the TATA-core **5** was successfully achieved *via* an aromatic nucleophilic substitution of the fluorine atom in *p*-fluoronitrobenzene with *p*-phenylenediamine in DMSO in the presence of potassium carbonate as a base.[43] Remarkably, this reaction provided compound **5** with almost quantitative yield. After the first addition of a nitrophenyl moiety on *p*-phenylenediamine, both amine functions (primary and secondary) become much less nucleophilic due to the electron-acceptor nature of a nitro group, which theoretically should favour the formation of less reactive diphenylamine. Nevertheless, as the secondary amine becomes probably even more acidic and undergoes deprotonation under these reaction conditions, the corresponding anion reacts with the second molecule of *p*-fluoronitrobenzene resulting in compound **5**. In order to obtain compound **6** two methodologies were used: (***i***) reduction using tin(II) chloride and (***ii***) catalytic reduction on palladium using hydrazine (which is a donor of electrons and hydrogen). Both methodologies work quite well providing corresponding aniline **6** with high yields. However, the use of tin(II) makes the work-up procedure more difficult because of the formation of amorphous tin(II)/tin(IV) hydroxides and the resulting amine cannot be stored for a long time. On the other hand, the second method is very practical when using large amount of materials. The product can be easily purified by recrystallization from ethanol and, more importantly, does not contain traces of transition metals, which could catalyse its oxidation, thus allowing its storage in the dark under argon for a longer time. The resulting aniline **6** was simply acylated with the corresponding acyl chlorides, previously described, to give the corresponding TATA molecules.

215. Buendía, J. *et al.* Helical supramolecular polymerization of C_3 - symmetric amides and retroamides: on the origin of cooperativity and handedness. **00,** 1–3 (2012).
216. Appel, W. P. J., Portale, G., Wisse, E., Dankers, P. Y. W. & Meijer, E. W. Aggregation of Ureido-Pyrimidinone Supramolecular Thermoplastic Elastomers into Nanofibers: A Kinetic Analysis. *Macromolecules* **44,** 6776–6784 (2011).
217. Hunsen, M. Carboxylic Acids from Primary Alcohols and Aldehydes by a Pyridinium Chlorochromate Catalyzed Oxidation. *Synthesis (Stuttg).* 2487–2490 (2005). doi:10.1055/s-2005-872085
218. Bowden, K., Heilbron, I. M., Jones, E. R. H. & Weedon, B. C. L. 13. Researches on acetylenic compounds. Part I. The preparation of acetylenic ketones by oxidation of acetylenic carbinols and glycols. *J. Chem. Soc.* 39 (1946). doi:10.1039/jr9460000039
219. Harding, K. E., May, L. M. & Dick, K. F. Selective oxidation of allylic alcohols with chromic acid. *J. Org. Chem.* **40,** 1664–1665 (1975).

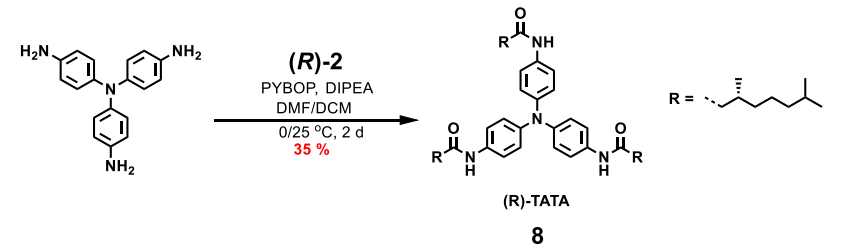

Scheme 5 | The scheme of reaction procedure of **(*R*)-TATA** synthesis using the peptide coupling procedure.

(*R*)-TATA can be obtained as well using a peptide coupling procedure (**Scheme 5**). This procedure was used to synthetize **(*R*)-TATA** directly from acid **(*R*)-2** and compound **6**, using PYBOP as activating agent. However, the final yield in this case, was somehow lower because of a tedious column chromatography purification.

B. Self-Assembly Characterization

i. Solubility and Gelation properties

(*S*)-, **(C_9)-**, **(C_{14})- TATAs** exhibit good gelation properties in various organic solvents (**Table 4**). although nonpolar solvents such as alkanes do not dissolve the studied TATAs. It should be mentioned that for physical gels the use of "*critical gelation concentration*" is not correct, because the concentration of organogelator is in this case not a critical parameter, unlike, for example, the critical micelle concentration (CMC). Therefore, this parameter should be used carefully, when different compounds are compared at identical conditions (volume of solvent, vial, *etc.*). Thus, here we are using the term "*onset gelation concentration*" (OGC). *i.e.* the concentration, at which a gel, formed under particular conditions is not destroyed during the tube inversion test. Gelation experiments were carried out in screw cap vials with 2 mL of solvent after dissolving the corresponding amount of TATA by heating at reflux. The gelation properties were estimated by the tube inversion test after the solutions were cooled down to room temperature. OGC values are reported for the lowest concentration at which a self-supporting gel was formed (**Figure 52**). A maximal concentration of 20 g/L was used to test the gelation abilities. Near the OGC in all solvents, these gels could be easily destroyed by shaking the vial. The opacity of the studied gels increases with the concentration of TATA.

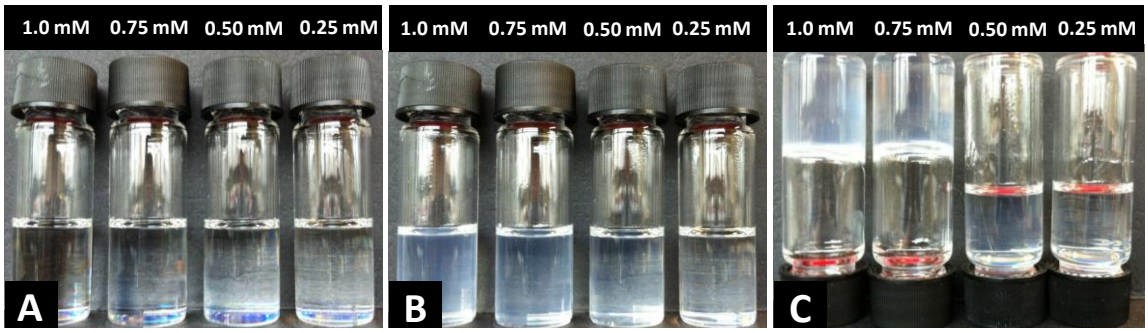

Figure 52 | Solutions and gels of **(*S*)-TATA** in toluene for different concentrations of organogelator. Concentration of **(*S*)-TATA** is 1.0, 0.75, 0.5 and 0.25 mM (from left to right). (**A**) Hot solutions of **(*S*)-TATA**; (**B**) **(*S*)-TATA** organogels, formed after cooling of the hot solutions to room temperature (the opacity of gels increases with increasing concentrations); (**C**) Tube inversion test experiment for various concentrations of **(*S*)-TATA** showing self-supporting gels for 0.75 and 1.0 mM.

The OGC for **(*S*)-TATA** was found to be 0.56 g/L (0.75 mM) and 2.5 g/L in toluene (**Figure 52**) and nitrobenzene respectively. The formation of thermoresponsive physical organogels was observed in chlorinated solvents as well, but at much higher concentrations (OGC of 2.1 g/L and 6.8 g/L in dichloroethane and dichloromethane respectively). No gels were observed in polar solvents such as DMSO, DMF, THF or methanol/toluene mixture even

at high concentrations. Obviously, gelation properties were shown to be dependent on the length and branching of the lateral chains. For instance, **(*S*)-TATA** is perfectly soluble in methanol/toluene mixture at a concentration of 20 mM while **(C_{14})-TATA** forms a thermoresponsive gel at the same concentration.

Table 4 | Solubility and gelation properties of **(S)-TATA** tested in different solvents

Compound	Solvent	Effect	C, g/L	C, mol/L
	Alkanes [a]	Poor solubility	-	-
	Diethyl ether	Poor solubility	-	-
	Nitromethane	Precipitation	5	0.6×10^{-2}
	Acetonitrile	Crystallization	10	1.3×10^{-2}
	Ethyl acetate	Precipitation	10	1.3×10^{-2}
	Acetone	Crystallization	15	2.0×10^{-2}
	Methanol	Precipitation	15	2.0×10^{-2}
	THF	Solution	20	2.6×10^{-2}
	DMSO	Solution	20	2.6×10^{-2}
(*S*)-TATA	DMF	Solution	20	2.6×10^{-2}
	Chloroform	Solution	20	2.6×10^{-2}
	Tetrachloroethane	Solution	20	2.6×10^{-2}
	Dichloromethane	Gel	6.8	9.0×10^{-3}
	Dichloroethane	Gel	2.1	2.8×10^{-3}
	Toluene	Gel	0.56	7.5×10^{-4}
	Chlorobenzene	Gel	0.62	8.3×10^{-4}
	Nitrobenzene	Gel	2.5	3.3×10^{-3}
	o-Xylene	Gel	0.80	1.1×10^{-3}
	Anisole	Gel	0.80	1.1×10^{-3}
(C_9)-TATA	Toluene	Gel	0.50	7.0×10^{-4}
(C_{14})-TATA	Toluene	Gel	0.66	7.2×10^{-4}

[a] pentane, cyclohexane, methylcyclohexane

ii. Microscopy studies

The structure of these self-assemblies was first investigated with optical microscopy as the size of aggregates was large enough (**Figure 53**). Long fibres, up to several hundreds of micrometres in length, were observed in both concentration regimes: below and above the OGC. For **(C_9)-TATA** (**Figure 53D-F**), the fibres appear shorter and more rigid than for **(*S*)-TATA** (**Figure 53A-C**). We believe that TATAs with chiral substituents (**(*S*)-TATA**) are stacked in a less compact way which, as a consequence, allows higher degree of flexibility than in the case of linear alkyl chains (**(C_9)-TATA**).

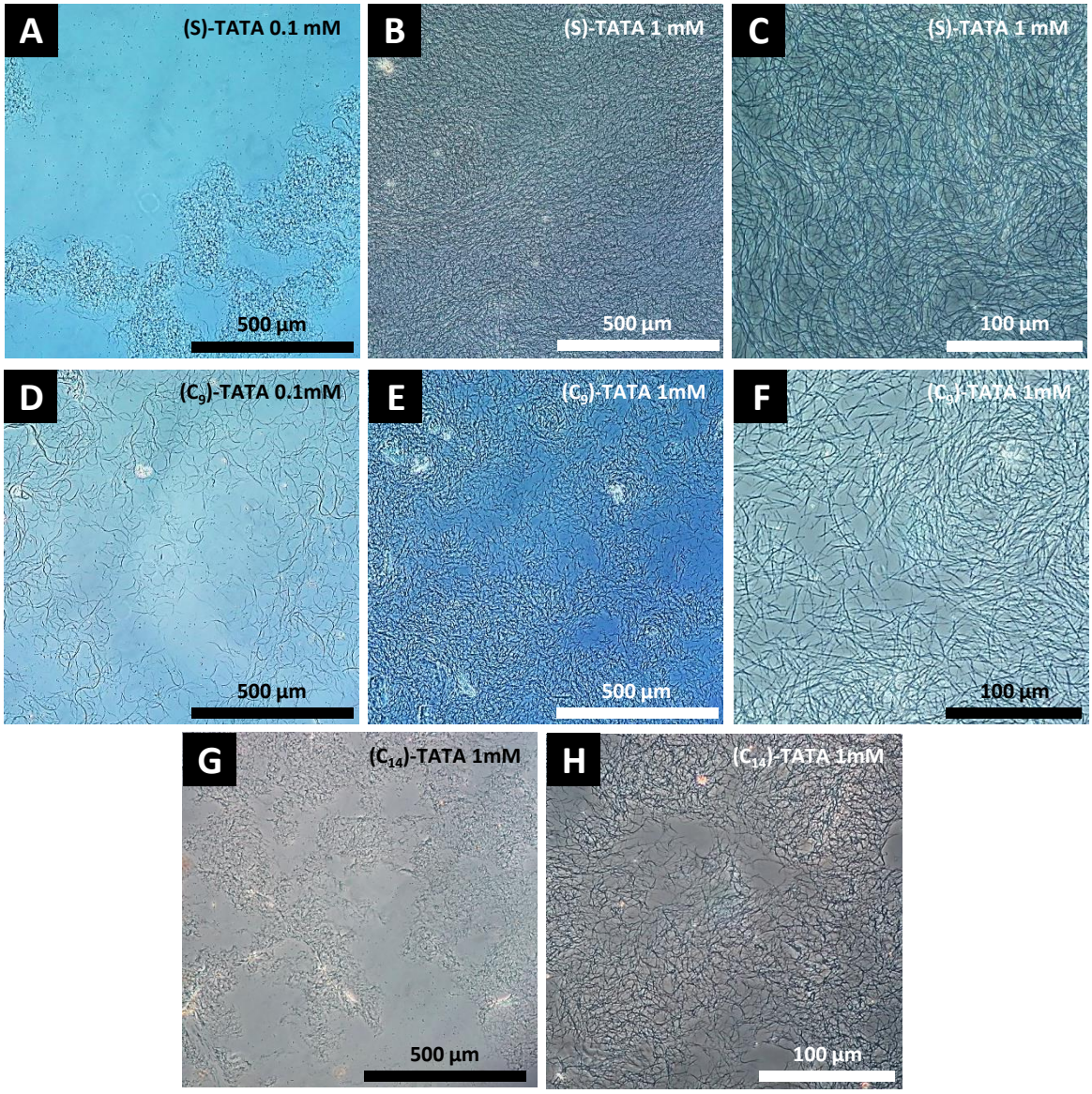

Figure 53 | OPM photographs of TATA self-assemblies in toluene at different concentrations. (**A – C**) **(*S*)-TATA**; (**D – F**) **(C_9)-TATA**; **(G,H) (C_{14})-TATA.** Images were obtained using a phase contrast mode.[220]

For **(C_9)-TATA,** after 2 weeks at room temperature, the formation of long (few millimetres) needle-like crystals with a high aspect ratio (few dozens) was surprisingly observed, indicating a possible transition from the kinetically trapped state (fibre) to a thermodynamic product, which is a crystal in this case (**Figure 54**).[221]

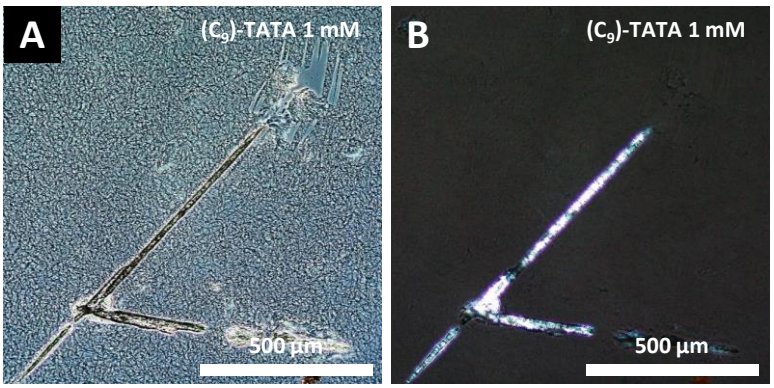

Figure 54 | OPM photographs of **(C_9)-TATA** self-assembly in toluene (1.0 mM), observed in (**A**) a phase-contrast mode, and (**B**) in a cross-polarised mode. A needle-like crystal of **(C_9)-TATA** is surrounded by fibres.

The formation of long needle-like crystalline structures have also been observed for **(*S*)-TATA** after the cooling of hot acetonitrile or acetone solutions (**Table 4, Figure 55**). The rigidity of these structures, which make them resemble at a Mikado-game, under a cross-polarised light together with a distinct birefringence suggest their crystalline organisation. These crystals could be possibly used as chiral waveguides, as we recently discovered such properties for organic framework, made of self-assembled triarylamines.[130]

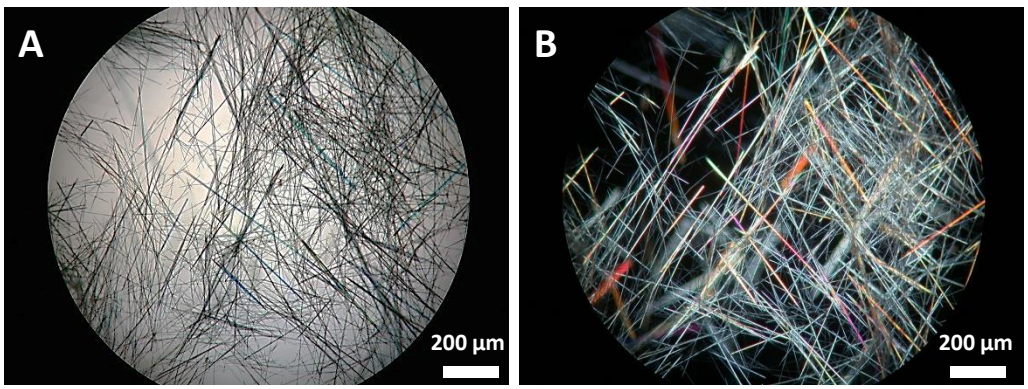

Figure 55 | OPM photographs of **(*S*)-TATA** needle-like crystals, obtained from saturated acetone solution. (**A**) Bright-field illumination; (**B**) Cross-polarised mode.

220. Quality of the OPM images was enhanced with contrast, brightness and sharpness filters. See **Figure S2** for the original images.
221. Wang, Y., Tang, L. & Yu, J. Investigation of Spontaneous Transition from Low-Molecular-Weight Hydrogel into Macroscopic Crystals. *Cryst. Growth Des.* **8,** 884–889 (2008).

We also studied the morphology of the fibres with electron microscopy. Transmission electron microscopy (TEM) and scanning electron microscopy (SEM) imaging shows that self-assembled TATA leads to the formation of fibrous bundles of few dozens of micrometres length and hundreds of nanometres in diameter.

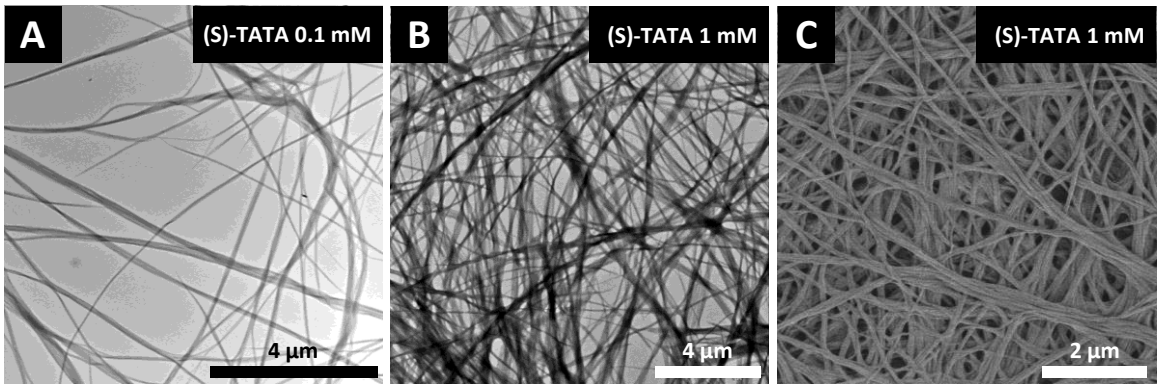

Figure 56 | Electron microscopy images of **(*S*)-TATA** self-assemblies in toluene. (**A, B**) TEM of 0.1 mM and 1 mM respectively; (**C**) SEM of 1 mM solution.

AFM imaging on the TEM samples also confirmed formation of super-twisted bundle of fibres (**Figure 57**), with diameter of the smallest fibril of around 1.5 nm which may correspond to the diameter of an individual columnar stack.

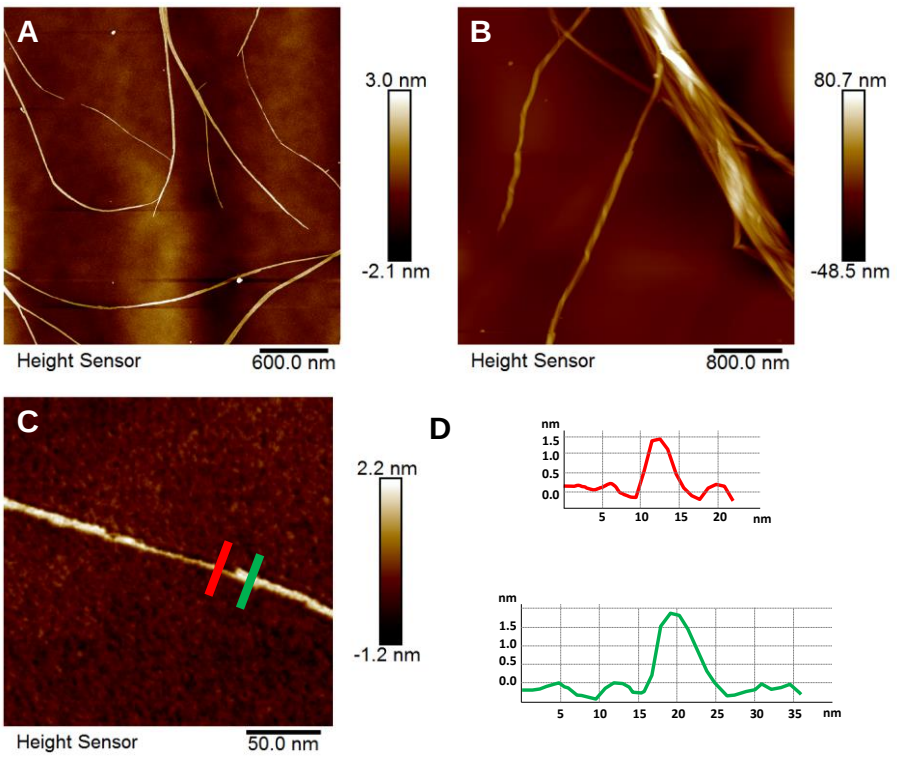

Figure 57 | AFM height images of **(*S*)-TATA** self-assemblies in toluene at (**A, C**) 0.1 mM and (**B**) 0.5 mM concentration. (**C**) AFM image of two fibres and (**D**) corresponding height profile of the cross-sections represented by green and red lines.

iii. NMR Spectroscopy

^{1}H NMR spectra of the synthetized TATAs were in agreement with previously reported compounds.[113] Compared to the 1st generation of triarylamines,[81] TATAs, and in particular **(*S*)-TATA**, **(C_9)-TATA** and **(C_{14})-TATA** assemble even without light irradiation in a variety of organic solvents such as chloroform, toluene or acetonitrile. Because of this self-assembly into long fibrillar aggregates, usually no signals are present for the TATA molecules in proton NMR at room temperature in these solvents. However, depending on the size of the aggregates, the signals corresponding to the lateral alkyl chains can sometimes be observed. In polar solvents, such as DMSO, DMF, THF or mixture of methanol and toluene, TATAs are molecularly dissolved and clear NMR spectra could be recorded (**Figure 58A**). As already discussed in the previous chapter, in the presence of just 5 % of chloroform, electron-rich TATA can be oxidized upon light irradiation into the corresponding triarylammonium radical-cation. The green colour, which appears during the irradiation process together with the disappearance of NMR signals, corresponds to the photo-induced oxidation of the TATA and to self-assembly process (**Figure 58C**).

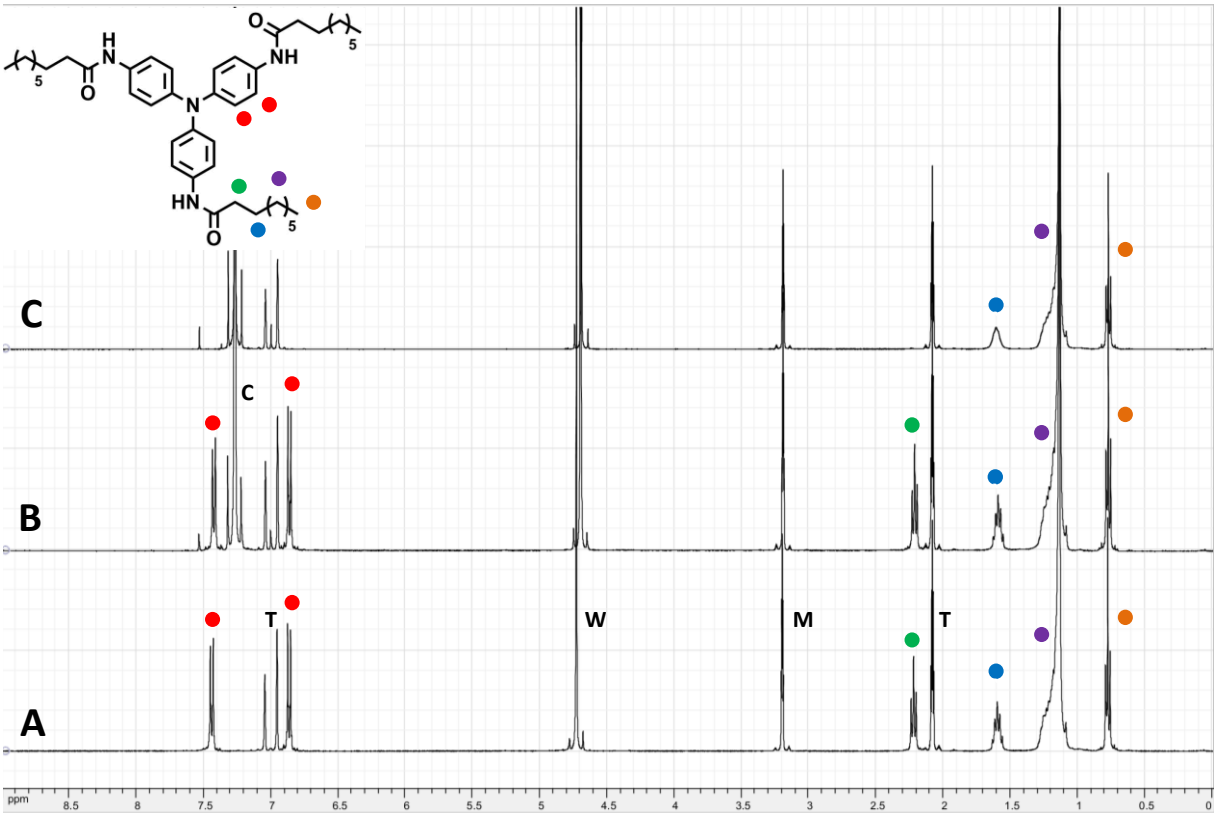

Figure 58 | ^{1}H NMR spectra of **(C_9)-TATA** in a mixture of deuterated methanol and toluene – 5:3 (**A**); after addition of 5% of chloroform (**B**); after irradiation with visible light for 1h, signals, correspondent to the aromatic TATA-core disappeared (**C**). (M, W, T, C assign residual signals of solvents: methanol, toluene, water and chloroform respectively).

Concentration dependent NMR studies of **(*S*)-TATA** in deuterated THF (see **Figure** 59) and methanol/toluene (**Figure S3** in annexes) have been performed. Upon dilution of the studied systems, we did not observe any significant change in the chemical shift for the signals corresponding to the aromatic core and to the amide protons in the studied range of concentrations,[222] indicating, that no self-assembly occurs at these conditions.

Temperature dependent NMR studies were also performed to study the self-assembling process of **(*S*)-TATA** in toluene. Upon gradual heating of the solution, the appearance of **(*S*)-TATA** resonance signals was observed, showing the transition from assembled to molecularly dissolved state.

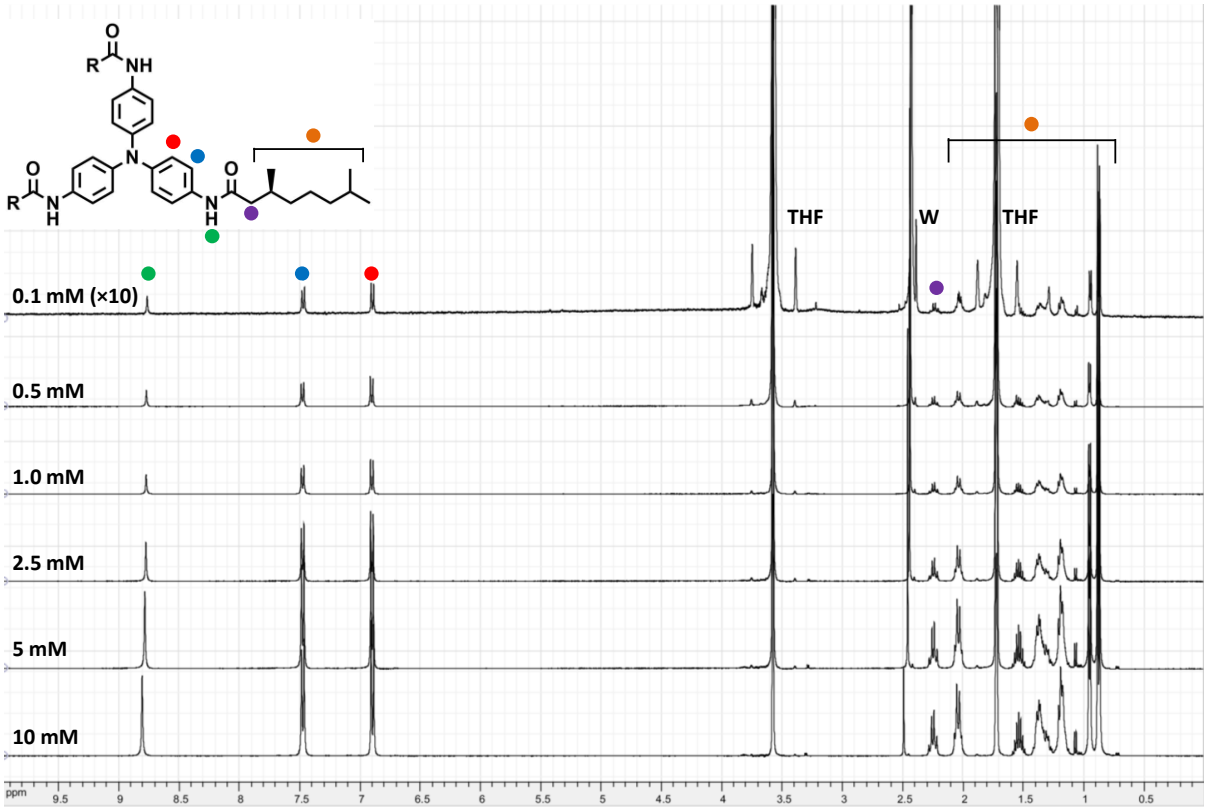

Figure 59 | ^{1}H NMR spectra of **(*S*)-TATA** in deuterated THF at different concentrations.

222. In methanol/toluene mixture, the amide signal could not be identified as it is positioned as the residual OH signal of methanol.

iv. Infrared Spectroscopy

Infrared (IR) spectroscopy proved to be very useful to study intermolecular hydrogen bonds. This technique has been widely used to identify and differentiate molecular packing through different types of hydrogen bonds in supramolecular polymers by numerous groups.[113,175,177,223,224]

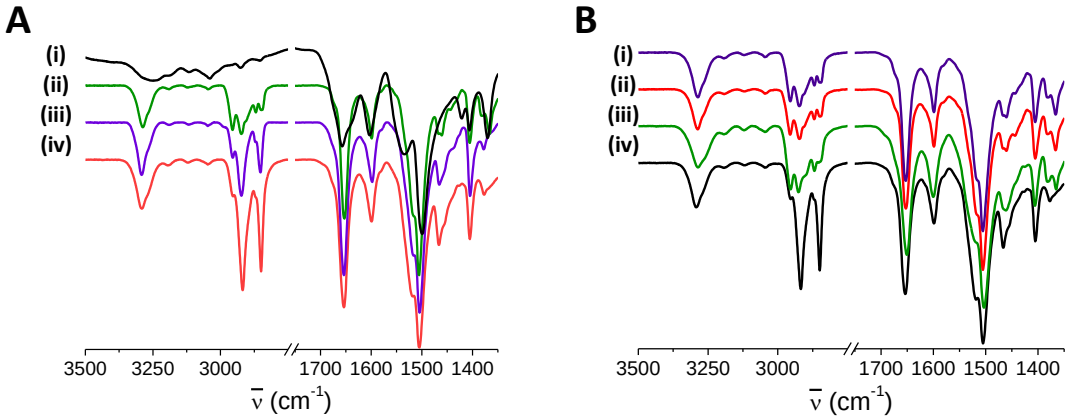

Figure 60 | FTIR spectra on solid samples for (**A**) TATAs as obtained after purification; (**i**) **TATA-Ac** (reported by Armao et al.[130] see **Figure 61**), (**ii**) **(*S*)-TATA**, (**iii**) **(C_9)-TATA**, (**iv**) **(C_{14})-TATA,** and (**B**) **(*S*)-TATA**, which was assembled in different solvents (**i**) acetonitrile, (**ii**) acetone, (**iii**) toluene, (**iv**) **(C_{14})-TATA** assembled in chloroform.[225]

FTIR spectra of TATAs with long alkyl chains as well as with acetamido groups (**Figure 61C**) in the solid state were recorded either from samples as obtained after the isolation (**Figure 60A**) and after the assembly in different solvents (**Figure 60B**). Well-defined bands at around 3290 and 1653 cm^{-1} correspond to the stretching vibrations of the N–H and C=O bonds respectively. Compared to stretching vibrations of free N–H and C=O groups (3500 – 3400 and ≈ 1685 cm^{-1} respectively)[226], they are shifted towards lower frequencies, which clearly indicates the presence of intermolecular hydrogen bonding between molecules. The high symmetry of the amide and carbonyl stretching vibration can indicate the existence of just one type of amide group, involved in hydrogen bonding between molecules.[175] Taking into account previously reported experimental evidence and theoretical calculations on achiral TATA[83,113] we can attribute these values of vibration frequencies to the formation of threefold helical-type intermolecular hydrogen bonding between neighbouring

223. Hanabusa, K., Koto, C., Kimura, M., Shirai, H. & Kakehi, A. Remarkable Viscoelasticity of Organic Solvents Containing Trialkyl-1,3,5-benzenetricarboxamides and Their Intermolecular Hydrogen Bonding. *Chem. Lett.* 429–430 (1997). doi:10.1246/cl.1997.429
224. Yasuda, Y., Takebe, Y., Fukumoto, M., Inada, H. & Shirota, Y. 4,4',4"-Tris(stearoylamino)triphenylamine as a novel material for functional molecular gels. *Adv. Mater.* **8,** 740–741 (1996).
225. Self-assemblies from different solvents were filtered under reduced pressure, dried and then studied using ATR-FTIR. **(C_{14})-TATA** was used instead of **(*S*)-TATA** in chloroform for the reason of much lower gelation concentration.
226. See Pretsch, E. Buhlmann, P.; Badertscher, M. Structure Determination of Organic Compounds, 4th ed.; Springer: New York, 2009 for spectroscopic data.

TATA molecules within columnar stack. A schematic representation of TATA dimer within stack is shown on the **Figure 61A,** together with the MM2 geometry optimisation model of **(*S*)-TATA** pentamer (**B**)[227] in agreement with DFT calculations on achiral TATAs.[113]

Table 5 | Summary of IR data for different TATAs from **Figure 60 A**

Band	(C_9)-TATA	(C_{14})-TATA	(*S*)-TATA	TATA-Ac
N-H	3292	3291	3287	3422/3253
C=O	1654	1653	1653	1658/1638
Amide II	1597	1599	1598	1604

IR spectra was found to be identical for **(*S*)-**, **(C_9)-** and **(C_{14})- TATA** molecules in the solid state, suggesting similar supramolecular arrangements (**Table 5**). However, the shape and the position of the amide-group vibrations for **TATA-Ac** (tris-acetamide triarylamine, see **Figure 61**) was found to be different from other TATAs, decorated with long alkyl chains (**Figure 60A(i)**). First of all, both N–H and C=O bands have lower symmetry as bands appear broader and have few shoulders. This indicates the presence of different types of amide groups and is a signature of a different types of molecular packing. Indeed, for **TATA-Ac** (**Figure 61C-E**),[130] the crystal structure revealed a columnar packing of TATA dimers, arranged in a "snow-flake" shape,[83] with all amide groups participating in the formation of an intracolumnar hydrogen bonding network. In general, such "snow-flake" pattern of organization happens to be more favoured for TAA crystallisation. From the various experimental evidence obtained by IR and molecular modelling, we can speculate that the presence of long alkyl chains prevents such "snow-flake" arrangement of the **(S)-**, **(C_9)-** and **(C_{14})-** TATAs. Furthermore, IR data suggest similar columnar arrangement in self-assemblies obtained in different solvents (**Figure 60B**).

227. DFT calculations performed by Armao et al. gave the following values for the distance between the central nitrogen atoms of 4.85 Å and 20° for the dihedral angle between neighbouring molecules.

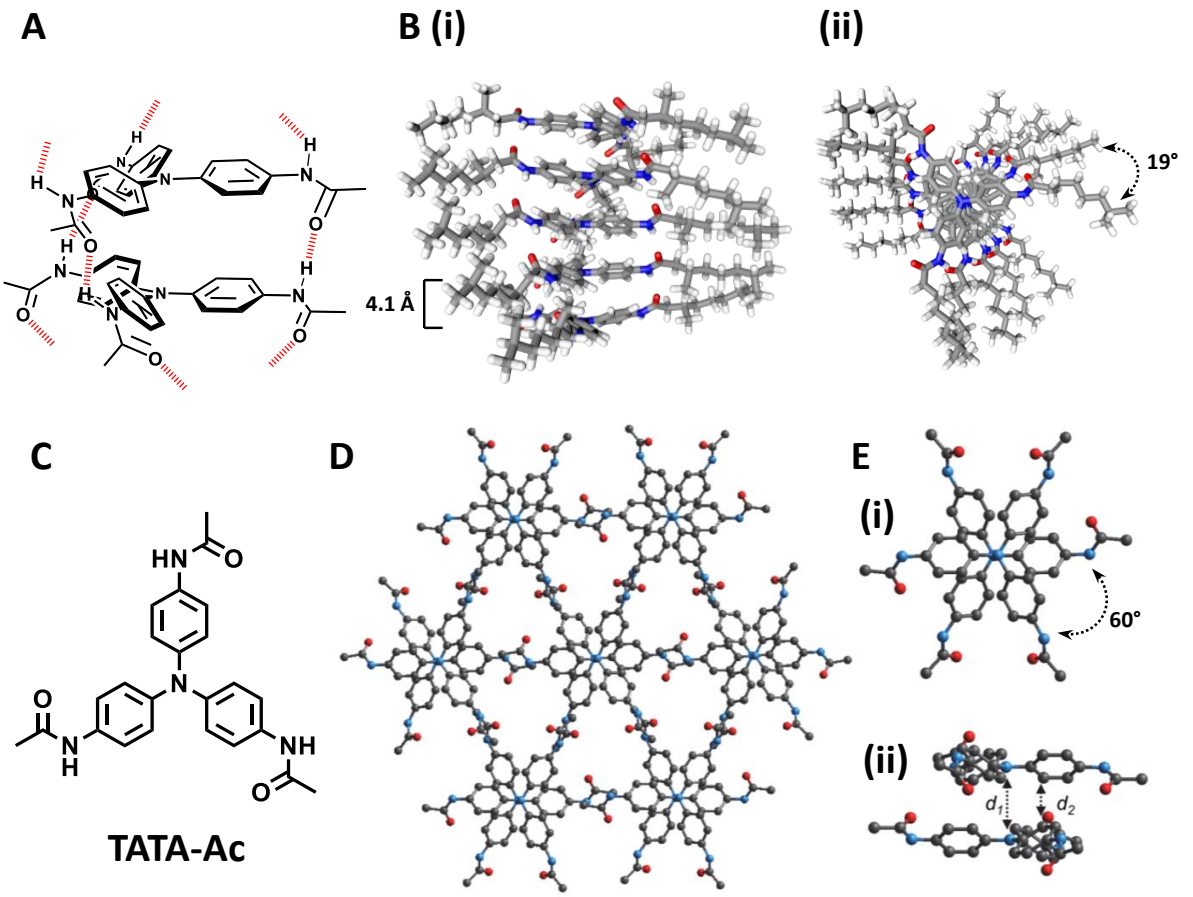

Figure 61 | (**A**) Schematic representation of a generic TATA dimer, connected together in an infinite column through intracolumnar hydrogen bonding; (**B**) Side view (**i**) and top view (**ii**) of the **(S)-TATA** pentamer, obtained using a MM2 geometry optimisation; (**C**) Molecular structure of **TATA-Ac**; (**D**) Crystal structure of **TATA-Ac** represented along the direction of columnar stacking; (**E**) TATA "snow-flake" dimer, top view (**i**), errow shows the dihedral angle between TATAs in a "snow-flake" dimer; and side view (**ii**), where d_1 is a N–N distance, d_2 the *o*-carbon distance[228]. **C-E** adapted from ref. 130

v. UV-Vis and Fluorescence Spectroscopy

Concentration dependent UV-Vis and fluorescence spectroscopy studies of TATAs in different solvents confirmed previously discussed results in this chapter about the self-assembly behaviour of TATAs in different solvents. Some general trends in the absorption and fluorescent behaviours of TATA were observed: (***i***) solvatochromism, (absorption/emission) maximum shifts towards higher wavelengths with solvent polarity; (***ii***) temperature independent emission and absorption spectra at concentrations of TATA below which self-assembly occurs (below 0.1 mM in toluene). At high concentrations of TATAs in solvents where self-assembly occurs, the absorption/emission maxima were shifted towards

228. The distance between central nitrogens – d_1 is 4.173 Å, and the distance between orto-carbons of neighbouring molecules – d_2 is 3.608 Å.

lower wavelength at low temperature, together with the increase of fluorescence intensity and decrease in absorption intensity. These data are summarized in **Table 6**.

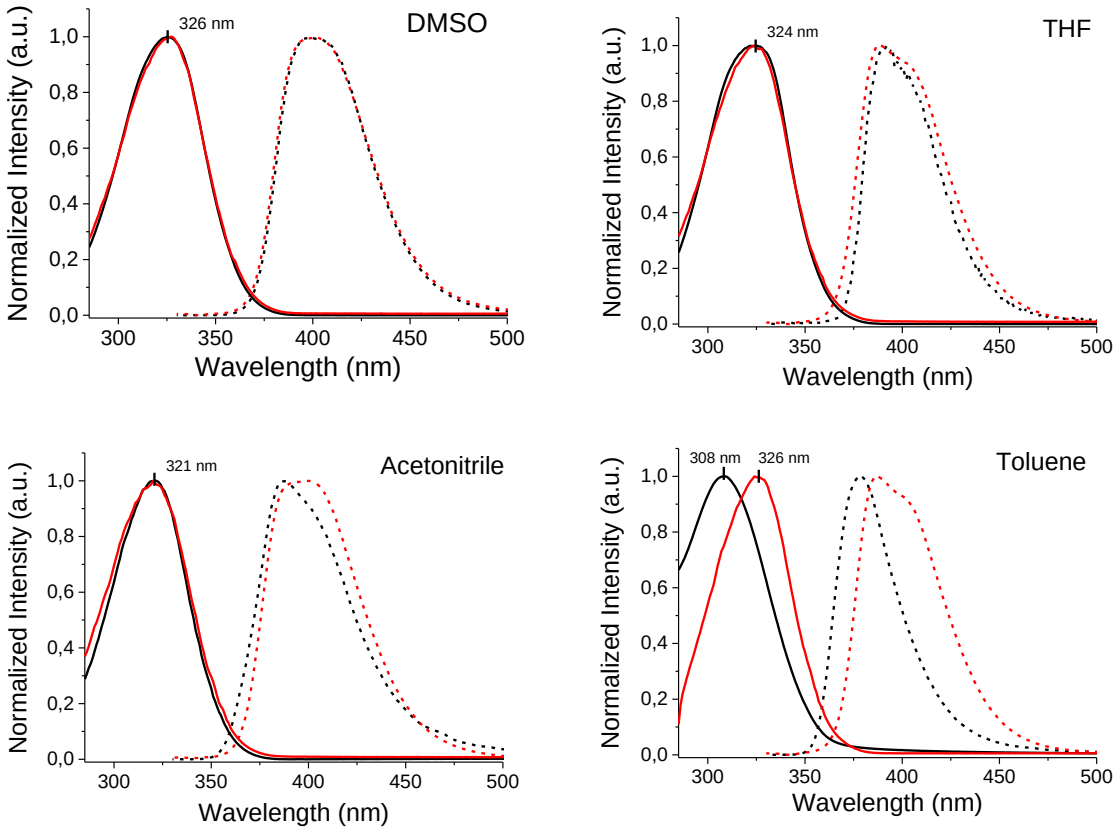

Figure 62 | UV-Vis (solid lines) and fluorescence (dashed lines) spectra of **(*S*)-TATA** in different solvents at 1 mM (black lines) and 0.01 mM (red lines). In the case of acetonitrile a concentration of 0.1 mM was used instead of 1 mM due to solubility issues at this concentration. Excitation wavelength: 310 nm.

In polar solvents, such as DMSO, THF or acetonitrile, TATA molecules are molecularly dissolved and thus there are no strong interactions between them. However, the shape of the emission spectrum appears more like a superposition of few bands with a shoulder at 403 nm along with a maximum of emission at 387 nm. This observation may indicate the presence of different luminophores in the system, such as monomers of different symmetry, dimers or oligomers for example[59,65,66]. In toluene, a hypsochromic shift for both absorption and emission spectra was observed when increasing the concentration of TATA at which it assembles, which may be explained by the π-π interactions between aromatic systems of TATAs.

Table 6 | Absorption end fluorescent properties of **(S)-TATA** in different solvents.

Solvent	λ_{max}^{Abs}, nm at 10^{-5} M/10^{-3} M	Shift, nm	λ_{max}^{Emit}, nm at 10^{-5} M/10^{-3} M	Shift, nm	Stokes shift, nm[b]
Toluene	326/308	18	387/379	8	61
ACN	321/321[a]	0	397/388	9	76
THF	324/324	0	389/392	3	65
DMSO	326/326	0	400/400	0	74

[a] this value was taken from 10^{-4} M solution because of crystallisation of the TATA at the concentration of 10^{-3} M.
[b] Stokes shift is determined using spectroscopy values obtained for 10^{-5} M samples.

vi. Circular Dichroism

Finally, chiral TATA molecules have been characterised by circular dichroism. Using the results of molecular modelling for the TATA packing within the columnar assemblies as a guide (**Figure 61,** also see Armao et. al.,[113] Nyrkova et. al.,[83] Kim et. al[121] and Kim *et al.*[120]), one can immediately see that neighbouring TATA molecules are positioned with an angular displacement of around 20° along the self-assembly axis. This gives a helical structure with a pitch of 6 TATA molecules.[229] Two possible helices exist: right handed helix (*P*) and left handed helix (*M*). When the TATA is achiral, these helices display enantiomeric relationship and should be formed during the self-assembling process in equal quantities. However, if TATA is decorated with chiral substituents, such as (*S/R*)-TATAs, (*M*) and (*P*) helices will be diasteriomeric, hence having different energies. In this case, one of the helices may be formed in an excess, leading of an optically active absorption of the TAA core in CD. One should keep in mind as well that TAAs already exhibit propeller chirality at molecular level because of their propeller-like structure, which due to intramolecular rotation in solution will not be detected, but may influence chiral-self-assembly as was commented by Kim *et al.*[121]

Chiral discotic assemblies have been widely studied by numerous groups using circular dichroism (CD) spectroscopy, providing information on the self-assembly process.[146,150,166,168] The CD spectra of **(*S*)-TATA** in different solvents at the concentration of 0.5 mM are reported in **Figure 63**. All spectra were obtained after cooling hot solutions inside the quartz cuvette. It is clear that chiral aggregates are formed during the cooling process for solvents where gelation was observed. However, surprisingly no sign of chiral assemblies is

229. The actual full pitch contains 18 TATA molecules, but because of the C3-symmetry, this number can be reduced to 6.

present in dichloromethane, chloroform or 1,1,2,2-tetrachloroethane under these conditions. Interestingly, in all aromatic solvents negative CD signal was observed, while in 1,2-dichloroethane and acetonitrile positive, suggesting plausible different structures of self-assemblies.

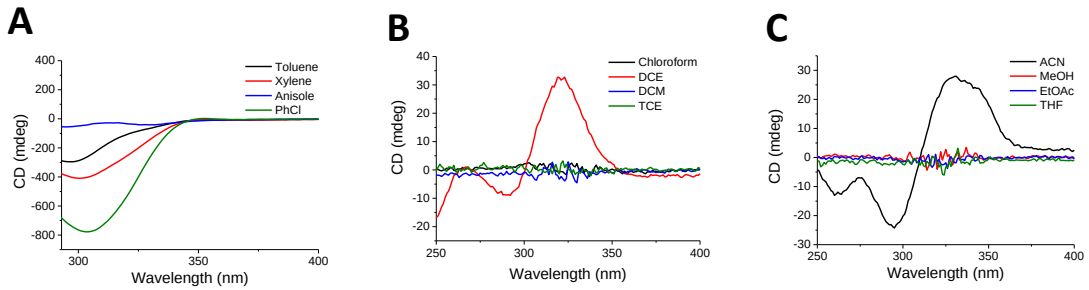

Figure 63 | CD spectra of 0.5mM solutions of **(*S*)-TATA** in different solvents recorded at a temperature of 273 K. (**A**) Aromatic solvents: toluene (black line), *o*-xylene (red), anisole (blue), chlorobenzene (green); (**B**) Chlorinated solvents: chloroform (black), dichloroethane (red), dichloromethane (blue), tetrachloroethane (green); (**C**) Some common nonchlorinated solvents: acetonitrile (black), methanol (red), ethyl acetate (blue), tetrahydrofuran (green).

With the "static" characterization of self-assemblies in hand, we further investigated the self-assembly process using different temperature dependent spectroscopic techniques.

C. Study and Modelling of the Self-Assembly Mechanism

Temperature dependent UV-Vis spectroscopy measurements were performed in order to investigate the self-assembly behaviour of TATAs and to distinguish between isodesmic (equal-K) and cooperative (nucleation-and-growth) supramolecular polymerisation models.

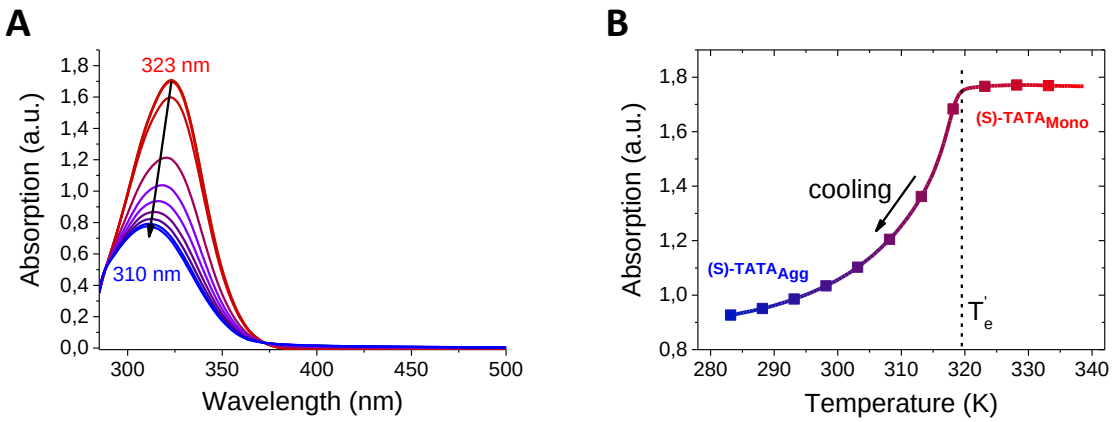

Figure 64 | (A) Temperature-dependent absorption spectra of a 0.5 mM toluene solution of **(*S*)-TATA** recorded during the cooling process from 338 (red lines) to 283 (blue lines) K at a rate of 1 K/min. Arrow indicates the shift of the absorption maximum. **(B)** Evolution of the absorption at 315 nm as a function of the temperature for the same solution.

Experimentally, each studied solution in toluene was heated up to 90 °C to ensure that TATA is molecularly dissolved – **(*S*)-TATA$_{Mono}$**. After 5 min of re-equilibration, the solutions were cooled slowly to study the aggregation process. After the end of this cooling cycle, the heating cycle was immediately performed again, starting from the final temperature reached during cooling. **Figure 64A** represents UV-Vis spectra of a 0.5 mM solution of **(*S*)-TATA** in toluene with decreasing temperature (338 – 283 K with 5 K increment). Upon cooling, a decrease in absorption intensity was observed together with a hypsochromic shift of the absorption maximum from 322 nm to 310 nm. These changes indicate the transition from the molecularly dissolved state to the aggregated state – **(*S*)-TATA$_{Agg}$**, which is consistent with the microscopy data.

The cooling trace (**Figure 64B**) shows a decreasing of the absorption intensity measured at 315 nm with temperature. The non-sigmoidal character of the curve, together with the presence of two temperature regimes, clearly indicate a nucleation-and-growth mechanism for the self-assembly process.[147] The regime observed at relatively high temperatures, where the absorption practically does not change *i.e.* TATA is molecularly dissolved, corresponds to the "nucleation regime". The elongation regime, existing at lower temperatures, is characterised by a significant decrease in absorption intensity due to the aggregation of TATA. These regimes are separated by the elongation temperature T_e (of 322 K for this concentration) below which the self-assembly occurs.

We then studied the influence of the cooling rate on the behaviour of the system, monitoring the absorption intensity at 315 nm with changing temperature. Cooling was performed at different rates: 10, 5, 2, 1 and 0.5 K/min. As shown on (**Figure 65A**), traces that correspond to a cooling rate of 2 – 0.5 K/min have almost the same shape and could be used to extract thermodynamic data. Yet, we decided to choose a rate of 1 K/min for further experiments as the optimal conditions. The consequent cooling-heating cycles revealed the existence of thermal hysteresis at all cooling/heating rates. This indicates a difference between the critical elongation temperature during the cooling T_e' and the heating process T_e (**Figure** 65) and suggests the existence of a kinetic barrier in the self-assembly of TATA during the cooling process.[151,200]

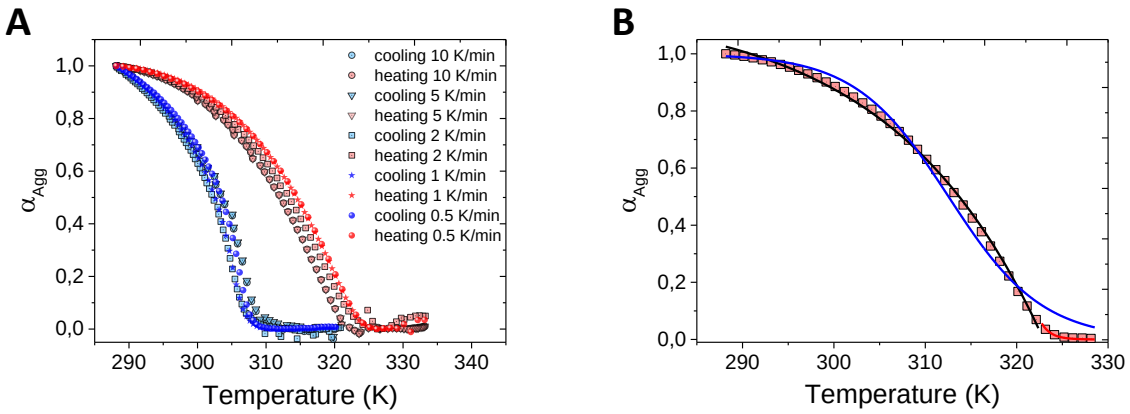

Figure 65 | (A) Temperature dependent degree of aggregation $\boldsymbol{\alpha_{Agg}}$, calculated from the spectroscopic data of the self-assembling process of **(*S*)-TATA** in toluene, $\boldsymbol{C_T}$ = 0.21 mM, recorded at different rates of cooling (blue) and heating (red). (**B**) Temperature dependent melting curve of the self-assembling process of **(*S*)-TATA** in toluene, $\boldsymbol{C_T}$ = 0.21 mM (red squares). Solid lines represent the fitted data using the isodesmic (blue line, R = 0.989) and cooperative (black and red lines, R = 0.997) models.[230]

We then investigated the temperature dependent behaviour of TATAs at different concentrations (**Figure 66**). Melting curves $\alpha_{Agg} = f(T)$ were obtained by recording the absorption intensity at 315 nm during the cooling-heating processes of the studied solutions at a rate of 1 K^{-1} (**Figure 66B-D**, **Figure S4**). The nons-igmoidal curves observed for all concentrations were fitted with both isodesmic and nucleation-growth models, as optimised by Meijer and co-workers for the modelling of unidimensional supramolecular polymerisation.[146] Data suggests that supramolecular polymerisation of TATAs occurs through a cooperative mechanism (**Figure 65B**).[147]

230. Temperature dependent degree of aggregation was calculated by normalizing the experimental UV-Vis traces.

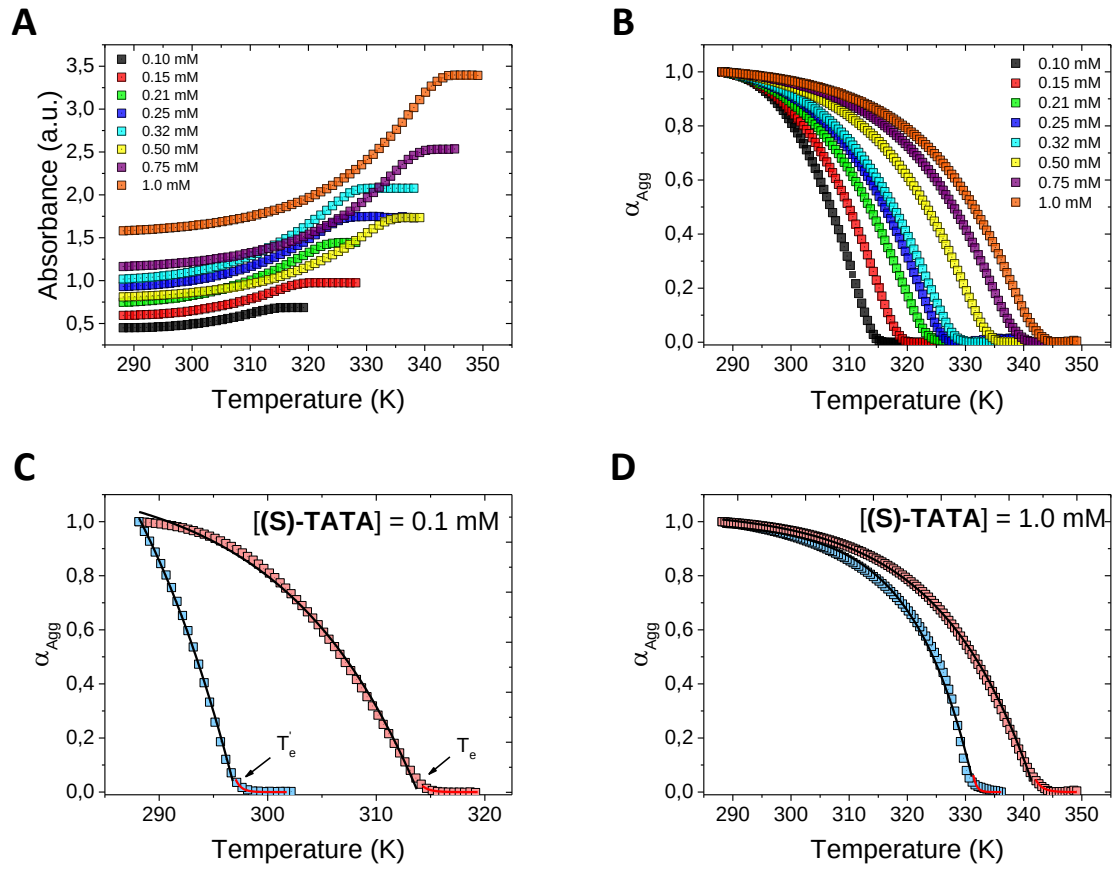

Figure 66 | (A) Temperature dependent absorption intensities recorded at 315 nm during the heating of **(*S*)-TATA** self-assembly in toluene at different concentrations.[231] **(B)** Melting curves (temperature dependent degree of aggregation – $\boldsymbol{\alpha_{Agg}}$) obtained by normalisation of experimental UV data; **(C-D)** Temperature dependent degree of aggregation ($\boldsymbol{\alpha_{Agg}}$) of **(*S*)-TATA** at 0.1 mM (**C**) and 1.0 mM (**D**) in toluene, and calculated from the temperature dependent UV data, recorded at 315 nm, obtained during the cooling (blue squares) and heating (red squares) processes at a rate of 1 K^{-1}. Solid lines represent the cooperative polymerisation fit in the nucleation (red) and the elongation (black) regimes.

Cooperative fit of the data gave the elongation enthalpy of $\Delta H_e = -66 \pm 1$ kJ mol^{-1} and T_e = 313.8 K at a concentration of 1.0×10^{-4} M and average elongation enthalpy $\Delta H_e = -58 \pm 1$ kJ·mol^{-1} (see **Table S3** in annexes for obtained parameters at other concentrations). Alternatively, the van 't Hoff equation could be used to extract the standard thermodynamic parameters as ΔH_e° and ΔS_e° (**Eq. (36)**). For that, we have plotted the natural logarithm of the reciprocal concentration C_T as a function of the reciprocal T_e and we observed the linear relationship between both (**Figure 67**). By fitting the data with **Eq. (36)** in the case of **(*S*)-TATA** in toluene, the standard enthalpy change ΔH_e° and the standard entropy change ΔS_e° for the elongation were found to be -72 ± 1 kJ·mol^{-1} and -153 ± 4 J·mol^{-1}·K^{-1} respectively. These values are in good agreement with the values in **Table S3** (see annexes).

231. Cuvettes with different path lengths were used during the measurements: 2 mm for 0.1 – 0.32 mM solutions and 1 mm for 0.5 – 1.0 mM solutions.

The average value for the activation equilibrium constant K_e 6.4×10^{-5}. The elongation equilibrium constant K_e (298 K) = 4.0×10^{4} M^{-1} was calculated using extracted standard enthalpy and entropy values following **Eq. (34)**.

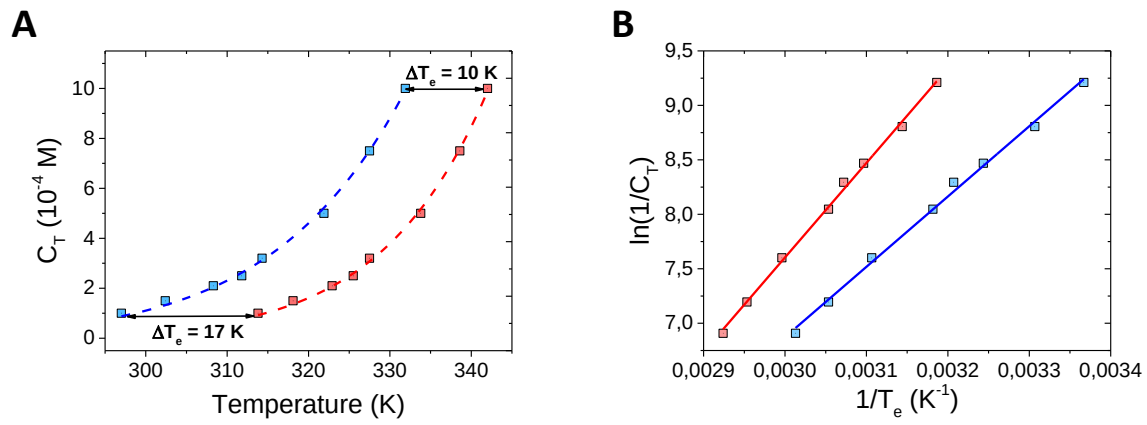

Figure 67 | (A) Evolution of the total concentration of molecules C_T as a function of elongation temperature T_e for **(*S*)-TATA** in the cooling (blue squares) and the heating (red squares) regimes. Dashed lines represent the nonlinear fit of the experimental data. **(B)** Evolution of the natural logarithm of the reciprocal concentration C_T as a function of the reciprocal T_e for **(*S*)-TATA** in cooling (blue squares) and heating (red squares) regimes. Solid lines show the linear relationship, whose slope is proportional to the ΔH_e°.

We then studied (***i***) the influence of the structure and length of the side alkyl chains and (***ii***) the influence of a solvent composition on the self-assembling behaviour of **TATAs**. For this, UV melting curves were recorded for **(C_9)-** and **(C_{14})**-TATAs in toluene, and for **(*S*)-TATA** in a mixture of toluene/methylcyclohexane 1:1 v/v. In all cases, the systems exhibited similar thermal hysteresis, characterized by two elongation temperatures T_e' and T_e (**Figure S5** in annexes). The graphical relationship between the concentration and the elongation temperature during the heating process for all studied systems is represented in **Figure 68A** and the corresponding van 't Hoff plots are represented in **Figure 68B**.

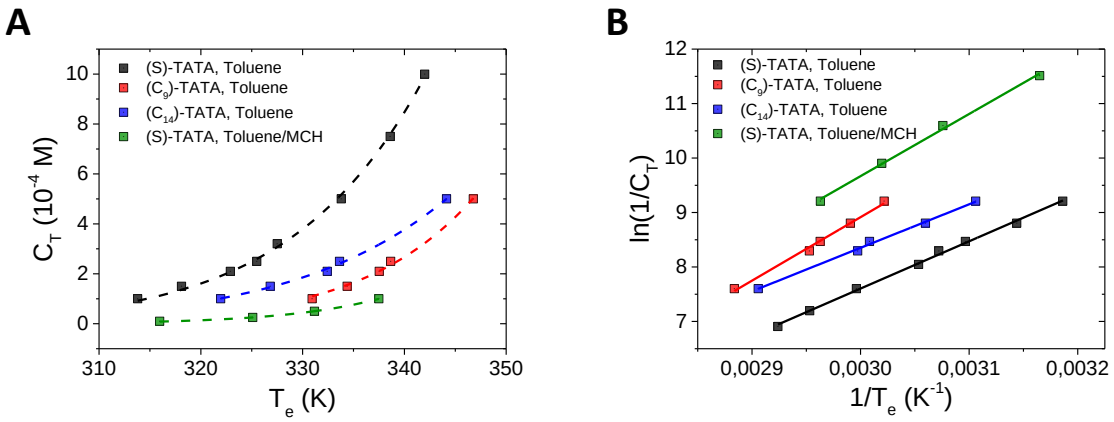

Figure 68 | (A) Evolution of the total concentration of molecules C_T as a function of T_e during the heating process for **(*S*)-TATA** (black squares), **(C_9)-TATA** (red squares), **(C_{14})-TATA** in toluene (blue squares) and **(*S*)-TATA** in a 1:1 mixture of toluene/MCH (green squares). Dashed lines represent the nonlinear fit of the experimental data. (**B**) Evolution of the natural logarithm of the reciprocal concentration C_T as a function of the reciprocal T_e during the heating process for **(*S*)-TATA** (black squares), **(C_9)-TATA** (red squares), **(C_{14})-TATA** in toluene (blue squares) and **(*S*)-TATA** in a 1:1 mixture of toluene/MCH (green squares). Solid lines represent the linear fit of the experimental data.

For the same concentration of the various TATAs in toluene solutions, a lower T_e is observed for the **(*S*)-TATA**, **(C_9)-TATA** and is characterised by the highest T_e. This effect can be explained by the less compact packing of the branched alkyl chains, in comparison with linear ones. As for the trends depending on the chain length, additional experiments are needed to properly explain experimental observations.

Table 7 | Thermodynamic parameters recorded for the self-assembly of different TATAs in pure toluene and in the mixture of toluene and MCH (1/1 v/v) extracted from the van't Hoff plots, which were obtained after fitting of the experimental temperature dependent spectroscopic data.

Compound	Solvent	ΔH_e°, kJ mol^{-1}	ΔS_e°, J mol^{-1} K^{-1}	K_e, M^{-1}
(*S*)-TATA [a]	Toluene	– 72 ± 1	– 153 ± 4	4.0×10^4
(*S*)-TATA [b]	Toluene	– 68 ± 8	– 142± 23	3.2×10^4
(C_9)-TATA [a]	Toluene	– 97 ± 4	– 216 ± 13	5.2×10^5
(C_{14})-TATA [a]	Toluene	– 66 ± 2	– 129 ± 7	6.7×10^4
(*S*)-TATA [a], [c]	Toluene/MCH	– 95 ± 3	– 204 ± 10	10×10^5

[a] parameter obtained from the UV-Vis data; [b] parameter obtained from the CD data

It is well known that the polarity of the solvent can influence the self-assembly. As expected, for **(*S*)-TATA** the T_e is much higher in a mixture of toluene/MCH than in pure toluene (337.5 K vs 318 K respectively) and the standard enthalpy of elongation ΔH_e° in a toluene/MCH mixture and pure toluene is – 95 ± 3 and – 72 ± 1 kJ·mol^{-1} respectively clearly indicates, that the energy of interaction between TATA molecules is higher in a less polar solvent. The thermodynamic values extracted from the van 't Hoff plots are represented in **Table 7**.

We then took advantage of temperature dependent CD spectroscopy to study the aggregation process of **(*S*)-TATA** in details. Our investigations were focused on the self-assembling behaviour of **(*S*)-TATA** in toluene at different concentrations and for different temperature regimes (**Figure 69, Figure 70, Figure S6 , Figure S7**).

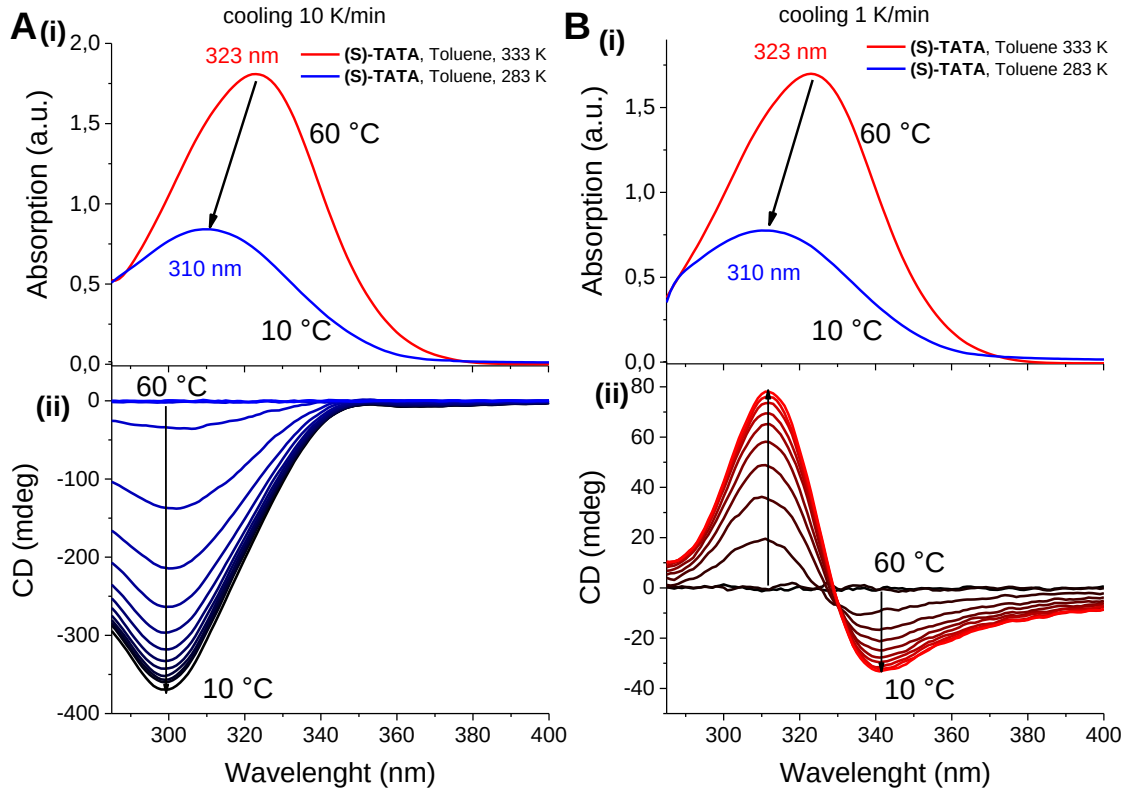

Figure 69 | Comparison of UV-Vis (***i***) and CD (***ii***) spectra for 0.5 mM solutions of **(*S*)-TATA** at different cooling rates. (**A**) fast cooling and (**B**) – slow cooling regimes.

We first studied the evolution of the CD signal for different cooling rates at a fixed concentration. During the slow cooling of a 0.5 mM solution of **(*S*)-TATA** (1 K/min), the CD signal showed an increased intensity for an intense positive maximum at 314 nm and a negative maximum of low intensity at 344 nm. On the other hand, when a hot solution is cooled quickly (10 K/min), the CD signal displays only an increasing negative intensity

maximum at 302 nm (**Figure 69**). This may signify the presence of different self-assembly pathway during the slow and fast cooling regimes. We then monitored the evolution of the CD intensity at 315 nm with temperature for different concentrations (**Figure 70, Figure S6** and **Figure S7** in annexes). At high temperatures, where TATA molecules are molecularly dissolved, the CD is silent. However, below the elongation temperature in all cases, a sharp change in the CD intensity is recorded, which is in agreement with the UV-Vis data. For concentrations lower than 0.5 mM, the CD signal of **(*S*)-TATA** is negative independently of the cooling rate. For concentrations between 0.5 mM and 0.75 mM, the CD signal proved to be negative when the solution is cooled down fast (10 K/min), and positive for slow cooling (1 K/min). For a concentration of 1.0 mM, the CD is positive for both cooling regimes.[232]

Due to the sophisticated shape of some melting curves, fitting of the experimental data was performed using temperature dependent CD experiments, obtained after fast cooling (**Figure S8** in annexes). The thermodynamic parameters extracted from the van 't Hoff plot are summarized in **Table 7** and are in good agreement with the ones extracted from UV-Vis data.

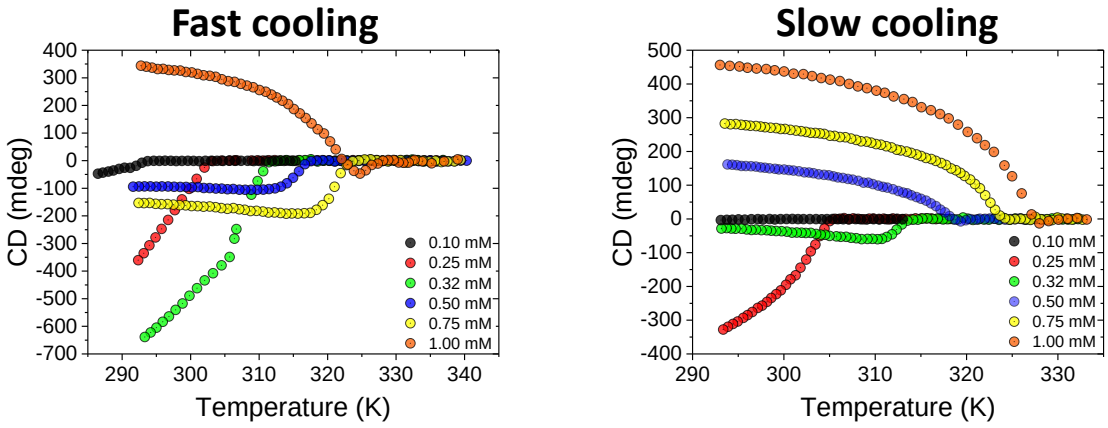

Figure 70 | Temperature dependent CD measurements of toluene solutions of **(*S*)-TATA** at different concentrations and for different cooling regimes. CD intensities are recorded at 315 nm. (**A**) Slow cooling regime (1 K/min). (**B**) Fast cooling regime (10 K/min).

This different behaviour could be possibly explained by the following reasoning. As already mentioned in the bibliography section of this chapter, circular dichroism is a difference in absorption by the sample of *R*-CPL and *L*-CPL. For most of the chiral compounds, which do not self-assemble, the CD spectrum should be constant at any temperature, in the same way as the UV-Vis spectrum, thus corresponding to the molecular

232. It should be mentioned, however, that it was possible to obtain negative CD for the high concentrations of **(*S*)-TATA** if cooling a hot solution on an ice bath (i.e. very fast cooling).

circular dichroism. However, for molecules capable of aggregation, such as **(*S*)-TATA** for example, the observed CD spectrum is the result of the combination of molecular CD, the aggregation-induced CD of first order (the CD which occurs because of the spatial organisation of chromophores in the primary aggregates – single fibres, for instance) and the aggregation-induced CD of higher orders (the CD which is caused by further aggregation of the primary assemblies into superstructures like bundle of fibres, ribbons *etc.*). Importantly, because of the highly dynamic nature of the triarylamine propeller-like structure in solution, no signal corresponding to molecular CD should be observed. However, upon aggregation, the conformation of propeller is immobilised, which should result in the appearance of molecular-propeller contribution to resulting CD.

In our example, the negative CD is possibly related to the formation of unique TATA-fibres, because such behaviour occurs in the relatively diluted solutions, where mainly primary assemblies form independently of the cooling rate. On the contrary, the positive CD is possibly the result of higher order self-organisation of primary fibres of **(*S*)-TATA**, as this situation occurs mainly at higher concentrations, at which the amount of dissolved material is enough to start the formation of superstructures. In these cases, the CD depends on the cooling rate. For example: at [**(*S*)-TATA**] = 0.5 mM (**Figure S7**) the CD constantly increases during the slow cooling below the T_e, to the values of around 150 mdeg; whereas during the fast cooling the CD first decreases, to the value of – 100 mdeg, and then remains constant. (**Figure S6 , Figure S7** in annexes).

Considering that the reversible reaction of *disassembling* is highly improbable below the T_e', one can suppose that this plateau exists due to the appearance of the positive component in CD, related either to enantiomeric helies or to the superstructures.

The temperature dependent CD cooling and heating curves as well as the UV-Vis also exhibit the thermal hysteresis. Moreover, they show a *memory effect* – the heating curve repeats the path of the cooling curve (which is shifted and broadened however). This may implicate that the structure, formed during the cooling process conserve primary aggregates as they are, and disassembles in a retrograde way.

It is reasonable, in our opinion, to assume the following: ***a***) at low concentrations, independently on the cooling rate, the growth of single fibres or/and growth of bundles containing small number of fibres is a dominant process of unidirectional self-assembly, which is characterised by negative CD. ***b***) at higher concentrations, additional level of self-assembly occurs (formation of super-aggregates, bundles of fibres), which may be noticed

when comparing shapes of UV and CD melting curves for different concentrations. The positive CD is a result of this super aggregation.

The nucleation step for both cases may include the formation of a single fibrils, which aggregate laterally resulting in a superhelical nuclei. When the size of these nuclei is larger than some critical value – strong entanglement takes plase.

The analysis of the AFM images of self-assemblies obtained from 0.5 mM solutions for both cooling gradients are shown in **Figure 71.** For both regimes of cooling, the entanglement of fibres (superhelicity) was observed. However, interestingly, in the case for fast cooling process, this entanglement is limited and occurs over long distances (with a helical pitch of order of 1 μm). In the case of slow cooling, the character of superhelical arrangement of fibres is much stronger, with a larger amount of turns for the same distance. The difference in entanglement might be the cause of their different CD response.

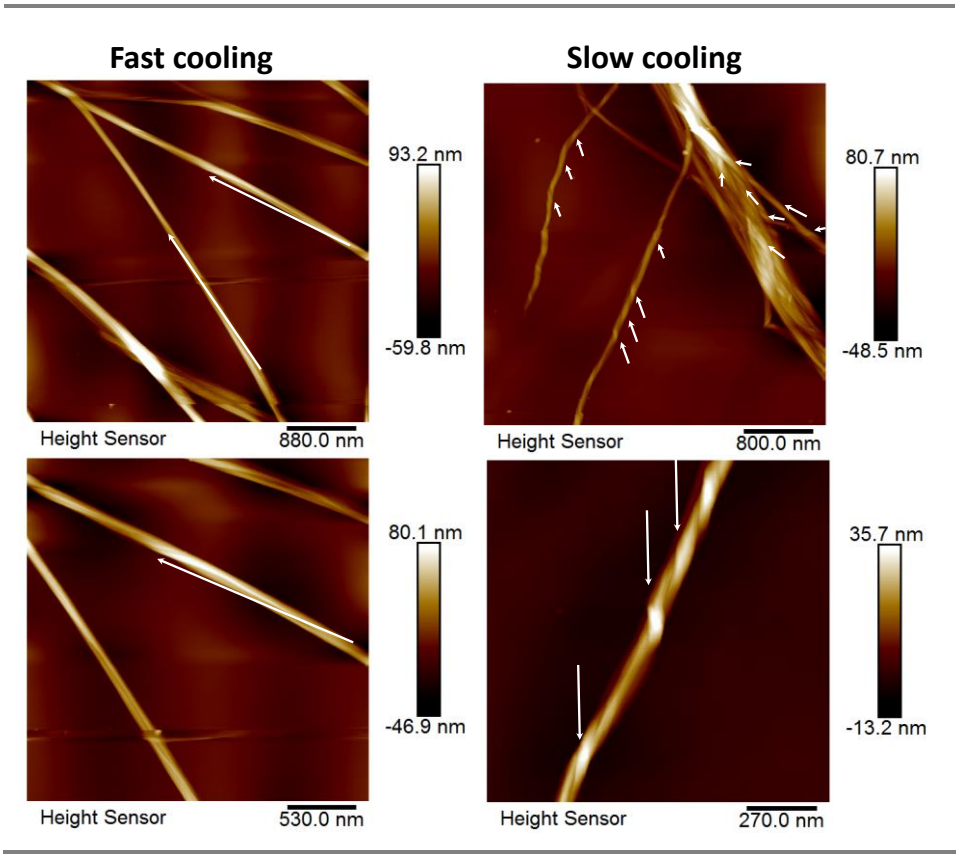

Figure 71 | AFM height image of **(*S*)-TATA** self-assemblies in 0.5 mM solution in toluene.

AFM imaging of self-assemblies, obtained from 0.1 mM concentration, revealed the presence of laterally aggregated fibres, demonstrated in **Figure 72**. We hypothesised, that good resolution of the AFM image could come from the aligned positioning of the helical grooves of several fibres.

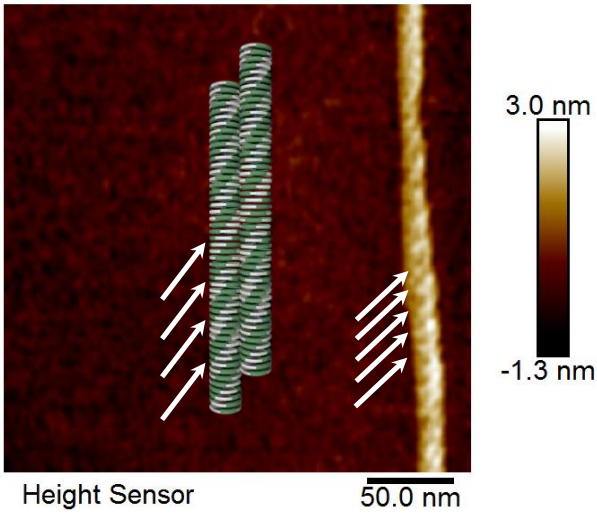

Figure 72 | AFM height image of **(*S*)-TATA** self-assemblies in 0.1 mM solution in toluene and schematic representation of lateral aggregation of fibrils.

The self-assembly process of **(*S*)-TATA** was also investigated with temperature dependent fluorescence spectroscopy. In toluene, the shape of the emission band at concentrations lower than 10^{-4} M is neither concentration nor temperature dependent, which means that TATA exists in the molecularly dissolved state (**Figure 73**). However, at higher concentrations the shape of the emission band does depend on temperature (at high temperature, when no aggregation is observed and TATA is molecularly dissolved, the shape of the emission band is similar to these for TATA at low concentrations). At low temperatures, *i.e.* below the aggregation temperature, the emission maximum shifts hypsochromically from 387 nm to 379 nm with the simultaneous increase of the fluorescent intensity, which indicates a self-assembly induced emission phenomenon (SAIE). Tracing the intensity of fluorescence at 385 nm with the temperature change provided melting curves, which were fitted with cooperative model, providing similar parameters to those obtained by UV and CD (**Table S2**).

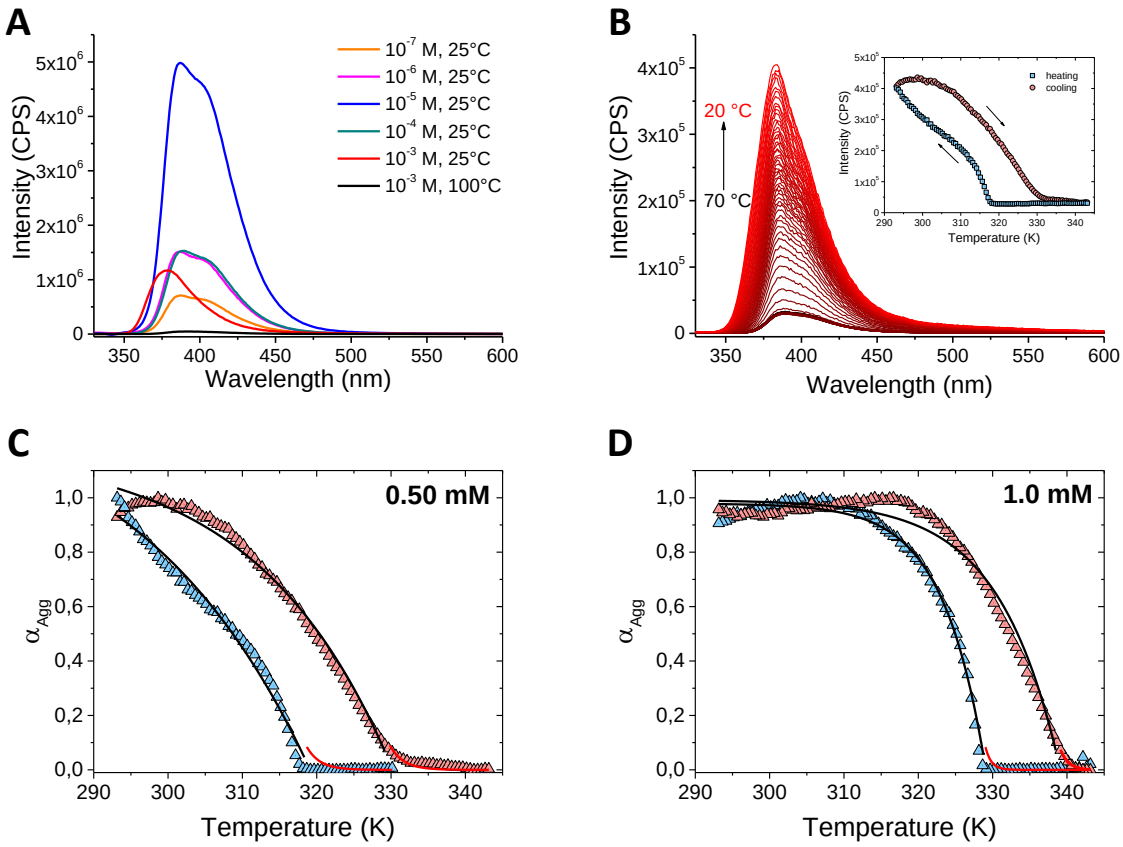

Figure 73 | (**A**) Fluorescent spectra of **(*S*)-TATA** in toluene at different concentrations and temperatures. (**B**) Temperature dependent fluorescent spectra of **(*S*)-TATA** in toluene for a 0.5 mM concentration of TATA. Inset shows the temperature dependence of fluorescence intensity at 385 nm (cooling and heating curves – blue squares and red circles respectively). (**C, D**) Temperature dependent degree of aggregation calculated from fluorescence intensity at 385 nm for 0.5 mM (**C**) and 1.0 mM (**D**) solutions.

4. CONCLUSIONS

To summarise, we studied the mechanism of thermoactivated self-assembly of TATA molecules bearing chiral and achiral substituents using different spectroscopic techniques (FTIR, UV-Vis, fluorescence and CD) and microscopy studies (OPM, TEM, SEM, AFM).

All studied TATAs self-assembly following nucleation and growth model. The presence of thermal hysteresis for the assembly and disassembly process was observed, indicating the existence of a kinetic barrier during the aggregation process, which is related to a particular propeller-like shape of the TATA molecules, with two possible components: *i*) entropic (might be a major one), related to the intramolecular rotation and *ii*) conformational, related to the heterochirality mismatch of the *Δ* and *Λ* conformers, which cannot produce a dimer. The thermodynamic parameters, extracted during the fitting of experimental data lays within reported range of values for similar three-fold hydrogen bonded systems.

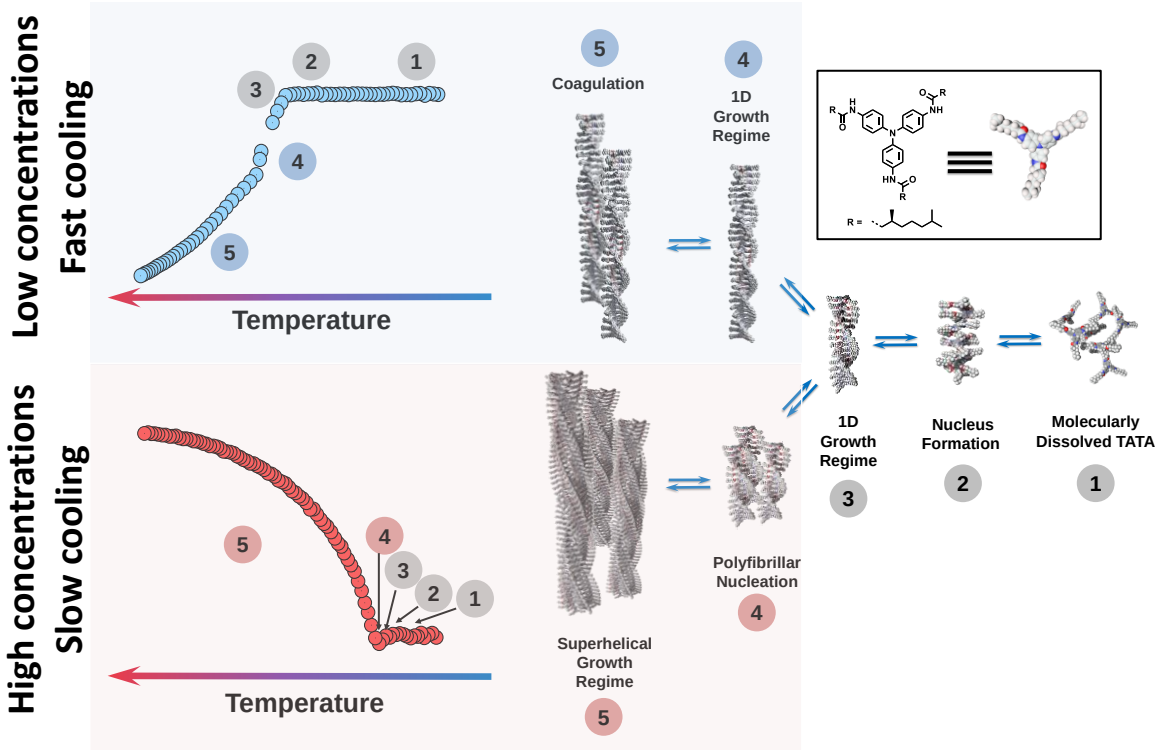

Figure 74 | Schematic representation of **(*S*)-TATA** self-assembly pathways.

Different self-assembly pathways were observed using CD spectroscopy depending on the cooling speed (**Figure 74**). The kinetic analysis of the CD melting curves as well as the AFM imaging suggest that the difference of the chirality is related to the formation of structures of higher orders, which readily form upon slow cooling. During the fast cooling

process, at higher concentrations fibres tend to aggregate as well, however due to the fast decrees in temperature the degree of entanglement is much lower. This type of fine tuning of the self-assembly might be of importance to change the functions of these materials but also it has a considerable fundamental value.

CHAPTER III. BIOCATALYTIC SELF-ASSEMBLY OF TRIARYLAMINE-PEPTIDE CONJUGATES

1. INTRODUCTION

In the *Chapter I*, we discussed that the columnar arrangement of the triarylamine units within nanowires, which was achieved *via* the introduction of amide groups around the TAA core, is crucial to their outstanding conducting properties. It was demonstrated that such supramolecular fibres can be used for different applications such as liquid crystals,[125] organic waveguides[130], plasmonic interconnects[129] or in spintronic technologies.[126,127] In our group, we were also interested in exploring further different supramolecular approaches, in order to controll the arrangement of the triarylamine functions within the self-assemblies.

When looking for structuring motifs, nature is an abundant source of inspiration, as it uses the simple building blocks, such as amino acids, carbohydrates, lipids and nucleotides to construct objects of high complexity – the living organisms.[233]. In recent decades such bottom-up approach[234] has been successfully applied by supramolecular chemists to design new functional materials in all fields of nanoscience, from biomedical applications to soft-matter electronics.[235,236] One of such hierarchical strategy is focused on using different bioconjugates made of functional building-blocks and self-assembling peptides, which are responsible for the controlled structuring of the functional moiety. In recent years, this approach resulted in the construction of different supramolecular systems based on peptide

233. Swiegers, G. F. *Bioinspiration and biomimicry in chemistry reverse-engineering nature*. (Wiley, 2012).
234. Iqbal, P., Preece, J. A. & Mendes, P. M. in *Supramolecular Chemistry* (John Wiley & Sons, Ltd, 2012). doi:10.1002/9780470661345.smc195
235. Busseron, E., Ruff, Y., Moulin, E. & Giuseppone, N. Supramolecular self-assemblies as functional nanomaterials. *Nanoscale* **5,** 7098 (2013).
236. De Santis, E. & Ryadnov, M. G. Peptide self-assembly for nanomaterials: the old new kid on the block. *Chem. Soc. Rev.* **44,** 8288–8300 (2015).
237. Afrasiabi, R. & Kraatz, H.-B. Small-Peptide-Based Organogel Kit: Towards the Development of Multicomponent Self-Sorting Organogels. *Chem. Eur. J.* **19,** 15862–15871 (2013).
238. Nalluri, S. K. M. *et al.* Conducting nanofibers and organogels derived from the self-assembly of tetrathiafulvalene-appended dipeptides. *Langmuir* **30,** 12429–37 (2014).
239. Nalluri, S. K. M., Berdugo, C., Javid, N., Frederix, P. W. J. M. & Ulijn, R. V. Biocatalytic Self-Assembly of Supramolecular Charge-Transfer Nanostructures Based on n-Type Semiconductor-Appended Peptides. *Angew. Chem. Int. Ed.* **53,** 5882–5887 (2014).
240. Nalluri, S. K. M. & Ulijn, R. V. Discovery of energy transfer nanostructures using gelation-driven dynamic combinatorial libraries. *Chem. Sci.* **4,** 3699–3705 (2013).
241. Adhikari, B., Nanda, J. & Banerjee, A. Pyrene-Containing Peptide-Based Fluorescent Organogels: Inclusion of Graphene into the Organogel. *Chem. Eur. J.* **17,** 11488–11496 (2011).
242. Gao, Y. *et al.* Enzyme-instructed self-assembly of peptide derivatives to form nanofibers and hydrogels. *Biopolymers* **94,** 19–31 (2010).
243. Williams, R. J., Mart, R. J. & Ulijn, R. V. Exploiting biocatalysis in peptide self-assembly. *Biopolymers* **94,** 107–117 (2010).
244. Zelzer, M., Todd, S. J., Hirst, A. R., McDonald, T. O. & Ulijn, R. V. Enzyme responsive materials: design strategies and future developments. *Biomater. Sci.* **1,** 11–39 (2013).

conjugates including ferrocene,[237] azobenzene, tetrathiafulvalene,[238] naphthalene,[239,240] pyrene[237,241] units and displaying interesting electronic properties. Moreover, the additional use of biomolecules with specific functions, such as enzymes, for examples, was shown to produce nanostructures, which are not accessible by conventional techniques.[242–244] Recently, such a biocatalytic approach was used by the group of Ulijn to obtain n-type naphthalene diimide-peptide hydrogel with interesting optoelectronic properties.[239]

Inspired by these results, we were curious to see whether this approach might be used to organise conducting triarylamines. In this chapter, we report on the synthesis and study of the supramolecular properties of triarylamines decorated with amino acids and peptides in the native state and in the presence of different enzymes.

The study concerning the biocatalytic self-assembly was performed in collaboration with the group of Prof. R.V. Ulijn. The experiments were partly conducted at the University of Strathclyde, UK together with Dr. S.K.M. Nalluri as a part of the mobility program within the Marie Curie Action ITN ReAd.

2. BIBLIOGRAPHY

A. General Overview

When discussing biomolecules from the point of view of their functions, the main structural components of living systems are: (***i***) polysaccharides, such as cellulose or chitin; (***ii***) polyphenols, such as lignin; (***iii***) proteins; (***iv***) various lipids and (***v***) nucleic acids (the nucleic acids do not play a structural role in the living systems, they only store genetic information; however, their particularly interesting supramolecular features, such as programmed complementarity made them extremely popular in the domain of DNA nanotechnology). Except for lipids, all other classes of molecules are high molecular weight macromolecules. All living organisms, but also self-assembled objects, such as viruses, evolved to have the complex machinery to build these biopolymers from small building blocks: sugars, amino acids, nucleosides. Biomacromolecules then undergo further programmed aggregation, yielding various supramolecular structures such as nanotubes, nanofibers, nanocapsules *etc.* by means of noncovalent interactions.[245–247]

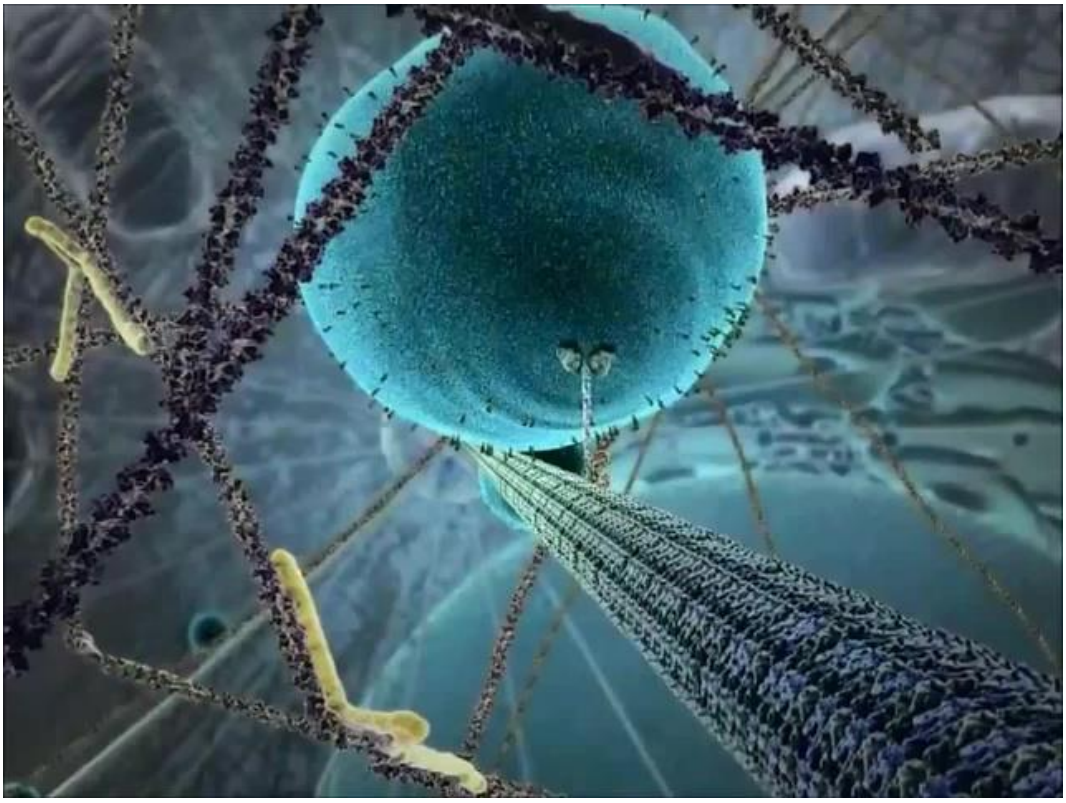

Figure 75 | Kinesin (protein motor) walking up the microtubule (protein self-assembly) and transporting vesicle (lipid self-assembly) inside the living cell (complex supramolecular system). Figure is adapted from ref. 248

The particular interest in proteins lies in their wide structural diversity, provided by the variability of the relatively small number of natural building blocks, *i.e.* proteinogenic amino acids (**Figure S9** in annexes). Each of these small natural molecules have different characteristic features, such as pK_a, hydrophobicity/hydrophilicity, charge, presence of an aromatic function, structural strain, which define the properties of the secondary and tertiary structures of the proteins, in which they are combined.

The variety of possible structures which may be formed from protein/peptide self-assemblies is impressively large and diverse, going from 1D structures such as nanofibers, nanorods and tubes to 2D structures, such as sheets and membranes or even 3D structures (entangled networks, nanoparticles, micelles *etc.*) (**Figure 76**).[236,249,250]

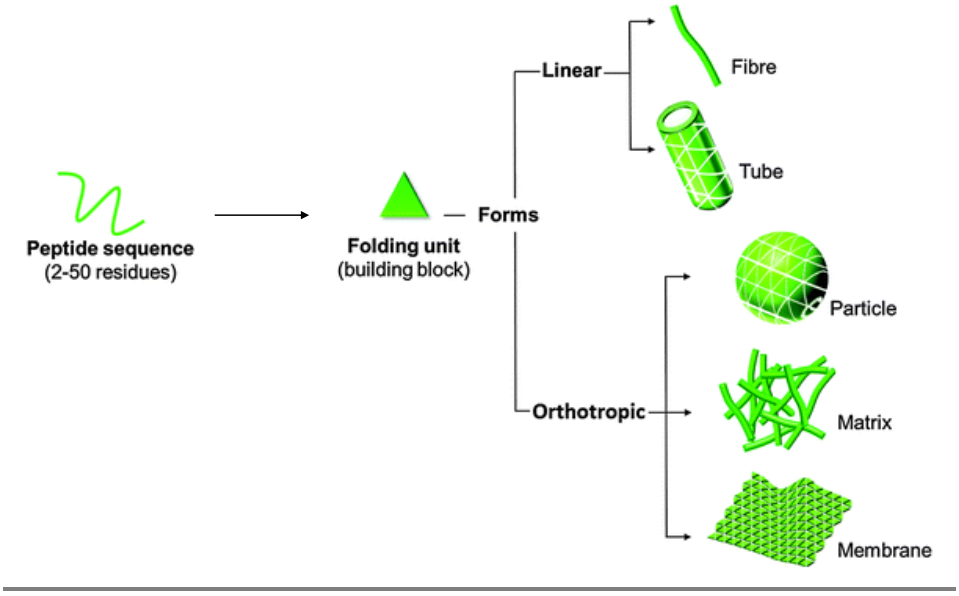

Figure 76 | Schematic representation of the different topologies which may be obtained from peptide building blocks. Figure is reproduced from ref. 236

The structural features of proteins, which allows them to assemble, have been extensively studied over the last fifty years, providing some indications regarding the mechanism of protein aggregation.[251] It is important to remember that these structures are the result of billions years of evolution, which we, unfortunately, do not have billion years at our disposal. However, technological progress provides us with powerful tools to analyse and

245. Seeman, N. C. DNA in a material world. *Nature* **421,** 427–431 (2003).
246. McLaughlin, C. K., Hamblin, G. D. & Sleiman, H. F. Supramolecular DNA assembly. *Chem. Soc. Rev.* **40,** 5647 (2011).
247. Lim, Y., Moon, K.-S. & Lee, M. Recent advances in functional supramolecular nanostructures assembled from bioactive building blocks. *Chem. Soc. Rev.* **38,** 925 (2009).
248. *The Inner Life of the Cell*. (Harvard University, 2006). at <http://www.xvivo.net/animation/the-inner-life-of-the-cell/>
249. Fleming, S., Debnath, S., Frederix, P. W. J. M., Tuttle, T. & Ulijn, R. V. Aromatic peptide amphiphiles: significance of the Fmoc moiety. *Chem. Commun.* **49,** 10587 (2013).
250. Hartgerink, J. D., Beniash, E. & Stupp, S. I. Peptide-amphiphile nanofibers: A versatile scaffold for the preparation of self-assembling materials. *Proc. Natl. Acad. Sci.* **99,** 5133–5138 (2002).
251. Invernizzi, G., Papaleo, E., Sabate, R. & Ventura, S. Protein aggregation: Mechanisms and functional consequences. *Int. J. Biochem. Cell Biol.* **44,** 1541–1554 (2012).

select the important structural features which are responsible for a particular phenomenon of interest modelled using small molecules, which could be synthesised by conventional synthetic techniques.[252,253]

B. Peptide-Based Self-Assemblies

Although today we are able to synthesise complex proteins using synthetic approaches and biotechnology,[252,254] their use in materials science remains quite limited considering their price, synthetic scale and stability. The use of small peptides instead, inspired from naturally occurring sequences or designed *de novo*, is more practical and could be highly promising in biomedical applications, such as tissue regeneration.[236,255]

The majority of peptide-based supramolecular systems known today are built from two classes of peptidic molecules: (***i***) naturally occurring morphologies composed purely of amino acids such as α-helices (which can assemble in coiled-coil structures) and β-sheets (formed from the β-strands) (**Figure 77**); (***ii***) small-aromatic peptides, such as FF dipeptide and *de novo* designed peptide-conjugates, consisting of one peptidic part and a conjugated non-peptidic moiety such as an aromatic, aliphatic or other functionalities which then give rise to various self-assembled architectures.

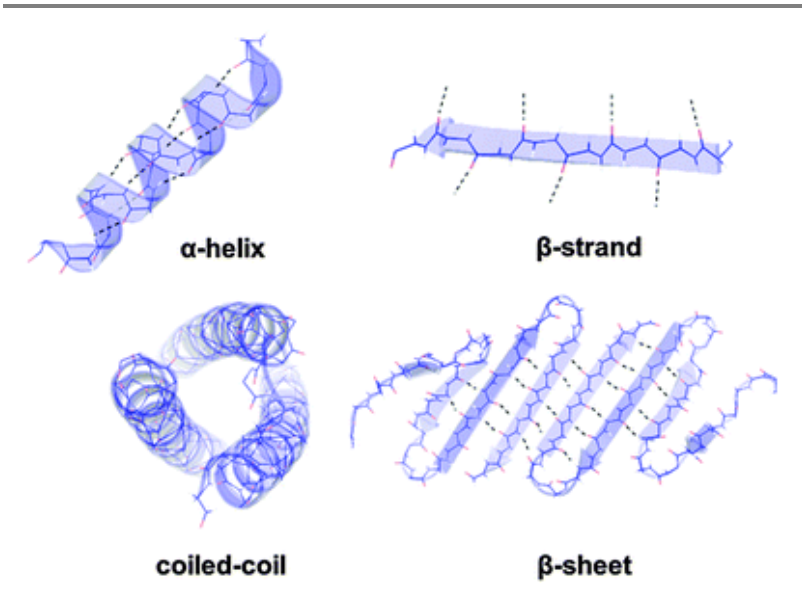

Figure 77 | α-Helix and β-strand protein folding elements and their oligomerization states – coiled coils and β-sheets. Dotted lines indicate hydrogen bonds. Figure is reproduced from ref. 236

In the following section, we will briefly discuss the different classes of peptidic moieties used to build peptide-based self-assemblies.

i. α-Helical Peptides

The α-helical motif is one of the most abundant secondary structures of natural proteins.[256,257] Typically, an α-helix has a right-handed helical conformation in which each NH group of the peptide backbone is bound to the CO group of the 3rd or 4th residue through a hydrogen bond. This conformation is also denoted as 3.6_{13}-helix, where 3.6 stand for the average number of amino acid residues per one helical turn, which is made of 13 membered ring including hydrogen bonds. The propensity of different amino acids to assist in the formation and stabilisation of α-helical structure depends mainly on the side group (see **Figure S10A** in annexes). Two amino acids in particular have the lowest propensity to stabilise an α-helix: proline (due to its rigid structure and the absence of NH group after the formation of a peptide bond) and glycine (due to its high flexibility).

Several synthetic α-helical motifs have been used to build self-assembled nanostructures.[256,258–261] The structural features governing the self-assembly process are well understood and generalised, so that specialised computer programs such as MultiCoil, *etc.* can be used to predict if a designed sequence will self-assemble into an α-helical coiled-coil.[258–260] The simplest example of such assemblies, which contains two α-helices, is so called coiled-coil motif. The individual helix is a 3.5-α-helix heptamer peptide (or heptade) described as (*a-b-c-d-e-f-g*), which has two helical turns for a heptade sequence that may be repeated few times in the sequence as depicted in **Figure 78**. The amino acids in the first and fourth positions (*a* and *d*) should be hydrophobic, such as V, L or I, rendering one of the faces of the helix hydrophobic. The aggregation of these faces through hydrophobic interactions drives the formation of the coiled-coil structure between two or more helices. The incorporation of charged residues in the fifth and seventh positions (*e* and *g*) brings additional stabilisation to the coiled-coil structure *via* electrostatic interactions. Other types of interactions, such as additional hydrogen bonding, cation-π interaction were shown to play a role in the stabilisation of these structures as well.

252. Chandrudu, S., Simerska, P. & Toth, I. Chemical Methods for Peptide and Protein Production. *Molecules* **18,** 4373–4388 (2013).
253. Mitchell, A. R. Bruce Merrifield and solid-phase peptide synthesis: A historical assessment. *Biopolymers* **90,** 175–184 (2008).
254. Gräslund, S. *et al.* Protein production and purification. *Nat. Methods* **5,** 135–146 (2008).
255. Stephanopoulos, N., Ortony, J. H. & Stupp, S. I. Self-assembly for the synthesis of functional biomaterials. *Acta Mater.* **61,** 912–930 (2013).
256. Cavalli, S., Robson Marsden, H., Albericio, F. & Kros, A. Peptide Self-Assembly. *Supramol. Chem.* (2012). doi:10.1002/9780470661345.smc088
257. Brändén, C.-I. & Tooze, J. *Introduction to Protein Structure*. (Garland Pub., 1999).
258. Lupas, A., Van Dyke, M. & Stock, J. Predicting coiled coils from protein sequences. *Science* **252,** 1162–1164 (1991).
259. Alva, V., Nam, S.-Z., Söding, J. & Lupas, A. N. The MPI bioinformatics Toolkit as an integrative platform for advanced protein sequence and structure analysis. *Nucleic Acids Res.* **44,** W410–W415 (2016).
260. Wolf, E., Kim, P. S. & Berger, B. MultiCoil: A program for predicting two-and three-stranded coiled coils. *Protein Sci.* **6,** 1179–1189 (1997).

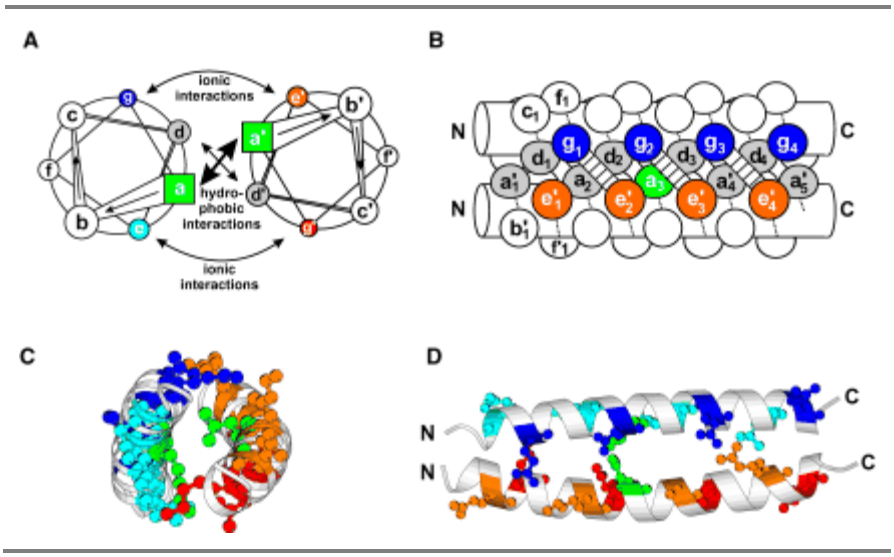

Figure 78 | (**A**, **B**) Schematic representation of a parallel dimeric coiled-coil. (**C**, **D**) X-ray structure of the leucine zipper of GCN47 as ribbon plot. Figure is reproduced from ref. 262

Woolfson and colleagues took advantage of the tunability of such structures to design coiled-coils with "sticky ends" by incorporating oppositely charged amino acids in the *b* and *c* positions.[263] Such modifications caused their aggregation in nanofibers *via* electrostatic interactions, which led ultimately to a thickening of the fibre and their precipitation from the solution, thus preventing gelation. When the charged amino acids in positions *b* and *c* were replaced by alanine or glutamine, gel formation occurred. This example highlights how the structure/properties relationship in peptide systems, can be tuned by using different amino acids.

An interesting example describing the use of *de novo* designed α-helical proteins as electronic switches was reported by N. Ashkenasy and co-workers.[261] The authors studied the influence of the peptide conformation on their electrical properties. 21-amino-acid peptidic sequence, forming dimeric "Velcro" coiled-coils with three different conformations, were synthesised and their dimers were anchored on a gold surface (**Figure 79B**). The different conformations of the coiled-coil structures were shown to yield large difference in the resulting molecular dipole moment, as determined by Kelvin probe measurement of their contact potential difference.

Moreover, these peptides were also tested as molecular bridges between a gold surface and a gold-coated AFM tip (**Figure 79C)**. Remarkably, for a parallel orientation (PN and PC), the current-voltage relationships were asymmetric (**Figure 79C)**, (red and blue curves respectively), showing a rectifying behaviour with opposite polarity. On the other hand, for an

261. Shlizerman, C., Atanassov, A., Berkovich, I., Ashkenasy, G. & Ashkenasy, N. De Novo Designed Coiled-Coil Proteins with Variable Conformations as Components of Molecular Electronic Devices. *J. Am. Chem. Soc.* **132,** 5070–5076 (2010).

antiparallel conformation, a symmetric ohmic-like behaviour was recorded (**Figure 79C** green curve), highlighting the importance of the peptide conformation on the electronic properties of the molecular bridges.

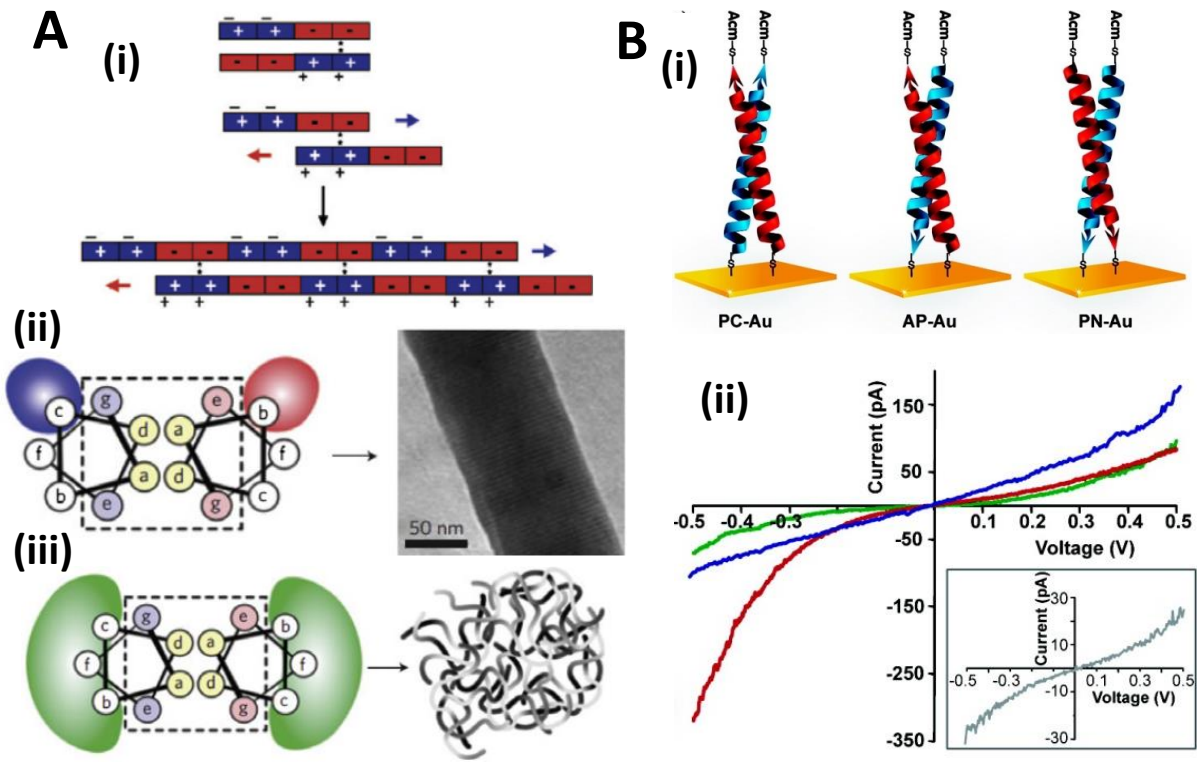

Figure 79 | (**A**) (**i**) Schematic illustration of the "sticky-end" driven self assembly of α-helices. (**ii**) Coiled-coil motif with charged residues at *b* and *c* positions, which aggregate forming thick precipitating fibres.(*iii*) Coiled-coils with Ala or Gln which self-assemble causing hydrogelation. (**B**) (**i**) Illustration of the parallel and antiparallel coiled coils adsorbed onto gold surfaces. Red is used for glutamic acid rich peptides and blue for lysine rich peptides. **(ii)** I−V curves of coiled-coil monolayers: **PC** (red), **PN** (blue), and **AP** (green). Figure is adapted from refs. 255,261,263

ii. β-Sheet Forming Peptides

Another widespread natural secondary structure motif of peptides/proteins is β-sheet, which is formed by hydrogen bonding between β-strands, an almost fully extended peptide backbone, in which the side-groups of neighbouring amino acids are oriented in opposite directions (**Figure 77**)[257]. Two basic arrangements are possible for β-sheet peptides: parallel, when C and N termini strands are oriented in the same direction and antiparallel, when they alternate. Typically, amphipathic peptides, in which hydrophobic (X) and polar/charged (Z) amino acids alternate, in a sequence such as $(XZXZ)_n$, are known to form β-sheet structures.[264,265] The relative propensity of different amino acids to produce such structures is represented on **Figure S10B** (see annexes).

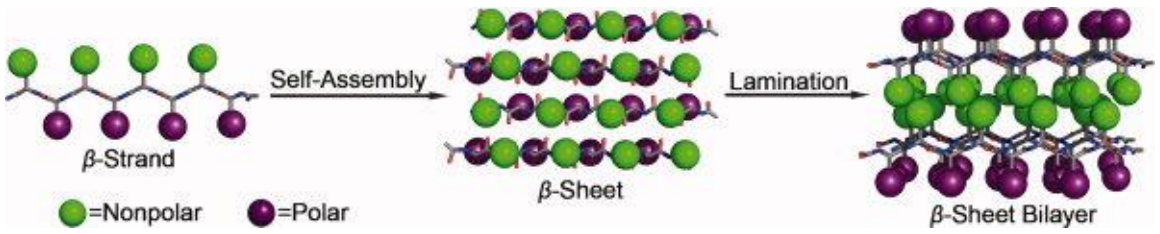

Figure 80 | Proposed self-assembly of an amphipathic peptide sequence and arrangement of amino acid side chains in the β-sheet bilayer. Figure is adapted from ref. 265

Taking these structural characteristics into account, different groups took advantage of this rational design to investigate β-sheet self-assembling peptides. The group of Zhang reported one of the first examples of bio-inspired self-assembly of β-sheets.[266]

The chosen peptide sequence $(RARADADA)_2$ named "RAD" but also "Lego" was designed to have a complementary pattern of charged residues on the polar face of the β-sheet (e.g. + + – – + + – –). Upon further face-to-face aggregation of RAD β-sheets the multilayer fibrils were formed, resulting in gel formation at a very low concentration (< 1% w). Interestingly, the ability of these fibres to reform after mechanical destruction was demonstrated, underlying the self-healing behaviour of those self-assemblies thanks to noncovalent interactions. These hydrogels were also found to be biocompatible and used in regenerative medicine as matrices for cell growth.[266]

β-sheet peptides have a tendency to self-assemble in various hierarchical structures such as tapes, ribbons, fibrils and fibres.[255,264] One of the important aspects to control is the formation of these structures not only through physico-chemical parameters such as pH, temperature or salt concentration but also through the primary structure of the building units. Systematic studies of the β-sheet peptide aggregation with various di-, tri- and tetrameric sequences such as $(\mathbf{F}K\mathbf{F}E)_n$, $(\mathbf{I}K\mathbf{I}E)_n$ or $(\mathbf{V}K\mathbf{V}E)_n$ revealed a number of observations.[255] In particular, peptides with a higher ratio of aromatic residues as well as long peptides have lower aggregation concentration.

262. Mason, J. M. & Arndt, K. M. Coiled Coil Domains: Stability, Specificity, and Biological Implications. *ChemBioChem* **5,** 170–176 (2004).
263. Banwell, E. F. *et al.* Rational design and application of responsive α-helical peptide hydrogels. *Nat. Mater.* **8,** 596–600 (2009).
264. Bowerman, C. J. & Nilsson, B. L. Review self-assembly of amphipathic β-sheet peptides: Insights and applications. *Biopolymers* **98,** 169–184 (2012).
265. Bowerman, C. J. & Nilsson, B. L. Self-assembly of amphipathic β-sheet peptides: insights and applications. *Biopolymers* **98,** 169–84 (2012).
266. Loo, Y., Zhang, S. & Hauser, C. A. E. From short peptides to nanofibers to macromolecular assemblies in biomedicine. *Biotechnol. Adv.* **30,** 593–603 (2012).
267. Pochan, D. J. *et al.* Thermally Reversible Hydrogels via Intramolecular Folding and Consequent Self-Assembly of a de Novo Designed Peptide. *J. Am. Chem. Soc.* **125,** 11802–11803 (2003).

Another subclass of peptides designed to produce β-sheets was communicated by the group of Schneider, who used a so-called hairpin peptide, which consists of two β-strands connected *via* a turn sequence -^{D}PP-: VKVKVKVKV^{D}PPTKVKVKV, where ^{D}P stands for the D-Proline. At pH 5.5, this sequence has a random structure due to electrostatic repulsion between charged lysine residues, however upon basification to pH 9.0, β-sheet hairpin forms thanks to the intramolecular hydrogen bonding. Subsequent self-assembly of the hairpins leads to the formation of aggregates of higher hierarchy, causing gelation of the solution. Detailed studies of these systems revealed a series of interesting dynamic properties such as self-healing and thermoresponsiveness.[267] As depicted in **Figure 81**, the increasing temperature causes the dehydration of the nonpolar residues, resulting in the self-assembly of the β-hairpins, which then undergo hydrophobic collapse and gel formation.

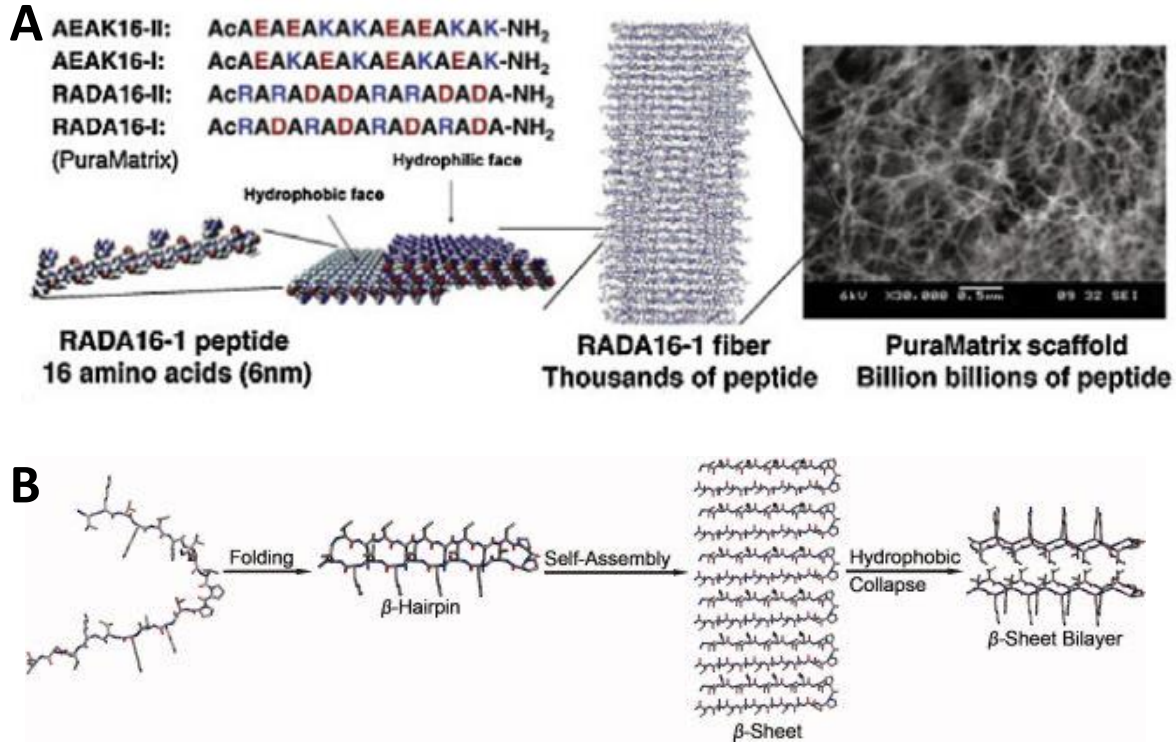

Figure 81 | (**A**) Schematic of the ionic self-complementary peptides developed by Zhang and co-workers. The peptides pack into sheets and fibers based on hydrophobic interactions on one face of the molecule, and complementary ionic interaction on the other. These fibers then form a highly porous hydrogel. (**B**) Proposed mode of self-assembly for Schneider's β-hairpin amphipathic peptides. Figure is adapted from ref.265

Overall, the self-assembly of β-peptides gives rise to a new class of biocompatible materials which are used in regenerative medicine, *etc.*[268] Together with theoretical studies on this process, better understanding and thus improved treatments for some neurodegenerative

diseases such as Alzheimer's, which is caused by the formation of aggregates of amyloid peptides, may be possible. [269]

iii. Dipeptides

So far, we have discussed the self-assembling properties of quite large peptides. However, from a practical points of view, the shorter the sequence the better it is.

One of the first examples of such short peptides was shown to be the FF sequence, which is believed to play an important role in the aggregation of Alzheimer's Aβ peptides. It was demonstrated, that upon cooling hot aqueous solutions, FF dipeptide undergo self-assembling through a combined hydrogen bonding and strong π-π interactions and form a very long (up to 100 μm) nanotubes.[270] These nanotubes represent high thermal and mechanical stability and are believed to be one of the stiffest bio-material obtained through the self-assembly process.[271]

Interestingly, the outcome of the self-organization can be tuned by using co-solvent. Huang *et al.* recently reported on the self-assembly of FF-dipeptide in a mixture of water/acetonitrile (**Figure 82**).[272] Remarkably, when changing the solvent composition structures with different morphology were obtained. Nanotubes were formed in systems with high water content (**Figure 82C(i,ii)**) while in the solutions with high ratio of acetonitrile nanofibers were observed (**Figure 82C(iii)**), mixtures of both kind of aggregates were formed in solvent mixtures with acetonitrile content (10-98%).

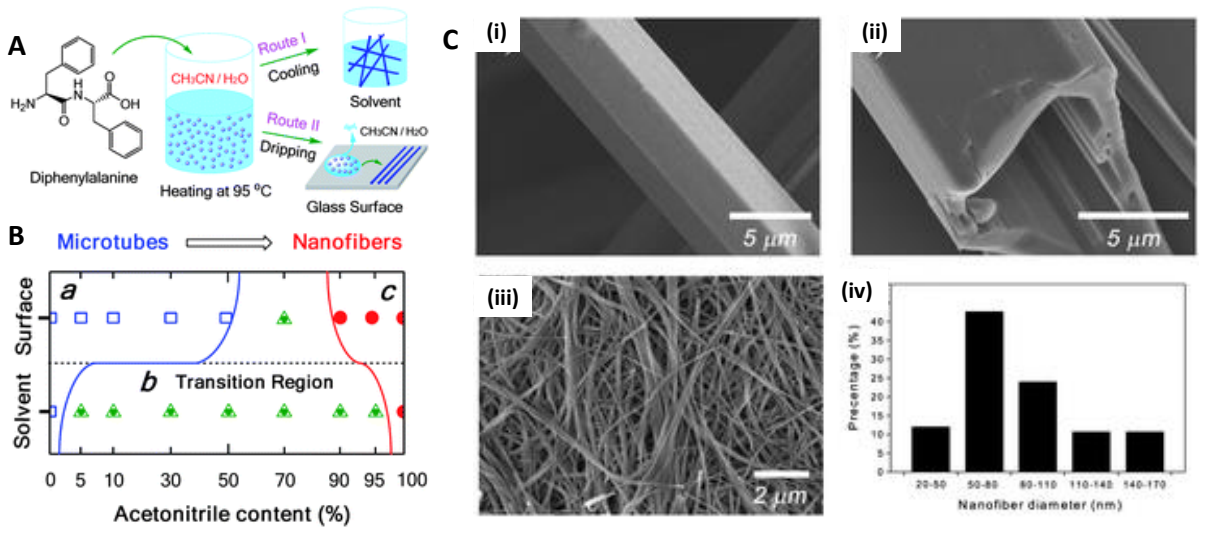

Figure 82 | (A) A schematic illustration of the diphenylalanine self-assembly. (**B**) A 'phase diagram'-like picture showing the structural transition of peptide assemblies from microtubes into nanofibers with the increasing acetonitrile content. (**C**) SEM images of diphenylalanine microtubes (**i** and **ii**) and nanofibers (**iii**), which were formed in pure water and acetonitrile (Route I), respectively. (**iv**) A statistical distribution of nanofibers diameters. Figure is reproduced from ref. 272

When the authors deposited hot solutions of FF in solvent mixtures on the cold glass surface (Route II) the phase diagram was shifted, allowing only for the formation of microtubules or nanofibers in a broader range of solvent compositions (**Figure 82B**).

Other phenylalanine-containing dipeptides were shown to aggregate in aqueous medium. Ventura and colleagues highlighted the influence small structural changes on the macroscopic effects in peptide self-assemblies.[273] They studied the gelation properties of hydrophobic VF and IF dipeptides. Remarkably, the isoleucine containing peptide assembled, inducing hydrogelation at already at 2% w/w, while valine containing dipeptide remained in the solution.

Recently Frederix *et al.* developed a methodology to estimate the theoretical propensity of gelation for 400 di- and 800 tri- peptides using molecular dynamics computational methods (**Figure 83** and **Figure S16**).[274,275] These calculations include peptidic sequences with free C- and N-termini. Using methods of molecular dynamics, the authors propose an aggregation propensity score for each studied sequence. Sequences with high score have a big chance to aggregate, while sequences with a low score do not. **Figure 83** represents a theoretical propensity score diagram, which shows scores for studied dipeptides: red colour indicates high aggregation propensity. From this chart is clear, that aromatic dipeptides, containing Phe or Try have the highest aggregation propensities with highest scores for FF and WW dipeptides.

268. Hosseinkhani, H., Hong, P.-D. & Yu, D.-S. Self-Assembled Proteins and Peptides for Regenerative Medicine. *Chem. Rev.* **113,** 4837–4861 (2013).
269. Serpell, L. C. Alzheimer's amyloid fibrils: structure and assembly. *Biochim. Biophys. Acta - Mol. Basis Dis.* **1502,** 16–30 (2000).
270. Reches, M. & Gazit, E. Casting metal nanowires within discrete self-assembled peptide nanotubes. *Science* **300,** 625–7 (2003).
271. Yan, X., Zhu, P. & Li, J. Self-assembly and application of diphenylalanine-based nanostructures. *Chem. Soc. Rev.* **39,** 1877 (2010).
272. Huang, R., Qi, W., Su, R., Zhao, J. & He, Z. Solvent and surface controlled self-assembly of diphenylalanine peptide: from microtubes to nanofibers. *Soft Matter* **7,** 6418 (2011).
273. de Groot, N. S., Parella, T., Aviles, F. X., Vendrell, J. & Ventura, S. Ile-Phe Dipeptide Self-Assembly: Clues to Amyloid Formation. *Biophys. J.* **92,** 1732–1741 (2007).
274. Frederix, P. W. J. M. *et al.* Exploring the sequence space for (tri-)peptide self-assembly to design and discover new hydrogels. *Nat. Chem.* **7,** 30–37 (2014).
275. Frederix, P. W. J. M., Ulijn, R. V., Hunt, N. T. & Tuttle, T. Virtual Screening for Dipeptide Aggregation: Toward Predictive Tools for Peptide Self-Assembly. *J. Phys. Chem. Lett.* **2,** 2380–2384 (2011).

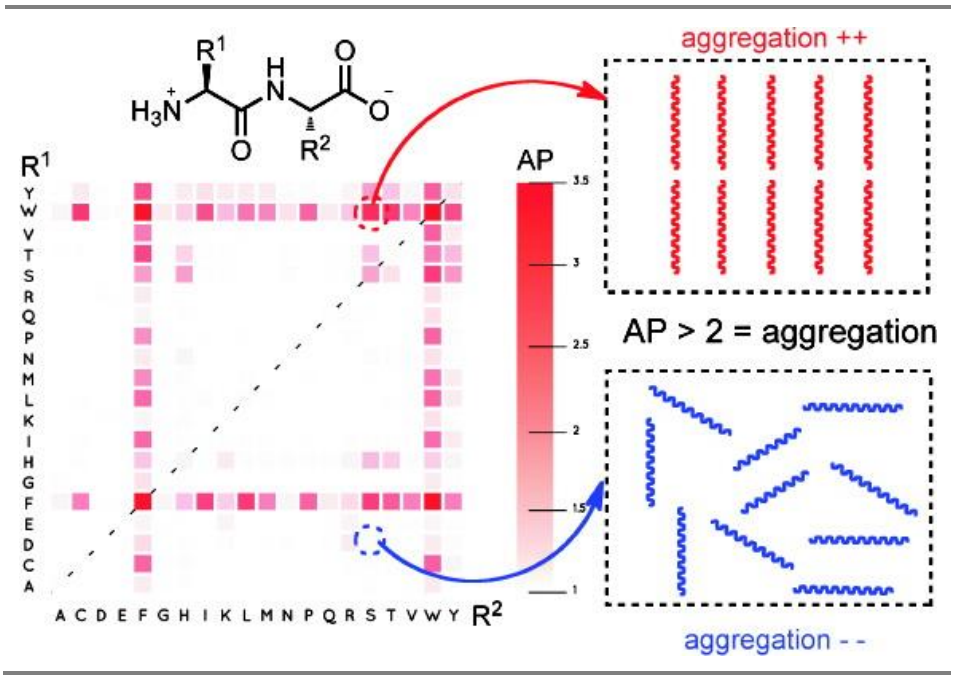

Figure 83 | Two-dimensional grids indicating the aggregation propensity score for dipeptides. Horizontal and vertical axes show the amino acid one-letter codes for the first (N-terminus) and second (C-terminus) amino acid, respectively.Figure is reproduced from ref. 275

Even though the predicted properties may not be always supported by experimental results[276] it can still be used as a prediction tool for the design of self-assembling peptides.

276. For instance the IF and VF have similar high aggregation propensities, however in an example above it was shown that VF does not aggregate under the same conditions.

C. Peptide Amphiphiles Self-Assemblies

i. Peptide-Conjugate Amphiphiles

Hitherto, we have discussed supramolecular structures resulting from peptides containing only amino acids. However, structures assembled from so-called peptide amphiphiles (PA) received a wide interest over the last decade.[163,249,277] Peptide amphiphiles consist of a hydrophilic peptide part (typically 5-10 residues), decorated with a hydrophobic nonpeptidic part (fatty acid residues for example), making them similar to lipids (**Figure 84A**). The self-assembly of these peptide amphiphiles were extensively studied by the group of Stupp.[250,255,278]

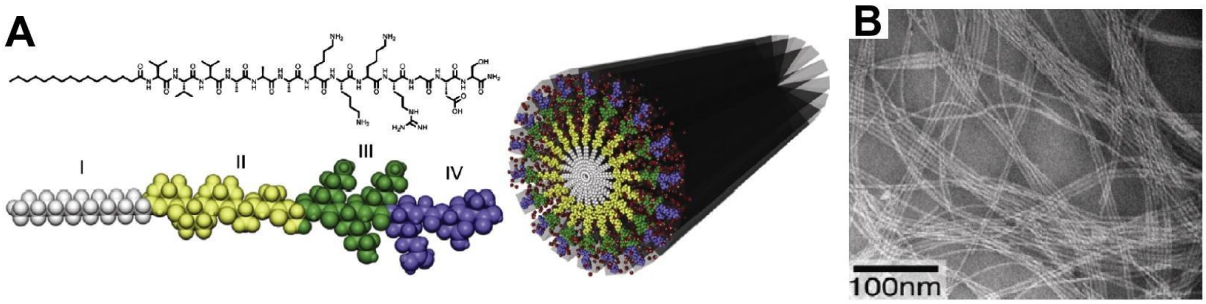

Figure 84 | (A) Chemical structure of a representative peptide amphiphile (PA), and its assembly into nanofibers, with four primary regions highlighted in colour. Region I: unbranched alkyl (usually C16) tail; region II: a β-sheet forming segment to promote H-bonding along the fibre axis; region III: charged amino acids for solubility; region IV: a peptide epitope to impart the material with biological signalling properties. (**B**) TEM image demonstrating the self-assembly of PAs into high aspect ratio nanofibers, often of several microns in length. Figure is adapted from ref. 255

In aqueous media, these amphiphiles assemble into nanorods with high aspect ratio. Fatty acid chains aggregate together to form a hydrophobic core, while the hydrophilic shell consists of the peptidic residues. The shell can be modified with various chemical groups in order to achieve a desired functionality such as fluorescence for bio-imaging, bio-recognition, *etc.* (**Figure 84A** region **IV**).[250,278] It was shown that the peptide sequence close to hydrophobic core (region **II**) is important for the formation of a hydrogen bonding network between the amphiphiles *via* β-sheet structures. In many cases, the self-assembly of PA leads to gelation, which found multiple biomedical applications.[268]

277. Zhao, X. *et al.* Molecular self-assembly and applications of designer peptide amphiphiles. *Chem. Soc. Rev.* **39,** 3480–3498 (2010).
278. Cui, H., Webber, M. J. & Stupp, S. I. Self-assembly of peptide amphiphiles: from molecules to nanostructures to biomaterials. *Biopolymers* **94,** 1–18 (2010)

ii. Short Aromatic Peptide Conjugates

Systematic studies of peptidic self-assemblies showed that highly aromatic peptides such as FF can readily form supramolecular structures. It was also discovered, that even uniquely aromatic amino acids, conjugated with aromatic blocks (usually classical protecting groups such as Fmoc) readily self-assemble in water as well.[163] This type of peptide conjugate, where the nonpeptidic part is an aromatic moiety, is called an aromatic peptide amphiphile (APA) (**Figure 85**). Typically, APAs consist of four main structural components: a peptide part, which could be one amino acid or relatively short peptide (2-3 residues) with free C-terminus or modified (R = -OH, $-NH_2$ for instance) and an aromatic part connected to the peptide through a linker. Together with other peptide-based materials, this class was extensively studied during the last decade, resulting in large variety of new functional systems.[163] The relative robustness of these materials allowed their application not only in the biomedical field but also in various domains of nanoscience such as organic electronics for example.[162,279]

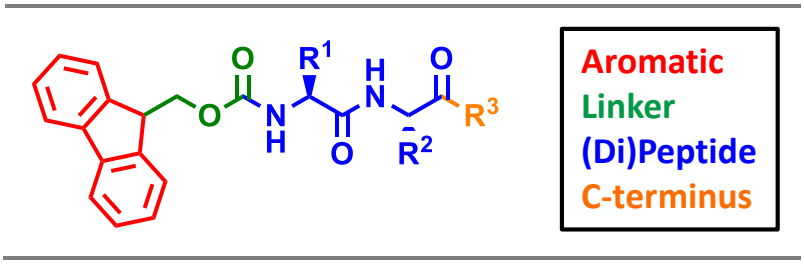

Figure 85 | Generic structure of an aromatic peptide amphiphile (APA). Fmoc dipeptide is used as a typical example. Figure is adapted from ref. 163

1) Aromatic part

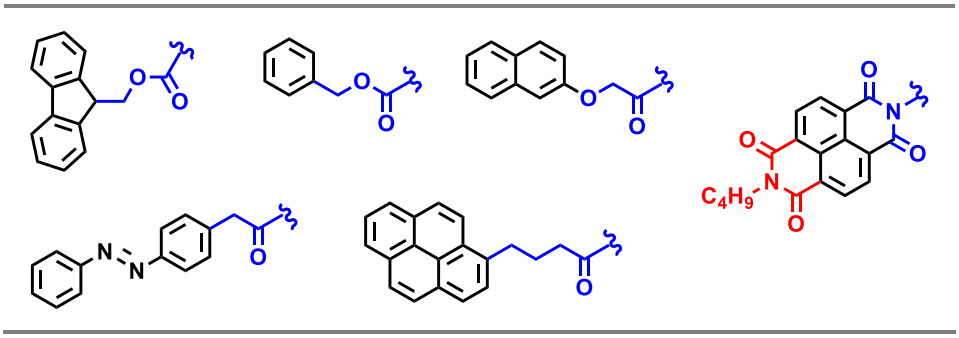

Figure 86 | A selection of some aromatic moieties and linkers reported in the literature classified according to the structure. Red indicates a substituent not part of the core aromatic functionality, whilst blue indicates the linker that connects to the N-terminus of a peptide sequence. Figure is adapted from ref. 163

The first examples of APA self-assemblies were reported for Fmoc protected peptides, such as Fmoc-LD for example, which formed a thermoresponsive hydrogel.[280] Importantly,

although Fmoc and Boc groups are both hydrophobic, it was shown that Boc-peptides do not form self-assemblies, underlying the importance of aromatic properties of the function at the N-terminus for the self-assembling and gelation properties.[281] To date, short peptides have been decorated with different synthetic aromatic functions to tune and improve the gelation properties or to introduce a functionality for conductivity or charge transfer (**Figure 86** and **Figure S11** in annexes).[163]

2) Linker

The linker, connecting the aromatic part to the peptide or amino acid also plays an important role in the gelation process. For instance, methoxynaphthyl peptide conjugates (***a*** - ***c***) were shown to form hydrogels, while the equivalent naphthyl-peptides with shorter linkers did not produce gels (**Figure 87**).[282] Molecular modelling suggested unfavourable conformations for the peptides with shorter linker precluding an efficient association. The authors suggested that the presence of the methoxy group also might bring additional stabilisation *via* possible H-bonding.[282]

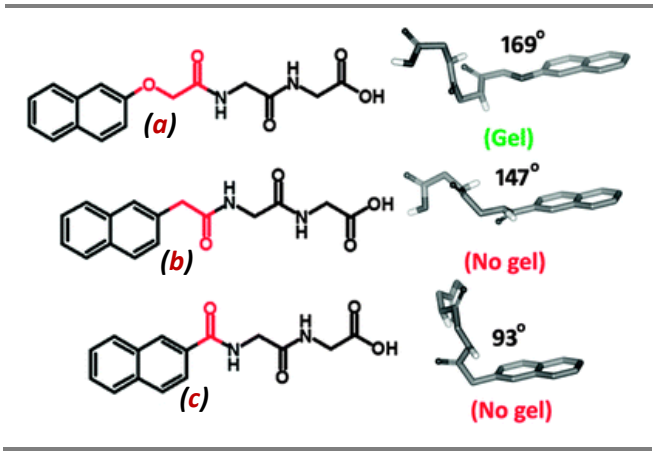

Figure 87 | Effects of the nature of the linker on the overall molecular geometry; with a relatively linear conformation being optimal for gelation. Figure is adapted from ref. 163

279. Ardoña, H. A. M. & Tovar, J. D. Peptide π-Electron Conjugates: Organic Electronics for Biology? *Bioconjug. Chem.* **26,** 2290–2302 (2015).
280. Vegners, R., Shestakova, I., Kalvinsh, I., Ezzell, R. M. & Janmey, P. A. Use of a gel-forming dipeptide derivative as a carrier for antigen presentation. *J. Pept. Sci.* **1,** 371–378 (1995).
281. Debnath, S., Shome, A., Das, D. & Das, P. K. Hydrogelation through self-assembly of fmoc-peptide functionalized cationic amphiphiles: potent antibacterial agent. *J. Phys. Chem. B* **114,** 4407–15 (2010).
282. Yang, Z., Liang, G., Ma, M., Gao, Y. & Xu, B. Conjugates of naphthalene and dipeptides produce molecular hydrogelators with high efficiency of hydrogelation and superhelical nanofibers. *J. Mater. Chem.* **17,** 850–854 (2007).

3) Peptide part

The second key part of peptide amphiphile is obviously the peptidic moiety. We have already discussed the structural features of primary peptide sequence leading to α-helix or β-sheet structures. When considering short aromatic peptide conjugates, general tendencies have been observed as well.[163] Scott and Ulijn recently analysed literature data on the gelation properties of aromatic peptide amphiphiles made of either one of the 20 natural amino acids or 400 dipeptide sequences (**Figure 88**).[283]

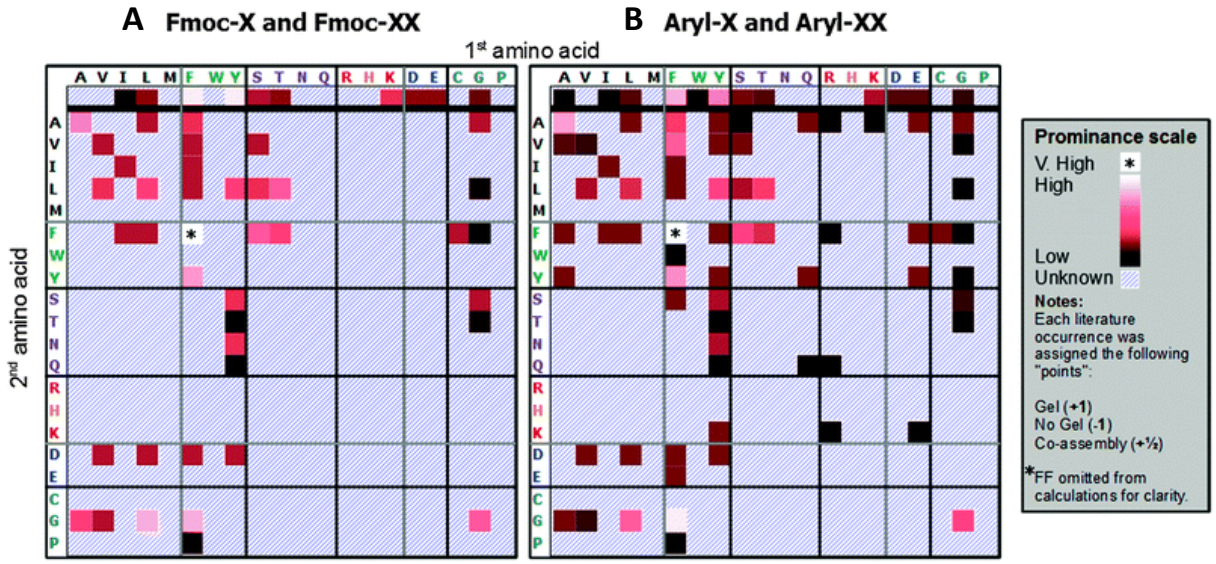

Figure 88 | Literature/self-assembly prominence summary for all natural amino acid and dipeptides (respectively separated by thick black horizontal lines) containing (**A**) Fmoc and (**B**) N-terminal aromatics in general as hydrophobic part. Thin black lines define hydrophobic, hydrophilic, charged, and other side chain classifications. Thin grey lines define subcategories (as far as reasonably possible) – *i.e.* aliphatic/aromatic and positive/negative. Figure is adapted from ref. 163

Among all known peptide amphiphiles, aromatic and hydrophobic amino acids and peptides, were analysed as the best gelating APAs, conjugated with FF sequence being the most popular. In general, however, the choice of a sequence should be based on a balance between its hydrophobic/hydrophilic properties, so that the aggregation is favoured in the solution and precipitation does not occur.

The theoretical simulations could be used to some extent predict to a certain degree, whether a chosen sequence has a tendency to self-assemble in aqueous media or not as was discussed in a previous section. [274,275]

283. For each sequence find in literature, points were attributed: +1 if it gelated, -1 if it did not form gel and +0.5 if it formed co-assembly with other compounds. Thus, the lighter the colour of the square, representing aromatic dipeptide conjugate, it was reported to form gel more frequently than if the colour is dark.

4) C-terminus

For short APAs, the self-assembling properties may strongly depend on the C-terminus: free acid, ester, amide, *etc.*

Leaving the C-terminus of the peptide amphiphile unchanged, offers the possibility to tune the balance between the free carboxylic acid (-COOH) and its conjugated base ($-COO^-$), by adjusting the pH of the system. pH titration of Fmoc-FF amphiphile reported by Saiani and colleagues highlights the importance of the C-terminus group and the influence of the pH on the self-organisation (**Figure 89**).[284] Upon acidification of a basic Fmoc-FF solution, a transition from solution to a translucent gel was observed at pH 9.5, which then transformed into a turbid viscous solution at pH 6.2 and finally phase separation occurred below pH 5.2.

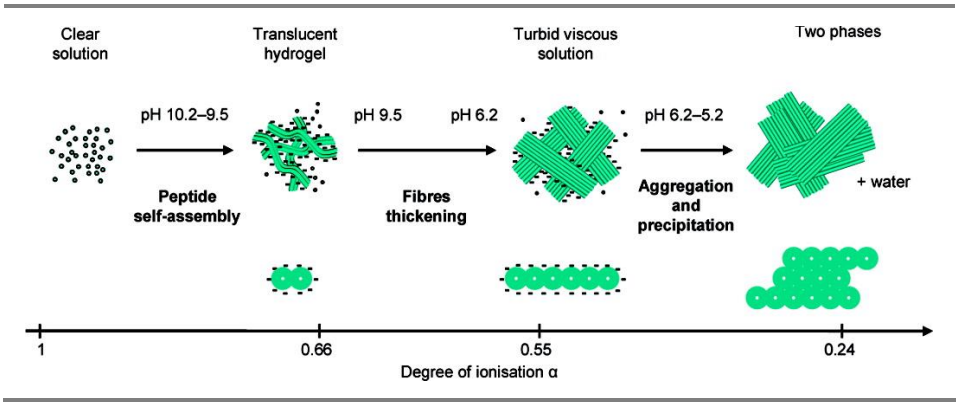

Figure 89 | Proposed self-assembly mechanism of Fmoc-FF from high to low pH above the critical gelation concentration as a function of the peptide degree of ionisation, α. Figure is reproduced from ref. 284

Interestingly, the authors report also on the aggregation-induced shift of the pKa of the diphenylalanine amphiphile, which occurred twice during the titration procedure, meaning that self-association influences the acid/base properties of the carboxyl unit present on the peptide.

The modification of the C-terminus can also be a powerful tool to tune the self-assembly propensity. While amphiphiles with a free acid group have different self-assembling properties depending on pH, the methoxy esters (-COOMe) are stable in a broader range of pH. The introduction of an ester groups however, makes the compound more hydrophobic, thus with a higher tendency to precipitate. Therefore, the incorporation of hydrophilic residues in a sequence may balance this effect. For instance, studies on the gelation properties of Fmoc-protected fluorinated phenylalanines with different C-terminus modifications

284. Tang, C., Smith, A. M., Collins, R. F., Ulijn, R. V. & Saiani, A. Fmoc-Diphenylalanine Self-Assembly Mechanism Induces Apparent p K a Shifts. *Langmuir* **25,** 9447–9453 (2009).

revealed the following trend: –COOH terminus promotes gelation, methyl ester (-COOMe) promotes precipitation and amide (-$CONH_2$) makes peptides more soluble.[163]

iii. Applications

With this knowledge in hand, chemists have designed new peptide-based materials with multiple applications.[236] For instance, Nalluri *et al.* took advantage of the ability of short peptides (FF and LLL) to assemble into fibrous structures in organic solvents in order to organise the semiconducting molecules such as tetrathiafulvalene in a controlled fashion.[238]

In this study, a p-active tetrathiafulvalene (TTF) was decorated with either amide C-terminus diphenylalanine peptide or methyl ester C-terminus trileucine peptide (**Figure 90A**). The FF conjugate was shown to assemble in common organic solvents into one directional structures, leading to the gelation of the solvent. Interestingly the LLL conjugate did not form organogels, being completely soluble or precipitating under the same conditions as the FF compound. This highlights the importance of a balance between hydrogen bonding, aromatic interactions and solvation in organic solvents to induce gelation.

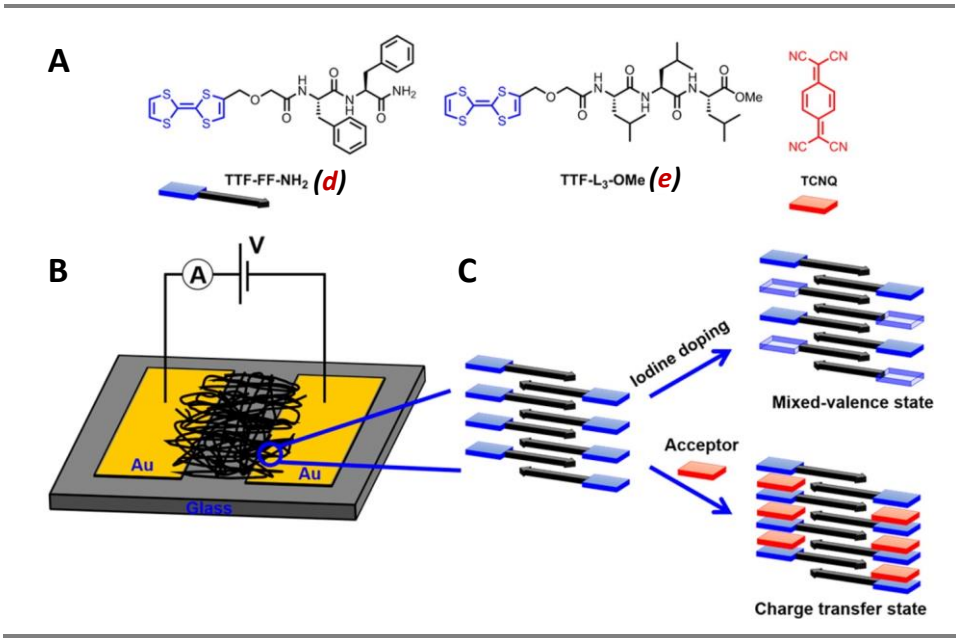

Figure 90 | (A) Molecular structures of p-type TTF-peptide bioconjugates: TTF−diphenylalanine amide **(*d*)** (TTF-FF-NH_2) and TTF-trileucine methyl ester **(*e*)** (TTF-L_3-OMe) derivatives, and TCNQ acceptor used in this study. Schematic representation of (**B**) the method of electrical conductivity measurements of xerogel nanofiber networks drop-casted between gold electrodes on a sodium-free glass substrate and (**C**) the proposed mechanism of the nonaqueous self-assembly process of TTF−peptide bioconjugates and the formation of charge transfer and mixed-valence states upon doping with TCNQ and iodine, respectively. Figure is reproduced from ref. 238

The authors further investigated the electrochemical properties of the gels. TTF residues within fibres were oxidised electrochemically, or with a chemical oxidant such as

iodine to form the mixed valence state. The presence of a charge transfer band in the NIR region of the absorption spectrum suggests the close arrangement of TTF-moieties within nanofibers. Charge-transfer complexes were also obtained upon addition of an electron-accepting molecule such as tetracyanoquinodimethane (TCNQ) to the assemblies (**Figure 90**). Remarkably, conductivity measurements revealed an increase in conductivity by few orders of magnitude from 1.9×10^{-10} for undoped conjugate to 3.6×10^{-4} S·cm^{-1} and 6.4×10^{-7} S·cm^{-1} when doped with TCNQ and iodine vapour respectively.

This example illustrates the possibility to use bioconjugates for the construction of electroactive soft materials.

D. Biocatalytic Induction of Self-Organisation

So far, we have discussed peptidic supramolecular structures obtained when a single compound was dissolved at room or elevated temperature in either aqueous media or organic solvents and spontaneously formed self-assemblies (or when the self-assembly process was triggered by a pH change) (**Figure 91**A). We have also mentioned that some peptide-conjugates do not form assemblies but precipitate due to inappropriate balance between hydrophobic and hydrophilic characters. However, in some cases, assemblies constructed from these insoluble building blocks can be obtained using both their soluble precursors and enzymes in order to catalyse their *in situ* transformation. This approach is called biocatalytic and is often used to obtain nanomaterials, which cannot be synthesised by other means (**Figure 91**B).[243]

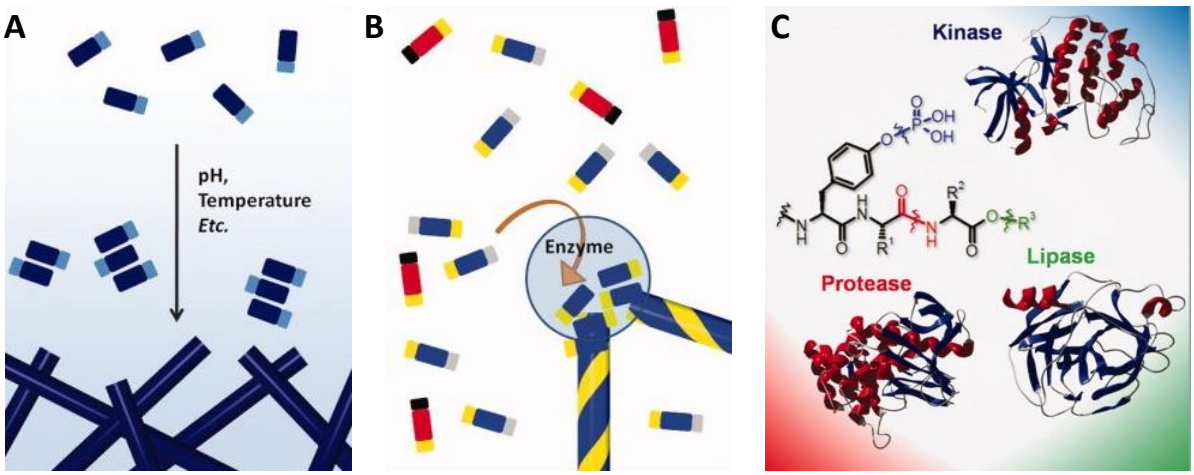

Figure 91 | Comparing environmentally (bulk) (**A**) versus chemically triggered (localised) (**B**) self-assembly. Light-blue rectangles represent enzymatically cleavable blocking groups that prevent self-assembly of precursors. (**C**) Examples of enzymes that may be used to control molecular self-assembly and the chemical bonds that they affect. Figure is adapted from ref. 243

In the last decade, enzymes have been used frequently to produce enzyme-based supramolecular materials.[243,285] There are a few pathways reported to reach such materials: (***i***) enzyme triggered self-assembly, when enzyme catalyses the chemical transformation of the precursor(s) which leads to the aggregation event; (***ii***) enzyme catalysed dynamic assembly, when one form of assembly transforms into another, thanks to the enzyme action. Additionally, different enzymes have been utilised for this purpose, among them kinases (dephosphorylation), proteases (peptide bond cleavage) and lipases (ester bond cleavage) are the most popular (**Figure 91**C).

From the point of view of thermodynamics, these processes can be classified into two groups related to the free energy change. In the first group, the precursor is less favoured than the actual building block, thus leading to self-assembly (**Figure 92A**). In the second group, the building block is the least favoured species; however, due to a gain in energy during the self-assembly process, the equilibrium can be shifted towards aggregate formation (**Figure** 92**B**).[286]

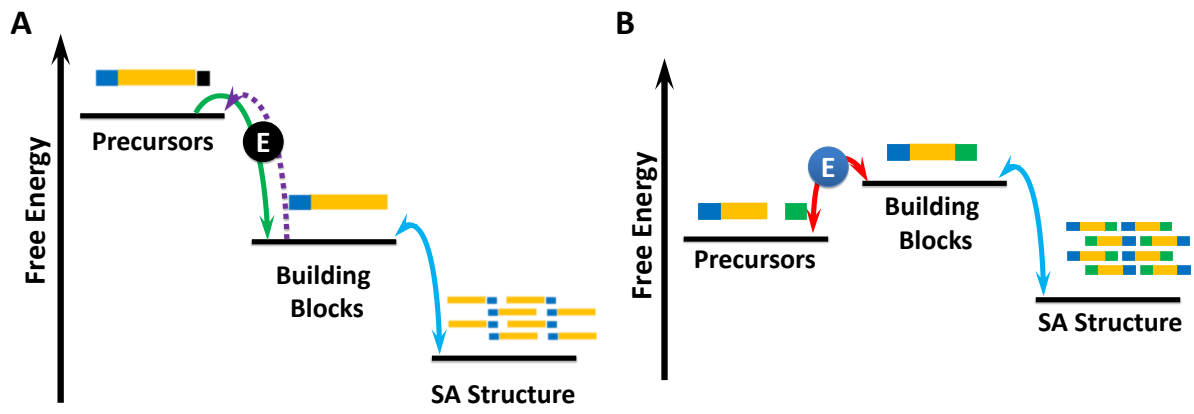

Figure 92 | Free energy diagrams for two possible scenarios in enzymatic self-assembly (e-SA). (**A**) The enzymatic reaction and self-assembly process are both thermodynamically favoured. In some cases, these systems can be made reversible, *e.g.*, if the forward reaction is driven by phosphate ester hydrolysis, the reverse may be possible by exploiting a kinetic-controlled system, e.g., by exploiting an ATP-dependant enzyme (e.g., kinase). (**B**) e-SA under thermodynamic control: formation of SA building blocks is thermodynamically unfavored in isolation, however, may occur in reversible fashion when coupled to a sufficiently favourable SA. Figure is adapted from ref. 243

285. Zhou, J., Du, X., Yamagata, N. & Xu, B. Enzyme-Instructed Self-Assembly of Small α-Peptides as a Multiple-Step Process for Selectively Killing Cancer Cells. *J. Am. Chem. Soc.* **138,** 3813–3823 (2016).
286. Williams, R. J. *et al*. Enzyme-assisted self-assembly under thermodynamic control. *Nat. Nanotechnol.* **4,** 19–24 (2009).

To conclude this bibliographic section, we would like to demonstrate the potential of these enzymatic approaches using a few examples, mainly by the group of Prof. Ulijn.

This group reported on the biocatalytic self-assembly of Fmoc-protected dipeptides such as FF, FY, YL, VL and FL starting from their methyl ester precursors (**Figure 93**). Whereas methylated precursors formed turbid suspensions at 55 °C and pH 8, due to their high hydrophobicity, the addition of the subtilisin, which hydrolyzes methyl ester groups, initiated the self-assembly process. The tube inversion test confirmed translucent gel formation while FTIR spectroscopy showed the appearance of vibration bands corresponding to the formation of antiparallel β-sheets. An increase of the fluorescence intensity of the fluorene groups together with the appearance of a pronounced CD signal suggested additional π-π interactions between neighbouring Fmoc groups. Finally, AFM imaging demonstrated the formation of monodisperse nanofibers at the origin of the gelation process (**Figure 93C**).

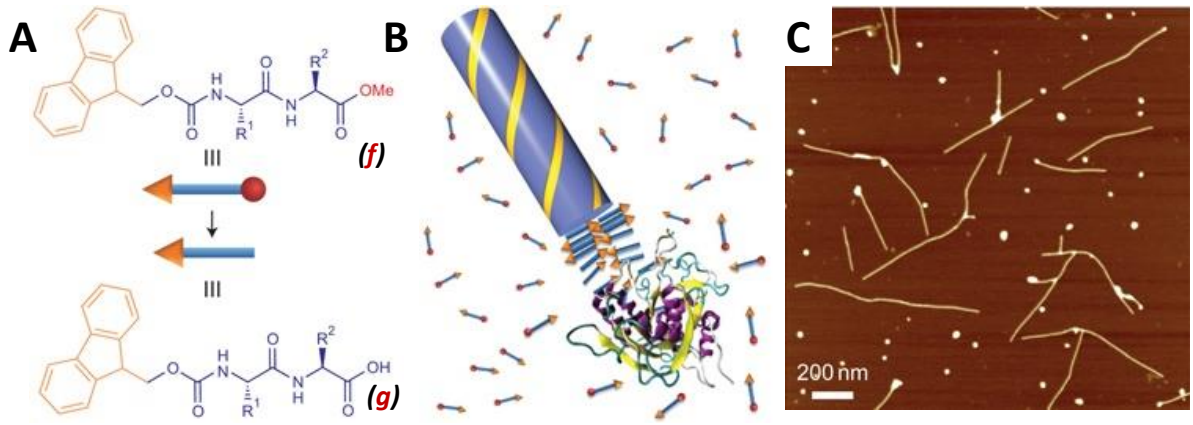

Figure 93 | (**A**) Chemical structure of Fmoc-dipeptide methyl esters (***f***) studied in the paper (orange, fluorenyl moiety of the Fmoc group; blue, dipeptide sequence; red, enzyme cleavable methoxy group). Subtilisin catalyses the hydrolysis of these esters to Fmoc-peptide gelators. (**B**) Schematic representation of the nucleation and growth mechanism of self-assembly controlled by subtilisin. (**C**) AFM analysis of initial stages of the self-assembly process. Figure is adapted from ref. 287

287. Hirst, A. R. *et al.* Biocatalytic induction of supramolecular order. *Nat. Chem.* **2,** 1089–94 (2010).
288. Sadownik, J. W., Leckie, J. & Ulijn, R. V. Micelle to fibre biocatalytic supramolecular transformation of an aromatic peptide amphiphile. *Chem. Commun.* **47,** 728–730 (2011).

In another example, the same group reported on the interesting enzymatically induced dynamic supramolecular transformation process of one type of supramolecular aggregates (micelles) into another type (fibres) (**Figure 94**).[288] Fmoc protected FY peptide amphiphile, phosphorylated at the tyrosine residue Fmoc-F*p*Y (***h***) was reported to form micelles, at pH 8 above a CMC of 5 mM, due to the ionisation of the phosphate groups. The 5 nm size of these micelles, analysed by DLS, suggested the structure represented in **Figure 94** (taking into consideration the molecule size ≈ 2 nm), where the Fmoc groups created a hydrophobic core with the phosphates groups generated a hydrophilic surface. Interestingly, the addition of alkaline phosphatase initiated hydrogel formation, as this enzyme is known to cleave the phosphoester bond, thus rendering the peptide amphiphile less polar, which consequently self-assembled into fibres.

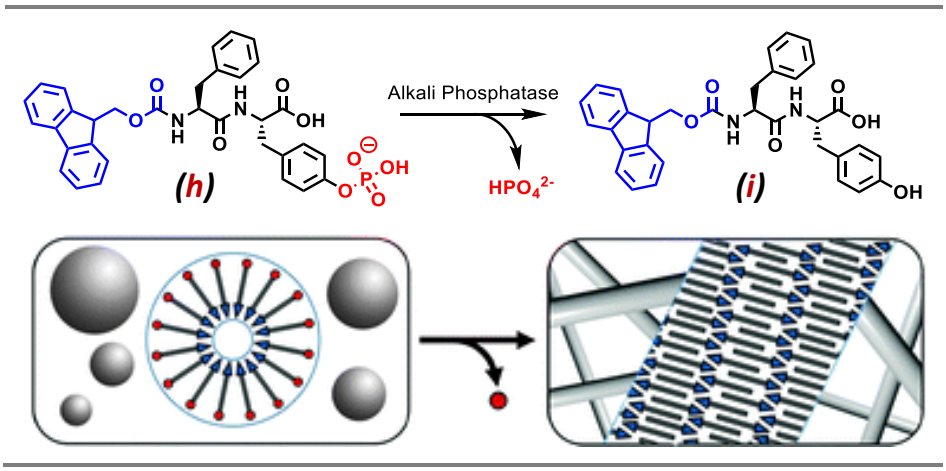

Figure 94 | Enzyme-catalyzed dephosphorylation reaction of Fmoc-F*p*Y (***h***) and a schematic representation of the transformation from micelles to fibres. Figure is reproduced from ref. 288

Remarkably, in both examples, different precursors were used to produce the same building block Fmoc-FY (***i***), which then further assembled into the same supramolecular architecture, *i.e.* nanofibers.

The formation of an amide bond was also exploited to generate *in situ* the building blocks necessary for the self-assemblies. To do so, the zinc protease thermolysin was used for instance to catalyse the condensation of tyrosine-naphthalene conjugate precursor with different amino acids such as F, L, V, Y, A and G with an amide in the C-terminus (**Figure 95**).[240] While thermolysin is usually known to cleave peptides into amino acids[289]if the thermodynamics favours the formation of the assemblies, the reaction will be shifted toward the condensation of amino acids (**Figure 92B**, **Figure 95A**).

289. The specificity of this enzyme is not very high, however for a sequence such as -X-YZ- where X is any amino acid, Y is hydrophobic and Z is any amino acid except proline, cleavage takes place between X and Y positions.

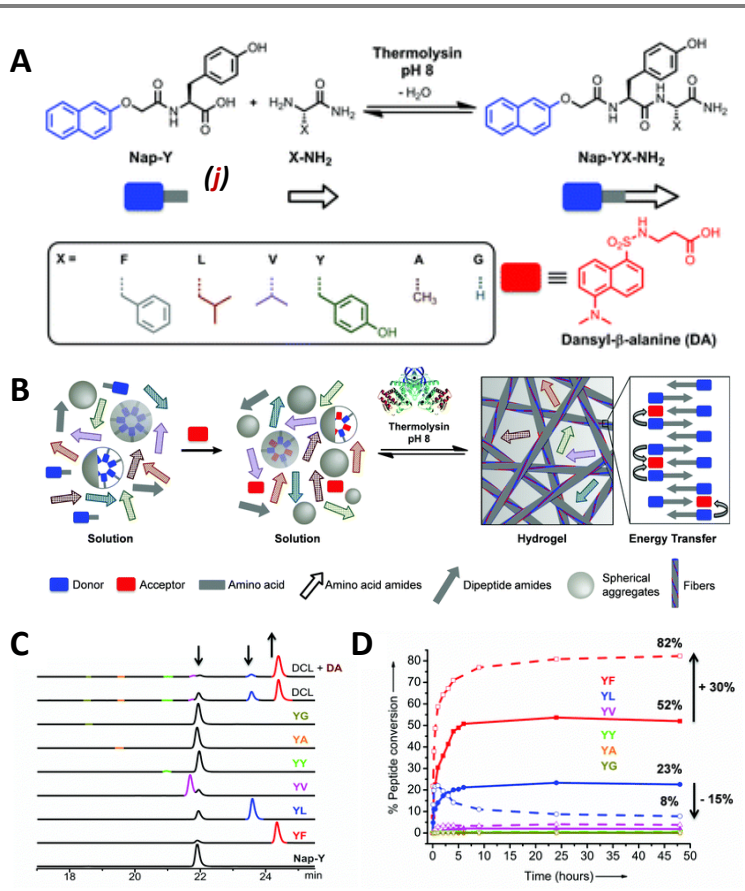

Figure 95 | (**A**) Formation of naphthoxy-substituted dipeptide amphiphiles by a fully reversible thermolysin-catalysed condensation reaction and the molecular structure of dansyl-β-alanine (DA) used in this study. (**B**) Schematic representation of thermolysin-triggered development of a bicomponent hydrogel composed of naphthalene donors and dansyl acceptors, showing efficient energy transfer from a library of eight different amino acid non-assembling precursor components. (**C**) The enzymatic conversion of Nap-Y (*j*) and X-NH_2 into Nap-YX-NH_2 amphiphiles was shown by part of the reversed-phase HPLC traces in isolation (all except top two traces) as well as in dynamic combinatorial library (top two traces) and (**D**) time course of the percentage conversion in dynamic combinatorial library by HPLC as measured in the absence (solid traces) and presence (dashed traces) of DA. Figure is adapted from ref. 240

Conversion of the condensation reactions with different amino acids was monitored by HPLC and the results were in agreement with visual observations of hydrogelation: gels formed for systems where high conversions were achieved (F, L, V amino acids). Additionally, the authors took advantage of dynamic combinatorial chemistry[290,291] to select the best gelator. For this purpose, thermolysin was added to the mixture of amino acids and Nap-Y precursor, which caused hydrogelation after 24 hours. HPLC chromatogram (**Figure** 95**C**) showed that YF was the major product (52%) with 23% of YL formed. Importantly, amplification of YF (from 52 to 82%, see **Figure 95D**) was achieved upon addition of an electron acceptor, dansyl alanine (DA), which intercalated between the naphthyl moieties giving additional stabilisation to the supramolecular structure. Because of the interaction of

DA with peptide self-assemblies, charge transfer complexes were formed, as confirmed by fluorescence spectroscopy.

Inspired by these results, which demonstrate the power of enzymatic approach for the construction of functional materials, we were interested to explore this biocatalytic induction of supramolecular order, with regard to triarylamine units.

290. Lehn, J.-M. Dynamic Combinatorial Chemistry and Virtual Combinatorial Libraries. *Chem. Eur. J.* **5,** 2455–2463 (1999).
291. Corbett, P. T. *et al.* Dynamic combinatorial chemistry. *Chem. Rev.* **106,** 3652–711 (2006).

3. RESULTS AND DISCUSSIONS

The outcome of this project is a result of a collaboration between the Ulijn group and our group, which combines the experiences from two fields: biocatalysis in supramolecular chemistry and supramolecular chemistry of triarylamines.

A set of triarylamine-based building block precursors (amino acid and peptide conjugates) were been synthesised to construct assemblies with the help of different enzymes (**Figure 96**). Two types of molecules were been designed with TAA core as aromatic unit of APA: the first type, with one peptide branch and two methoxy groups around the TAA core (**23, 25, 27, 31** and **32**); and the second type, decorated with two peptide branches and possessing an amide group (**24, 28, 30, 33** and **34**). While the first type of aromatic peptide amphiphiles (with other aromatic moieties) was reported several times, the second type, with two amino acid/peptide branches connected to one hydrophobic core has, to the best of our knowledge, never been reported.

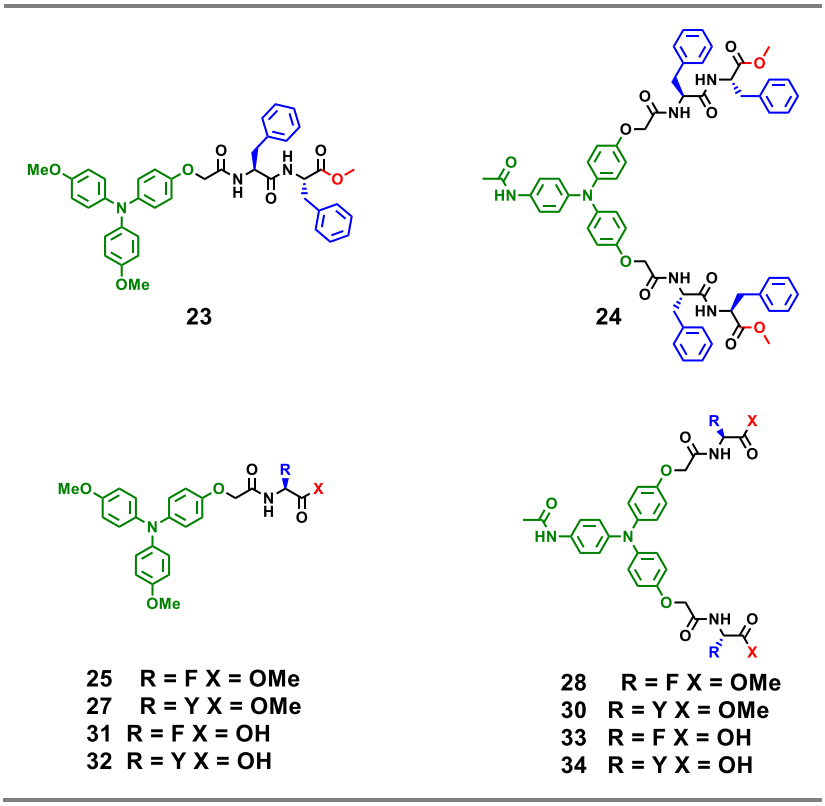

Figure 96 | Chemical structures of studied TAA-amino acid and peptide conjugates.

One set of TAA molecules was decorated with FF dipeptides terminated at the C-terminus with a methoxy group for subtilisin catalysed self-assembly; another one was decorated with F and Y, terminated with methyl esters, as substrates for the chymotrypsin

induced dynamic aggregation and a last set of TAAs modified with free F and Y acids was designed for dipeptide formation catalysed by thermolysin.

A. Synthesis

The synthesis of the TAA peptide-conjugates consists of three parts: (***i***) the synthesis of TAA cores, (***ii***) the synthesis of the peptidic parts and (***iii***) conjugation between the TAA core and the peptidic part. We designed two approaches: ***1***) first, modification of the TAA with a reactive group to graft any amino acid (**Scheme 6A**), and ***2***) modification of the amino acid with the functional group, which can then react with the TAAs (**Scheme 6B**). We decided to choose the second method, as it should allow to decorate different TAAs with the modified amino acid or peptide derivatives without additional functionalization of TAAs.

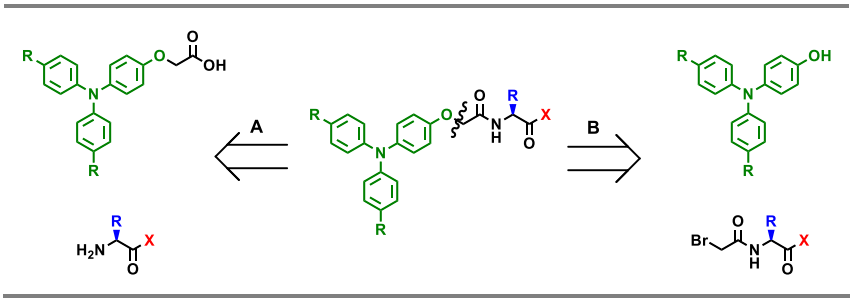

Scheme 6 | Retrosynthetic scheme of the TAA-bioconjugate synthesis.

i. Synthesis of the TAA-Core

The synthesis of the methoxy substituted TAA-core was achieved *via* the Buchwald-Hartwig coupling between commercially available benzyloxyaniline and 4-methoxy-bromobenzene, affording triarylamine **11** in high yields (**Scheme 7**). The benzyl group was then removed by hydrogenolysis using palladium on charcoal, affording hydroxyl triarylamine **12** which could be used in subsequent decoration with the functionalized amino acid derivatives.

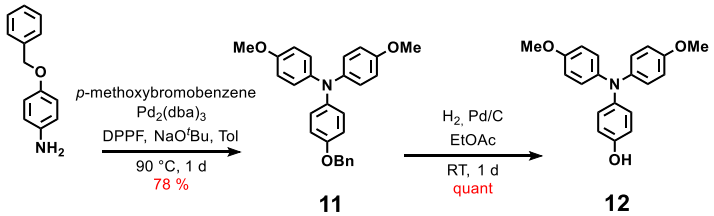

Scheme 7 | Synthesis of the methoxy TAA precursor **12.**

Triarylamine **17** was synthesised using a modified Ullmann copper-catalysed coupling procedure, as key step, as reported in our previous papers[81,119]. Briefly, the iodobenzyloxy benzene **13** was obtained by reacting iodophenol with benzyl bromide under basic conditions. Nitro compound **14** was then obtained *via* Ullmann coupling and further reduced with tin(II) chloride to afford the amino compound, which was immediately reacted with acetyl chloride to yield benzyloxy TAA **16**. The hydroxyl TAA precursor **17** was obtained after deprotection of the benzyl groups by hydrogenolysis using the same conditions as described for **12**.

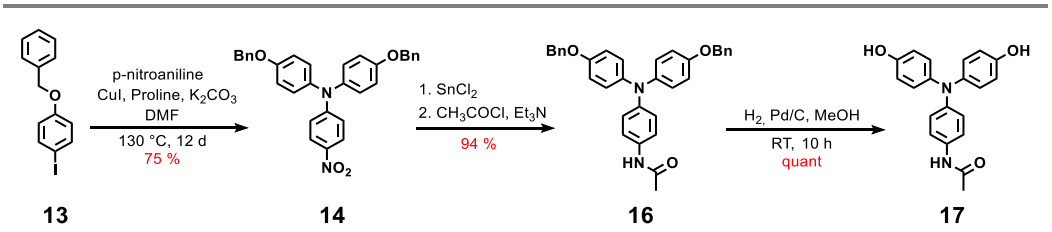

Scheme 8 | Synthesis of TAA amide **17.**

ii. Synthesis of the Peptidic Unit

The FF methyl ester **20** was synthesised in three steps with high yield (**Scheme 9A**). In the first step, the Boc-protected FF peptide **18** was obtained *via* the classical peptidic coupling procedure between Boc-protected phenylalanine and phenylalanine methyl ester hydrochloride using HOBt and EDC-HCl as coupling reagents. The corresponding amine was obtained after Boc deprotection with TFA and further immediate coupling with bromoacetyl chloride to provide the desired dipeptide precursor **20** in good yield.

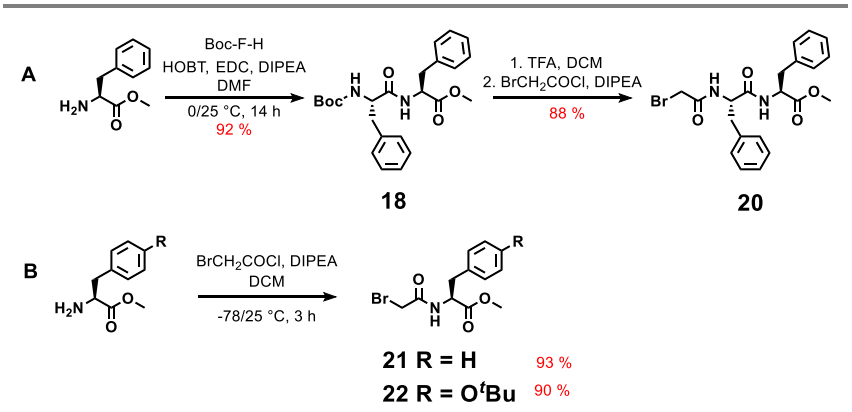

Scheme 9 | Synthesis of the peptidic and amino acid derivatives **20**, **21** and **22.**

The corresponding amino acid derivatives **21** and **22** were obtained in one step by acetylation of the methyl esters of amino acids by bromoacetyl chloride with excellent yields.

iii. Synthesis of TAA-Peptide Conjugates

The TAA-peptide conjugates were finally obtained after grafting amino acid/peptide derivatives **20**, **21** and **22** on TAA cores *via* nucleophilic substitution in DMF in the presence of potassium or cesium carbonate as a base (**Scheme 10**). TAA decorated with methyl esters dipeptides (**23** and **24)**, and phenylalanine conjugates (**25** and **28**) were purified by column chromatography and used in enzymatic reactions with subtilisin and chymotrypsin respectively.

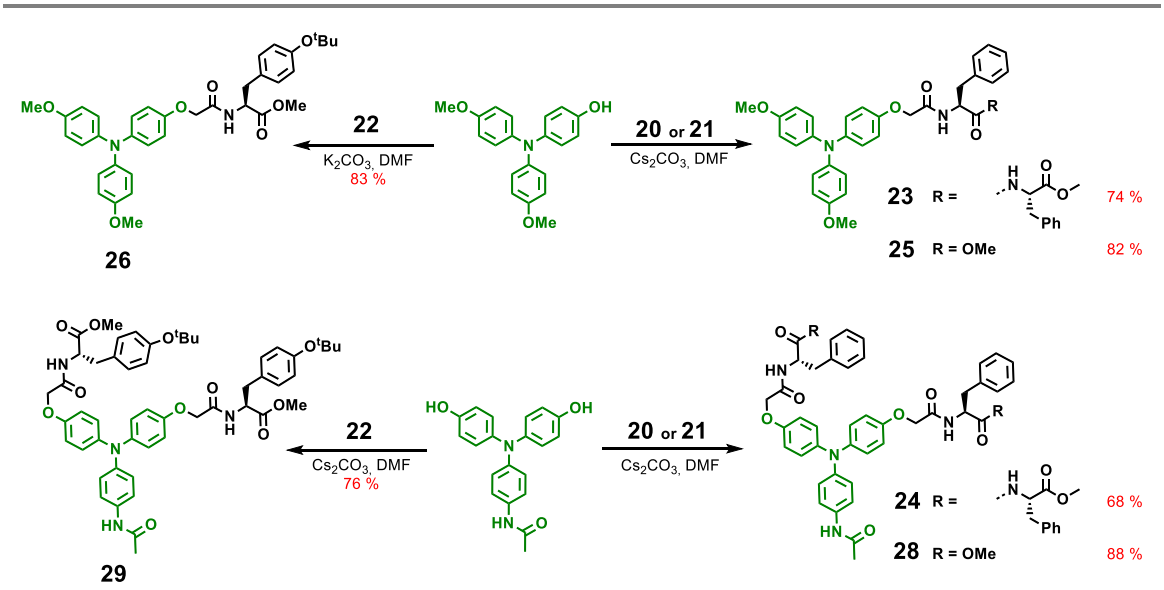

Scheme 10 | Synthesis of the TAA-bioconjugates **23** - **26**, **28** and **29** from TAA precursors and amino acid/peptide derivatives**.**

As for the tyrosine derivatives, the hydroxyl group was deprotected using TFA to give the methyl ester derivatives **27** and **30** (**Scheme 11**).

The free amino acid derivatives **31**, **32**, **33** and **34** were obtained after saponification reaction with potassium hydroxide in dioxane-water mixture after purification using reverse-phase preparative HPLC (see **Figure S13**).

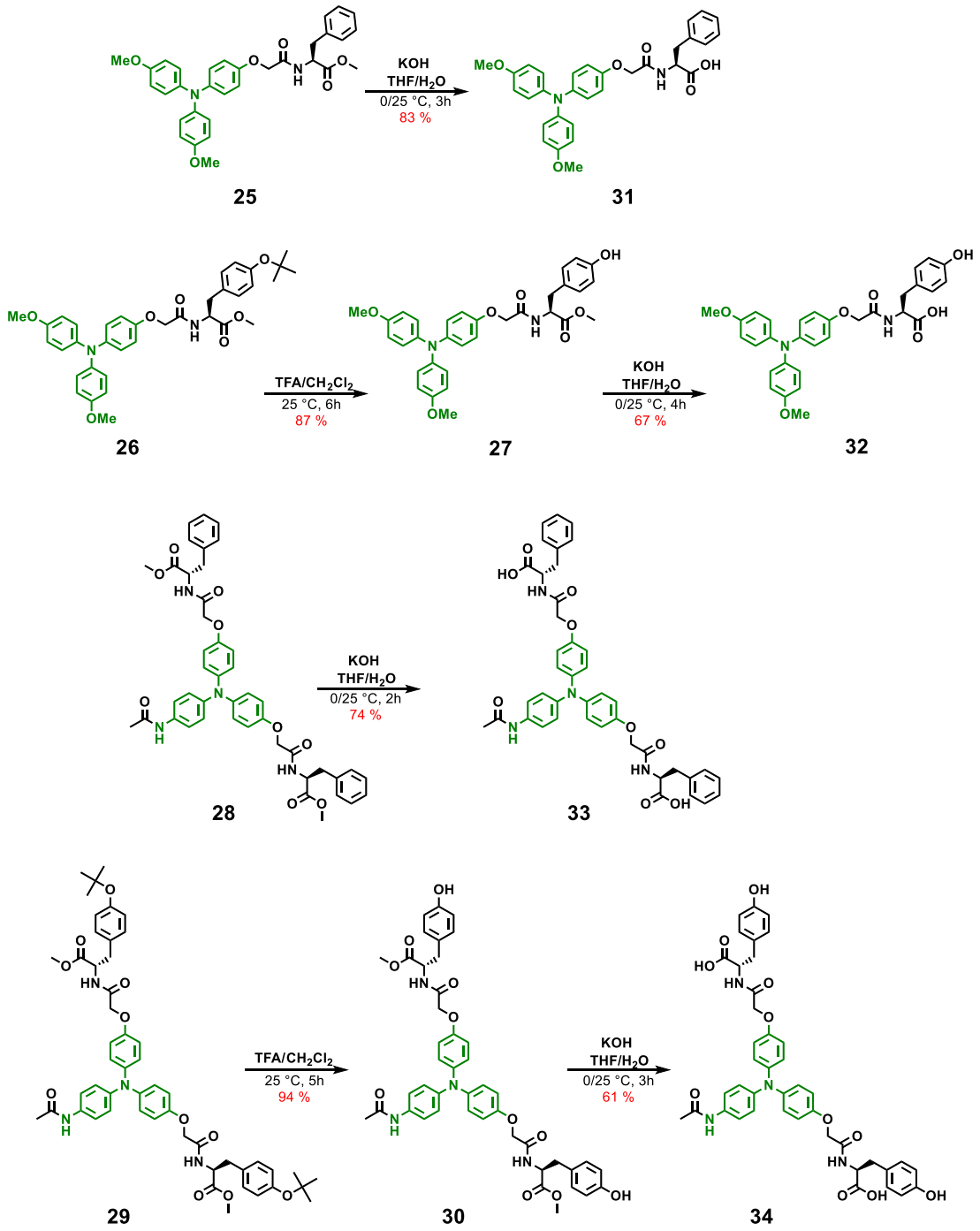

Scheme 11 | Synthesis of TAA-amino acid derivatives from protected precursors.

Before starting our investigation of enzyme catalysed self-assemblies in water, we were interested to know whether the conjugation of our TAA with amino acids and peptides would influence their photosensitivity. Thus, we investigated the behaviour of the TAA-amino acid/peptide conjugates in organic solvents. Satisfyingly, all compounds revealed the classical electron-rich TAA behaviour under light exposure: ***a***) the appearance of a green/cyan colour, indicating the formation of triarylammonium radical cations; and ***b***) disappearance of

NMR signals corresponding to the TAA core. However, TEM analysis of the samples obtained after irradiation of 0.1 mM chloroform solutions did not reveal any organised structures. Although no gelation was observed for TAA-peptide conjugates **31 – 34** in common organic solvents such as toluene, acetone, acetonitrile, chloroform, ethyl acetate, methanol and ethanol, compounds **23** and **24** led to gel-like structures upon sonication in diethyl ether.

Then the enzyme responsive properties of our molecules were investigated using the different biocatalytic approaches described in the bibliographic introduction.

B. Enzymes screening for biocatalytic self-assembly

To evaluate the enzyme responsiveness of our molecules we chose three enzymes namely: subtilisin, chymotrypsin and thermolysin.

i. Subtilisin

Dipeptide FF methyl ester conjugates **23** and **24** were evaluated in the hydrolysis reaction catalysed by subtilisin, Unfortunately, both compounds were found to be quite insoluble in an aqueous medium, possibly due to their highly hydrophobic structure. Increasing the temperature together with ultrasonication did not improve the situation, so that no changes could be observed either by necked eye nor from HPLC analysis even after the addition of enzyme.

ii. Chymotrypsin

Chymotrypsin is known to cleave the peptide bond on the carboxyl side of aromatic amino acids such as phenylalanine, tyrosine or tryptophan, but also to hydrolyze esters. Interestingly, in the presence of a stronger nucleophile than water, such as free amino group of an amino acid for instance, this enzyme can also catalyse the reaction of de-esterification/amidation, producing the peptide bond. Chymotrypsin was tested with the methyl ester single amino acid substrates **25**, **27**, **28** and **30** with addition of L-phenylalanine amide in a phosphate buffer medium at pH 8.

During the tests with these molecules, we observed their quite poor solubility. However, ultrasonication of the systems resulted in relatively stable suspensions, to which the enzyme was added. Unfortunately, no transition was observed for any of the compounds.

Table 8 | Summary of enzyme screening for biocatalytic self-assembly.

Substrate	Enzyme	Observation
TAA-FF-OMe	**Subtilisin**	Not soluble in water
TAA-AA-OMe + H-F-NH_2	**Chymotrypsin**	No gel formation
TAA-AA-OH + H-F-OMe	**Thermolysin**	No gel formation
TAA-AA-OH + H-F-NH_2	**Thermolysin**	Gelation

iii. Thermolysin

Finally, the protease thermolysin was employed to catalyse the formation of the peptide bond between the free amino acid TAA conjugates **31** – **34** and amino acids amides and methyl esters (H-F-NH_2 and H-F-OMe respectively) at pH 8.

In this case, the solubility of compounds **32** – **34** was good, even at relatively high concentrations of 20 mM, resulting in clear solutions, however, TAA **31** resulted in a colloidal solution showing temperature and concentration dependent transition. The colloidal system was obtained for concentration above 5 mM Increasing the temperature above 45 – 50 °C for the 20 mM emulsion resulted in a clear solution, suggesting the probable formation of micelles for compound **31** in analogy with the structure reported for the Fmoc-*p*Y conjugate (see **Figure 94**).[288] Temperature-dependent NMR studies reveal the appearance of the resonance signals for the conjugates upon temperature increase indicating transition from the aggregated to the molecular state (**Figure S15**).

After these successful solubility tests, the enzymatic reactions were performed. Briefly, the compound was solubilized in screw cap vial in 1 mL of 100 mM phosphate buffer at pH 8, to obtain 20 mM solutions. The corresponding phenylalanine amide or methyl ester was added in a 4-fold excess relatively to the TAA core. Finally, 1 mg of thermolysin was added to the solutions, followed by subsequent intense mixing using a vortex apparatus and ultrasonication for one minute each. The systems were then left standing to reach equilibrium for 24 hours. After that time, gelation was observed for all the systems containing TAA-conjugates and phenylalanine amide, while in the vials with phenylalanine methyl ester, no gelation was observed.

Considering the results obtained during the enzymatic screening, we continued our investigations on enzymatic TAA hydrogelation using TAA amino acids **31** – **34** with phenylalanine amide (H-F-NH_2) in the presence of thermolysin. For the sake of clarity, we will present data for each set of TAA conjugates in two different sections.

C. Thermolysin Triggered TAA Self-Assembly

i. Two-Branched TAA-Conjugates

The novelty of compounds **33** and **34** lies in the presence of two potentially reactive branches, a feature that has never been reported before. We were curious how the self-assembly will influence the enzymatic transformation of the conjugates and vice-versa. From **Scheme 12** we have to consider that two products can be obtained during the condensation reaction between two-branched TAA-conjugates **33**, **34** and H-F-NH_2, either the half or the fully condensed products.

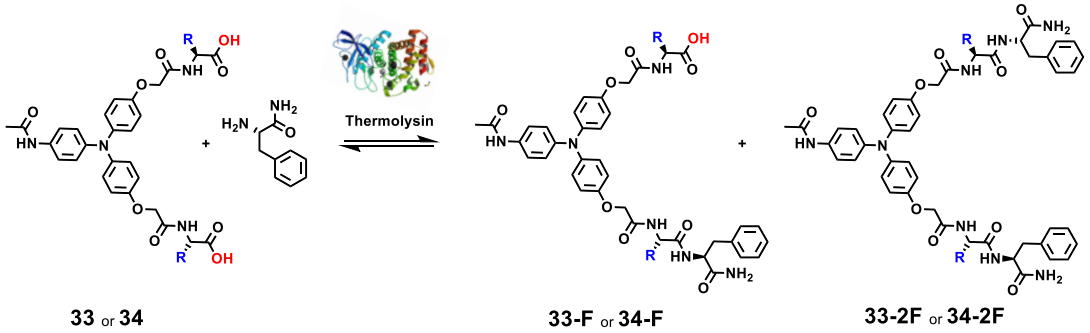

Scheme 12 | Reactional scheme of the biocatalytic reaction of two-branched TAA-amino acid conjugates **9** and **10** with phenylalanine amide, catalysed by thermolysin.

We first studied the biocatalysed gelation process for different concentrations of substrates. The digital photographs of gels, obtained for 5, 10 and 20 mM concentrations of substrates after 24 h of reaction are represented in **Figure 97**. The tube inversion test confirmed the formation of self-supporting gels for all systems except 5 mM tyrosine conjugate **34**, which gave a viscous liquid.

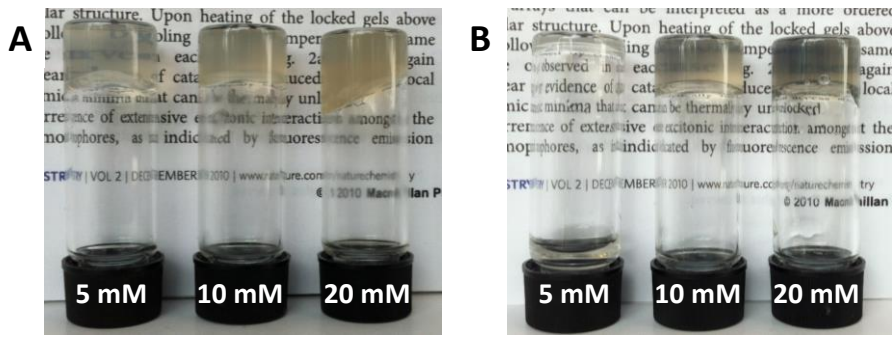

Figure 97 | Digital photographs of hydrogels formed as a result of biocatalytic self-assembly of TAA peptide conjugates (**A**) phenylalanine derivative **33** and (**B**) tyrosine derivative **34**.

HPLC analyses of the composition of the obtained systems for 20 mM samples after 24 hours of equilibration showed a total conversion of 93% and 89% for the phenylalanine

(**33**) and tyrosine (**34**) conjugates, respectively. Interestingly, the ratio of mono- and di-condensed products in both cases was almost the same: corresponding to 77% and 15% for **33** and 76% and 13% for **34**, suggesting that once the noncondensed product is trapped within the self-assembly, it is no more accessible to the enzyme.

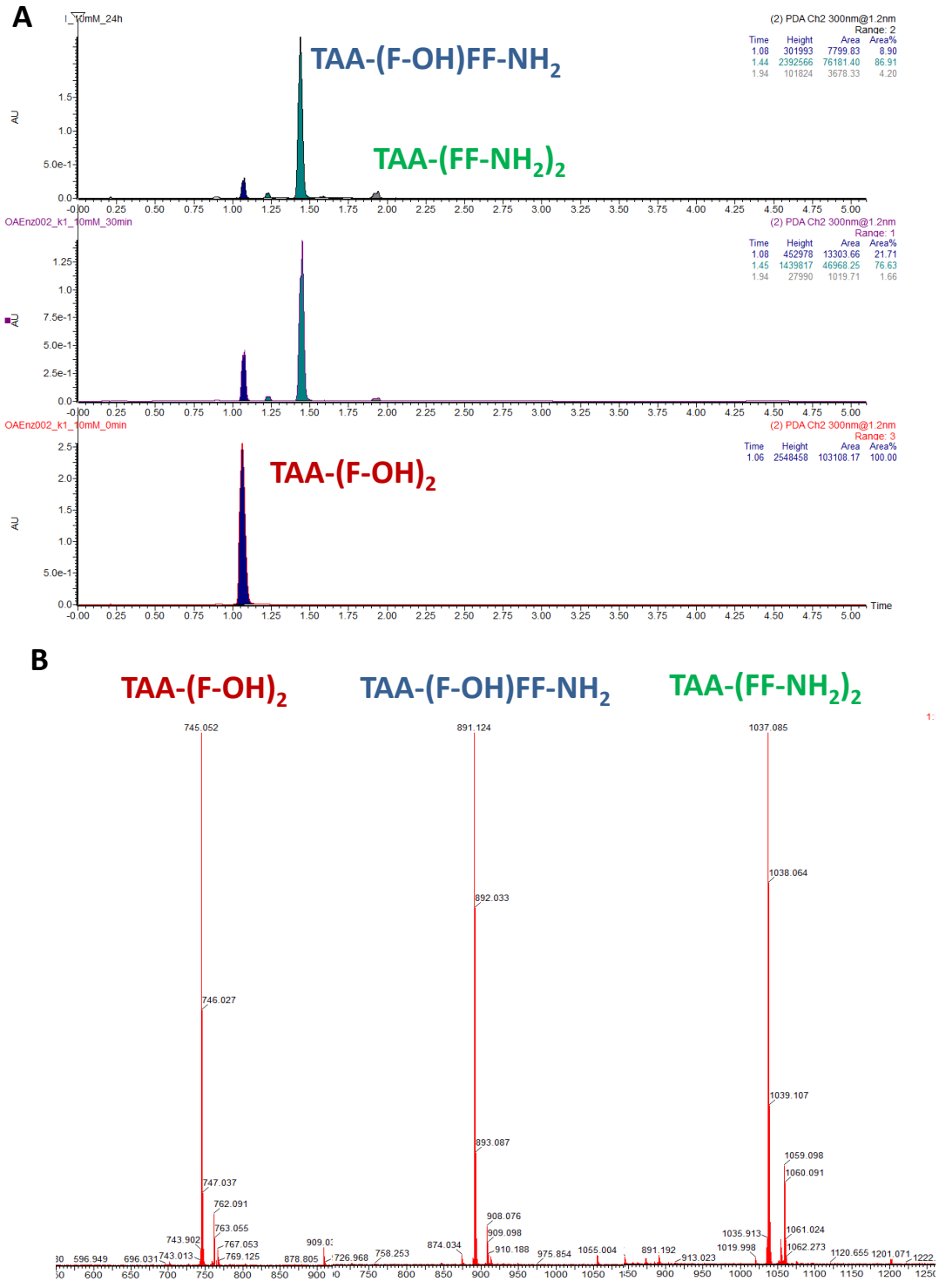

Figure 98 | LC-MS analysis of the distribution of products of enzymatic reaction of **33** with phenylalanine amide at concentration 10 mM. (**A**) UPLC traces with peak integration. (**B**) Mass spectra of corresponding spesies.

The kinetic study of the condensation for **33** revealed a slightly different picture for the product distribution after 24 hours of equilibrium. The total conversion was nearly 90% for all concentrations, with a larger difference in the distribution of mono and di-condensed products: 81.2/7.4% for 5 mM, 87.1/4.0% for 10 mM and 87.7/1.5% for 20 mM. This deviation with the data, obtained during the enzyme screening procedure, might be related to the distortion and mixing issues of the kinetically investigated systems.[292,293] The kinetic curves suggest an asymptotic character of the reaction, with a half-time for substrate conversion of around 45, 12 and 15 min for 5, 10 and 20 mM concentrations respectively.

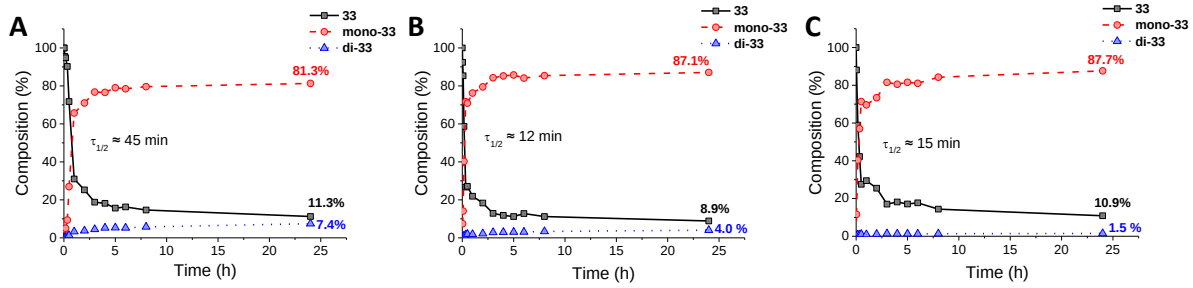

Figure 99 | Conversion kinetics of compound **33** at different starting concentrations. (**A**) 5 mM, (**B**) 10 mM and (**C**) 20 mM.

292. For each point, the mixture was sonicated and vortexed for homogenisation and gel distortion.
293. The second possible explanation could be related to enzyme functioning, which may decrease over time. The first gelation experiments were carried out in the Ulijn group with commercial thermolysin, which was already in use for some time by the group membe.

TEM studies of the gels proved the formation of entangled networks of nanofibers with high aspect ratio, few micrometres in length and around 9±1 nm for **33** and 11±2 nm for **34** in width. **Figure 100** shows typical TEM images for the 5 mM gels made of **33** (**A**) and for of **34** the 20 mM (**B**) and for 5 mM (**C, D**).

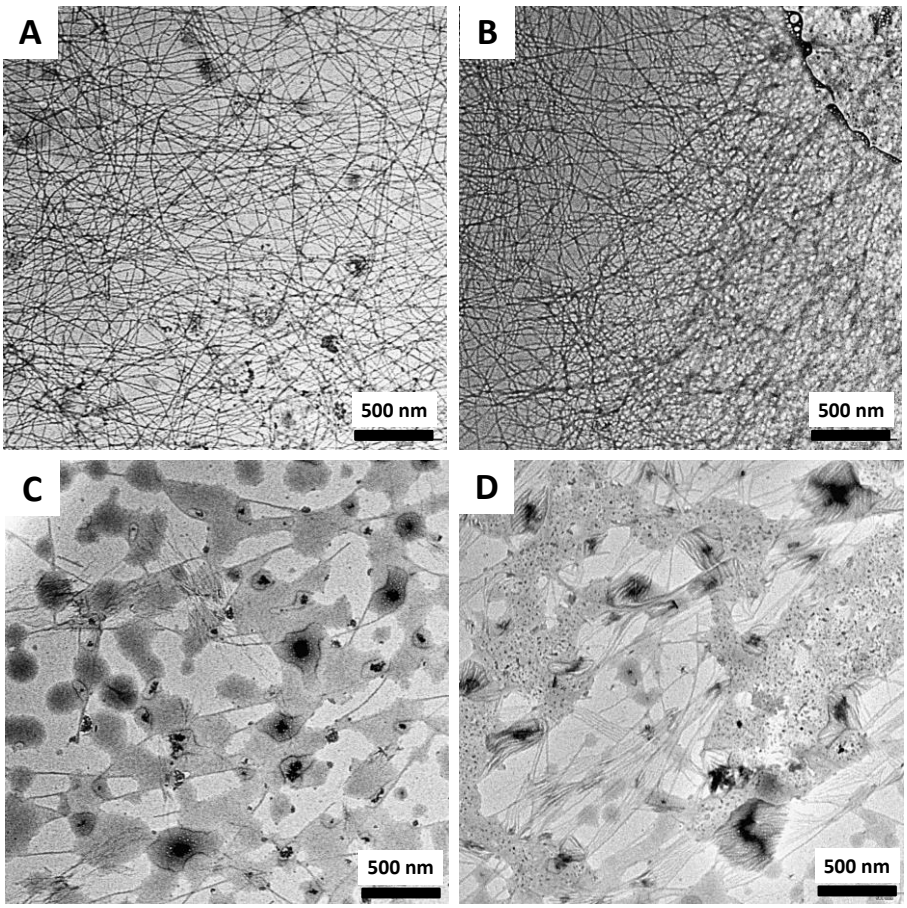

Figure 100 | TEM images of the enzyme triggered self-assemblies of 5 mM phenylalanine TAA conjugate **33** (**A**), and tyrosine TAA conjugate **34,** 20 mM (**B**) and 5 mM (**C,D**).

Interestingly, at a concentration of 5 mM of TAA-conjugate **34,** shorter fibres were observed and bundles of fibres with the size of 12±2 nm.

AFM analysis also confirmed formation of helical fibrillar structures (**Figure 101**).

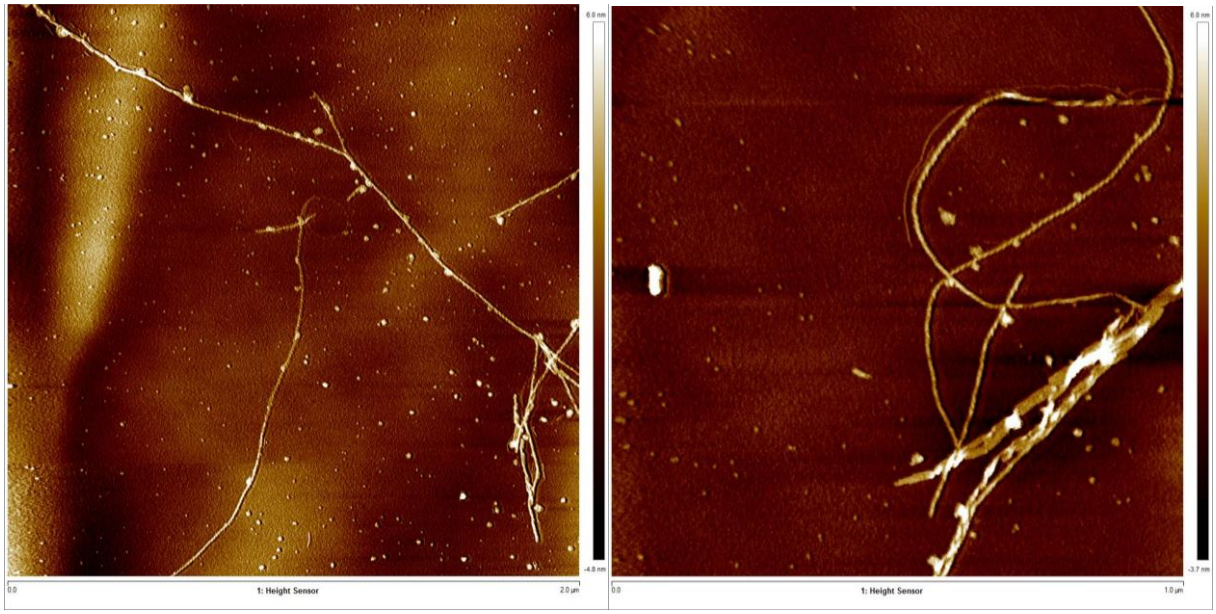

Figure 101 | AFM height image of biocatalytic assemblies of phenylalanini TAA conjugate **33**.

The optical absorption and fluorescence spectroscopy measurements performed during the gelation process revealed a respective decrease in absorption and increase in fluorescence of the TAA core as a result of self-assembly formation (**Figure 102**). No shift, neither in absorption nor in fluorescence, was present, which could mean that no strong interactions between the TAA centres exist in these assemblies. No shift of the fluorescence maxima was detected neither for TAA conjugate **34** (**Figure S17**).

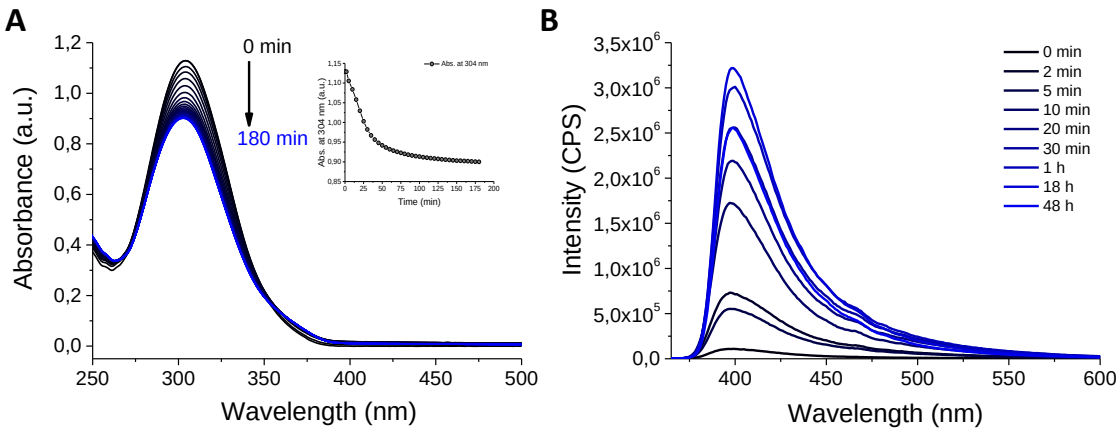

Figure 102 | Spectroscopy studies of the enzymatically triggered self-assembly of phenylalanine TAA conjugate **33**. (**A**) Time-dependent UV-Vis absorption spectroscopy. (**B**) Time-dependent fluorescence spectroscopy.

The circular dichroism spectra for **33** and **34** characterised with a distinct Cotton effect in the TAA absorption region, indicating the formation of chiral supramolecular structures in both cases, which confirms AFM observations. The difference in the spectra for compounds **33** and **34** may suggest different arrangements of the triarylamine cores within these assemblies (**Figure 103**). This observation again highlights that small structural differences within building blocks may cause big differences at a level of self-assembly.

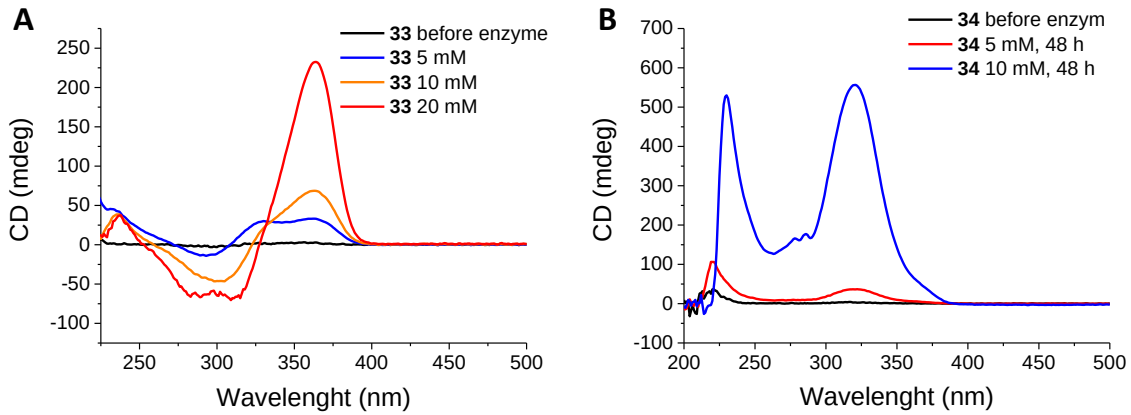

Figure 103 | CD spectra for self-assemblies of (**A**) phenylalanine TAA conjugate **33** and (**B**) tyrosine TAA conjugate **34**.

The additional structural analyses are currently in progress in order to propose the mechanism and structures of assembly including: WAXS/SAXS which can afford intermolecular distances and other structural parameters; FTIR, giving information about the peptide stacking conformation and additional high resolution AFM imaging, which could provide information about the relationship between structure of a TAA-bioconjugates and the chirality of a supramolecular assembly. We also intend to investigate the conducting properties of single fibres using conducting AFM.

ii. Single branched TAA conjugates

TAA decorated with one amino acid residue were also susceptible to the enzymatically triggered self-assembly process with thermolysin. In this case, the only product of condensation is an amide terminated dipeptide TAA-FF-NH_2 or TAA-YF-NH_2 depending on the used precursor (**Scheme 13**).

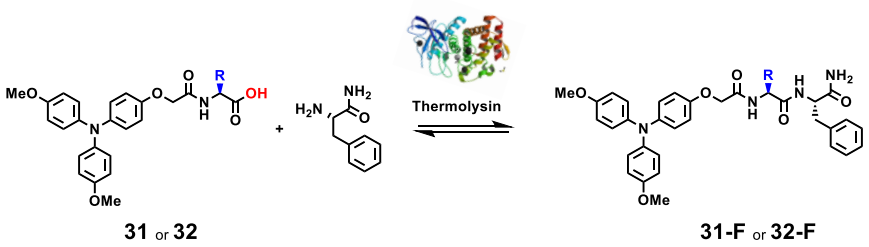

Scheme 13 | Scheme of the enzymatically catalysed dipeptide formation starting from one branch TAA-conjugates **31** and **32**.

After the 24 h of enzymatic reaction, visual changes were observed for all systems. For TAA conjugate **31** self-supporting opaque hydrogels were formed (**Figure 104A**). In the case of tyrosine conjugate **32,** viscous solutions with a jelly precipitate was formed starting from clear solutions before the addition of thermolysin (**Figure 104B**).

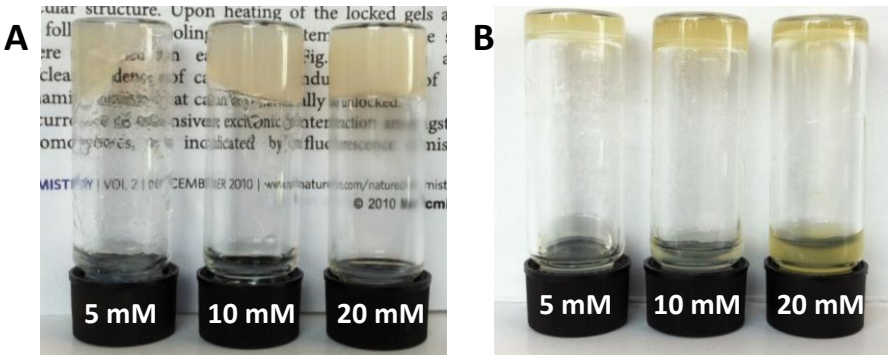

Figure 104 | Tube-inversion test for the different substrates at different concentrations after 24 h of enzymatic reaction. **(A)** TAA-F-OH **31** and **(B)** TAA-Y-OH **32.**

Kinetic measurements for all studied systems showed asymptotic profiles with conversions between 75 and 87% for **31** and between 35 and 60% for **32** depending on the initial concentration (**Figure 106**). Interestingly, unlike conjugates **33** and **34** with two branches, one-branched conjugates **31** and **32** displayed the higher conversions for the lowest concentrations. Additionally, the conversion for the tyrosine version **32** was almost twice lower than that for the phenylalanine analogue, suggesting the crucial influence of the hydrophobicity balance on the self-assembly process.

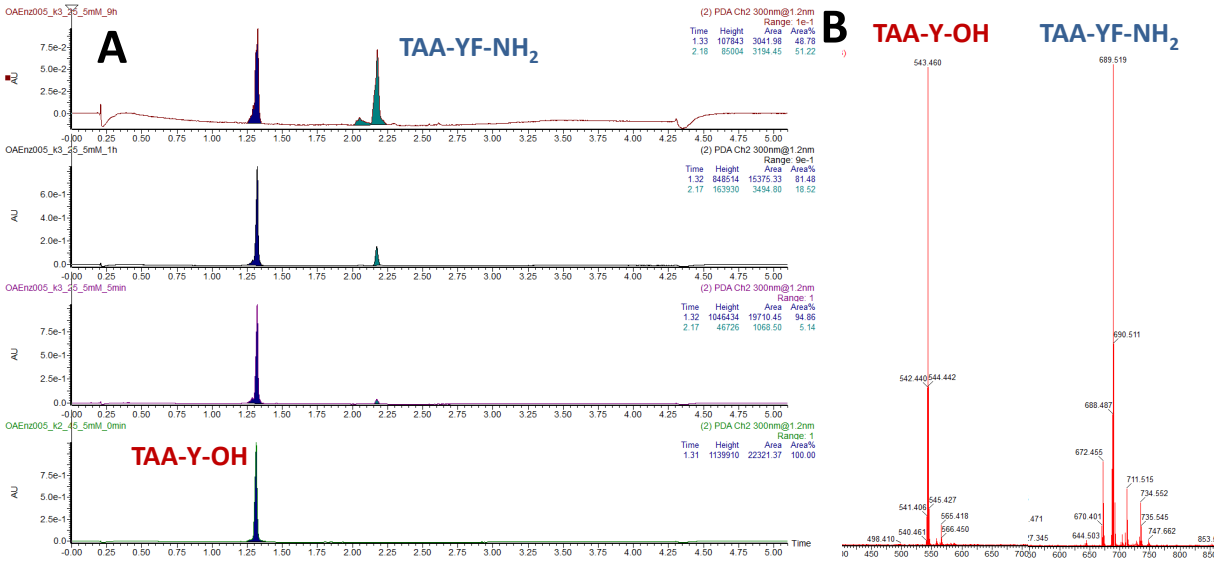

Figure 105 | LC-MS analysis of the distribution of products of enzymatic reaction of **32** with phenylalanine amide. (**A**) UPLC traces with peak integration. (**B**) Mass spectra of corresponding spesies.

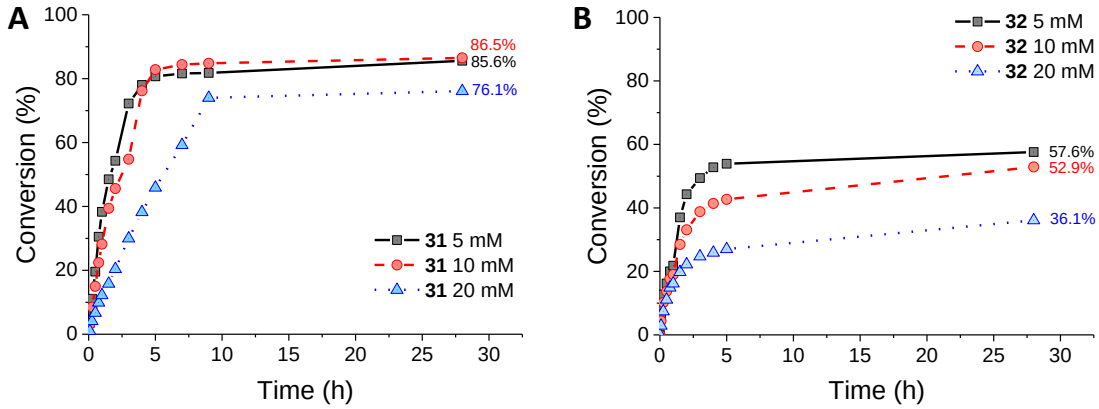

Figure 106 | Kinetic curves for the enzymatic reactions between phenylalanine amide and TAA peptide conjugates (**A**) **31** and (**B**) **32**.

Microscopy studies demonstrated the formation of fibrous aggregates for both phenylalanine and tyrosine conjugates (**Figure 107**). Remarkably, in the case of **31**, relatively short (280±50 nm) length and 14±4 nm width fibres were formed, while for **32** very long nanowires (13±3 nm width) were observed. This effect may be explained by the higher hydrophobicity of compound **31** compared to **32**, which might cause a decrease in the critical concentration value necessary for self-organization, increasing consequently the number of nuclei, which in turn gave shorter fibres. The width of the assemblies, however, seems to be quite constant for tested substrates tested.

Fluorescence spectroscopy measurements performed during the enzymatically triggered self-assembly revealed an increase in fluorescence intensity for compound **32** (**Figure** 108**B**) together with the appearance of small shoulders in a red-shifted part of the spectra, which were not observed for previous compounds. However, only a small fluctuation of the fluorescence intensity was detected for the phenylalanine conjugate **31** (**Figure 108A**). We suggest that this effect takes place because the starting fluorescence intensity corresponding to spherical assemblies of **31** is already quite high (**Figure S14** and **Figure S16** in annexes), and the micelle to fibre transition does not influence that much the fluorescence. Our hypothesis can be supported by temperature dependent fluorescence measurements made on **31** in a buffer solution, which clearly indicates a drastic decrease in fluorescence with temperature increase (**Figure S16** in annexes).

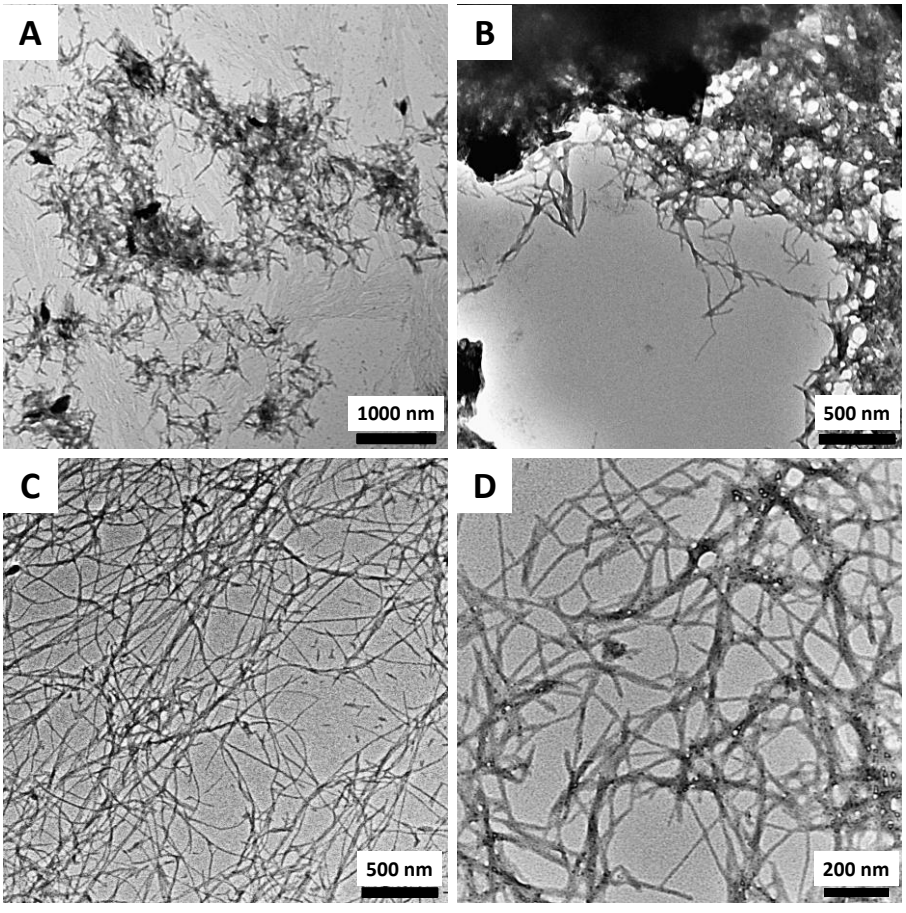

Figure 107 | TEM images of the enzymatically triggered self-assemblies of **31** (**A, B**) (5 mM) and **32** (**C, D**) (5 mM).

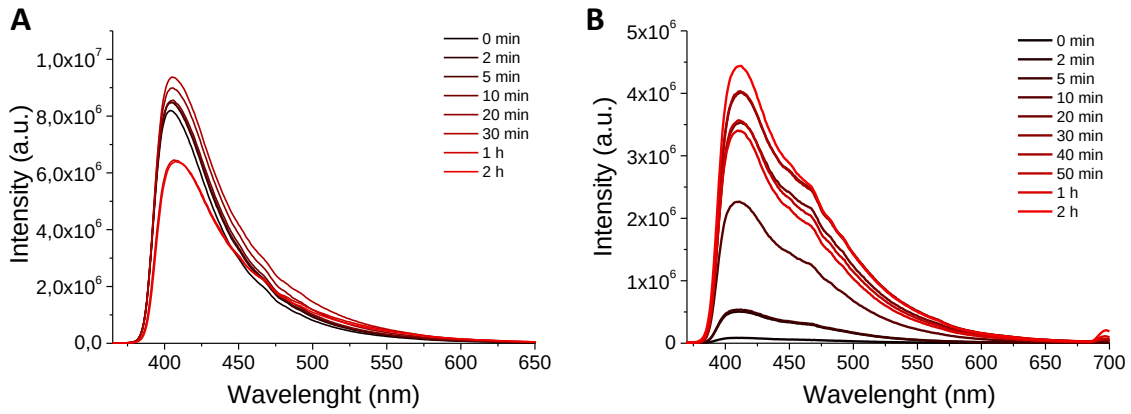

Figure 108 | Fluorescence spectra recorded during the enzymatic reactions for 5 mM solutions of phenylalanine derivative **31** (**A**) and for tyrosine derivative **32** (**B**)

A very interesting observation was made during the CD measurements of these self-assembled systems. For **31** and **32,** a distinct Cotton effect was observed, which was different from the ones recorded for two-branched TAA-conjugates (**Figure 109** and **Figure S18**). When comparing the CD spectra of the enzymatically triggered self-assemblies of **31** and **32,** the CD spectra of the phenylalanine derivative appeared to be almost the mirror image of the CD spectra recorded from the tyrosine derivative. This observation can suggest an identical organisation of the TAA conjugates within the assemblies but with opposite chirality.

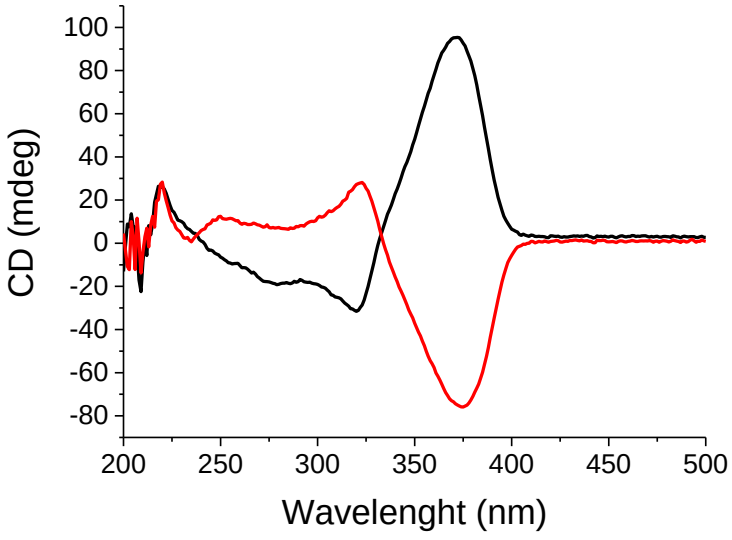

Figure 109 | CD spectra of the 10 mM self-assemblies of **31** (black line) and **32** (red line).

This observation highlights the influence of small structural changes in the building blocks on the final supramolecular structure.

Here FTIR analysis will be performed to understand the conformation of the peptide self-assembly, together with additional AFM measurements.

iii. Temperature dependence of enzymatic reactions

It is known that thermolysin remains active at quite high temperatures.[294] We were interested to know whether changing the temperature during the enzymatic reaction would produce any changes on the system. Thus, the measurements at 45 and 65 °C were performed (**Figure 110**). TAA conjugates with one branch were chosen as model compounds, for temperature dependent measurements for they have just one reactive group, which simplifies the analysis of the resulting mixtures. In all cases, the following trends were observed: ***a***) upon temperature increase maximum of conversion was reached faster; ***b***) conversion decreased with increasing temperature.

When the systems were cooled down to room temperature, for all samples starting from phenylalanine derivative **31**, hydrogelation was observed, while in the case of tyrosine conjugate **32,** viscous liquids were formed.

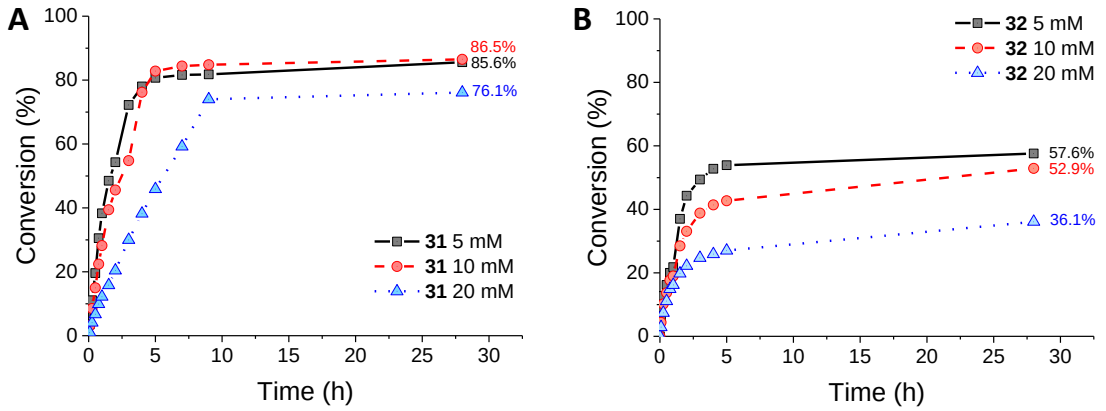

Figure 110 | Kinetics of product formation in the enzymatic reactions at 45 °C (**A** and **B**) and at 65 °C (**C** and **D**) for substrates **31** (**A**, **C**) and **32** (**B**, **D**).

Morphology analysis by TEM revealed drastic changes in the structure of the aggregates for the phenylalanine compound (**Figure 111**). Compared to aggregates obtained at room temperature (**Figure 107A,B**), the observed fibres were much longer (dozens of

294. Fujita, S. C., Go, N. & Imahori, K. Melting-profile analysis of thermal stability of thermolysin. A formulation of temperature-scanning kinetics. *Biochemistry* **18,** 24–28 (1979).

microns in length) with a high aspect ratio, along with a higher diameter of the fibres (23±3 nm) than previously observed.

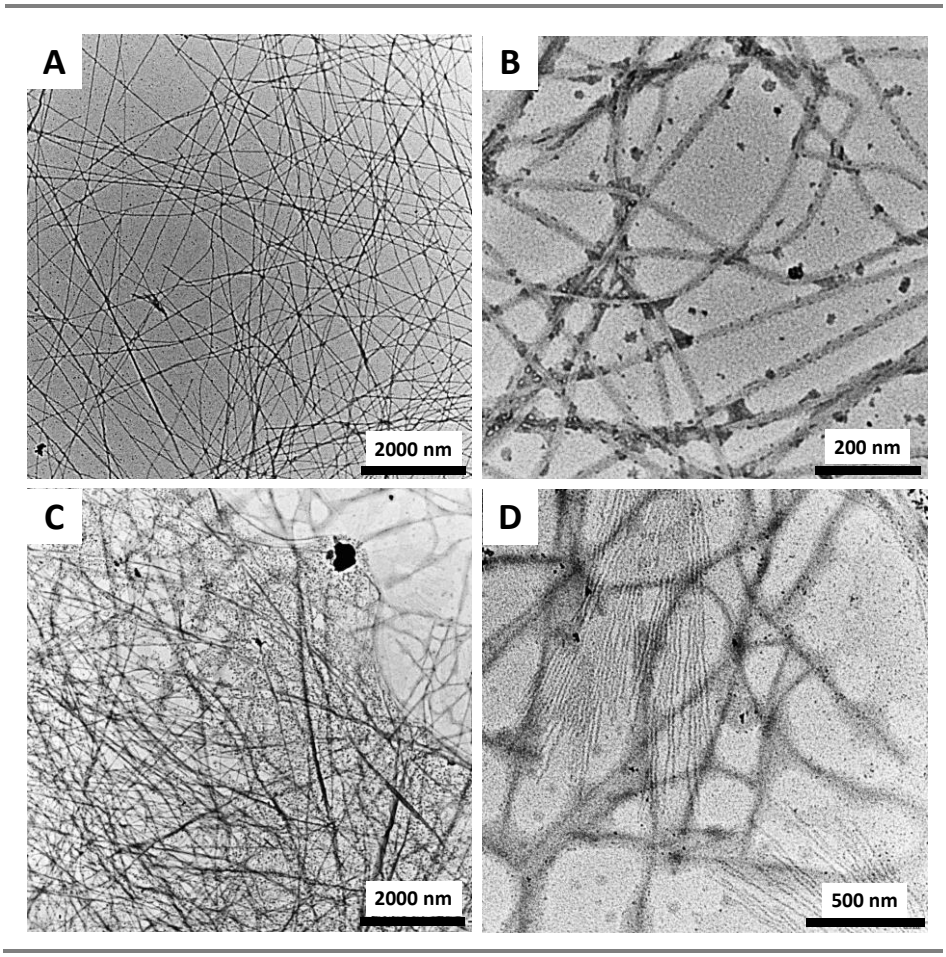

Figure 111 | TEM images for the enzymatically triggered self-assemblies of phenylalanine derivative **31** at 65 °C. (**A, B**) for 5 mM concentration and (**C, D**) for 20 mM concentration.

The morphology of aggregates obtained at 65 °C starting from **32** was also improved (**Figure 112**) comparing to those obtained at room temperature (**Figure 107C,D**) in a similar way as for molecule **31**, even though the enzymatic conversion in this case proved to be rather low (4 – 8%).

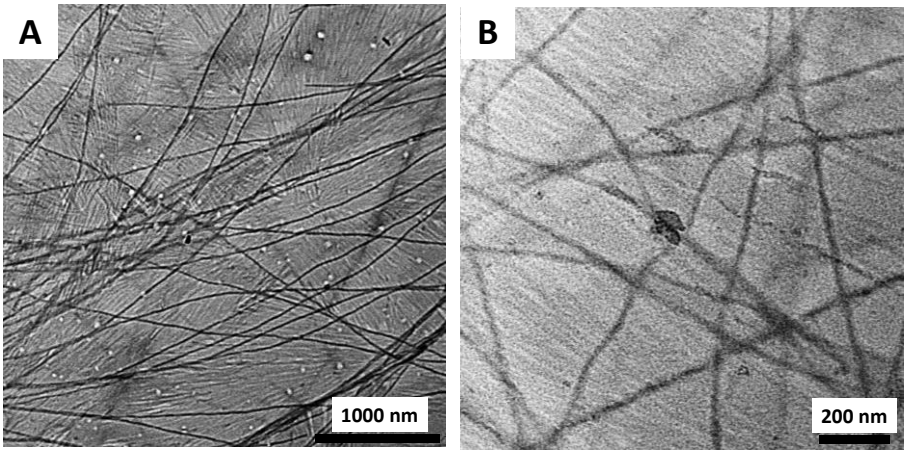

Figure 112 | TEM images of the self-assemblies of tyrosine derivative **32** at 65 °C for 5 mM concentration.

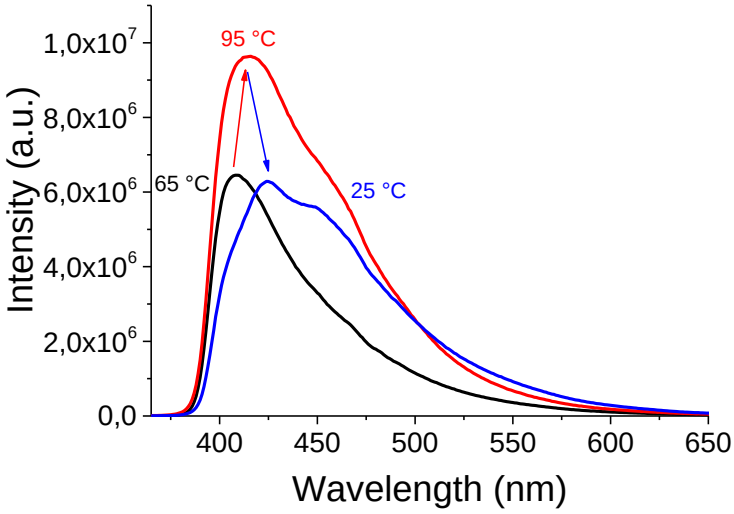

Figure 113 | Fluorescent spectra recorded for the self-assemblies of phenylalanine TAA-conjugate **31** at different temperatures. Spectra recorded at 65 °C, where the enzymatic reaction was conducted (black line). Spectra at 95 °C recorded for the same sample heated up to this temperature and held for 10 min (red line). Spectra recorded after the system was cooled down to room temperature from 95 °C for 30 min (blue line).

Changes in fluorescence spectra were also observed for the phenylalanine conjugate **31** (**Figure 113**). The spectrum recorded at the incubation temperature (65 °C) was identical to the one, obtained for this system at room temperature. When the sample was heated to 95 °C, the fluorescence intensity increased slightly. However, after the sample was cooled to

room temperature, a completely different picture was revealed: the fluorescent spectrum appears to consist of spectra, which correspond to different kind of species. Further investigation should be performed to understand this phenomenon in detail.

Another peculiar type of behaviour was noticed, *i.e.* the chirality of the tyrosine TAA conjugate assemblies was switched to the opposite upon heating. **Figure 114** represents the CD spectra of structures produced from enzymatically triggered self-assembly starting from tyrosine TAA conjugate **32**. As shown before at room temperature, an intense negative signal at 375 nm is observed (**Figure 114A** red and pink line). Remarkably, when a 5 mM solution of **32** was incubated with an enzyme at 45 °C overnight and after cooling down the system to room temperature, a positive mirror image signal was recorded, indicating a switch of chirality.

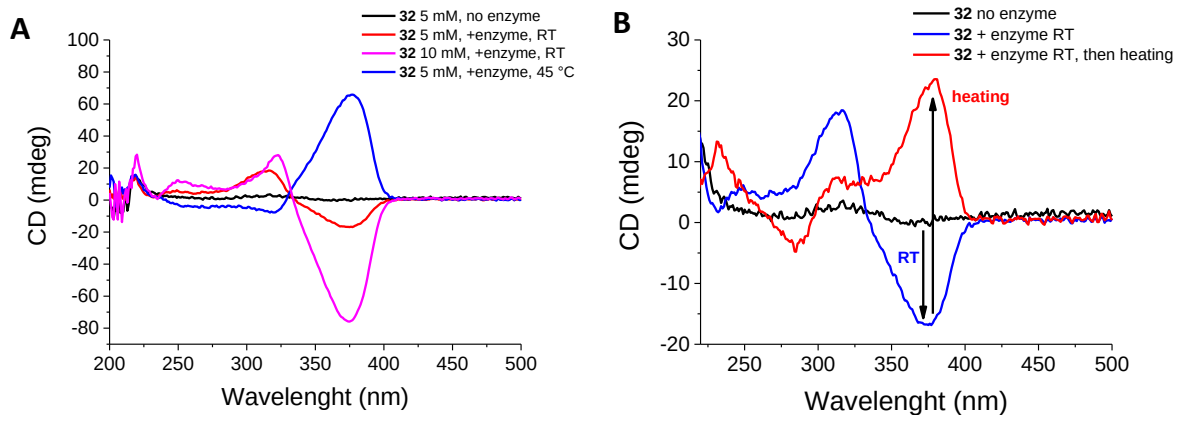

Figure 114 | CD spectra for enzymatically triggered self-assemblies of **32** (**A**) incubated at different temperatures and (**B**) Thermal chirality switching.

Furthermore, when already formed assemblies of **32** at a concentration of 5 mM were heated at 65 °C for 2 hours, the initially recorded CD signal changed to its mirror image (**Figure 114B**).

As for compound **31** it seems that incubation at different temperatures does not have an influence on the shape of the CD spectra (**Figure 115**), confirming the fluorescence spectroscopy studies and possibly indicating, that the internal structure, of the aggregates remains identical, even though on macroscopic level, the morphology changes dramatically.

Remarkably, however, after the same heating procedure that was performed for the fluorescence measurements reported on **Figure 113,** considerable changes in the CD spectrum (**Figure 115**). They consist of an intensity increase corresponding to the electron transitions of TAA core together with the dramatic increase of the band at 218 nm, which can correspond to the phenyl absorption, but also the higher energy TAA-core transitions are not excluded. This

observation together with fluorescence suggest occurrence of temperature induced structural rearrangement within self-assemblies.

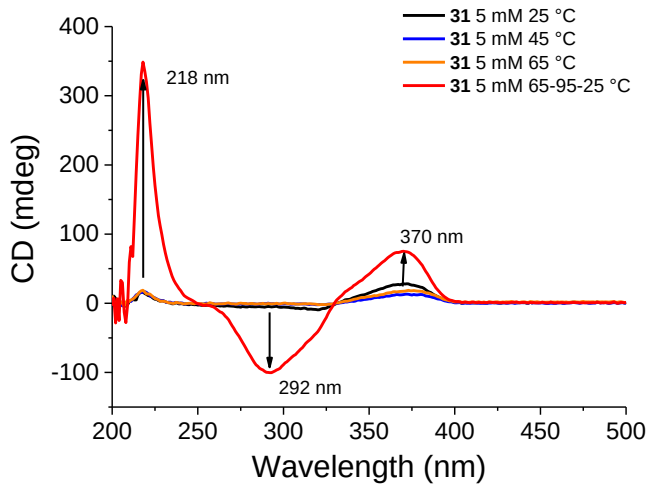

Figure 115 | CD spectra for enzymatically triggered self-assemblies of **31** at different temperatures.

This observations become even more interesting in light of some natural phenomena such as temperature dependent sex determination in some reptilian specimen for instance, where small differences in environment temperature cause large differences at the organism levels producing animals of different genders.[295,296]

Further studies of this effect should help to elucidate how small environmental changes might be amplified and expressed at the supramolecular level.

iv. Control experiment

A triarylamine diphenylalanine amide conjugate (TAA-FF-NH_2, **35**) was synthetized *via* peptide coupling procedure to test, whether self-assemblies could be formed from the compound obtained directly by conventional chemical synthesis (see **Figure S19**).

The synthetized compound precipitated from DMF reaction mixture and was barely soluble even in solvents such as DMF or DMSO. Its solubility in aqueous media was negligible. The heating and ultrasonication produced no effect. Moreover, incubation with thermolysin, which theoretically could hydrolyse this dipeptide, leading to some changes, had no effect both at room temperature and at elevated temperatures, underlying again the power of an enzymatic approach for the in building of the structures inaccessible starting from such precursors.

4. CONCLUSIONS AND PERSPECTIVES

In this chapter, we investigated the possibility to use biomolecules such as amino acids and peptides to trigger the self-assembly of triarylamines in aqueous medium. We have shown that biocatalytic approaches prove very useful to produce hierarchical self-assemblies in the form of hydrogels, when such materials are not accessible directly from the synthetic precursors. The TEM analysis confirmed the formation of high aspect ratio 1D nano-objects which are at the origin of the gel formation. Moreover, a thermal chirality inversion was observed for Y-TAA-bioconjugate self-assemblies, suggesting a possible transition from the kinetic product to the thermodynamic one.

Further analyses will be oriented to determine the conductivity of these nanofibers using conducting AFM, but also elucidate by FTIR and SAXS the molecular arrangement, giving rise to the helical fibres as determined by CD experiments and microscopies.

Further understanding of subtle temperature dependent effects will also be continued.

CHAPTER IV.
SELF-ASSEMBLING TRIARYLAMINES AS THE HOLE-TRANSPORTING MATERIALS IN PEROVSKITE SOLAR CELLS

1. INTRODUCTION

It is established that global energy consumption will increase by 50% within the next fifteen years *i.e.* going from around 20 TW in 2010 to 30 TW by 2030,[297]; the majority of this energy is supplied by fossil fuels, such as gas, oil or coal. The long-term consequence of the use of these fuels is the emission of greenhouse gases (mainly CO_2). Moreover, the supply of these materials is quite limited. For these reasons, a shift towards renewable sources of energy such as wind, water, thermal and solar powers, is one of the main priorities for humanity today.

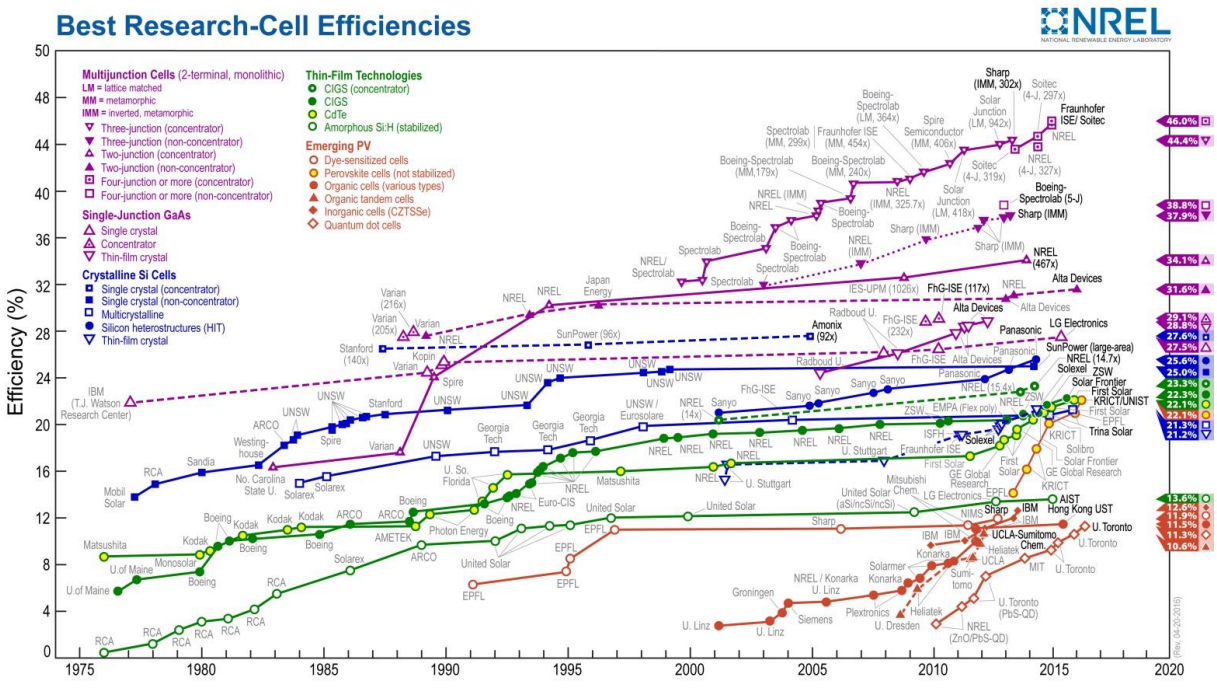

Figure 116| Timeline chart of the certified reported photoconversion efficiencies of the most common types of solar cells recorded since 1975. Chart is taken from the web page of the National Renewable Energy Laboratory. 298

297. Pandey, A. K., Tyagi, V. V., Selvaraj, J. A., Rahim, N. A. & Tyagi, S. K. Recent advances in solar photovoltaic systems for emerging trends and advanced applications. *Renew. Sustain. Energy Rev.* **53,** 859–884 (2016).
298. NREL Chart. at <http://www.nrel.gov/ncpv/images/efficiency_chart.jpg>

The development and use of photovoltaic systems, among others sources, is of great importance as photovoltaics can directly convert solar energy into electricity. Today the market for solar cells is almost fully occupied by single crystalline silicon solar cells.[297] However, the cost of production of crystalline silicon is high, and the corresponding solar panels are heavy and rigid. On the other hand, other types of photovoltaic materials such as organic photovoltaics or thin film solar cells have been considered to substitute monocrystalline silicon, due to their price and ease of processability.[297,299–301] Nevertheless, to date their photoconversion efficiencies prove lower than silicon.

The search for new and more efficient materials is of particular interest for scientists in the photovoltaic community. For instance, a real breakthrough was achieved a few years ago with a discovery of highly efficient photovoltaics based on hybrid tin(II)/lead(II) halides with a perovskite-like structure.[302–306] The chart in **Figure 116** shows the evolution of certified photoconversion efficiencies for major types of photovoltaic materials in recent years. Remarkably, perovskite solar cells have doubled in performance from 10% in 2012 up to over 22% in 2016 (red outlined circles with yellow filling, **Figure 116**).[298] A hole transporting material (HTM) is used in such solar cells to extract and conduct holes from the photoactive perovskite layer to the electrode. One of the most used HTM is based on a triarylamine derivative, so called *spiro*-MeOTAD (2,2',7,7'-Tetrakis-(N,N-di-4-methoxyphenylamino)-9,9'-spirobifluorene see **Figure 124** on page 175).[302]

Inspired by these remarkable results, our team (including Dr. T. Ellis, Dr. J.J. Armao IV) has developed new series of triarylamine-based self-assembling molecules for use them as HTM in perovskite solar cells. The incorporation in the devices and solar cell performance was performed by Dr. P. Gratia in the group of Prof. M. Grätzel and Prof. Md.K. Nazeeruddin at the École Polytechnique Fédérale de Lausanne in Switzerland.

After a brief introduction to the state of the art in the field of perovskite solar cells, we will report on the results of this collaborative work.

299. Hagfeldt, A. & Grätzel, M. Molecular Photovoltaics. *Acc. Chem. Res.* **33,** 269–277 (2000).
300. Troshin, P. A. & Sariciftci, N. S. in *Supramolecular Chemistry* **5,** 2725–2788 (John Wiley & Sons, Ltd, 2012).
301. Polman, A., Knight, M., Garnett, E. C., Ehrler, B. & Sinke, W. C. Photovoltaic materials: Present efficiencies and future challenges. *Science* **352,** aad4424–aad4424 (2016).
302. Jung, H. S. & Park, N.-G. Perovskite Solar Cells: From Materials to Devices. *Small* **11,** 10–25 (2015).
303. Green, M. A., Ho-Baillie, A. & Snaith, H. J. The emergence of perovskite solar cells. *Nat. Photonics* **8,** 506–514 (2014).

2. BIBLIOGRAPHY

A. Historical overview

In 1839, French physicist Alexandre-Edmond Becquerel, inspired by the photography process, observed the generation of an electric current during the illumination of platinum electrodes, which were covered with silver halides, in an electrolytic cell.[307,308] This observation was named *photovoltaic effect* – the generation of electric voltage or current in a material upon illumination. Another early example of photovoltaic effect was observed for solid selenium in 1867 by Adams and Day, who studied the conductivity of bulk selenium and observed its anomalous behaviour under light irradiation.[309] In 1883, the first photovoltaic device was constructed from a thin film of selenium placed between two different metals electrodes,[310] and showed an efficiency less than 1%. These discoveries remained unrecognised until almost 50 years later, when new findings of photovoltaic effect in copper(I) oxide and thallous sulphide reawakened the interest in this field, which remains one of the most developed one (renewable energy and photovoltaics) from since that time.

B. Photovoltaics

i. Principle of work

The photovoltaic effect is very similar to the photoelectric effect, for which A. Einstein received the Nobel Prize in 1921.[311] In both phenomena, the absorption of light causes the excitation of an electron. The photoelectric effect is characterised by the ejection of the excited electron out of the material in vacuum, while in the photovoltaic effect, the excited electron and the corresponding hole remain in the material. An electric current is then generated, when an electron and the corresponding positively charged hole are separated and transported to the opposite electrodes. Such separation may be induced by a difference of potentials between the used electrodes, which are made of different materials.

304. Boix, P. P., Nonomura, K., Mathews, N. & Mhaisalkar, S. G. Current progress and future perspectives for organic/inorganic perovskite solar cells. *Mater. Today* **17,** 16–23 (2014).
305. Grätzel, M. The light and shade of perovskite solar cells. *Nat. Mater.* **13,** 838–842 (2014).
306. Stranks, S. D. & Snaith, H. J. Metal-halide perovskites for photovoltaic and light-emitting devices. *Nat. Nanotechnol.* **10,** 391–402 (2015).
307. Bequerel, E. A. Recherches sur les effets de la radiation chimique de la lumiere solaire au moyen des courants electriques. *C. R. Hebd. Seances Acad. Sci.* **9,** 145–149 (1839).
308. Grätzel, M. Photoelectrochemical cells. *Nature* **414,** 338–344 (2001).
309. Adams, W. G. & Day, R. E. The Action of Light on Selenium. *Proc. R. Soc. London* **25,** 113–117 (1876).
310. Fritts, C. E. On a new form of selenium cell, and some electrical discoveries made by its use. *Am. J. Sci.* s**3-26,** 465–472 (1883).
311. The Nobel Prize in Physics 1921. at <http://www.nobelprize.org/nobel_prizes/physics/laureates/1921/>
312. eco2solar. at <http://eco2solar.co.uk/>
313. Theory of solar cells. at <https://en.wikipedia.org/wiki/Theory_of_solar_cells>

A solar cell (SC) is a device, made of a semiconducting material (placed between electrodes) as a photoactive layer, which transforms solar light into electricity *via* the photovoltaic effect (**Figure 117A**). One of the electrodes is usually made of a thin metal film such as gold, silver aluminium, *etc*., while the other electrode, also called substrate electrode, is made of glass covered with a transparent conductive oxide (TCO) thin film, usually indium tin oxide (ITO).

The design of a solar cell strongly depends on the nature of the photoactive material, however, the general working principle remains the same. The scheme of the simplest solar cell (at the same time the most common one), based on one p-n junction of silicon, is represented in **Figure 117**. In this type of SC, the p-doped and n-doped semiconducting silicon layers are in contact with one another, creating a large p-n junction. The absorption of photons with energy higher than the bandgap of silicon, excites the electron, which moves from the valence band to the conduction band, causing charge separation (**Figure 117B**). The generated charge carriers then migrate to the opposite electrodes, creating an electric current.

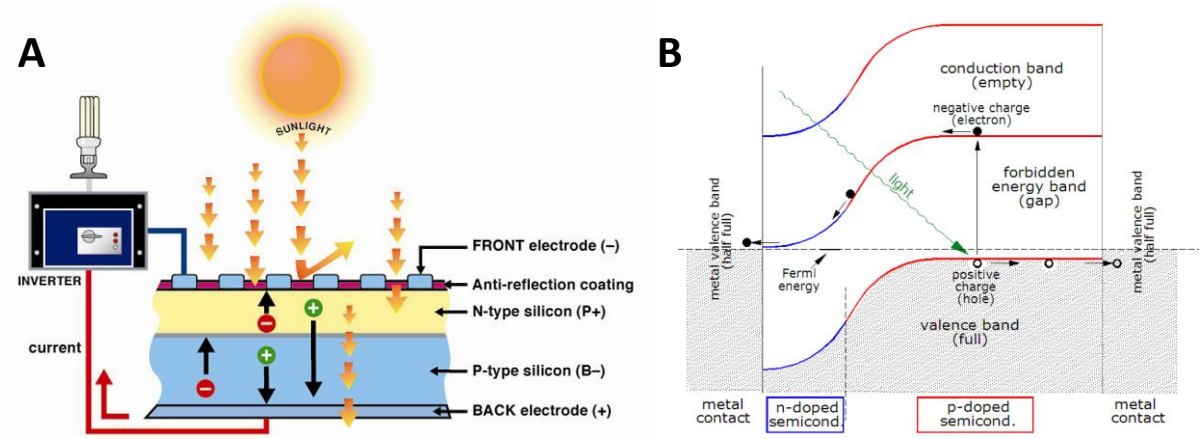

Figure 117 | (**A**) Scheme of the structure and functioning of a silicon solar cell. The incident light of appropriate energy is absorbed by the silicon, which generates charge separated state. The electrons end holes migrate in opposite directions creating an electric current. The figure is adapted from the web page of eco2solar.[312] (**B**) Scheme of the photovoltaic mechanism occuring in a single-junction silicon solar cell. Figure is adapted from the Wikipedia web page.[313]

ii. Characteristics and limitations of solar cells

The performance of solar cells is characterised by a few key parameters (**Figure 118A**). The *open circuit voltage*, V_{oc} corresponds to the maximum voltage that can be generated in the solar cell. In reality, this value is always smaller, than the energy band-gap,

312. eco2solar. at http://eco2solar.co.uk/
313. Theory of solar cells. at https://en.wikipedia.org/wiki/Theory_of_solar_cells
314. alternative energy tutorials. at http://www.alternative-energy-tutorials.com/energy-articles/solar-cell-i-v-characteristic.html

due to thermodynamic reasons. The *short-circuit current* I_{sc} is the current obtained in the solar cell when working in the short-circuited regime. Again, in practice, the I_{sc} is always smaller than theoretically predicted values. The output power of the solar cell is calculated as a product of maximal current and maximal corresponding voltage. At boundary conditions *i.e.* in a short-circuited or open-circuited regimes, this power equals zero. Therefore, the current and voltage, at which the output power is maximal, P_{max}, are defined as I_{mp} and V_{mp} respectively, and these parameters are smaller than their maximal values I_{sc} and V_{oc} respectively. One of the most important parameters, which is used when comparing different solar cells is the *efficiency of the solar cell* or *photoconvercion efficiency* (PCE), η. The PCE is calculated as a ratio between P_{max} of the solar cell to the input solar light power:

$$\eta = \frac{P_{max}}{P_{in}} = \frac{V_{os} I_{sc} FF}{P_{in}} \qquad \textbf{(39)}$$

where P_{in} corresponds to the input light power and FF is a fill factor, which is characterized as a ratio between the P_{max} to the product of I_{sc} and V_{os}:

$$FF = \frac{P_{max}}{V_{oc} I_{sc}} = \frac{V_{mp} I_{mp}}{V_{oc} I_{sc}} \qquad \textbf{(40)}$$

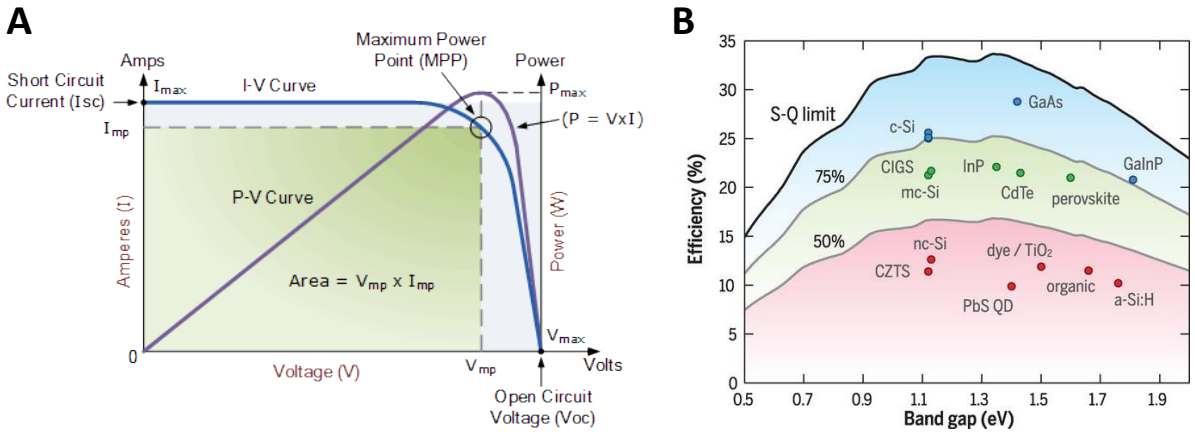

Figure 118 | (**A**) Typical V-I curve (blue) of a photovoltaic device and its corresponding power curve (purple). The figure is adapted from the web page of the Alternative energy tutorials.[314] (**B**) Graphical dependence of the efficiency of the single junction photovoltaic device depending on the band-gap of the material. Black curve represents the Shockley–Queisser fundamental limit. Colored zones represent the range of efficiencies relative to the S-Q limit: 0 – 50% (red zone), 50 – 75% (green zone), 75 – 100% (blue zone). The colour circles represent the certified record of PCE for the most common classes of single junction photovoltaic systems. Figure is adapted from ref. 301

While the lower limit of a SC efficiency is obviously zero, the upper-efficiency limit depends on various parameters, such the bandgap of the material, irradiation conditions, architecture of the cell, *etc.* It is defined by one of the most fundamental model for photovoltaics, so called the Shockley–Queisser (S-Q) limit.[301] Accordingly to the S-Q model, the efficiency limit for a single component single-junction solar cell with an optimal bandgap of 1.34 eV is equal to 33.7%. This means that out of all the energy received by the solar cell, only 33.7% can be theoretically transformed into an electric power. The relationship between the S-Q efficiency and the bandgap of a material is described on **Figure 118B**. The S-Q limit can be exceeded by using multicomponent solar cells with multiple junctions, however, the cost of their production is so high, that they cannot be competitive on the market.

The optimal way, to deal with the S-Q limit, is to approach it and make the production of photovoltaic devices less expensive. Among others, the newly emerged type of perovskite solar cell offers interesting promises for multiple reasons, which will be detailed in the next section.

C. Perovskite solar cells

It is appropriate to say that the field of organic-inorganic hybrid perovskite solar cell, or simply called perovskite solar cells (PSCs) is one of the fastest developing direction of photovoltaics today.[301–306] The timeline of PCS discovery started more than a century ago. The complex alkali-metal and tin/lead halides were synthesised in 1893.[305] The structure and properties of such compounds, however, were determined only 64 years later by Moller in 1958, describing the formula of caesium lead halides to be $CsPbX_3$ (X = Cl, Br or I), and the photoconductive properties of these materials, suggesting their semi-conductive nature. By replacing the alkali-metal for a methyl ammonium cation, Weber obtained the first organic-inorganic hybrid perovskite in 1978.[305]

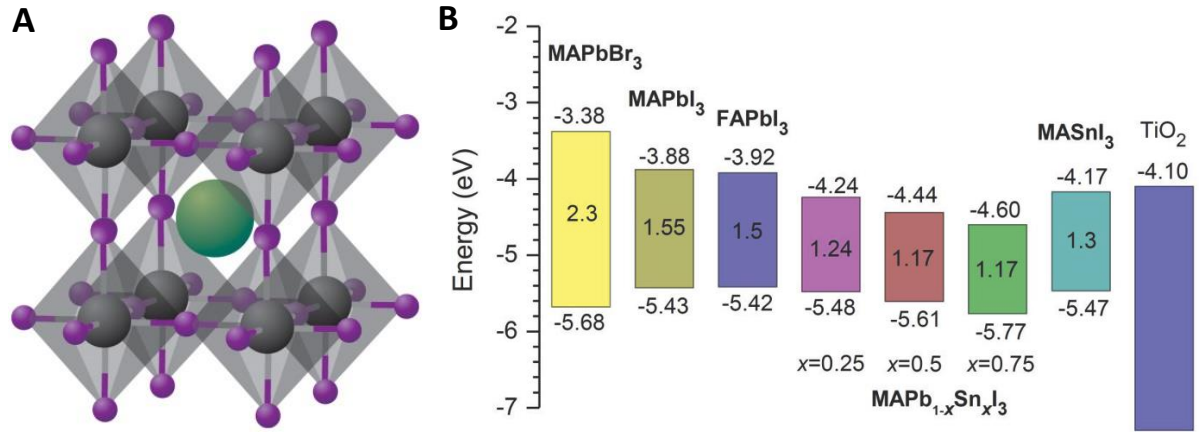

Figure 119 | (**A**) Typical crystal structure of a perovskite. (**B**) Band-gap energy levels of different lead/tin halide perovskites and TiO_2. Figures are adapted from refs. 302,305

The name "perovskite", comes from the structural similarity of these compounds with the natural mineral perovskite, a calcium titanate $CaTiO_3$, where small titanium atoms are surrounded in an octahedral manner by six oxygen atoms and the larger calcium ions occupy the cubooctahedral voids formed by 12 oxygen atoms.[315] The general formula of perovskite-like photovoltaic materials thus is $\mathbf{ABX_3}$, where **A** is a large cation (such as Cs^+, $CH_3NH_3^+$ or $HC(NH_2)_2^+$), **B** is Pb(II) or Sn(II) and **X** is a halide anion (Cl, Br or I) (**Figure 119A**).

The optical end electronic properties of methylammonium lead(II) iodide, ($CH_3NH_3PbI_3$) interested scientists for decades, mainly concerning their applications in LED technologies.[306] The absorption coefficient of its thin film deposited on nanocrystalline TiO_2 was estimated to be 1.5×10^4 cm^{-1},[303] which is comparable with other conventional PV materials such as GaAs, GaTe, and CIGS (copper indium gallium selenide). Although $CH_3NH_3PbI_3$ does not possess a panchromatic absorption, due to its bandgap value of 1.55 eV puting an onset absorption at 800 nm, it is possible to tune bandgap by replacing the methylammonium cation by a formyl ammonium, which has a larger size. This exchange lowers the bandgap by around 0.07 eV or extends the absorption by 40 nm. It is also possible to decrease this bandgap value by partial replacement of the lead atoms with tin(II) from 1.55 eV to 1.17 eV.[302] Obviously, variation of the halides has an influence on the photoelectronic properties of perovskites as well, as demonstrated by the energy diagrams of common perovskites depending on their composition (**Figure 119B)**.

The exciton binding energy in perovskites is very low (about 0.030 eV), meaning that, once formed, they rapidly dissociate, producing free charge carriers, with high mobility

315. Navrotsky, A. Energetics and Crystal Chemical Systematics among Ilmenite, Lithium Niobate, and Perovskite Structures. *Chem. Mater*. **10,** 2787–2793 (1998).

values, up to 25 cm^2 $V^{-1}s^{-1}$ for both electrons and holes.[302,305] Surprisingly, despite these remarkable properties being known for more than 20 years, no information on their use as PV materials have been reported, mainly due to the toxicity of lead and the poor robustness of less toxic tin analogues. Just ten years ago, in 2006, Miyasaka and colleagues, reported on the first use of $CH_3NH_3PbBr_3$ in liquid-based dye-sensitized solar cells with an efficiency of 2.2%.[303] When bromide was substituted by iodide, the efficiency was raised to 3.8% in 2009, however, the performance was not stable due to the fast degradation of perovskites in organic solvents.[303] After the modification of the TiO_2 treatment procedure, in 2011, the group of Park reported on an increased efficiency up to 6.5%, however, the issue associated to perovskite solubilisation was still not solved.[303] These results stimulated the development of solid-state perovskite cells, where the problematic electrolyte is replaced by a solid hole transporting material (HTM). In 2012, Grätzel and Park[316] and almost simultaneously Snaith[317] reported on the use of *spiro*-MeOTAD (that was originally developed for use in OLEDs), which not just doubled the efficiency but also dramatically improved the stability of the solar cells. These pioneering works catalysed an enormous interest in solid state perovskite photovoltaics in the last few years, leading to the advancement of this technology with reported certified PCE values exceeding 20%.[298]

Generally, perovskite solar cells have three main components: (***i***) a perovskite light absorption layer; (***ii***) a mesoporous semiconducting material to accept electrons from the excited perovskite and (***iii***) a hole-transporting material. These components are sandwiched between metal electrodes. In the device, these components can be arranged in two ways, a mesoscopic nanostructure and planar structure, as depicted in **Figure 120A**.

In a mesoscopic device architecture, a perovskite layer blended with TiO_2 (which increases the surface area, and conduct electrons) is deposited on the top of a mesoporous material, such as TiO_2, playing the role of an electron conductor, after injection of the electrons from the perovskite. The presence of a compact TiO_2 layer on the substrate is important for hole blocking. Various nanomaterials have been tested instead of TiO_2, such as ZnO nanorods, TiO_2 nanoparticles/ITO composites, Al_2O_3 nanoparticles, *etc.* Interestingly, for solar cells with a planar architecture, *i.e.* without mesoporous material, the performance was comparable, if not higher, suggesting that perovskite may be an efficient electron transporter due to the balanced mobility of charge carriers. The diffusion lengths for electrons

316. Kim, H.-S. *et al.* Lead Iodide Perovskite Sensitized All-Solid-State Submicron Thin Film Mesoscopic Solar Cell with Efficiency Exceeding 9%. *Sci. Rep.* **2,** 583–585 (2012).
317. Lee, M. M., Teuscher, J., Miyasaka, T., Murakami, T. N. & Snaith, H. J. Efficient hybrid solar cells based on meso-superstructured organometal halide perovskites. *Science* **338,** 643–7 (2012).

and holes in a perovskite prepared by mixing $PbCl_2$ and excess of CH_3NH_3I were estimated to be around 1069 nm and 1213 nm respectively.[302] The close values of these diffusion lengths suggested the possibility to use the perovskites in the HTM-free architectures, which led to the development of cells with a certified efficiency of 12.8%.[302]

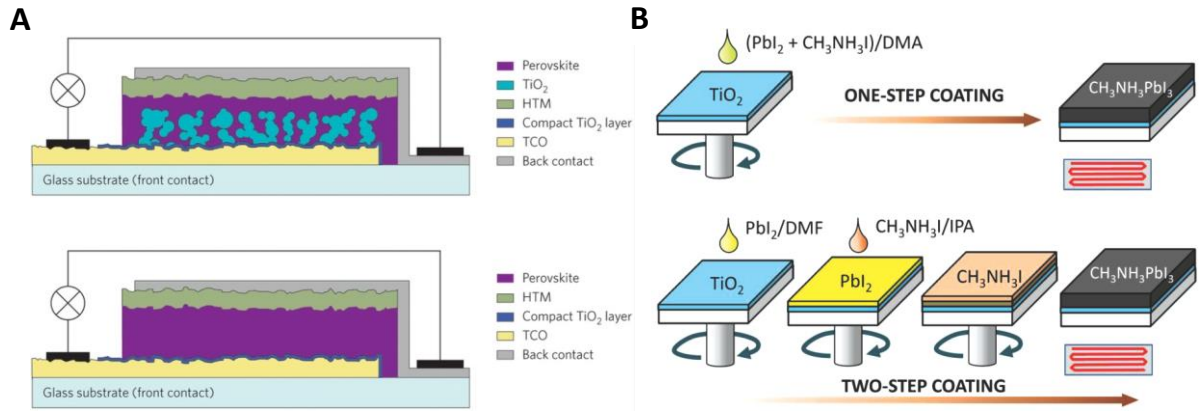

Figure 120 | (**A**) The two most common types of perovskite solar cell architecture: mesoscopic (top) and planar (bottom). (**B**) Methods of preparation and deposition of lead halide perovskites: (top) direct method, when the mixture of led(II) iodide and methylammonium iodide in an organic solvent is coated on the substrate, and (bottom) two-step deposition, when lead(II) iodide is deposited first, followed by coating with the solution of methylammonium iodide. Figures are adapted from refs. 302,305

It was shown that the deposition method also influences the PCE of perovskite solar cells (**Figure 120B**).[305] Initially, a single step methodology was mainly used for perovskite deposition, which included the casting of the solution of both PbX_2 and CH_3NH_3X (X = Cl, Br or I) in appropriate solvents such as DMF or DMSO. Unfortunately, this method afforded the perovskite deposition with various morphologies which happened to be poorly reproducible. In order to have a better control, a two-step deposition was developed, which consisted in the consecutive deposition of a DMF solution containing led(ii) iodide on a mesoporous TiO_2 substrate followed by the deposition of an isopropanol solution of a methylammonium iodide (**Figure 120B**). The resulting perovskite semiconductor was formed *in situ* in the pores of titanium dioxide. This method allowed a better control over the perovskite morphology and as a consequence to reproducible PCR results.

D. Hole-transporting materials in perovskite solar cells

Even though the performance of perovskite solar cells was dramatically improved, mainly due to the development of new deposition techniques of the perovskite material which allowed better control over its nanostructure, the hole-transport material still remains an

important component of perovskite solar cells. The main role of the HTM is to improve the hole-transporting characteristics, such as hole extraction from the perovskite material and hole transport to the cathode. Moreover, correctly chosen HTM can play the role of an electron blocking layer, preventing the recombination of charge carriers.

There are the following requirements that the HTM must fulfill:[28–30]

(***i***) The absorption of the HTM should not superimpose with the absorption of the perovskite material because of the excellent photo-absorption properties of perovskite in the visible region. It is desirable that the HTM have its absorption in the UV region or/and in the red/NIR region, where perovskite is a bad light-harvester.

(***ii***) Appropriate HOMO-LUMO levels of the HTM compared to perovskite. Two factors are particularly important: ***a***) for an efficient hole extraction and transport, the HOMO level of the HTM should be in a range between the level of the valence band of the perovskite and the potential of the cathode in order to create sufficient electron-driving force. In the case of $CH_3NH_3PbI_3$ and a gold cathode, this range is located between -5.43 and -5.1 eV, respectively; ***b***) the V_{oc} of a solar cell depends on the energy level of electrons on the TiO_2 and on the HOMO of the HTM. Therefore, the lower HOMO level is the higher V_{oc} can be obtained.

(***iii***) High hole mobility values for the HTM, ensuring efficient transport of holes from the perovskite layer to the electrode. In order to increase the mobility values, p-dopants were used in numerous works.[28–30] So far, however, the role of the dopants is under debate.

Taking these requirements into consideration, various small molecules and polymeric hole-transporting materials have been designed and tested in PSCs in recent years,[28–30] and here we will try to briefly summarise these data.

i. Triarylamine derivative HTMs

1) Spiro-derivatives

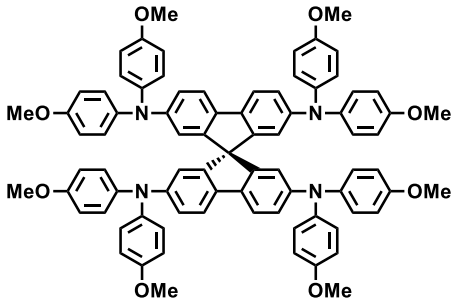

spiro-MeO-TAD

(a)

Figure 121 | Chemical structure of a gold standatd *spiro*-MeOTAD.

To date, the highest PCE of perovskite solar cells was recorded for devices having triarylamines-based HTMs.[28–30] The most popular one is a twisted molecule 2,2',7,7'-Tetrakis-(N,N-di-4-methoxyphenylamino)-9,9'-spirobifluorene or simply *spiro*-MeOTAD (***a***) (**Figure** 121), so called the "gold" standard. As a rule, the performance of a solar cell, developed with a new HTM, is compared with the performance of the same batch of solar cells containing *spiro*-MeOTAD. PCE as high as 15-19% were obtained using spiro-MeOTAD HTM. Due to the low hole mobility of pure *spiro*-MeOTAD, it is usually doped with additives such as lithium bis(trifluoromethane sulfonyl)imide salt LiTFSI, 4-*tert*-butylpyridine (*t*BP) and cobalt(III) complexes (FK 209). The role of these dopants is not well understood, however, it is suggested that LiTFSI promotes the oxidation of the *spiro* compound by oxygen, under light and stabilises the *spiro* radical cation. FK 209 plays the role of an oxidant itself. The influence of these additives on the PCE is not clear either. Some authors propose that their use may corrupt the perovskite layer and diminish the performance. Improvements in this direction were achieved by using the dicationic salt of *spiro*-compound, *spiro*-MeOTAD$(TFSI)_2$ as a dopant. Using this approach, no other dopants or oxidants, as *spiro*-MeOTAD$(TFSI)_2$ will oxidise neutral molecule giving two radical cations in result following the reaction **(2)** p. 38 in bibliography section.

One of the advantages of *spiro*-molecule is its high glass transition temperature (T_g around 120 °C), keeping it in amorphous state, which seems to be very important to achieve a high surface contact between the electrode and the HTM. Therefore, it is better to design new materials which do not crystallise under the deposition conditions.

2) Structure-Properties Relationship

The influence of the position of the methoxy groups on *spiro*-molecules was studied by Seok and colleagues (Figure 122).[318] *Para* (***a***), *meta* (***b***) and *ortho* (***c***) methoxy-substituted compounds were tested in perovskite cells, showing high performance for all the molecules, however, the highest performance was found for the *ortho*-substituted compound ***c*** (16.7% against 15.2% for commercial gold-standard *spiro*). The authors relate this increase in efficiency with the highest level of LUMO, which gives better electron blocking properties to this material.[318]

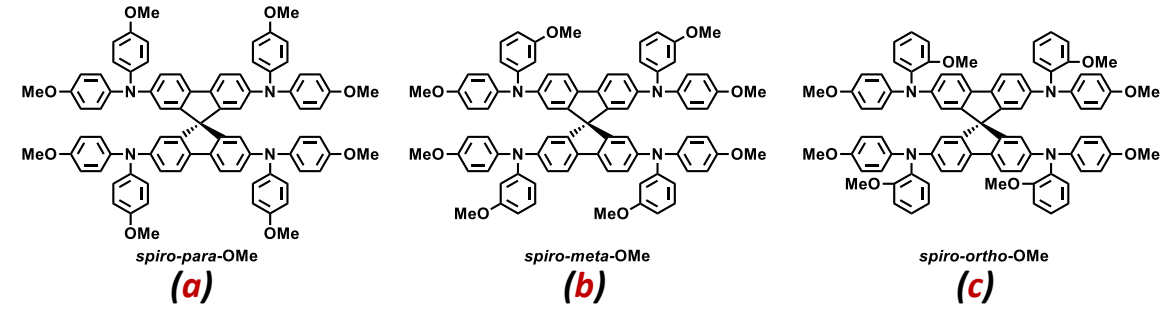

Figure 122 | Chemical structures of *spiro*-MeOTAD molecules with different positions of methoxy groups.

The group of Leo studied a series of *spiro* analogues molecules ***d*** – ***h*** in order to investigate how the HOMO energy can be tuned by changing the substituents at the *para*-positions.[319] Molecules ***e*** and ***f*** demonstrated the highest efficiency of 10.9% (7.8% with the *spiro*-MeOTAD (***a***) molecule at the same conditions) (**Figure 123**). The molecule ***g*** having a border HOMO energy level demonstrated lower performance while molecule ***h***, having HOMO energy level, lower than one of perovskite was inactive. This examples demonstrates how important it is to carefully design HTM with an appropriate electronic properties. Promisingly high PCE demonstrated solar cells with compound ***d***, which much cheaper and more readily available, from a synthetic point of view. Indeed, the cost of *spiro*- type of compounds is relatively high, which significantly increases the electricity production cost (compare: 1 g of *spiro*-MeOTAD ***a*** costs near 300 euro *vs* 200 euro for 1 g of MeOTPD ***d***).[320] For this reason, the search for new HTM is a very competitive field with large number of alternatives for gold standard *spiro*-MeOTAD ***a*** developed in few recent years.[28–30]

318. Jeon, N. J. *et al.* o -Methoxy Substituents in Spiro-OMeTAD for Efficient Inorganic–Organic Hybrid Perovskite Solar Cells. *J. Am. Chem. Soc.* **136,** 7837–7840 (2014).
319. Polander, L. E. *et al.* Hole-transport material variation in fully vacuum deposited perovskite solar cells. *APL Mater.* **2,** 081503 (2014).
320. Sigma-Aldrich. at <http://www.sigmaaldrich.com/>

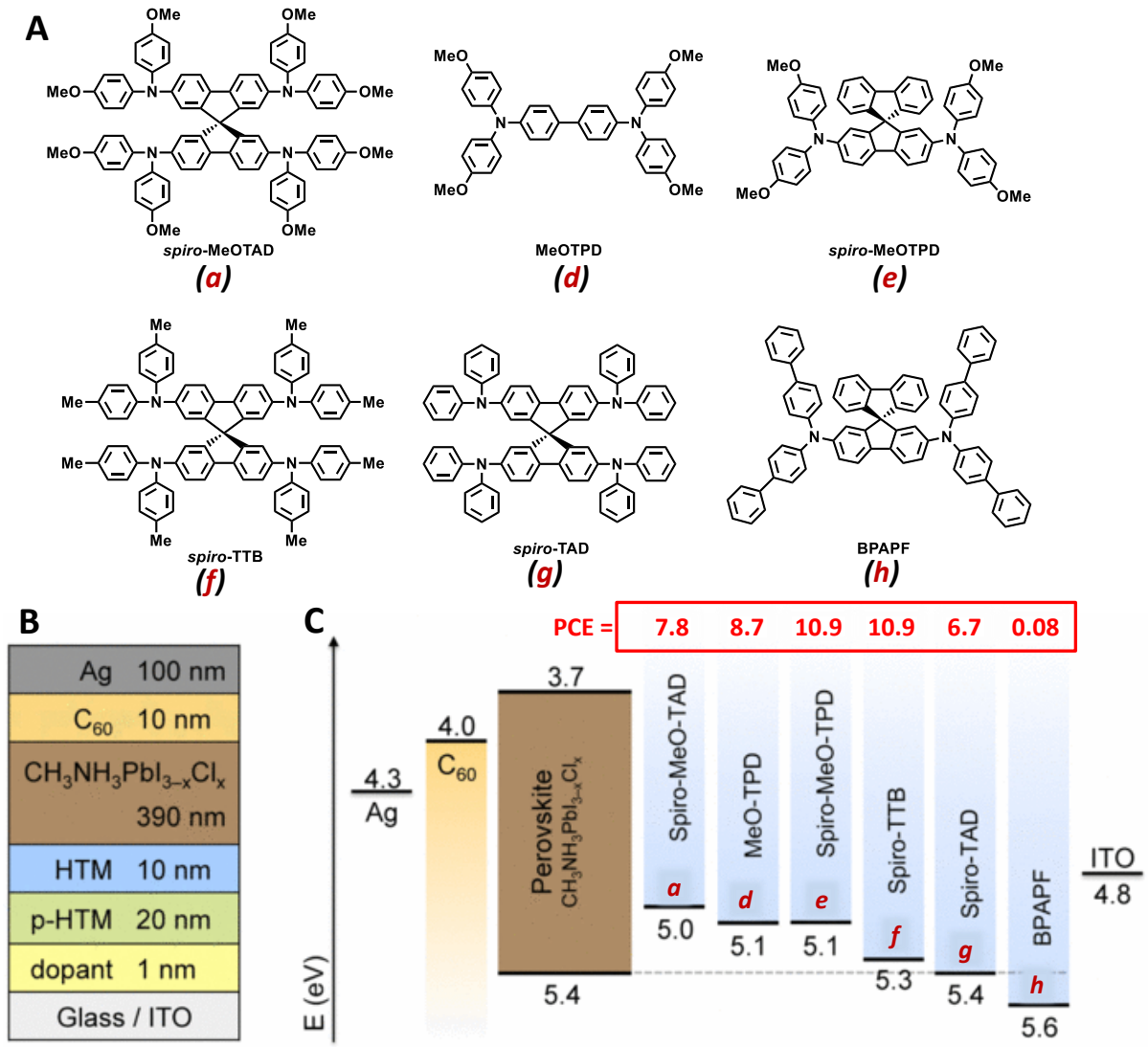

Figure 123 | (**A**) Chemical structures of some examples of spiro-class of molecules, used as HTM in perovskite solar cells. (**B**) Scematic representation of a perovskite solar cell. (**C**) Energy level diagram comparing HOMO energy levels for molecules ***a***, ***d*** – ***h***. Figure is adapted from ref. 319

Much focus still remains on *spiro*-type compound, due to their good processibility. For instance, the two-step synthesis of the compound ***k*** the analogue of ***a*** comprising synthesis of an analogous *spiro*-core and its grafting to a diarylamines function *via* the Buchwald-Hartwig procedure was recently reported by Hagfeld and Gratzel.[321] The molecule showed the PCE of 19.8% against 20.8% for the gold standard in the doped state.

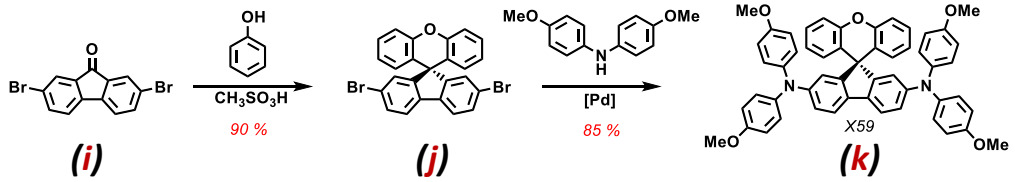

Scheme 14 | Synthesis of compound ***k***.[321]

3) Other Triarylamine Conjugates

Other types of molecule, containing electron donor triarylamine derivatives have been developed and investigated in perovskite solar cells.

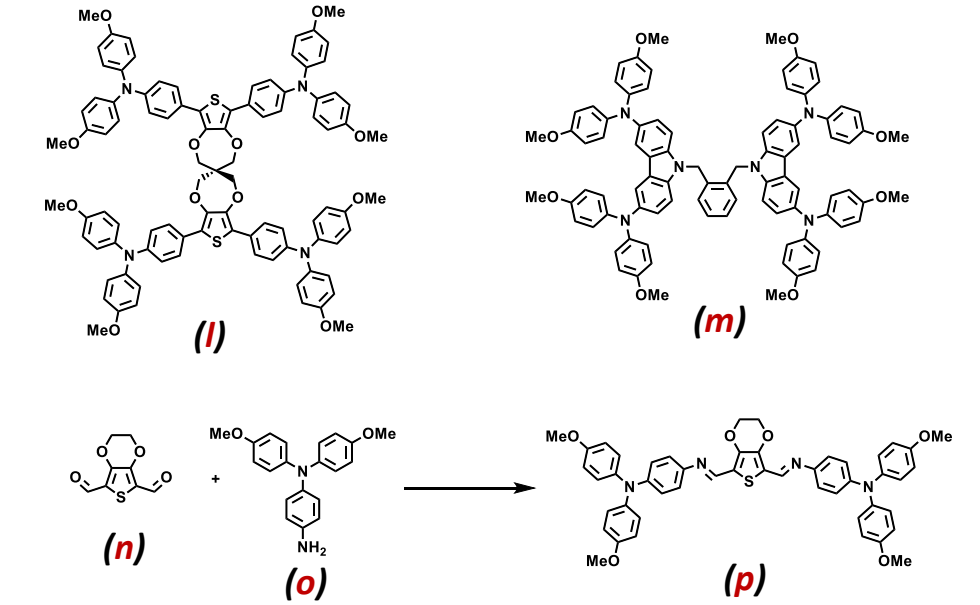

Figure 124 | Chemical structures of different TAA-based compounds used in perovskite solar cells as HTM: thiophene derivative ***l*** and ***m***, carbazole derivative ***p***.

For instance, Grimsdale and colleagues reported on the bis-triarylamine ***thiophene derivative*** showing comparable PCEs with the gold standard (13.2% and 13.7% respectively),[322]. Inspired by this success, Nazeeruddin and co-workers recently reported on the synthesis of the compound ***l***[323], which is a combination of an aliphatic *spiro*-moiety and a

molecule reported by Grimsdale.[322] Remarkably, in comparison with *spiro*-MeOTAD molecule ***a***, where the TAA parts are twisted by 90°, compound ***l*** was found to be quite planar in the crystalline state. The PCE for ***l*** was reported to slightly exceed the gold standard 13.4% vs 12.2% respectively.[323] Petrus *et al.* have developed fast and cheap method for the synthesis of efficient compounds.[324] The authors took advantage of azomethine chemistry, to synthesise the thiophene-based TAA-derivative ***p*** starting from thiophene dialdehyde precursor (***n***) and amino-TAA (***o***) in chloroform. Resulting ***p*** demonstrated high PCE (11.0 % *vs* 11.3% for *spiro*-MeOTAD). This examples shows the possibility for the potential use of dynamic combinatorial chemistry in this field.

Carbazole is another popular scaffold for the construction of HTMs used by several groups. Gratia *et al.* have developed a fast two-step synthesis of a carbazole-based compound ***m*** in which dendritic carbazoles were connected *via* dimethylenebenzene linker, allowing their flexibility. The PCE for compound ***m*** was recorded to be 16.9% *vs* 18.4% for the *spiro*-MeOTAD.[325] Other groups have also reported on high PCE with various carbazole derivatives.[326,327]

Inspired by the success of PSCs with *spiro*-TAA derivatives, numerous groups tested the performance of HTMs based on planar ***triarylamines***. Ko, Nazeeruddin and co-workers synthesized star-shape TAA derivative ***q*** and its more rigid analogue ***r***.[328] The idea behind this design was to increase the lifetime of the charge separated state by increasing the delocalisation area of the formed radical cation due to the planarization of the TAA core in ***r***. The recorded PCE were 12.3% and 13.6% for ***q*** and ***r*** respectively *vs* 14.7% for the *spiro*-***a*** and 6.9% for the naked perovskite cell. Interestingly, in another study reported by the same group, the efficiency of the rigidified TAA-compound was also higher, than in the case of the its propeller-like analog.[329]

---

321. Bi, D. *et al.* Facile synthesized organic hole transporting material for perovskite solar cell with efficiency of 19.8%. *Nano Energy* **23,** 138–144 (2016).
322. Li, H. *et al.* A Simple 3,4-Ethylenedioxythiophene Based Hole-Transporting Material for Perovskite Solar Cells. *Angew. Chem. Int. Ed.* **53,** 4085–4088 (2014).
323. Ganesan, P. *et al.* A simple spiro-type hole transporting material for efficient perovskite solar cells. *Energy Environ. Sci.* **8,** 1986–1991 (2015).
324. Petrus, M. L., Bein, T., Dingemans, T. J. & Docampo, P. A low cost azomethine-based hole transporting material for perovskite photovoltaics. *J. Mater. Chem. A* **3,** 12159–12162 (2015).
325. Gratia, P. *et al.* A Methoxydiphenylamine-Substituted Carbazole Twin Derivative: An Efficient Hole-Transporting Material for Perovskite Solar Cells. *Angew. Chem. Int. Ed.* **54,** 11409–11413 (2015).
326. Sung, S. Do *et al.* 14.8% perovskite solar cells employing carbazole derivatives as hole transporting materials. *Chem. Commun.* **50,** 14161–14163 (2014).
327. Xu, B. *et al.* Carbazole-Based Hole-Transport Materials for Efficient Solid-State Dye-Sensitized Solar Cells and Perovskite Solar Cells. *Adv. Mater.* **26,** 6629–6634 (2014).
328. Choi, H. *et al.* Efficient Perovskite Solar Cells with 13.63 % Efficiency Based on Planar Triphenylamine Hole Conductors. *Chem. Eur. J.* **20,** 10894–10899 (2014).
329. Choi, H. *et al.* Efficient star-shaped hole transporting materials with diphenylethenyl side arms for an efficient perovskite solar cell. *J. Mater. Chem. A* **2,** 19136–19140 (2014).
330. Song, Y. *et al.* Energy level tuning of TPB-based hole-transporting materials for highly efficient perovskite solar cells. *Chem. Commun.* **50,** 15239–15242 (2014).

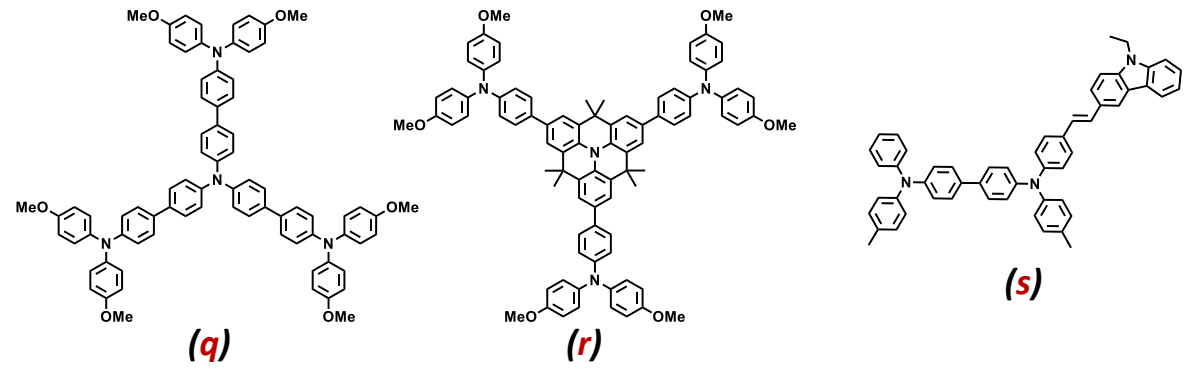

Figure 125 | Chemical structures of other TAA derivatives ***q*** - ***s***, used as HTM in perovskite solar cells.

Smaller TAA structures also have been exploited. Meng and colleagues synthesised derivatives of tetraphenyl benzidine (***s***) starting from commercially available dimethyl tetraphenyl benzidine in two steps *via* formylation and subsequent Wittig reactions with an appropriate precursor. The PCEs of this material in perovskite solar cells was 13.1% and 8.06% without addition of dopants and with dopants respectively *vs* 13.3% for the ***a***, making this type of compound possible candidates to replace *spiro*-molecule.[330]

ii. Other Small Molecules

Screening for HTMs is not only confined to aniline derivatives. Some recent examples highlight this tendency. The first example of the use of dopant-free tetrathiafulvalene (***t***) as a HTM in highly efficient PSCs was published by Han and colleagues.[331] The authors report the efficiency of pristine ***t*** to be as high as 11.0% in comparison with a PCE for the doped ***a*** of 11.4%. Moreover, the stability of solar cells to high humidity was higher comparing to the ***a*** analogue.

Small molecule TIPS pentacene (***u***), reported by Ahmad, exhibits an appropriate HOMO level with respect to the perovskite and relatively high mobility values.[332] The performance of ***u*** in the pristine state was higher than with the addition of dopant (11.5% *vs* 8.2%) and then the *spiro*-standard, which efficiency was recorded at 9.8%.[332]

331. Liu, J. *et al.* A dopant-free hole-transporting material for efficient and stable perovskite solar cells. *Energy Environ. Sci.* **7,** 2963 (2014).
332. Kazim, S. *et al.* A dopant free linear acene derivative as a hole transport material for perovskite pigmented solar cells. *Energy Environ. Sci.* **8,** 1816–1823 (2015).
333. Qin, P. *et al.* Low band gap S,N-heteroacene-based oligothiophenes as hole-transporting and light absorbing materials for efficient perovskite-based solar cells. *Energy Environ. Sci.* **7,** 2981 (2014).
334. Javier Ramos, F. *et al.* Non-aggregated Zn(ii)octa(2,6-diphenylphenoxy) phthalocyanine as a hole transporting material for efficient perovskite solar cells. *Dalt. Trans.* **44,** 10847–10851 (2015).

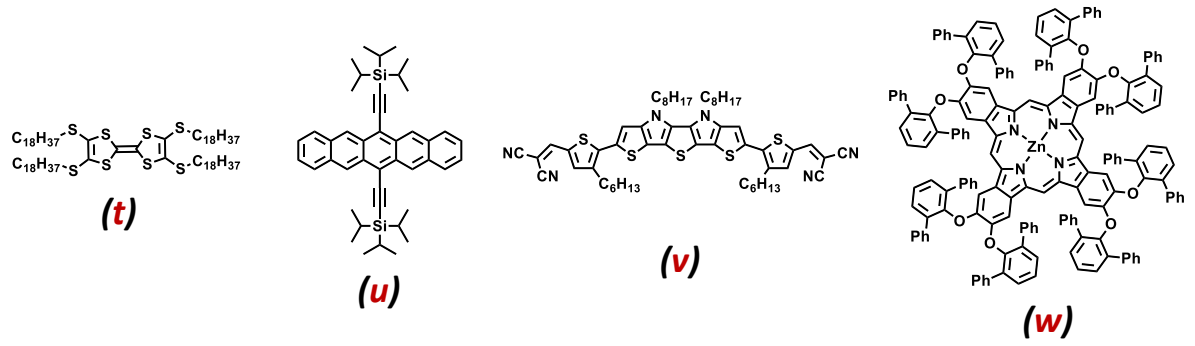

Figure 126 | Chemical structures of other various small molecules used as HTM in perovskite solar cells with quite high PCEs.

The group of Grätzel reported on the use of S,N-pentacene (***v***) with excellent electronic properties to be an appropriate hole transporter in perovskite solar cells. Moreover, ***v*** absorbs light in the low energy region, and hence can contribute to light harvesting. The PCE for ***v*** was found to be 10.5% *vs* naked perovskite 7.6%.[333]

The Zn(II) phthalocyanine derivative (***w***), decorated with bulky substituents to ensure a low level of crystallinity, was also used as a hole transporting material in perovskite solar cells.[334] The efficiency of the conversion was demonstrated to be 6.7% *vs* 10.3% for the *spiro*-MeOTAD.

These examples demonstrate the large varieties of different HTMs, which can be designed from small organic molecules as well as coordination compounds.

Overall, although the number of tested HTM is already large and is constantly growing, no systematic studies have been carried out, which could predict their performance in the perovskite solar cell, except for the HOMO-level prediction. Therefore, simple screening is used to choose the candidates with appropriate energy level, and then synthetize and test them.

Importantly, almost no examples of the use of supramolecular systems have been reported to the best of our knowledge, thus we were interested to exploit this field using discovered in our group light-triggered self-assembly of triarylamines.

3. Results and Discussions

Inspired by the incredible boost of perovskite-based photovoltaics, and having experience in with conducting self-assembling materials based on triarylamines, we were interested in appling our class of systems as the hole transporting material in perovskite solar cells. We hypothesized that the self-assembly of HTM molecules might improve charge transport from the perovskite layer to the electrode.

Two sets of triarylamine-based molecules with two and three nitrogen redox centres have been developed, based on theoretical calculations of HOMO-LUMO levels, to ensure that the molecules have the appropriate energy levels to match with the one of perovskite. Each molecule was designed with alkoxy substituents (such as methoxy, butoxy, octyloxy and benzyloxy), primarily, for their electronic properties and, secondly, to control crystallinity/amorphousness as well as solubility in organic solvents. In order to probe the effect of self-assembly on the PCE, most molecules were designed with amide groups to ensure the formation of columnar aggregates *via* hydrogen bonds, as already reported by our group.[81,113] One of the two-centred molecules was decorated with four benzyloxy moieties, as a control molecule (**Figure 127**).

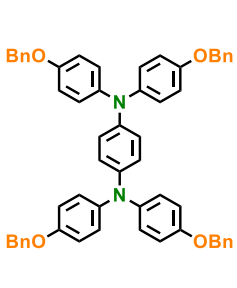

38 2N4Bn-TAA

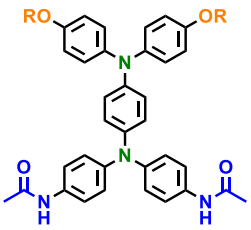

43	Me (2N2Me2A-TAA)
47	Oct (2N2Oct2A-TAA)
50	Bn (2N2Bn2A-TAA)
52	Bu (2N2Bu2A-TAA)

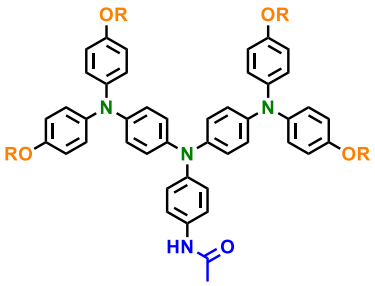

57	Me (3N4Me1A-TAA)
64	Oct (3N4Oct1A-TAA)
67	Bn (3N4Bn1A-TAA)
69	Bu (3N4Bu1A-TAA)

Figure 127 | Chemical structures of designed two and three centre triarylamine derivatives.

A. Synthesis of Triarylamine-Based HTMs

i. Synthesis of Triarylamines with Two Redox Centres

Two strategies were designed to obtain the dinitro precursors **41, 45 and 48** of the two-nitrogen triarylamine derivatives. The first method provides methoxy substituted molecule **41** in three steps, including aromatic nucleophilic substitution (S_NAr), reduction of

the nitro group and a second S_NAr (**Scheme 14**). Molecule **39** was synthesized from commercially available 4,4'-dimethoxydiphenylamine and *p*-fluoronitrobenzene in DMF in the presence of an excess of potassium carbonate. The resulting nitro compound **39** was reduced with tin(II) chloride and the corresponding amine **40** was used in the next S_NAr reaction with *p*-fluoronitrobenzene to afford compound **41** with 47% yield.

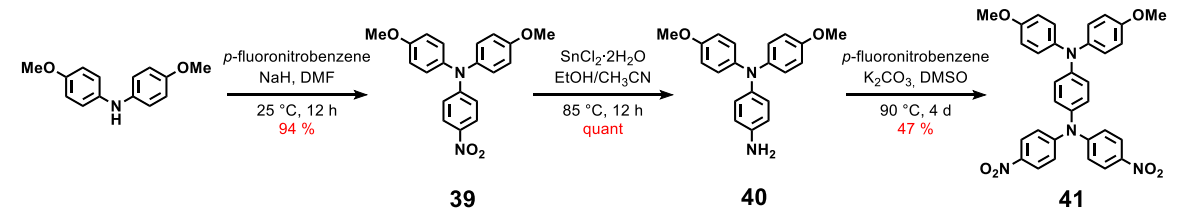

Scheme 15 | Synthesis of two-center nitro precursor with methoxy substituents.

The second strategy was used to synthesise octyloxy (**45**) and benzyloxy precursors (**48**). The choice of the benzyloxy substituent is important, as such an approach allows easy exchange of the benzyl groups with any substituent *via* two-step hydrogenolysis/nucleophilic substitution (*vide infra*). Compound **5**, which was obtained following the procedure described in *Chapter II*, was reacted with 4-octyloxyiodobenzene (**44**) or 4-benzyloxyiodobenzene (**13**) using Buchwald-Hartwig conditions, providing dinitro compounds **48** and **48** with reasonable yields at the gram scale.

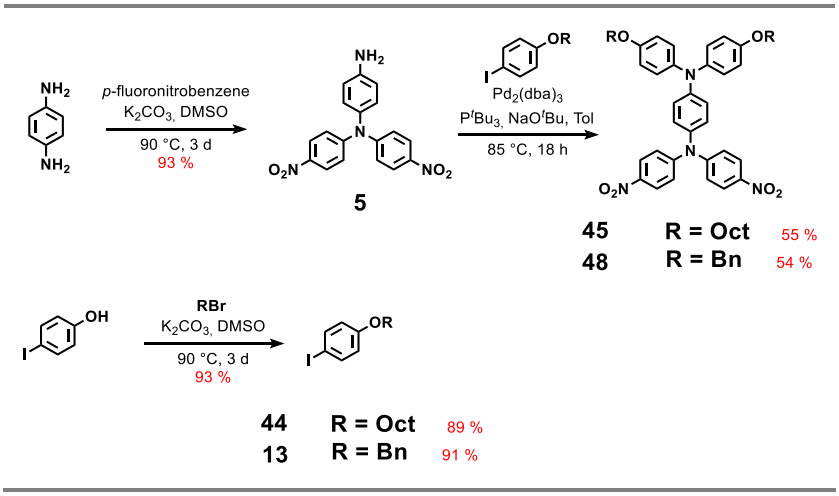

Scheme 16 | Synthesis of two-center nitro precursors with benzyloxy and octyloxy substituents.

After reduction of the nitro compounds **41, 45** and **48** with tin(II) chloride, the corresponding anilines were acetylated with acetyl chloride in dichloromethane in good yields (**Scheme 17**). Butoxy substituted triarylamine **52** was obtained in two steps starting from the freshly prepared benzyloxy compound **50**. The benzyl groups were first removed under an

atmosphere of hydrogen using palladium on charcoal as a catalyst, affording the free phenol derivative, which then reacted with iodobutane to produce molecule **52**. All compounds were purified by recrystallization except for the octyloxy derivative **47** which required column chromatography.

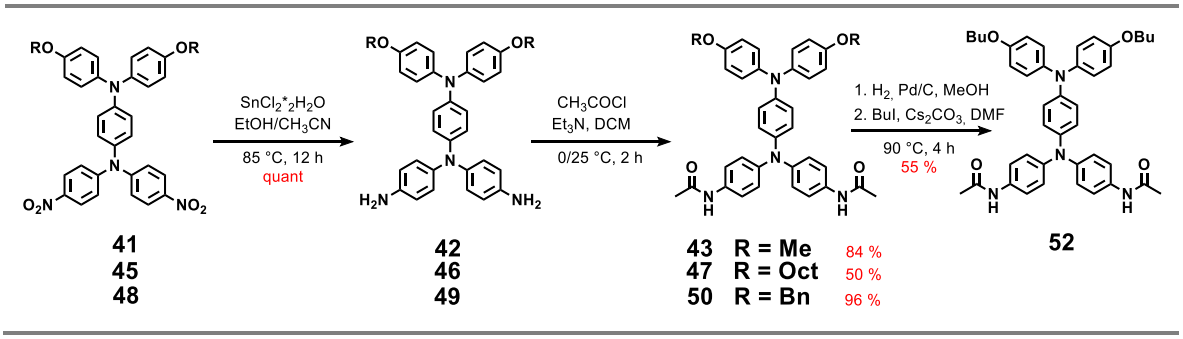

Scheme 17 | Synthesis of two-center TAA derivatives **43, 47, 50** and **52**.

The control molecule **38** was obtained using a two-step Buchwald-Hartwig methodology (**Scheme 18**). In the first step, the 4,4'-dibenzyloxydiphenylamine (**37**) was synthesised from commercial 4-(benzyloxy)aniline hydrochloride and *p*-benzyloxy bromobenzene (**36**) using $Pd_2(dba)_3$ and DPPF as a sterically hindered ligand, to ensure the formation of the mono-coupling product. In the second step, molecule **37** reacted with 1,4-dibromobenzene under classical Buchwald-Hartwig conditions with *tert*-butylphosphine as a ligand to provide compound **38** with a high yield.

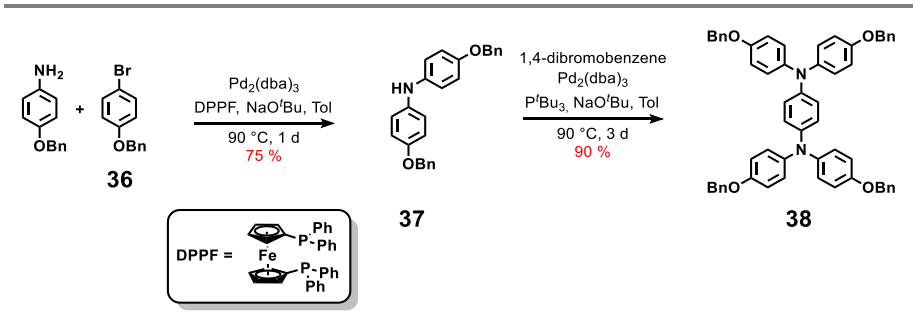

Scheme 18 | Synthesis of two-center tetrabenzyloxy compound **38**.

ii. Synthesis of Triarylamines with Three Redox Centres

The three-centred TAA derivatives were synthesized in five to seven steps according to **Scheme 19**. The nitro triarylamine **53** was obtained *via* S_NAr between commercially available *p*-fluoronitrobenzene and diphenylamine in DMF in the presence of sodium hydride as a base with high yield. The bromination of **53** with N-bromosuccinimide afforded the dibromonitro triarylamine **54**, which was then reacted with the corresponding alkoxy substituted diphenylamine (**37**, **61** and commercially available 4,4'-dimethoxydiphenylamine)

under Buchwald-Hartwig conditions to result in three redox centre nitro precursors **55**, **62** and **65**. Compounds **37** and **61** were synthetized *via* Buchwald-Hartwig coupling using the DPPF as bulky ligand. Subsequent reduction of the nitro group with tin(II) chloride and acetylation of obtained aniline yields the methoxy **57**, octyloxy **64** and benzyloxy **67** triarylamine derivatives with reasonable to high yields. The resulting three-N butoxy derivative **69** was synthesised in a similar way as compound **52**: after hydrogenolysis of the benzyl groups and subsequent alkylation with butyl iodide.

All final compounds and intermediates were characterised by ^{1}H, ^{13}C NMR and mass spectrometry (see experimental section).

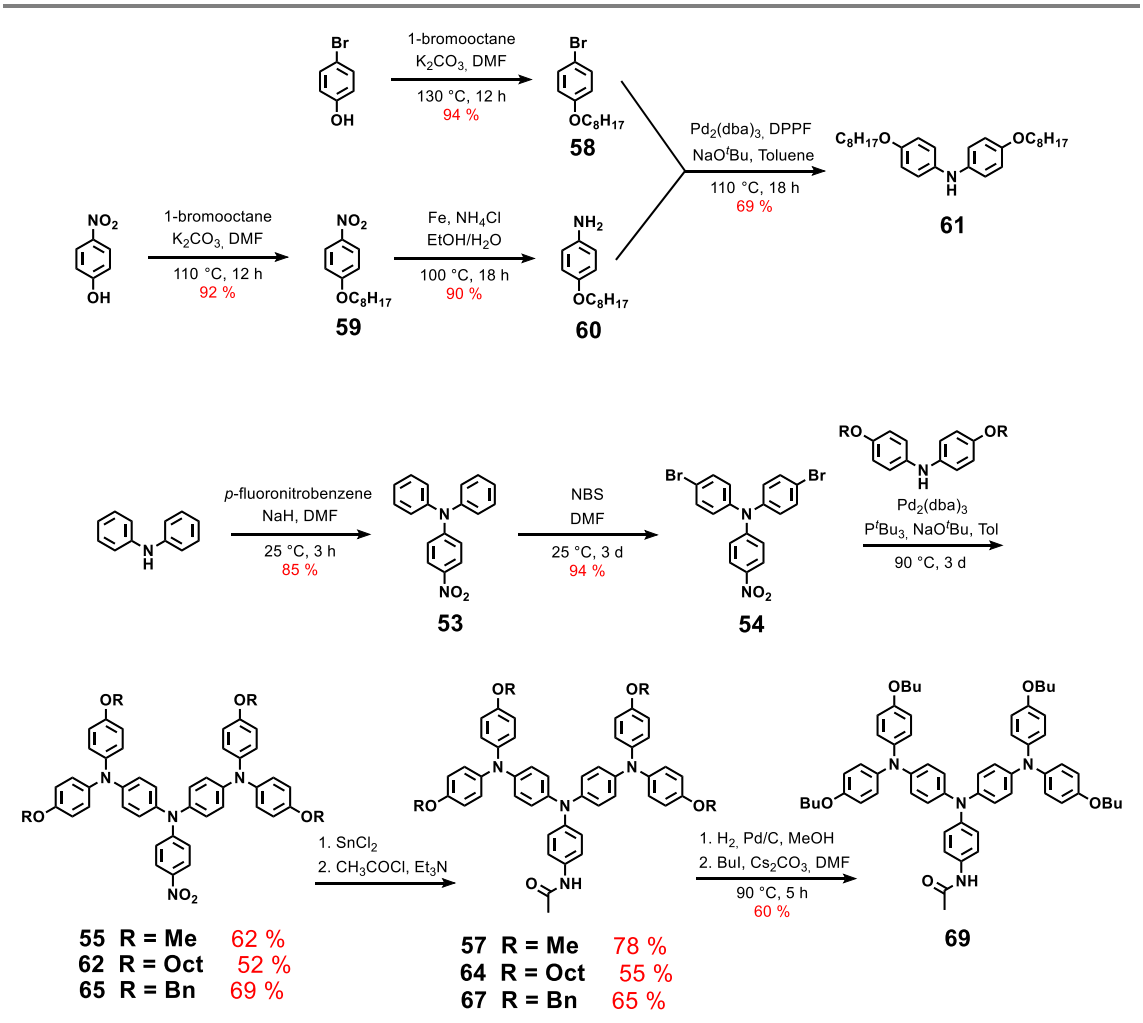

Scheme 19 | Synthesis of three-center TAA derivatives.

B. Electrochemical Properties

In order to investigate the electronic properties of the synthesised candidates for HTM, we first characterised the methoxy-substituted compounds **43** and **57** using UV-Vis spectroscopy (**Figure 128A)**. As expected, due to the increased number of phenyl groups, the absorption maximum at λ= 340 nm undergo red-shift in comparison with triarylamine of the first generation as reported by Moulin *at al.*[81] When comparing two and three redox centre compounds **43** and **57**, the latter is shifted by 9 nm towards lower energies (334 nm and 343 nm for **43** and **57** respectively).

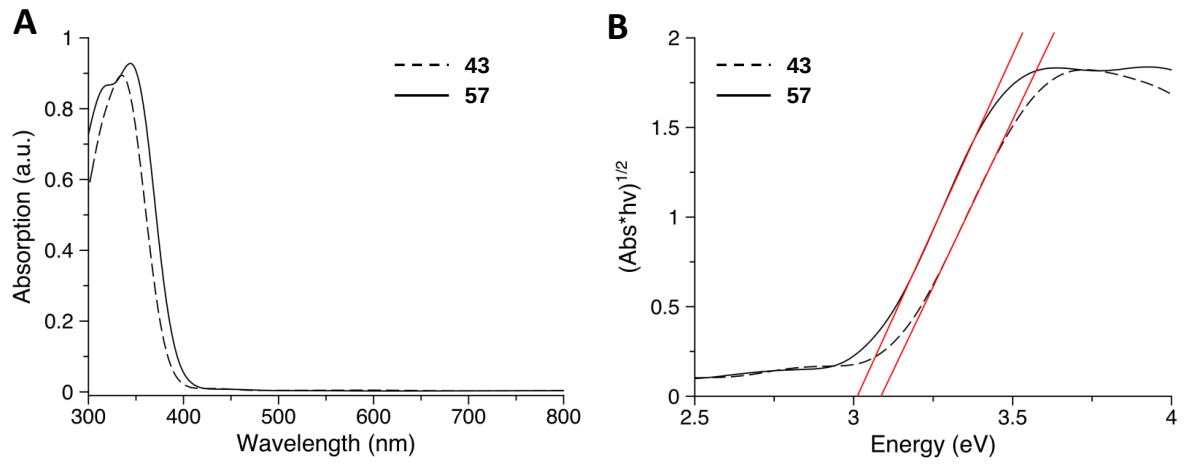

Figure 128 (A) UV-Vis absorption spectra of the unoxidized TAAs **43** (dashed line) and **57** (solid line). (**B**) Tauc plots for the determination of the absorption onset. Red lines represent the extrapolation of the linear region of Tauc plots.

The onset absorption values for both molecules were determined using the Tauc plot (**Figure 128B**). Though this method is generally used to determine the band-gap in bulk semiconducting materials, it can be applied to molecules or polymers in solution or/and film as well.[335] Typical Tauc plots are built from the square root of the product of absorption (Abs) and light energy (hν) as a function of light energy (hν). Extrapolation of the linear regime of the resulting curve to the X axis affords the band-gap value. In the case of two- and three-redox centre TAAs these values were found to be 3.1 and 3.0 eV respectively.

Cyclic voltammetry (CV) studies revealed the expected electrochemical behaviour for all two- and three- redox centre triarylamines, *i.e.* the presence of two and three reversible oxidation peaks respectively as shown in **Figure 129**. Importantly, from these data, we can calculate the HOMO level of our TAA derivatives by determining the redox potential ($E_{1/2}$)

335. Hwang, S.-W. & Chen, Y. Photoluminescent and Electrochemical Properties of Novel Poly(aryl ether)s with Isolated Hole-Transporting Carbazole and Electron-Transporting 1,3,4-Oxadiazole Fluorophores. *Macromolecules* **35,** 5438–5443 (2002).

for the first oxidation peak with respect to vacuum, using an internal ferrocene (Fc) standard as a reference. In our studies, ferrocene strongly interferes with almost all of the triarylamines, as its redox potential is located in the same region as the first oxidation peak of TAAs, therefore we use decamethyl ferrocene (DmFc) instead as its redox potential is located near 0 V. The electrochemical data for all studied compounds are summarised in **Table 3**. The redox potentials for two centre TAAs range from -5.27 V to -5.25 V (*vs* vacuum), which correspond to the HOMO energy level from -5.15 to -5.18 eV. For the three centre TAAs the redox potential for the first oxidation peak is slightly higher –ranging from -5.14 to -5.18 V (*vs* vacuum), and corresponding to HOMO energy level located between -5.04 and -5.07 eV. Interestingly, for the control molecule **38**, with four benzyloxy groups, the HOMO level was found to be the highest one at -4.94 eV. Comparing this value with one recorded for **50** TAA, suggests that the alkoxy groups are stronger electron donors than the amide groups, rendering molecule **38** more easily prompt to oxidation.

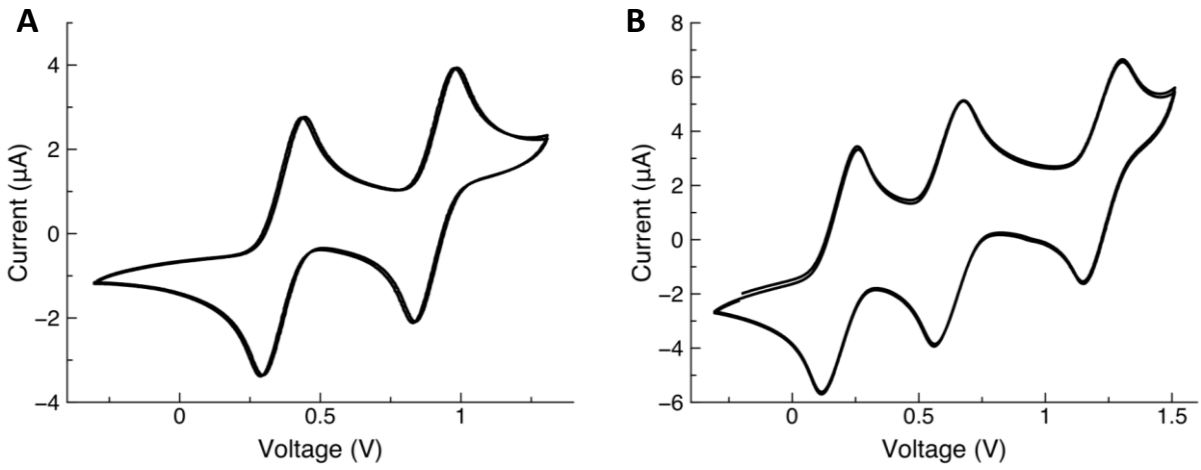

Figure 129 | Cyclic voltammograms of (**A**) two- and (**B**) three redox-center TAA derivatives **43** and **57** respectively in TCE at a concentration of 0.1 mM in TCE with 0.1 M TBAHPF as electrolite at a scan rate of 100 mV/s.

Compared with the HOMO energy levels recorded for the first and second generations of triarylamines (see chapter V), which range from -5.7 to -5.6 eV and to the valence band of the perovskite located at -5.44 eV, the HOMO levels of both two and three redox centre TAAs match the level of the valence band of perovskite and thus, their application as HTMs can be considered. The LUMO levels were calculated from the HOMO levels obtained by CV experiments and the band-gap values retrieved from the Tauc plots.

Table 9 | Summarised electrochemical data for the HTMs candidates

Compound	E_{Onset}[a] V	$E_{1/2}$ vs Fc[b] V	$E_{1/2}$ vs Vac[c] V	HOMO[d] eV	LUMO[e] eV
38	0.187	-0.051	-5.254	-4.94	---
43	0.342	-0.036	-5.268	-5.16	-2.06
52	0.407	-0.058	-5.246	-5.15	-2.05
47	0.422	-0.052	-5.252	-5.18	-2.08
50	0.358	-0.031	-5.274	-5.16	-2.06
57	0.315	-0.135	-5.169	-5.05	-2.05
69	0.310	-0.168	-5.137	-5.06	-2.06
64	0.302	-0.139	-5.165	-5.07	-2.07
67	0.289	-0.120	-5.184	-5.04	-2.04
TAA-BTA	0.642	0.252	5.556	-5.41	---

[a] Position of E_{Onset} corresponds to the minimal energy needed to eject an electron from molecule. It is obtained at the intersection of a baseline with the tangent build to the slope of the oxidation peak; [b] $E_{1/2}$ defines the redox potential of the compound, as a potential at which the ratio between oxidised and reduced form is 1 to 1. It is calculated as a median between oxidation and reduction peaks and its position is referred to an internal standard or standard electrode; [c] Redox potential of a Fc/Fc^+ couple is below the vacuum level for 4.8 eV. [d] HOMO is calculated as: HOMO = - (E_{Onset}Ox *vs* Fc) – 4.8 eV. [e] LUMO level can be calculated using the onset of reduction peak or the optical bandgap oncet.

Interestingly, the HOMO levels of the two redox centre TAAs are comparable to the HOMO levels of known compounds such as ***k*** (**Scheme 14**), ***q*** and ***r*** (**Figure 125**) (-5.15, -5.13 and -5.14 eV respectively), ***l*** (-5.15 eV) (**Figure 124**); three centre TAAs (-5.04 – -5.07 eV) with tetrathiafulvalene (***t***) (-5.05 eV) (**Figure 126**). The LUMO levels for both two and three centre TAAs is almost the same as for *spiro*-OMeTAD (-2.05 eV/-2.28 eV).[336]

Overall, the determination of these HOMO levels and their comparison with promising compounds, already reported in the literature, suggest the potential of our TAA derivatives for use in perovskite solar cells.

C. Self-Assembly in Solution

We then studied the self-assembling properties of out TAA candidates for use as HTMs. NMR studies in chloroform revealed the classic behaviour observed for self-assembling TAAs upon light irradiation, namely a significant broadening and flattening of the signals corresponding to the aromatic core, thus indicating the possible self-assembly of all studied molecules (**Figure 130**). Interestingly, the control compound **38** was without amide

336. Here, however there is a small confusion, because some authors report value for LUMO as -2.05 eV and others as -2.28 eV. What is even more confusing, that in the same review articles these values can be found simultaneously!

groups was found to self-assemble upon light irradiation with a 405 nm LED, in agreement with the higher HOMO level determined by CV experiments (**Figure 130A**) However, it should be noted that the broaden NMR spectra recorded for molecules **50** and **67** with amide groups without light irradiation might indicate partially assembled systems.

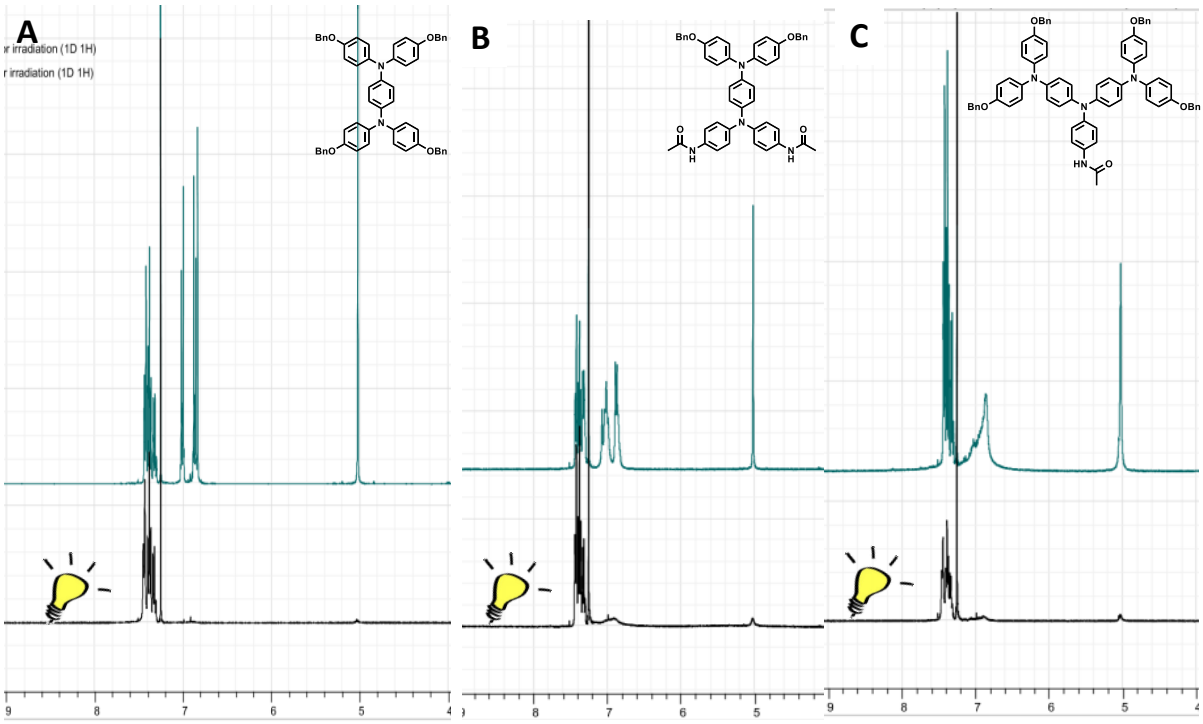

Figure 130 | NMR spectra recorded for different benzyloxy-substituted TAA derivatives in $CDCl_3$. Before irradiation with light (blue line) and after 30 s irradiation (black line) (**A**) Control tetrabenzyloxy two redox center compound **38**. (**B**) Two redox center TAA derivative **50**. (**C**) Three redox center TAA derivative **67**.

Each of the studied compound also underwent photoinduced oxidation in chlorinated solvents. **Figure 131** represents the evolution of the absorption of 0.05 mM solutions of **43** and **57** in tetrachloroethane upon irradiation with a 390 nm LED light for 30 seconds. For both compounds, the decrease in the intensity of absorption of the band near 340 nm, which corresponds to the neutral molecules, was observed together with the appearance of an intense charge transfer band in the near infra-red region (with absorption maximum near 1100 nm and 1350 nm for **43** and **57** respectively), indicating the formation of an intramolecular mixed-valence state after oxidation of one nitrogen centre to its corresponding radical cation. Taking into account, that the charge transfer band reaches its maximum upon irradiation and does not decrease upon further irradiation, one can assume that photo-induced oxidation occurs only once for the process: $TAA \rightarrow TAA^{\bullet+}$ and does not go further.

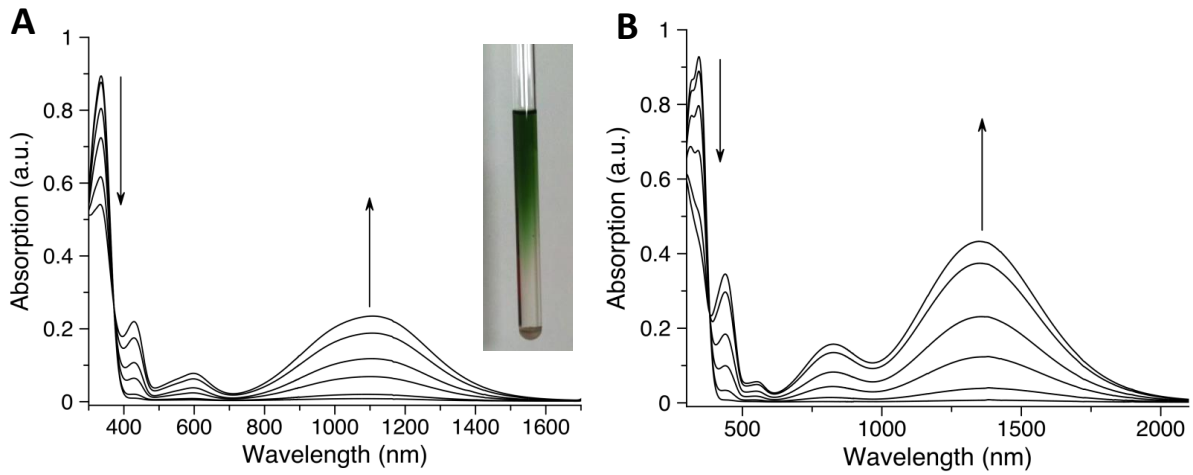

Figure 131 | UV-Vis-NIR spectra of methoxy substituted (**A**) two redox center TAA **43** and (**B**) three redox center TAA **57** in tetrachloroethane at a concentration of 0.05 mM upon light irradiation. The arrows indicate the increase/decrease in the intensities of absorption bands. The inset in (**A**) shows a photograph of an NMR tube of compound **43** in chloroform, the solution in upper part of the tube was irradiated with daylight, and the bottom part was covered with aluminium foil, clearly indicating the photooxidation in the upper part.

Further investigation of these solutions by TEM revealed the presence of fibril self-assemblies (**Figure 132**). Aggregates were observed also for the control molecule **38**; however, in this case, the structure of these aggregates seemed quite amorphous (**Figure S20**).

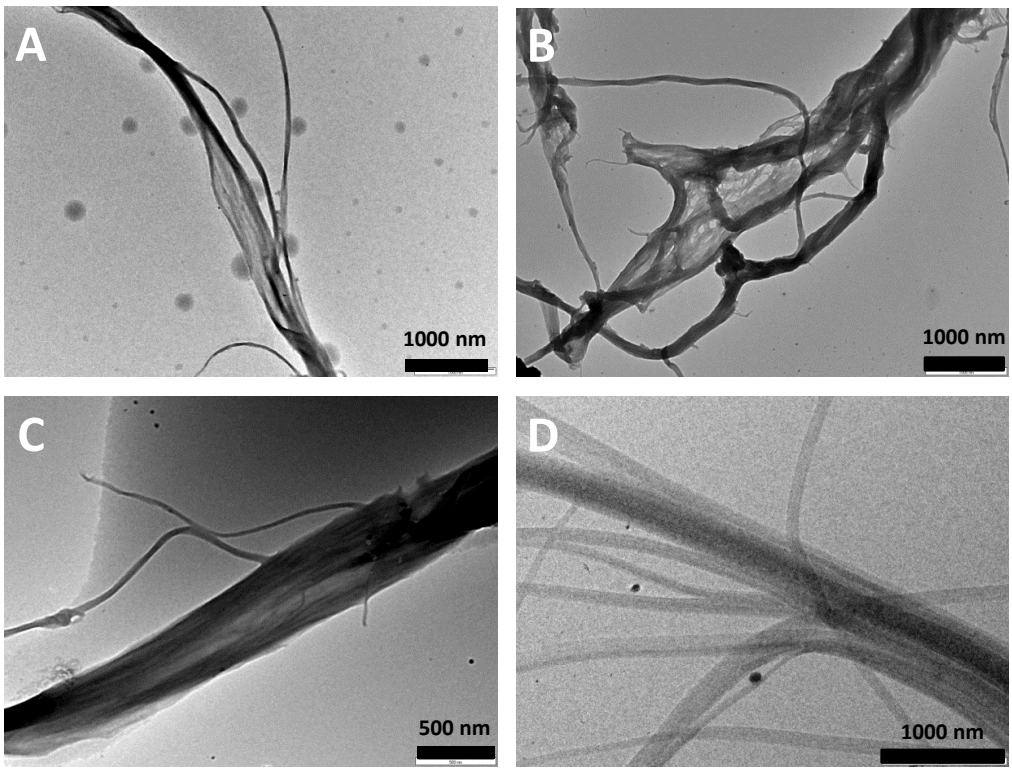

Figure 132 | TEM images of self-assemblies obtained from 1 mM chloroform solutions for **47** (**A**), **50** (**B**), **57** (**C**) and **64** (**D**).

D. Solar Cell Performance

Firstly, triarylamines with octyloxy substituent were evaluated in perovskite solar cells in collaboration with BASF R&D laboratory in Ludwigshafen, Germany. The cells were built as such (**Figure 133A**): ***a***) conductive fluorine-doped tin oxide (FTO) was deposited on a patterned glass substrate, followed by deposition of a compact layer of TiO_2 playing the role of a hole-blocking material; ***b***) lead(II) iodide perovskite in DMF was then spin coated on the prepared substrate, and ***c***) after drying, the studied HTM either in tetrachloroethane or chlorobenzene was deposited on the top of the perovskite layer, followed by final deposition of a thin film gold electrode by evaporation.

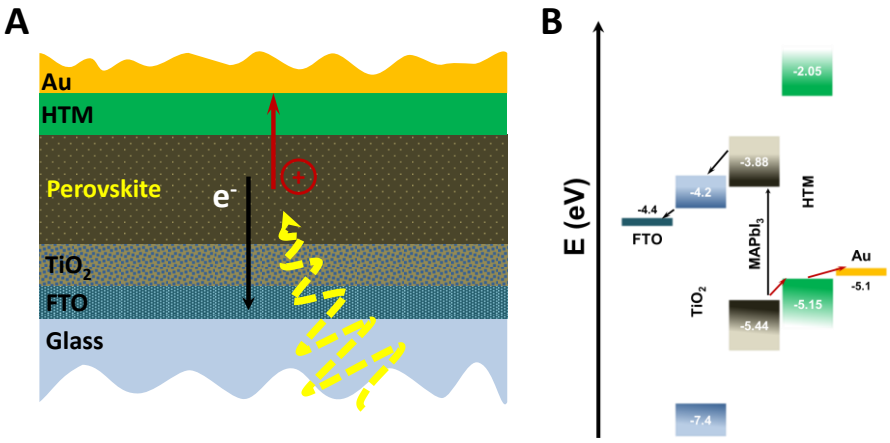

Figure 133 | (**A**) Scheme of the perovskite solar cell device with planar architecture, used to study TAA derivatives as HTMs. (**B**) Energy level diagram of a perovskite solar cell buit from **52** as example of HTM.

The HTM layer was prepared either from chlorobenzene or tetrachloroethane with chemical doping (LiTFSI, *t*BP), photo-initiated doping, or without any dopant.

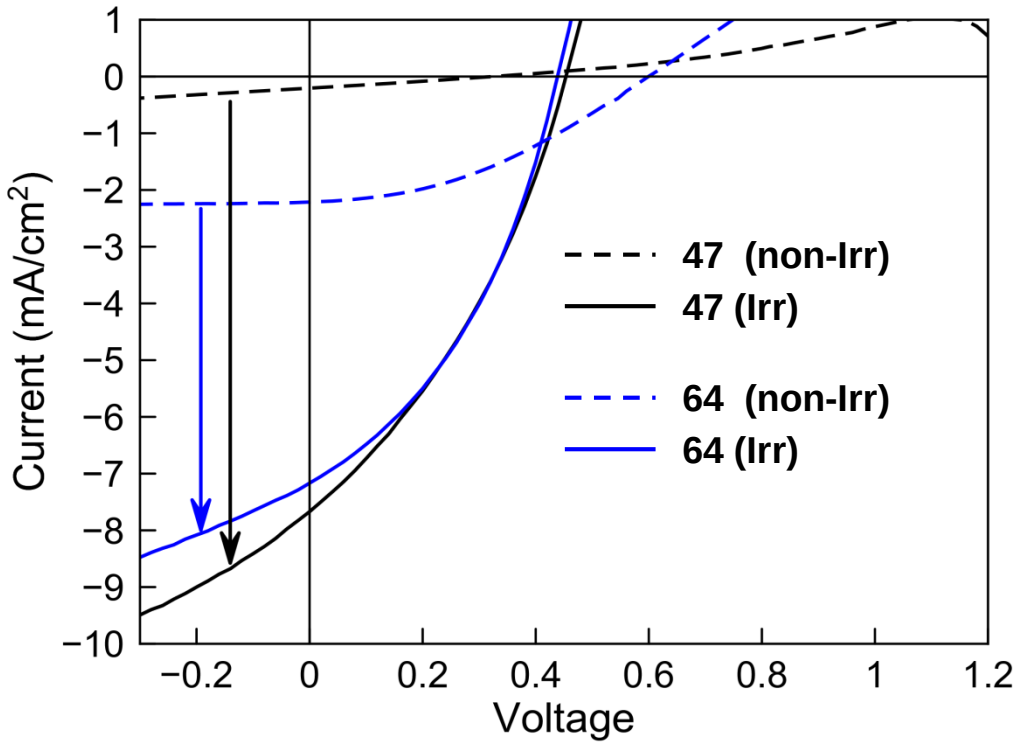

Figure 134 | I-V curve of the perovskite photovoltaic devices with incorporated two redox center TAA **47** (black lines) and three redox center TAA **64** (blue lines) as HTMs. Arrows indicate the improvement of the performance of the device when using photo-doped TAAs (solid lines) in comparison with undoped ones (dashed lines).

The performance of the solar cells with the addition of dopant was poor. The best PCE results were obtained for the solar cells built with HTMs prepared in tetrachloroethane by photo-induced doping, as demonstrated in **Figure 134**. When deposited from chlorobenzene, no dependence on the irradiation was observed. However, the efficiency for compound **64** deposited from tetrachloroethane doubled after photo-oxidation from 0.5% to 1.0% (**Table 10**). For TAA **47**, 10% of methanol was used to completely dissolve the material in the tetrachloroethane. Importantly, the results improved from a nonfunctioning device without irradiation to a device with a PCE of 1.1%. Nevertheless, these data are far from the PCE recorded for solar cells prepared in the same batch with *spiro*-MeOTAD (8.5%).

Table 10 | Characteristics of the performance of photovoltaic devices, incorporating octyloxy substituted TAAs

Compound in TCE	I_{sc} (mA/cm^2)	V_{oc} (mV)	FF (%)	PCE %
***spiro*-OMeTAD**	-16.04	780	63	8.5
47 non-irr	-0.29	520	30	0
64 non-irr	-3.36	540	35	0.5
47 irr	-7.17	440	39	1.1
64 irr	-7.67	460	34	1.0

Analyses of these data suggest that the fill factor is quite low, compared to *spiro*-MeOTAD, indicating problems with charge transport.

Tests on other molecules were performed in collaboration with Dr. P. Gratia from the group of Prof. Grätzel and Prof. Nazeeruddin in EFPL in Switzerland using the same type of cell architecture.

First, we tested the solubility of our compounds in chlorobenzene and tetrachloroethane at a standard concentration of 60 mg/mL. Unfortunately, compounds **43** and **57** bearing methoxy substituents as well as compound **52** with butyloxy substituents had solubility problems in these solvents at such high concentrations and even the addition of up to 10% methanol could not improve the situation. The high crystallinity of these TAAs makes them bad candidates for use in devices. The control molecule **38** had a very good solubility, but formed a poor quality film and the device showed poor performance related to current extraction problems.

The solubility of benzyloxy compounds **50** and **67** was good enough to prepare films with good quality. Remarkably, these devices showed PCEs as high as 7.5% and 5.7% TAAs **50** and **67** respectively without the use of any additives (**Figure 135** and **Table 11**). For compound **50** the performance of the device did not depend on photo-doping, however strong dependence was observed for the thickness of the HTM layer. Devices prepared with less concentrated solution performed better, with a PCE of 2.6% *vs* 7.5% for 60 mg/mL and 30 mg/mL concentrations, respectively. For compound **67**, the performance increased both with photo-doping and with decreasing concentration.

Table 11 | Characteristics of the performance of photovoltaic devices, incorporating benzyloxy substituted TAAs

Compound in TCE	I_{sc} (mA/cm^2)	V_{oc} (mV)	FF (%)	PCE %
Spiro-OMeTAD	---	---	75	15.5
50 non-irr 30 mg	18.3	947	39	7.0
50 irr 30 mg	18.8	936	42	7.5
50 non-irr 60 mg	11.7	881	22	2.3
50 irr 60 mg	12.8	882	22	2.6
67 irr 30 mg	17.0	890	33	5.0
67 non-irr 60 mg	12.7	859	24	2.7
67 irr 60 mg	17.3	914	36	5.7

Analysis of the I-V curves confirmed what was observed for octyloxy TAAs **47** and **64** *i.e.* low fill factor value, confirming problems of charge transport. We suggest that series resistances are the main reason for the low fill factor observed, indicating that the conductivity of the material is quite low. Better performance for thinner films confirms this hypothesis.

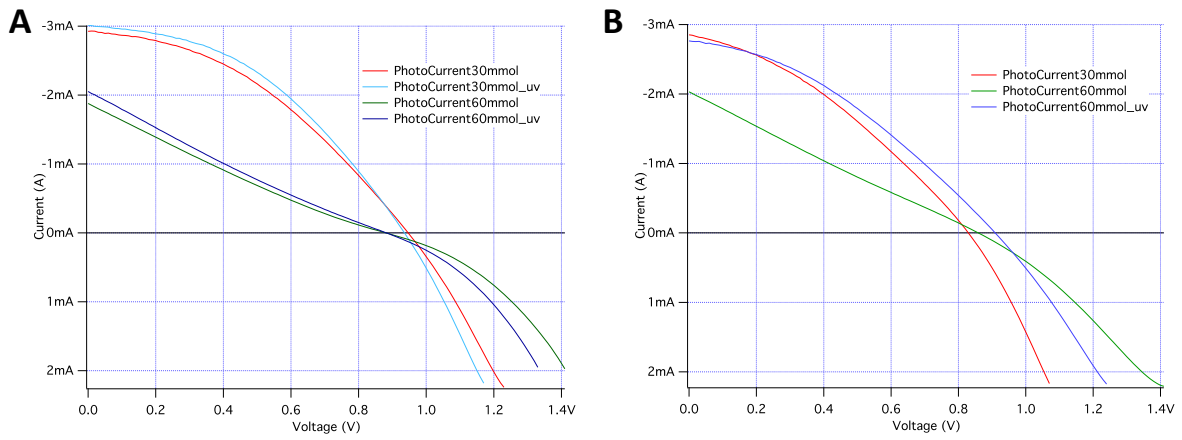

Figure 135 | The I-V curves for the benzyloxy substituted TAAs. (**A**) Two redox center TAA **50** and (**B**) three redox center TAA **64**.

4. CONCLUSION AND PERSPECTIVES

We have developed a series of TAA derivatives incorporating several redox centres included in the aromatic system. While these molecules retain their self-assembling properties upon light irradiation, CV experiments have shown that these TAAs could be suitable in terms of energy levels for use as HTM in perovskite solar cells.

So far, we have demonstrated that TAAs, having an appropriate energy level can be used as HTMs in perovskite solar cells without any additives. We also found that photo-doping increases the performance of the devices. Although PCE as high as 7.5% could be recorded for same derivatives, all the synthesised molecules could not outperform the performance of gold standard in these cells.

Furthermore, one of our main questions yet remains unanswered, whether the self-assembly process has any influence on the PCEs of the devices. We are planning now to build photovoltaic cells using deposition of our HTMs from solvents where our TAAs do not assemble, such as THF, and to compare the performance of these devices with those built using standard procedures.

CHAPTER V.
SPATIALLY ADDRESSED SUPRAMOLECULAR POLYMERIZATION OF TRIARYLAMINES IN AN ELECTRIC FIELD

1. INTRODUCTION

Detailed mechanistic studies and analyses on the self-assembly process of the first generation of TAAs have demonstrated that a critical amount of radicals (above a critical concentration of 10 nM), generated by photo- or chemo-oxidation (using tetrabromobenzoquinone for instance), triggers the supramolecular polymerisation of TAAs into conductive nanowires.[81–83] Moreover, we proved that the quantities of radical cation nuclei can be tuned using different light sources leading to the control of the morphology of TAA-based nanostructures.[114]

We were also curious to know whether it would be possible to induce and control the self-assembly of TAAs by using an electric current, as the oxidant. Indeed, electrochemical methods find large number of applications in different fields of science and technology such as galvanoplasty, electrolysis (production of different materials and compounds such as aluminium *etc.* or electrochemical synthesis of compounds with exotically high oxidation states for example) because electricity is the most powerful oxidant, but at the same time, it is the strongest reducing agent known. Moreover, electrochemistry allows the manipulation of very delicate substances,[337] due to the technical possibility to easily control various parameters of the electric current such as type, field strength, density of current, *etc.* In the field of organic electronics, electrochemistry was successfully used to build various covalent conductive polymers such as polyanilines, polithiophenes, polypyrenes, polypyrroles.[338–341]

337. Selectively oxidize/reduce compound having similar redox potentials.
338. Diaz, A. F., Kanazawa, K. K. & Gardini, G. P. Electrochemical polymerization of pyrrole. *J. Chem. Soc. Chem. Commun.* 635 (1979). doi:10.1039/c39790000635
339. Bachman, J. C. *et al.* Electrochemical polymerization of pyrene derivatives on functionalized carbon nanotubes for pseudocapacitive electrodes. *Nat. Commun.* **6,** 7040 (2015).
340. Wang, B., Tang, J. & Wang, F. Electrochemical polymerization of aniline. *Synth. Met.* **18,** 323–328 (1987).
341. Wei, Y., Chan, C. C., Tian, J., Jang, G. W. & Hsueh, K. F. Electrochemical polymerization of thiophenes in the presence of bithiophene or terthiophene: kinetics and mechanism of the polymerization. *Chem. Mater.* **3,** 888–897 (1991).
342. Peng, L. *et al.* Electrochemical redox responsive supramolecular self-healing hydrogels based on host–guest interaction. *Polym. Chem.* **6,** 3652–3659 (2015).
343. Feng, A., Yan, Q., Zhang, H., Peng, L. & Yuan, J. Electrochemical redox responsive polymeric micelles formed from amphiphilic supramolecular brushes. *Chem. Commun.* **50,** 4740 (2014).
344. Guo, D.-S. & Liu, Y. Calixarene-based supramolecular polymerization in solution. *Chem. Soc. Rev.* **41,** 5907 (2012).

Yet, there are only a handful of examples of electrochemically triggered supramolecular polymerisations in literature.[342–344] In these examples the supramolecular polymer form due to host-guest interactions, which can be influenced by electrochemical stimuli, by changing the association constant between host and guest upon their oxidation/reduction.

In this chapter, we report on a successful collaborative work with Dr. T. Ellis (former post-doctoral researcher in SAMS Group), Dr. J.J. Armao IV (former PhD student in the SAMS Group) and Dr. D. Martel (permanent researcher in the institute) on the electrochemically induced supramolecular polymerisation of mono-amide-TAA. Moreover, we will demonstrate the possibility to use the DC electric field for the *in situ* macroscopic alignment of TAA nanofibers between gold microelectrodes of different morphologies.

2. BIBLIOGRAPHY

A. Generalities

The controlled placement of unidirectional supramolecular structures is of a high fundamental and practical interest due to their potential application in material sciences especially in organic electronics.[345] A high degree of order at the nano- and micro- levels is expected to produce materials with unique mechanical, optical and electronic properties.[345,346] Different methodologies have been developed to induce ordering of polymeric, inorganic and supramolecular materials. For instance, nanoimprint lithography, liquid crystal assisted alignment, geometry restricted evaporation induction, magnetic and electric field inductions, are the most popular.[345]

The electric field induced alignment is of a great practical interest, as it should allow to address nanostructures in a controlled way, directly between the electrodes. In the following section, we will show how the electric field has so far been used to induce order in supramolecular systems.

B. Electric Field Induction of Order

Manipulation and alignment of anisotropic objects by dielectrophoretic forces induced by electric field have been used to arrange different types of objects: metallic nanoparticles and nanorods, various inorganic nanoparticles and nanowires, as well as organic molecules such as covalent and supramolecular polymers.[345,347–349] The majority of these examples, however, describe the *manipulation* of already existing nanoobjects using electric fields, and there is a couple of examples reporting on the use of electric field to align 1D supramolecular structures.[345] Additionally, in recent decades, a few examples have been published regarding the *in situ* formation of supramolecular structures under electric fields. In this chapter, we will cover all the known examples of electric field induction of order in supramolecular systems, classifying them in two groups:

(***i***) Electric field manipulation of already formed supramolecular structures

(***ii***) Electric field directed *in situ* self-assembly

i. Electric Field Manipulation

Manipulation of neutral objects by the non-uniform electric field is called dielectrophoresis.[350,351] Dielectrophoresis occurs due to polarization of the object (nanoparticle, nanowire or even living cell), caused by the field inhomogeneity and it is widely used for microscopic manipulation of small objects in biomedical field[352] for cell separation or in electronics for bridging of electrodes with nanowires when constructing single-wire transistors.[347,353–355] Usually these nanowires are constructed from metals, inorganic semiconductors, nanotubes or polymer molecules. However, several groups report on the dielectrophoretic alignment of supramolecular objects for application in electronics or electrochromic devices and in this section we will discuss the recent developments in this field.

1) Supramolecular Systems in Organic Media

To our knowledge, the first example of alignment of supramolecular structures by an electric field was reported by Stupp and co-workers.[356,357] It was shown[358], that so called dendron rodcoil molecules, DRC (***a***)[359], represented on the **Figure 136A**, self-assemble in various organic solvents (such as toluene, for example) to form organogels at low concentrations. Morphology investigations and theoretical studies suggest that primarily formed head-to-head ***a*** dimers assemble further into long nanoribbons, due to strong π-π stacking of the rod-like parts.

345. Su, B., Wu, Y. & Jiang, L. The art of aligning one-dimensional (1D) nanostructures. *Chem. Soc. Rev.* **41,** 7832 (2012).
346. Moulin, E., Cid, J.-J. & Giuseppone, N. Advances in supramolecular electronics - from randomly self-assembled nanostructures to addressable self-organized interconnects. *Adv. Mater.* **25,** 477–87 (2013).
347. Freer, E. M. *et al.* High-yield self-limiting single-nanowire assembly with dielectrophoresis. *Nat. Nanotechnol.* **5,** 525–530 (2010).
348. Jiang, L., Dong, H. & Hu, W. Controlled growth and assembly of one-dimensional ordered nanostructures of organic functional materials. *Soft Matter* **7,** 1615–1630 (2011).
349. Brown, D. A. *et al.* Electric Field Guided Assembly of One-Dimensional Nanostructures for High Performance Sensors. *Sensors* **12,** 5725–5751 (2012).
350. Barnaby, E., Bryant, G. & Wolfe, J. What is 'dielectrophoresis'? *J. Electroanal. Chem. Interfacial Electrochem.* **253,** 347–352 (1988).
351. Lapizco-Encinas, B. H. & Rito-Palomares, M. Dielectrophoresis for the manipulation of nanobioparticles. *Electrophoresis* **28,** 4521–4538 (2007).
352. Pethig, R. Dielectrophoresis: Status of the theory, technology, and applications. *Biomicrofluidics* **4,** 022811 (2010).
353. Boote, J. J. & Evans, S. D. Dielectrophoretic manipulation and electrical characterization of gold nanowires. *Nanotechnology* **16,** 1500–1505 (2005).
354. Raychaudhuri, S., Dayeh, S. A., Wang, D. & Yu, E. T. Precise Semiconductor Nanowire Placement Through Dielectrophoresis. *Nano Lett.* **9,** 2260–2266 (2009).
355. Li, J., Zhang, Q., Yang, D. & Tian, J. Fabrication of carbon nanotube field effect transistors by AC dielectrophoresis method. *Carbon N. Y.* **42,** 2263–2267 (2004).
356. Messmore, B. W., Hulvat, J. F., Sone, E. D. & Stupp, S. I. Synthesis, Self-Assembly, and Characterization of Supramolecular Polymers from Electroactive Dendron Rodcoil Molecules. *J. Am. Chem. Soc.* **126,** 14452–14458 (2004).
357. Li, L. *et al.* Assembling a lasing hybrid material with supramolecular polymers and nanocrystals. *Nat. Mater.* **2,** 689–694 (2003).
358. Zubarev, E. R., Pralle, M. U., Sone, E. D. & Stupp, S. I. Self-assembly of dendron rodcoil molecules into nanoribbons. *J. Am. Chem. Soc.* **123,** 4105–4106 (2001).
359. DRCs, are amphiphilic molecules, consisting of three parts: a polar dendron moiety (1st generation of 3,5-dihydroxy benzoic ester dendritic segment), a rigid rod-like part (aromatic rings) and a flexible third part (various feasible coil-like segments).

Casting the preformed assemblies from toluene solutions under an alternating current (AC) electric field resulted in the formation of a birefringent film, consisting of supramolecular nanostructures (**Figure 136B**). The authors speculate that in the electric field, the nanostructures become charged and start to oscillate due to the electrophoresis. Shear forces cause the alignment of the ribbons parallel to the electric field, as observed by OPM. On the contrary, the film produced from a THF solution, where ***a*** are molecularly dissolved, led to amorphous structure. Interestingly, the conductivity of the film, produced from a toluene solution, was three orders of magnitudes higher than the film obtained from THF. The authors explain this observation by a better π orbital overlap between the molecules within preformed supramolecular structures. Direct observation by AFM (**Figure 136C**) also confirmed the alignment of ***a*** fibres along the lines of electric field.

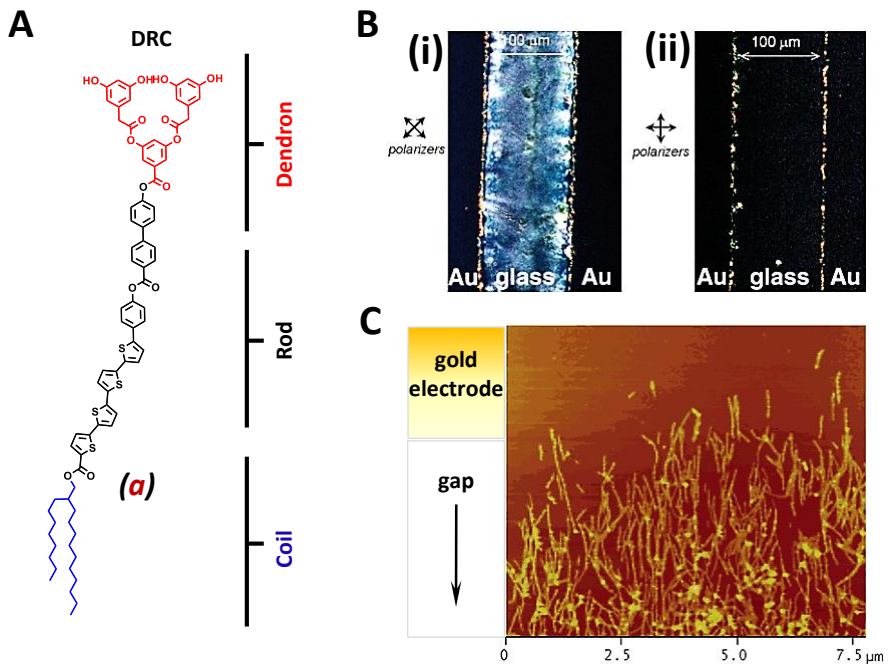

Figure 136 | (A) Structure of a tetrathiophene member (***a***) of the DRC family of molecules. (**B**) OPM image of a *a* film aligned in an AC electric field. Rotation of a sample by 45° along the optical axis causes the bright sample (**i**) to switch to dark (**ii**) indicating uniaxial orientation of the optical axis of the film. (**C**) AFM image of aligned ribbons of ***a*** on Au/Cr patterned mica substrate. The diagram (left) depicts where the edge of the gold electrode begins on the substrate. Ribbons are aligned in the gap. Figure was adapted from ref. 356

Co-assemblies of DRCs with ZnO nanorods were also successfully aligned using a similar approach.[357]

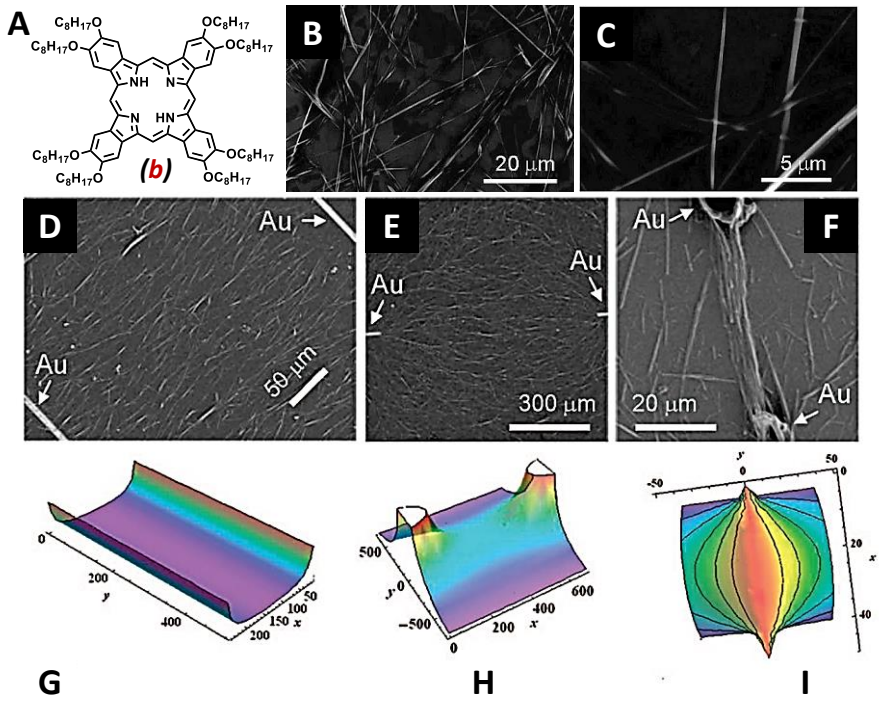

Figure 137 | (**A**) Molecular structure of the studied phtalocyanine (***b***). (**B, C**) SEM images of fibres obtained during ***b*** self-assembly in dodecane. (**D – F**) SEM images of ***b*** nanofibres drop-cast onto the surface with applied inhomogenous electric field in one or two directions, generated by patterned Au electrodes. The respective calculated geometries of electric fields (**G, H**) between the two Au electrodes of the two shapes are shown. Figure **I** represents the electric field in the geometry as in figure **H**, however the strength of the electric field was normallized to the central line connecting the two electrodes. The strength of the electric field is given in arbitrary units and the length x,y are in microns. Figure is adapted from ref. 360

In another example, Duzhko at al.[360,361] reported on the alignment of supramolecular fibres made of discotic phtalocyanine (***b***) derivative under an applied direct current (DC) electric field (**Figure 137**). These PCs assemble into long fibres upon cooling a hot dodecane solution. When preformed fibres were drop-casted on the surface with inhomogeneous electric field, created between gold electrodes of different geometrics, alignment of the nanofibers along the lines of the electric field was clearly observed in all cases. Experimental observations of alignment pattern are in good agreement with the calculations of the electric field intensity map between the electrodes which is represented on the **Figure 137**(**D – I**).

Interestingly, if the alignment was carried out during illumination with light, a significantly larger number of nanofibers was found in the area between the electrodes. Furthermore, the degree of order during alignment upon illumination was much higher than

360. Duzhko, V., Du, J., Zorman, C. A. & Singer, K. D. Electric field patterning of organic nanoarchitectures with self-assembled molecular fibers. *J. Phys. Chem. C* **112,** 12081–12084 (2008).
361. Duzhko, V. & Singer, K. D. Self-Assembled Fibers of a Discotic Phthalocyanine Derivative: Internal Structure, Tailoring of Geometry, and Alignment by a Direct Current Electric Field. *J. Phys. Chem. C* **111,** 27–31 (2007).

when alignment was performed in dark. The authors suggest that this effect takes place due to an efficient spatial separation of the photogenerated charges within PC self-assemblies in the electric field, which is a dominant mechanism under illumination. Indeed, charge separation induces the formation of a dipole moment, thus increasing the energy of interaction between the fibres and the field. On the other hand, in the dark, the separation and distribution of thermally generated charges together with the polarisation in the electric field preferentially takes place, but this effect is less pronounced. The authors claim that this approach allows easy manipulation of nanofibers, which was illustrated by the deposition of a single ***b*** nanofiber between two gold electrodes within a 7 μm gap.

In a similar way, self-assembled amyloid peptide nanotubes (SAPNT) were manipulated and immobilized on gold electrodes using dielectrophoretic forces, under an electric field.[362] For this purpose, a dielectrophoretic four-contact microchip was fabricated by optical lithography. By tuning the parameters of the electric field (frequency and amplitude) both single as well as a bundle of SAPNTs were manipulated and placed between the electrodes. The authors propose to use this method to study the electric properties of bionanoassemblies and to use them in bioelectronic devises such as biosensors and field-effect transistors.

A very interesting and quite unique example was reported by Kuwahara *et al.*,[363] who took advantage of the electric field to control the alignment of organometallic supramolecular polymers (**Figure 138**). A diruthenium complex was used as building block, bridged with halogen atoms whereas gallate units decorated with fatty chains were utilized as ligands, rendering the ruthenium complex soluble in organic media, such as decane, cyclohexane or toluene.

Both chlorine (***c***) and iodine (***d***) bridged coordination polymers were found to form lyotropic liquid crystals in decane and to respond to an applied AC electric field. Without the electric field, the *n*-decane dispersion of both polymers were transparent to light, due to the birefringence of the liquid crystalline phase. Conversely, when an AC electric field was applied, the area between the ITO electrodes became dark, indicating the perpendicular orientation of the polymer chains to the ITO electrodes *i.e.* parallel to the lines of the electric field.

362. Castillo, J., Tanzi, S., Dimaki, M. & Svendsen, W. Manipulation of self-assembly amyloid peptide nanotubes by dielectrophoresis. *Electrophoresis* **29,** 5026–5032 (2008).
363. Kuwahara, R., Fujikawa, S., Kuroiwa, K. & Kimizuka, N. Controlled Polymerization and Self-Assembly of Halogen-Bridged Diruthenium Complexes in Organic Media and Their Dielectrophoretic Alignment. *J. Am. Chem. Soc.* **134,** 1192–1199 (2012).

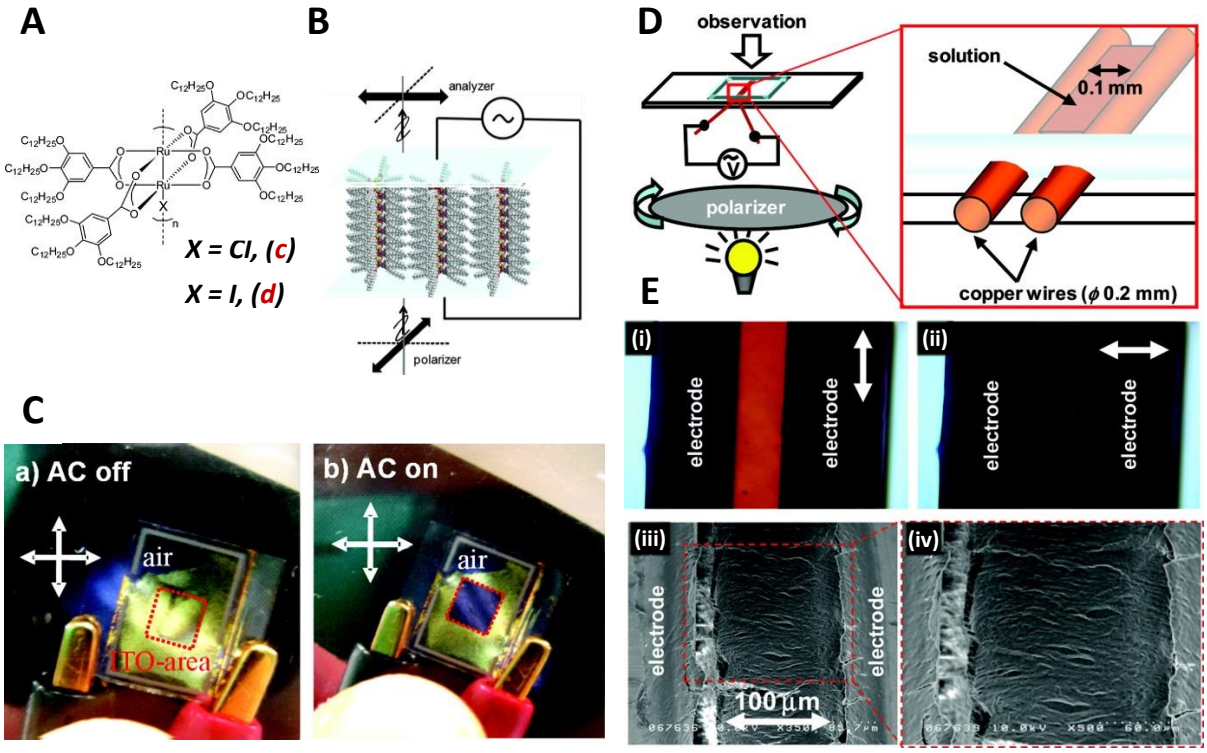

Figure 138 | (**A**) Chemical structure of the diruthenium unit which composes the 1D coordination polymer. (**B**) Schematic representation of the polymer alignment along the lines of the electric field, parallel to the ITO electrodes. (**C**) Photographs of the ITO cell filled with a dodecane suspension of the bridged containing polymer under polarised light, before the AC field was applied (left), and under the electric field (right). (**D**) Scheme of the alignement set-up between two copper electrodes. (**E**) Imaging of the self-assemblies between the electrodes (**i-ii**) OPM photographs (**iii-iv**) SEM image of freeze-dried sample. Figure is adapted from ref. 363

Orientation of the diruthenium coordination polymers was also achieved in two dimensions. An *n*-decane solution of ***c*** was placed between parallel-oriented copper electrodes with a gap of 100 µm. Due to the dynamic nature of the studied coordination polymers, the immobilization of the aligned structures directly in the set-up, by freeze-drying, allowed them to be imaged with SEM and to observe the effect of electric field on the alignment (**Figure** 138**(D,E)**).

2) Supramolecular Systems in Aqueous Media

Working with electric fields in aqueous media is quite challenging. Indeed, the low susceptibility of soft materials requires high electric fields, which may lead to multiple parasitic phenomena, when using electrodes immersed in an electrolyte, such as polarization, Faradaic reactions on the electrodes (causing fast degradation of the material), Joule heating and presence of convective flows.[364]

An elegant approach, originally developed by Michot and colleagues,[364] was recently used by the group of Kouwer[365] to align supramolecular fibres in an aqueous medium. Peptide amphiphile (***e***) represented on **Figure 139A** were shown to form long supramolecular polymers in water solutions, as demonstrated by TEM imaging (**Figure 139B**).

To circumvent possible problems associated with the work in aqueous media, the peptide self-assemblies (which have quite low dielectric susceptibility) were manipulated with the electric field through an intermediate (template) compound which has high level of electro-responsiveness in the isolated glass capillary (**Figure 139C**). This allows the use of high potentials without any secondary reactions, as the electrodes are not immerged in the solution.

Colloidal Goethite was chosen as such an anisotropic electrically responsive material. Goethite (α-FeO(OH)), the form of iron oxide which exists as board-shape nanoparticles (**Figure 139D**), and form nematic liquid crystalline phase in water at certain concentrations, was shown to align under electric field. When peptide assemblies were introduced in this system, anisotropic alignment of the fibres was observed parallel to the electric field, caused by the priory alignment of Goethite nanoparticles. Moreover, because of the anisotropy of the electric field, fibres migrated to the region with the strongest field (**Figure 139E**).

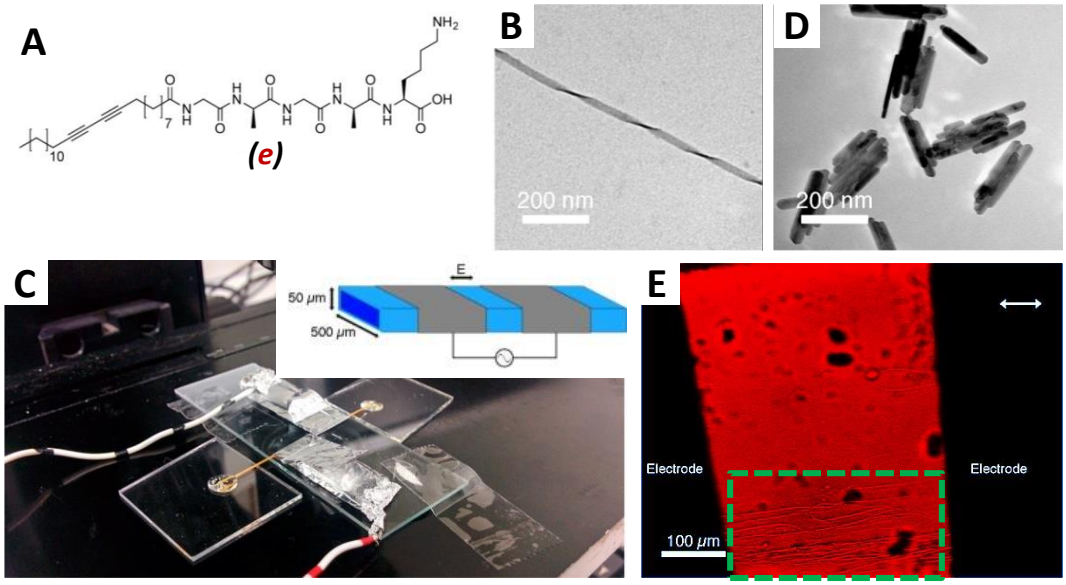

Figure 139 | (**A**) Molecular structure of studied peptide amphiphile (***e***). (**B**) TEM image of a nanoribbon formed from PA in 0.20 mg/mL water solution. (**C**) Photograph of the electric field capilary setup, installed under the microscope. The strips of aluminium foil are attached to the power source and function generator The inset shows a schematic representation of the set-up. (**D**) TEM image of Goethite nanoparticles. (**E**) OPM photograph of aligned nanofibres under an inhomogeneous electric field. Fibres migrated towards the stronger field at the bottom of the image. Figure is adapted from ref. 365

These examples highlight the possibility to use the electric field for alignment of organic and organometallic supramolecular self-assemblies both in organic solutions and even in aqueous media.

ii. Electric Field Directed In situ Self-Assembly

In comparison with electric field manipulation or electrophoresis, where already prepared objects are manipulated by the inhomogeneity of electric field, *in situ* construction of supramolecular aggregates deals with the electric field directed self-assembly. This approach proved useful when constructing conducting nanocircuits from self-assembling TAAs under light irradiation,[82] and could be used for similar proposes in organic micro and nano electronics. However, to the best of our knowledge, few examples have been reported on the exploitation of this approach.

In 2006 van Esch and co-workers[366] reported the first example of electric field directed *in situ* formation of aligned of supramolecular nanowires. A known gel-forming 1,3,5-triamide *cis*,*cis*-cyclohexane derivative (***f***) was chosen due to its properties to assemble in different organic solvents and in aqueous medium (**Figure** 140**A**).[367] The presence of three amide groups ensures the cooperative formation of hydrogen bonds with neighbouring molecules, causing ***f*** to self-assemble in long fibres (**Figure** 140**B**). The authors suggested that because of the dipolar nature of an amide group, supramolecular fibres, formed by means of the hydrogen bonds, should have large dipole moment, making them ideal candidates to study the influence of an electric field.

364. Dozov, I. *et al.* Electric-Field-Induced Perfect Anti-Nematic Order in Isotropic Aqueous Suspensions of a Natural Beidellite Clay. *J. Phys. Chem. B* **115,** 7751–7765 (2011).
365. van der Asdonk, P., Kragt, S. & Kouwer, P. H. J. Directing Soft Matter in Water Using Electric Fields. *ACS Appl. Mater. Interfaces* acsami.6b03910 (2016). doi:10.1021/acsami.6b03910
366. Sardone, L. *et al.* Electric-Field-Assisted Alignment of Supramolecular Fibers. *Adv. Mater.* **18,** 1276–1280 (2006).
367. Heeres, A. *et al.* Orthogonal Self-Assembly of Low Molecular Weight Hydrogelators and Surfactants. *J. Am. Chem. Soc.* **125,** 14252–14253 (2003).

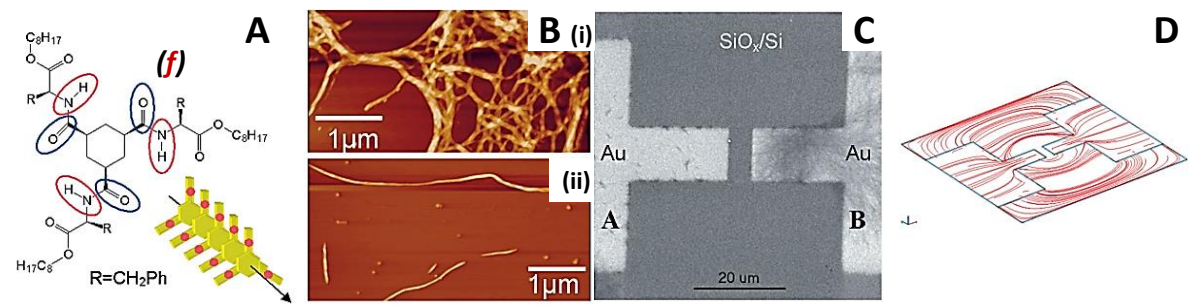

Figure 140 | (**A**) Chemical structure of CTG (***f***) and schematic representation of 1D supramolecular assembly, constructed by means of hydrogen bonds. (**B**) AFM images of ***f*** nano-fibres. (**C**) SEM image of the set-up and fibres, deposited on the right electrode. (**D**) Theoretical map of the electric field between the electrodes. Figure is adapted from ref. 366

In order to test this hypothesis, a hot solution of ***f*** in 1-octanol (where ***f*** exist in molecularly dissolved state) was cast on the electrode surface, under an applied DC electric field. The substrate was then gradually cooled below its sol-gel transition temperature. During the cooling process, nanofibers formed on the negatively charged electrode (**Figure 140C**). Statistical analysis of the SEM images proved that, the directionality of the growth occurs along the lines of the electric field (**Figure 140D**).

In order to understand the influence of molecular dipole moment on the alignments in an electric field, the group of Kato synthesized a set of self-assembling molecules (***g*** – ***k***), which form self-supportive thermoreversible fibrous organogels in various organic solvents (**Figure** 141**A**).[368] To test the alignment under an electric field, a gel in dodecylbenzene was heated to above the sol-gel transition to obtain a solution of molecularly dissolved molecules, which was deposit then between gold electrodes on the glass substrate. Then, the system was slowly cooled down below the sol-gel transition temperature under an applied electric field. For compounds ***g*** and ***k***, aligned fibres bridging the electrodes were formed under the application of an AC electric field (1.0 V/μm, 1 kHz) (**Figure 141D**), whereas without electric field, randomly entangled fibres were formed in the gap (**Figure 141E**). Interestingly, compound ***j*** did not form aligned structures under an electric field, probably due to the low dipole moment of ***j*** in comparison with ***i*** (**Figure 141F**). The influence of parameters related to the electric field was also studied. Alignment was observed for a magnitude of the electric field above 0.5 V/μm at a frequency of 1 kHz, and for frequencies ranging between 100 Hz and 10 kHz under the field of 1.0 V/μm. In contrast, when the self-assembly of ***g*** was carried out under a DC electric field, no alignment was detected.

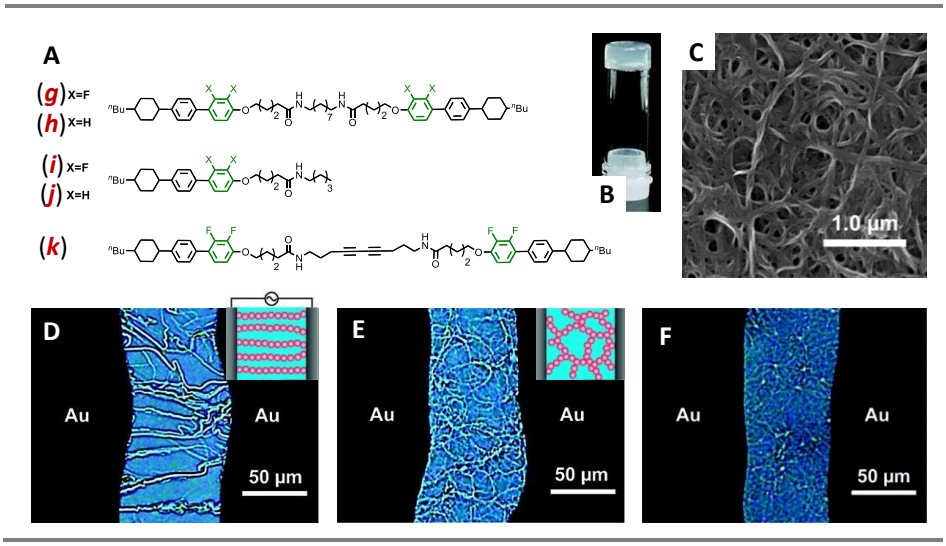

Figure 141 | (A) Molecular structure of studied compounds. (**B**) Self-supporting thermoresponsive organogel obtained from ***g*** in dodecylbenzene. (**C**) SEM image of supramolecular structures made of ***g*** formed during the self-assembling process. (**D-F**) Digital photographs of microscopy observations. (**D**) alignement of ***g*** nanofibres under an AC electric field. (**E**) Random growth of fibres made of ***g*** without electric field. (**F**) Image of the entangled ***j*** nanofibres under an electric field, showing no alignement. Figure is adapted from ref. 368

In other work, these authors successfully applied the previously described technique to obtained aligned nanostructures made of similar molecules (decorated with dithiophene moiety instead of cyclohexyl) between ITO glass electrodes *in situ*.[369] These assemblies exhibited photoconductive behaviour, showing a conductivity of 300 nA under a DC electric field upon irradiation with UV light. However almost no difference in photoconductivity was observed between aligned and randomly assembled structures.

As it was discussed in the bibliography chapter on self-assembling triarylamines, our group demonstrated the possibility to construct *in situ* nanocircuits made of supramolecular conducting fibres on the hundred nanometes scale.[82] In brief, the self-assemblies produced upon irradiation and under a DC electric field leads to spatially precise interconnections between gold electrodes with an outstanding conductivity.

As one can see, there are quite a limited number of works, reporting on the use of the electric field alignment of supramolecular structures. Moreover, there are even fewer examples of *in situ* construction of such structures under applied field. Having experience in aligning the conducting nanofibers between gold electrodes on the scale of 100 nm we were interested to extend this distance to a micrometre scale or beyond.

368. Yoshio, M., Shoji, Y., Tochigi, Y., Nishikawa, Y. & Kato, T. Electric Field-Assisted Alignment of Self-Assembled Fibers Composed of Hydrogen-Bonded Molecules Having Laterally Fluorinated Mesogens. *J. Am. Chem. Soc.* **131,** 6763–6767 (2009).
369. Shoji, Y., Yoshio, M., Yasuda, T., Funahashi, M. & Kato, T. Alignment of photoconductive self-assembled fibers composed of π-conjugated molecules under electric fields. *J. Mater. Chem.* **20,** 173–179 (2010).

3. RESULTS AND DISCUSSIONS

We chose the first generation TAA to study self-assembly induced electrochemically and to control the fibre growth with an electric field.

A. Synthesis

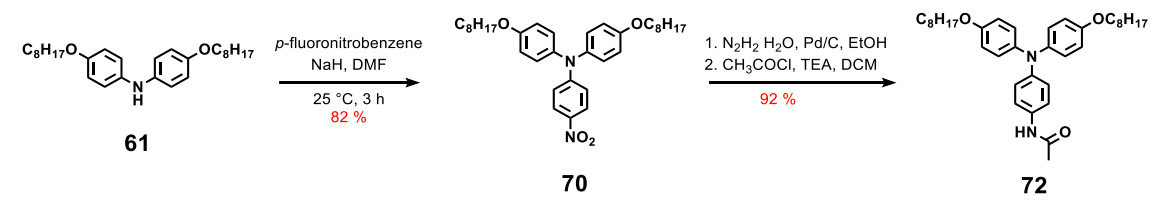

Scheme 20 | Scheme for the synthesis of triarylamine mono-amide, **72.**

The synthesis of TAA **72** was performed through the nitro derivative **70**, which was obtained *via* aromatic nucleophilic substitution of the fluorine atom in *p*-fluoronitrobenzene by the nitrogen atom of diarylamine **61** (**Scheme 20**). Compound **70** can be easily obtained *via* the second methodology, initially described by our group, which requires a one-step copper catalysed Ullmann reaction between *p*-nitroaniline and *p*-octyloxyiodobenzene.[81] Although both methodologies provide the desired product **70** with high yields, the Ullmann methodology requires a much longer reaction time. The nitro derivative **70** was then reduced using palladium on charcoal and hydrazine as hydrogen source into the corresponding aniline, which was finally acetylated to afford the desired TAA **72** in excellent yield.

B. Electrochemically Triggered Self-Assembly of Mono-Amide Triarylamine Nanowires

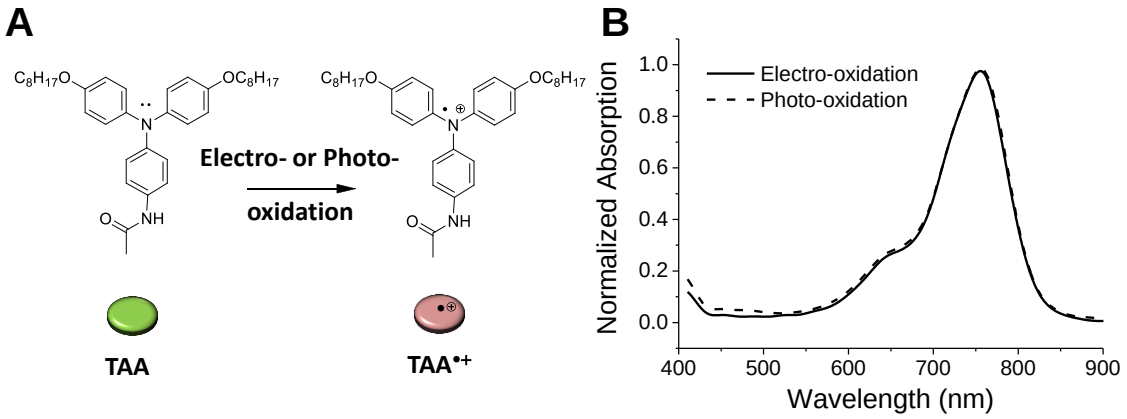

Figure 142 | (**A**) Electro- or photo-triggered oxidation of TAA **72** in its radical cation. (**B**) Normalized absorption spectra of electro- and photo-oxidized **72**$^{\bullet+}$.

We first evaluated some key parameters associated with the light activated supramolecular polymerization process.

In previous chapters, we have mentioned that electron-rich TAA can undergo photo-oxidation process using different light sources such as UV lamp, halogen lamp[81,82,113,115] or even sunlight[114]. Here, we wanted to precisely characterize different light sources that could be used for the photo-oxidation process. First, we recorded the irradiation spectra of all commonly used light sources (**Figure S21** in annexes). We observed that (***i***) the spectrum recorded for the resistance halogen lamp commonly used in our experiments[81–83,113] shows a broad absorption band spanning from 350 to 1100 nm; (***ii***) the one recorded for xenon lamps shows absorption only between 400 and 720 nm and (***iii***) that the absorption spectrum of sunlight spans from 250 up to 2500 nm. Importantly, we notice that, whereas sunlight and the halogen lamp can be used to induce the light triggered self-assembly, xenon lamps never give rise to any photo-oxidation of the triarylamines. This observation suggests that wavelengths corresponding to the UV spectrum (*i.e.* below 400 nm) are responsible for inducing the self-assembly process. To confirm this, we irradiated a TCE solution of compound **72** with the excitation laser of a fluorescent spectrometer, at different wavelength, in order to induce the photo-oxidation.[370] As expected, from 780 nm down to 420 nm, no changes were observed in

370. The time of irradiation was equal to the time needed to record the spectrum.

the UV-Vis spectrum of these irradiated solutions. When the laser was set to 400 nm or even better at 395 nm *i.e.* closer to the absorption band of neutral **72** starting at 400 nm, the radical absorption band at 800 nm grew steadily (**Figure 143A**).

Taking into account these results, we decided to use the LED light centred at the 395 nm wavelength, which provides controlled light energy in relatively narrow range for the following studies.

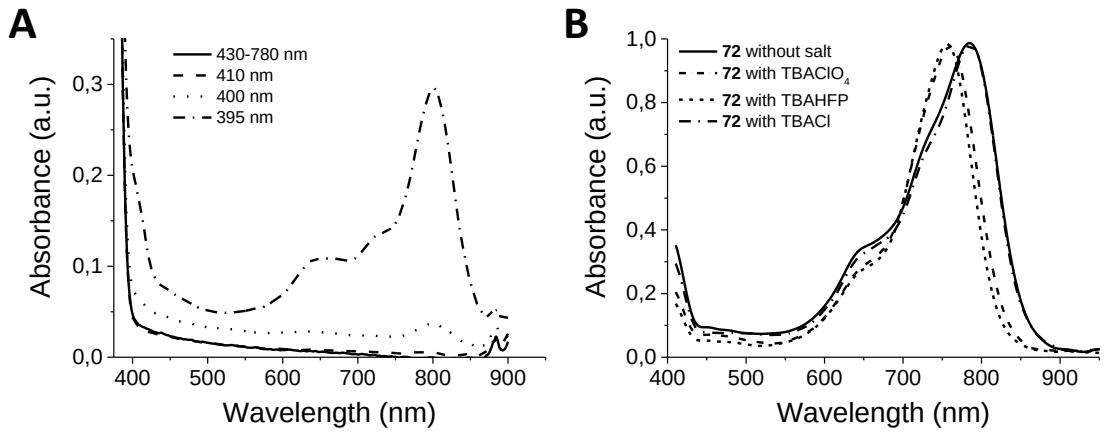

Figure 143 | (**A**) Comparison of the UV-Vis spectra of **72** at 0.1 mM in TCE after exposure to different wavelengths irradiation. (**B**) UV-Vis spectra of **72** at 1 mM in TCE after photo-induced self-assembly in the presence (or the absence) of various counter ion salts at a concentration of 0.1 M. (All spectra normalized for clarity).

In order to check whether it will be possible to trigger the self-assembly of the TAA **72** by electrochemical stimulus (**Figure 142A**), we first studied the possibility to photo-oxidize **72** in the presence of a high concentration of commonly used electrolytes ([**72**] = 1 mM; [*electrolyte*] = 100 mM in tetrachloroethane (TCE)).

Importantly, we should mention that, although the photo-oxidation of **72** in chlorinated solvents produces chloride counter anions, ^{35}Cl NMR was unable to detect a signal in irradiated systems, indicating that the chloride ion is highly associated with the TAA radical (as expected from theoretical values giving an energy of 57 k_BT for the ion pair).[83] This point is of particular importance for our electrochemical experiments which are typically performed in solution with a higher concentration of electrolyte. Thus, we first tried to understand (***i***) the effect of changing the counter-anion on the self-assembly, and (***ii***) the effect of higher concentration of electrolyte on the self-assembly (**Figure 143B**).

Photo-oxidation of **72** in a tetrachloroethane (TCE) solution containing 0.1 M tetrabutylammonium chloride (TBACl) gave the same stable absorption spectrum as the control solution in pure TCE, indicating the triggering of a stable self-assembly at even higher

concentration of electrolyte. In order to test the effect of various counter ions, compound **72** was then dissolved in a solution of TCE with 0.1 M either the common electrochemical tetrabutylammonium (TBA) perchlorate salts ($TBAClO_4$) or TBA hexafluorophosphate salt (TBAHFP). The results show that the self-assembly is still present with all counter-ions and that those ones are tightly associated to $\mathbf{72}^{\bullet+}$ as the absorption bands corresponding to the radical cation (~785 nm) are hypsochromically shifted (~760 nm) depending on their nature. To summarize, we confirmed the effective photo-induced oxidation in the presence of high concentrations of electrolytes such as tetrabutyl ammonium perchlorate ($TBAClO_4$), hexafluorophosphate (TBAHFP), or chloride (TBACl).

We then studied the electrochemical behavior of compound **72** by performing cyclic voltammetry (CV) experiment at a scan rate of 100 $mV{\cdot}s^{-1}$ in TCE and with TBAHFP as electrolyte (**Figure 144A**). We observed a first oxidation associated with radical cation $\mathbf{72}^{\bullet+}$ ($E_{1/2}$ = -71 mV *vs* Fc/Fc^+), and a second oxidation leading to the corresponding dication $\mathbf{72}^{2+}$ ($E_{1/2}$ = 704 mV *vs* Fc/Fc^+). Spectroelectrochemistry was also performed on this solution, showing the expected UV-Vis spectrum of $\mathbf{72}^{\bullet+}$ as it passes over the first oxidation potential (**Figure 144B**). The resulting spectrum perfectly matches with the one observed upon photo-irradiation (**Figure 143B**, plain line).

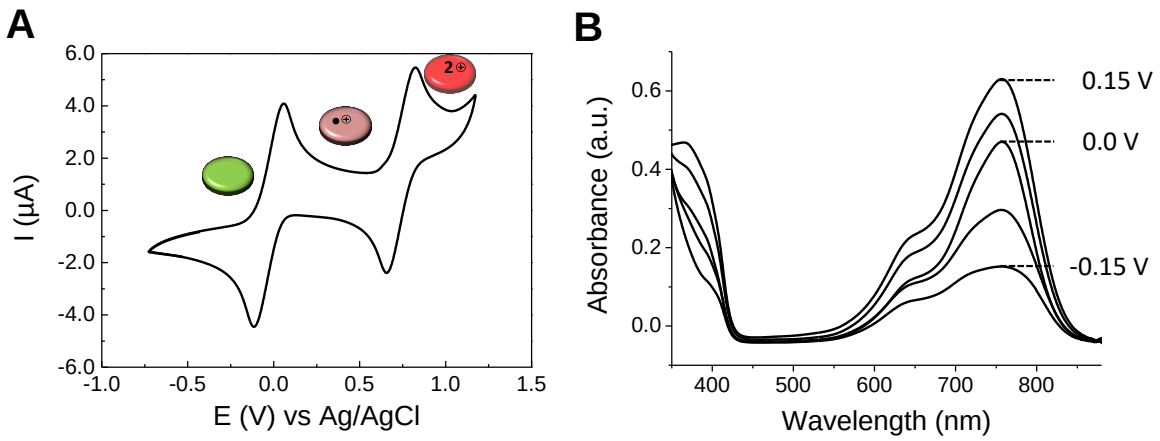

Figure 144 | (**A**) Cyclic voltamogram of compound **72** at a concentration of 1 mM in TCE with 0.1 M TBAHFP and at a speed of 100 $mV{\cdot}s^{-1}$. (**B**) Spectroelectrochemical behavior of **72** for different potential scans over the first oxidation wave in the range -0.15 to 0.15 V *vs* Fc/Fc^+ in TCE with 0.1 M TBAHFP.

We further tested whether the wires can be self-assembled by an electrochemical stimulus from **72** and $\mathbf{72}^{\bullet+}$ in the presence of the electrolyte. For that, we probed the behaviour of a solution of **72** in deuterated chloroform (5 mM) and in the presence of TBAHFP (100 mM) by ^1H NMR spectroscopy, while holding a potential of 0.2 V *vs* Fc/Fc^+

for 30 min. This time of electro-oxidation involves the production of approximately 1% of **72**$^{\bullet+}$ in the solution as determined by coulometry (see **Figure S22** in annexes and associated discussions). **Figure** 145**A** shows that, after this electrochemical treatment, the aromatic proton resonance signals of the TAA fully disappear as observed for the light-induced self-assembly process.

Electro-oxidation of **72** was also performed in the absence of electrolyte with a high potential of 25 V held for 30 min in deuterated TCE, showing the same disappearance of the aromatic signals resonance (**Figure 145B**). This NMR observation is another typical signature of the self-assembly process and is explained by the formation of large and rigid anisotropic stacks of TAA molecules.[81]

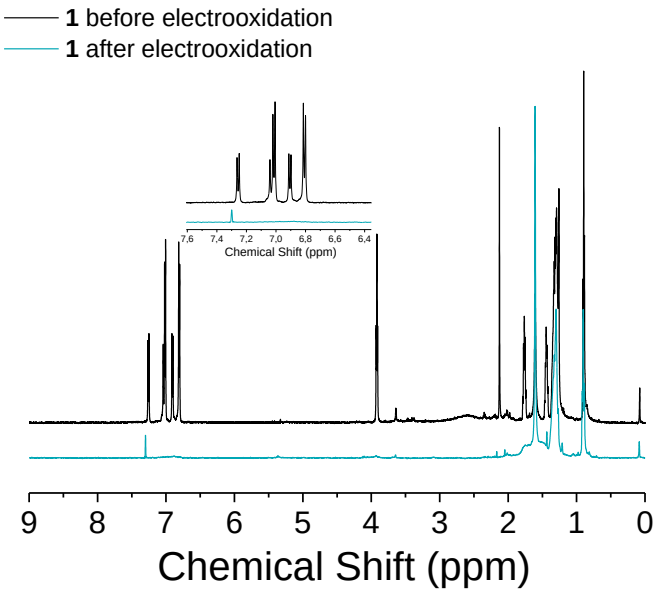

Figure 145 | Comparison of ^{1}H NMR spectra before and after electrolysis of a solution of **72** in TCE-d_2 held at 25 V for 30 min without electrolyte.

Drop cast samples from this solution were imaged by both TEM and AFM, confirming the formation of supramolecular TAA nanowires (**Figure 146A**). By analogy with our previous investigations, we postulate that the electrochemically triggered self-assembly mechanism involves the following sequence (**Figure 146, B**): (***i***) diffusion of a neutral molecule **72** into the double layer, (***ii***) oxidation of the neutral species at the electrode surface producing **72**$^{\bullet+}$, (***iii***) migration of the radical cation into the diffusion layer, (***iv***) nucleation of the radical species, and (***v***) growth of the supramolecular fibres by addition of neutral monomers on the nuclei. As a control experiment, we found that it is possible to suppress the self-assembly pathway by simply introducing a redox couple in excess, e.g.

decamethylferrocene (DmFc), which reduces **72**$^{\bullet+}$ before it can nucleate the process (**Figure** S24 in annexes and following discussions).

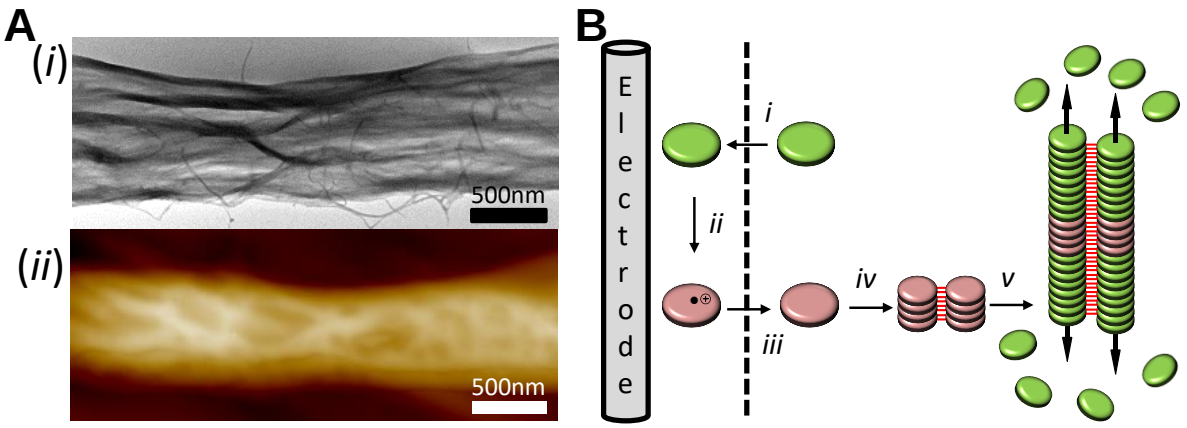

Figure 146 | (**A**) ***(i)*** TEM and ***(ii)*** AFM height images of TAA **72** fibers formed from electrochemically triggered process. (**B**) Simplified electrochemical mechanism of the nucleation/growth supramolecular polymerization activated by electro-oxidation.

To further probe the nucleation step, we studied in more details the CV of the redox process **72/72**$^{\bullet+}$ which occurs when illuminating the system. The CV curves always show (independently of the illumination time) a classical reversible behaviour with $|E_p - E_p/2| \sim 52$ mV where E_P is (**Figure S25A** in annexes). However, a measured effect of the illumination is that the peak oxidation current (iOx) drops whereas the equivalent background reduction current (iR) does not, is unexpected from the oxidized species injection to the solution. This effect can be seen more clearly with a microelectrode setup (**Figure S25B** in annexes). Importantly, the addition of DmFc after 3 min of light irradiation shows the return of the peak current to its pre-illumination value, thus excluding the deposition of a chemical species at the electrode (which would had changed the current height). The peak height of the non-irradiated solution analysed for various scan rates and using the Randles-Sevcik equation gives a diffusion coefficient of 2.38×10^{-10} $m^2 \cdot s^{-1}$ for compound **72.**[371] It is consistent with its diffusion coefficient determined by DOSY NMR in TCE (2.03×10^{-10} $m^2 \cdot s^{-1}$, **Figure 147**). By considering our previously described theoretical model for the nucleation process, we believe that the current drop of the oxidation potential is consistent with the formation of oligomeric

371. The diffusion constant of **72** in the presence of decamethylferrocene was determined using the Randles–Sevcik equation:

$$i_p = 0.446\, nFAC\left(\frac{nFvD}{RT}\right)^{\frac{1}{2}}$$

where i_p is current maximum (A), n equals to number of transferred electrons, A is electrode area (cm^2), F is a Faraday's constant ($C \cdot mol^{-1}$), D, diffusion coefficient (cm^2/s), C is concentration (mol/L) and v is a scan rate in V/s.

chains of nuclei (dipoles involving **72**$^{\bullet+}$ separated by chlorine anions), thus decreasing the statistical average diffusion coefficient.[372]

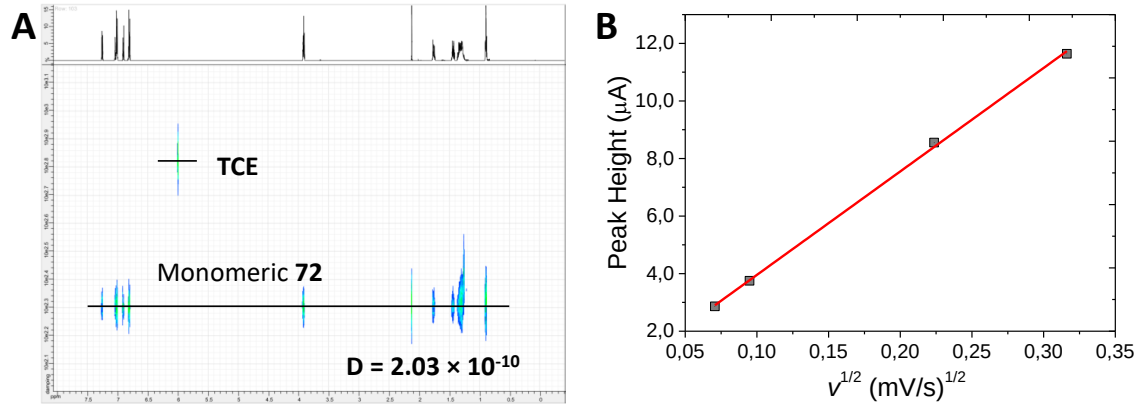

Figure 147 | (A) DOSY NMR spectrum of molecule **72** in TCE-d_2. **(B)** Peak height versus the square root of the scan rate for the oxidation of the **72** in the presence of decamethylferrocene solution and the resulting diffusion constant determined by peak height.

These experiments prove that the self-assembly process can be triggered by electrochemical stimuli, both in pure solvent and in the presence of high concentrations of electrolytes.

C. *In situ* Electric Field Directed Self-Assembly of Triarylamines

Knowing the possibility to electrochemically trigger the nucleation of supramolecular triarylamine fibres, and to grow them from a surface by supramolecular recognition, we then investigated the possibility to directly polymerize and align these fibres between commercially available electrodes and in the presence of an electric field. Although such an alignment was already observed by photo-irradiation and over very short path length of 100 nm,[82] reaching such an organization over longer distances did not succeed with similar experimental procedures. We postulated that a reason for this failure partly came from the use of chloroform or tetrachloroethane to dissolve the TAA molecules and to trigger their oxidation with light. Given their redox potential windows and dielectric constants, the large electric field necessary to align the wires on long distances would be shielded by the

372. The increase in diffusion constant by non-interacting redox polymers has been well described by Anson and co-workers, and follows the Mark-Houwink-Sakurada equation:

$$\frac{D_p}{D_m} = \left(\frac{M_m}{M_p}\right)^a$$

Where D_p and D_m are the diffusion coefficients of the polymer and monomer respectively, M_m and the M_p are the molecular mass of the monomer and polymer respectively, and a is constant, dependent on the interaction of polymer with the solvent. Thus a polymerization of increasing the effective molecular mass, will result in a decrease of diffusion coefficient and thereby a peak current height.

electrogenerated (or photo-generated) triarylammonium radical cations and their respective chloride counter ions. If this effect can indeed be overcome by using nanoelectrodes in which the Debye length is larger than the electrode gap, a solvent selection should be operated for higher length scales with a lower dielectric constant. However, solvents of lower dielectric constants are less suitable for solubilizing TAA molecules which precludes the unique advantage of triggering an oriented nucleation/growth process at the electrode surface.

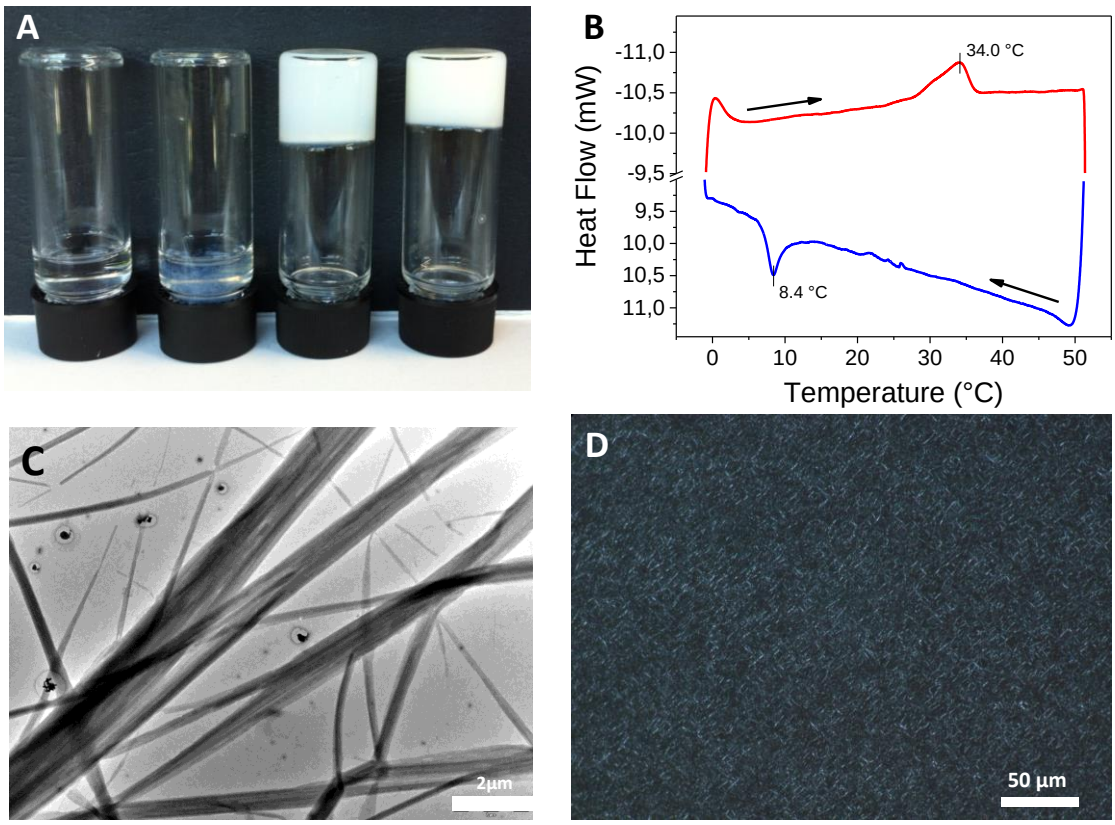

Figure 148 | (**A**) Photo-stable room temperature gelation of TAA **72** in heptane after cooling to 0 °C with concentrations of 1, 2, 5, 10 mg/mL (left to right). (**B**) Differential Scanning Calorimetry (µDSC) traces from the second pass of heptane gel of TAA **72**, at a concentration of 26 mg/mL recorded at scan rate of 0.5 °C/min. Heating (red) and cooling (blue) cycles. Endothermic peak at 34 °C corresponds to gel melting, exothermic peak at 8.4 °C correspond to gelation process (**C**) TEM image of the self-assemblies, formed upon gelation of 5 mg/mL haptane solution of **72**. (**D**) OPM image of a gel.

Interestingly, we found that TAA **72** can dissolve at elevated temperatures in alkanes, such as heptane which was the focus of this study, and that it forms a thermoresponsive organogel upon subsequent cooling (with onset gelation concentration of 2.5 mg/mL at T ≈ 10 °C). (**Figure 148, A**). An interesting property of this system is its large thermal hysteresis showing that, after gelation occurs, the gel is fairly stable up to T = 30 °C (**Figure 148, B**) We thus turned to potentially more informative devices using the lateral geometry of gold and

platinum interdigitated electrodes (IDE) separated by parallel gaps with a distance comprised between 10 and 50 μm, and using a field's strength of 5×10^7 V·m^{-1}. The deposition procedure involved: (***i***) heating of the material (5 mg/mL) until the system fully dissolved; (***ii***) cooling the solution to room temperature (5 °C above the gelation temperature); and (***iii***) drop-casting of the solution (typically 5 μL) onto the interdigitated substrate in the presence of the DC electric field, and until evaporation of the solvent. The substrates were then analyzed by POM and AFM showing the homogeneous alignment of mono-disperse wires filling all gaps with an orientation parallel to the applied electric field (**Figure 149 A-C, Figure S26**). A control experiment using the same procedure but without electric field, revealed only the presence of amorphous and unlocalised material (**Figure S27**).

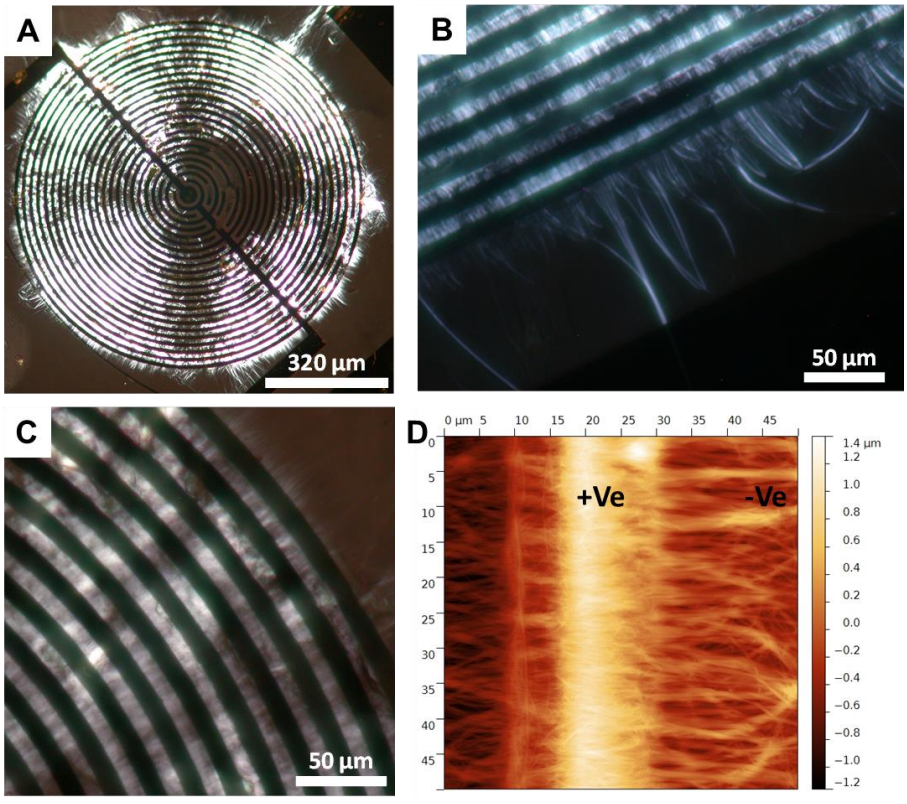

Figure 149 | (**A-C**) Optical microscopy images of aligned wires under cross-polarization from a 5 mg/mL solution of **72** dropped on an IDE with an applied field of 5×10^7 V·m^{-1}. (**D**) AFM image of the same IDE sample shown in (**B**). (**A, C**) Optical microscopy images of the concentric circular IDE electrode under cross-polarization after the drop cast of **72** with an electric field of 5×10^7 V·m^{-1} and leading to a full radial alignment in the device.

In addition, by applying an electric field on a device with a more complex geometry, that is using circular concentric interdigitated electrodes, we unambiguously proved that the wires precisely follow the field's lines (**Figure 150**). As a final test, using a microarray electrode, we were able from the same deposition procedure to grow thin bundles of wires

between pores separated by a distance of 50 μm, and only when these pores are aligned in the field direction (**Figure 150, B**). We determined with this set up that the minimum field strength required for the assembly and alignment of the wires is ≈ 1×10^5 $V \cdot m^{-1}$.

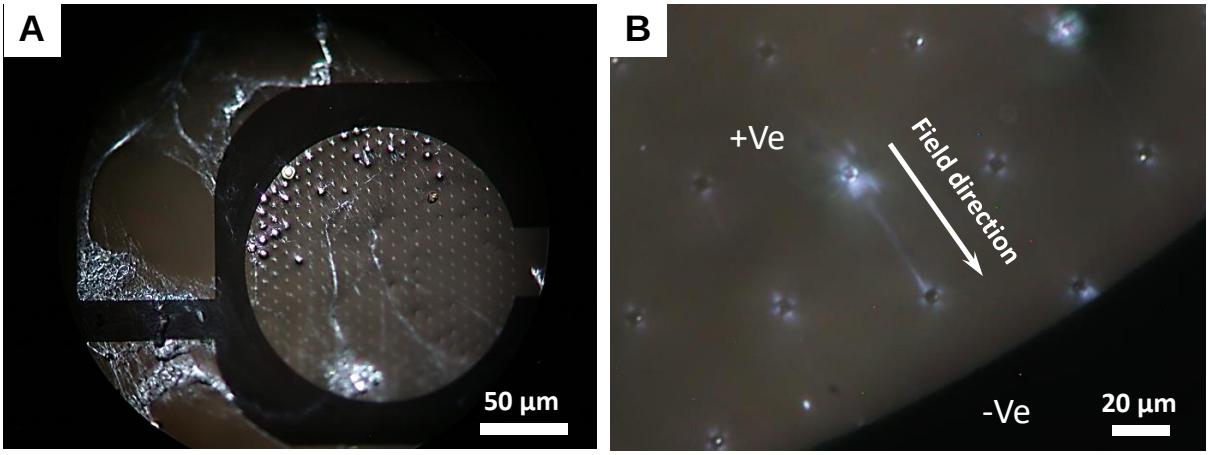

Figure 150 | (**A**) Microelectrode array, showing the wires growth in places of higher fields strength, and realizing precise interconnections over 50 μm distances as illustrated in the zoomed region (**B**).

In order to investigate, whether the contact of TAA **72** with electrodes is necessary for the directional growth of the fibres we performed the alignment of fibres in the cell with blocked ITO layer by a photoresist to ensure that triarylamine molecules will not contact with the electrode surface. Remarkably, no organisation was observed, suggesting that the oxidation of the TAA at the electrode surface plays a crucial role in the self-assembly under an electric field.

The necessity of the electrical contact for complete wire formation indicates that although there is no electrolyte to be used as counter ions, the immediate contact of the electrode in such high field is able to oxidize the molecule, thus creating a seeding surface from which neutral TAA can nucleate and grow. This is consistent with the fact that wires always grow from the positive electrode and follow the field lines toward the negative electrode.

4. CONCLUSIONS

We have demonstrated the possibility to achieve placement and orientation of supramolecular polymers by combining a nucleation/growth mechanism with an electrical potential applied between electrodes over tens of micrometres. For this, we used triarylamine molecules that display key features to achieve such entirely controlled process and, in particular: (***i***) the ability to nucleate electrochemically, (***ii***) a high stability at electrode surface, (***iii***) the ability to initiate wire growth at the electrode without permanent redox processes, (***iv***) the ability to align in electric fields over relatively large distances. The relatively high fields required for this alignment limits the type of solvents that can be used – typically excluding solvents with high dielectric constants, which will electrochemically reduce or oxidize at the interface – but experimental solutions can be found, as shown in this study. Such high control in every aspect of supramolecular polymerization processes, including localization, and orientation on such large distances, is at the moment quite unique in the literature. Potential implementations resulting from these experiments include: (***i***) spatial control over the self-assembly process in various optoelectronic devices requiring efficient charge transport, ranging from sensors to solar cells, (***ii***) use of redox couples to create out-of-equilibrium redox environments for dynamic self-assemblies, (**iii**) 3D electrical wiring in organogels.

CHAPTER VI.
ANISOTROPIC ORDERING OF PLASMONIC NANOPARTICLES AND SUPRAMOLECULAR FIBRES AT THE LIQUID-LIQUID INTERFACE

1. INTRODUCTION

The possibility to manipulate light through plasmon coupling between plasmonic nanoparticles (mainly noble metals) excites the interest of scientists from different fields of nanoscience.[373–377] This technology has been exploited for sensing applications such as surface-enhanced Raman scattering (SERS),[378,379] biosensing,[380,381] plasmonic nano-rulers,[382–384] for the construction of photonic chips and light sources[373] and even for solar cells.[375] Plasmonic nanotechnology is expected to bring computer science to a qualitatively new level, and overcome its current limitations.[373]

However, it has always been a big challenge to control the alignment of such plasmonic structures, which has so far resulted in the development of advanced engineering and bioengineering strategies.[385–393]

In this chapter, after a brief bibliographical overview on the basics of the plasmonic phenomena in nanoscience, we will report on a new fast and easy method of alignment of gold nanoparticles (AuNPs) at the liquid-liquid interface (LLI), using self-assembling triarylamines. This method was discovered in our group by Dr. J.J. Armao IV, and further development of this approach resulted in this collaborative work between the researchers in our group as well as Dr. R. Arenal from the Institute of Nanoscience of Aragon in Zaragosa and theory group from our institute (Dr. I. Nyrkova and Dr. A. Semenov).

373. Ozbay, E. Plasmonics: Merging Photonics and Electronics at Nanoscale Dimensions. *Science* **311,** 189–193 (2006).
374. Nie, Z., Petukhova, A. & Kumacheva, E. Properties and emerging applications of self-assembled structures made from inorganic nanoparticles. *Nat. Nanotechnol.* **5,** 15–25 (2010).
375. Atwater, H. A. & Polman, A. Plasmonics for improved photovoltaic devices. *Nat. Mater.* **9,** 205–213 (2010).
376. Hentschel, M. *et al*. Transition from Isolated to Collective Modes in Plasmonic Oligomers. *Nano Lett.* **10,** 2721–2726 (2010).
377. Focusing in on applications. *Nat. Nanotechnol.* **10,** 1–1 (2015).
378. Schlücker, S. Surface-Enhanced Raman Spectroscopy: Concepts and Chemical Applications. *Angew. Chem. Int. Ed.* **53,** 4756–4795 (2014).
379. Lal, S. *et al.* Tailoring plasmonic substrates for surface enhanced spectroscopies. *Chem. Soc. Rev.* **37,** 898 (2008).
380. Hill, R. T. Plasmonic biosensors. *Wiley Interdiscip. Rev. Nanomedicine Nanobiotechnology* **7,** 152–168 (2015).
381. Anker, J. N. *et al*. Biosensing with plasmonic nanosensors. *Nat. Mater.* **7,** 442–453 (2008).
382. Liu, N., Hentschel, M., Weiss, T., Alivisatos, A. P. & Giessen, H. Three-Dimensional Plasmon Rulers. *Science* **332,** 1407–1410 (2011).

2. BIBLIOGRAPHY

Gold is usually thought of as a yellow metal, however, suspensions of gold nanoparticles can give rise to a different colour, usually red or purple, depending on their size. This feature of colloidal gold was exploited more than 2000 years ago to produce stained glasses in pottery and ceramics (**Figure 151**).

Figure 151 | Lycurgus Cup. A 4th-century Roman glass cage cup made of a dichroic glass, containing dispersed gold. Figure is reproduced from the Wikipedia web page.[394]

This interesting effect could not be explained by classical Rayleigh scattering, which is common for colloids. Only at the beginning of the 20th century, Mie proposed a theory which easily predicted far-field properties of spherical metallic nanoparticles using Maxwell's equations of classical electromagnetism.[395]

383. Wu, L. & Reinhard, B. M. Probing subdiffraction limit separations with plasmon coupling microscopy: concepts and applications. *Chem. Soc. Rev.* **43,** 3884 (2014).
384. Jain, P. K., Huang, W. & El-Sayed, M. A. On the Universal Scaling Behavior of the Distance Decay of Plasmon Coupling in Metal Nanoparticle Pairs: A Plasmon Ruler Equation. *Nano Lett.* **7,** 2080–2088 (2007).
385. Maier, S. A. *et al.* Local detection of electromagnetic energy transport below the diffraction limit in metal nanoparticle plasmon waveguides. *Nat. Mater.* **2,** 229–232 (2003).
386. Bek, A. *et al.* Fluorescence Enhancement in Hot Spots of AFM-Designed Gold Nanoparticle Sandwiches. *Nano Lett.* **8,** 485–490 (2008).
387. Maragò, O. M., Jones, P. H., Gucciardi, P. G., Volpe, G. & Ferrari, A. C. Optical trapping and manipulation of nanostructures. *Nat. Nanotechnol.* **8,** 807–819 (2013).
388. Tan, S. J., Campolongo, M. J., Luo, D. & Cheng, W. Building plasmonic nanostructures with DNA. *Nat. Nanotechnol.* **6,** 268–276 (2011).
389. Ross, M. B., Ku, J. C., Vaccarezza, V. M., Schatz, G. C. & Mirkin, C. A. Nanoscale form dictates mesoscale function in plasmonic DNA–nanoparticle superlattices. *Nat. Nanotechnol.* **10,** 453–458 (2015).
390. Dujardin, E., Peet, C., Stubbs, G., Culver, J. N. & Mann, S. Organization of Metallic Nanoparticles Using Tobacco Mosaic Virus Templates. *Nano Lett.* **3,** 413–417 (2003).
391. Wang, H. *et al.* Cylindrical Block Co-Micelles with Spatially Selective Functionalization by Nanoparticles. *J. Am. Chem. Soc.* **129,** 12924–12925 (2007).
392. Akcora, P. *et al.* Anisotropic self-assembly of spherical polymer-grafted nanoparticles. *Nat. Mater.* **8,** 354–359 (2009).
393. Huang, J., Kim, F., Tao, A. R., Connor, S. & Yang, P. Spontaneous formation of nanoparticle stripe patterns through dewetting. *Nat. Mater.* **4,** 896–900 (2005).

A. Plasmon Resonance

The electrons in bulk metal exist in a form of so-called electron gas (free moving valence electrons within the crystal lattice).[396] At equilibrium, the electrons' movement is quite chaotic, however, under applied electric field this movement can be organised, causing an electric current for example.[395]

Light, as electromagnetic radiation, has an electric component, which means that it can also affect the movement of electron gas in metals. When the size of a metal nanoparticle is smaller than the wavelength of the incident light, the interaction with light causes the electron gas to move from its equilibrium state. The collective movement of electrons induces the formation of a dipole in the metallic nanoparticle (**Figure 152A**). Moreover, at the appropriate wavelength, the oscillation of the electric component of light causes the collective coherent oscillations of plasma in nanoparticles. This oscillation is also called *localised surface plasmon resonance* (LCPR) (**Figure 152B**).[395,397]

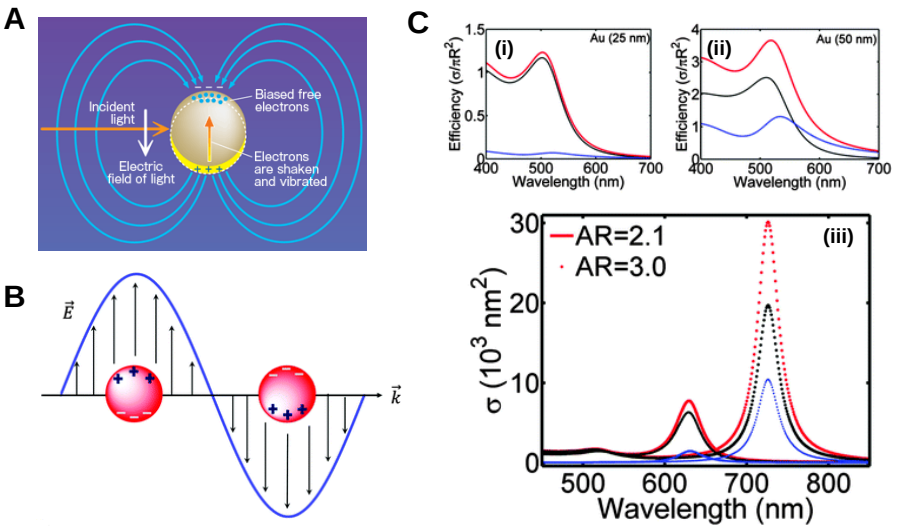

Figure 152 | (A) Illustration of the processes happening in the metallic nanosphere under light irradiation. (**B**) Illustration of the formation of localised surface plasmons in metallic nanoparticles. Dipoles are oriented with the lines of electric component of light. (**C**) Theoretical calculations of the extinction (red), scattering (blue) and absorption (black) of spherical Au nanoparticle of radius 25 nm (**i**), 50 nm (**ii**), an ellipsoid particle with different aspect ratios (AR) (**iii**). Figure is reproduced from ref.395.

The plasmon resonance of gold NPs takes place at energies that correspond to the visible region of the spectrum, thus causing the appearance of a characteristic colour. In

394. at <https://en.wikipedia.org/wiki/Lycurgus_Cup>
395. Olson, J. *et al.* Optical characterization of single plasmonic nanoparticles. *Chem. Soc. Rev.* **44,** 40–57 (2015).
396. This electron gas sometimes is called plasma, from where comes the term plasmonic, as a hybrid of plasma oscillations (plasmons) and electronics.

comparison with the electron spectroscopy of small molecules, for NPs the decrease in intensity of the incident light as a function of wavelength is called the extinction spectrum due to the intensity extinction consisting of two components: absorption and scattering. Different parameters such as the size, shape and composition of the nanoparticle, together with the refractive index of the surrounding medium, determine the spectral (far-field) properties of plasmonic NPs. For instance, the contribution to the extinction of incident light by absorption and scattering for 25 nm and 50 nm gold nanoparticles is compared in **Figure 152C**, indicating increasing scattering contribution with increasing NP size. The shape of plasmonic NPs also has a large influence on the characteristics of plasmon resonance, which is demonstrated on **Figure 152C(iii)** for anisotropic NP with different aspect ratios, suggesting a larger contribution of the scattering phenomenon for the NPs with a higher level of anisotropy.[395]

Plasmon resonance generates strong responses in both near- and far- field effects for gold NPs. Far-field effects are considered when talking about the absorption and scattering of the colloid systems; their understanding is important for the design of new materials with macroscopic properties, e.g. colour.[395] On the other hand, the near-field properties influence the environment of the NPs at scales equal or lower than the wavelength of light. The optical interaction between nearby NPs depends on the near-field effects, which is used in analytical techniques such as Surface Enhanced Raman Spectroscopy (SERS).[378,398] For these reasons the study and understanding of near-field properties are important for various applications in nanosciences.

397. Myroshnychenko, V. *et al.* Modelling the optical response of gold nanoparticles. *Chem. Soc. Rev.* **37,** 1792 (2008).
398. Stiles, P. L., Dieringer, J. A., Shah, N. C. & Van Duyne, R. P. Surface-Enhanced Raman Spectroscopy. *Annu. Rev. Anal. Chem.* **1,** 601–626 (2008).
399. Prodan, E., Radloff, C., Halas, N. J. & Nordlander, P. A hybridization model for the plasmon response of complex nanostructures. *Science* **302,** 419–22 (2003).
400. Wang, H., Brandl, D. W., Nordlander, P. & Halas, N. J. Plasmonic Nanostructures: Artificial Molecules. *Acc. Chem. Res.* **40,** 53–62 (2007).
401. Halas, N. J., Lal, S., Chang, W.-S., Link, S. & Nordlander, P. Plasmons in Strongly Coupled Metallic Nanostructures. *Chem. Rev.* **111,** 3913–3961 (2011).
402. Zohar, N., Chuntonov, L. & Haran, G. The simplest plasmonic molecules: Metal nanoparticle dimers and trimers. *J. Photochem. Photobiol. C Photochem. Rev.* **21,** 26–39 (2014).

B. Plasmon Coupling

We have shown in the previous section that plasmon resonance characteristics strongly depend on the morphology and size of nanoparticles. Thus, by controlling these parameters, we should be able to tune the optical properties of such plasmonic materials. Fundamental and practical interest in this field resulted in the development of efficient and controlled methods for the synthesis and proliferation of different plasmonic nanoobjects of various morphologies: from spherical to star-shape and even more sophisticated shapes (**Figure 153**).[388]

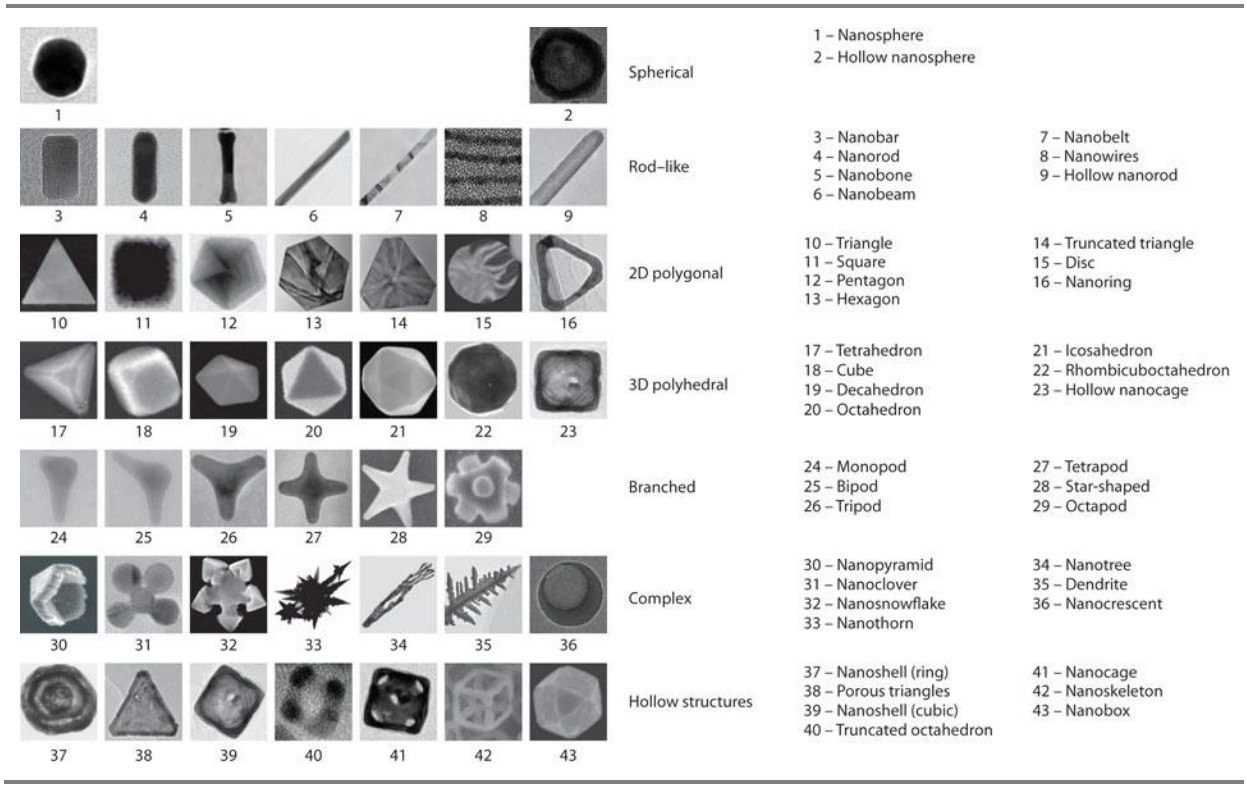

Figure 153 | A "periodic table" of plasmonic atoms. Figure is reproduced from ref. 388.

It is also possible to change the optical characteristics of such plasmonic nanoparticles when placing them in close proximity to one another, at a distance far less than the NP diameter. The near-field coupling between the particles will cause a change of their properties and hence the system will behave as a new individual object. **Figure 154** displays the theoretical calculations of the plasmon resonance energy for a system consisting of two 100 nm size spherical particles depending on the distance *s* between them.[397] The results predict a distinct red-shift with decreasing distance, which is consistent with several experimental observations.[379,381] While the plasmon resonance of spherical metallic nanoparticles can be described using classical electromagnetic theory, in the case of more complex systems elaborated numerical methods have been established, such as discrete dipole

approximation (DDA) and finite difference time domain (FDTD).[397] These methods are widely used to predict near- and far-field optical properties of more complex plasmonic systems; however, they are time and resources consuming.

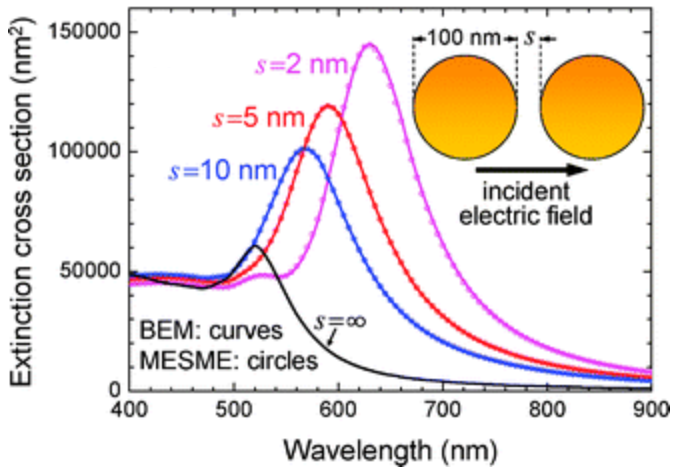

Figure 154 | Theoretically calculated extinction of gold dimers for longitudinal field illumination depending on the distance between the particles' surfaces. Figure is reproduced from ref. 397.

A real break in the paradigm was proposed recently with the development of *plasmon hybridization* theory, which was designed to better understand and intuitively predict the origin of plasmons and properties of plasmonic systems.[399] The idea was to consider the behaviour of virtual elementary particles, plasmons in plasmonic nanoparticles in a similar way as electrons in atoms. When two atoms are bound together, a linear combination of atomic orbitals results in a formation of molecular bonding and antibonding orbitals. Similarly, when two individual plasmonic particles (or *plasmonic* "*atoms*") interact, it results in an appearance of a set of hybridised energy levels, so-called bonding mode and antibonding mode (**Figure 155**).[399,400] In such a case, two plasmon orbitals, with the resulting dipole oriented parallel to the axis of the dimer, are formed (here we can see the analogy with σ and σ^* in theory of molecular orbitals) with the binding plasmon orbital, which has a net dipole, having the lowest energy. This set of modes is responsible for the interaction with light, and is called *"bright" plasmon mode* (**Figure 155A**, l = 1).[397,399–401] Additionally, two degenerate plasmon orbitals are formed when dipoles oriented perpendicular to the axis connect two plasmon atoms (analogous to the π and π^* molecular orbitals). This set of plasmon modes does not have net dipole moments and therefore cannot interact with planewave incident light; these modes are called "*dark*" (**Figure 155A,** l = 2).[397,399–401]

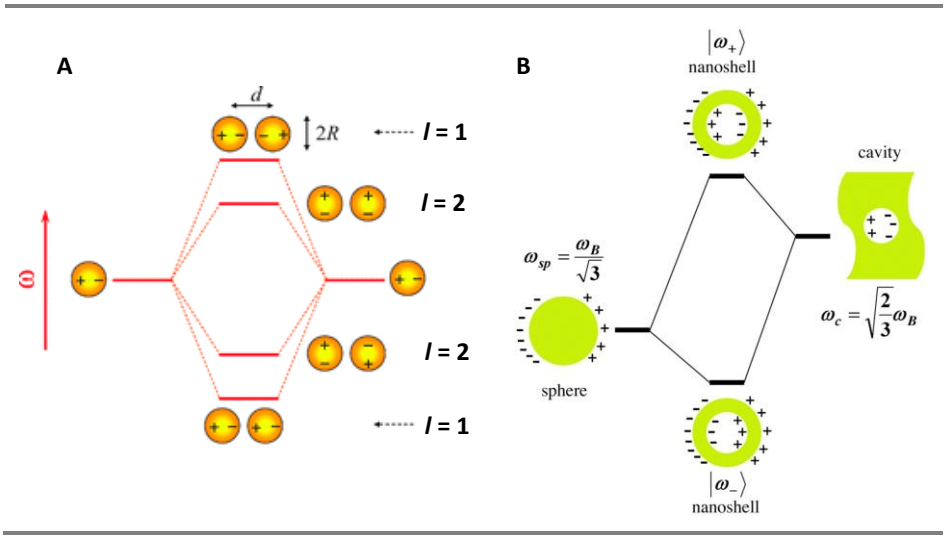

Figure 155 | (**A**) Energy diagram of plasmon hybridization in interacting spherical nanoparticles, producing two bright plasmon modes (*l* = 1) and two dark plasmon modes (*l* = 2). **(B)** Energy-level diagram describing the plasmon hybridization in nanoshells, resulting from the interaction between the sphere and cavity plasmons. Figures are adapted from refs. 397,399

Using plasmon hybridization theory, plasmonic properties of complex systems have been successfully predicted (**Figure 155B**).[399–401] The interaction between plasmons of a spherical particle with cavity in bulk gold results in a plasmon hybridization in a nanoshell, with a symmetrical low energy bonding mode and antisymmetrical coupled high-energy antibonding mode.

Following the analogy with atoms, complex structures of plasmonic nanoparticles (artificial atoms) are called *plasmonic* (artificial) *molecules*,[400–403] and, as when moving from diatomic plasmonic molecules to triatomic, things start to become more complex. The group of Haran demonstrated how the symmetry of plasmonic molecules influences its optical properties.[403] In order to explain the experimental results, the authors successfully applied Group Theory[404–406] (which is widely used in molecular spectroscopy) to describe the plasmon coupling modes (**Figure 156**). The authors studied silver nanoparticle trimers by light scattering. Depending on the symmetry of the trimers, the number of plasmon mode varies. For the highly symmetrical triangular plasmonic molecules with D_{3h} symmetry, plasmonic modes are degenerate. Interestingly, when the symmetry is lowered by gradual opening of the triangle, this degeneration disappears, giving rise to multiple plasmon modes.

403. Chuntonov, L. & Haran, G. Trimeric Plasmonic Molecules: The Role of Symmetry. *Nano Lett.* **11,** 2440–2445 (2011).
404. Rosenthal, J. E. & Murphy, G. M. Group Theory and the Vibrations of Polyatomic Molecules. *Rev. Mod. Phys.* **8,** 317–346 (1936).
405. Herman, M. & Lievin, J. Group theory. From common objects to molecules. *J. Chem. Educ.* **54,** 596 (1977).
406. White, J. E. An introduction to group theory for chemists. *J. Chem. Educ.* **44,** 128 (1967).
407. Slaughter, L. S. *et al.* Toward Plasmonic Polymers. *Nano Lett.* **12,** 3967–3972 (2012).

The number of these modes and their character was determined by using tables of characters for different symmetry groups.

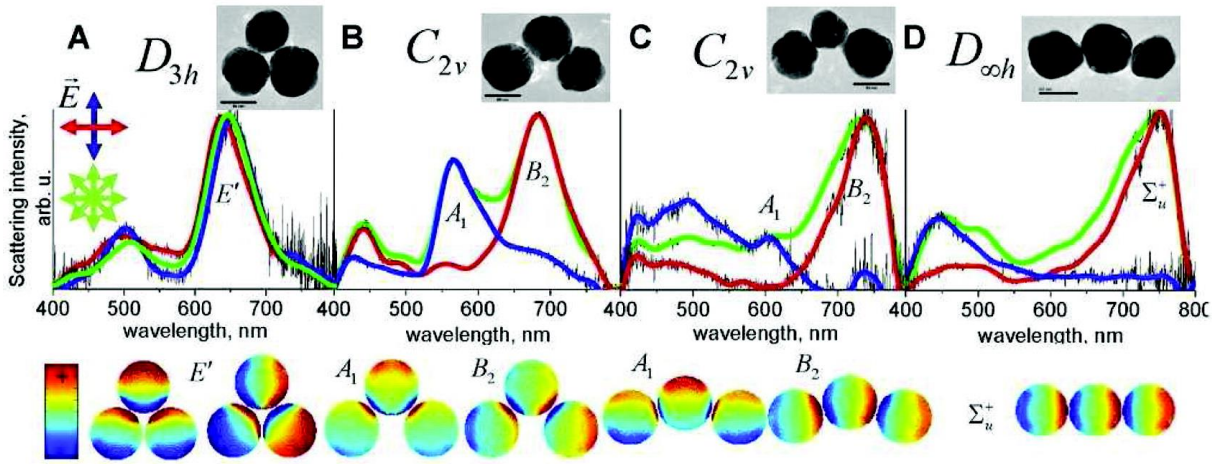

Figure 156 | Scattering spectra of silver nanoparticle trimers showing mode splitting due to the gradual opening of the vertex angle. The clusters are excited by either nonpolarized light (green) or light linearly polarised along the longitudinal (red) and transverse (blue) directions (which are indicated by arrows of matching colours). Plasmon mode symmetries of the bonding modes are marked. TEM images of the clusters are shown in the insets (the bars are 50 nm). Calculated surface charge distributions of the selectively excited bonding modes are shown below the spectra Red colour represents the high density of positive charges and blue colour represents the high density of negative charges. Figure is reproduced from ref 403.

Going further, when plasmonic atoms are placed in an extended array we may obtain "*plasmonic polymers*".[407] In these polymers the plasmonic mode can be coupled, and extended to the size of the whole structure, with potential application as plasmonic waveguides. The plasmon hybridization modes of such oligomers were imaged using the electron energy loss spectroscopy technique (EELS).[408] This analytical technique is based on measuring the energy loss of electrons after their interaction with matter. Briefly, the high kinetic energy electron beam is directed on a sample causing some of the electrons to scatter unelastically due to the absorption of energy by the sample (in the case of plasmonic particle the energy of interactions with plasmons). The detector then measures the number of scattered electrons depending on their energy. The combination of EELS with TEM/SEM can afford the atomic resolution of the studied objects, allowing precise positioning of the electron beam. Additionally, the use of electron beam monochromator can afford the selection of electrons with particular energy with high accuracy (up to 0.1 eV),[409] allowing the mapping of the plasmonic modes around the nanostructures with unprecedented precision. As expected, the authors observed one dipolar plasmonic mode for a single spherical nanoparticle (**Figure**

157), and two modes (longitudinal and transverse) for a nanoparticle dimer. Moreover, EELS is able to detect higher energy "dark" mode (L2 peak), which does not interact with light.

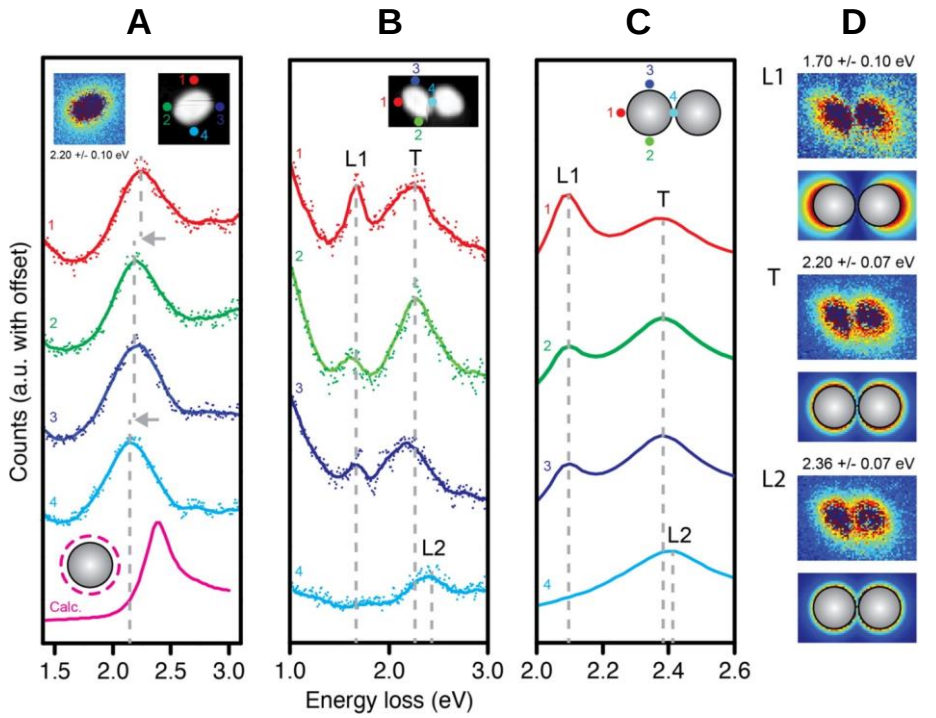

Figure 157 | Electron Energy Loss Spectroscopy Spectra (EELS) of Au nanoparticles. (**A**) Experimental EELS map of the sphere. Experimental (**B**) and modelled (**C**) EELS spectra of a nanoparticle dimer taken at the locations indicated by the numbers in the insets. Inset of (**B**) shows a dark-field image of the dimer. (**D**) Experimental (upper) and modelled (lower) EELS maps of the (L1) *l* = 1, (T) transverse, and (L2) *l* = 2 modes present within the dimer. Numbers in the insets indicate the locations of the spectrum measurements. Figure is reproduced from ref. 408.

The plasmon coupling effect is not only of fundamental interest, attention has also been paid from a practical side. For example, Irudayaraj and co-workers took advantage of the strong dependence of the plasmon coupling on the distance between particles to study the presence of precise mRNA strands in living cells (**Figure 158**).[410] DNA probes, specific to a targeted region within an mRNA sequence, were conjugated with 40 nm gold NPs. When these probes were hybridised to an mRNA strands and found to be located in close regions, plasmon coupling occurred due to the small interparticle distance, resulting in a change of the spectral characteristics of the system, and allowing the detection of single mRNA in living cells. This example highlights the potential of such technologies in bioimaging and sensing.[380–382]

408. Barrow, S. J., Rossouw, D., Funston, A. M., Botton, G. A. & Mulvaney, P. Mapping Bright and Dark Modes in Gold Nanoparticle Chains using Electron Energy Loss Spectroscopy. *Nano Lett.* **14,** 3799–3808 (2014).
409. Egerton, R. F. Electron energy-loss spectroscopy in the TEM. *Reports Prog. Phys.* **72,** 016502 (2009).
410. Lee, K., Cui, Y., Lee, L. P. & Irudayaraj, J. Quantitative imaging of single mRNA splice variants in living cells. *Nat. Nanotechnol.* **9,** 474–480 (2014).

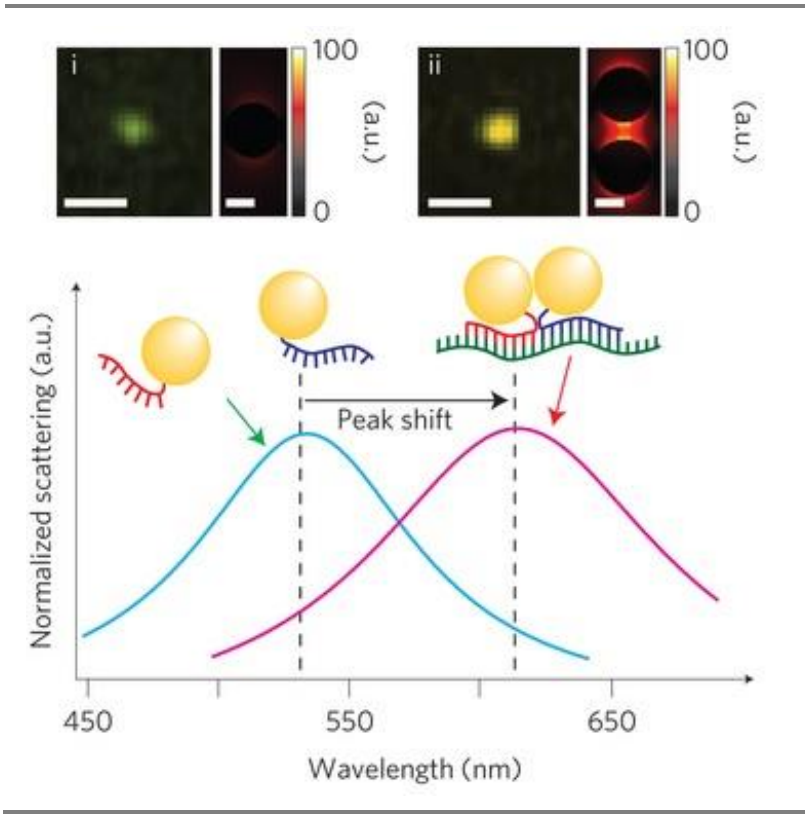

Figure 158 | Schematic design of sequence-selective single mRNA detection.. (**Top**): Real-colour images (left panels) and (FDTD) simulation results (right panels) of the nanoparticle monomer (**i**) and dimer (**ii**). (**Bottom**) Spectral characteristics of Au NPs structures. Monomers (light blue line) and dimers (purple line)Figure is adapted from ref. 410.

All of these examples demonstrate the importance and the influence of the order in plasmonic systems on their properties. The development of technologies, allowing a high degree of control over the alignment of plasmonic structures is thus of a high importance as well. The strategies, which have been used to achieve this task, could be divided into three main groups: (***i***) top-down methodologies such as nanolithography[385,386] (***ii***) organisation by means of different templating substrates in solutions, such as DNA,[388,389] viruses,[390] and polymers;[391,392] and (***iii***) organisation at the interface, including liquid-air (Langmuir-Blodgett),[393] liquid-solid[411] and liquid-liquid interfaces (LLI).[412,413]

The first two groups allow extremely high level of control in the ordering of plasmonic NPs (see **Figure 159A** for example). However, they require the use of costly instruments and time. On the other hand, the third group of methods does not require any sophisticated

411. Mistark, P. A. *et al*. Block-Copolymer-Based Plasmonic Nanostructures. *ACS Nano* **3,** 3987–3992 (2009).
412. Edel, J. B., Kornyshev, A. A. & Urbakh, M. Self-Assembly of Nanoparticle Arrays for Use as Mirrors, Sensors, and Antennas. *ACS Nano* **7,** 9526–9532 (2013).
413. Radziuk, D. & Moehwald, H. Prospects for plasmonic hot spots in single molecule SERS towards the chemical imaging of live cells. *Phys. Chem. Chem. Phys.* **17,** 21072–21093 (2015).
414. Fang, P.-P. *et al*. Conductive Gold Nanoparticle Mirrors at Liquid/Liquid Interfaces. *ACS Nano* **7,** 9241–9248 (2013).
415. Cecchini, M. P., Turek, V. A., Paget, J., Kornyshev, A. A. & Edel, J. B. Self-assembled nanoparticle arrays for multiphase trace analyte detection. *Nat. Mater.* **12,** 165–171 (2012).

equipment, has low cost, is easily applicable and fast. The films, obtained using the LLI technique are self-healing and easily renewable. The isotropic films of NPs, obtained at the LLI have been recently used in the following ways: as conductive mirror-like coatings,[414] and sensors *via in-situ* surface enhanced Raman scattering.[415]

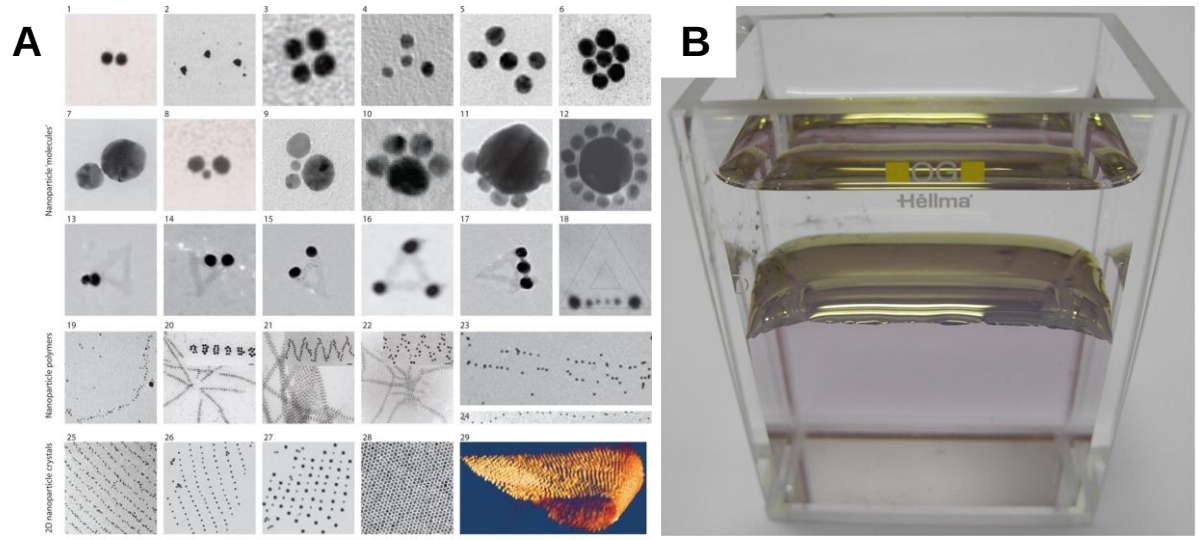

Figure 159 | (**A**) Variety of morphologies of plasmonic nanostructures organised using DNA from "plasmonic atoms". (**B**) The mirror-like film of gold NPs formed at the LLI between the organic layer, containing heptane and dichloroethane and water layer. Figures are adapted from the refs. 388,414

In the first example, the authors obtained a mirror-like film, consisting of gold NPs at the liquid-liquid interface (heptane, dichloroethane)/water. The obtained film demonstrated high reflectance and electric conductivity properties. However, the electron microscopy studies showed random isotropic positioning of gold NPs at the interface (**Figure 159B**).[414]

In the second example, Edel and co-workers utilised the self-assembly of gold NPs at the interface LLI and LAI fro detection of different analytes by SERS. No studies have been performed in this work towards the structural features of these plasmonic self-assemblies.[415]

Remarkably, to our knowledge, there are no reports in the literature on the anisotropic alignment of plasmonic NPs at the LLI.

3. RESULTS AND DISCUSSIONS

In this section, we will demonstrate how TATA self-assemblies, doped by photo-irradiation, can be used to produce nanoparticles alignment at the LLI. The studied TATA (**74**) was synthetized following the procedure described in *chapter II*.

A. Film formation

Knowing that TATAs self-assemble into long charged nanofibers upon light irradiation, we were curious to see if it may be possible to obtain gold NPs-TAA conjugate materials, in which NPs would be organised along these fibres. Our hypotheses were as follows: (***i***) the TATA nano-fibres, when doped with radical cations during the light irradiation, are charged positively, with stabilizing chlorine counter-ions.[83] (***ii***) On the other hand, positively charged gold NPs, when stabilised in solution with citrate molecules, are negatively charged.[416] (***iii***) Due to the electrostatic interactions between the negatively charged double layer of NPs and positively charged TATA nanowires, it might be possible to obtain a hybrid AuNPs-TATA material.

To prove our hypothesis, a biphasic system, containing TAA nanowires and Au NPs was prepared (**Figure 160**). The lower layer contained a chloroform solution of TATA nano-wires, preliminary doped with around 50% quantity of radical cations by photo-induced oxidation (solutions were irradiated for around 1 h). The upper, aqueous layer contained the colloidal solution of citrate stabilised 13 nm Au NPs. After only 10 – 15 s of shaking an interesting observation was made. The colour of the chloroform layer changed from intense green to slightly yellow, with the simultaneous decrease in the intensity in colour of water layer, indicating a decrease of concentration for both TATA and Au NPs in the corresponding solutions (**Figure 160A(i)**). Moreover, an intense dark-blue coloured[417] film was formed at the interface of this biphasic system. Equally, the film was formed when the biphasic system was left undisturbed overnight. Importantly, no film formation was observed when using non-irradiated nanowires, indicating the importance of doping the wires with positively charged radical cations. This suggests that electrostatic interactions play a major role in the film formation.

416. Wuithschick, M. *et al*. Turkevich in New Robes: Key Questions Answered for the Most Common Gold Nanoparticle Synthesis. *ACS Nano* **9,** 7052–7071 (2015).
417. The colour of the film depended on the angle of observation. In a transmitted light the film was dark-blue, however in a reflected light the colour was golden with metallic reflectance.

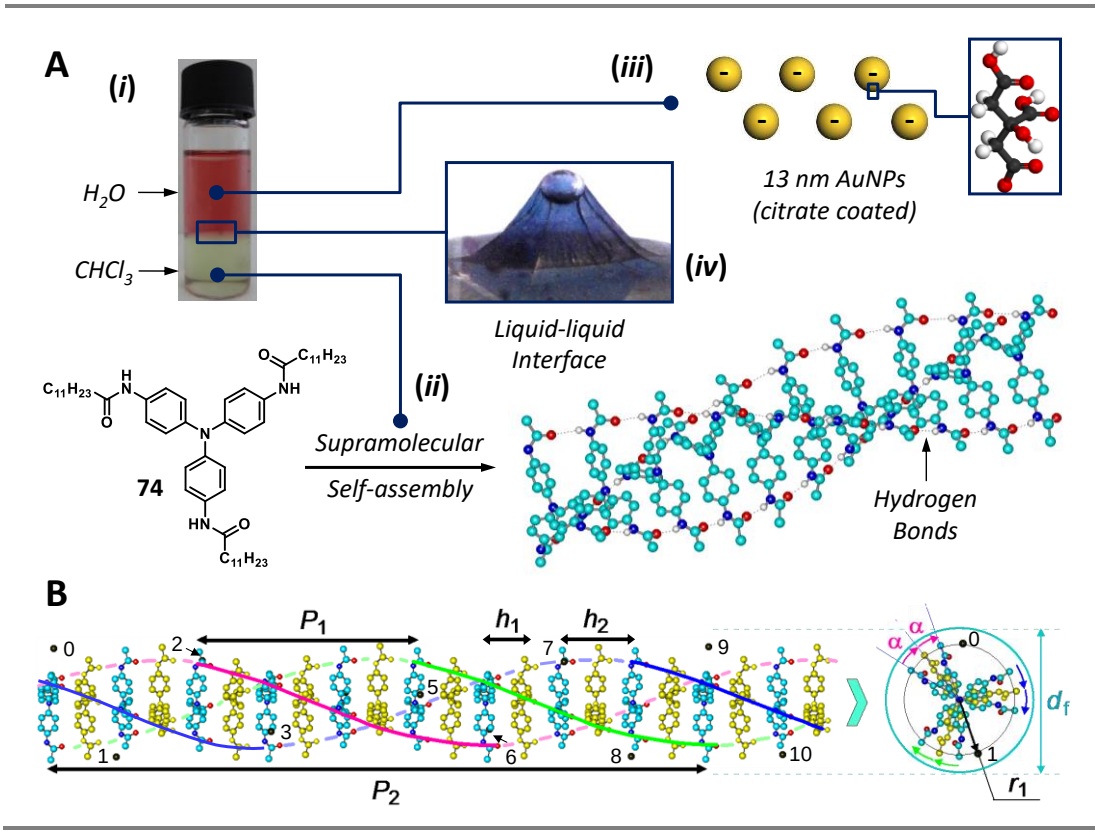

Figure 160 | (**A**) Different components involved in the formation of the hybrid TATA/Au film at the liquid/liquid interface. (**i**) Photograph of the biphasic system with chloroform (lower layer) and water phases (upper layer) after shaking. (**ii**) The chloroform layer contains TATA supramolecular nanowires, doped upon light irradiation with TATA radical cations. (**iii**) The aqueous layer contains a suspension of citrate stabilized 13 nm size gold nanoparticles (Au NPs). (**iv**) An air bubble, trapped under the hybrid film, formed at the interface. (**B**) Characteristics of a TATA nanofiber doped with radical cations, composed from 22 TATA units. Chlorine counterions are marked as black dots numbered from 0 to 10; coloured lines represent the three chains of H-bonded amide groups; h_1 = 0.485 nm, distance between the central nitrogens of neighbouring TATA molecules; $P_1 = 6h_1$, apparent helical period; $P_2 = 3P_1 = 18h_1$, full helical period; $h_2 = 2h_1$ contour length per radical.

UV-Vis absorption measurements revealed a 90 nm red-shift of the NPs extinction peak in this hybrid film compared to the solution, clearly indicating the aggregation of plasmonic NPs on the film (**Figure 161A**).[401] Study of the film with a confocal Raman microscope demonstrated surface enhanced Raman scattering. Importantly, the SERS from TATAs was observed only when focusing the laser on the areas with TATA nanofibers together with gold NPs, while no response was observed when focusing on the areas containing only nanofibers (**Figure 161B**), indicating the close contact between the NPs and the nanowires.

TEM imaging showed that the film was composed of nanofibres and NPs, however, no ordering of the wires nor for the NPs was observed. Moreover, AFM imaging revealed that the NPs remain on one side of the film, while the nanowires are located on the other, meaning that that NPs do not intercalate in the TATA layer, rather stay on its surface (**Figure 161C**).

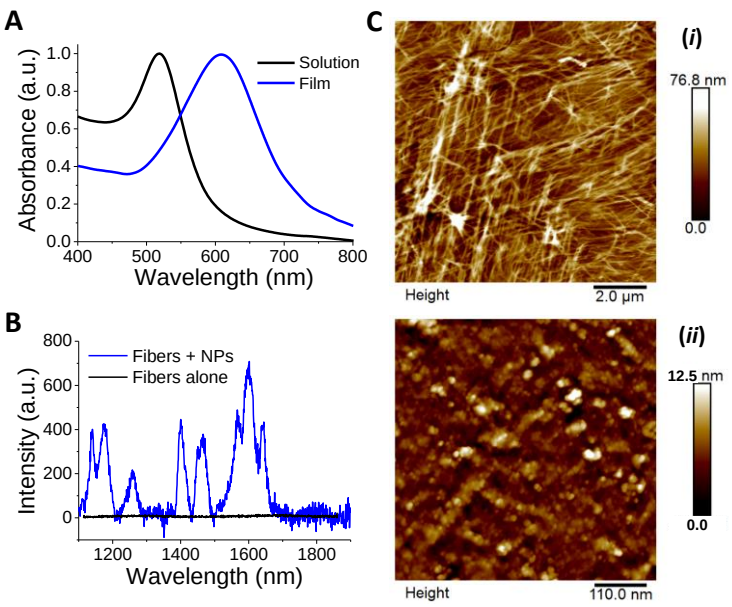

Figure 161 | (**A**) Extinction spectra of the plasmonic film of Au NPs (blue line) and a colloidal solution (black line). (**B**) SERS spectra of the film recorded at different positions. (**C**) AFM image of the film (**i**) chloroform layer side, (**ii**) aqueous layer side.

B. Ordering at the Liquid-Liquid Interface

Considering that shaking is an important parameter in the hybrid film formation, we decided to study the influence of stirring and centrifugation on this process.

Stirring

In order to have better control over the agitation of the biphasic mixture we decided to use magnetic stirring, while continuously irradiating the system with light. To a 1 mM chloroform solution of TATA in a screw-cap vial (with a diameter of 12 mm) a suspension of Au NPs with the concentration as obtained after synthesis was carefully added. A stirring speed of 800 RPM was chosen so that vortexing of the system could be observed without significant distortions of the interphase. After 1 h of stirring the formation of a visually homogeneous film was observed. Remarkably, by TEM we observed the partial anisotropic alignment of the fibres and NPs in some regions of the film (**Figure 162**). Optimisation of different parameters for the film formation and gold NP ordering showed the best results at high concentrations of TATA (1 – 5 mM), long irradiation times (1 h), and relatively high stirring speed (800 – 1000 RPM). Interestingly, when a disordered film, obtained by simply shaking, was subjected to stirring, no improvement in order was observed, suggesting a static nature to the film, as opposed to the dynamic nature of TATA self-assemblies in solution.

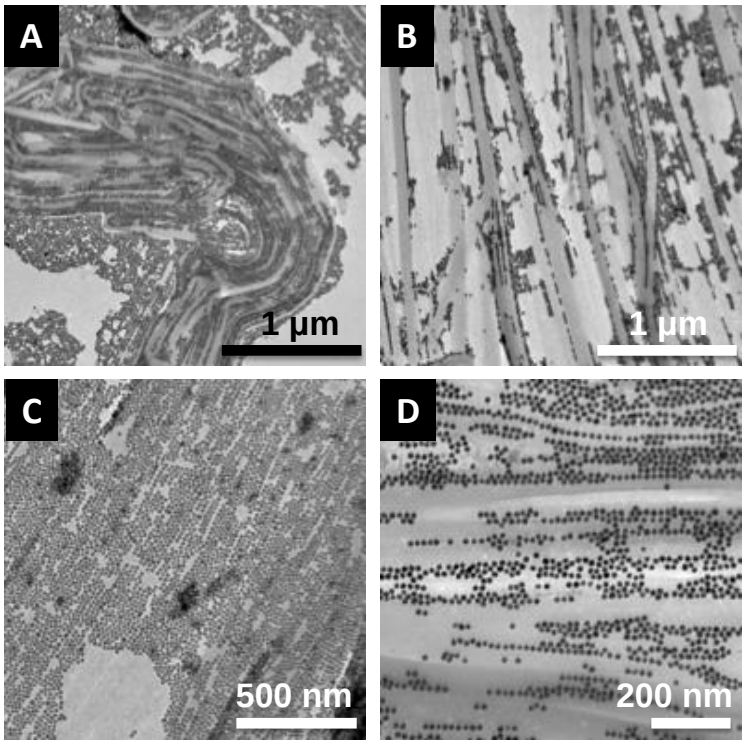

Figure 162 | Typical TEM images of a hybrid film, formed at the LLI during the stirring process at 800 RPM for 1h. Images represent different zones of NPs alignment along the TATA nanowires.

Centrifugation

Considering the results obtained by magnetic stirring, we then hypothesised that the lateral force applied to the interface during stirring might be responsible for this partial alignment. Thus, we decided to use centrifugation at a controlled speed of rotation, to isolate the centrifugation force, parallel to the interface, and to avoid turbulent flows existing during the stirring process.

We first evaluated the relative centrifugal force (RF_C) created during stirring at 800 RPM, taking into account the following equation:

$$RF_C = \frac{r\omega^2}{g} \qquad \textbf{(41)}$$

where ω is the angular frequency, r is the radius from the centre of rotation and g is the gravitational constant. Considering that the distance from the centre of the vortex to the interphase is 0.3 cm, the relative centrifugal force in the units of "g" will be:

$$RF_C = 1.118 \times 10^{-5} \times 0.3 \times 800^2 = 2.15\ g$$

After centrifugation at a speed corresponding to 2.15 g, film formation with partial ordering of the NPs was observed, proving our hypothesis about the role of the centrifugal force in the ordering event. All further studies were done using 1 or 5 mM concentration of TATA and a concentration of gold NPs of 7.08 pM at pH 6.0. The stoichiometric ratio of gold NPs was calculated with a consideration, that they would cover the available surface area of the film with monolayer. The SPR extinction peak at 518 nm with a value of 0.865 gave a concentration of Au NP of 6.23×10^{-9} M. Using an average diameter for NPs of 13 nm, a stoichiometric ratio of Au NPs to a surface area (1 mL solution volume)/available thin film surface area (diameter of vial is 1.2 cm) was achieved by 8.8 times dilution of the original concentration.

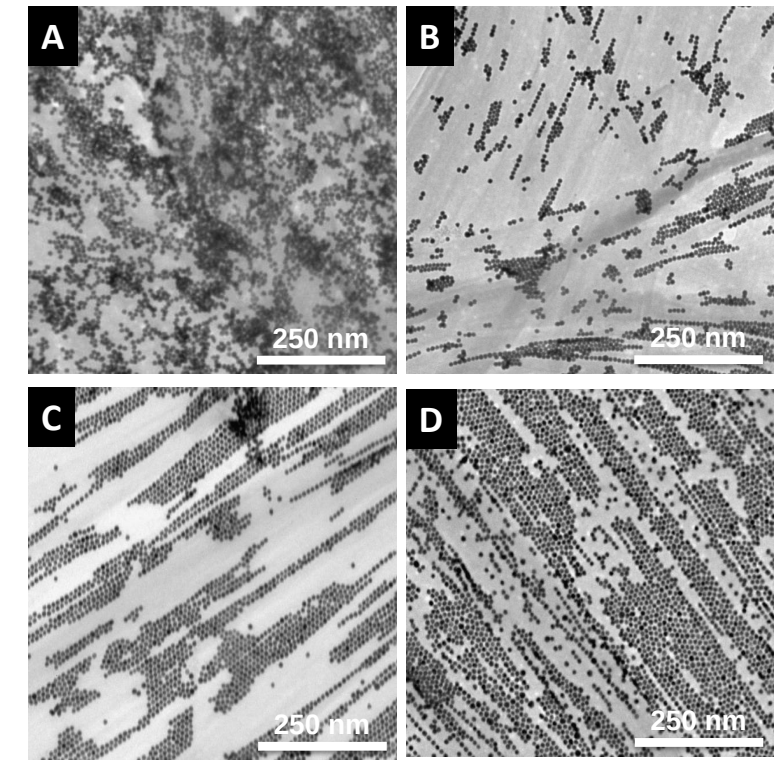

Figure 163 | Typical TEM images of a hybrid film formed at the LLI at (**A**) 0 g overnight diffusion, (**B**) 5 g for 1 h, (**C**) 100 g for 1 h and (**D**) 1000 g for 1 h.

TEM images of the films were obtained for different centrifugal forces (*g*), applied to the biphasic system made of a 5 mM TATA solution and a stock solution of Au NPs (7.08 pM) (**Figure 163**). **Figure 163A**, corresponding to the control non-centrifuged sample, *i.e.* which was left standing overnight, revealed a little ordering on the film. The images corresponding to the centrifuged samples, however revealed a strong dependence on the centrifugal force of the ordering of the NPs, clearly indicating improved ordering with

increasing *g* (**Figure 163B-D**). Long-range ordering was also evidenced by OPM, showing the formation of a nematic liquid crystalline phase with large domain size when increasing the centrifugal force (**Figure 164**).

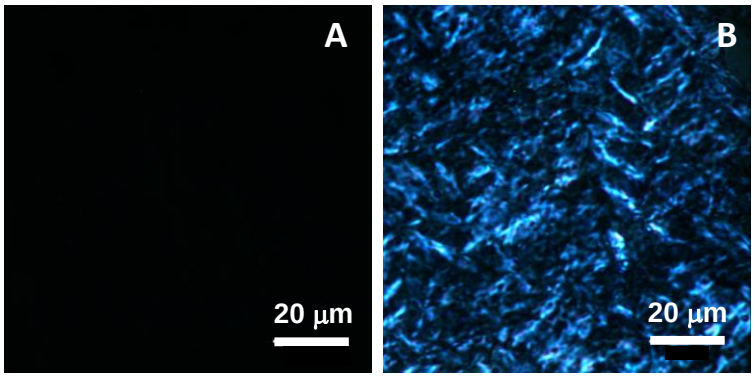

Figure 164 | Cross-polarised optical microscopy images of the films, obtained using different conditions. (**A**) 0 g overnight diffusion and (**B**) 1000 g for 1 h.

C. Quantification of the Ordering

In order to quantify the level of anisotropy of ordering for different centrifugal forces, we performed a statistical analysis on the TEM images over three different surface areas from 2.25 to 25 μm^2. The orientational parameter S ($0 \leq S \leq 1$), which is defined as:

$$S = 2\cos^2\theta - 1 \qquad \textbf{(42)}$$

was used for the quantification of the ordering: the higher value of S the higher is the degree of orientation.[418]

For all considered surface areas, an increase of the orientational parameter was observed with increasing the centrifugal force (**Figure 165**). For instance, for a 5 mM solution of TATA, a S value of 0.76 was reached at 10 g while, at 0 g S was equal to 0.18 for a surface area of 25 μm^2. Interestingly, for a concentration of TATA of 1 mM, even higher degrees of order were achieved: S increased from 0.18 to 0.96 at 10 g indicating almost perfect ordering. For identical concentrations, when the S parameter was calculated for smaller surface areas, a partial anisotropic ordering was observed even without centrifugation (S = 0.62 for 9 μm^2 and S = 0.73 for 2.25 μm^2.

418. Schneider, C. A., Rasband, W. S. & Eliceiri, K. W. NIH Image to ImageJ: 25 years of image analysis. *Nat. Methods* **9,** 671–675 (2012).

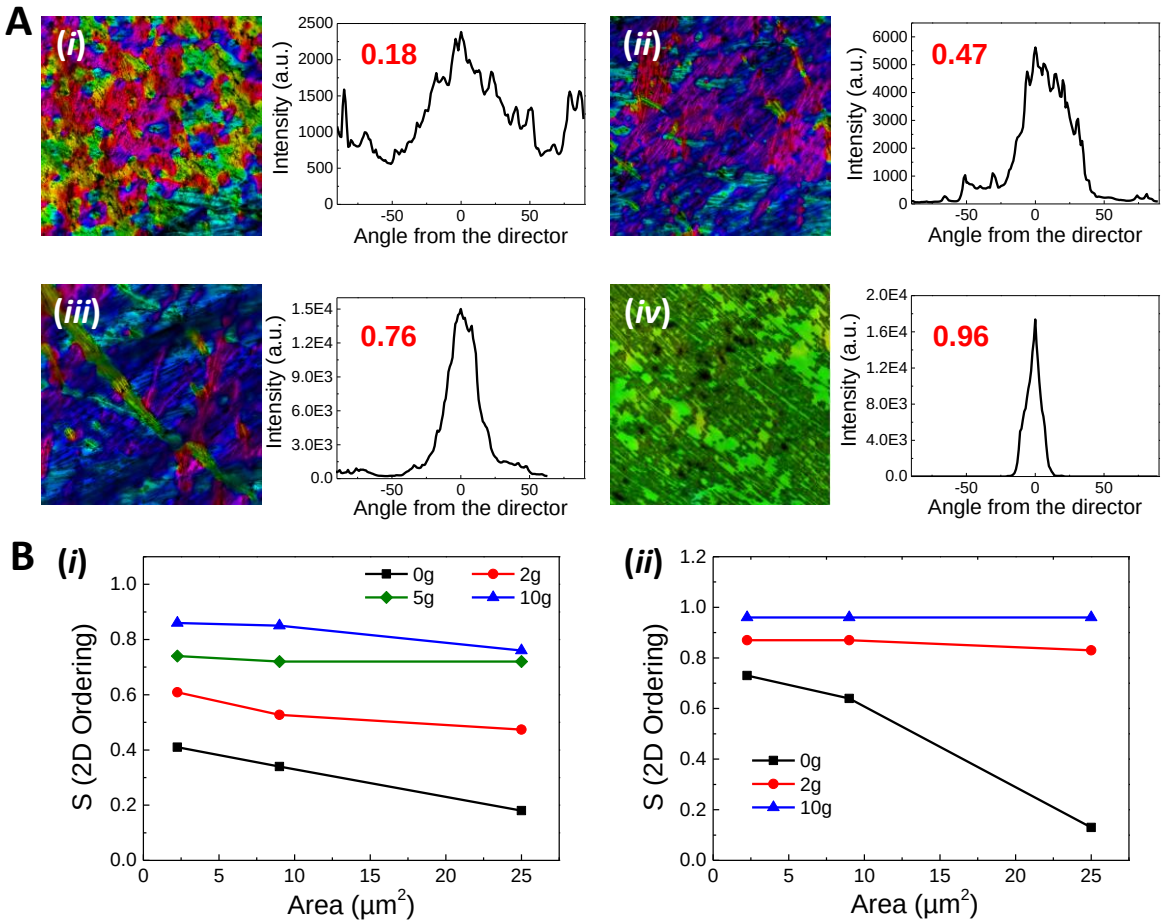

Figure 165 | Characterisation of the anisotropy within hybrid films formed at LLI. (**A**) TEM images over a surface of 25 μm^2, analysed to determine the parameter of order ***S***, given in red, as a function of the angle with the main director, different colour represent a particular orientation of the NPs strings. (**i**) 5 mM solution of TATA, no centrifugation, (**ii**) 5 mM solution of TATA under centrifugation of 2 g, (**iii**) 5 mM solution of TATA under centrifugation of 10 g, (**iv**) 1 mM solution of TATA under centrifugation of 10 g. (**B**) Orientational parameter ***S*** as a function of surface area for different centrifugation forces for (**i**) 5 mM and (**ii**) 1mM solution of TATA.

D. Electron Energy Loss Spectroscopy Studies

Plasmon coupling between NPs ordered in the hybrid film was studied using the scanning transmission electron microscopy-electron energy loss spectroscopy (STEM-EELS) technique, which was briefly discussed in the bibliography section. The local plasmonic response was investigated on the films, prepared from 5 mM solution of TATA at 10 g.

Figure 166A represents a low magnification high angle annular dark-field (HAADF) scanning transmission electron microscopy (STEM) image of two Au nanoparticles (NPs). As it can be deduced from the high-resolution (HR) STEM-HAADF image, see **Figure 166B**, all the NPs are highly crystalline.

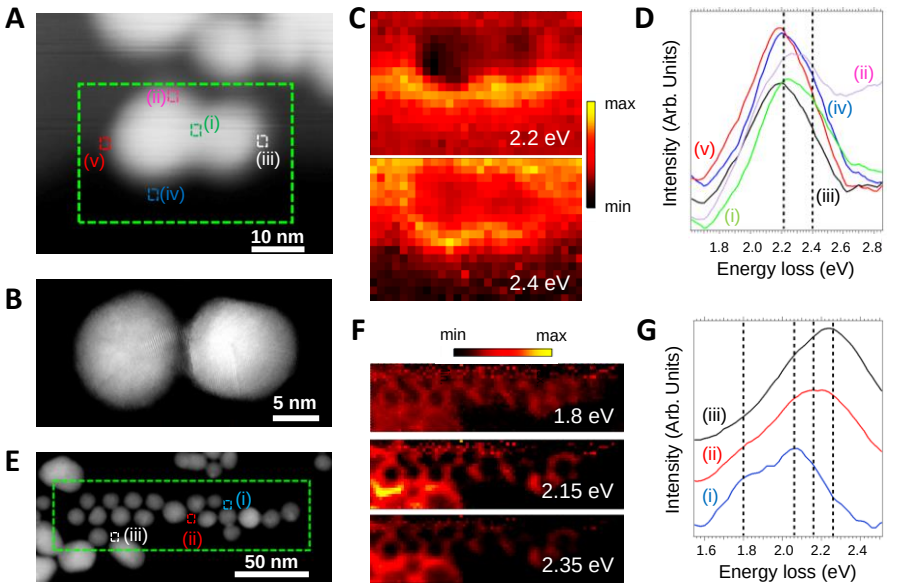

Figure 166 | STEM-EELS measurements. (**A**) Low magnification high angle annular dark-field (HAADF) scanning transmission electron microscopy (STEM) image of two merged AuNPs. (**B**) High-resolution HAADF-STEM image of two other AuNPs, showing their high crystalline quality degree (X-ray energy-dispersive spectroscopy (EDS) also confirmed that the NPs are composed exclusively of pure gold). (**C**) Intensity maps extracted from the EELS-SPIM recorded in the green marked area of **Fig. 16A**, after removing the zero-loss peak (ZLP). These intensity maps show the spatial distribution of the LSPR mode of these AuNPs. (**D**) EEL spectra (each of them corresponds to the sum of 4 spectra) extracted from the EELS-SPIM in the areas marked in the **Fig. 16A** and labelled as (i) - (v), respectively. (**E**) Low magnification HAADF-STEM image of an aggregate of AuNPs. An EELS-SPIM has been recorded in the area square marked in green. (**F**) Intensity maps extracted from the EELS-SPIM after removing the ZLP and showing the spatial distribution of the LSPR modes. (**G**) EEL spectra (each of them corresponds to the sum of 4 spectra) obtained from the EELS-SPIM in the regions marked in **Fig. 16E**.

In order to investigate local optical properties of merged Au NPs, we performed high-energy resolution electron energy loss spectroscopy (HR-EELS) on the nanostructure in the green marked area of **Figure 166A**. An EELS spectrum-image (SPIM) in the low-loss region (below 50 eV) was recorded. **Figure 166C** depicts the intensity maps of the local surface plasmons resonances (LSPR) extracted from this EELS-SPIM, after the subtraction of zero-loss peak (ZLP). EEL spectra (sum of 4 spectra), obtained from different areas of the SPIM marked by numbered squares in **Figure 166A**, are plotted in **Figure 166D**. It is commonly known that the LSPR strongly depend on the shape, size and local dielectric environment of the plasmonic NPs. In the case of these two NPs in **Figure 166A**, a small blue-shifts can be observed together with broadenings of the dipolar LSPR mode at ~2.2 eV (**Figure 166D)**. These shifts and broadenings are caused by the presence of the carbon support of the TEM grid and by the fact that these two NPs are merged and their shape is more ellipsoidal than the spherical shape of each individual NP.

Figure 166E, corresponding to a low-magnification STEM-HAADF image, shows an aggregate of gold NPs. A low-loss EELS-SPIM has been recorded on the area, marked with a green rectangle, of this micrograph. The intensity maps extracted from this EELS-SPIM show the spatial distribution of the excited LSPR modes (**Figure 166F**). These modes correspond to plasmon resonance couplings of the different NPs. **Figure 166G** displays some EEL spectra obtained from the EELS-SPIM. The peaks observed in these spectra correspond to LSPR (different (dark and bright) transversal/longitudinal) modes showed in the intensity maps. It is worth mentioning that due to the fact of the complex arrangement of these NPs, a proper assignment of these resonances is complicated. From these maps, one can observe that the maximal enhancement of the electromagnetic field is in the hot spots (gap between the NPs), where these fields are concentrated due to the surface plasmon coupling effects. These results confirm previous results in larger NPs also showing some (linear-chain) alignments.

E. Theoretical Aspects of the Formation of Triarylamine /Gold Hybrid Film

In order to have a better fundamental understanding of the phenomenon, occurring at the LLI, a theoretical model explaining our observations was developed by Dr. Semenov and Dr, Nyrkova (ICS).

Briefly, the mechanism of the film formation at the LLI comprises several steps: (***i***) photochemical oxidation of preformed supramolecular nano-fibres of TATA, which are doped with around 50% of radical cation molecules; (***ii***) diffusion of a fraction of chloride counter ions, produced during the parallel photoreduction of chloroform, in the aqueous layer, followed by diffusion of the positively charged nanowires to the LLI and their absorption and organisation at the interface; (***iii***) diffusion/sedimentation of AuNPs to the LLI, and their aggregation on the positively charged layer of TAA nanowires. In the following section, we will try to elucidate these different steps.

iii. Processes in Chloroform Layer

The mechanism of photoinduced self-assembly of TAA has been extensively studied in our previous works.[81,83] We will summarise it here shortly, with regard to the present study. All-atom calculated model of the supramolecular fibril, formed during the self-assembly process of TATA in chloroform is shown on the **Figure 160B**. These self-assembled structures are constructed mainly due to the formation of threefold intracolumnar hydrogen

bonding between amide groups of neighbouring TATA molecules. During the photochemical oxidation for 1 h, the fibrils become doped by 50% with corresponding radical cations. The chlorine anions, produced during the simultaneous reduction of chloroform, are associated with the fibrils due to the low dielectric constant of chloroform.

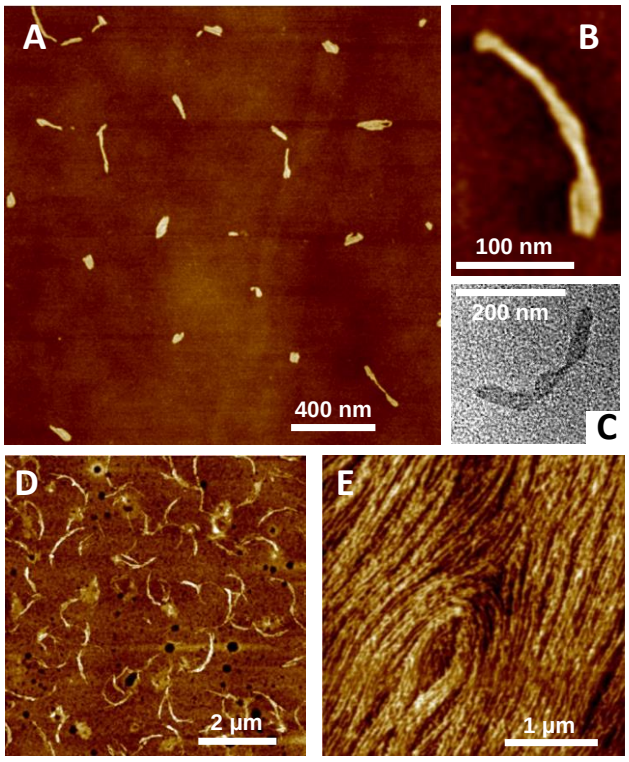

Figure 167 | AFM images of the TATA fibrils from chloroform solutions (**A-C**) at concentrations of 0.1 mM, (**D**) 1 mM and (**E**) 5 mM. (**C**) TEM image of the similar object as represented in **Fig. B**.

Additional stabilization of the 1D aggregates by aromatic and dipole-dipole interactions explains the quite high fibril scission energy ($E_{SC} \sim 24.5\ k_B T$), which ensures a very low critical aggregation concentration. For low concentrations of TATAs, theoretical calculations predict a mean fibril length of around 1 µm for a 1 mM solution, which is in agreement with experimental observations giving an average length of 2 µm (**Figure 167**). In a hierarchical organisation process, two fibrils attract each other side-to-side due to electrostatic interactions between radical cations and chlorine anions. Nevertheless, the entropic penalty at low concentrations is too high, and it overcomes the electrostatic attraction. At higher concentrations, however the bundles of fibres readily form and are quite stable, leading to the formation of organogels.

iv. Triarylamine Fibres at the Liquid-Liquid Interface

We then studied the diffusion phenomenon of the fibres at the LLI. When the water layer is added, and the biphasic system is formed, chlorine anions strongly prefer the aqueous phase to chloroform, despite their electrostatic binding to the positively charged TATA fibrils (**Figure 168A**).

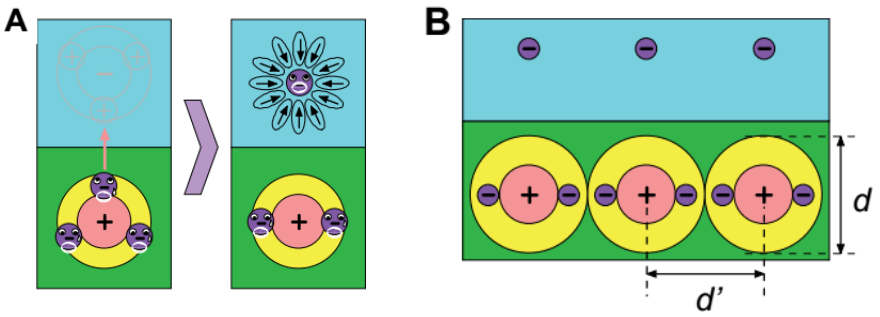

Figure 168 | Charged TAA fibrils at the LLI. (**A**) Chloride anion transfer at the interface. (**B**) Chloride anion transfer from a bound state in chloroform to a free state in water. One-third of the chloride ions (among those bound initially to a triarylamine fibril) can migrate to water.

The transition of chlorine anions to the water phase leaves the fibres charged positively. Due to the strong electrostatic attraction with the counter ions located in the aqueous phase, the nanowires migrate to the interface (**Figure 168B**). The energy gain on fibril absorption at the LLI is $\Delta F \approx -5k_BT$ per contour length segment $\Delta L = h_2 \approx 1\,nm$ for optimal fraction $f_t \approx \frac{1}{3}$ of transferred counter ions; where ΔF is a free energy gain and f_t is a fraction of chloride counter anions transferred to the aqueous phase. Because of the strong electrostatic attraction to the LLI, the fibres tend to form a dense absorbed monolayer. At thermodynamic equilibrium, due to geometric constraints and because of their side-to-side electrostatic attraction, the fibres must be aligned almost parallel with a high nematic order *i.e.* with the orientation parameter S close to one. The charged monolayer of fibrils induces a positive potential in water close to the interface with chloroform, which is compensated by the layer of anions (mainly citrate) near the interface. In reality however, the ordering process is quite slow, due mainly to the slow dynamics of 1 μm long fibrils at the confined space at LLI, and because of defects such as fibre crossing.

v. Film Formation

Gold NPs prepared using the Turkevich procedure,[416,419] are stabilized by the formation of a double layer consisting of citrate molecules, which are directly adsorbed at the gold surface, and of positively charged hydrated sodium cations. The thickness of the inner layer h_{st} is calculated to be approximately 1.5 nm and it is necessary for the steric stabilisation of NPs. The double layer provides electrostatic stabilisation to the NPs, which works for larger distances, due to its zeta-potential $\zeta_i = -1.9\ k_B T/e$.

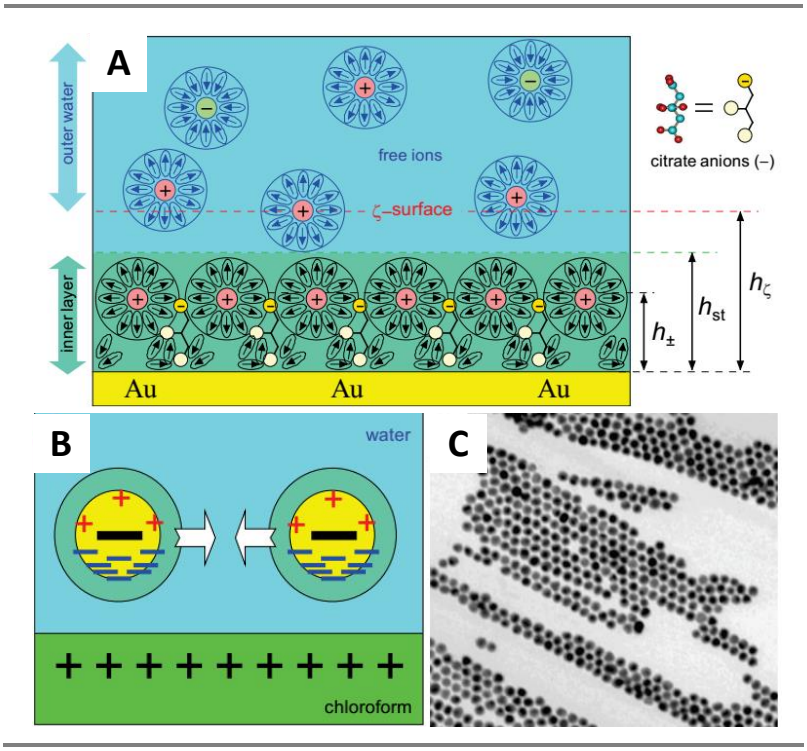

Figure 169 | (**A**) Local ionic organization near the gold surface of the nanoparticle. The inner layer is formed of adsorbed citrate and sodium ions (in their solvated state). (**B**) Electric charge redistribution on the Au NP surfaces (due to attraction to the positively charged border with chloroform) and the resultant side-to-side attraction of AuNPs near the water-chloroform interface. (**C**) TEM image of adsorbed NPs forming clusters at the interface.

The Au NPs are thus attracted to the interface, which is oppositely charged, because of the TATA fibrils. At a distance of around 5 nm, the condensed interfacial anions are driven away by electrostatic repulsion with the NP, increasing in such a way the effective positive charge at the interface by a factor of 5. This results in an attraction energy of about 110 $k_B T$, ensuring strong adsorption of AuNPs on the TATA film at the LLI. Interestingly, even neutral AuNPs could be adsorbed on the TATA film, as the net attraction energy is about 10 $k_B T$ due to the electrostatic negative charge induction at the surface of the NP close to the interface.

The kinetics of the NPs adsorption is governed by their diffusion/sedimentation, which increases during centrifugation.

The NPs tend to form a hexagonal structure at the surface, as soon as a significant surface coverage is achieved. However, in less dense regions, TEM images show the formation of ordered elongated clusters of NPs, following the orientation of the aligned fibres (**Figure 169C**). This peculiar effect could be explained by the attraction of NPs one to another due to the redistribution of their surface charges caused by the positively charged fibrils (**Figure 169B**).

4. CONCLUSIONS

To conclude, a new simple and fast method for the formation of hybrid TATA/Au plasmonic film was developed. The key steps of this process involved: (***i***) doping of TATA nanowires with positively charged radical cation molecules; (***ii***) migration and alignment of these fibres to the LLI, caused by the phase transfer of chloride anions to the aqueous phase, and followed by electrostatic interaction between the interface and the nanowires; (***iii***) centrifugation-enhanced diffusion of Au NPs to the LLI and adsorption on the TATA layer. Due to fibre alignment and to the lateral attraction between Au NPs, which is caused by the additional polarisation by the TATAs, structures with a high order of anisotropy were obtained. Importantly, we think that this method could be universal for any supramolecular structure, which is able to form 1D organised charged assembly, making it a useful tool for the preparation of anisotropically ordered plasmonic nanostructures.

GENERAL CONCLUSIONS AND PERSPECTIVES

In this manuscript, I described the results of my PhD work oriented towards the understanding of different fundamental aspects of the supramolecular chemistry of triarylamines and their potential applications.

In *Chapter II*, I elucidated the mechanism of thermally activated supramolecular polymerizations of triarylamine trisamides. It was shown that the assembly process proceeds *via* a cooperative nucleation and growth mechanism. The presence of thermal hysteresis between the assembly and dissociation processes indicates the existence of a kinetic barrier, that can be related to the inherent "propeller chirality" of triarylamines. Supramolecular chirality of the hierarchical assemblies depends on the rate of temperature change, as shown by CD spectroscopy and AFM imaging. This finding may contribute to a better control over the functional properties based on these supramolecular polymers and materials thereof. Further studies should be performed in the future to correlate the optical, electronic, magnetic, and plasmonic properties depending on the pathway used for the self-assembly.

In *Chapter III*, in collaboration with the group of Prof. R. Ulijn, we demonstrated the possibility to use an enzymatic approach for the construction of TAA-based structures which are inaccessible by other means. Incubation of the enzymatically triggered self-assembly at different temperatures allowed control over the morphology and chirality of the assemblies. It was shown that small changes in the TAA-peptide structure, such as the interchange of Tyr by Phe, lead to large changes on the macroscopic level. Here, again, optical and conductivity measurements should be performed in the future to extract a structure/function relationship of these systems.

Chapter IV describes the application of two and three centred derivatives of self-assembling TAAs as dopant-free hole transporting materials in perovskite-type solar cells. The photoconversion efficiencies of the devices incorporating our molecules demonstrated very good values, yet not competing with the best reference devices due to charge extraction and series resistance issues. However, we clearly highlighted the beneficial aspect of the supramolecular self-assembly on the photo-conversion.´

In *Chapter V*, we have demonstrated the possibility to trigger supramolecular polymerization electrochemically. The unidirectional growth of the fibres was performed under a sole electric field in situ at the micrometre scale between the electrodes. This type of

self-construction process opens many opportunities for the design of complex systems, such as 3D nanowiring for instance.

Chapter VI described the exploitation of the structural features of triarylamines. We described the process of the formation of hybrid organic-inorganic films at the liquid-liquid interface between TAA nanowires and gold nanoparticles due to their electrostatic attraction. An unprecedented high degree of ordering of gold nanoparticles was observed when an additional gravitational force was introduced to facilitate film formation, using simple centrifugation of a biphasic system. We believe that this simple and fast method can be used as a tool for the preparation of anisotropically ordered materials in general.

Overall, in my opinion, these findings push our knowledge and understanding of the supramolecular chemistry of triarylamine molecules a little further, which will help for the development of new systems with enhanced properties. More broadly, we attempted to make a contribution to the understanding of complex relationships between the structure of small molecules and the way in which it is expressed at the supramolecular level under the influence of environmental changes. I hope, that this small piece of research will contribute to the future development of supramolecular chemistry as "*somewhere, something incredible is waiting to be known*."

EXPERIMENTAL PART

1. General Procedures

A. Solvents and Chemicals

All reagents and solvents were purchased at the highest commercial quality and used without further purification unless otherwise noted. Dry solvents were obtained using a double column SolvTech purification system. Water was deionized by using a milli-gradient system (Millipore, Molsheim, France). All reactions were carried out under argon atmosphere except when water was used as a solvent.

B. Chromatographic Methods

Thin Layer Chromatographies were performed using silica on TLC Al foils (silica gel matrix with fluorescent indicator 254 nm, thickness: 500 µm, Sigma-Aldrich). The visualisation of TLC was performed using *Bioblock VL-4C* UV-Lamp (6 W, 254 nm and/or 365 nm), iodine vapour, phosphomolybdic acid and/or Cerium ammonium molybdate staining solutions. Preparative Column Chromatographies were performed using silica gel (60 Å, 230 – 400 mesh, 40 – 63 µm, Sigma-Aldrich). Preparative Ultra Performance Liquid Chromatographies were performed using a *Waters AutoPurify* system equipped with a UV detector (set at 310 nm), a *3100* mass spectrometer, reverse phase columns (Waters, Sun Fire Prep C_{18} 5.0 µm, 19 × 150 mm; Waters, XBridge Prep C_{18} 5.0 µm, 19 × 150 mm) running with a water/methanol gradient as eluent, and the MassLynx 4.1 – XP software.

C. Analytical Methods and Instruments

i. Ultra-High Performance Liquid Chromatography (UPLC)

Ultra-Performance Liquid Chromatographies coupled to Mass Spectroscopy (UPLC-MS) were carried out on a *Waters Acquity UPLC-SQD* apparatus equipped with a PDA detector (190–500 nm, 80Hz), a SQD mass spectrometer, using a reverse phase column (Waters, BEH C_{18} 1.7 µm, 2.1 mm × 50 mm), the MassLynx 4.1 – XP software and a gradient (water-acetonitrile + 0.1 % formic acid) as eluent.

ii. Nuclear Magnetic Resonance Spectroscopy

^{1}H NMR spectra were recorded on a *Bruker Avance 400* spectrometer at 400 MHz and ^{13}C NMR spectra at 100 MHz. The spectra were internally referenced to the residual solvent peaks (see ref[420] for information). For ^{1}H NMR assignments, the chemical shifts are given in ppm. Coupling constants *J* are given in Hz. Peaks are described as singlet (s), doublet (d), triplet (t), quartet (q), multiplet (m) and broad (br).

iii. Mass Spectrometry

Electrospray – Mass Spectroscopy (ESI-MS) were recorded using a *Waters SQD* mass spectrometer either by direct infusion or after UPLC chromatography using the MassLynx 4.1 – XP software.

iv. UV-Vis-NIR Spectroscopy

UV-Vis-NIR spectra were recorded on a UV-Vis-NIR spectrophotometer Cary 5000 Scan Varian. The Peltier 12 cuvette sample holder was used to control the temperature. Quartz cells with an appropriate path length (depending on the concentration of the studied solution) of 0.1 mm, 1 mm, 2 mm and 10 mm were used for the experiments.

v. FluorescenceSpectroscopy

Fluorescence emission spectra were recorded on a FluoroMax-4 (Horiba Jobin-Yvon) spectrofluorometer with the following settings: excitation wavelength (λ_{ex} = 310 nm), slit width = 2 nm; emission region 330 – 600 nm, slit width = 5 nm, increment = 1 nm, integration time = 0.1 s in quartz glass cuvette with 1.0 cm optical path. Temperature was controlled using a Peltier system.

vi. Circular Dichroism Spectroscopy

CD spectra were recorded on a Jasco J-810 spectropolarimeter. Quartz cells with an appropriate path length (depending on the concentration of the studied solution) of 0.1 mm, 1 mm, 2 mm and 10 mm were used for the experiments. Each spectrum was recorded at a scan rate of 100 nm/min, a response time of 1 s and a bandwidth of 1 nm. Temperature was controlled with a Peltier system.

420. Fulmer, G. R. *et al.* NMR chemical shifts of trace impurities: Common laboratory solvents, organics, and gases in deuterated solvents relevant to the organometallic chemist. *Organometallics* **29,** 2176–2179 (2010).

vii. Infra-Red Spectroscopy

InfraRed (IR) spectra were recorded on a Fourier transform infrared spectrometer VERTEX 70 (Bruker).

viii. Dynamic light scattering experiments

DLS experiments were performed using a ZetaSizer Nano ZS (Malvern Instruments, Worcestershire, UK).

ix. Optical Microscopy

Polarizing optical microscopy (POM) experiments were performed by using a Leica DMR polarization microscope (Leica) equipped with a digital camera (COOLPIX995, Nikon).

x. Transmission Electron Microscopy (TEM)

TEM experiments were performed using a CM12 Philips microscope equipped with a MVIII (SoftImaging System) CCD camera. Samples were analyzed in Bright Field Mode with a LaB6 cathode and 120 kV tension. Image treatments were performed by using analySIS (Soft Imaging System) software. For the sample preparation, a carbon-coated copper grid was placed on a Whatman filter paper. Then, a 5 μL drop was casted on the grid and the grid was left to dry at air before analysis.

xi. Scanning Electron Microscopy (SEM)

Scanning electron microscopy (SEM) experiments were performed using a SU8000 Hitachi microscope. All the samples were prepared by dropcasting a toluene solution on a silicon wafer. The solvent was evaporated under ambient conditions. Before analysis, a drop of colloidal silver was deposited on the side of the wafer to ensure conductivity of the sample. Abbreviations: WD – Working Distance; AV – Accelerating Voltage; DV – Decelerating Voltage; SE – Secondary Electrons mode; BSE – Back Scattered Electrons mode; U – Upper detector; L – Lower detector.

xii. Atomic Force Microscopy (AFM)

Atomic force microscopy (AFM) images were obtained by scanning the samples using a Nanoscope 8 (Bruker) operated in Peak-Force tapping mode. Peak-Force AFM is based on Peak force tapping technology, during which the probe is oscillated in a similar fashion as it is in tapping mode, but at far below the resonance frequency. Each time the tip and the sample are brought together, a force curve is captured. These forces can be controlled at levels much lower than contact mode and even lower than tapping mode allowing operation on even the most delicate soft samples. Ultra-sharp silicon cantilevers were used. During AFM imaging, the force was reduced in order to avoid dragging of molecules by the tip. Integral gain was adjusted to give sharp images. All analyses of the images were conducted in integrated software.

2. SYNTHESIS AND CHARACTERIZATION

A. Chapter II

Compounds (S)-1 and (R)-1

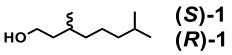

(3S)-3,7-dimethyloctan-1-ol/(3R)-3,7-dimethyloctan-1-ol

*Compounds **(S)-1/(R)-1** were synthesised according to a reported procedure.*[216] **(3S)-3,7-dimethyloct-6-en-1-ol/(3R)-3,7-dimethyloctan-1-ol** (5.0 g, 31.7 mmol) was dissolved in a mixture of ethyl acetate (15 mL) and methanol (15 mL) in 100 mL round bottom flask. Palladium on charcoal (200 mg) was added carefully to this solution under an argon atmosphere. The flask was closed with a Septa cork, vacuumed and a balloon with hydrogen was then connected. The reaction mixture was stirred under a hydrogen atmosphere at 50 °C overnight. When the volume of the balloon did not change anymore, the reaction mixture was cooled down to room temperature and the catalyst was removed by filtration through a pad of Celite®, which was washed few times with ethyl acetate (200 mL). The solvent was evaporated under reduced pressure, and the resulting residue was dried *in vacuo* to give **(3S)-3,7-dimethyloctan-1-ol** (**(*S*)-1**) or **(3R)-3,7-dimethyloctan-1-ol** (**(*R*)-1**) (4.9 g, 98 %) as a colourless oily liquid, which was clean enough to be used in the next step without purification. *Analyses were in accordance with the literature.*[216]

^{1}H NMR (400 MHz, $CDCl_3$, 25 °C): δ = 3.74 – 3.60 (m, 2H), 1.65 – 1.45 (m, 3H), 1.42 – 1.33 (m, 1H), 1.33 – 1.20 (m, 4H), 1.19 – 1.06 (m, 3H), 0.92 – 0.80 (m, 9H).

^{13}C NMR (100 MHz, $CDCl_3$, 25 °C): δ = 61.4, 40.2, 39.4, 37.5, 29.6, 28.1, 24.8, 22.8, 22.7, 19.8.

Compounds (S)-2 and (R)-2

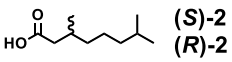

(3S)-3,7-dimethyloctanoic acid/(3R)-3,7-dimethyloctanoic acid

*Compounds **(S)-2/(R)-2** were synthesised according to a reported procedure.*[216] Periodic acid (7.2 g, 31.4 mmol) was dissolved in acetonitrile (100 mL) under vigorous stirring at room temperature for 40 min. Then, pyridinium chlorochromate (2 %, 0.06 g, 0.278 mmol) was

added. The solution was cooled down to 0°C using an ice bath and compound **(*S*)-1/(*R*)-1** (2.2 g, 13.9 mmol) in acetonitrile (30 mL) was added dropwise. The reaction mixture was stirred for 1 hour at 0 °C and for 3 hours at room temperature. After that time, acetonitrile was evaporated under reduced pressure. Ethyl acetate (200 mL) was added and the organic layer was extracted with water/brine 1:1 v/v (400 mL), saturated $NaHSO_3$ (300 mL) and again brine (500 mL). The organic phase was dried over Na_2SO_4, filtered and evaporated under vacuum. The resulting crude liquid was distilled using the kugelrohr to provide **(3S)-3,7-dimethyloctanoic acid** (**(*S*)-2**) or **(3R)-3,7-dimethyloctanoic acid** (**(R)-2**) (2.2 g, 92 %) as a colourless viscous liquid. *Analyses were in accordance with the literature.*[216]

^{1}H NMR (400 MHz, $CDCl_3$, 25 °C): δ = 2.35 (dd, *J* = 14.9, 5.8 Hz, 1H), 2.15 (dd, *J* = 14.9, 8.2 Hz, 1H), 2.01 – 1.90 (m, 1H), 1.60 – 1.46 (m, 1H), 1.38 – 1.10 (m, 6H), 0.97 (d, *J* = 6.7 Hz, 3H), 0.87 (d, *J* = 6.7 Hz, 6H).

Compound (S)-3

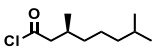

(*S*)-3

(3S)-3,7-dimethyloctanoyl chloride

The synthetic procedure was adapted from ref.[421] Compound **1d** (2.2 g, 12.8 mmol) was dissolved in chloroform (10 mL) and thionyl chloride (5 mL, 68.9 mmol) was added. The reaction mixture was stirred at reflux for 3 hours. After that time, it was cooled down to room temperature, solvent was removed under reduced pressure and **(3S)-3,7-dimethyloctanoyl chloride** (**(*S*)-3**) (2.4 g, 99 %) was obtained as a colourless oil after distillation using the kugelrohr. *Analyses were in accordance with the literature.*[216]

^{1}H NMR (400 MHz, $CDCl_3$, 25 °C): δ = 2.88 (dd, *J* = 16.0, 5.8 Hz, 1H), 2.68 (dd, *J* = 16.0, 8.0 Hz, 1H), 2.14 – 2.01 (m, 1H), 1.60 – 1.46 (m, 1H), 1.38 – 1.10 (m, 6H), 0.99 (d, *J* = 6.6 Hz, 3H), 0.87 (d, *J* = 6.6 Hz, 6H).

^{13}C NMR (100 MHz, $CDCl_3$, 25 °C): δ = 137.4, 54.4, 39.0, 36.5, 30.9, 3.03, 24.6, 22.8, 22.7, 19.4.

421. Koniev, O. *et al.* Selective Irreversible Chemical Tagging of Cysteine with 3-Arylpropiolonitriles. *Bioconjug. Chem.* **25,** 202–206 (2014).

Compound 4

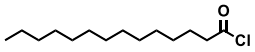

4

Myristoyl chloride

The synthetic procedure was adapted from refs.[421,422] Tetradecanoic acid (35.0 g, 153 mmol) was dissolved in chloroform (200 mL) and thionyl chloride (22.2 mL, 306 mmol) was added. The reaction mixture was stirred at reflux overnight. Chloroform and the excess of thionyl chloride were removed under reduced pressure. Pure **myristoyl chloride** (**4**) (35.0 g, 93 %) was obtained as a colourless liquid after vacuum distillation (*bp* 75 – 78 °C at 1 Torr). *Analyses were in accordance with the literature.*[422]

^{1}H NMR (400 MHz, $CDCl_3$, 25 °C): δ = 2.88 (t, *J* = 7.2 Hz, 2H), 1.71 (tt, *J* = 7.2, 7.2 Hz, 2H), 1.43 – 1.20 (m, 20H), 0.88 (t, *J* = 7.0 Hz, 3H).

^{13}C NMR (100 MHz, $CDCl_3$, 25 °C): δ = 173.8, 47.2, 32.1, 29.79, 29.76, 29.68, 29.51, 29.48, 29.2, 28.6, 25.2, 22.8, 14.2.

Compound 5

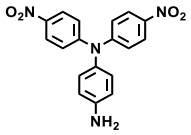

5

1-N,1-N-bis(4-nitrophenyl)benzene-1,4-diamine

*Compound **5** was synthesised according to a reported procedure.*[43] 1,4-benzenediamine (3.5 g, 32.4 mmol) and potassium carbonate (17.9 g, 129 mmol) were dissolved in a 250 mL Schleck flask in dry DMSO (50 mL). 4-fluoronitrobenzene (6.87 mL, 64.7 mmol) was added to the colourless reaction mixture and the reaction mixture was heated for 3 days at 90 °C. The colour changed to dark-red. Upon completion, as monitored by UPLC-MS, the solution was allowed to cool down to room temperature, and further diluted with water (300 mL) leading to the formation of a dark red precipitate. This solid was filtered, washed several times with water (5 × 50 mL) and then dried to provide **1-*N*,1-*N*-bis(4-nitrophenyl)benzene-1,4-diamine** (**5**) (10.4 g, 92 %) as a dark red solid. *Analyses were in accordance with the literature.*[43]

^{1}H NMR (400 MHz, $CDCl_3$, 25 °C): δ = 8.12 (d, *J* = 9.3 Hz, 4H), 7.13 (d, *J* = 9.3 Hz, 4H), 6.96 (d, *J* = 8.6 Hz, 2H), 6.73 (d, *J* = 8.6 Hz, 2H), 3.84 (brs, 2H).

422. Tautz, L. & Rétey, J. A Highly Convergent Synthesis of Myristoyl-carba(dethia)-coenzyme A. *European J. Org. Chem.* **2010,** 1728–1735 (2010).

^{13}C NMR (100 MHz, $CDCl_3$, 25 °C): δ = 152.2, 146.1, 142.3, 135.2, 129.1, 125.6, 121.6, 116.6.

MS (ESI): *m/z* calcd for $C_{18}H_{14}N_4O_4$ $[M]^+$ 350.10, found 350.29; calcd for $C_{18}H_{15}N_4O_4$ $[M+H]^+$ 351.11, found 351.29.

Compound 6

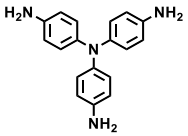

6

1-N,1-N-bis(4-aminophenyl)benzene-1,4-diamine

*Compound **6** was synthesised according to a reported procedure.*[423] Compound **5** (10.5 g, 30 mmol) was dissolved in a mixture of ethanol (200 mL) and dioxane (100 mL) in a 500 mL round-bottom two-neck flask equipped with a reflux condenser. Palladium on charcoal (0.8 g) was added carefully under an atmosphere of argon. The reaction mixture was heated up to 80 °C. Hydrazine hydrate (35 mL, 719 mmol) was added dropwise under vigorous stirring over a period of 3 hours, and the reaction mixture was further stirred under reflux overnight. Then, the reaction was cooled down to room temperature. The catalyst was removed by filtration through a pad of Celite®, which was washed few times with methanol (200 mL). The filtrate was poured into water (1 L). The precipitate was filtered off and dried to provide a crude product, which was recrystallized from boiling ethanol to provide compound **6** (7.1 g, 82 %) as a grey solid. *Analyses were in accordance with the literature.*[43]

^{1}H NMR (400 MHz, Acetone-d_6, 25 °C): δ = 6.71 (d, *J* = 8.7 Hz, 6H), 6.55 (d, *J* = 8.8 Hz, 6H), 4.28 (brs, 6H).

^{13}C NMR (100 MHz, Acetone-d_6, 25 °C): δ = 143.9, 140.7, 125.3, 116.0.

MS (ESI): *m/z* calcd for $C_{18}H_{18}N_4$ $[M]^+$ 290.15, found 290.38; calcd for $C_{18}H_{19}N_4$ $[M+H]^+$ 291.16, found 291.38.

423. Tzeng, B.-C., Chao, A., Selvam, T. & Chang, T.-Y. Polyrotaxane frameworks containing N,N′,N″-(4,4′,4″-nitrilotris(4,1-phenylene))triisonicotinamide: structural and luminescent properties. *CrystEngComm* **15,** 5337 (2013).

Compound **7**

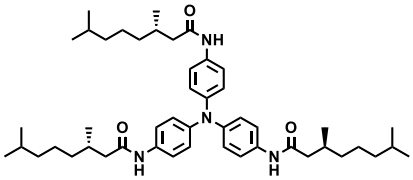

(S)-TATA
7

(3S)-N-{4-[bis({4-[(3S)-3,7-dimethyloctanamido]phenyl})amino]phenyl}-3,7-dimethyloctanamide

The synthetic procedure was adapted from ref.[113] Triarylamine **6** (420 mg, 1.45 mmol) was dissolved in dry dichloromethane (30 mL) in a 100 mL round bottom flask. Triethylamine (800 µL, 5.79 mmol) was added and the reaction mixture was cooled down to 0°C using an ice bath. A solution of compound **(*S*)-3** (965 mg, 5.06 mmol) in dry dichloromethane (10 mL) was added dropwise and the reaction mixture was stirred at room temperature overnight. The reaction mixture was diluted with dichloromethane (200 mL), and the organic phase was washed with a saturated solution of NH_4Cl (2 × 25 mL), brine (25 mL) and dried over anhydrous Na_2SO_4. After the solid was removed by filtration, solvent was evaporated under reduced pressure. The residue was washed with a minimum amount of methanol and the resulting white precipitate was collected. The methanol solution was evaporated and this operation repeated was several times to yield compound **7** (950 mg, 87 %) as a white solid.

^{1}H NMR (400 MHz, DMSO-*d*$_6$, *25 °C*): δ = 9.78 (s, 3H), 7.48 (d, *J* = 8.9 Hz, 6H), 6.88 (d, *J* = 8.9 Hz, 6H), 2.25 (dd, *J* = 13.9, 6.3 Hz, 3H), 2.08 (dd, *J* = 13.9, 8.1 Hz, 3H), 1.99 – 1.86 (m, 3H), 1.51 (m, 3H), 1.36 – 1.20 (m, 9H), 1.18 – 1.07 (m, 9H), 0.89 (d, *J* = 6.7 Hz, 9H), 0.85 (d, *J* = 6.7 Hz, 18H).

^{13}C NMR (100 MHz, DMSO-*d*$_6$, *25 °C*): δ = 170.4, 142.7, 134.2, 123.5, 120.3, 44.0, 38.6, 36.4, 30.2, 27.3, 24.1, 22.5, 22.4, 19.5.

MS (ESI): *m/z* calcd for $C_{48}H_{72}N_4O_3$ $[M]^+$ 752.56, found 752.77; calcd for $C_{48}H_{73}N_4O_3$ $[M+H]^+$ 753.57, found 753.76.

Compound 8

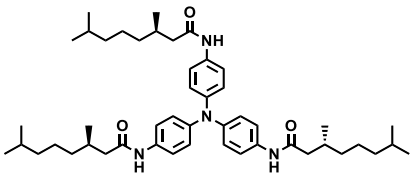

(R)-TATA
9

(3R)-N-{4-[bis({4-[(3R)-3,7-dimethyloctanamido]phenyl})amino]phenyl}-3,7-dimethyloctanamide

Triarylamine **6** (0.23 g, 0.792 mmol) was dissolved in a 100 mL Schlenk flask in a mixture of DMF (6 mL) and dichloromethane (6 mL). Compound **(*R*)-2** (0.409 g, 2.38 mmol) was added and the solution was cooled down to 0°C using an ice bath. PYBOP (1.28 g, 2.46 mmol) and diisopropylethylamine (0.69 mL, 3.96 mmol) were added and the reaction mixture was stirred for 2 days at room temperature. The reaction mixture was diluted with ethyl acetate (250 mL). The organic phase was washed with saturated sodium bicarbonate (50 mL), brine (2 × 50 mL) and dried over anhydrous Na_2SO_4. The solvent was evaporated, the resulting solid residue was purified by column chromatography (SiO_2, cyclohexane/ethyl acetate 90/10 → 50/50) and further recrystallized from acetone to provide compound **8** (0.209 g, 35 %) as a white solid.

^{1}H NMR (400 MHz, DMSO-*d*$_6$, *25 °C*): δ = 9.78 (s, 3H), 7.48 (d, *J* = 8.9 Hz, 6H), 6.88 (d, *J* = 8.9 Hz, 6H), 2.25 (dd, *J* = 13.9, 6.3 Hz, 3H), 2.08 (dd, *J* = 13.9, 8.1 Hz, 3H), 1.99 – 1.86 (m, 3H), 1.58 – 1.45 (m, 3H), 1.36 – 1.20 (m, 9H), 1.18 – 1.07 (m, 9H), 0.89 (d, *J* = 6.7 Hz, 9H), 0.85 (d, *J* = 6.7 Hz, 18H).

^{13}C NMR (100 MHz, DMSO-*d*$_6$, *25 °C*): δ = 170.4, 142.7, 134.2, 123.5, 120.3, 44.0, 38.6, 36.4, 30.2, 27.3, 24.1, 22.5, 22.4, 19.5.

MS (ESI): *m/z* calcd for $C_{48}H_{72}N_4O_3$ $[M]^+$ 752.56, found 752.77; calcd for $C_{48}H_{73}N_4O_3$ $[M+H]^+$ 753.57, found 753.76.

Compound 9

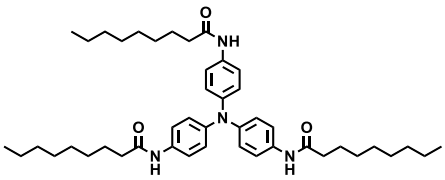

C9-TATA
9

N-{4-[bis(4-nonanamidophenyl)amino]phenyl}nonanamide

The synthetic procedure was adapted from ref.[113] Triarylamine **6** (1.0 g, 3.44 mmol) was dissolved in a mixture of dichloromethane (50 mL) and THF (25 mL). Triethylamine (1.9 mL, 13.8 mmol) was added and the solution was cooled down to 0 °C using an ice bath, followed by the addition of nonanoyl chloride (2.43 g, 13.8 mmol). The reaction mixture was stirred for 15 min at 0 °C and then for 1 hour at room temperature. The solvent was then evaporated and the crude solid was dissolved in THF (300 mL). The organic phase was washed subsequently with 1M HCl/brine – 1:2 v/v (100 mL), 1M NaOH/brine – 1:2 v/v (2 × 50 mL), saturated NH_4Cl (50 mL) and brine (100 mL) and then dried over anhydrous Na_2SO_4. After evaporation of the solvents under reduced pressure, the crude residue was recrystallized from boiling ethanol, the precipitate was filtered, washed with cold ethanol (50 mL) and diethyl ether (250 mL) and finally dried under vacuum to provide compound **3** (2.3 g, 94 %) as a white solid.

^{1}H NMR (400 MHz, DMSO-*d*$_6$, *25 °C*): δ = 9.76 (s, 3H), 7.47 (d, *J* = 8.8 Hz, 6H), 6.87 (d, *J* = 8.9 Hz, 6H), 2.26 (t, *J* = 7.3 Hz, 6H), 1.57 (tt, *J* = 7.2, 7.2 Hz, 6H), 1.35 – 1.15 (m, 31H), 0.86 (t, *J* = 7.2 Hz, 9H).

MS (ESI): *m/z* calcd for $C_{45}H_{66}N_4O_3$ $[M]^+$ 710.51, found 710.64; calcd for $C_{45}H_{67}N_4O_3$ $[M+H]^+$ 711.52, found 711.63.

Compound 10

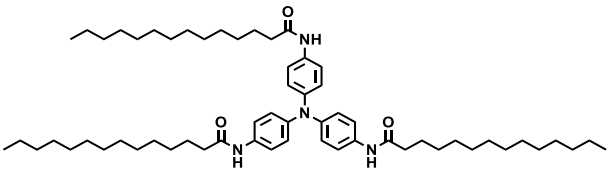

C14-TATA
10

N-{4-[bis(4-tetradecanamidophenyl)amino]phenyl}tetradecanamide

The synthetic procedure was adapted from ref.[113] Triarylamine **6** (400 mg, 1.38 mmol) was dissolved in a mixture of dichloromethane (50 mL) and THF (50 mL). Triethylamine (766 µL, 5.51 mmol) was added and the solution was cooled down to 0 °C using an ice bath. Myristoyl

chloride (**4**) (1.36 g, 5.51 mmol) was then added dropwise to the stirred solution and the reaction mixture was warmed up and stirred for 1 h at room temperature. The solvent was then evaporated and the crude solid was dissolved in THF (250 mL). The organic phase was washed subsequently with 1M HCl/brine – 1:2 v/v (100 mL), 1M NaOH/brine – 1:2 v/v (2 × 50 mL), saturated NH_4Cl (50 mL) and brine (100 mL) and then dried over anhydrous Na_2SO_4. After evaporation of the solvents under reduced pressure, the crude residue was recrystallized from boiling ethanol, the precipitate was filtered, washed with cold ethanol (150 mL) and diethyl ether (150 mL) and finally dried under vacuum to provide compound **10** (1.1 g, 87 %) as a white solid.

^{1}H NMR (400 MHz, CD_3OD/Toluene-d_8, 25 °C): δ = 7.55 (d, *J* = 8.9 Hz, 6H), 6.98 (d, *J* = 8.9 Hz, 6H), 2.33 (t, *J* = 7.3 Hz, 6H), 1.71 (tt, *J* = 7.5, 7.5 Hz, 6H), 1.42 – 1.20 (m, 60H), 0.89 (t, *J* = 6.8 Hz, 9H).

^{13}C NMR (100 MHz, CD_3OD/Toluene-d_8, 25 °C): δ = 174.0, 145.1, 134.8, 125.0, 122.2, 44.0, 32.9, 30.7 (br.), 30.6, 30.5, 30.4, 30.3, 26.9, 23.6, 14.6.

B. Chapter III

Compound 11

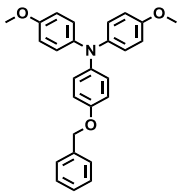

11

N-[4-(benzyloxy)phenyl]-4-methoxy-N-(4-methoxyphenyl)aniline

Tris(dibenzylideneacetone)dipalladium(0) (249 mg, 0.272 mmol) and tri-*tert*-butylphosphine (1 M in Toluene, 1.09 mL, 1.09 mmol) were dissolved in degassed toluene (10 mL) in a 100 mL Schlenk, and the deep-purple coloured mixture was stirred for 15 min at room temperature. After this time, 4-bromoanisole (7.93 g, 42.4 mmol) was added, the colour changed to red-orange, followed by addition of sodium *tert*-butoxide (6.52 g, 67.9 mmol) and 4-(benzyloxy)anilinium chloride (4.0 g, 17.0 mmol). The reaction mixture was stirred at 100 °C for 1 day and then, after cooling down to room temperature, toluene was evaporated and the crude residue was dissolved in diethyl ether (300 mL). The organic phase was washed with a saturated solution of NH_4Cl (2 × 100 mL), water (100 mL), brine (2 × 50 mL) and dried over anhydrous Na_2SO_4. The solvent was evaporated and the crude product was purified by column chromatography (SiO_2, cyclohexane/ethyl acetate: 80/20) to give compound **11** (6.2 g, 89 %) as a colourless amorphous solid.

^{1}H NMR (400 MHz, Acetone-d_6, 25 °C): δ = 7.49 – 7.44 (m, 2H), 7.41 – 7.35 (m, 2H), 7.35 – 7.28 (m, 1H), 6.93 (d, *J* = 9.0 Hz, 6H), 6.83 (d, *J* = 9.0 Hz, 6H), 5.06 (s, 2H), 3.75 (s, 6H).

^{13}C NMR (100 MHz, Acetone-d_6, 25 °C): δ = 156.2, 155.1, 143.1, 142.8, 138.6, 129.2, 128.6, 125.7, 125.3, 116.4, 115.4, 70.8, 55.7.

MS (ESI): *m/z* calcd for $C_{27}H_{25}NO_3$ $[M]^+$ 411.18, found 411.24; calcd for $C_{27}H_{26}NO_3$ $[M+H]^+$ 412.19, found 412.26.

Compound 12

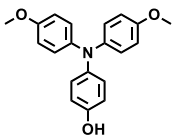

12

4-[bis(4-methoxyphenyl)amino]phenol

Compound **11** (4.5 g, 10.9 mmol) was dissolved in a mixture of methanol (20 mL) and ethyl acetate (30 mL) in a 100 mL round bottom flask. Palladium on charcoal (0.116 g) was added carefully and a balloon of hydrogen was connected to the flask. The reaction mixture was stirred for 2 hours at room temperature, as monitored by UPLC-MS, and then filtered through a pad of Celite® and washed with methanol (150 mL). The solvent was evaporated under reduced pressure affording compound **12** (3.48 g, 99 %) as a slightly greenish solid, which was pure enough to be used immediately in the next step.

MS (ESI): *m/z* calcd for $C_{20}H_{19}NO_3$ $[M]^+$ 321.14, found 321.18; calcd for $C_{20}H_{20}NO_3$ $[M+H]^+$ 322.14, found 322.18.

Compound 13

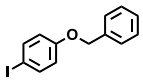

13

1-(benzyloxy)-4-iodobenzene

4-iodophenol (25.0 g, 113 mmol) was dissolved in acetone (400 mL) in a 500 mL round-bottom flask. Potassium carbonate (31.4 g, 227 mmol) was added and the reaction mixture was stirred for 10 min, followed by the addition of benzyl bromide (14.3 mL, 119 mmol), which resulted in slightly yellow suspension. The reaction mixture was stirred overnight at reflux and then, acetone was removed under reduced pressure. The solid residue was dissolved in ethyl acetate (500 mL) and washed with water (100 mL), NaOH 1M (200 mL) and brine (50 mL). The organic phase was dried over anhydrous Na_2SO_4, filtered and the solvent was removed under reduced pressure. Compound **13** (32.0 g, 91 %) was recovered as a white solid after recrystallization from ethanol. *Analyses were in accordance with literature.*

^{1}H NMR (400 MHz, $CDCl_3$, 25°C): δ = 7.56 (d, *J* = 9.0 Hz, 2H), 7.43 – 7.30 (m, 5H), 6.76 (d, *J* = 9.0 Hz, 2H), 5.04 (s, 2H).

^{13}C NMR (100 MHz, $CDCl_3$, 25°C): δ = 158.9, 138.5, 136.8, 128.8, 128.3, 127.6, 117.5, 83.3, 70.3.

Compound 14

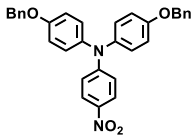

14

4-(benzyloxy)-N-[4-(benzyloxy)phenyl]-N-(4-nitrophenyl)aniline

*Compound **14** was synthesised according to a reported procedure.*[81] *p*-nitroaniline (1.36 g, 9.87 mmol), compound **13** (12.3 g, 39.5 mmol), potassium carbonate (10.9 g, 79.0 mmol), copper(I) iodide (752 mg, 3.95 mmol) and L-proline (0.91 g, 7.9 mmol) were suspended in dry DMF (40 mL). The reaction mixture was heated for 5 days at 150°C resulting in a dark-red coloured mixture. After that time, the solution was cooled down to room temperature, poured into a saturated solution of NH_4Cl (150 mL) and the aqueous solution was extracted with ethyl acetate (2 × 200 mL). The combined organic phase was washed with a solution of EDTA (2 × 50 mL), water (2 × 100 mL), brine (2 × 50 mL) and dried over anhydrous Na_2SO_4. Evaporation under reduced pressure followed by purification by column chromatography (SiO_2, cyclohexane/dichloromethane 50/50) provided compound **14** (3.2 g, 64 %) as an orange-red solid. *Analyses were in accordance with the literature.*[81]

^{1}H NMR (400 MHz, $CDCl_3$, 25°C): δ = 8.00 (d, *J* = 9.2 Hz, 2H), 7.47 – 7.31 (m, 10H), 7.13 (d, *J* = 8.9 Hz, 4H), 6.98 (d, *J* = 8.9 Hz, 2H), 6.77 (d, J = 9.2 Hz, 2H), 5.07 (s, 4H).

^{13}C NMR (100 MHz, $CDCl_3$, 25°C): δ = 157.0, 154.2, 139.2, 138.6, 136.8, 128.8, 128.2, 128.2, 127.6, 125.7, 116.2, 116.0, 70.4.

MS (ESI): *m/z* calcd for $C_{32}H_{26}N_2O_4$ $[M+H]^+$ 503.20, found 503.23.

Compound 16

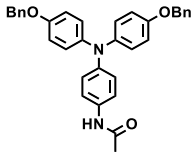

16

1-N,1-N-bis[4-(benzyloxy)phenyl]benzene-1,4-diamine

*Compound **16** was synthesised according to a reported procedure.*[81] Compound **14** (770 mg, 1.53 mmol) and tin (II) chloride dihydrate (3.46 g, 15.3 mmol) were dissolved in a mixture of acetonitrile (20 mL) and ethanol (20 mL) in a 100 mL flask. The orange reaction mixture was stirred at reflux overnight and, after cooling down to room temperature, it was diluted with ethyl acetate (200 mL). The organic phase was washed with NaOH 3M (3 × 75 mL), water (3

× 100 mL), brine (2 × 100 mL), then dried over anhydrous Na_2SO_4. Further evaporation under reduced pressure provided compound **15** as a yellowish solid, which was used in the next step without purification.

To a cooled (0 °C) solution of compound **15** (1.88 g, 3.98 mmol) and triethylamine (3.3 mL, 23.9 mmol) in dichloromethane (50 mL), acetyl chloride (1.56 g, 19.9 mmol) was added dropwise. The reaction mixture was stirred for 5 min at 0 °C and then was warmed up to room temperature. Upon completion, as monitored by UPLC-MS, the reaction mixture was diluted with dichloromethane (200 mL). The organic phase was washed with HCl 1M (2 × 50 mL), a saturated solution of Na_2CO_3 (2 × 50 mL), water (2 × 100 mL) and brine (100 mL), and then over anhydrous Na_2SO_4. After evaporation of the solvent under reduced pressure, the brownish crude residue was purified by column chromatography (SiO_2, cyclohexane/ethyl acetate 50/50) to provide compound **16** (1.93 g, 94 %) as a white solid. *Analyses were in accordance with the literature*.[81]

^{1}H NMR (400 MHz, Acetone-*d*$_6$, *25 °C*): δ = 9.02 (s, 1H), 7.53 – 7.44 (m, 6H), 7.42 – 7.36 (m, 4H), 7.35 – 7.28 (m, 2H), 7.00 - 6.92 (m, 8H), 6.86 (d, *J* = 8.9 Hz, 2H), 5.09 (s, 4H), (CH_3 signal overlaps with the solvent residual peak).

^{13}C NMR (100 MHz, Acetone-*d*$_6$, *25 °C*): δ = 168.4, 155.7, 145.1, 142.55, 138.5, 134.7, 129.3, 128.6, 128.4, 126.3, 123.2, 121.0, 116.5, 70.8.

MS (ESI): *m/z* calcd for $C_{34}H_{30}N_2O_3$ $[M]^+$ 514.23, found 514.35; calcd for $C_{34}H_{31}N_2O_3$ $[M+H]^+$ 515.23, found 515.39.

Compound 17

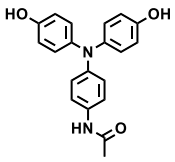

17

N-{4-[bis(4-hydroxyphenyl)amino]phenyl}acetamide

*Compound **17** was synthesised according to a reported procedure.*[114] To a solution of compound **16** (480 mg, 0.933 mmol) in a mixture of methanol (15 mL) and ethyl acetate (15 mL), palladium on charcoal (30 mg) was added under argon atmosphere and a balloon of hydrogen was connected to the flask. The reaction mixture was stirred for 8 hours at room temperature, and upon completion of the reaction, as monitored by UPLC, the reaction mixture was filtered through a pad of Celite® which was washed few times with methanol (40 mL). Further evaporation under reduced pressure afforded compound **17** (311 mg,

quantitative) as a greenish-coloured solid, which was used without purification in the next step. *Analyses were in accordance with the literature.*[114]

MS (ESI): *m/z* calcd for $C_{20}H_{18}N_2O_3$ $[M]^+$ 334.13, found 334.30; calcd for $C_{20}H_{19}N_2O_3$ $[M+H]^+$ 335.14, found 335.31.

Compound 18

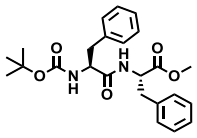

18

Methyl (tert-butoxycarbonyl)-L-phenylalanyl-L-phenylalaninate

To a solution of N-(*tert*-butoxycarbonyl)- L-phenylalanine (6.0 g, 22.4 mmol), EDC • HCl (4.34 g, 22.4 mmol), HOBt hydrate (3.43 g, 22.4 mmol) and diisopropylethylamine (11.1 mL, 67.2 mmol) in DMF (100 mL) was added at 0 °C to a solution of L-phenylalanine methyl ester hydrochloride (4.39 g, 20.4 mmol) and diisopropylethylamine (11.1 mL, 67.2 mmol) in DMF (100 mL). The reaction mixture was stirred for 10 min at 0 °C, for 12 h at room temperature, and then diluted with ethyl acetate (200 mL). The organic phase was washed with a solution of citric acid (100 mL), NaOH 1M (100 mL), water (2 × 100 mL), brine (100 mL) and dried over anhydrous Na_2SO_4. After evaporation under reduced pressure, the resulting yellowish crude product was recrystallized form ethyl acetate/cyclohexane: (50/50) affording compound **18** (8.0 g, 92 %) as a white solid.

^{1}H NMR (400 MHz, $CDCl_3$, 25°C): δ = 7.32 – 7.15 (m, 8H), 7.01 – 6.95 (m, 2H), 6.25 (brd, *J* = 7.1 Hz, 1H), 4.91 (brs, 1H), 4.78 (td, *J* = 7.6, 6.1 Hz, 1H), 4.41 – 4.20 (m, 1H), 3.67 (s, 3H), 3.12 – 2.96 (m, 4H), 1.40 (s, 9H).

^{13}C NMR (100 MHz, $CDCl_3$, 25°C): δ = 171.5, 170.9, 155.4, 136.6, 135.8, 129.5, 129.4, 128.8, 128.7, 127.3, 127.1, 80.4, 55.8, 53.4, 52.4, 38.4, 38.1, 28.4.

MS (ESI): *m/z* calcd for $C_{24}H_{31}N_2O_5$ $[M+H]^+$ 427.22, found 427.40; calcd for $C_{24}H_{30}N_2O_3Na$ $[M+Na]^+$ 449.21, found 449.38.

Compound 20

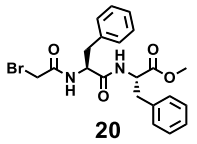

20

Methyl (2-bromoacetyl)- L-phenylalanyl- L-phenylalaninate

The synthetic procedure was adapted from ref.[421] To a solution of compound **18** (1.54 g, 3.61 mmol) in dichloromethane (40 mL) was added TFA (4.0 mL, 54.2 mmol). The reaction mixture was stirred for 2 hours at room temperature and then, the solvent was removed under reduced pressure. The resulting white solid was suspended in toluene (20 mL), and the solution was then evaporated in order to remove residual TFA. This operation was repeated few times providing **H-L-Phe-L-Phe-OMe TFA salt** (**19**) as a white solid which was used in the next step without purification.

To the suspension of crude compound **19** (1.57 g, 3.57 mmol) in dry dichloromethane (200 mL) was added diisopropylethylamine (1.77 mL, 10.7 mmol). The reaction mixture was stirred at room temperature for 10 min until dissolution of all the starting material, and after cooling down to -78 °C, bromoacetyl chloride (355 µL, 4.29 mmol) was added dropwise using a syringe pump over 30 minutes. The reaction medium was then stirred at -78 °C for 30 min and at room temperature for 1 hour. It was then washed with 1M HCl (2 × 50 mL), water (100 mL), brine (100 mL) and then dried over anhydrous Na_2SO_4. Further evaporation under reduced pressure followed by purification by column chromatography (SiO_2, cyclohexane/ethyl acetate: 100:0 → 70/30) provided compound **20** (1.4 g, 88 %) as an off-white solid.

^{1}H NMR (400 MHz, $CDCl_3$, 25°C): δ = 7.33 – 7.16 (m, 8H), 7.00 – 6.92 (m, 3H), 6.10 – 6.02 (m, 1H), 4.76 (td, *J* = 7.6, 6.1 Hz, 1H), 4.63 – 4.53 (m, 1H), 4.00 – 3.75 (m, 2H), 3.70 (s, 3H), 3.16 – 2.93 (m, 4H).

^{13}C NMR (100 MHz, $CDCl_3$, 25°C): δ = 171.3, 169.7, 165.5, 136.0, 135.6, 129.6, 129.3, 128.9, 128.8, 127.4, 127.3, 55.0, 53.5, 52.5, 38.1, 37.9, 28.7.

MS (ESI): *m/z* calcd for $C_{21}H_{24}BrN_2O_4$ $[M+H]^+$ 447.09/449.09, found 447.26/449.25.

Compound 21

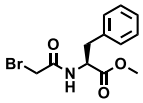

21

Methyl (2S)-2-(2-bromoacetamido)-3-phenylpropanoate

The synthetic procedure was adapted from ref.[421] To a suspension of L-phenylalanine methyl ester hydrochloride (2.0 g, 9.27 mmol) in dichloromethane (200 mL) was added diisopropylethylamine (3.6 g, 4.6 mL, 27.8 mmol). The reaction mixture was stirred for 10 min at room temperature and after dissolution of all the starting material, the solution was cooled down to -78 °C and bromoacetyl chloride (1.01 mL, 11.5 mmol) in dichloromethane (20 mL) was added slowly using a syringe pump (30 minutes) resulting in orange-coloured solution. This solution was warmed up to room temperature and stirred for another 3 hours before being washed with 1M HCl (2 x 50 mL), water (100 mL), brine (100 mL), and dried over anhydrous Na_2SO_4. Further evaporation under reduced pressure and purification by column chromatography (SiO_2, cyclohexane/ethyl acetate: 100/0 → 70/30) provided compound **21** (2.59 g, 93 %) as white solid.

^{1}H NMR (400 MHz, $CDCl_3$, 25°C): δ = 7.36 – 7.22 (m, 3H), 7.16 – 7.08 (m 2H), 6.84 (brd, *J* = 6.8 Hz, 1H), 4.90 – 4.81 (m, 1H), 3.87 – 3.78 (m, 2H), 3.74 (s, 3H), 3.22 – 3.07 (m, 2H).

^{13}C NMR (100 MHz, $CDCl_3$, 25°C): δ = 171.4, 165.2, 135.5, 129.3, 128.8, 127.5, 53.8, 52.6, 37.9, 28.7.

MS (ESI): *m/z* calcd for $C_{12}H_{14}BrNO_3$ $[M+H]^+$ 300.02/302.02, found 300.21/300.22.

Compound 22

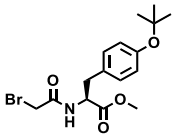

22

Methyl (2S)-2-(2-bromoacetamido)-3-[4-(tert-butoxy)phenyl]propanoate

The synthetic procedure was adapted from ref.[421] To a stirred solution of (2S)-3-[4-(*tert*-butoxy)phenyl]-1-methoxy-1-oxopropan-2-aminium chloride (5.00 g, 17.4 mmol) in dichloromethane (400 mL) was added diisopropylethylamine (8.61 mL, 52.1 mmol). The resulting solution was cooled down to -78 °C and a solution of bromoacetyl chloride (1.88 mL, 21.5 mmol) in dichloromethane (20 mL) was added dropwise resulting in a brownish solution, which was warmed up to room temperature and stirred for another 1 hour. After that

time, the reaction mixture was washed with 1M HCl (2 × 100 mL), water (100 mL) and brine (100 mL) and dried over anhydrous Na_2SO_4. Further evaporation under reduced pressure and purification by column chromatography (SiO_2, cyclohexane/ethyl acetate: 100/0 → 70/30) provided compound **22** (5.8 g, 90 %) as a slightly yellow oil.

^{1}H NMR (400 MHz, $CDCl_3$, 25°C): δ = 7.00 (d, *J* = 8.6 Hz, 2H), 6.91 (d, *J* = 8.6 Hz, 2H), 6.81 (brd, *J* = 7.6 Hz, 1H), 4.8 (td, *J* = 7.9, 5.9 Hz, 1H), 3.88 – 3.76 (m, 2H), 3.71 (s, 3H), 3.15 – 3.03 (m, 2H), 1.32 (s, 9H).

^{13}C NMR (400 MHz, $CDCl_3$, 25°C): δ = 171.4, 165.2, 154.8, 130.2, 129.8, 124.4, 78.6, 53.9, 52.5, 37.2, 29.0, 28.8.

MS (ESI): *m/z* calcd for $C_{16}H_{23}BrNO_4$ $[M+H]^+$ 372.08/374.08, found 372.25/374.25.

Compound 23

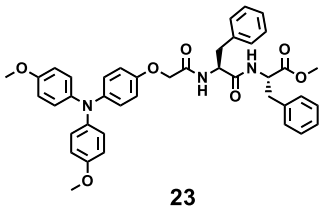

23

Methyl 2-[(2S)-2-(2-{4-[bis(4-methoxyphenyl)amino]phenoxy}acetamido)-3-phenylpropanamido]-3-phenylpropanoate

Compounds **12** (445 mg, 1.38 mmol) and **20** (743 mg, 1.66 mmol) and potassium carbonate (382 mg, 2.77 mmol) were dissolved in dry DMF (8 mL) in a 25 mL flask. The reaction mixture which become red-brown was stirred at room temperature for 2 days, and then diluted with ethyl acetate (200 mL). The organic phase was washed with water (3 × 50 mL) and brine (50 mL) and dried over anhydrous Na_2SO_4. Further evaporation of the solvent provided an orange oil, which was washed few times with acetone (3×15 mL) to afford compound **23** (700 mg, 74 %) as a white solid.

^{1}H NMR (400 MHz, CD_3OD, 25°C): δ = 7.30 – 7.10 (m, 10H), 6.90 (d, *J* = 9.0 Hz, 4H), 6.86 – 6.77 (m, 6H), 6.70 (d, *J* = 9.0 Hz, 2H), 4.78 – 4.71 (m, 1H), 4.70 – 4.63 (m, 1H), 4.41 – 4.29 (m, 2H), 3.75 (s, 6H), 3.66 (s, 3H), 3.12 (dt, *J* = 14.2, 5.7, Hz, 2H), 3.01 – 2.84 (m, 2H).

^{13}C NMR (100 MHz, CD_3OD, 25°C): δ = 171.8, 168.1, 168.0, 153.7, 143.1, 141.3, 137.3, 134.2, 129.2, 128.4, 126.7, 125.5, 123.3, 120.5, 115.9, 67.1, 53.2, 52.2, 36.5, 24.0.

MS (ESI): *m/z* calcd for $C_{41}H_{41}N_3O_7$ $[M]^+$ 687.29, found 687.26; calcd for $C_{41}H_{42}N_3O_7$ $[M+H]^+$ 688.30, found 688.27.

Compound 24

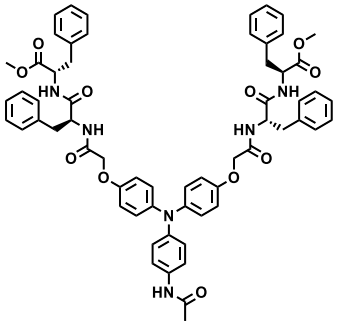

24

(2S)-2-[(2S)-2-(2-{4-[(4-acetamidophenyl)({4-[({1-[(1-methoxy-1-oxo-3-phenylpropan-2-yl)carbamoyl]-2-phenylethyl}carbamoyl)methoxy]phenyl})amine

Compounds **17** (165 mg, 0.493 mmol), compound **20** (485 mg, 1.09 mmol) and caesium carbonate (482 mg, 1.48 mmol) were dissolved in dry DMF (3 mL) in a 10 mL flask. The reaction mixture, which become reddish-brown, was stirred at room temperature for 2 days and then, diluted with ethyl acetate (400 mL). The organic phase was washed with water (3 × 50 mL) and brine (50 mL) and dried over anhydrous Na_2SO_4. Further evaporation of the solvent provided an orange oil, which was washed few times with acetone (15 mL) to afford compound **24** (360 mg, 68 %) as a white solid.

^{1}H NMR (400 MHz, DMSO-*d*$_6$, 25 °C): δ = 9.82 (s, 1H), 8.56 (d, *J* = 7.7 Hz, 2H), 8.02 (d, *J* = 7.7 Hz, 2H), 7.44 (d, *J* = 9.0 Hz, 2H), 7.33 – 6.97 (m, 20H), 6.87 – 6.77 (m, 6H), 6.73 (d, *J* = 9.2 Hz, 4H), 4.70 – 4.60 (m, 2H), 4.55 – 4.46 (m, 2H), 4.36 (s, 4H), 3.59 (s, 6H), 3.09 – 2.90 (m, 6H), 2.87 – 2.78 (m, 2H), 2.01 (s, 3H).

MS (ESI): *m/z* calcd for $C_{62}H_{62}N_6O_{11}$ $[M]^+$ 1066.45, found 1066.32; calcd for $C_{62}H_{63}N_6O_{11}$ $[M+H]^+$ 1067.45, found 1067.38.

Compound 25

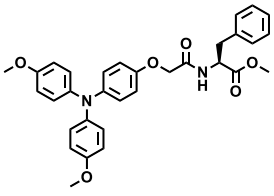

25

Methyl 2-(2-{4-[bis(4-methoxyphenyl)amino]phenoxy}acetamido)-3-phenylpropanoate

Compound **12** (647 mg, 2.01 mmol), compound **21** (725 mg, 2.42 mmol) and potassium carbonate (556 mg, 4.03 mmol) were dissolved in dry DMF (10 mL) in a 10 mL flask. The reaction mixture, which became brownish, was stirred at room temperature overnight, and

then diluted with ethyl acetate (300 mL). The organic phase was washed with water (3 × 50 mL) and brine (50 mL) and dried over anhydrous Na_2SO_4. Further evaporation under reduced pressure and purification by column chromatography (SiO_2, cyclohexane/ethyl acetate: 20/80) provided compound **25** (890 mg, 82 %) as a white solid.

^{1}H NMR (400 MHz, $CDCl_3$, 25 °C): δ = 7.30 – 7.20 (m, 3H), 7.11 – 7.05 (m, 2H), 7.03 – 6.88 (m, 6H), 6.80 (d, *J* = 9.0 Hz, 4H), 6.73 (d, *J* = 9.0 Hz, 2H), 5.00 – 4.92 (m, 1H), 4.49 – 4.37 (m, 2H), 3.78 (s, 6H), 3.73 (s, 3H), 3.15 (d, *J* = 5.9 Hz, 2H).

^{13}C NMR (100 MHz, $CDCl_3$, 25 °C): δ = 171.7, 168.3, 155.5, 152.3, 143.7, 141.8, 135.8, 129.4, 128.9, 127.5, 125.5, 124.1, 115.7, 114.8, 68.0, 55.7, 52.6, 52.5, 38.2.

MS (ESI): *m/z* calcd for $C_{32}H_{32}N_2O_6$ $[M]^+$ 540.23, found 540.28; calcd for $C_{32}H_{33}N_2O_6$ $[M+H]^+$ 541.23, found 541.27.

Compound 26

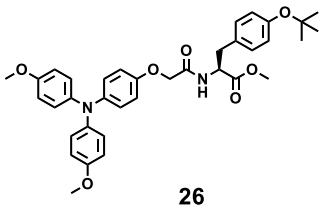

26

Methyl (2S)-2-(2-{4-[bis(4-methoxyphenyl)amino]phenoxy}acetamido)-3-[4-(tert-butoxy)phenyl]propanoate

Compounds **12** (950 mg, 2.96 mmol), compound **22** (1.32 g, 3.55 mmol) and potassium carbonate (817 mg, 5.91 mmol) were dissolved in dry DMF (15 mL) in a 10 mL flask. The reaction mixture was stirred at room temperature for 2 days and then diluted with ethyl acetate (350 mL). The organic phase was washed with water (3 × 50 mL) and brine (50 mL) and dried over anhydrous Na_2SO_4. Further evaporation under reduced pressure and purification by column chromatography (SiO_2, cyclohexane/ethyl acetate: 20/80) provided compound **26** (1.5 g, 83 %) as a white solid.

^{1}H NMR (400 MHz, $CDCl_3$, 25 °C): δ = 7.01 – 6.91 (m, 8H), 6.88 (d, *J* = 8.5 Hz, 2H), 6.79 (d, *J* = 9.0 Hz, 4H), 6.73 (d, *J* = 9.2 Hz, 2H), 4.97 – 4.89 (m, 1H), 4.48 – 4.36 (m, 2H), 3.78 (s, 6H), 3.70 (s, 3H), 3.15 – 3.03 (m, 2H), 1.31 (s, 9H).

MS (ESI): *m/z* calcd for $C_{36}H_{40}N_2O_7$ $[M]^+$ 612.28, found 612.31; calcd for $C_{36}H_{41}N_2O_7$ $[M+H]^+$ 613.29, found 613.32.

Compound 27

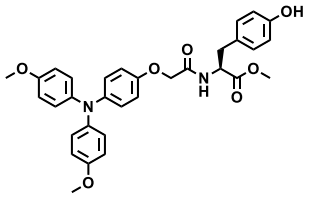

27

Methyl (2S)-2-(2-{4-[bis(4-methoxyphenyl)amino]phenoxy}acetamido)-3-(4-hydroxyphenyl)propanoate

To a cooled (0°C) solution of compound **26** (1.3 g, 2.12 mmol) in dichloromethane (50 mL) TFA (5.0 mL, 67.3 mmol) was added dropwise. The reaction mixture was then stirred at room temperature for 6 hours and upon completion of the reaction, as monitored by UPLC-MS, the solvent was evaporated. The resulting green coloured residue was dissolved in water (50 mL), and the pH was adjusted to 6 – 7 with a solution of sodium bicarbonate. The aqueous phase was extracted with ethyl acetate (3 × 100 mL) and the combined organic phase was washed with water (100 mL), brine (100 mL) and dried over anhydrous Na_2SO_4. Further evaporation under reduced pressure and purification by column chromatography (SiO_2, ethyl acetate: 100%) afforded compound **8** (1.03 g, 87 %) as a white solid..

^{1}H NMR (400 MHz, $CDCl_3$, 25 °C): δ = 7.03 (brd, *J* = 8.3 Hz, 1H), 7.00 – 6.88 (m, 8H), 6.80 (d, *J* = 9.1 Hz, 4H), 6.75 – 6.65 (m, 4H), 5.56 – 5.28 (brs, 1H), 4.98 – 4.88 (m, 1H), 4.48 – 4.37 (m, 2H), 3.78 (s, 6H), 3.73 (s, 3H), 3.12 – 2.99 (m, 2H).

^{13}C NMR (100 MHz, $CDCl_3$, 25 °C): δ = 171.7, 168.5, 155.4, 155.2, 152.2, 143.7, 141.8, 130.5, 127.4, 125.5, 124.1, 115.8, (2C) 114.8, 68.0, 55.7, 52.8, 52.6, 37.4.

MS (ESI): *m/z* calcd for $C_{32}H_{32}N_2O_7$ $[M]^+$ 556.22, found 556.23; calcd for $C_{32}H_{33}N_2O_7$ $[M+H]^+$ 557.23, found 557.19.

Compound 28

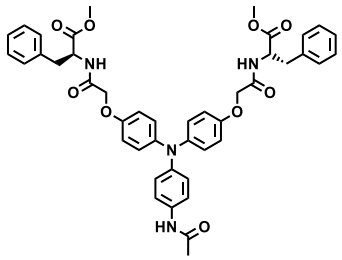

28

Methyl (2S)-2-(2-{4-[(4-acetamidophenyl)(4-{[(1-methoxy-1-oxo-3-phenylpropan-2-yl)carbamoyl]methoxy}phenyl)amino]phenoxy}acetamido)-3-phenylpropanoate

To a solution of compound **17** (312 mg, 0.933 mmol) and cesium carbonate (912 mg, 2.8 mmol) in DMF (5 mL) was added compound **21** (700 mg, 2.33 mmol) and the reaction mixture was stirred at room temperature overnight. After that time, it was diluted with ethyl acetate (250 mL) and the organic phase was washed with NaOH 1M (50 mL), saturated NH_4Cl (100 mL), water (2 × 50 mL), brine (100 mL) and dried over anhydrous Na_2SO_4. Further evaporation under reduced pressure followed by purification by column chromatography (SiO_2, cyclohexane/ethyl acetate: 30/70 → 0/100) provided compound **28** (634 mg, 88 %) as a colourless solid.

^{1}H NMR (400 MHz, CD_3OD/Toluene-d_8, 25 °C): δ = 7.37 (d, *J* = 8.9 Hz, 2H), 7.26 – 7.20 (m, 4H), 7.19 – 7.13 (m, 6H), 6.93 (d, *J* = 9.0 Hz, 4H), 6.87 (d, *J* = 8.9 Hz, 2H), 6.80 (d, *J* = 9.0 Hz, 4H), 4.51 – 4.38 (m, 4H), 3.71 (s, 6H), 3.24 – 3.18 (m, 2H), 3.10 – 3.02 (m, 2H), 2.99 (brs, 1H), 2.86 (brs, 1H), 2.10 (s, 3H).

MS (ESI): *m/z* calcd for $C_{44}H_{44}N_4O_9$ $[M]^+$ 772.31, found 772.44; calcd for $C_{44}H_{45}N_4O_9$ $[M+H]^+$ 773.32, found 773.44.

Compound 29

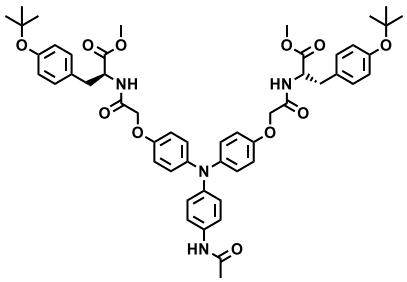

29

Methyl (2S)-3-[4-(tert-butoxy)phenyl]-2-{2-[4-({4-[({3-[4-(tert-butoxy)phenyl]-1-methoxy-1-oxopropan-2-yl}carbamoyl)methoxy]phenyl}(4-acetamidophenyl)

Compounds **17** (342 mg, 1.02 mmol), compound **22** (837 mg, 2.25 mmol) and cesium carbonate (1.0 g, 3.07 mmol) were dissolved in dry DMF (5 mL) in a 10 mL flask. The reaction mixture, which became reddish-brown, was stirred at room temperature for 2 daysand was then diluted with ethyl acetate (300 mL). The organic phase was washed with water (3 × 50 mL) and brine (50 mL) and dried over anhydrous Na_2SO_4. Further evaporation under reduced pressure and purification by column chromatography (SiO_2, cyclohexane/ethyl acetate: 20/80) provided compound **29** (710 mg, 76 %) as a white solid.

^{1}H NMR (400 MHz, CD_3OD, 25 °C): δ = 7.38 (d, *J* = 9.0 Hz, 2H), 7.06 (d, *J* = 8.3 Hz, 5H), 6.95 (d, *J* = 9.0 Hz, 4H), 6.91 – 6.84 (m, 7H), 6.80 (d, *J* = 9.0 Hz, 4H), 4.78 (dd, *J* = 8.7, 5.5 8.7 Hz, 2H), 4.51 – 4.39 (m, 4H), 3.71 (s, 6H), 3.17 (dd, *J* = 13.9, 5.2 Hz, 2H), 3.08 – 3.97 (m, 4H), 2.09 (s, 3H), 1.27 (s, 18H).

^{13}C NMR (400 MHz, CD_3OD, 25 °C): δ = 173.0, 171.4, 171.1, 155.5, 155.0, 146.1, 143.7, 132.9, 130.8, 126.7, 125.3, 123.8, 122.5, 117.0 (2C), 79.5, 68.5, 54.6, 52.9, 37.5, 29.2, 23.6.

MS (ESI): *m/z* calcd for $C_{52}H_{60}N_4O_{11}$ $[M]^+$ 916.43, found 916.38; calcd for $C_{52}H_{61}N_4O_{11}$ $[M+H]^+$ 917.43, found 917.41.

Compound 30

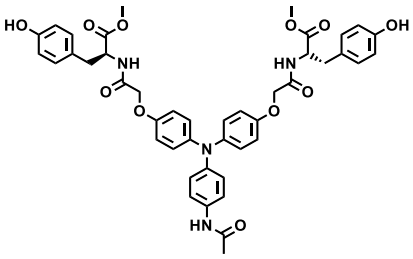

30

Dimethyl 2,2'-((2,2'-((((4-acetamidophenyl)azanediyl)bis(4,1-phenylene))bis(oxy))bis(acetyl))bis(azanediyl))(2S,2'S)-bis(3-(4-hydroxyphenyl)propanoate)

To a cooled (0°C) solution of compound **29** (700 mg, 0.763 mmol) in dichloromethane (20 mL) was added TFA (3.89 mL, 52.4 mmol). The intense blue-green mixture was stirred for 5 hours at room temperature and then, the solvent was evaporated. The resulting green residue was dissolved in a 1:1 mixture of water/brine (100 mL) and the pH was adjusted to 6 – 7 with a solution of sodium bicarbonate. The aqueous phase was extracted with THF (2 × 100 mL) and the combined organic phase was washed with brine (2 × 50 mL) and dried over anhydrous sodium sulphate. Further evaporation under reduced pressure and purification by column chromatography (SiO_2, ethyl acetate/methanol: 99/1) provided compound **30** (580 mg, 94 %) as a white solid.

^{1}H NMR (400 MHz, CD_3OD, 25 °C): δ = 7.35 (d, *J* = 8.6 Hz, 2H), 7.09 – 6.92 (m, 10H), 6.92 – 6.77 (m, 6H), 6.88 (d, *J* = 8.34 Hz, 4H), 4.73 (dd, J = 8.4, 5.3, Hz, 2H), 4.52 – 4.40 (m, 4H), 3.71 (s, 6H), 3.09 (dd, *J* = 13.9, 5.5 Hz, 2H), 3.02 – 2.92 (m, 2H), 2.09 (s, 3H).

^{13}C NMR (400 MHz, CD_3OD, 25 °C): δ = 173.2, 171.4, 171.1, 157.5, 155.0, 148.3, 143.7, 133.8, 131.3, 128.4, 126.8, 123.7, 122.6, 116.9, 116.4, 68.5, 54.8, 52.8, 37.4, 23.6.

MS (ESI): *m/z* calcd for $C_{44}H_{44}N_4O_{11}$ $[M]^+$ 804.30, found 804.24; calcd for $C_{44}H_{45}N_4O_{11}$ $[M+H]^+$ 805.31, found 805.31.

Compound 31

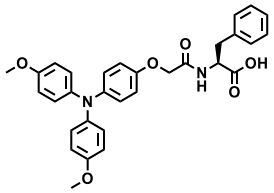

31

2-(2-{4-[bis(4-methoxyphenyl)amino]phenoxy}acetamido)-3-phenylpropanoic acid

Compound **25** (466 mg, 0.862 mmol) was dissolved in THF (12 mL), and the solution was cooled down to 0 °C followed by the dropwise addition of a solution of potassium hydroxide

(120 mg, 2.15 mmol) in water (6 mL). The reaction mixture was stirred at 0 °C for 1 hour, as monitored by UPLC-MS, and then, it was acidified with 2M HCl (1.5 mL) to pH 1 – 2. The aqueous phase was extracted with ethyl acetate (200 mL), and the organic phase was dried over anhydrous Na_2SO_4. Further evaporation under reduced pressure afforded a green solid which was sonicated several times with diethyl ether (20 mL). The resulting white suspension was centrifuged and further filtration and drying of the remaining solid afforded compound **31** (375 mg, 83 %) as a white solid.

^{1}H NMR (400 MHz, DMSO-*d*$_6$, 25 °C): δ = 12.8 (brs, 1H), 8.20 (d, *J* = 8.3 Hz, 1H), 7.28 – 7.17 (m, 4H), 7.17 – 7.10 (m, 1H), 6.92 – 6.83 (m, 8H), 6.82 – 6.73 (m, 4H), 4.57 – 4.49 (m, 1H), 3.44 – 3.34 (m, 2H), 3.71 (s, 6H), 3.15 – 3.08 (m, 1H), 3.02 – 2.95 (m, 1H).

^{13}C NMR (100 MHz, DMSO-*d*$_6$, 25 °C): δ = 172.6, 167.7, 154.8, 152.8, 142.0, 141.2, 137.4, 129.1, 128.1, 126.4, 124.8, 123.7, 115.5, 114.8, 67.0, 55.2, 52.9, 36.4.

MS (ESI): *m/z* calcd for $C_{31}H_{30}N_2O_6$ $[M]^+$ 526.21, found 526.23; calcd for $C_{31}H_{31}N_2O_6$ $[M+H]^+$ 527.22, found 527.24.

Compound 32

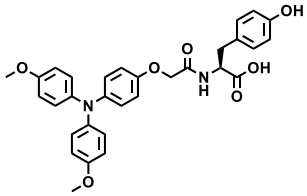

32

(2S)-2-(2-{4-[bis(4-methoxyphenyl)amino]phenoxy}acetamido)-3-(4-hydroxyphenyl)propanoic acid

Compound **27** (650 mg, 1.17 mmol) was dissolved in THF (16 mL) at 0 °C and the solution of potassium hydroxide (200 mg, 3.56 mmol) in water (8 mL) was added dropwise. The reaction mixture was stirred at 0 °C for 3 additional hours, as monitored by UPLC-MS, and then diluted with 1M $KHSO_4$ (20 mL). The aqueous medium was extracted with ethyl acetate (300 mL) and the organic phase was washed with brine (100 mL) and dried over anhydrous Na_2SO_4. Further evaporation of the solvent followed by purification using preparative reverse phase HPLC (basic water/methanol gradient) afforded compound **32** (360 mg, 57 %) as a greenish solid in ammonium salt form.

^{1}H NMR (400 MHz, DMSO-*d*$_6$, 25 °C): δ = 9.05 (br.s, 1H), 7.63 (d, *J* = 7.1 Hz, 1H), 6.93 – 6.77 (m, 13H), 6.56 (d, *J* = 8.5 Hz, 2H), 4.37 (s, 2H), 4.13 (dd, *J* = 6.2, 6.2, 1H), 3.71 (s, 6H),

3.44 (broad hill, corresponding to NH^{4+}), 2.97 (dd, *J* = 13.6, 5.1 Hz, 1H), 2.87 (dd, *J* = 13.6, 6.1 Hz, 1H).

^{13}C NMR (100 MHz, DMSO-*d*$_6$, 25 °C): δ = 172.5, 166.6. 155.6, 154.8, 152.7, 142.2, 141.2, 130.3, 128.4, 124.8, 123.8, 115.7, 114.8, 114.7, 67.5, 55.2, 54.6, 36.2.

MS (ESI): *m/z* calcd for $C_{31}H_{30}N_2O_7$ $[M]^+$ 542.21, found 542.22; calcd for $C_{31}H_{31}N_2O_7$ $[M+H]^+$ 543.21, found 243.24.

Compound 33

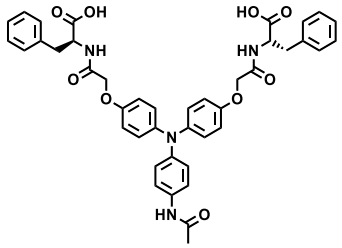

33

2-[2-(4-{[4-({[(1S)-1-carboxy-2-phenylethyl]carbamoyl}methoxy)phenyl](4-acetamidophenyl)amino}phenoxy)acetamido]-3-phenylpropanoic acid

Compound **28** (470 mg, 0.608 mmol) was dissolved in THF (12 mL), the solution was cooled to 0 °C using an ice bath, and then a solution of potassium hydroxide (170 mg, 3.04 mmol) in water (8 mL) was added dropwise. The reaction mixture was stirred at 0 °C for one additional hour, as monitored by UPLC-MS, and it was then diluted with 1M $KHSO_4$ (20 mL). The aqueous solution was extracted with ethyl acetate (300 mL) and the organic phase was washed with brine (2 × 50 mL) and dried over anhydrous Na_2SO_4. Further evaporation of the solvent followed by purification using preparative reverse phase HPLC (basic water/methanol gradient) afforded compound **33** (380 mg, 84 %) as a white solid.

^{1}H NMR (400 MHz, DMSO-*d*$_6$, 25 °C): δ = 9.88 (s, 1H), 7.79 (d, *J* = 7.3 Hz, 2H), 7.44 (d, *J* = 8.8 Hz, 2H), 7.20 – 7.05 (m, 10H), 6.89 – 6.74 (m, 10H), 4.25 (dt, *J* = 7.0, 5.2, Hz, 2H), 3.11 (dd, *J* = 14.0, 4.7 Hz, 2H), 2.98 (dd, *J* = 14.0, 7.0 Hz, 2H), 2.00 (s, 3H).

^{13}C NMR (100 MHz, DMSO-*d*$_6$, 25 °C): δ = 172.6, 167.8, 166.8, 153.3, 143.2, 141.4, 138.4, 133.7, 129.4, 127.8, 125.9, 125.0, 122.5, 120.3, 115.8, 67.4, 54.2, 37.0, 23.8.

MS (ESI): *m/z* calcd for $C_{42}H_{40}N_4O_9$ $[M]^+$ 744.28, found 744.30; calcd for $C_{42}H_{41}N_4O_9$ $[M+H]^+$ 745.29, found 745.27.

Compound 34

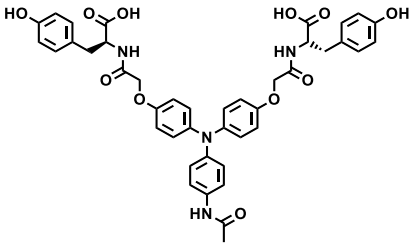

34

(2S,2'S)-2,2'-((2,2'-((((4-acetamidophenyl)azanediyl)bis(4,1-phenylene))bis(oxy))bis(acetyl))bis(azanediyl))bis(3-(4-(tert-butoxy)phenyl)propanoic acid)

To a solution of compound **10** (460 mg, 0.502 mmol) in THF (10 mL) was added dropwise a solution of potassium hydroxide (140 mg, 2.51 mmol) in water (7 mL) at 0 °C. The reaction mixture was stirred for 30 min at 0 °C, as monitored by UPLC-MS, and the pH was then adjusted to pH 1 – 2 with 1M H_2SO_4 (1 mL). The aqueous solution was extracted with ethyl acetate (200 mL) and the organic phase was washed with brine (100 mL) and dried over anhydrous Na_2SO_4. Further evaporation of the solvent followed by purification using preparative reverse phase HPLC (basic water/methanol gradient) afforded compound **14** (210 mg, 54 %) as an off-white solid.

^{1}H NMR (400 MHz, DMSO-d_6, 25 °C): δ = 9.83 (s, 1H), 7.80 (d, *J* = 7.6 Hz, 2H), 7.42 (d, *J* = 8.9 Hz, 2H), 6.96 – 6.76 (m, 14 H), 6.60 (d, *J* = 8.6 Hz, 4H), 4.25 (dt, *J* = 7.4, 5.2 Hz, 4H), 3.40 (br.s.), 2.98 (dd, *J* = 13.7, 5.0 Hz, 2H), 2.86 (dd, *J* = 13.7, 7.3 Hz, 2H), 2.00 (s, 3H).

^{13}C NMR (100 MHz, DMSO-d_6, 25 °C): δ = 172.7, 167.8, 167.0, 155.7, 153.3, 143.3, 141.5, 133.6, 130.2, 128.0, 125.0, 122.4, 120.3, 115.8, 114.8, 67.2, 54.1, 36.1, 23.8.

MS (ESI): *m/z* calcd for $C_{42}H_{40}N_4O_{11}$ $[M]^+$ 776.27, found 776.26; calcd for $C_{42}H_{41}N_4O_{11}$ $[M+H]^+$ 777.28, found 777.22.

Compound 35

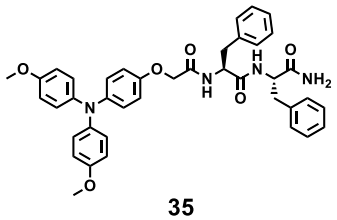

35

(2S,2'S)-2,2'-((2,2'-((((4-acetamidophenyl)azanediyl)bis(4,1-phenylene))bis(oxy))bis(acetyl))bis(azanediyl))bis(3-(4-(tert-butoxy)phenyl)propanoic acid)

To a solution of compound **31** (500 mg, 0.946 mmol), EDC • HCl (201 mg, 1.04 mmol), HOBt hydrate (159 mg, 1.04 mmol) and diisopropylamine (260 µL, 1.56 mmol) in DMF (5

mL) was added a solution of H-F-NH_2 • HCl (209 mg, 1.04 mmol) and diisopropylethylamine (260 µL, 1.56 mmol) in DMF (5 mL) at 0 °C. The reaction mixture was stirred at 0 °C for 10 minutes and at room temperature for 12 hours. It was then diluted with ethyl acetate (200 mL) and the organic phase was washed with solution of citric acid (100 mL), 1M NaOH (100 mL), water (2 × 100 mL), brine (100 mL) and dried over anhydrous Na_2SO_4. Further evaporation under reduced pressure afforded a yellowish residue which was subsequently washed under sonication with ethanol (200 mL) and diethyl ether (200 mL) to provide compound **35** (550 mg, 86%) as a white solid.

^{1}H NMR (400 MHz, DMSO-*d*$_6$, 25 °C): δ = [8.44 (d, *J* = 8.8 Hz) and 8.18 (d, *J* = 8.2 Hz) 1H], [7.99 (d, *J* = 8.2 Hz) and 7.91 (d, *J* = 8.2 Hz) 1H], 7.56 – 6.30 (m, 25H), 4.65 – 4.53 (m, 1H), 4.52 – 4.41 (m, 1H), 4.34 (s, 2H), 3.71 (s, 6H), 3.09 – 2.92 (m, 2H), 2.88 – 2.67 (m, 2H).

MS (ESI): *m/z* calcd for $C_{40}H_{40}N_4O_6$ $[M]^+$, 672.29; found 672.46. calcd for $C_{40}H_{41}N_4O_6$ $[M+H]^+$, 673.30; found 673.50.

C. Chapter IV

Compound 36

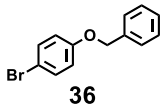

36

1-(benzyloxy)-4-bromobenzene

To a white suspension of 4-bromophenol (25.3 g, 146 mmol) and potassium carbonate (40.4 g, 292 mmol) in acetone (400 mL) in a 500 mL round-bottom flask was added benzyl bromide (17.5 mL, 146 mmol). The reaction mixture was stirred for 1 day at reflux and then, acetone was evaporated under reduced pressure. The solid residue was suspended in diethyl ether (500 mL) and the organic phase was washed with water (100 mL), 1M NaOH (200 mL) and brine (2 × 50 mL) and then dried over anhydrous Na_2SO_4. Further evaporation under reduced pressure followed by recrystallization from boiling ethanol provided compound **36** (37.2 g, 97 %) as a white solid.

^{1}H NMR (400 MHz, $CDCl_3$, 25 °C): δ = 7.47 – 7.30 (m, 7H), 6.86 (d, *J* = 9.0 Hz, 2H), 5.05 (s, 2H).

^{13}C NMR (100 MHz, $CDCl_3$, 25 °C): δ = 158.1, 136.8, 132.5, 128.9, 128.3, 127.6, 116.9, 113.4, 70.5.

Compound 37

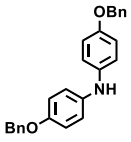

37

4-(benzyloxy)-N-[4-(benzyloxy)phenyl]aniline

Diphenylphosphinoferrocene (DPPF) (0.657 g, 1.15 mmol) and tris(dibenzylideneacetone)dipalladium(0) (0.163 g, 0.173 mmol) were dissolved in dry toluene (60 mL) in a 100 mL Schlenk flask. After stirring for 15 minutes, compound **36** (7.57 g, 28.8 mmol) and sodium *tert*-butoxide (11.1 g, 115 mmol) were added, followed by 4-(benzyloxy)anilinium chloride (8.13 g, 34.5 mmol) five minutes later and then, the reaction mixture was stirred at 110 °C overnight. After that time, the reaction mixture was cooled down to room temperature, diluted with water (200 mL) and the aqueous phase was extracted with dichloromethane (2 × 250 mL). The combined organic phase was washed with water (100 mL), brine (2 × 100 mL) and was dried over anhydrous Na_2SO_4. Further evaporation

under reduced pressure afforded a crude brown residue, which was recrystallized from boiling isopropanol. The resulting crystals were filtered, washed with diethyl ether (30 mL) and dried *in vacuo* to afford compound **37** (9.5 g, 87 %) as a grey powder.

^{1}H NMR (400 MHz, $CDCl_3$, 25 °C): δ = 7.44 – 7.28 (m, 14H), 6.84 (d, *J* = 9.0 Hz, 4H), 5.02 (s, 4H), 1.53 (brs, 1H).

^{13}C NMR (100 MHz, $CDCl_3$, 25 °C): δ = 153.6, 138.2, 137.5, 128.7, 128.0, 127.6, 119.6, 116.0, 70.7.

MS (ESI): *m/z* calcd for $C_{26}H_{23}NO_2$ $[M]^+$ 381.17, found 381.36; calcd for $C_{26}H_{24}NO_2$ $[M+H]^+$ 382.18, found 382.37.

Compound 38

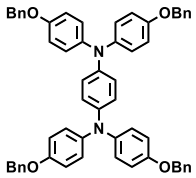

38

1-N,1-N,4-N,4-N-tetrakis[4-(benzyloxy)phenyl]benzene-1,4-diamine

1,4-dibromobenzene (76.4 µL, 0.596 mmol), compound **16a** (500 mg, 1.31 mmol), sodium *tert*-butoxide (171 mg, 1.79 mmol), tri-*tert*-butylphosphine (1 M, 0.179 mL, 0.179 mmol) and tris(dibenzylideneacetone)dipalladium(0) (27.3 mg, 0.0298 mmol) were dissolved in dry toluene (10 mL) in a 100 mL Schlenk. The reaction mixture was stirred at 90 °C for 3 days, and then, after cooling down to room temperature, toluene was evaporated. The crude residue was dissolved in dichloromethane (200 mL) and the organic phase was washed with water (2 × 50 mL) and dried over anhydrous Na_2SO_4. Further evaporation of the solvents under reduced pressure afforded a brownish residue, which was washed with acetone (2 × 10 mL) and diethyl ether (2 × 10 mL) to provide compound **16** (450 mg, 90 %) as a yellowish solid.

^{1}H NMR (400 MHz, $CDCl_3$, 25 °C): δ = 7.47 – 7.29 (m, 20H), 7.02 (d, *J* = 9.0 Hz, 8H), 6.87 (d, *J* = 9.0 Hz, 8H), 6.84 (s, 4H), 5.03 (s, 8H).

^{13}C NMR (100 MHz, $CDCl_3$, 25 °C): δ = 154.4, 142.6, 141.8, 137.2, 128.6, 127.9, 127.5, 125.3, 123.3, 115.6, 70.4.

MS (ESI): *m/z* calcd for $C_{58}H_{48}N_2O_4$ $[M]^+$ 836.36, found 836.51; calcd for $C_{58}H_{49}N_2O_4$ $[M+H]^+$ 837.37, found 837.47.

Compound 39

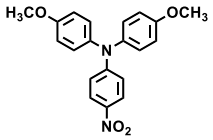

39

4-methoxy-N-(4-methoxyphenyl)-N-(4-nitrophenyl)aniline

4,4'-dimethoxydiphenylamine (1.0 g, 4.36 mmol) was dissolved in dry DMF (20 mL) and then, sodium hydride (210 mg, 5.23 mmol) was added inducing a colour change from white to greenish. *p*-fluoronitrobenzene (510 µL, 4.8 mmol) was added dropwise over 30 min, leading to an exothermic reaction, which colour changed from greenish to brownish. The reaction mixture was stirred at room temperature overnight, as monitored by UPLC-MS, and it was then diluted with water (150 mL). The aqueous medium was extracted with diethyl ether (300 mL) and the organic phase was dried over anhydrous Na_2SO_4. Purification by column chromatography (SiO_2, pentane/diethyl ether: 50/50) afforded compound **39** (1.43 g, 94 %) as orange crystals. *Analyses were in accordance with the literature.*[81]

^{1}H NMR (400 MHz, $CDCl_3$, 25 °C): δ = 7.99 (d, *J* = 9.4 Hz, 2H), 7.13 (d, *J* = 9.0 Hz, 4H), 6.91 (d, *J* = 9.0 Hz, 4H), 6.75 (d, *J* = 9.4 Hz, 2H), 3.82 (s, 6H).

^{13}C NMR (100 MHz, $CDCl_3$, 25 °C): δ = 157.8, 154.3, 139.2, 138.4, 128.3, 125.7, 115.9, 115.4, 55.7.

MS (ESI): *m/z* calcd for $C_{20}H_{18}N_2O_4$ $[M]^+$ 350.13, found 350.31; calcd for $C_{20}H_{19}N_2O_4$ $[M+H]^+$ 351.13, found 351.31.

Compound 41

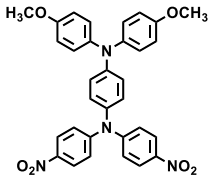

41

4-methoxy-N-(4-methoxyphenyl)-N-(4-nitrophenyl)aniline

The synthetic procedure was adapted from ref [81]. Compound **39** (1.0 g, 2.85 mmol) and tin (II) chloride dihydrate (5.15 g, 22.8 mmol) were dissolved in a mixture of acetonitrile (25 mL) and ethanol (25 mL) in a 100 mL flask. The reaction mixture was stirred at reflux overnight and, after cooling down to room temperature, it was diluted with ethyl acetate (250 mL). The organic phase was washed with NaOH 1M (3 × 75 mL), water (100 mL), brine (50

mL), and then dried over anhydrous Na_2SO_4. Further evaporation under reduced pressure provided compound **40**, which was used in the next step without purification.

Compound **40** (0.90 g, 2.85 mmol) and potassium carbonate (1.58 g, 11.4 mmol) were dissolved in DMSO (10 mL) in a 25 mL Schlenk-tube. *p*-fluoronitrobenzene (636 µL, 5.99 mmol) was added to the yellowish reaction mixture inducing a colour change to red. The reaction mixture was heated at 100 °C for 4 days, as monitored by UPLC-MS, and after cooling down to room temperature and dilution with water (200 mL), a dark red solid precipitated. The residue was extracted with dichloromethane (500 mL), the organic phase was washed with water (200 mL) and dried over anhydrous Na_2SO_4. After evaporation of the solvent under reduced pressure, purification by column chromatography (SiO_2, cyclohexane/dichloromethane: 50/50 → 0/100) afforded compound **17-1b** (750 mg, 47 %) as a dark red solid.

^{1}H NMR (400 MHz, $CDCl_3$, 25 °C): δ = 8.14 (d, *J* = 9.3 Hz, 4H), 7.16 (d, *J* = 9.3 Hz, 4H), 7.12 (d, *J* = 9.1 Hz, 4H), 6.93 – 6.89 (m, 4H), 6.87 (d, *J* = 9.1 Hz, 4H), 3.80 (s, 6H).

^{13}C NMR (100 MHz, $CDCl_3$, 25 °C): δ = 156.7, 152.1, 148.2, 142.5, 140.1, 136.0, 128.3, 127.4, 125.6, 121.8, 120.4, 115.1, 55.7.

MS (ESI): *m/z* calcd for $C_{32}H_{26}N_4O_6$ $[M]^+$ 562.19, found 562.35; calcd for $C_{32}H_{27}N_4O_6$ $[M+H]^+$ 563.19, found 563.35.

Compound 43

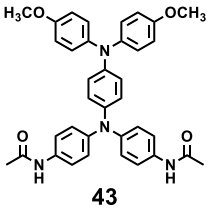

43

N-[4-({4-[bis(4-methoxyphenyl)amino]phenyl}(4-acetamidophenyl)amino)phenyl]acetamide

The synthetic procedure was adapted from ref [81]. Compound **41** (0.7 g, 1.24 mmol) and tin (II) chloride dihydrate (2.81 g, 12.4 mmol) were dissolved in a mixture of acetonitrile (15 mL) and ethanol (10 mL). The reaction mixture was stirred at reflux for 4 hours, as monitored by UPLC-MS and, after cooling down to room temperature, it was diluted with ethyl acetate (300 mL). The organic phase was washed with NaOH 2M (3 × 100 mL), water (100 mL), brine (50 mL), and then dried over anhydrous Na_2SO_4. Further evaporation under reduced pressure provided compound **42**, which was used in the next step without purification.

To a cooled (0 °C) solution of compound **42** (625 mg, 1.24 mmol) and triethylamine (519 µL, 3.73 mmol) in dry dichloromethane (30 mL), was added dropwise acetyl chloride

(266 µL, 3.73 mmol), and the reaction mixture was allowed to stir for 1 hour at room temperature, as monitored by UPLC-MS. The reaction mixture was then diluted with dichloromethane (350 mL), and the organic phase was washed with a saturated solution of sodium bicarbonate (50 mL), brine (50 mL), and dried over anhydrous Na_2SO_4. Further evaporation under reduced pressure afforded a yellowish solid, which was washed with acetone (2 × 20 mL), diethyl ether (3 × 10 mL) and recrystallized from boiling acetone to provide compound **43** (613 mg, 84 %) as a white solid.

^{1}H NMR (400 MHz, DMSO-*d*$_6$, 25 °C): δ = 9.83 (s, 2H), 7.45 (d, *J* = 8.9 Hz, 4H), 6.97 (d, *J* = 9.0 Hz, 4H), 6.93 – 6.85 (m, 8H), 6.83 (d, *J* = 8.9 Hz, 2H), 6.75 (d, *J* = 9.0 Hz, 2H), 3.72 (s, 6H), 2.00 (s, 6H).

^{13}C NMR (100 MHz, DMSO-*d*$_6$, 25 °C): δ = 167.8, 155.2, 143.3, 142.7, 140.8, 140.6, 134.1, 125.7, 124.5, 123.4, 121.9, 120.3, 114.8, 55.2, 23.8.

MS (ESI): *m/z* calcd for $C_{36}H_{34}N_4O_4$ $[M]^+$ 586.26, found 586.42; calcd for $C_{36}H_{35}N_4O_4$ $[M+H]^+$ 587.27, found 587.40.

Compound 44

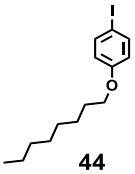

44

p-octoxy-iodobenzene

To a white suspension of 4-iodophenol (14.5 g, 66 mmol) and potassium carbonate (13.2 g, 95.8 mmol) in acetone (400 mL) in a 500 mL round-bottom flask was added 1-bromooctane (12.1 mL, 69.4 mmol). The reaction mixture was stirred for 1 day at reflux and then, acetone was evaporated under reduced pressure. The solid residue was suspended in diethyl ether (500 mL) and the organic phase was washed with water (100 mL), NaOH 1M (200 mL), brine (2 × 50 mL) and dried over anhydrous Na_2SO_4. Further evaporation under reduced pressure afforded compound **44** (19.5 g, 89 %) as a white solid. *Analyses were in accordance with the literature.*

^{1}H NMR (400 MHz, $CDCl_3$, 25 °C): δ = 7.55 (d, *J* = 8.8 Hz, 2H), 6.67 (d, *J* = 8.8 Hz, 2H), 3.92 (t, *J* = 6.4 Hz, 2H), 1.73 (quint, *J* = 6.8, 2H), 1.35 – 1.25 (m, 10H), 0.88 (t, *J* = 6.4 Hz, 3H).

^{13}C NMR (100 MHz, $CDCl_3$, 25 °C): δ = 159.1, 138.2, 117.0, 82.5, 68.2, 31.9, 29.4, 29.3, 29.27, 26.1, 22.8, 14.2.

Compound 45

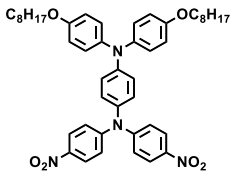

45

N1,N1-bis(4-nitrophenyl)-N4,N4-bis(4-(octyloxy)phenyl)benzene-1,4-diamine

Tris(dibenzylideneacetone)dipalladium(0) (70 mg, 0.075 mmol) and tri-*tert*-butylphosphine (1M in Toluene, 75 µL, 0.075 mmol) was stirred in toluene (10 mL) for 10 minutes in a Schlenk flask. Then, compound **5** (175 mg, 0.5 mmol) was added, along with compound **44** (500 mg, 1.5 mmol) and sodium *tert*-butoxide (685 mg, 3.05 mmol). The mixture was heated for 24 hours at 100 °C. Afterwards, the reaction medium was diluted with ethyl acetate (100 mL) and the solution was passed over a plug of silica gel, which was washed with ethyl acetate (200 mL). After evaporation of the solvent under reduced pressure, purification by column chromatography (SiO_2, cyclohexane/ethyl acetate: 10/1 → 0/1) afforded compound **45** (350 mg, 89 %) as a dark red solid.

^{1}H NMR (400 MHz, $CDCl_3$, 25 °C): δ = 8.13 (d, *J* = 9.2 Hz, 4H), 7.16 (d, *J* = 9.2 Hz, 4H), 7.10 (d, *J* = 8.9 Hz, 4H), 6.89 (s, 4H), 6.85 (d, *J* = 8.9 Hz, 4H), 3.93 (t, *J* = 13.1 Hz, 4H).

Compound 47

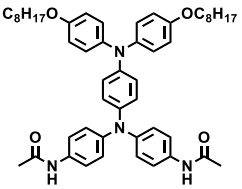

47

N,N'-(((4-(bis(4-(octyloxy)phenyl)amino)phenyl)azanediyl)bis(4,1-phenylene))diacetamide

Compound **45** (880 mg, 1.16 mmol) and tin (II) chloride dihydrate (2.62 g, 11.6 mmol) were dissolved in a mixture of acetonitrile (30 mL) and ethanol (20 mL). The reaction mixture was stirred at reflux for 18 hours, as monitored by UPLC-MS and, after cooling down to room temperature, it was diluted with diethyl ether (300 mL). The organic phase was washed with NaOH 2M (3 × 100 mL), water (100 mL), brine (100 mL), and then dried over anhydrous Na_2SO_4. Further evaporation under reduced pressure provided compound **46**, which was used in the next step without purification.

To a cooled (0 °C) solution of compound **42** (810 mg, 1.16 mmol) and triethylamine (480 µL, 3.5 mmol) in dry dichloromethane (30 mL), was added dropwise acetyl chloride (248 µL, 3.5

mmol), and the reaction mixture was allowed to stir for 1 hour at room temperature, as monitored by UPLC-MS. The reaction mixture was then diluted with dichloromethane (350 mL), and the organic phase was washed with a saturated solution of sodium bicarbonate (50 mL), brine (50 mL), and dried over anhydrous Na_2SO_4. Further evaporation under reduced pressure afforded a dark coloured solid, which was purified by column chromatography (SiO_2, cyclohexane/dichloromethane/TEA: 30/70/1) afforded compound **47** (450 mg, 50 %) as a white solid.

Compound 48

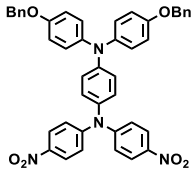

48

1-N,1-N-bis[4-(benzyloxy)phenyl]-4-N,4-N-bis(4-nitrophenyl)benzene-1,4-diamine

Tris(dibenzylideneacetone)dipalladium(0) (392 mg, 0.428 mmol) was stirred with tri-*tert*-butylphosphine (1 M in Toluene, 428 µL, 0.428 mmol) in toluene (40 mL) for 10 minutes in a Schlenk flask. Then, compound **5** (1.0 g, 2.85 mmol) was added, along with compound **13** (5.4 g, 17.4 mmol) and sodium *tert*-butoxide (1.67 g, 17.4 mmol). The mixture was heated for 24 hours at 100 °C and then, toluene was removed under reduced pressure. The resulting brown residue was dissolved in a minimal volume of dichloromethane the solution and was filtrated though a pad of silica gel to remove the catalyst. Further purification by column chromatography (SiO_2, cyclohexane/dichloromethane: 30/70) afforded compound **48** (1.6 g, 78 %) as a deep coloured red solid.

^{1}H NMR (400 MHz, $CDCl_3$, 25 °C): δ = 8.14 (d, *J* = 9.2 Hz, 4H), 7.47 – 7.30 (m, 10H), 7.16 (d, *J* = 9.2 Hz, 4H), 7.11 (d, *J* = 9.0 Hz, 4H), 6.94 (d, *J* = 9.0 Hz, 4H), 6.91 (s, 4H), 5.05 (s, 4H).

MS (ESI): *m/z* calcd for $C_{44}H_{34}N_4O_6$ $[M+H]^+$ 715.25 , found 715.34.

Compound 50

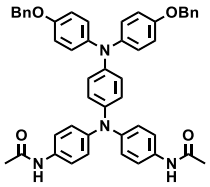

50

1-N,1-N-bis(4-aminophenyl)-4-N,4-N-bis[4-(benzyloxy)phenyl]benzene-1,4-diamine

Compound **48** (1.5 g, 2.1 mmol) and tin (II) chloride dihydrate (4.74 g, 21.0 mmol) were dissolved in a mixture of acetonitrile (25 mL) and ethanol (15 mL). The reaction mixture was stirred at reflux for 18 hours, as monitored by UPLC-MS and, after cooling down to room temperature, it was diluted with ethyl acetate (400 mL). The organic phase was washed with NaOH 2M (3 × 100 mL), water (100 mL), brine (100 mL), and then dried over anhydrous Na_2SO_4. Further evaporation under reduced pressure provided compound **49**, which was used in the next step without purification.

To a cooled (0 °C) solution of compound **49** (1.37 g, 2.09 mmol) and triethylamine (879 µL, 6.32 mmol) in dry dichloromethane (50 mL), was added dropwise acetyl chloride (447 µL, 6.27 mmol), and the reaction mixture was allowed to stir for 30 minutes at room temperature, as monitored by UPLC-MS. The reaction mixture was then diluted with dichloromethane (600 mL), and the organic phase was washed with a saturated solution of sodium bicarbonate (100 mL), brine (100 mL), and dried over anhydrous Na_2SO_4. Further evaporation under reduced pressure afforded a yellowish solid, which was washed with acetone (2 × 15 mL), diethyl ether (2 × 10 mL) to provide compound **50** (1.48 g, 96 %) as a white solid.

^{1}H NMR (400 MHz, DMSO-d_6, 25 °C): δ = 9.84 (s, 2H), 7.49 – 7.42 (m, 8H), 7.39 (dd, *J* = 7.3, 7.3 Hz, 4H), 7.32 (dd, *J* = 7.3, 7.3 Hz, 2H), 7.00 – 6.93 (m, 8H), 6.90 (d, *J* = 8.9 Hz, 4H), 6.83 (d, *J* = 9.0 Hz, 2H), 6.77 (d, *J* = 9.0 Hz, 2H), 5.04 (s, 4H), 2.01 (s, 6H).

^{13}C NMR (100 MHz, DMSO-d_6, 25 °C): δ = 167.8, 154.3, 143.1, 142.7, 141.0, 140.8, 137.1, 134.1, 128.4, 127.8, 127.7, 125.5, 124.3, 123.4, 122.2, 120.3, 115.7, 69.5, 23.8.

MS (ESI): *m/z* calcd for $C_{48}H_{42}N_4O_4$ $[M]^+$ 738.32, found 738.44; calcd for $C_{48}H_{43}N_4O_4$ $[M+H]^+$ 739.33, found 739.42.

Compound 52

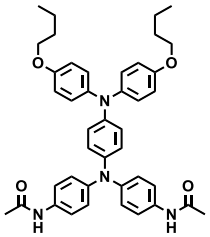

52

N-[4-({4-[bis(4-hydroxyphenyl)amino]phenyl}(4-acetamidophenyl)ami-no)phenyl]acetamide

To a solution of compound **50** (200 mg, 0.271 mmol) in a mixture of methanol (40 mL) and ethyl acetate (20 mL), palladium on charcoal (30 mg) was added under argon atmosphere and a balloon of hydrogen was connected to the flask. The reaction mixture was stirred for 15 hours at room temperature, and upon completion of the reaction, as monitored by UPLC, the reaction mixture was filtered through a pad of Celite® which was washed few times with methanol (50 mL). Further evaporation under reduced pressure afforded compound **51** as a greenish-coloured solid, which was used without purification in the next step.

To a stirred solution of compound **51** (151 mg, 0.27 mmol) and cesium carbonate (264 mg, 0.811 mmol) in dry DMF (5 mL) in a 25 mL Schlenk-tube was added 1-iodobutane (130 µL, 1.13 mmol). The reaction mixture was heated up to 90 °C for 4 hours, as monitored by TLC, and after cooling down to room temperature, it was diluted with dichloromethane (250 mL). The organic phase was washed with water (100 mL), brine (50 mL) and dried over anhydrous Na_2SO_4. Further evaporation under reduced pressure followed by recrystallization from acetone afforded compound **52** (101 mg, 56 %) as a white solid.

^{1}H NMR (400 MHz, DMSO-d_6, 25 °C): δ = 9.82 (s, 2H), 7.45 (d, *J* = 8.8 Hz, 4H), 6.95 (d, *J* = 8.8 Hz, 4H), 6.92 – 6.84 (m, 8H), 6.82 (d, *J* = 9.1 Hz, 2H), 6.75 (d, *J* = 9.1 Hz, 2H), 3.91 (t, *J* = 6.4 Hz, 4H), 2.00 (s, 6H), 1.67 (tt, *J* = 6.4, 6.4 Hz, 4H), 1.42 (tt, *J* = 7.3, 7.3 Hz, 4H), 0.92 (t, *J* = 7.3 Hz, 6H).

^{13}C NMR (100 MHz, DMSO-d_6, 25 °C): δ = 167.8, 154.6, 143.3, 142.7, 140.7, 140.5, 134.1, 125.6, 124.4, 123.3, 121.8, 120.3, 115.3, 67.3, 30.8, 23.8, 18.7, 13.7.

MS (ESI): *m/z* calcd for $C_{42}H_{46}N_4O_4$ $[M]^+$ 670.50, found 670.35; calcd for $C_{42}H_{47}N_4O_4$ $[M+H]^+$ 671.36, found 671.46.

Compound 53

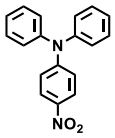

53

4-nitro-N,N-diphenylaniline

To a stirred solution of diphenylamine (10 g, 59.1 mmol) in dry DMF (250 mL), sodium hydride (2.85 g, 71.3 mmol) was added portionwise. Then *p*-fluoronitrobenzene (6.9 mL, 65 mmol) was added dropwise during 30 min. The reaction mixture was stirred at room temperature overnight, as monitored by UPLC-MS, and then poured into cooled water (600 mL). The resulting yellow precipitate was filtrated and recrystallized from boiling toluene, providing compound **53** (15.0 g, 88 %) as orange crystals.

^{1}H NMR (400 MHz, $CDCl_3$, 25 °C): δ = 8.04 (d, *J* = 9.4 Hz, 2H), 7.41 – 7.34 (m, 4H), 7.25 – 7.14 (m, 6H), 6.92 (d, *J* = 9.4 Hz, 2H). We need a range for a multiplet. Please modify accordingly

MS (ESI): m/z calculated for $C_{18}H_{14}N_2O_2$ $[M]^+$ 290.11, found 290.27.

Compound 54

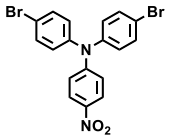

54

4-bromo-N-(4-bromophenyl)-N-(4-nitrophenyl)aniline

Compound **53** (3.0 g, 10.3 mmol) was dissolved in DMF (20 mL) in a 100 mL 2 necked flask. Then, N-bromosuccinimide (4.27 g, 24 mmol) in DMF (15 mL) was added dropwise at room temperature to this orange solution. After stirring for 12 hours, an orange precipitate appeared, and the reaction mixture was stirred for 2 additional days. It was then diluted with water (200 mL). The orange precipitate was filtered under reduced pressure, dried at 95 °C and then dissolved in minimal volume of dichloromethane (50 mL). Cold methanol was finally added slowly until a precipitate appeared (for 50 mL of dichloromethane, 150 mL of methanol were used) providing compound **54** (4.35 g, 94 %) as yellow crystals.

^{1}H NMR (400 MHz, $CDCl_3$, 25 °C): δ = 8.06 (d, *J* = 9.2 Hz, 2H), 7.48 (d, *J* = 8.8 Hz, 4H), 7.03 (d, *J* = 8.8 Hz, 4H), 6.96 (d, *J* = 9.2 Hz, 2H).

^{13}C NMR (100 MHz, $CDCl_3$, 25 °C): δ = 152.7, 144.7, 141.3, 133.3, 127.8, 125.6, 119.4, 119.0.

MS (ESI): *m/z* calcd for $C_{18}H_{12}Br_2N_2O_2$ $[M]^+$ 446.93, found 447.05.

Compound 55

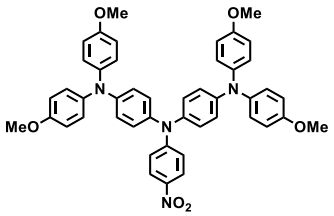

55

1-N-{4-[bis(4-methoxyphenyl)amino]phenyl}-4-N,4-N-bis(4-methoxyphenyl)-1-N-(4-nitrophenyl)benzene-1,4-diamine

Compound **54** (444 mg, 0.991 mmol), 4 4'-dimethoxydiphenylamine (500 mg, 2.18 mmol), sodium *tert*-butoxide (285 mg, 2.97 mmol), tri-*tert*-butylphosphine (1 M in Toluene, 150 µL, 0.149 mmol) and tris(dibenzylideneacetone)dipalladium(0) (136 mg, 0.149 mmol) were dissolved in dry toluene (19 mL) in a 50 mL Schlenk. The reaction mixture was stirred at 90 °C for 3 days. Further evaporation under reduced pressure followed by purification by column chromatography (SiO_2, dichloromethane) provided compound **55** (457 mg, 62 %) as a deep-red solid.

MS (ESI): *m/z* calcd for $C_{46}H_{40}N_4O_6$ $[M]^+$ 744.29, found 744.39; calcd for $C_{46}H_{41}N_4O_6$ $[M+H]^+$ 745.30, found 745.37.

Compound 57

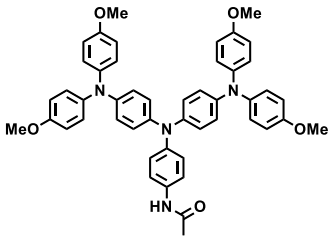

57

1-N,1-N-bis({4-[bis(4-methoxyphenyl)amino]phenyl})benzene-1,4-diamine

The synthetic procedure was adapted from ref.[81] A solution of compound **55** (300 mg, 0.403 mmol) and tin (II) chloride dihydrate (908 mg, 4.03 mmol) in a mixture of ethanol (4 mL) and acetonitrile (4 mL) was stirred overnight at reflux. After that time, the solution was cooled down to room temperature and diluted with ethyl acetate (250 mL). The organic phase was washed with 1M NaOH (3 × 100 mL), water (50 mL) and brine (100 mL), and dried over anhydrous Na_2SO_4. Further evaporation under reduced pressure provided compound **56** which was used in the next step without purification.

A solution of compound **56** (290 mg, 0.406 mmol) and triethylamine (85 µL, 0.609 mmol) in dry dichloromethane (10 mL) was cooled down to 0 °C using an ice bath. After stirring for 5 minutes, acetyl chloride (45 µL, 0.609 mmol) was added dropwise, and the mixture was allowed to stir overnight at room temperature. After that time, the reaction mixture was diluted with dichloromethane (100 mL), and the organic phase was washed with a saturated solution of sodium bicarbonate (25 mL), brine (50 mL) and dried over anhydrous Na_2SO_4. Further evaporation under reduced pressure and purification by column chromatography (SiO_2, cyclohexane/ethyl acetate: 90/10 → 0/100) provided compound **57** (239 mg, 78 %) as an off-white solid.

^{1}H NMR (400 MHz, DMSO-*d*$_6$, 25 °C): δ = 9.81 (s, 1H), 7.44 (d, *J* = 8.9 Hz, 2H), 6.96 (d, *J* = 9.0 Hz, 8H), 6.93 – 6.80 (m, 14H), 6.75 (d, *J* = 9.0 Hz, 4H), 3.71 (s, 12H), 2.00 (s, 3H).

^{13}C NMR (100 MHz, DMSO-*d*$_6$, 25 °C): δ = 167.8, 155.2, 143.2, 142.8, 140.9, 140.6, 133.9, 125.6, 124.4, 123.0, 121.9, 120.3, 114.8, 55.2, 23.8.

ESI (MS): *m/z* calcd for $C_{48}H_{44}N_4O_5$ $[M]^+$ 756.33, found 756.50; calcd for $C_{48}H_{45}N_4O_5$ $[M+H]^+$ 757.34, found 757.46.

Compound 58

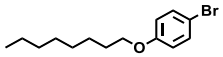

58

1-bromo-4-(octyloxy)benzene

To a colourless solution of 4-bromophenol (10.0 g, 57.8 mmol) in DMF (40 mL) in a Schlenk flask was added potassium carbonate (14.5 g, 105 mmol). After stirring for 10 minutes, 1-bromooctane (9.14 mL, 52.5 mmol) was added and the reaction suspension was then stirred for 12 hours at 130 °C. After that time, the reaction mixture was cooled down to room temperature, and diluted with water (200 mL) and 3M NaOH (200 mL). The aqueous solution was extracted with diethyl ether (2 × 200 mL). The combined organic phase was washed with 1M NaOH (100 mL), brine (100 mL) and dried over anhydrous Na_2SO_4. Further evaporation under reduced pressure followed by distillation under reduced pressure (*bp* 112 – 114 °C at 0.02 Torr) provided compound **58** (14.1 g, 94 %) as a colourless oil.

^{1}H NMR (400 MHz, CDCl$_3$, 25 °C): δ = 7.36 (d, *J* = 8.9 Hz, 2H), 6.77 (d, *J* = 8.9 Hz, 2H), 3.91 (t, *J* = 6.7 Hz, 2H), 1.77 (tt, *J* = 6.7, 6.7 Hz, 2H), 1.47 – 1.41 (m, 2H), 1.39 – 1.24 (m, 8H), 0.89 (t, *J* = 6.7 Hz, 3H).

^{13}C NMR (100 MHz, CDCl$_3$, 25 °C): δ = 158.4, 132.3, 116.5, 112.7, 68.4, 32.0, 29.5, 29.4, 29.3, 26.2, 22.8, 14.2.

Compound 59

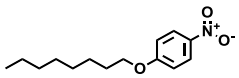

59

p-nitrophenyl octyl ether

To a colourless solution of 4-nitrophenol (8.0 g, 57.5 mmol) in DMF (50 mL) in a Schlenk was added potassium carbonate (13.2 g, 95.8 mmol) and the reaction mixture turned yellow. After stirring for 10 minutes, 1-bromooctane (9.26 g, 47.9 mmol) was added and the reaction mixture was stirred for 12 hours at 110 °C. After that time, it was cooled down to room temperature and diluted with diethyl ether (300 mL). The organic phase was washed with saturated NH_4Cl (100 mL), 1M NaOH (2 × 50 mL), saturated sodium bicarbonate (2 × 50 mL), water (3 × 50 mL), brine (2 × 50 mL), and then dried over anhydrous Na_2SO_4. Further evaporation under reduced pressure followed by distillation using Kugelrohr (*bp* 110 – 120 °C at 0.1 – 0.5 Torr) afforded compound **59** (11.1 g, 92 %) as a colourless oil.

^{1}H NMR (400 MHz, $CDCl_3$, 25 °C): δ = 8.19 (d, *J* = 9.4 Hz, 2H), 6.94 (d, *J* = 9.2 Hz, 2H), 4.04 (t, *J* = 6.7 Hz, 2H), 1.82 (tt, *J* = 6.5, 6.5 Hz, 2H), 1.52 – 1.41 (m, 2H), 1.40 – 1.19 (m, 8H), 0.89 (t, *J* = 6.7 Hz, 3H).

Compound 60

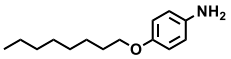

60

4-octoxyaniline

To a solution of compound **59** (11.1 g, 44.2 mmol) in a mixture of ethanol (170 mL) and water (20 mL) was added ammonium chloride (23.6 g, 441 mmol). The yellowish solution was stirred for 5 min, then iron (9.87 g, 176 mmol) was added and the reaction mixture was stirred for 12 hours at reflux. After that time, the brown-red reaction mixture was cooled down to room temperature, the solid residue was filtered, and the filtrate was concentrated under reduced pressure. Saturated EDTA (200 mL) was added to the resulting residue and pH was adjusted to 11 with 3M NaOH (50 mL). The aqueous phase was extracted with ethyl acetate (2 × 200 mL). The combined organic phase was washed with water (2 × 100 mL), brine (2 × 100 mL) and dried over anhydrous Na_2SO_4. Further evaporation under reduced pressure followed by distillation using the kugelrohr (*bp* 110 – 120 °C at 0.1 – 0.5 Torr) provided compound **60** (8.8 g, 90 %) as a colourless oil.

^{1}H NMR (400 MHz, $CDCl_3$, 25 °C): δ = 6.74 (d, *J* = 8.9 Hz, 2H), 6.64 (d, *J* = 8.9 Hz, 2H), 3.88 (t, *J* = 6.7 Hz, 2H), 3.45 (brs, 2H), 1.74 (tt, *J* = 6.7, 6.7 Hz, 2H), 1.49 – 1.38 (m, 2H), 1.38 – 1.20 (m, 8H), 0.89 (t, *J* = 7.2 Hz, 3H).

MS (ESI): *m/z* calcd for $C_{14}H_{24}NO$ $[M+H]^+$ 222.19, found 222.40.

Compound 61

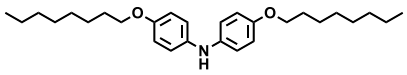

61

4-(octyloxy)-N-[4-(octyloxy)phenyl]aniline

Diphenylphosphinoferrocene (DPPF) (657 mg, 1.15 mmol) and tris(dibenzylideneacetone) dipalladium(0) (160 mg, 0.169 mmol) were dissolved in dry toluene (50 mL) in a 100 mL Schlenk flask. After stirring for 15 minutes, distilled compound **58** (8.2 g, 28.8 mmol) and sodium *tert*-butoxide (5.42 g, 56.4 mmol) were added. After 5 minutes, freshly distilled aniline **60** (7.0 g, 31.6 mmol) was added and the reaction mixture was stirred at 110 °C overnight. After that time, the reaction mixture was cooled down to room temperature and diluted with dichloromethane (250 mL). The organic phase was washed subsequently with saturated NH_4Cl (2 × 100 mL), water (100 mL), brine (2 × 100 mL) and dried over anhydrous Na_2SO_4. Further evaporation under reduced pressure, purification by column chromatography (SiO_2, dichloromethane/TEA: 100/1) and recrystallization from boiling *i*-propyl alcohol afforded compound **61** (8.5 g, 69 %) as a grey-pearl powder.

^{1}H NMR (400 MHz, Acetone-*d*$_6$, 25 °C): δ = 6.95 (d, *J* = 8.9 Hz, 4H), 6.81 (d, *J* = 8.9 Hz, 4H), 6.69 (brs, 1H), 3.92 (t, *J* = 6.5 Hz, 4H), 1.74 (tt, *J* = 6.8, 6.8 Hz, 4H), 1.47 (tt, *J* = 6.8, 6.8 Hz, 4H), 1.41 – 1.25 (m, 16H), 0.89 (t, *J* = 7.0 Hz, 6H).

^{13}C NMR (100 MHz, Acetone-*d*$_6$, 25 °C): δ = 154.3, 139.4, 119.7, 116.2, 69.0, 32.6, 30.3, 30.2, 30.1, 26.9, 23.4, 14.4.

MS (ESI): *m/z* calcd for $C_{28}H_{43}NO_2$ $[M]^+$, 425.33; found 425.51. calcd for $C_{28}H_{44}NO_2$ $[M+H]^+$, 426.34; found 426.52.

Compound 62

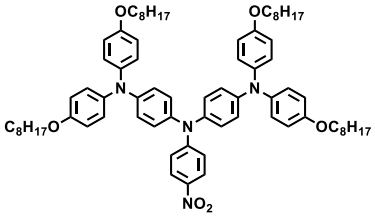

62

1-N-(4-{bis[4-octyloxy)phenyl]amino}phenyl)-1-N-(4-nitrophenyl)-4-N,4-N-bis[4-(octyloxy)phenyl]benzene-1,4-diamine

Compound **54** (431 mg, 1.01 mmol), compound **61** (212 mg, 0.474 mmol), tris(dibenzylideneacetone)dipalladium(0) (62 mg, 0.0674 mmol), and sodium *tert*-butoxide (134 mg, 1.39 mmol) were dissolved in dry toluene (8.5 mL). After dissolution, tri-*tert*-butylphosphine (1 M in Toluene, 0.05 mL, 0.005 mmol) was added and the resulting mixture was stirred for 3 days at room temperature, as monitored by UPLC-MS. The solution was filtered through a pad of silica gel, which was washed with dichloromethane (300 mL). Further evaporation under reduced pressure and purification by column chromatography (SiO_2, cyclohexane/diethyl ether 100/0 → 90/10) afforded compound **62** (280 mg, 52%) as a red solid.

^{1}H NMR (400MHz, $CDCl_3$, 25 °C): δ = 8.01 (d, *J* = 9.4 Hz, 2 H), 7.08 (d, *J* = 9.0 Hz, 8 H), 6.98 (d, *J* = 8.9 Hz, 4 H), 6.89 (d, *J* = 8.9 Hz, 4 H), 6.84 (d, *J* = 9.0 Hz, 10H), 3.94 (t, *J* = 6.6 Hz, 8 H), 1.92 - 1.69 (m, 8 H), 1.53 - 1.21 (m, 44 H), 0.90 (t, *J* = 6.6 Hz 12 H).

MS (ESI): *m/z* calcd for $C_{74}H_{96}N_4O_6$ $[M]^+$,1136.73; found 1137.11.

Compound 64

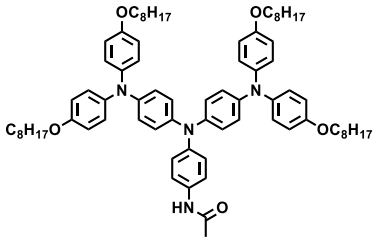

64

N-(4-(bis(4-(bis(4-(octyloxy)phenyl)amino)phenyl)amino)phenyl)acetamide

A solution of compound **62** (280 mg, 0.245 mmol) and tin (II) chloride dihydrate (1.31 g, 6.9 mmol) in a mixture of ethanol (4 mL) and acetonitrile (4 mL) was stirred overnight at reflux. After that time, the solution was cooled down to room temperature and diluted with ethyl acetate (200 mL). The organic phase was washed with 1M NaOH (3 × 100 mL), water (100 mL) and brine (100 mL), and dried over anhydrous Na_2SO_4. Further evaporation under reduced pressure provided compound **63** which was used in the next step without purification.

A solution of compound **63** (271 mg, 0.245 mmol) and triethylamine (35 µL, 0.246 mmol) in dry dichloromethane (5 mL) was cooled down to 0 °C using an ice bath. After stirring for 5 minutes, a solution of acetyl chloride (30 µL, 0.42 mmol) in dichloromethane (1 mL) was

added dropwise, and the mixture was allowed to stir overnight at room temperature. After that time, the reaction mixture was diluted with a saturated solution of ammonium chloride (100 mL) and the mixture was extract with diethyl ether (500 mL). The organic phase was washed with water (200 mL), brine (100 mL) and dried over anhydrous Na_2SO_4. Further evaporation under reduced pressure and purification by column chromatography (SiO_2, cyclohexane/diethyl ether: 1/1) provided compound **64** (154 mg, 55 %) as an off-white solid. The compound self-assembled in DMSO so that no signal could be observed.

MS (ESI): *m/z* calcd for $C_{76}H_{100}N_4O_5$ $[M]^+$,1148.77; found 1149.03.

Compound 65

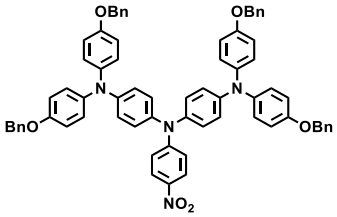

65

1-N,1-N-bis[4-(benzyloxy)phenyl]-4-N-(4-{bis[4-(benzyloxy)phenyl]ami-no}phenyl)-4-N-(4-nitrophenyl)benzene-1,4-diamine

Compounds **54** (747 mg, 1.67 mmol), **37** (1.40 g, 3.67 mmol), sodium *tert*-butoxide (480 mg, 5 mmol), tri-*tert*-butylphosphine (1 M in Toluene, 0.25 mL, 0.25 mmol) and tris(dibenzylideneacetone)dipalladium(0) (229 mg, 0.25 mmol) were mixed in dry toluene (32 mL) in a 100 mL Schlenk. The reaction mixture was stirred at 90 °C for 3 days. Further evaporation under reduced pressure followed by purification by column chromatography (SiO_2, dichloromethane) afforded compound **65** (1.2 g, 69 %) as a deep-red solid.

^{1}H NMR (400 MHz, $CDCl_3$, 25 °C): δ = 8.02 (d, *J* = 9.4 Hz, 2H), 7.48 – 7.31 (m, 20H), 7.09 (d, *J* = 8.8 Hz, 8H), 7.00 (d, *J* = 8.8 Hz, 4H), 6.95 – 6.90 (m, 12H), 6.84 (d, *J* = 9.4 Hz, 2H), 5.05 (s, 8H).

^{13}C NMR (100 MHz, $CDCl_3$, 25 °C): δ = 155.4, 154.2, 146.8, 140.9, 139.0, 137.6, 137.1, 128.7, 128.1, 127.6, 126.8, 125.7, 121.3, 119.6, 116.0, 115.9, 70.5.

MS (ESI): *m/z* calcd for $C_{70}H_{56}N_4O_6$ $[M]^+$ 1048.42, found 1048.51; calcd for $C_{70}H_{57}N_4O_6$ $[M+H]^+$ 1049.43, found 1049.43.

Compound 67

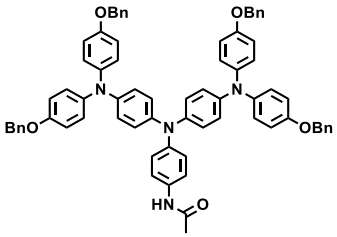

67

N-{4-[bis(4-{bis[4-(benzyloxy)phenyl]amino}phenyl)amino]phenyl}acet-amide

A solution of compound **65** (1.20 g, 1.14 mmol) and tin (II) chloride dihydrate (2.58 g, 11.4 mmol) in a mixture of ethanol (20 mL) and acetonitrile (20 mL) was stirred overnight at reflux. After that time, the solution was cooled down to room temperature and diluted with ethyl acetate (250 mL). The organic phase was washed with 1M NaOH (3 × 50 mL), water (100 mL), brine (100 mL), and dried over anhydrous Na_2SO_4. Further evaporation under reduced pressure provided compound **66** which was used in the next step without purification.

A solution of compound **66** (1.164 g, 1.14 mmol) and triethylamine (250 µL, 1.78 mmol) in dry dichloromethane (25 mL) was cooled down to 0 °C using an ice bath. After stirring for 5 minutes, acetyl chloride (125 µL, 1.76 mmol) was added dropwise, and the mixture was allowed to stir for 3 hours at room temperature. After that time, the reaction mixture was diluted with dichloromethane (300 mL), and the organic phase was washed with a saturated solution of sodium bicarbonate (50 mL), brine (30 mL) and dried over anhydrous Na_2SO_4. Further evaporation under reduced pressure afforded a reddish solid which was washed with acetone (30 mL), diethyl ether (10 mL) and dried under vacuum to provide compound **67** (787 mg, 65 %) as an off-white solid.

^{1}H NMR (400 MHz, DMSO-*d*$_6$, 25 °C): δ = 9.82 (s, 1H), 7.50 – 7.30 (m, 22H), 6.96 (s, 16H), 6.91 (d, *J* = 9.0 Hz, 2H), 6.85 (d, *J* = 8.9 Hz, 4H), 6.77 (d, *J* = 8.9 Hz, 4H), 5.04 (s, 8H), 2.00 (s, 3H).

^{13}C NMR (100 MHz, DMSO-*d*$_6$, 25 °C): δ = 167.8, 154.3, 143.0, 142.8, 141.0, 140.8, 137.1, 133.9, 128.4, 127.8, 127.6, 125.5, 124.3, 123.2, 122.2, 120.3, 115.7, 69.5, 23.8.

MS (ESI): *m/z* calcd for $C_{72}H_{60}N_4O_5$ $[M]^+$ 1060.46, found 1060.57; calcd for $C_{72}H_{61}N_4O_5$ $[M+H]^+$ 1061.46, found 1061.54.

Compound 69

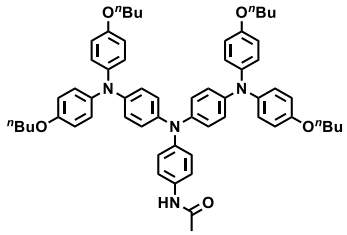

69

N-{4-[bis({4-[bis(4-butoxyphenyl)amino]phenyl})amino]phenyl}acetamide

To a solution of compound **67** (200 mg, 0.188 mmol) in a mixture of methanol (30 mL) and ethyl acetate (20 mL), palladium on charcoal (25 mg) was added under argon atmosphere and a balloon of hydrogen was connected to the flask. The reaction mixture was stirred for 14 hours at room temperature, and upon completion of the reaction, as monitored by TLC, the reaction mixture was filtered through a pad of Celite® which was washed few times with methanol (100 mL). Further evaporation under reduced pressure afforded compound **68** (311 mg, quantitative) as a marine-coloured solid, which was used without purification in the next step.

To a stirred solution of compound **68** (132 mg, 0.188 mmol) and cesium carbonate (368 mg, 1.13 mmol) in dry DMF (5 mL) in a 25 mL Schlenk-tube was added 1-iodobutane (200 µL, 1.72 mmol). The reaction mixture was heated up to 90 °C for 5 hours, as monitored by TLC, and after cooling down to room temperature, it was diluted with dichloromethane (300 mL). The organic phase was washed with water (100 mL), brine (50 mL) and dried over anhydrous Na_2SO_4. Further evaporation under reduced pressure followed by recrystallization from acetone afforded compound **69** (104 mg, 60 %) as a white solid.

^{1}H NMR (400 MHz, DMSO-*d*$_6$, 25 °C): δ = 9.82 (s, 1H), 7.45 (d, *J* = 9.0 Hz, 2H), 6.95 (d, *J* = 9.0 Hz, 8H), 6.90 (d, *J* = 8.9 Hz, 2H), 6.89 – 6.81 (m, 12H), 6.75 (d, *J* = 8.9 Hz, 4H), 3.92 (t, *J* = 6.5 Hz, 8H), 2.01 (s, 3H), 1.70 – 1.74 (m, 8H), 1.46 – 1.42 (m, 8H), 0.93 (t, *J* = 7.3 Hz, 12H).

^{13}C NMR (100 MHz, DMSO-*d*$_6$, 25 °C): δ = 167.8, 154.6, 143.2, 142.8, 140.8, 140.5, 133.9, 125.6, 124.3, 123.0, 121.9, 120.3, 115.3, 67.3, 30.8, 23.8, 18.7, 13.7.

MS (ESI): *m/z* calcd for $C_{60}H_{68}N_4O_5$ $[M]^+$ 924.52, found 924.67; calcd for $C_{60}H_{69}N_4O_5$ $[M+H]^+$ 925.53, found 925.62.

D. Chapter V

Compound 70

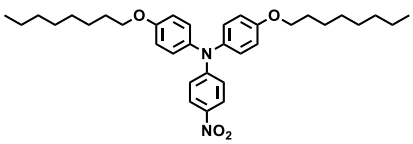

70

N-(4-nitrophenyl)-4-(octyloxy)-N-[4-(octyloxy)phenyl]aniline

To a solution of compound **61** (3.78 g, 8.88 mmol) in DMF (20 mL) was added sodium hydride (240 mg, 9.77 mmol). The reaction mixture was stirred for 15 minutes at room temperature and then, *p*-fluoronitrobenzene (1.57 g, 11.1 mmol) was added dropwise over a period of 30 minutes, leading to a colour change to deep-orange/red. The reaction mixture was stirred for 2 additional hours and then diluted with diethyl ether (250 mL). The organic phase was washed with saturated NH_4Cl (2 × 100 mL), water (5 × 50 mL), brine (100 mL) and dried over anhydrous Na_2SO_4. Further evaporation of the solvents under reduced pressure afforded a dark-red viscous oil which was purified by column chromatography (SiO_2, pentane/dichloromethane: 1/1) providing compound **70** (4.0 g, 82 %) as an orange-red viscous oil. *Analyses were in accordance with the literature.*[81]

^{1}H NMR (400 MHz, $CDCl_3$, 25 °C): δ = 7.99 (d, *J* = 9.4 Hz, 2H), 7.11 (d, *J* = 9.0 Hz, 4H), 6.89 (d, *J* = 9.0 Hz, 4H), 6.75 (d, *J* = 9.4 Hz, 2H), 3.95 (t, *J* = 6.6 Hz, 4H), 1.79 (tt, *J* = 6.6, 6.6 Hz, 4H), 1.51 – 1.41 (m, 4H), 1.41 – 1.21 (m, 16H), 0.89 (t, *J* = 7.2 Hz, 6H).

MS (ESI): *m/z* calcd for $C_{34}H_{46}N_2O_4$ $[M]^+$, 546.35; found 546.48. calcd for $C_{34}H_{47}N_2O_4$ $[M+H]^+$, 547.35; found 547.51.

Compound 72

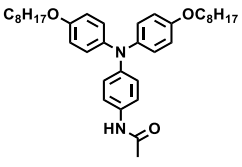

72

N-(4-{bis[4-(octyloxy)phenyl]amino}phenyl)acetamide

The synthetic procedure was adapted from ref [81]. Compound **70** (1.2 g, 2.19 mmol) was dissolved in ethanol (25 mL) in a 100 mL round-bottom two-neck flask equipped with a reflux condenser. Palladium on charcoal (50 mg) was added carefully under an atmosphere of argon. The reaction mixture was heated up to 80 °C. Hydrazine hydrate (2 mL, 41.1 mmol)

was added dropwise under vigorous stirring over a period of 30 minutes, and the reaction mixture was further stirred under reflux for 30 minutes more. Then, the reaction was cooled down to room temperature. The catalyst was removed by filtration through a pad of Celite®, which was washed few times with methanol (30 mL). Further evaporation under reduced pressure provided compound **71** as yellowish solid which was used in the next step without purification.

A stirred solution of freshly prepared compound **71** (1.0 g, 1.94 mmol) and triethylamine (538 μL, 3.87 mmol) in dichloromethane (20 mL) was cooled to 0 °C using an ice bath, and then acetyl chloride (276 μL, 3.87 mmol) was added dropwise. The reaction mixture was warmed up to room temperature, stirred for 30 minutes and then diluted with dichloromethane (200 mL). The organic phase was washed with 1M HCl (2 × 50 mL), 1M NaOH (2 × 50 mL), water (2 × 100 mL), brine (100 mL) and then dried over anhydrous Na_2SO_4. Further evaporation under reduced pressure and purification by column chromatography (SiO_2, cyclohexane/ethyl acetate: 85/15) afforded compound **72** (1.0 g, 92 %) as an off-white solid. *Analyses were in accordance with the literature.*[81]

^{1}H NMR (400 MHz, CD_3OD, 25 °C) δ: 7,3 (d, *J* = 9.0, 2H), 6.89 (d, *J* = 9.0 Hz, 4H), 6.81 (d, *J* = 9.0 Hz, 2H), 6.76 (d, *J* =9,0 Hz, 4H), 3.88 (t, *J* = 6.5 Hz, 4H), 2.08 (s, 3H), 1.77 – 1,67 (m, 4H), 1.50 – 1.39 (m, 4H), 1.40 – 1.23 (m, 16H), 0.89 (t, *J* = 7.0 Hz, 6H).

^{13}C NMR (100 MHz, CD_3OD, 25 °C): δ = 171.3, 156.5, 146.7, 142.5, 133.1, 127.0, 122.8, 122.4, 116.4, 69.3, 33.0, 30.51, 30.48, 30,43, 27.2, 23.7, 23.6, 14.5.

MS (ESI): *m/z* calcd for $C_{36}H_{50}N_2O_3$ $[M]^+$, 558.38; found 558.64.

E. Chapter VI

Compound 73

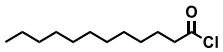

73

Lauroyl chloride

The synthetic procedure was adapted from ref.[421] Lauric acid (10.0 g, 49.9 mmol) was dissolved in chloroform (100 mL) and thionyl chloride (7.2 mL, 99.8 mmol) was added. The reaction mixture was stirred at reflux overnight. Chloroform and the excess of thionyl chloride were removed under reduced pressure. Pure lauroyl chloride (**73**) (10.5 g, 96 %) was obtained as a colourless liquid after vacuum distillation (*b.p.* 110 – 112 °C at 1 Torr). *Analyses were in accordance with the reported data.*[424 e]

^{1}H NMR (400 MHz, $CDCl_3$, 25 °C): δ = 2.88 (t, *J* = 7.3 Hz, 2H), 1.70 (tt, *J* = 7.3, 7.3 Hz, 2H), 1.44 – 1.10 (m, 16H), 0.88 (t, *J* = 6.5 Hz, 3H).

^{13}C NMR (100 MHz, $CDCl_3$, 25 °C): δ = 173,8. 47.2, 32.0, 29.71, 29.67, 29.5 (2C), 29.2, 28.6, 25.2, 22.8, 14.1.

Compound 74

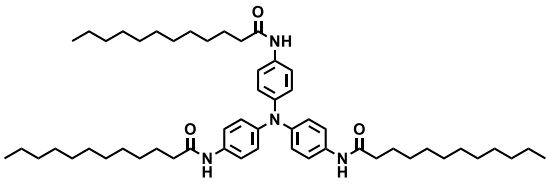

74

N-{4-[bis(4-dodecanamidophenyl)amino]phenyl}dodecanamide

*Compound **74** was synthesised according to a reported procedures* [113,129]. Compound **6** (0.75 g, 2.58 mmol) was dissolved in a mixture of dichloromethane (100 mL) and THF (100 mL). Triethylamine (1.44 mL, 10.3 mmol) was added and the solution was cooled down to 0 °C using an ice bath. Lauroyl chloride (2.26 g, 10.3 mmol) was then added dropwise to the stirred solution and the reaction mixture was warmed up to room temperature and then stirred for an additional hour. The solvent was evaporated and the resulting solid was dissolved in THF (350 mL). The organic phase was washed subsequently with 1M HCl/brine – 1:2 v/v (100 mL), 1M NaOH/brine – 1:2 v/v (2 × 50 mL), saturated NH_4Cl (50 mL), brine (100 mL), and then dried over anhydrous Na_2SO_4. Further evaporation under reduced pressure followed by recrystallization from boiling ethanol, washing of the collected solid with cold ethanol (50

424. Spectral Database for Organic Compounds, SDBS. at <Spectral Database for Organic Compounds, SDBS>

mL) and diethyl ether (100 mL) afforded compound **20** (1.8 g, 83 %) as a white solid. *Analyses were in accordance with the literature.*[113,129]

^{1}H NMR (400 MHz, CD_3OD/Toluene-d_8, 25°C): δ = 7.54 (d, *J* = 9.0 Hz, 6H), 6.97 (d, *J* = 9.0 Hz, 6H), 2.33 (t, *J* = 7.5 Hz, 6H), 1.70 (tt, *J* = 7.5, 7.5 Hz, 6H), 1.43 – 1.18 (m, 48H), 0.89 (t, *J* = 7.0 Hz, 9H).

^{13}C NMR (100 MHz, CD_3OD/Toluene-d_8, 25°C): δ = 174.0, 145.1, 134.8, 125.0, 122.2, 37.9, 32.9, 30.7, 30.6 (2C), 30.5, 30.4, 30.3, 26.9, 23.6, 14.6.

MS (ESI): *m/z* calcd for $C_{54}H_{84}N_4O_3$ $[M]^+$ 836.65, found 836.89.

3. SPECIFIC PROCEDURES

A. Procedures Specific to Chapter III

Enzymatic reaction setup

The biocatalytic reactions were performed either in screw-cap vials or in Eppendorfs using the following procedure.

1 equivalent of a triarylamine substrate and 4 equivalents of phenylalanine amide were dissolved in 1 mL of 100 mM phosphate buffer at pH 8. In some cases, solubilization was promoted by sonication and heating, and thus the solutions were cooled down to room temperature before addition of an enzyme. The enzyme (1.0 mg) was then added to the solution, following by vortexing and sonication for 1 min and the systems were left standing for 24 hours for equilibration. Hydrogelation was evaluated by the tube-inversion test.

The enzymatic conversion was monitored by UPLC-MS performing an integration of the peaks detected using the 310 nm absorption wavelength, which corresponds to the TAA absorption for all species, and which we can be considered constant over the course of the reaction under these conditions. Each sample was prepared by dissolving an aliquot of the enzymatic mixture in a acetonitrile:water mixture 50/50 v/v containing 1% of TFA.

B. Procedures Specific to Chapter V

Organogelation of TAA

An appropriate quantity of compound **72** was dissolved upon heating in heptane (1 mL) in a screw-cap vial. The solutions were then cooled down using an ice bath to promote faster gelation. The onset gelation concentration was determined by the tube-inversion test.

C. Procedures Specific to Chapter VI

i. Synthesis of gold nanoparticles

Gold nanoparticles, used for the construction at the LLI, were prepared according to the literature procedure of Turkevich and Frens,[419] consisting of a reduction of tetrachloroauric acid with sodium citrate.

Before the synthesis, all glassware was cleaned with aqua regia followed by a subsequent rinsing with distilled water and mili-Q water.

Tetrachloroauric acid trihydrate ($H[AuCl_4] \bullet 3H_2O$, 39.4 mg) was dissolved in mili-Q water (90 mL) in a 250 mL Erlenmeyer flask. The solution was boiled with vigorous stirring, followed by the addition of the solution of trisodium citrate ($Na_3Cit \bullet 2H_2O$, 102.9 mg in 10 mL of mili-Q water) at once. The reaction mixture was heated for 10 additional minutes and then allowed to cool down to room temperature.

The size of the obtained NPs was measured by TEM, revealing an average size of 13±1 nm.

ii. Ordered self-assembly at the LLI

The TAA/AuNPs films at LLI were prepared using a simple set-up: the biphasic system containing chloroform and an aqueous layer was prepared in a screw-cap vial with a diameter of 12 mm by placing carefully the preirradiated (time of irradiation: 1 h; light source: halogen 20 W lamp; distance from the light source: 5 cm) chloroform solution of compound **20** at the appropriate concentration, followed by the addition of the aqueous layer containing the gold NPs. The biphasic system was then centrifuged at the appropriate rotation speed, corresponding to the centrifugal force *RCF*, which is given by the following formula:

$$RCF = 11.18 \times r \times \left(\frac{Q}{1000}\right)^2$$

where RCF is the relative centrifugal force in units of 'g' (gravitational acceleration), r is the radius from the center of the centrifuge to the interface, and Q is the speed of rotation in RPM. The formed films were deposited on TEM grids by placing the grid parallel to the interface and carefully lifting it up.

ANNEXES

1. ANNEXES CHAPTER I

Table S1 | Solvent effect on the TMPD photoionisation and fluorescence. Data reproduced from ref.76

Solvent	Dielectric constant	TMPD Fluorescence	TMPD Photo-oxidation
Acetonitrile	37.5	Slight	Slight
Cyclohexanone	18.3	Slight	Slight
Pyridine	12.3	No	No
CH_2Cl_2	9.1	No	Yes
CH_2Br_2	7.2	No	Yes
CH_3I	7.0	TMPD is insoluble	TMPD is insoluble
Methyl ether	5.0	Yes	No
$CHCl_3$	4.8	No	Yes
$CHBr_3$	4.4	No	Yes
Ethyl ether	4.3	Yes	No
o-Xylene	2.6	Yes	No
Toluene	2.4	Yes	No
CCl_4	2.2	No	Ppt formed

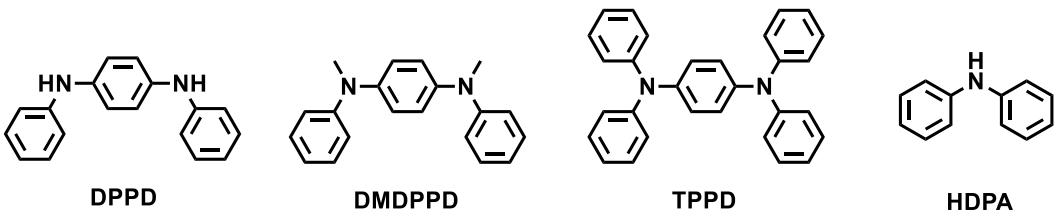

Figure S1 | Chemical structures of molecules studied by Richtol *et al.*[75]

2. ANNEXES CHAPTER II

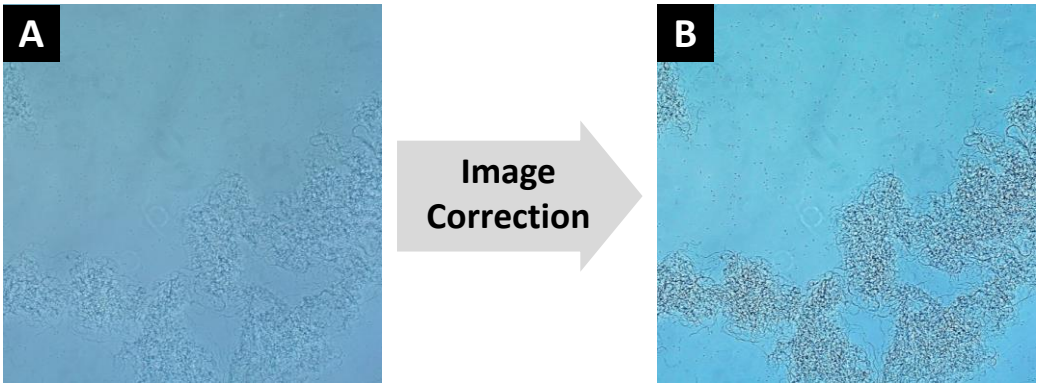

Figure S2 | OPM photographs of **(S)-TATA** self-assembly in toluene. (**A**) The original image; (**B**) image after the enhancement with sharpness, contrast and brightness filters.

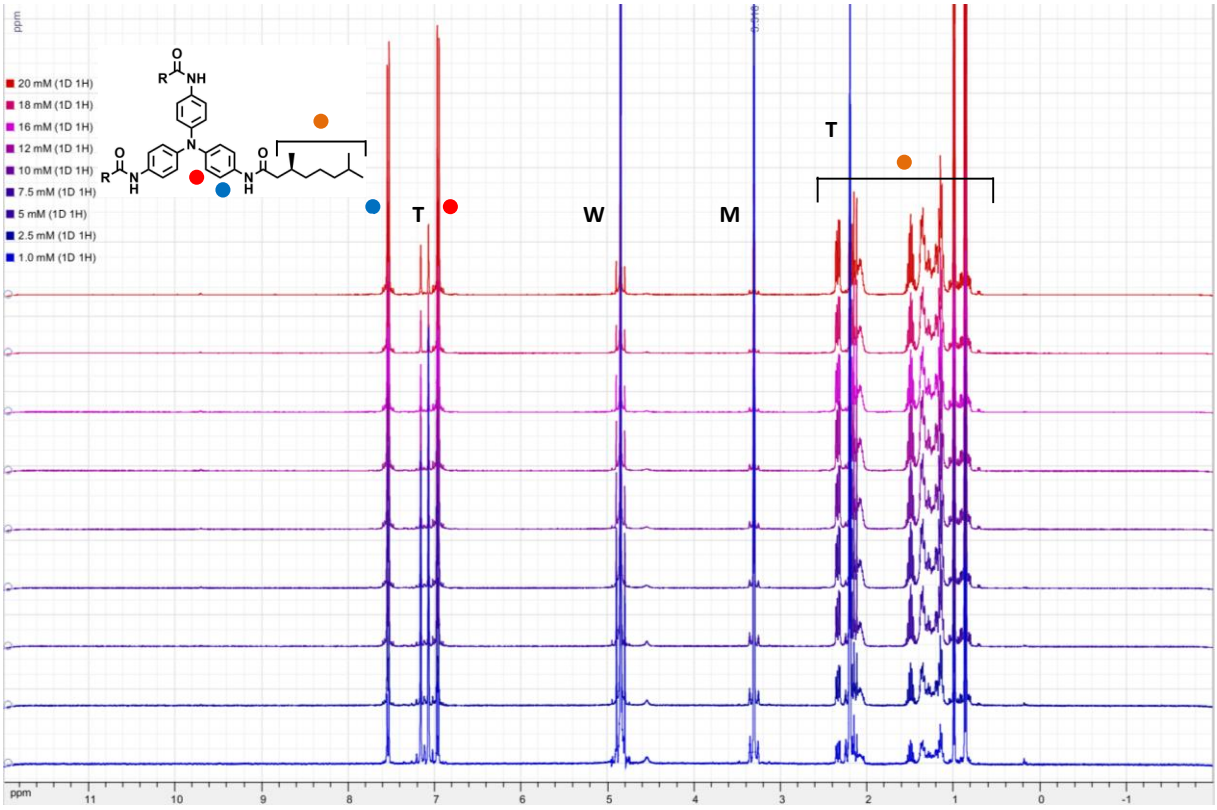

Figure S3 | Concentration dependent ^{1}H NMR experiment of **(S)-TAA** in a mixture of deuterated MeOH/Toluene 5:3 v/v. Letters T, M, W indicate the residual solvent signals of toluene, methanol and water.

Table S2 | Summary of IR data for different TATAs, assembled in different solvents

Band	Acetone	Acetonitrile	Toluene	Chloroform[a]
N–H	3288	3287	3286	3293
C=O	1653	1653	1651	1654
Amide II	1599	1599	1600	1599

[a] **(C_{14})-TATA**

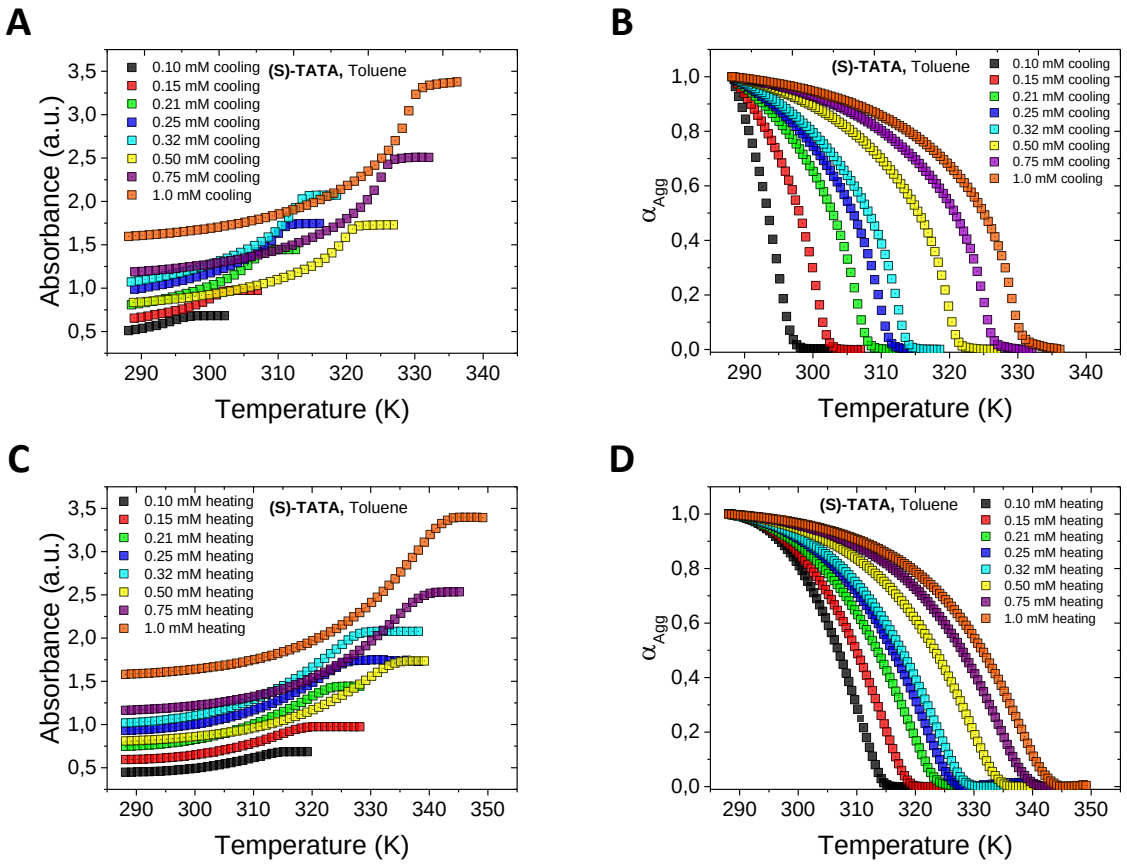

Figure S4 | (A, C) Temperature dependent absorption intensities of **(S)-TATA** in toluene recorded at 315 nm during the cooling and heating of **(S)-TATA** self-assembly in toluene at different concentrations respectively**. (B, D)** Melting curves (temperature dependent degree of aggregation – $\boldsymbol{\alpha_{Agg}}$) obtained by normalisation of experimental UV data, obtained during the cooling and heating cycle respectively.

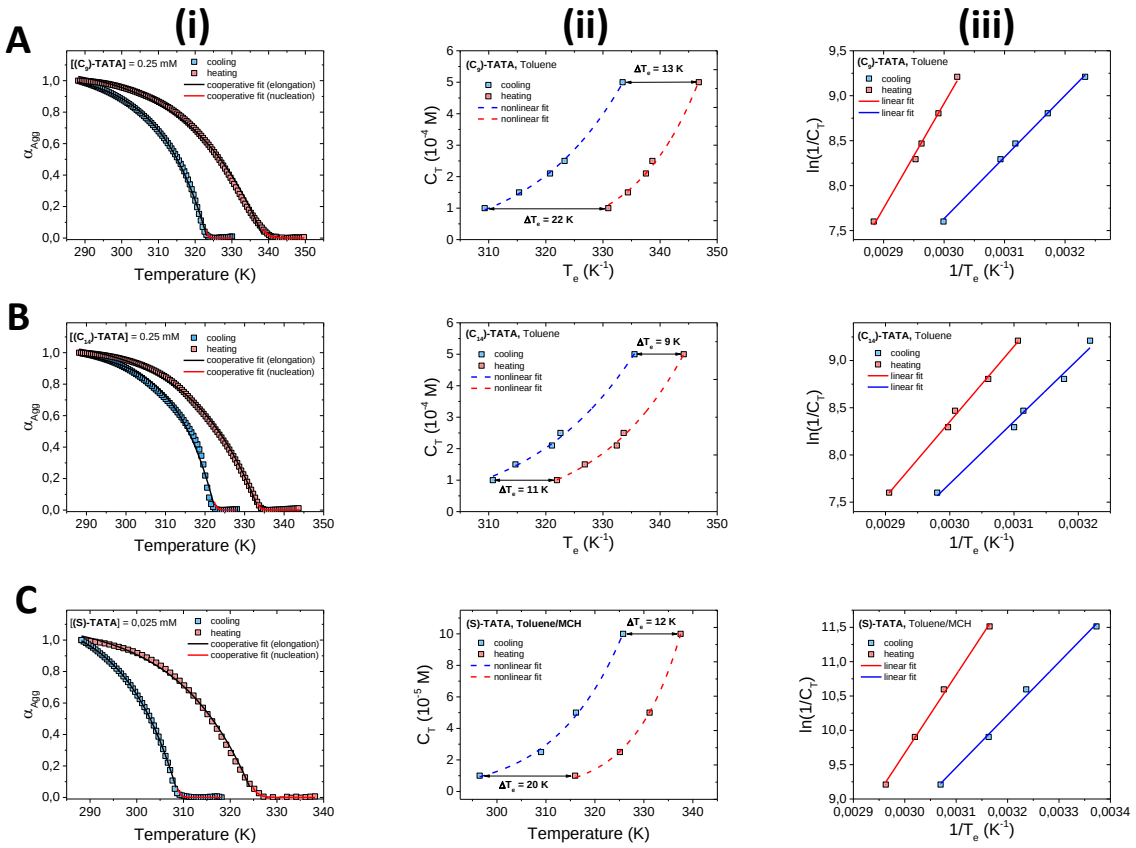

Figure S5 | (i) Temperature dependent degree of aggregation ($\boldsymbol{\alpha_{Agg}}$) of TATAs in 0.25 mM toluene solution calculated from the temperature dependent UV-Vis data, recorded at 315 nm, obtained during the cooling (blue squares) and heating (red squares) processes at a rate of 1 K^{-1}. Solid lines represent the cooperative polymerisation fit in the nucleation (red) and the elongation (black) regimes. **(ii)** $\boldsymbol{C_T}$ *vs* $\boldsymbol{T_e}$ for TATAs in the cooling (blue squares) and the heating (red squares) regimes. Dashed lines represent the nonlinear fit of the experimental data. (**iii**) The natural logarithm of the reciprocal concentration $\boldsymbol{C_T}$ *vs* the reciprocal $\boldsymbol{T_e}$ for TATAs in cooling (blue squares) and heating (red squares) regimes. The lines show the linear relationship, whose slope is proportional to the $\Delta \boldsymbol{H_e}$**. (C_9)-TATA (A), (C_{14})-TATA (B), (S)-TATA** in toluene/MCH 1/1 mixture at a concentration of 0.025 mM **(C)**.

Table S3. Thermodynamic parameters of the self-assembly of **(S)-TATA**, **(C_9)-TATA** and **(C_{14})-TATA** in toluene solutions of different concentrations, obtained using the nucleation-elongation model to fit the temperature dependant UV-Vis, CD and fluorescense spectroscopic data

Compound	C_T (M) x 10^{-4}	T'_e (K)	T_e (K)	ΔT_e (K)	α_{Sat}	ΔH_e (kJ mol^{-1})	$K_a \times 10^5$	$\langle N_n(T_e) \rangle$
(S)-TATA[a]	1.0	297.0	313.8	16.8	1.172 ± 0.007	-66 ± 1	4 ± 1	29 ± 1
	1.5	302.4	318.1	15.7	1.167 ± 0.005	-58.6 ± 0.7	5 ± 2	27 ± 1
	2.1	308.3	322.9	14.6	1.148 ± 0.004	-52.5 ± 0.5	7 ± 4	25 ± 1
	2.5	311.8	325.5	13.7	1.118 ± 0.003	-56.7 ± 0.4	6 ± 10	26 ± 2
	3.2	314.3	327.5	13.2	1.114 ± 0.003	-55.3 ± 0.4	6 ± 1	25 ± 1
	5.0	321.9	333.8	12.1	1.069 ± 0.002	-56.0 ± 0.4	4.8 ± 0.9	28 ± 1
	7.5	327.5	338.6	11.1	1.056 ± 0.002	-57.9 ± 0.3	8 ± 1	24 ± 1
	10	331.9	342.0	10.1	1.040 ± 0.001	-61.0 ± 0.3	10 ± 5	22 ± 1
C_9-TATA[a]	1.0	309.3	330.9	21.6	1.145 ± 0.005	-49.7 ± 0.6	0.6 ± 0.1	55 ± 3
	1.5	315.3	334.4	19.1	1.131 ± 0.004	-48.5 ± 0.5	6 ± 1	26 ± 2
	2.1	320.7	337.5	16.8	1.115 ± 0.004	-48.5 ± 0.4	11.7 ± 0.7	20 ± 1
	2.5	323.3	338.7	15.4	1.112 ± 0.004	-48.4 ± 0.5	9 ± 1	22 ± 1
	5.0	333.4	346.8	13.3	1.067 ± 0.002	-52.7 ± 0.3	17 ± 1	18 ± 1
C_{14}-TATA[a]	1.0	310.7	321.9	11.2	1.103 ± 0.004	-70.9 ± 0.8	65 ± 1	25 ± 1
	1.5	314.7	326.8	12.1	1.117 ± 0.005	-59.0 ± 0.7	65 ± 1	25 ± 1
	2.1	321.1	332.4	11.4	1.111 ± 0.004	-53.7 ± 0.5	4.0 ± 0.4	29 ± 1
	2.5	322.6	333.6	11.1	1.094 ± 0.002	-55.6 ± 0.4	1.8 ± 0.3	38 ± 2
	5.0	335.5	344.1	8.6	1.029 ± 0.001	-67.2 ± 0.2	1.2 ± 0.2	44 ± 2
(S)-TATA[b]	0.1	296.5	316.0	19.5	1.208 ± 0.012	-61 ± 1	4 ± 3	31 ± 8
	0.25	309.0	325.1	16.1	1.128 ± 0.005	-57.2 ± 0.7	9 ± 2	22 ± 1
	0.5	316.1	331.2	15.1	1.078 ± 0.003	-60.2 ± 0.4	12 ± 5	20 ± 3
	1.0	325.8	337.5	11.7	1.147 ± 0.006	-43.4 ± 0.5	8 ± 2	23 ± 2
(S)-TATA[c]	1.0		314.9		1,21 ± 0,03	-52 ± 3	24 ± 314	19 ± 2
	2.5		321.7		1,65 ± 0,03	-21,0 ± 0,5	18 ± 22	57 ± 4
	3.2		329.0		1,18 ± 0,01	-34,4 ± 0,9	20 ± 147	37 ± 9
	5.0		333.7		1,20 ± 0,04	-120 ± 10	141 ± 1456	19 ± 7
	7.5		339,7		1,4 ± 0,1	-90 ± 17	323 ± 3000	15 ± 4
(S)-TATA[d]	5.0	319.1	330.2	11.1	1.19 ± 0.03	-50 ± 3	23 ± 5	16 ± 1
	10.0	329.1	339.1	10.0	0.992 ± 0.008	-116 ± 5	45 ± 3	13 ± 1

[a] UV-Vis in toluene; [b] UV-Vis in toluene/methylcyclohexane; [c] CD in toluene; [d] Fluorescence in toluene

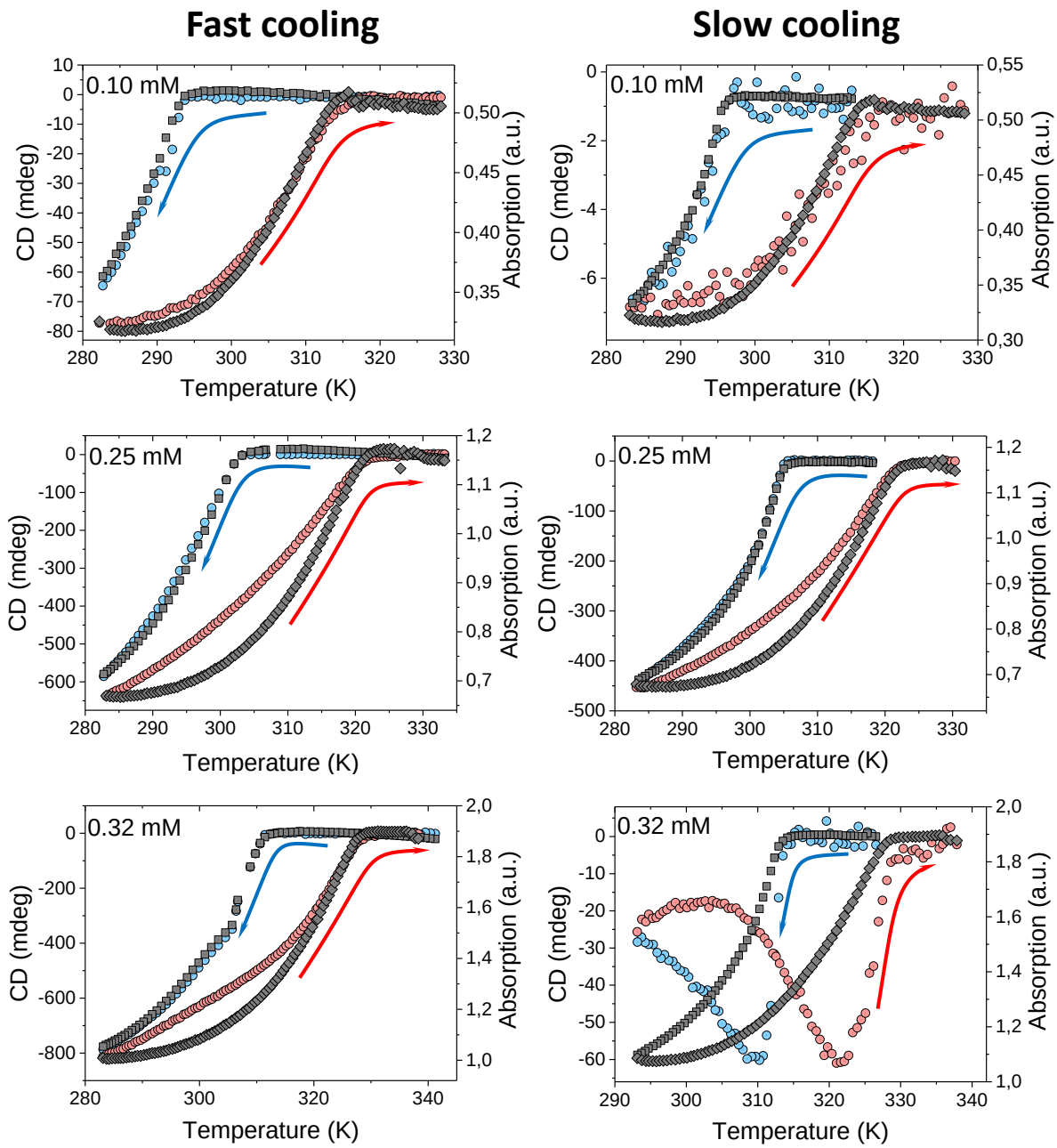

Figure S6 | Temperature dependent CD (blue and red circles) and UV (grey squares) curves of **(S)-TATA** in toluene at different concentrations and cooling regimes.

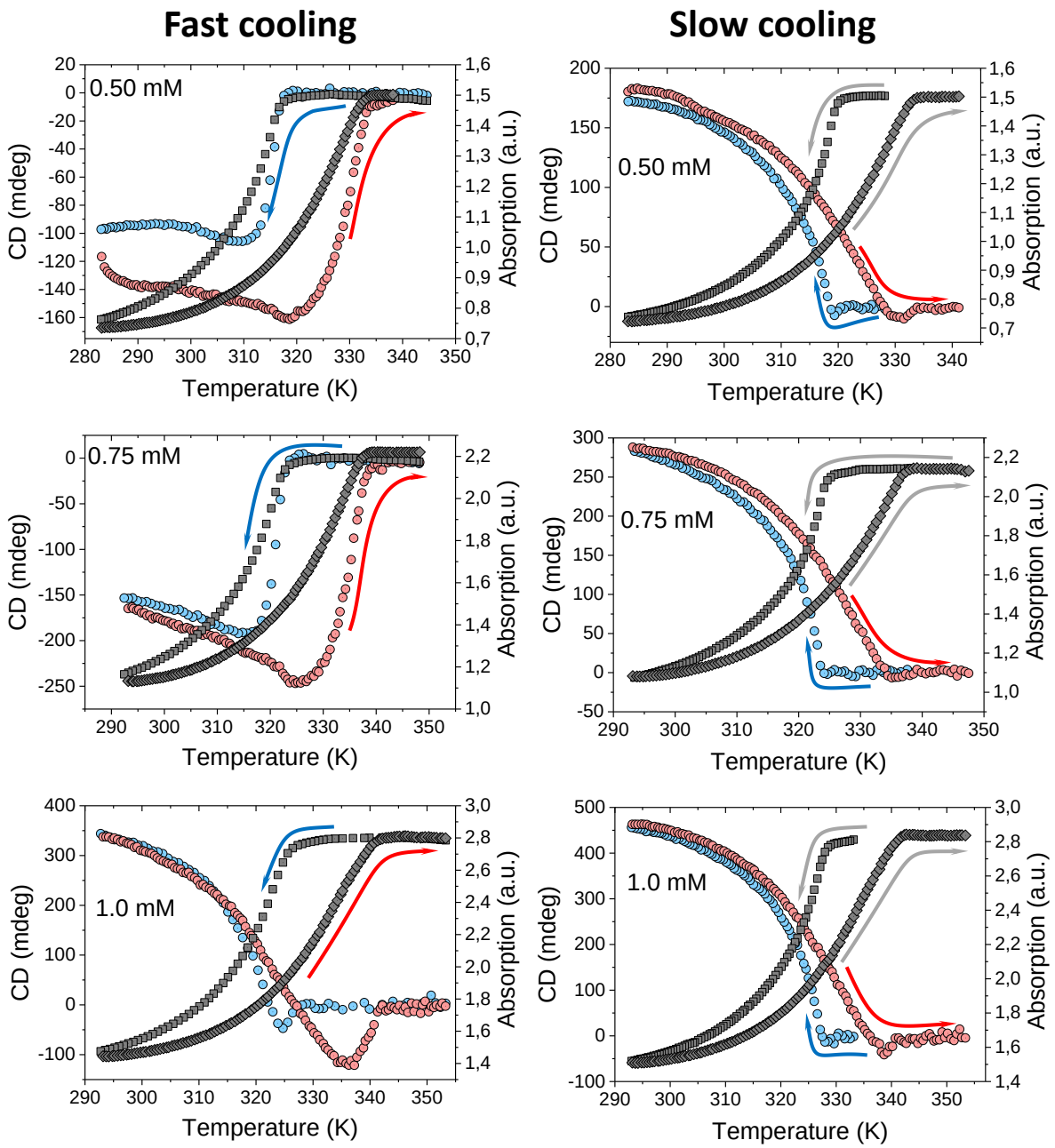

Figure S7 | Temperature dependent CD (blue and red circles) and UV (grey squares) curves of **(*S*)-TATA** in toluene at different concentrations and cooling regimes.

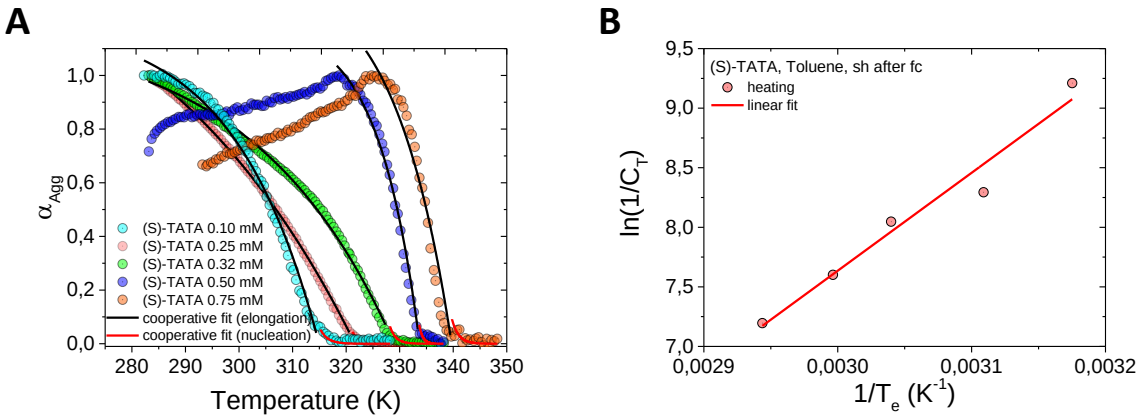

Figure S8 | (A) Temperature dependent degree of aggregation ($\boldsymbol{\alpha_{Agg}}$) of **(S)-TATA** in toluene solutions calculated from the temperature dependent CD data, recorded at 315 nm, during the slow heating at a rate of 1 K-1 after fast cooling regime. Solid lines represent the cooperative polymerisation fit in the nucleation (red) and the elongation (black) regimes. (**B**) Natural logarithm of the reciprocal concentration $\boldsymbol{C_T}$ vs the reciprocal $\boldsymbol{T_e}$ for for **(S)-TATA** in the heating (red circles) regime. Solid line shows the linear relationship, slope is proportional to the $\Delta\boldsymbol{H_e}$.

3. ANNEXES CHAPTER III

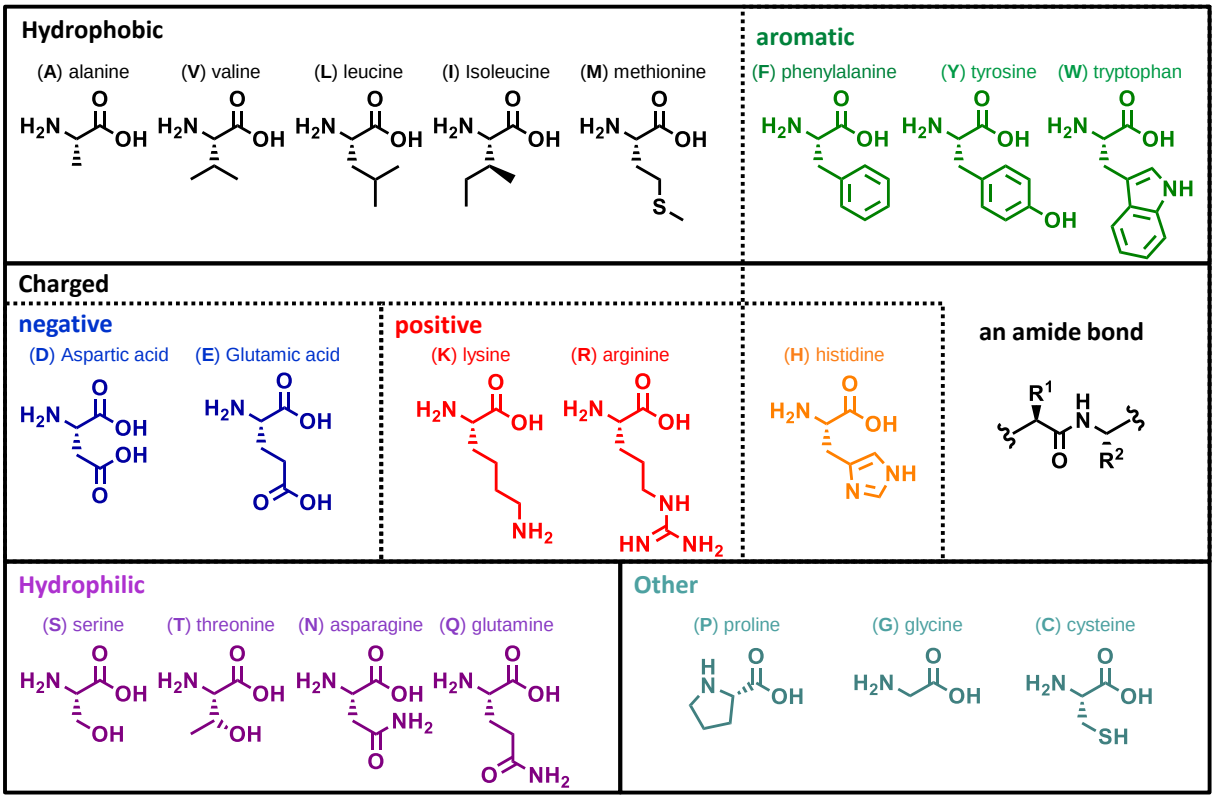

Figure S9 | Twenty gene encoded amino acids. Figure is adapted from ref. 163

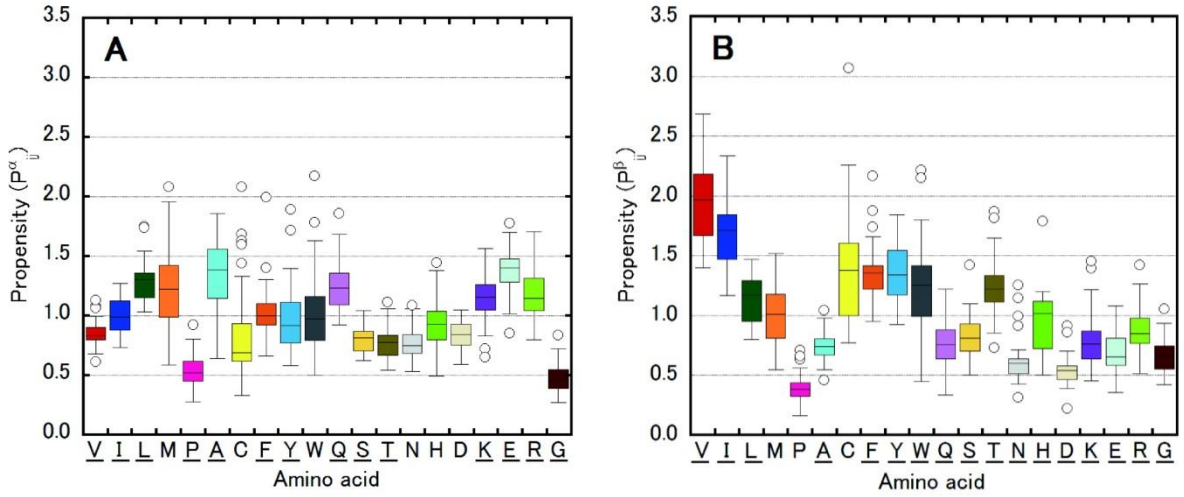

Figure S10 | Relative propensity of gene encoded amino acids to form (**A**) α-helical structures and (**B**) β-sheet structures. Figure is reproduced from ref.425

425. Fujiwara, K. *et al.* Dependence of alpha-helical and beta-sheet amino acid propensities on the overall protein fold type. *BMC Struct. Biol.* **12,** 18 (2012).

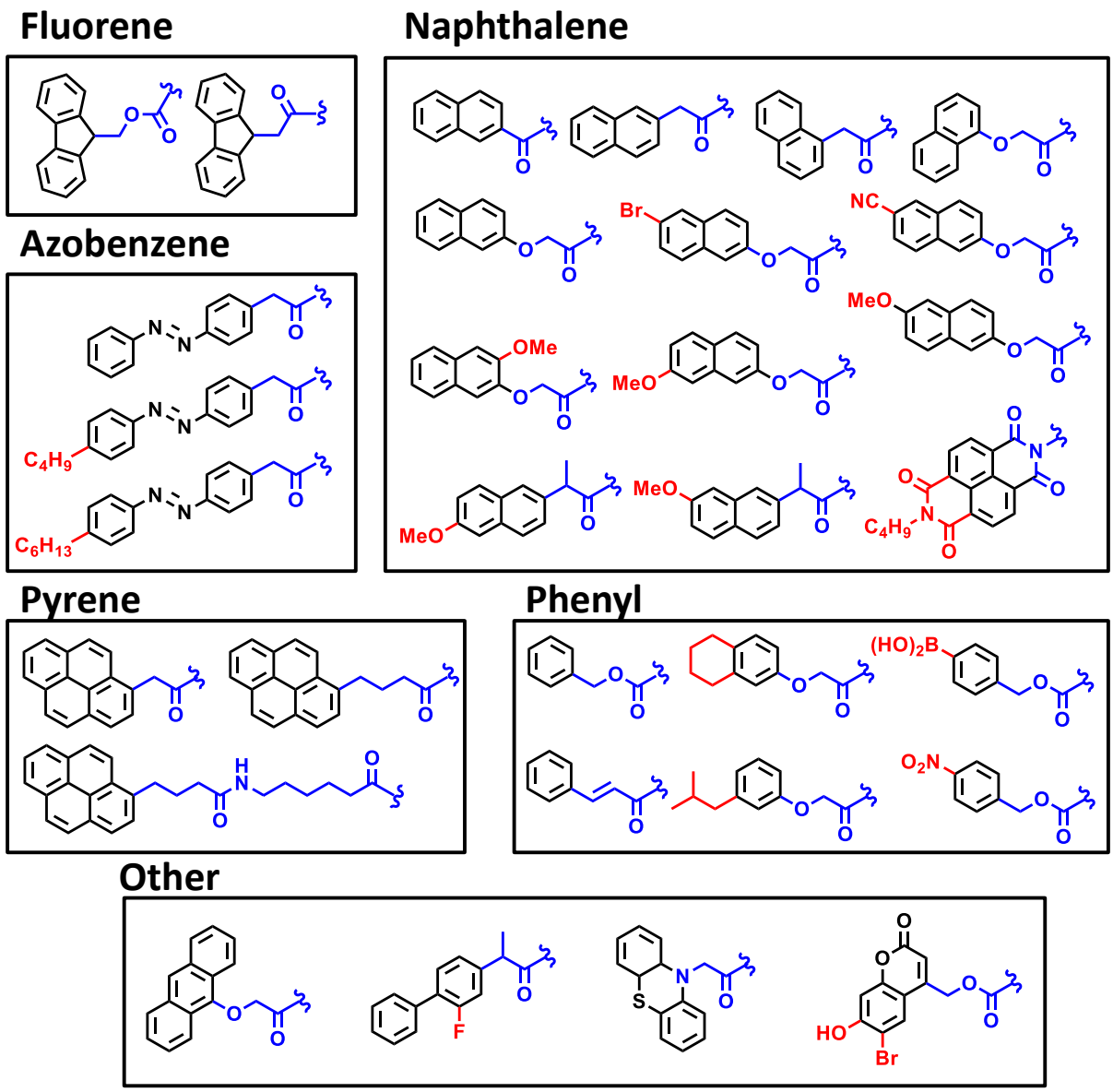

Figure S11 | Common synthetic aromatic functions reported in literature in aromatic peptide conjugates. Figure is adapted from ref.163

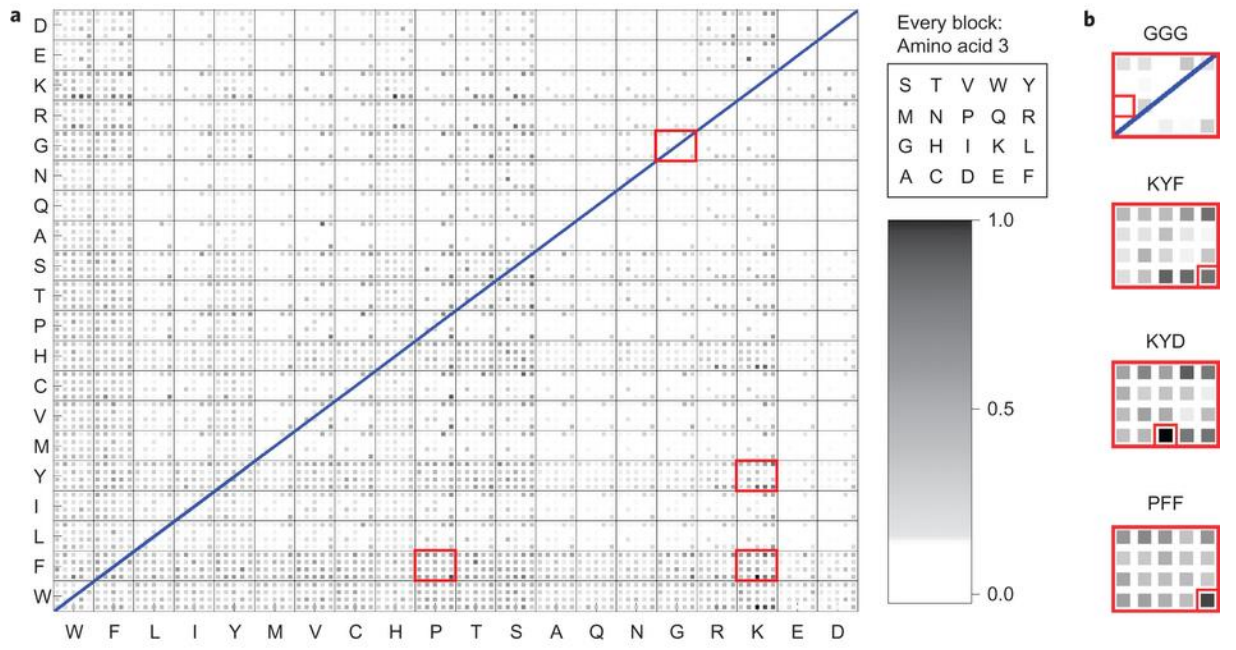

Figure S12 | Normalized aggregation propensity score for all 8,000 combinations of three amino acids after a 50 ns simulation. Within every rectangle, the third amino acid is represented by the position of the coloured square at the locations indicated in the legend on the right. A darker shade indicates a larger degree of aggregation.Figure is reproduced from ref. 274

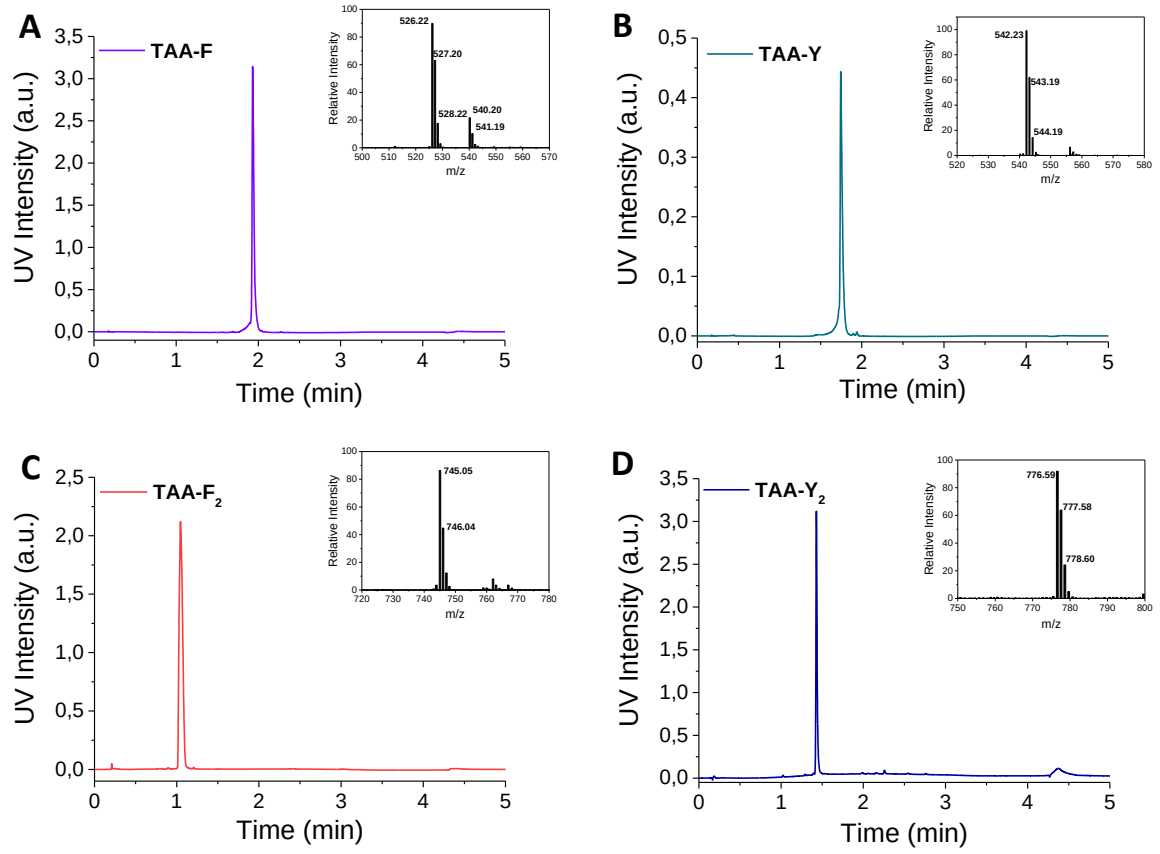

Figure S13 | UPLC chromatograms of purified triarylamine-based bioconjugates. (**A**) Compound **31**; (**B**) Compound **32**; (**C**) Compound **33**; (**D**) Compound **34**.

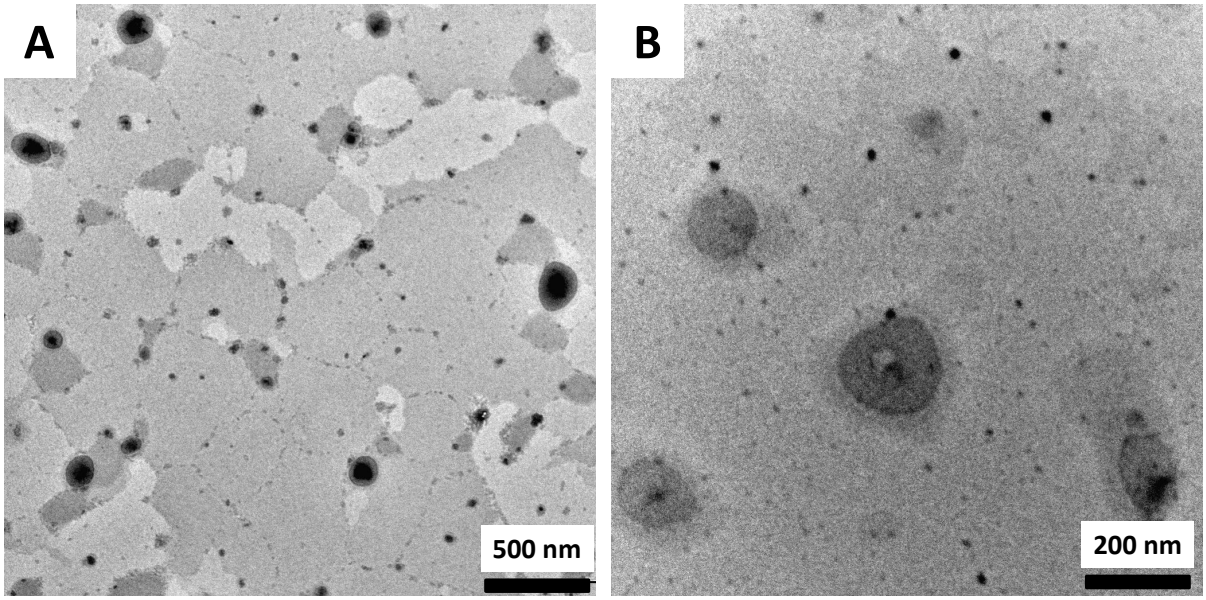

Figure S14 | TEM images of spherical aggregates formed from TAA-phenylalanine conjugate **31** at concentration 20 mM in 100 mM phosphate buffer at pH 8.

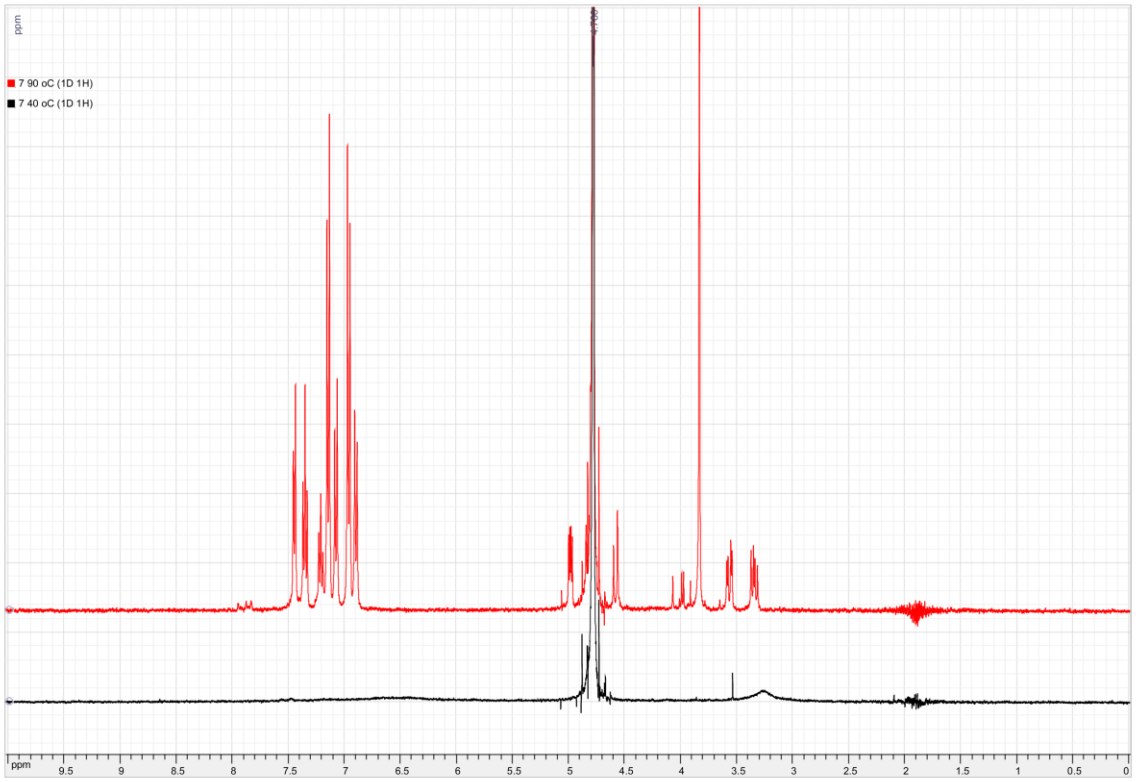

Figure S15 | 1H-NMR spectra recorded for 20 mM aqueous solution of phenylalanine TAA conjugate **31** at 40 °C (black line) no signal are observed, and at 90 °C (red line).

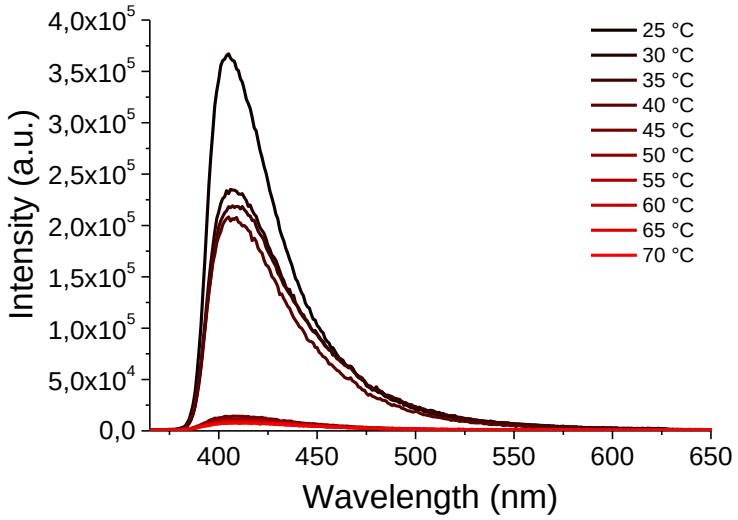

Figure S16 | Temperature dependent fluorescent spectra recorded for TAA-phenylalanine conjugate **31** at concentration 20 mM in 100 mM phosphate buffer at pH 8**.**

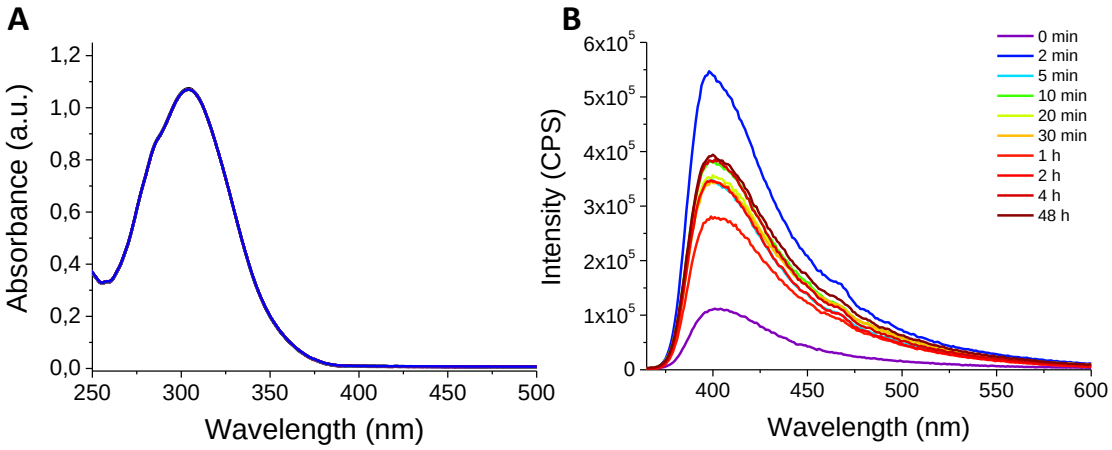

Figure S17 | Time dependent absorption (**A**) and fluorescense (**B**) for biocatalytic self-assembly of tyrosine TAA-conjugate **32**.

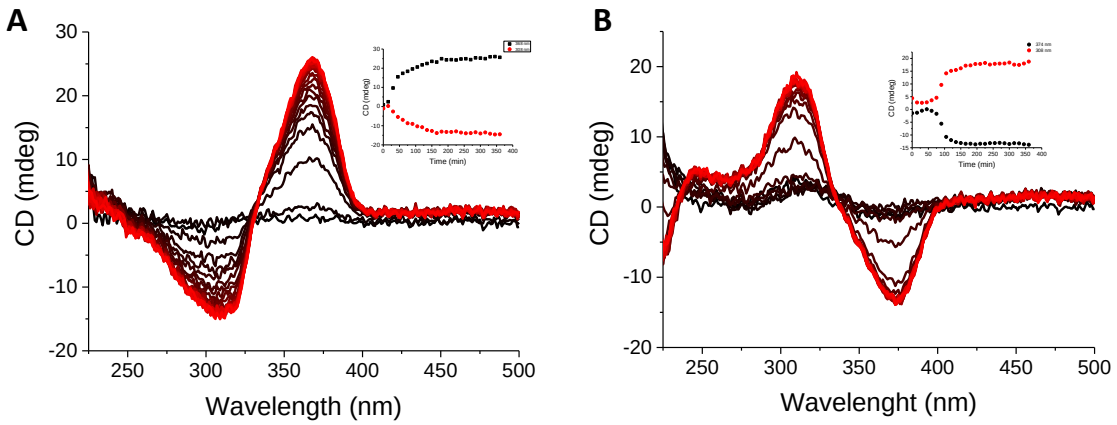

Figure S18 | Time dependent CD spectra recorded during enzymatically induced gelation of 5 mM TAA-bioconjugates (**A**) TAA-phenylalanine **31** and (**B**) TAA-tyrosine **32**.

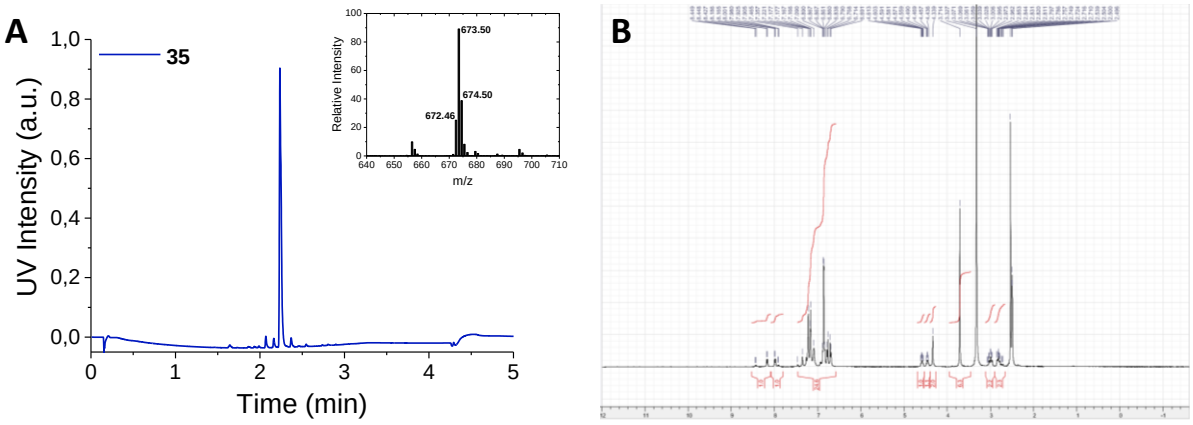

Figure S19 | (**A**) UPLC chromatograms of control molecule **35** and (**B**) corresponding ^{1}H NMR spectrum.

4. ANNEXES CHAPTER IV

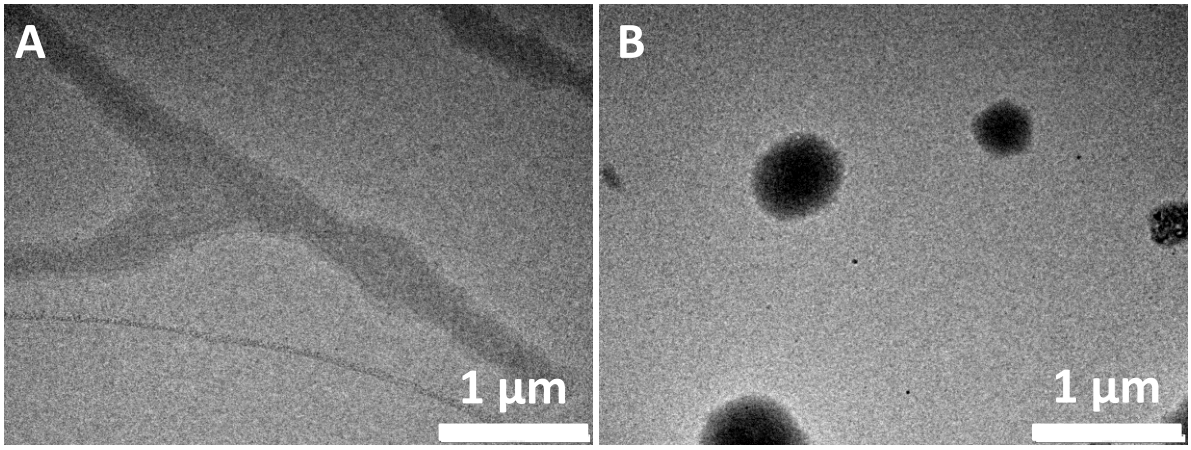

Figure S20 | TEM images of control compound **38** obtained after irradiation of 1 mM chloroform solution.

5. ANNEXES CHAPTER V

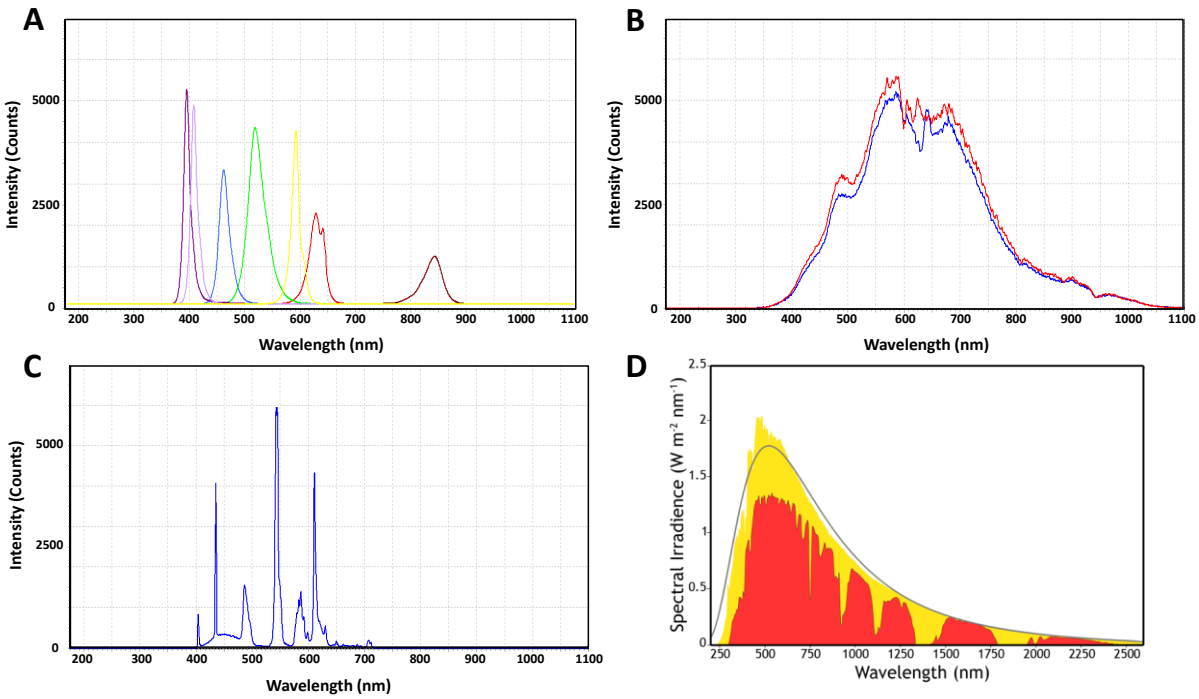

Figure S21 | Irradiative spectra of different light sources. (**A**) LEDs of (395, 400, 450, 520, 590, 625, 820)±5 nm, from left to right. 395 nm LED was used in all the experiments. (**B**) Halogen 20 W IKEA lamp. (**C**) Xenon lamp. (**D**) Sunlight spectrum.

72 (5.79 mg) was dissolved in a solution of 0.1 M TBAHFP in $CDCl_3$ (2 mL) resulting in a neutral electrolyte solution (5.2 mM). The solution was electro-oxidized with a three-probe system consisting of a platinum working electrode, silver wire reference electrode, and platinum counter electrode. The solution was treated with chrono-amperometric method (0.6 V *vs* Ag wire, 0.2 V *vs* Fc/Fc+) for 30 min.

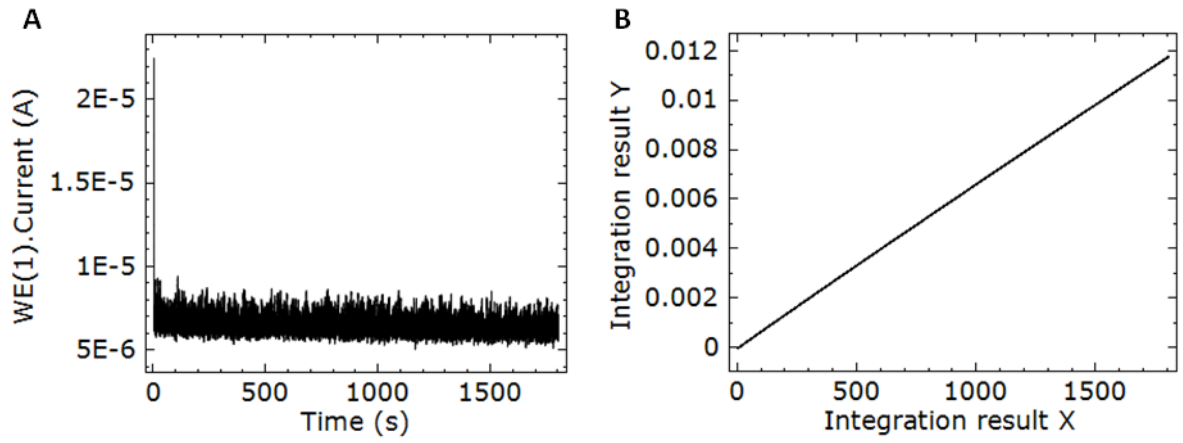

Figure S22 | (**A**) Current *vs* time result for the electrolysis of **72**, with the (**B**) current integration over time.

a) In order to determine quantity of oxidised TAA, we calculated quantity of charges, which flowed through the solution of TAA, by integrating current over a period of electro-oxidation time.
b) Integrating current results in 0.01178 C of current injected into the system (**Figure** S22). Applying faradays constant, chemical amount of radical cations of **72** in moles (n(**72**$^{\bullet+}$)):

$$n(72^{\bullet+}) = 0.01178\ C/96485\ C\ mol^{-1} = 1.22 \times 10^{-7}\ mol \text{ of radicals}$$

Concentration of radicals in the solution of electrolyte:

$$[72^{\bullet+}] = n(72^{\bullet+})/V(sol\text{-}n) = 1.22 \times 10^{-7}\ mol/0.002\ L = 6.10 \times 10^{-5}\ M$$

*Amount of radicals per neutral **72** in % (**φ(72**$^{\bullet+}$**)**):*

$$\varphi(72^{\bullet+}) = 100\ \% \times 6.1 \times 10^{-5}\ M/5.2 \times 10^{-3}\ M = 1.2\ \%.$$

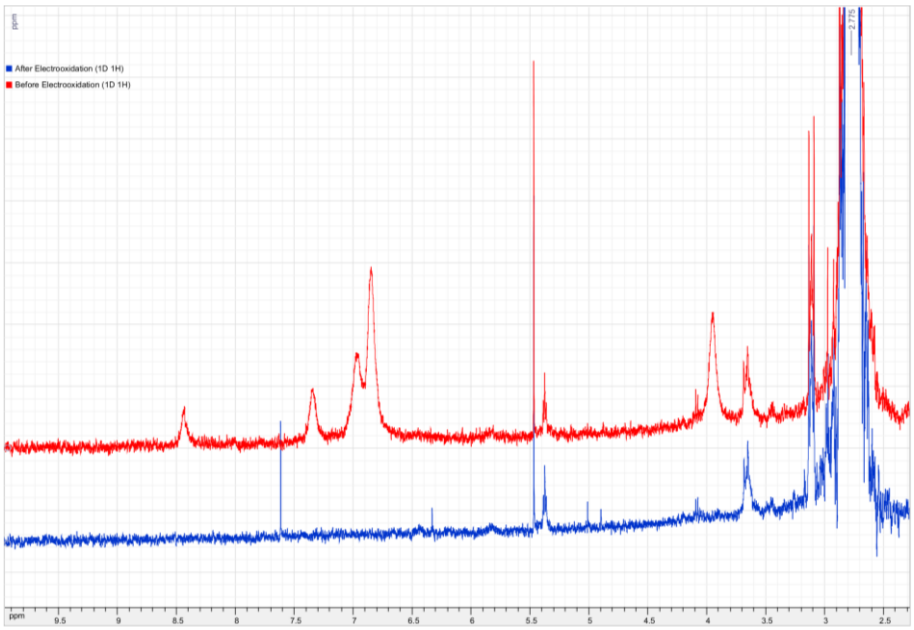

Figure S23 | Comparison of ^{1}H-NMR spectra before electrolytic treatment (red) and after electro-oxidation (blue) at 0.2 V *vs* Fc/Fc^{+} in a $CDCl_3$ with 0.1 M TBAHFP.

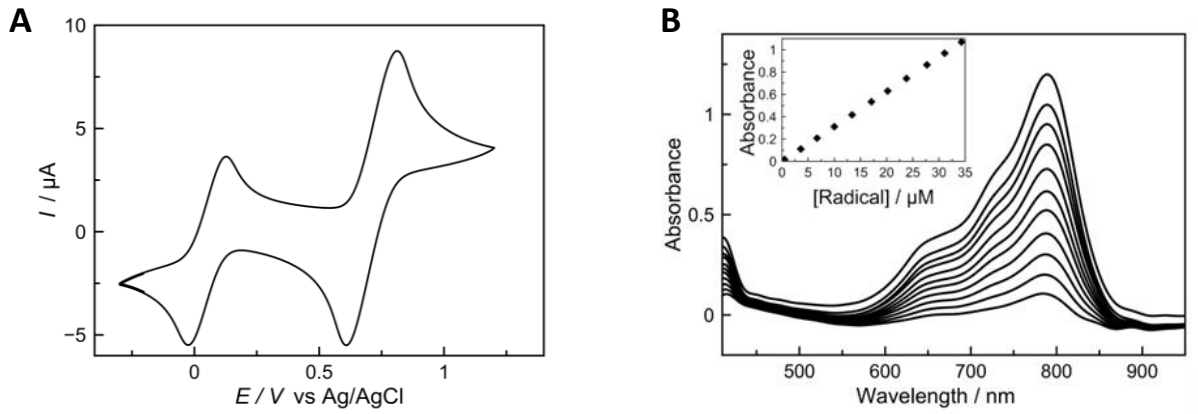

Figure S24 | (**A**) Cyclic voltammogramm of TCE solution of decamethylferrocene ($E_{1/2}$ = 0.1 V vs Ag/AgCl) and **72** ($E_{1/2}$=0.6 V vs Ag/AgCl). (**B**) Back titration of a solution of **72** with decamethylferrocene demonstrating the reduction of the radical cation

The interaction of supramolecular self-assemblies, composed of partially oxidized and neutral **72,** with decamethylferrocene was investigated by conducting a spectroscopic redox back-titration of the radical-cation (**Figure S24**).

We first exposed a solution of **72** to a LED irradiation until the absorbance of $\mathbf{72}^{\bullet+}$ reaches approximatively a value of 1.0 a.u. A solution of decamethylferrocene was then added to the solution of $\mathbf{72}^{\bullet+}$ with stirring, and the UV-Vis absorption spectra were taken after sequential addition.

The linear relationship between the quantity of added DmFc and radical band absorption indicates that DmFc does not participate in co-assembly process with TAA **72** but reacts completely. Assuming, that the DmFc and TAA radical cation react in proportions one to one:

$$DmFc + TAA^{\bullet+} \rightarrow DmFc^{+} + TAA$$

We can estimate the extinction coefficient for ration TAA **72** radical cation using Beer's law, which gives an extinction coefficient of ε = 31200±2600 $L \cdot mol^{-1} \cdot cm^{-1}$ (95% confidence) for $\mathbf{72}^{\bullet+}$. This extinction coefficient then allows an estimation of the charge saturation concentration of the wires by exposing **72** to UV light for 20 minutes (until absorbance ceased to increase on illumination). The system approaches a saturation of ~ 32% of radical without electrolyte. The fact that it is well below unity, supports that there must be neutral species to form the wires and stabilize the radical cation.

The radical stability was also tested against various common and stable electrochemical salts (at 0.1 M) to probe the effect of the chloride counter-ion. The saturation

concentration appears to be mostly independent of the salt ions used (TBAHFP: 32%, $TBAClO_4$: 36%). As the maximum saturation absorbance is approximately the same considering experimental error, the wire system is reasonably independent of the used counter ion. The notable exception is however, TBACl, which could only introduce half as many charges as the others for the same experimental, conditions (15%). Moreover, when using TBACl, the radical was strongly reduced within a day, while the typical green colour of the radical persisted for months in the presence of hexafluorophosphate and perchlorate. This is in agreement with our previously proposed light-induced mechanism where the chloride plays an active role in the radical reduction by forming Cl_2 molecules at the tips of double columnar fibrils following a second order rate reaction.[83] Here, in the presence of an excess chloride coming from the electrolyte, this reduction rate is enhanced.

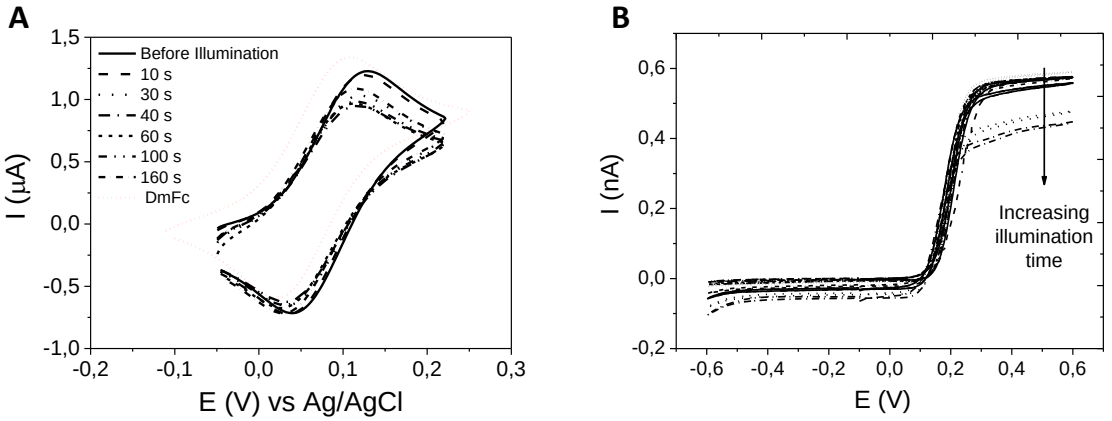

Figure S25 | Cyclic voltammogramms after various illumination times with the standard electrode setup (**A**) and with a microelectrode setup (**B**).

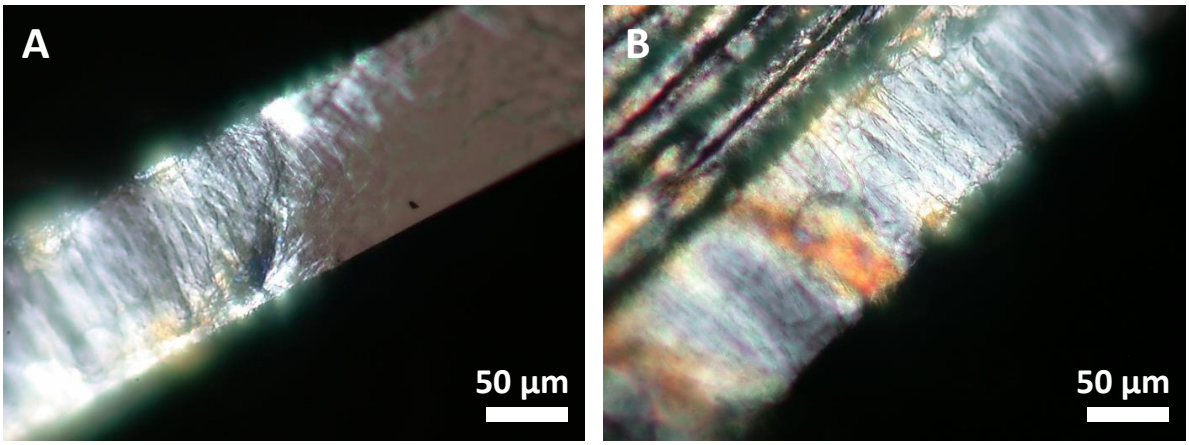

Figure S26 | OPM digital photographs of *in situ* assembling of **72** from 5 mg/mL heptane solution between the IDEs under applied DC electric field, cross-polarized mode. Wires are aligned perpendicular to electrodes *i.e.* parallel to the electric field

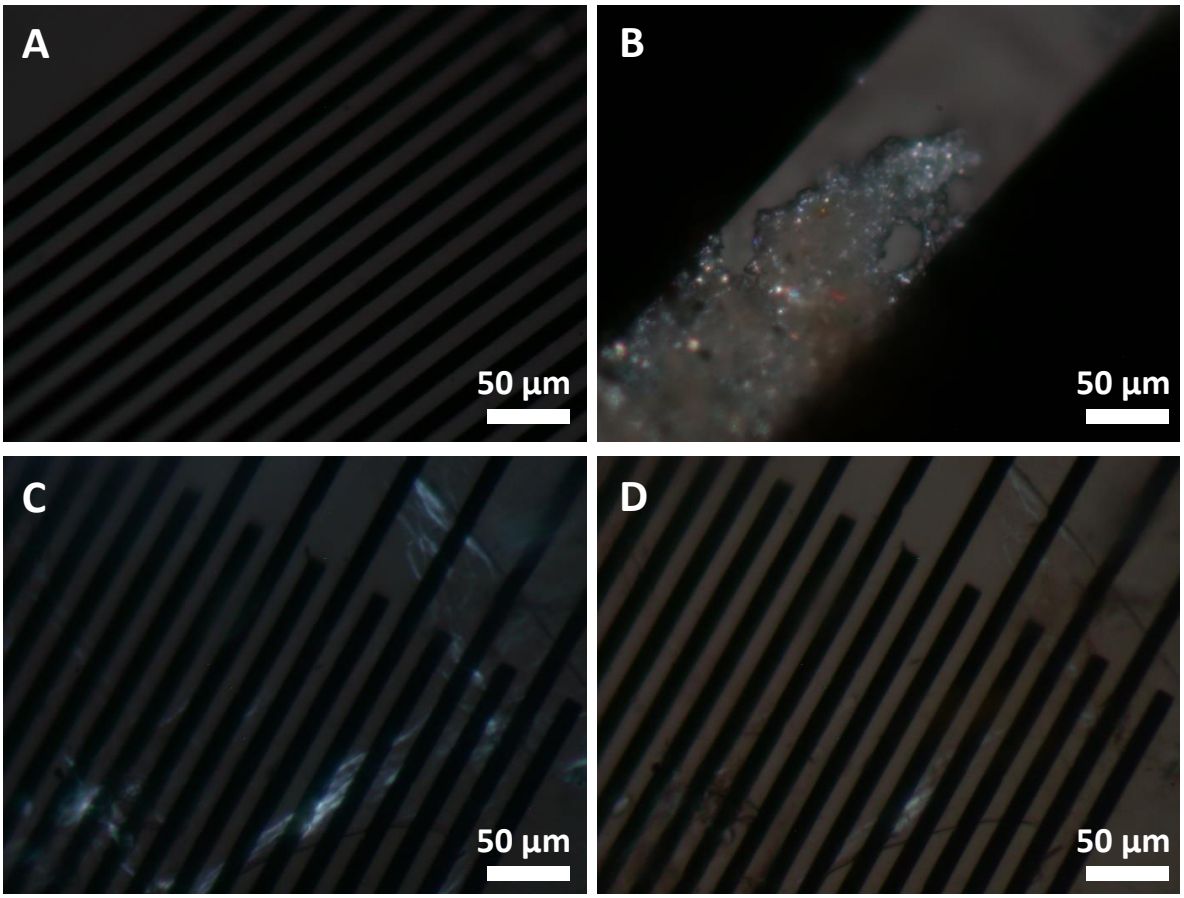

Figure S27 | OPM digital photographs of *in situ* assembling of **72** from 5 mg/mL heptane solution between the IDEs without applied DC electric field, cross-polarized mode. (**A**) No wires observed. (**B**) Amorphous deposition. (**C, D**) Few wires were observed with unorganized deposition

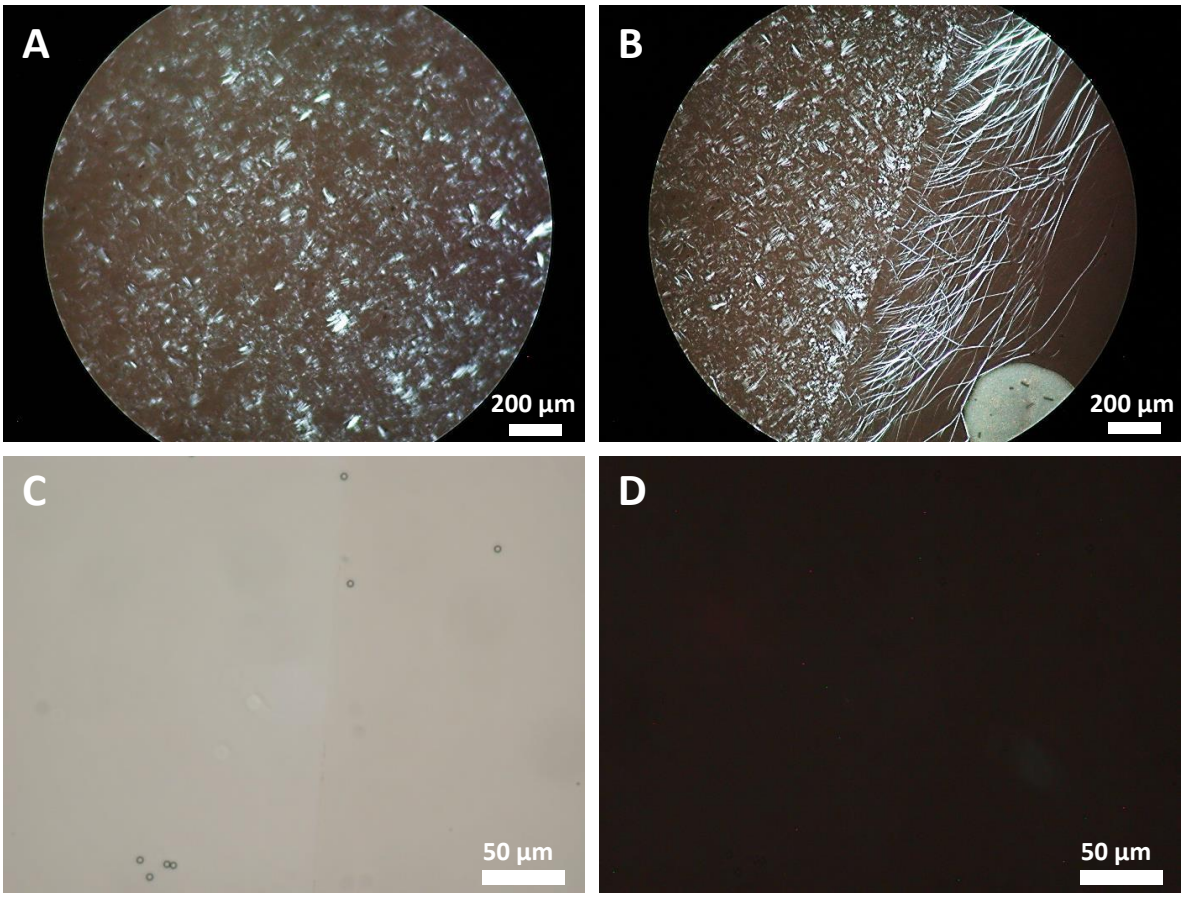

Figure S28 | OPM digital photographs of *in situ* assembling of **72** from 5 mg/mL heptane solution between the ITO covered glass electrodes without a photoresist, cross-polarized mode. (**A, B**) under applied DC electric field. (**C, D**) Without an electric field applied